The Production and Evaluation of Highly-aligned Nano-fibre Preforms Using Electro-spinning

By

SIHENG SHAO

A thesis submitted to
the University of Birmingham
for the degree of
DOCTOR OF PHILOSOPHY

School of Metallurgy and Materials
College of Engineering and Physical Sciences
University of Birmingham
May 2023

UNIVERSITY OF BIRMINGHAM

University of Birmingham Research Archive

e-theses repository

This unpublished thesis/dissertation is copyright of the author and/or third parties. The intellectual property rights of the author or third parties in respect of this work are as defined by The Copyright Designs and Patents Act 1988 or as modified by any successor legislation.

Any use made of information contained in this thesis/dissertation must be in accordance with that legislation and must be properly acknowledged. Further distribution or reproduction in any format is prohibited without the permission of the copyright holder.

ABSTRACT

Electro-spinning is an established manufacturing technique that is used to produce fibres in the nano-metre diameter. The electro-spun fibres are generally deposited on a grounded static electrode where the orientation of the deposited fibres is random. In the context of using these fibres as reinforcements in the production of composites, ideally, unidirectional and continuous fibres are desirable. Whilst a number of elegant and innovative techniques have been reported for producing aligned fibres, at the time of writing, there were no publications on techniques to extract the aligned fibres in an efficient manner to enable spooling and post-processing. Such a technique was developed in this study.

The starting point for the current project was COMSOL modelling where various electrode configuration and materials were considered. It transpired that by shielding the unwanted electric field lines between the charged spinneret (needle) containing a polymer solution, and modifying the geometry of the grounded static electrode, it was possible to control the trajectory of the electro-spun polymer jet, from the charged needle, to oscillate between the ends of the electrode. The ideal material for the shield was polytetrafluoroethylene (PTFE) and this new electro-spinning configuration is referred to as the 'Vee-shield' method because of the profile of shield. The fixture consists of a *V*-shaped PTFE shield at 60° with a 0.6 cm wide integral rectangular base that is mounted on a copper disk with a 10 cm diameter. The continuous extraction of the aligned nano-fibres was demonstrated using a motorised spooling unit. The polymer that was selected for this study was polyacrylonitrile (PAN) and the solvent was dimethyl sulfoxide (DMSO). In the static set-up, approximately 91% of the fibres

were deposited to within 3°. When the spooling rig was used, a tape of cellulose paper was used as a mobile substrate. It was hauled off at 0.07 mm/minute, where 78% of the fibres were aligned to within 3°. A patent was recently secured for this method for producing highly aligned nano-fibres (patent number: WO2020120985A1).

After the fibre alignment technique was developed, attention was given to improving the tensile properties of the electro-spun fibres. This required the development of an end-tabbing method that was repeatable, where the alignment of the fibres was assured, and where the gauge length of the tensile specimen was not compromised by the end-tab resin. The bonding adhesive selected was a photo-curable UV resin that fulfilled the above-mentioned requirements.

The feasibility of improving the tensile mechanical properties of the electro-spun fibres was investigated by cold-drawing. The Young's modulus at 0.015 strain, and the ultimate tensile strength of the as-spun and cold-drawn fibres were 2.9 ± 0.28 GPa and 76.7 ± 3.3 MPa and 8.5 ± 0.3 GPa and 88.9 ± 4.2 MPa, respectively.

Finally, the effect of oxidation of the electro-spun PAN fibres and the carbonisation temperature were studied. Since PAN shrinks during oxidation and carbonisation, a custom-designed rig was used to apply a constant tension, within a tube furnace, during the heat-treatment operation. The oxidation of PAN was carried out at 300 °C in air and the carbonisation at 600, 900 and 1,200 °C in a nitrogen atmosphere. The Young's modulus and the ultimate failure stress increased as a function of the heat-treatment temperature. For example, Young's modulus increased from 7.4 ± 0.7 GPa (as-spun fibre) to 37.2 ± 1.1 GPa

(carbonised at 900 °C). In the case of the ultimate failure stress, it increased from 195.0 ± 10.2 MPa to 378.1 ± 33.1 MPa for the as-spun and carbonised samples (at 900 °C), respectively.

XRD and Raman spectroscopy were used to study the graphitic characteristics of the oxidised and carbonised fibre where it was established that the sp^2 characteristics increased with heat-treatment temperature. With reference to the Raman spectra, the I_D/I_G ratio for the carbonised fibre was 0.87 ± 0.04 and it represents one of the highest values reported in literature for PAN samples that were treated at the same temperature.

A TEM-based technique was developed to estimate the fibre volume fraction for the carbonised fibres. This aspect was carried out in collaboration with the Electron Microscopy Centre in the School of Metallurgy and Materials at the University of Birmingham.

The work has shown that the tensile strength and the Young's modulus of electro-spun PAN fibres can be increased by cold-drawing.

LIST OF PUBLICATIONS

This thesis is based on the following peer-review journal paper and patent:

1. Shao, S., T. Ma, and G.F. Fernando, *Electro-spinning of highly-aligned polyacrylonitrile nano-fibres with continuous spooling.* Sci Rep, 2021. **11**(1): p. 21713.

2. Patent: *Electrospinning apparatus and method for forming aligned fibres.* Patent No. GB2594861B/WO2020120985A1. Inventor: Shao SIHENG Fernando GERARD.

Description of Author Contribution

My contribution to the original paper was that I designed and performed the experiments with advice from G. Fernando and wrote the paper along with G. Fernando. T. Mao aided with design of the initial concept.

ACKNOWLEDGEMENTS

I would like to express my deep and sincere gratitude to my supervisor, Professor Gerard Fernando, for his helpful supervision and support during my PhD. He gave me the golden opportunity to do this wonderful project. His invaluable guidance and patience helped me greatly with the research design, experimentation and analysis required to complete this thesis. No one deserves a bigger thank you than him.

I am thankful to my co-supervisor Dr Stephen Kukureka for his advice and support as well. My sincere thanks go to Frank Biddlestone, Amy Newell and Theresa Morris for training me to use the equipment in the laboratory. I am grateful to my friends and colleagues Dr Inam Khan, Dr Bongkot Hararak, Yuting Liu, Rohit Jassi, Zhongyuan Suen, Maximilian Hlatky and Madhav Ramesh, for their constant encouragement. I would also like to thank the staff at the School of Metallurgy and Materials, University of Birmingham, for their kindness.

Finally, I am incredibly grateful to my family for their unconditional love, care and support. Thank you for always standing by me.

CONTENTS

1. INTRODUCTON 11

1.1. Background to Electro-spinning and Key Issues 11

1.2. Aims 15

1.3. The Covid-19 Pandemic 15

2. LITERATURE REVIEW 16

2.1. Electro-spinning and Fibre Formation 16

2.1.1. The Polymer 16

2.1.2. The Solvent 19

2.1.3. Effect of Concentration, Molecular Weight, and Viscosity 23

2.1.4. Effect of Electric Charge, Conductivity and Surface Tension 25

2.1.5. Effect of Processing Parameters on Fibre Formation 29

2.1.6. Effect of Environmental Conditions on Fibre Formation 33

2.2. Fibre Alignment During Electro-spinning 35

2.2.1. Mechanical-based Nano-fibre Alignment Methods 37

2.2.2. Electro-spinning Under a Controlled Electric Field 41

2.2.3. Hybrid Alignment Methods 54

2.2.4. Other Nano-fibre Alignment Methods 61

2.3. Tensile Testing of Electro-spun Nano-fibre 69

2.3.1. Techniques to Determine the Tensile Properties of Electro-spun Nano-fibres 69

2.3.2. Improving the Tensile Properties of Nano-fibres through Drawing 79

2.4. PAN-based Carbon Nano-fibres 88

2.4.1. Manufacture and Pyrolysis of PAN-based CNFs 89

2.4.2. Factors that Influence the Tensile Properties of CFs and CNFs 94

3. EXPERIMENTAL 100

3.1. Materials 100

3.2. Electro-spinning Polyacrylonitrile/DMSO Solutions 104

3.2.1. Electro-spinning PAN Nano-fibres 105

3.2.2. Recovery and Storage of the As-spun Fibres 121

3.2.3. Drying Regime for the Electro-spun Nano-fibres 125

3.3. Pyrolysis of the Electro-spun PAN Nano-fibres 128

3.3.1. Temperature Gradient Within the Tube Furnace 128

3.3.2. Custom-designed Rig and Sample Preparation for the Thermal Treatment of the Electro-spun PAN Nano-fibres 130

3.3.3. Oxidation of the Electro-spun PAN Fibres 135

3.3.4. Carbonisation of the Oxidised PAN Nano-fibres 142

3.4. Preparation of Tensile Test Specimens 143

3.4.1. End-tabbing the As-spun Nano-fibre Bundles 144

3.4.2. End-tabbing the Oxidised and Carbonised Nano-fibres Bundles 145

3.5. Materials Characterisation 147

3.5.1. Rheometry 147

3.5.2. Electrical Conductivity 148

3.5.3. Surface Tension Measurements 149

3.5.4. High-speed Camera 150

3.5.5. Differential Scanning Calorimetry 150

3.5.6. Thermo-gravimetric Analysis 152

3.5.7. Weight of the Electro-spun PAN Nano-fibres 153

3.5.8. Scanning Electron Microscopy 153

3.5.9. Transmission Electron Microscopy 155

3.5.10. X-Ray Diffraction 156

3.5.11. Raman Spectroscopy 157

3.5.12. Fourier Transform Infrared Spectroscopy 158

3.5.13. Tensile Testing 159

3.6. COMSOL Modelling 167

4. RESULTS AND DISCUSSION 171

4.1. Electro-spinning of Highly Aligned PAN-based Carbon Nano-fibres 171

4.1.1. Reasons for Selecting PAN and DMSO 171

4.1.2. Morphology of the As-received PAN and Dissolution in DMSO 173

4.1.3. Viscosity 175

4.1.4. Electrical Conductivity 183

4.1.5. Surface Tension 185

4.1.6. Fibre Formation and Morphology of Electro-spun Fibres 186

4.1.7. The Effect of Drying Temperature on the Residual Solvent in PAN/DMSO Nano-fibres 199

4.1.8. Electro-spinning of Aligned PAN/DMSO Nano-fibres 204

4.1.9. Aligned Nano-fibres Obtained with Other Polymer Solutions Using the Vee-shield Set-up 227

4.1.10. Demonstration of Continuous Spooling in Conjunction with the Vee-shield 231

4.1.11. Production of Layers of Electro-spun Fibres at Specified Angles 237

4.2. Stabilisation and Carbonisation of Aligned PAN Nano-fibres 240

4.2.1. Establishing the Temperature Gradient within the Tube Furnace 243

4.2.2. Effect of Weight (tension) on the Stabilisation and Carbonisation of Aligned PAN Nano-fibres 247

4.2.3. Effect of Heat-treatment Temperature on Aligned PAN Nano-fibres 254

4.3. Tensile Testing of Randomly Oriented and Aligned PAN Nano-fibres.....271

4.3.1. Preparation of Randomly Oriented PAN Nano-fibres 271

4.3.2. Assessment of the Tensile Test Specimen using SEM 275

4.3.3. Effect of the End-tabbing Method on the Tensile Test Results 279

4.3.4. Tensile Testing of Randomly Oriented Electro-spun PAN Nano-fibres 285

4.3.5. Tensile Testing of As-spun Aligned PAN Nano-fibres 293

4.3.6. Improving the Tensile Properties of the Aligned Nano-fibres by Cold-Drawing 302

4.3.7. Tensile Testing of Aligned Heat-treated Nano-fibres 319

5. CONCLUSIONS AND RECOMMENDATIONS FOR FUTURE WORK 328

5.1. Conclusions.....328

5.2. Recommendations for Future Work.....331

REFERENCE 334

APPENDIX A.....358

APPENDIX B.....370

APPENDIX C.....384

1. INTRODUCTON

1.1. Background to Electro-spinning and Key Issues

Electro-spinning is a process that is used to produce polymer fibres with diameters in the sub-micrometre or nano-metre scale. Electro-spun fibres are used extensively in applications such as tissue engineereing [1], drug delivery [2], filtration [3], textiles [4] sensors [5] and catalysis [6]. A schematic illustration of the electro-spinning equipment and fibre production process is shown in Figure 1.1.1. With reference to Figure 1.1.1, a polymer solution is contained in a syringe that is connected to a metal needle. A screw-driven liquid dispenser is generally used to drive the plunger on the syringe to maintain a pendant drop of the polymer solution at the tip of the needle. A high electrical potential, positive or negative [7], is applied to the needle. A grounded electrode, generally referred to as the collector, is where the fibres are deposited. The applied potential between the needle and the grounded collector generates an electric field. As the intensity of the electric potential is increased, Coulomb repulsion forces [8] are generated between the polymer chains and charge accumulates on the surface of the polymer pendant drop. As the applied voltage is increased, the repulsion within the polymer chains, the accumulation of charge, and the attraction from the grounded collector causes the pendant polymer drop to deform into a conical shape and this is referred to as the Taylor cone [9]. As the applied voltage is increased further, there comes a point when surface tension of the polymer solution is exceeded, a fine polymer 'jet' is ejected from the Taylor cone and is propelled towards the grounded electrode [10]. The polymer jet follows a relative straight path for a certain distance from the tip of the Taylor cone and then its trajectory takes the

form of a 'whipping action' due to electrohydrodynamic instabilities [11]. Using high-speed photography with 18 ns exposure time Shin *et al.* [12] demonstrated that the whipping portion of the jet formed multiple loops instead of splaying. The whipping motion caused by bending instability causes the polymer jet to undergo stretching which is significantly more than that observed in the straight portion of jet. The path of jet elements formed by the bending instability grows in radius, and at the same time, thins and stretches [13]. The rapid movement of the polymer jet during the whipping action significantly elongates the fibre, resulting in a significant decrease in diameter. The whipping or bending instability during electro-spinning is said to be caused by an imbalance in the tangential stresses at the air/liquid interface [14]. These authors attributed this instability to be the result of the interactions between the surface accumulated charges and the external electric field that is tangential to the surface of the liquid in the axial direction. As the polymer jet propels towards the grounded electrode, the solvent in the fibre evaporates rapidly [15]. The evaporation of the solvent creates a skin on the surface of the fibre and this maintains the circular cross-section of the electro-spun fibres.

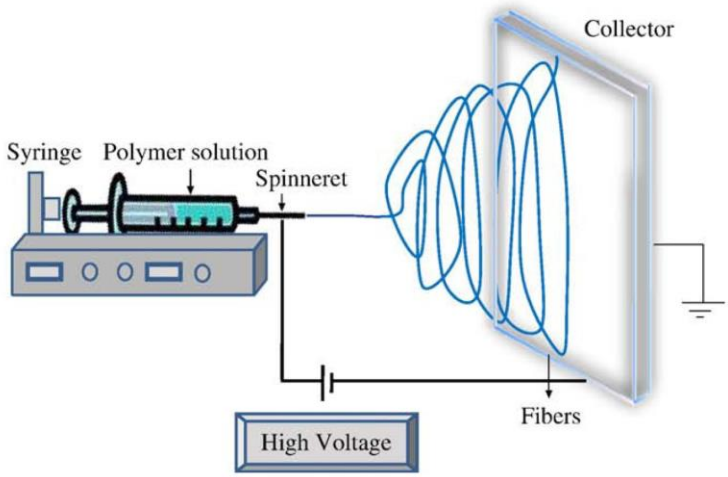

Figure 1.1.1 Typical experimental set-up for electro-spinning [16].

Although electro-spinning is generally reported in the literature to be a simple and straightforward technique to produce fibres in the nano-metre diameter, a number of factors affect the fibre morphology and the resultant mechanical properties. For example, the polymer and solution parameters, the processing conditions and the processing environment. These factors are presented in Table 2.1 (Page 17) and discussed in Section 2.1. The inter-relationship between these factors is far from simple where adjusting one parameter, for example changing the processing temperature will have an influence on the solution viscosity, humidity, the solubility of the polymer in the solvent and the evaporation rate of the solvent. It is apparent from Table 2.1 that a number of factors need to be considered and optimised to obtain the desired fibre morphology, diameter distribution, macroscopic orientation, and mechanical and physical properties [17].

In the context of the current work, the overall objective was to develop a practical method to electro-spin aligned fibres continuously, and also to develop a facility to haul them off continuously for post-processing. Whilst a number of previous authors have reported techniques to produce aligned electro-spun fibres [18-24], those methods do not permit the fibres to be extracted continuously. Hence, the fibres produced using those methods are not amenable for post-processing. For example, stretching to increase the degree of molecular orientation. It is generally appreciated that the mechanical properties of reinforcing fibres are influenced significantly by the degree of molecular alignment [25]. In an industrial setting, the stretching of the fibres is carried out as they are produced. However, this requires a large space to accommodate multiple rollers, take-up spools and control equipment [26, 27]. Once the electro-spun nano-fibres are produced, evaluating their mechanical properties is extremely challenging because of the dimensions involved, the sensitivity of the

load/displacement measurement equipment, required and the method of gripping the samples [28-31]. A common technique that is used to evaluate the mechanical properties of nano-fibres is atomic force microscopy (AFM) [32, 33]. However, the sampling volume is small and therefore not representative in terms of the true fibre volume fraction when they are used in composites [34]. In order to overcome the difficulties in evaluating the mechanical properties of single nano-fibres, the bundle test has been used [35, 36]. However, a review of the literature indicated that standard test procedures do not exist for such a tensile test method and in particular, for end-tabbing the specimen [37-39].

An issue that has puzzled researchers is the observation that the crystallinity and mechanical properties of electro-spun fibres are lower than those that are produced by conventional techniques such as wet, dry and melt-spinning [40]. The background to this is that there is extensive stretching that occurs during the whipping of the polymer jet, which should result in enhanced molecular alignment and crystallinity, but this is not the case.

The current research project was undertaken to address the issues mentioned above with regard to:

(i) establishing the optimum processing conditions to produce highly aligned electro-spun fibres. The polymer and solvent system that was chosen was polyacrylonitrile (PAN) and dimethyl sulfoxide (DMSO). PAN was selected as it offered a means for comparing the properties of the electro-spun fibres with those produced commercially via wet-spinning [41, 42]. DMSO was chosen as it is not toxic;

(ii) developing a method to prepare and end-tab a unidirectional array of electro-spun PAN fibres to enable tensile testing and stretching, and;

(iii) developing a rig to oxidise and carbonise the PAN fibres, followed by characterisation and tensile testing.

1.2. Aims

The primary aims of this research are as follows:

(i) To design, model and construct a rig to enable the production of randomly oriented, and highly aligned PAN nano-fibres with continuous spooling.

(ii) To characterise the electro-spun fibres using conventional analytical techniques and image analysis.

(iii) To develop a method to end-tab an array of unidirectional fibre bundles for tensile testing.

(iv) To design and construct a rig to enable the PAN nano-fibres to be oxidised and carbonised under tension.

(v) To demonstrate that other classes of polymers could be electro-spun using the Vee-shield method to produce aligned fibres.

1.3. The Covid-19 Pandemic

This research was affected by the pandemic where the lockdown period was used for the literature review and modelling of the electro-spinning rig. After the two lockdown periods, access to in-house equipment and those based in the other Schools within the University had to be managed because of the limited number of persons that were permitted in a laboratory and the demand for usage time by the research community.

2. LITERATURE REVIEW

2.1. Electro-spinning and Fibre Formation

Electro-spinning is a versatile technique for producing nano-fibres where a plethora of semi-crystalline and amorphous fibres have been electro-spun. The application areas include filters [3], scaffolds for tissue engineering [1], energy storage devices [43], actuators [44], sensors [5] and reinforcements [45]. In the case of the production of reinforcing fibres, ideally, the electro-spun fibres should be continuous, unfused and possess a circular cross-section. In order to produce electro-spun fibres with the desired properties in a consistent and repeatable manner, it is necessary to establish the influence and inter-relationships between a number of the materials' properties, the processing parameters and the processing environment [46]. A summary of some of the key parameters that can influence the properties of electro-spun fibres is presented in Table 2.1. The following section presents a review of the parameters mentioned in Table 2.1 in the context of electro-spinning the materials, processing parameters and environmental conditions including their influence on the macro and micro-structure of the fibres.

2.1.1. The Polymer

A wide range of polymers have been used for electro-spinning. Electro-spun fibres can be produced from either molten polymers [47, 48] or polymer solutions [49-51]. Melt-electro-spinning has generally been used with polymers such as polypropylene (PP), polyethylene terephthalate (PET), polycaprolactone (PCL) and polyethylene (PE), where no suitable solvent can be found at room temperature [52]. The semi-crystalline polymers are heated above their

melting temperature when melt-electro-spinning. The fibre diameter is generally in the range of 700 nm to 50 μm [48]. Fibre produced from melt-electro-spinning shows higher crystallinity and a smoother surface finish when compared to solution electro-spinning [53].

Table 2.1 A summary of materials, solution, electro-spinning parameters and environmental conditions that are known to influence the macro and micro-structure of electro-spun fibres using solution-based electro-spinning.

Materials and Solution Parameters	**Electro-spinning Parameters**	**Environmental Conditions**
Polymer	Applied Voltage	Temperature
Solvent	Working Distance	Humidity
Homogeneity	Solution Dispensing Rate	Pressure
Molecular Weight Distribution	Collector Geometry	Air Turbulence
Concentration	On-set of Whipping	Atmospheric Composition
Viscosity	The Needle	Health and Safety
Surface Tension	-	-
Electrical Conductivity	-	-
Dielectric Constant	-	-

With regard to solution electro-spinning, in general, as long as the polymer can be dissolved in a solvent, it should be electro-spinnable. Various polymer solutions have been electro-spun by researchers, such as poly(glycolide) (PGA)/1,1,1,3,3,3 hexafluoro-2-propanol [54]; poly(ε-caprolactone) (PCL)/methylene chloride [55]; poly(l-lactide) (PLA)/dimethylformamide (DMF)

[56]; poly(ethylene oxide) (PEO)/ethanol [57]; polystyrene (PS)/DMF [58]; cellulose acetate (CA)/acetone [59]; silk/hexafluoroacetone (HFA) [60]; chitosan/trifluoroacetic acid (TFA) [61]; gelatin/2,2,2-trifluoroethanol (TFE) [62]; collagen/1,1,1,3,3,3 hexafluoro-2-propanol (HFP) [63]; polyvinylidene fluoride (PVDF)/DMF [64]. Examples of other polymers include lignin/acetone/dimethyl sulfoxide (DMSO) [65]; polyvinyl acetate (PVA)/distilled water [66] and PAN/DMF [36], which are generally considered to be more suitable for solution electro-spinning. The selection of the polymer as well as the spinning method, is generally dictated by the desired end-use application. For example, in the case of scaffolds for tissue engineering, the polymer has to be bio-compatible [50]. Polymers such as PVDF that have piezoelectric properties have been used to fabricate sensors [67]. Carbonised PAN and lignin electro-spun fibre mats have been used as the electrodes for lithium-ion batteries [68, 69].

Electro-spinning is interlinked with the viscosity of the molten polymer or polymer solution. The viscosity is affected strongly by the molecular weight of the polymer and the concentration of the polymer solution [47, 52]. This can affect the conductivity and flowability, which influences the voltage applied, the selection of the needle size, and feed rate during electro-spinning. Since the viscosity has a critical influence for electro-spinnability [70, 71], and this will be discussed further in Section 2.1.3.

Although the effect of polymer properties such as conductivity and molecular weight on electro-spinning has been investigated and presented in review papers [4, 17, 47, 52], some characteristics of selected polymer components such as molecular weight distribution and solution homogeneity, as well as dielectric properties of the polymer with regard to its ability to be electro-spun, have not received any significant attention in the literature.

2.1.2. The Solvent

Due to the polarity of the acrylonitrile functional group, the inter-molecular attraction of PAN, and its high crystallinity (~35%) [72], the polymer starts to degrade prior to melting. Therefore the monomer, acrylonitrile, is co-polymerised for melt-spinning and wet-spinning, and electro-spinning is used for solution-based production of PAN nano-fibres [73]. The focus of the current work is on electro-spinning solutions and therefore, detailed attention is not given to melt electro-spinning. A good solvent is required to form a homogeneous polymer solution. The mechanism of polymer dissolution can be described as the solvent molecules' disentanglement of the polymer chain. The interaction between the solvent-polymer should be higher than the polymer-polymer interaction to initiate dissolution [74]. The solution property depends on the geometric array of the polymer and the magnitude of force operating between the molecules. For electro-spinning purposes, the ideal solvent system requires an equal interaction between solvent and polymer. In contrast, the interaction between polymer chains must be sufficient to enable a high degree of drawing during electro-spinning [75]. The criteria for selecting a suitable solvent for a given polymer can be based on the solubility parameter. Hansen [76] proposed that the interaction between polymer molecules can be divided into three different forces; dispersion forces (δ_d), polar interactions (δ_p) and hydrogen bonding (δ_h). The Hansen solubility parameter (δ) can be found using Equation (2.1):

$$\delta^2 = {\delta_d}^2 + {\delta_p}^2 + {\delta_h}^2 \tag{2.1}$$

Hansen stated that a good solvent for a given polymer should have a solubility parameter that is close to that of the polymer. This can be determined using the Hansen solubility parameter difference described in Equation (2.2):

$$R_a{}^2 = 4(\delta_{d2} - \delta_{d1})^2 + (\delta_{p2} - \delta_{p1})^2 + (\delta_{h2} - \delta_{h1})^2 \quad (2.2)$$

where R_a stands for the parameter difference between two selected substances (d_1, d_2 etc.). A smaller R_a value is required for an ideal polymer solution system [76]. The solubility parameters for PAN are 21.7 (δ_d), 14.1 (δ_p) and 9.1 (δ_h). The solubility parameter for selected solvents is presented in Table 2.2.

On inspecting Table 2.2, dimethylacetamide (DMAa), dimethylformamide (DMF) and dimethyl sulfoxide (DMSO) will dissolve PAN. During the dissolution of PAN, solvent bridges are formed by the orientation of the polarised solvent molecules between the nitrile groups of PAN (see Figure 2.1.1a and b) [77]. Mei *et al.* [78] calculate the Flory-Huggins parameter for PAN, DMF, DMAc and NMP. The Flory-Huggins parameter (χ) is a dimensionless quantity that describes the interactions between different components in a polymer solution [78]. According to the regular solution theory, the relationship between the Flory-Huggins interaction parameter and the solubility parameters is described by Equation (2.3):

$$\chi_{12} = \frac{\upsilon_1}{RT}(\delta_1 - \delta_2)^2 \quad (2.3)$$

where χ is the Flory-Huggins interaction parameter, υ is the molar volume (cm^3/mole), δ_1 and δ_2 are the solution parameter of substances 1 and 2, R is the universal gas constant (8.314 J/(mol. K)), and T is the absolute temperature [79]. Generally, the lower the Flory-Huggins parameter, the better the miscibility. Lindvig *et al.* [79] showed that the value of the Flory-Huggins parameter for PAN/DMF was the lowest (–0.792) compared with PAN/DMAc and PAN/NMP which were –0.313 and –0.115, respectively; hence it was deemed to be the ideal solvent among these three for dissolving PAN [80]. Due to the difference in the solubility parameter between DMF and PAN being more significant than that between DMSO and PAN

Table 2.2 Properties and solubility parameters for selected solvents [81-83].

Solvents	Toxicity	Hansen Solubility Parameters			Boiling Point (°C)	Enthalpy of Vaporisation (kJ/mol)	Freezing Point (°C)	Surface Tension (mN/m)	Electrical Conductivity (Ohm/m)	Dielectric Constant
		δ_D	δ_P	δ_H						
Acetone		15.5	10.4	7.0	56	31.3	-94.7	23.3	12.8×10^{-8}	20.7
Cyclohexanone		16.8	0.0	0.2	155	46.7	-47.2	36.5	7×10^{-8}	18.0
Dimethyl sulfoxide (DMSO)	Non-toxic	18.4	16.4	10.2	189	48.9	18.5	46.5	3×10^{-8}	36.7
Dimethylformamide (DMF)		17.4	13.7	11.3	153	43.0	-60.4	37.0	2.6×10^{-6}	46.7
Dimethylacetamide (DMAc)		16.8	11.5	10.2	165	38.5	-20.5	37.1	2×10^{-9}	37.2
N-methyl-2-pyrrolidone (NMP)		18	12.3	7.2	202	47.4	-23.5	36.6	2×10^{-8}	32.2
Tetrahydrofuran (THF)		16.8	5.7	8.0	66	31.9	-108.4	26.5	1×10^{-6}	7.6

(2.5 and 0.2, respectively), the solvent bridge in DMSO is longer than that for DMF (see Figure 2.1.1c). Furthermore, DMF can dissolve PAN two times faster than DMSO. However, PAN solutions containing DMSO are more homogenised and stable to changes in temperature due to its fixed charge distribution in its chemical structure, high dipole moments (3.96 D) and long solvent bridge [77]. DMF is more frequently used for electro-spinning [84-87], whereas DMSO is more commonly used for wet-spinning [88-92]. This is probably due to the boiling point of DMF (153 °C) being 36 °C lower than DMSO (189 °C), which means a faster evaporation rateduring electro-spinning. The viscosity and surface tension of DMSO is higher than DMF due to its higher polarity [93]. However, as seen in Table 2.2, DMSO is a non-toxic solvent.

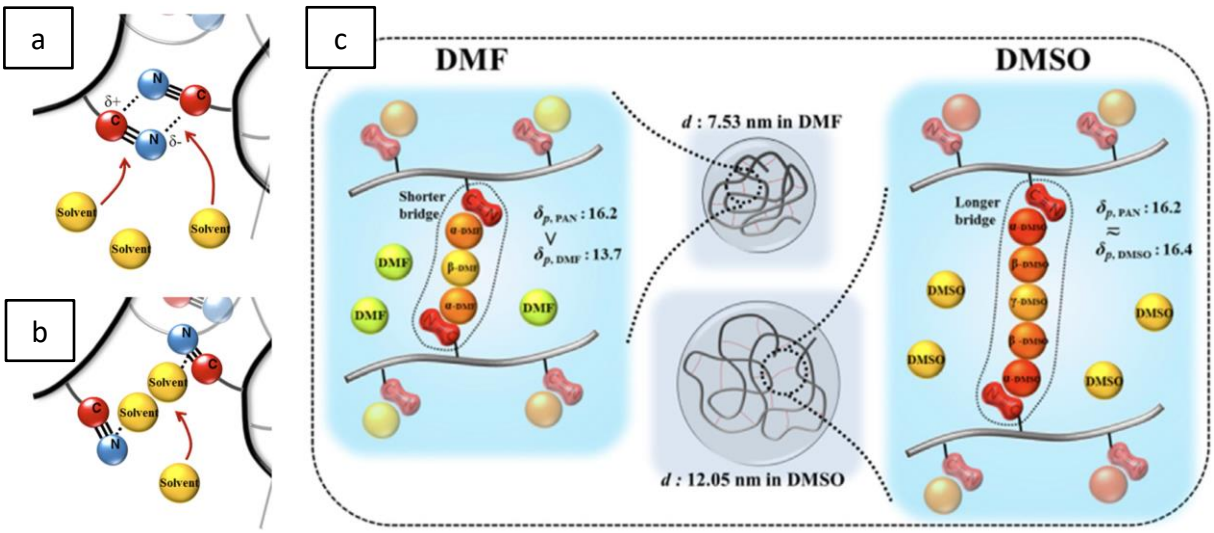

Figure 2.1.1 Schematic diagram of dissolution mechanism of PAN in DMF and DMSO; carbons are shown in red, nitrogens in blue, and solvent molecules in yellow. (a) Step 1: Penetration of solvent molecules into the polymer molecules by breaking up the polar-polar interaction of the nitrile groups of PAN. (b) Step 2: Formation of solvent bridges by orienting the polarised solvent molecules between the nitrile groups of PAN. (c) Schematic presentation of coil dimensions of PAN chain in the solvents and equilibrium solvent bridges [77].

2.1.3. Effect of Concentration, Molecular Weight, and Viscosity

With regard to electro-spinning, the viscosity of the polymer solution is known to have a major influence on the production of fibres. The viscosity can be altered by adjusting the concentration of the polymer, the molecular weight and/or the temperature [94]. Increasing the concentration or the molecular weight increases the probability of entanglement of the polymer chains [95-97]. An increase in the degree of chain entanglement leads to an increase in the intrinsic viscosity [98]. The relation between the intrinsic viscosity (η) and molecular weight distribution (M) can be found in the Mark-Houwink-Sakurada Equation (2.4) [99]:

$$[\eta] = KM^{a} \tag{2.4}$$

where K and α are constants depending on the polymer type, solvent and temperature.

Previous researchers realised that a minimum value of solution viscosity, known as critical viscosity (C*), was required to form fibres during electro-spinning. Solutions below this critical value result in electro-spraying [100]. Beadless fibres are generally formed within the semi-dilute region where the concentration of polymer solution (C) is greater than critical viscosity (C*). For a specific polymer/solvent combination, the critical viscosity is determined by measuring the viscosity of the polymer solution as a function of concentrations [101]. Typically, a change in the gradient is seen on the viscosity versus concentration plot, where the intersection indicates the critical viscosity. Colby and Rubinstein [102], pointed out that this turning point in the viscosity, known as the entanglement concentration (C_e), appears to be due to the polymer conformation changing from a semi-dilute un-entangled to a semi-dilute entangled state. Shenoy *et al.* [98] carried out a study to determine the role of chain entanglements on fibre formation during electro-spinning. In their study, they determine the

relationship between molecular weight, polymer concentration and the entanglement number in the solution. Equation (2.5) was established based on these parameters and can be used to predict fibre formation. They also showed that the sharp upturn point in solution viscosity occurs when $(M_c)_{soln}/(M_e)_{soln}$ ~2.

$$(n_e)_{soln} = \frac{M_W}{(M_e)_{soln}} \tag{2.5}$$

where $(n_e)_{soln}$ is the entanglement number in solution. M_w is the molecular weight of the polymer. $(M_e)_{soln}$ stands for the entanglement molecular weight in solution. $(M_c)_{soln}$ stands for the critical molecular weight in solution. The entanglement molecular weight in the solution, $(M_e)_{soln}$, can be determined using Equation (2.6):

$$M_e \propto C_\infty^{-3} m_o^3 l_o^{-6} \rho^{-2} \tag{2.6}$$

The M_e of a polymer is a function of the characteristic ratio (C_∞), the average molecular weight per backbone bond (m_o), bond length (l_o) and density (ρ) [103]. In their prediction, if the spinning solutions corresponded to $(n_e)_{soln} < 2$, bead formation was said to be more likely. When $2 < (n_e)_{soln} < 3.5$, a mix of beads and fibre is predicted to be formed. When $(n_e)_{soln} > 3.5$, fibre formation was said to be the predominant feature. Several polymer/solvent combinations with different polymer concentrations were used to establish the accuracy of this prediction. This paper clearly shows the importance of entanglement in the electro-spinning process when using a polymer solution. However, changes in concentration and molecular weight affect the solution viscosity. For fibre formation during electro-spinning, the molecular weight becomes less important when sufficient entanglement occurs with increasing polymer concentration [104].

The majority of the papers in the literature show that increasing the polymer solution viscosity reduces the formation of beads and increases fibre diameter [10, 105-107]. However, depending on the polymer type, the formation of beadless fibre only occurs within a certain viscosity range. Koski *et al.* [66] and Demir *et al.* [108] illustrated that when C >> C*, curly, wavy and ribbon-like fibres were formed. This could be due to the drawing and deformation of the polymer jet becoming difficult when the viscosity is high. The surface of the polymer jet is not able to solidify to form a skin with the required thickness to maintain the shape and structure of fibre when it hits the collector [13, 51].

In addition to the bulk viscosity of the polymer solution, Rosic *et al.* [109] showed the importance of interfacial viscosity between air and polymer solution to predict fibre formation. Firstly, they pointed out that the polymer solution should possess viscoelastic properties. In addition, the plasticity of the solution must be greater than the elasticity to form a stable polymer jet during electro-spinning. Secondly, the jet diameter has to decrease dramatically within the whipping region from a micrometre scale to hundreds of nanometres. Moreover, they pointed out that solvent evaporation usually occurs at the fibre surface, which causes the polymer concentration at the surface of the jet to change. These factors make interfacial rheological properties more important than the bulk solution viscosity. This is because the thinner the jet diameter, the larger the surface area.

2.1.4. Effect of Electric Charge, Conductivity and Surface Tension

As mentioned previously, the electro-spinning process initiates when the Coulomb repulsive force exceeds the surface tension of the polymer solution. The repulsion of these charges at the surface, under the applied potential, causes deformation of the liquid sphere and

stretching of the jet. The conductivity of the solution can strongly affect the Coulomb repulsive force active on the surface of the solution. Therefore, both parameters strongly affect the electro-spinnability, fibre formation and fibre morphology. Surface tension can be defined as a liquid property indicating the cohesive strength between molecules [110]. The surface tension can be measured using a force tensiometer. The surface tension of the solvent dominates the value of the surface tension for a polymer solution due to its high concentration in the system, typically more than 70%. Surface tension was believed to be another significant factor affecting the formation of beads [105]. Furthermore, the formation of beads is considered as the capillary breakup of the electro-spinning jets by surface tension [111]. Researchers have also reported that forming beads is possibly due to the high concentration of free-solvent molecules that tend to congregate because of surface tension. The number of beads was reduced when the surface tension was low at the same viscosity level when working with PCL in methanol [112]. Researchers realised that more than a single solution parameter was needed to predict fibre formation during electro-spinning. Kim *et al.* [113] demonstrated that fibre formation during electro-spinning can be estimated using the surface tension and viscosity of the solution. The fibre formability number was calculated using Equation (2.7):

$$N_F = \frac{\sigma_s}{\mu R} \tag{2.7}$$

where N_F is the formability number, μ is the viscosity (cP), σ_s stands for the surface tension. R represents the radius of the nozzle. Throughout their experiments, Kim *et al.* used a fixed voltage and nozzle radius, and they classified the fibre formation behaviour into four ranges using various formability numbers. When N_F was equal to, or less than 25, both electro-spinning and electro-spraying were not observed. Between 25 and 420, electro-spinning took

place. Beads started to form when N_F was higher than 420 and less than 13333. Over 13333, electro-spraying dominated the process. However only one polymer, PVP, was tested in their study. More experiments involving other polymers are needed in order to corroborate the result [113-115].

It was found that the magnitude of the Coulomb repulsive force is strongly related to the amount of surface charge as determined by the conductivity of the solution, which controls the elongation of the polymer jet [116]. The surface tension can be understood as the pressure difference between the inside and outside of the liquid solution sphere and calculated using the Young-Laplace Equation (2.8) [117]:

$$P_i - P_o = \frac{2\gamma}{r} \tag{2.8}$$

where P_i and P_o represent the inner and outer pressures, γ is the surface tension, and r is the radius of the liquid sphere. When a potential is applied, the repulsive force generated from the charged particle can increase the outward pressure, which breaks the balance created by the surface tension. This pressure, P, created by the potential, V, can be found using Equation (2.9) [118]:

$$P = \frac{\varepsilon_0 V^2}{r^2} \tag{2.9}$$

where r is the radius of the droplet, ε_0 is the permittivity of free-space, V is the voltage applied and P is the pressure within the droplet. The relationship between the electric field strength E and the surface tension γ, also proposed by Doshi and Reneker [8], can be expressed as:

$$E = \sqrt{\frac{4\gamma}{\varepsilon_0 R_c}} \tag{2.10}$$

where R_c is the radius of the curvature of the solution drop and ε_0 is the permittivity of free-space. Since the conductivity represents the mobility of charges moving through the volume and the charge density of the solution system, a higher density results in a shorter distance (*d)* between 2 charged particles (q_1 and q_2); therefore, conductivity can eventually affect the Coulomb force (*Fc*). The relationship can be found in Equation (2.11) [118]:

$$F_c = \frac{1}{4\pi\varepsilon_0}\frac{q_1 q_2}{d^2} \tag{2.11}$$

The conductivity of a polymer solution is affected by the chemical structure of the polymer, solvent type, and additives that are used [119].

Researchers have claimed that electric repulsive forces are one of the primary factors that cause whipping and bending instabilities [13, 119]. These instabilities may cause the jet to break up and stop fibre formation, which causes electro-spraying or forming fibres with beads [46]. This is also because the polymer jet cannot withstand the surface tension and the electrostatic force [120]. Balancing the fluid jet instability, the solution conductivity and the applied potential are important parameters with regard to electro-spinning. Several researchers report that under the same processing parameters, higher conductivity causes longer elongation, which results in thinner fibres [121-125]. However, the result seems different when electro-spinning PAN solution with salt additives. Qin *et al.* [126] studied the effect of different salts on the electro-spinning of PAN solutions. LiCl, $NaNO_3$, NaCl, and $CaCl_2$ were tested using PAN/DMF solutions with different concentrations. Their results showed that adding salt to the solution can decrease the viscosity of the solution [127]. The solution containing LiCl had the highest conductivity. However, the fibre produced with LiCl showed the largest average fibre diameter with the worst morphology. Similar results have also been

reported by Heikkila & Harlin [86]. Carbon nanotubes (CNTs) and $ZnCl_2$ were added to 13 wt% PAN/DMF solution to increase the conductivity. Under the same processing parameters, although PAN and PAN/$ZnCl_2$ solutions had similar viscosities, the higher conductivity PAN/$ZnCl_2$ solution showed a higher average fibre diameter under all circumstances. The authors suggested this was due to the higher conductivity, which led to a higher mass flow of the solution. Furthermore, the salts that remained inside the fibre were difficult to remove. Such additives can act as impurities and defects that decrease the mechanical properties of the fibres before and after the carbonisation [86]. Zeng *et al.* [56] reported that adding a volatile salt additive such as pyridinium formate to the electro-spinning solution will not negatively affect the as-spun fibres. They argued that the additive would evaporate with the solvent as the fibre solidified. The solution conductivity can also be improved by using a binary solvent system. Adding pyridine to a formic acid/Nylon-6 solution was said to produce nano-fibres with fewer beads than the single formic acid solvent system [49].

To date, several researchers have developed strategies to understand the formation of electro-spun fibres. All the factors mentioned above have a significant influence on fibre formation. However, most of these strategies are generated using mathematical models. Therefore, more experimental parameters need to be considered to understand the fibre formation process during electro-spinning.

2.1.5. Effect of Processing Parameters on Fibre Formation

2.1.5.1. Applied Voltage

The solution parameters stated in Table 2.1 are not the only factors that can affect the electro-spinnability of the polymers and the morphology of the fibres; process parameters can also

have an effect on fibre morphology. As described in Section 1.1, a critical voltage is required to overcome the surface tension to initiate the polymer jet to be ejected from the Taylor cone, and this threshold was found to vary from solution to solution [9, 128]. A number of researchers have found that processing voltage can affect fibre diameter. Dhanalakshmi *et al.* [129] found that when the working distance (distance between the tip of the spinneret and the top of the collector) was set to 10 cm, under the same solution concentration (15 w/v%), the average diameter of electro-spun Nylon-11 fibre increased from 0.237 ± 0.052 μm to 0.375 ± 0.075 μm when the voltage applied increased from 5 kV to 20 kV. Bakar *et al.* [130] also reported similar results when electro-spinning PAN with DMF, whereby the average fibre diameter was increased from 1.81 μm (10 kV) to 2.32 μm (20 kV). However, the authors did not explain the mechanism behind this observation. Katti *et al.* [131] found that the average fibre diameter of poly(lactide-co-glycolide) was first decreased from 865 nm to 340 nm and then increased to 470 nm when the electric field strength was increased from 0.375 kV/cm to 1.0 kV/cm, and then to 1.5 kV/cm. Wannatong *et al.* [132] reported a similar trend when electro-spinning 10 w/v% PS in DMF: the average fibre diameter decreased from 0.7 μm to 0.57 μm when the spinning voltage was increased from 10 kV to 20 kV. However, the diameter increased to 0.72 μm when the voltage was increased to 30 kV. Decrease in fibre diameter generally occurs between low to moderate voltages (10 kV to 20 kV) when the effect of surface tension is greater than the Coulombic repulsive force [132]. Higher voltages (~30+ kV) cause a greater Coulombic repulsive force, which stretches the charged jet and results in a thinner fibre [131, 133]. When the voltage applied is increased above ~20 kV, the Coulombic repulsive force will dominate the effect on fibre morphology, thereby increasing the stretching in both longitudinal and transverse directions and resulting in larger diameter fibres [132].

2.1.5.2. Solution Dispensing Rate

The liquid dispensing rate is another important factor in controlling bead formation and fibre morphology during electro-spinning. The feed rate must be adjusted according to the voltage applied. Insufficient feed rate with excessive voltage will produce an inconsistent fibre jet and cause bead formation. On the other hand, an excessive feed rate can cause a large semi-spherical droplet to form at the needle tip [134]. The relationship between the voltage and feed rate when electro-spinning 10 wt% PAN/DMF has been studied by Fallahi *et al.* [135]. The quasi-stable voltages at different feed rates follow Equation (2.12):

$$y = 4.417x^{0.273} \tag{2.12}$$

where y is the voltage applied (kV) and x is the feed rate (μL/hour). The R^2 value of this relationship was 0.9906. Fallahi *et al.* [135] found that the weight of the fibre produced within 15 minutes was dominated by the feed rate rather than by the voltage applied. However, the effect of feed rate on the fibre diameter was not reported. When producing aligned electro-spun porous PCL fibre using the parallel electrode method, Beachley and Wen [136] found that when voltage is sufficient for fibre formation, excessive feed rate did not noticeably affect the fibre morphology. However, Zargham *et al.* [134] found that the average fibre diameter and range of diameters produced increased when electro-spinning Nylon-6 nano-fibre with a high feed rate. They suggest that the wider distribution was caused by the unstable Taylor cone geometry. Flattened web-like structures were reported, suggesting that the insufficient solvent evaporation was more directly linked to their formation, rather than the high feed rate [134].

2.1.5.3. Working Distance

Fibre morphology is also affected by the distance between the needle and collector (known as the 'working distance'). Controlling the electric field strength at 1 kV/cm, Ki *et al.* [137] electro-spun gelatin nano-fibres at different working distances from 7.5–20 cm. The effect of working distance on the nano-fibre diameter was minimal. The average fibre diameters were 79, 95 and 81 nm when electro-spinning at 7.5, 15 and 20 cm, respectively. However, electro-spinnability became poor and beads were formed when distance increased. This is because insufficiently charged droplets at the needle are difficult to draw into a fibre jet. Zhou *et al.* [138] reported that when working distance was low (15 cm), wider fibre diameter distributions were seen when spinning PEO with deionised water. This was caused by fibre merging and fusion due to insufficient solvent evaporation. Similarly, Ki *et al.* [137] observed solution droplet formation when working distance was increased to 20 cm, yielding larger fibre diameter. However, some researchers found the opposite result, reporting that average fibre diameter decreases as working distance increases for the electro-spinning of Nylon-11 [129], PVA [139] and PAN [140]. However, all three papers fail to explain the mechanisms behind such behaviour.

2.1.5.4. Collectors

For electro-spinning, collectors are generally conductive substrates used for collecting the charged fibres. Fibre morphology and fibre orientation can be affected by substrate material and geometry. Liu and Hsieh [59] reported that the packing density and morphology of non-woven cellulose acetate fibre was significantly influenced by the collector material. Highly electrically conductive substrates (water and Al foil) result in denser packing and thicker

membrane structure due to a more rapid residual charge deposition rate. Furthermore, in contrast with fibre collected from water, fibre collected on a paper substrate (low electrical conductivity) has a more uniform diameter and smoother surfaces [59]. The surface morphology and porosity of PS/THF, PVAc/methylene chloride (MC) and PLLA/MC nano-fibre was found to be influenced by the temperature of the collector [141]. The geometry of the collector can be changed to produce oriented nano-fibres; this will be explained in detail in Section 2.2.

2.1.6. Effect of Environmental Conditions on Fibre Formation

Temperature and relative humidity are two important environmental parameters that can affect electro-spinnability and fibre morphology [142]. Wang *et al.* [143] fabricated 6 wt% PAN/DMF at 32.2 °C and 88.7 °C and found that average fibre diameter decreased from 170.2 ± 38.2 nm to 83.6 ± 40.5 nm. This indicates that the viscosity of the solution decreased when increasing temperature. Mit-uppatham *et al.* [100] reported a similar trend when electro-spinning 20 w/v% PA-6/formic acid: increasing the spinning temperature from 30 °C to 60 °C reduced the viscosity of the solution from 517 cP to 212 cP, and the average fibre diameter decreased from 98.3 ± 8.2 nm to 89.7 ± 5.6 nm. However, Amiraliyan *et al.* [144] observed that the average fibre diameter of 12 w/v% silk/formic acid increased from 165 nm to 1883 nm when spun at 25 °C and 75 °C, respectively. The fibre became more ribbon-like due to excessive solvent evaporation at the fibre surface as the spinning temperature increased, causing the formation of a skin on the jet surface that inhibited the evaporation of the solvent in the core of the fibre. This caused the ribbon to collapse when the jet struck the collector.

Relative humidity can influence fibre morphology, primarily by affecting the charge dissipation rate of the jet [145] and the evaporation rate of the solvent [142]; the humidity of the electro-spinning chamber can be controlled using a saturated salt bath [142, 146]. Vrieze *et al.* [142] found that PVP/ethanol solution could not produce fibres when humidity reached 60%, possibly due to the absorption of water into the fibres. In the case of hydrophilic polymers, when the water content of the surrounding atmosphere (humidity) is greater than the water content in the fibres, water will be absorbed into the fibres, as a result solvent evaporation and therefore, solidification will be inhibited [142]. Vrieze *et al.* [142] also found that increasing the humidity from 20% to 40% resulted in decreased fibre diameter when spinning PVP/ethanol and cellulose acetate/DMAc solutions. They suggested that increasing the humidity to just below a critical value slows the solidification and favours a higher degree of elongation of the polymer jet. The effect of humidity on the fibre diameter of PAN/DMF was studied by Huang *et al.* [147], who found that the fibre diameter increased continually from 150 nm to 640 nm as relative humidity increased (from 0% to 60%). They suggest that higher moisture content in the air reduces the amount of charge on the polymer jet surface [148], resulting in a weaker electric field and less stretching of the polymer jet [147]. In fact, the effect of humidity on fibre formation is strongly related to the polymer's hydrophilicity [145]. As shown in Figure 2.1.2, the solidification rate of hydrophilic and hygroscopic polymers was decreased, and finer fibres could be produced when humidity was increased, whereas the solidification rate was increased when producing hydrophobic polymer fibres under high humidity, resulting in larger-diameter or even porous fibres [145]. In the case of fibre alignment, charges maintained on the jet surface were discharged by the moisture, thereby

decreasing the degree of alignment as the humidity increased, especially when using parallel electrodes [15, 149, 150].

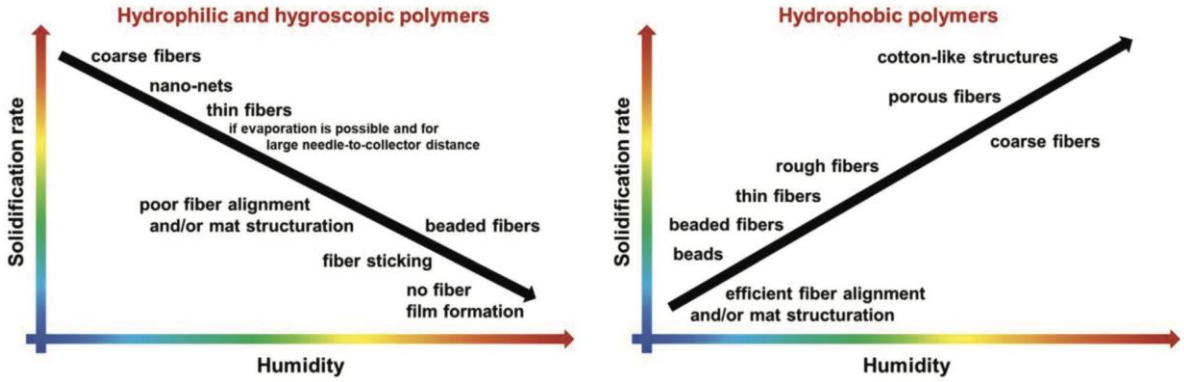

Figure 2.1.2 Electro-spun nano-fibre morphologies and mat structures as a function of humidity, solidification rate, and polymer hydrophilicity [145].

2.2. Fibre Alignment During Electro-spinning

Due to bending instability (the aforementioned whipping action) during electro-spinning, the electro-spun jets are usually deposited randomly on the collector, which gives a non-woven mat or mesh-like preform. The two-dimensional simulation of the electric field lines of a conventional electro-spinning set-up was demonstrated by Theron *et al.* [151] and Deitzel *et al.* [152]. Theron *et al.* [151] assumed the needle to be a positively charged circular point and the collector plate (grounded) to be of infinite size; they show equipotential arrowed lines of the electrostatic forces pointing from the needle to the collector. The field lines form an 'umbrella' shape that extends from the needle and becomes relatively parallel before reaching the grounded plate; this is illustrated in Figure 2.2.1a and b. These electric field lines were understood to be the main factor causing whipping instability [10, 13, 116].

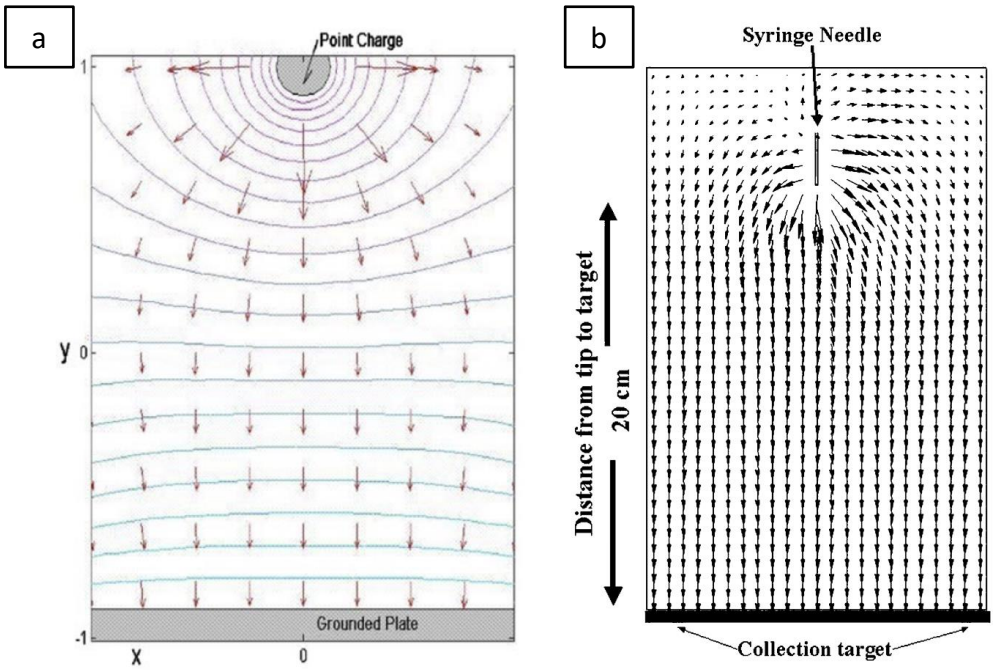

Figure 2.2.1 (a) The computational simulation of conventional electro-spinning set-up generated by Theron et al. [151] and (b) Deitzel et al. [152].

Non-woven structures are ideal for applications in filters and membranes because of their porous structure and large surface area. However, random electro-spun fibres cannot be applied to some areas where mechanical strength is required to maintain the geometry of the mat [153]. An aligned fibre array has greater stiffness than non-woven nano-fibre mat along the alignment direction [154], as demonstrated in the case of gas sensors or filters [155], fabrics and textiles [4], and vascular grafts or coating over stents [50]. Researchers also found that the aligned fibres were better able to support cell growth, proliferation, and neurite outgrowth than random fibres [156-158]. Aligned fibres also have the benefit of encouraging cell growth along the nano-fibres' axis of alignment, allowing the direction of cell growth to be controlled [159, 160]. Furthermore, unidirectional electro-spun fibre can also improve charge transport and increase power conversion efficiencies, which may be of interest for the

battery and energy-harvesting industries [161, 162]. Aligned nano-fibres can be obtained using high-speed rotating collectors [163] or by controlling the electric [150] and magnetic fields [20] during electro-spinning. This section reviews the methods reported in the literature for producing aligned fibres during electro-spinning. Appendix A presents a summary of the main electro-spinning fibre alignment methods and the associated processing parameters reported in the literature.

2.2.1. Mechanical-based Nano-fibre Alignment Methods

2.2.1.1. Rotating Collector

Aligned electro-spun fibres can be produced using a high-speed rotating drum or belt collector operating at around 12.9 m/s. A schematic illustration of a typical rotating collector is shown in Figure 2.2.2. Researchers have found that increasing the mandrel rotation speed will result in a higher degree of alignment [14, 19, 22, 63, 132, 164-170]. In fact, the rotation speed of the mandrel must match the whipping speed of the polymer jet in order to produce aligned fibres [14]. The whipping speed (or frequency) and deposited area of the polymer jet are typically controlled by the extension rate of the polymer jet [171] and the electric field strength of the system [172, 173]. Greenfeld *et al.* [173] reported that the extension rate of the electro-spinning jet varies from polymer to polymer. The extension rate of 3 wt% PEO was ~10^3 s^{-1}, whereas that for 15 wt% PMMA was around 7000 s^{-1}. They also found that the jet strain rate increased with the electric field strength and decreased with solution viscosity [173]. Therefore, the rotation speed of the mandrel must be adjusted for different polymers and processing conditions in order to produce aligned nano-fibres.

Researchers have also demonstrated that increasing the distance between the needle and collector to around 25–30 cm aids the alignment of the fibre on the rotating mandrel without changing the mandrel's rotation speed [174, 175]. The rotation-speed threshold to obtain aligned fibres varied from system to system: the minimum rotation speed for PET was 0.5 m/s [164], whereas the surface velocity to obtain aligned PAN fibres was 9.8 m/s [166].

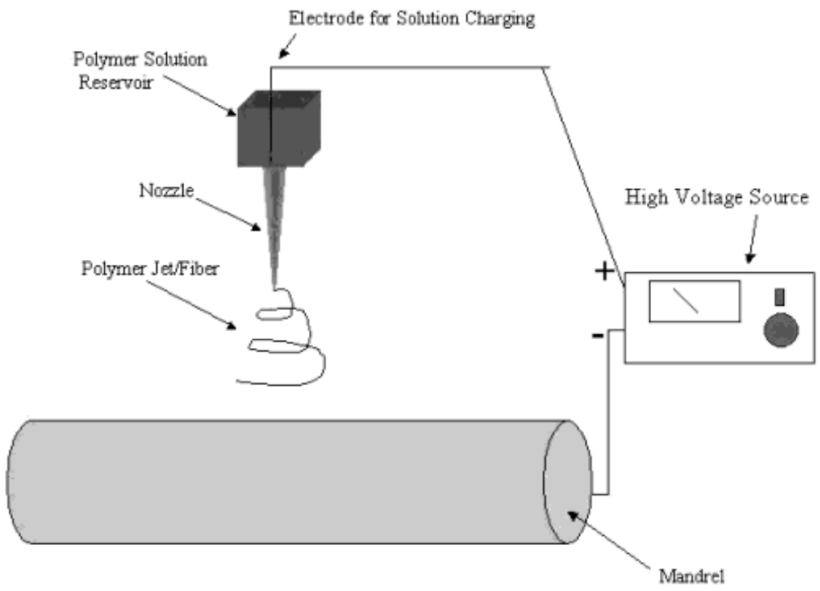

Figure 2.2.2 Schematic illustration of the rotating collector [63].

Increasing the take-up speed can also help stretch the fibre while spinning, leading to a decrease in the fibre diameter of highly aligned PLA fibres from 0.81 μm to 0.47 μm, respectively, when the collecting speed increases from 400 rpm to 1000 rpm [170]. Increasing the take-up speed from 0.25 m/s to 0.5 m/s, Kim *et al.* [164] found the tensile strength, Young's modulus and yield stress were around two times higher. However, high rotational speeds can generally lead to three problems: (i) the polymer jets must have sufficient elasticity and strength to avoid fracturing during production [164]; (ii) higher rotational speeds can lead to slower evaporation of the solvent, causing solvent-rich and flattened fibres to be deposited

[175]; and (iii) the air turbulence caused by the high mandrel rotation rates can cause fibre misalignment and even dislodge the fibres from the collector [164]. Air turbulence can be reduced by redesigning the electro-spinning rig. For example, Krishnamoorthy *et al.* [176] produced highly aligned fibres under fast rotation speeds (78 m/s) using an air-turbulence shield design (see Figure 2.2.3). Degree of fibre alignment starts to decrease as fibre mat thickness increases [177]. One possible explanation is that residual charges may accumulate as the mat gets thicker, thereby deflecting the incoming fibres and causing misalignment [178]. This problem can be addressed by using an alternating current (rather than a direct current) for electro-spinning. Fibres carrying both positive and negative charges becomes neutral upon reaching the collector [179]. These methods can produce large areas of aligned fibres efficiently.

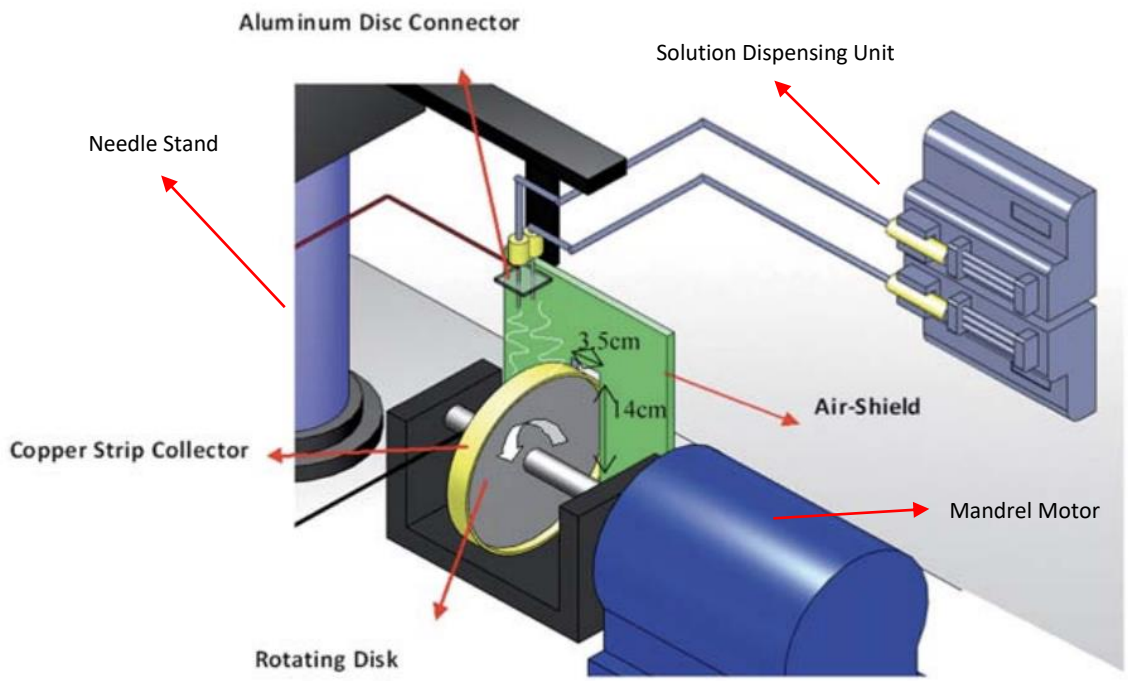

Figure 2.2.3 Schematic of the shielded rotating collector modified by Krishnamoorthy et al. [176] to generate aligned nano-fibre.

2.2.1.2. Centrifugal Alignment Method

Instead of using a rotating collector (mandrel) as discussed previously, in this case the spinneret is rotated, and the fibres are deposited onto the surface of a disc or the inner surface of a cylinder to produce aligned fibres. This method combines electro-spinning with centrifugal spinning to produce aligned fibres during electro-spinning; the centrifugal force is responsible for fibre alignment. Liu *et al.* [180] designed a rig wherein the spinning direction was perpendicular to the centrifugal force (see Figure 2.2.4a); highly aligned fibres were obtained with low spinneret rotation speed (420 rpm) and low voltage applied (3 kV). However, the fibre deposition area was restricted to the size of the ring collector, approximately between 14 cm (ID) and 16 cm (OD) diameter. Thus, a large area of fibre mat cannot be produced using their method.

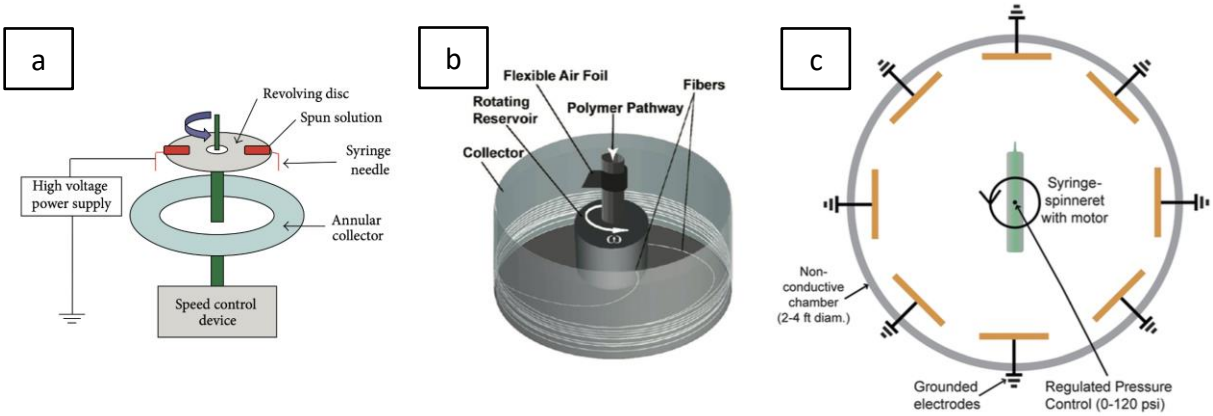

Figure 2.2.4 Schematic illustration of the centrifugal electro-spinning set-up designed by (a) Liu et al. [180], (b) Badrossamay et al. [181], and (c) Edmondson et al. [182].

Badrossamay *et al.* [181] rotated a solution reservoir that contained holes (see Figure 2.2.4b). The main advantage of this method is that with the help of centrifugal force, the voltage applied to initiate fibre formation was significantly reduced. Badrossamay *et al.* claimed that

the aligned fibre bundle can be produced without applying a voltage [181]. The authors also proposed a mathematical model to demonstrate how centrifugal force can form polymer jets and estimate the optimal processing parameters for the centrifugal spinning process. Edmondson *et al.* [182] used a similar idea to Badrossamay *et al.* [181]; however, they changed the collector from a continuous ring to several grounded plates. A schematic illustration of their set-up is shown in Figure 2.2.4c. The set-up yields a higher degree of alignment; however, it should be noted that a 15 kV voltage was also applied in this case. These two concepts were also compared by Kancheva *et al.* [183], who reached the same conclusion. It is assumed that, as with any mandrel-based collector approach, the centrifugal fibre alignment method will also produce fibres with an intrinsic curvature. It would likely prove difficult to unspool the fibres as a continuous length.

2.2.2. Electro-spinning Under a Controlled Electric Field

2.2.2.1. Parallel Electrodes

As described in Section 2.1.4, during electro-spinning, charges accumulate on the surface of the pendant polymer solution when a potential is applied across electrodes. These charges in the polymer solution follow the path of electric field lines, ultimately discharging themselves at the grounded electrode. The electric field lines can be altered by changing the shape of the grounded collector, thereby influencing the trajectory of the fibre towards the collector [119, 150]. The parallel electrode method is a very common and relatively simple, yet highly efficient, method for enabling fibre alignment. Li *et al.* [149] first introduced fibre alignment techniques using parallel electrodes; a schematic illustration of their set-up can be found in Figure 2.2.5a. Instead of using a rectangular or circular flat-plate grounded electrode, their set-up deployed

a pair of metallic grounded electrodes with an air gap between them. As seen in Figure 2.2.5b, Li *et al.* [149] also presented a schematic of the electric field lines between these electrodes. When the field gets close to the grounded parallel collectors, instead of pointing vertically, field vectors are attracted towards these electrodes. This cause the remaining charge on the fibre surface to be directed to the grounded electrode and deposited across the parallel electrodes (see Figure 2.2.5c).

The effect of gap distance was studied systematically by Liu and Dzenis [184], whose simulated results indicated that when gap size increases, the electric field component in the horizontal direction also increases, thereby favouring the alignment of nano-fibres. However, one of the main disadvantages of this set-up is that the width of the gap restricts the fibre length that can be produced. The whipping jet diameter must be wide enough to cover the width of the parallel plate; this can be altered by adjusting the voltage during production [12]. In this technique, the residual charge on the suspended fibres was reported to be responsible for repelling the incoming charged fibres. Therefore, a low electro-spinning time will result in a low fibre density with a correspondingly low degree of alignment because the fibres are not close enough to repel one another [150]. Moreover, a low-humidity environment is also necessary to slow the charge dissipation rate from the fibre surface [15]. Yusuf *et al.* [185] showed that increasing gap width decreased the fibre diameter from 629 ± 20 nm (5 mm) to 478 ± 2 nm (20 mm) when spinning with 15 wt% PVA. Liu and Dzenis [184] reported that alignment increased non-linearly with the increased gap size. Beachley *et al.* [84] reported that an excessive gap requires that the fibre have a high solidification rate, high stretchability, and sufficient strength to support its own weight to avoid fracturing after deposition. The choice of electrode material can also influence the orientation of the electro-spun fibres.

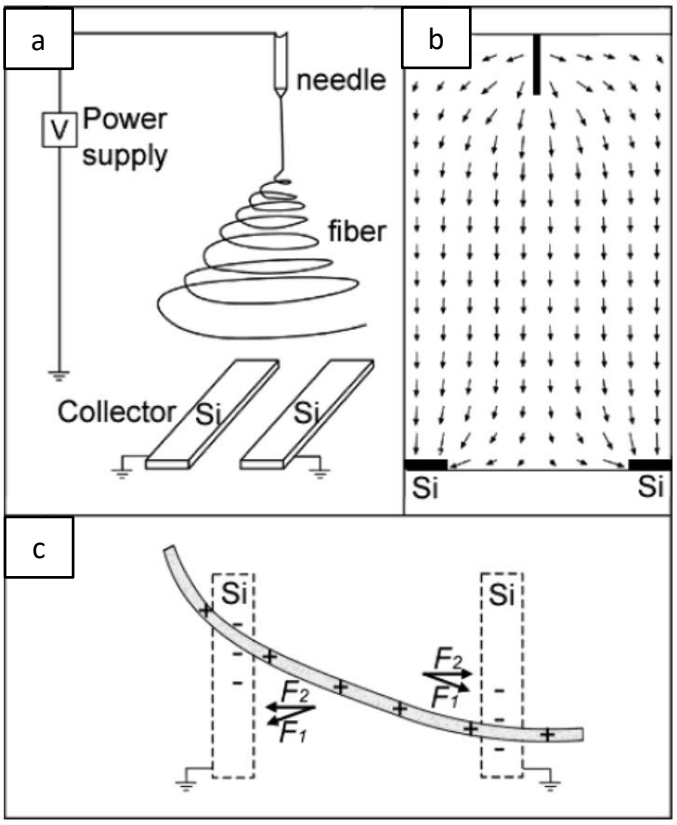

Figure 2.2.5 (a) Schematic illustration of the parallel electrode set-up using a pair of conductive silicon stripes for electro-spinning to generate uniaxially aligned nano-fibres. (b) Simulated electric field strength vectors in the region between the needle and the collector. (c) Electrostatic force analysis of a charged nano-fibre spanning across the gap. The electrostatic force (F1) resulting from the electric field and the Coulomb interactions (F2) between the positive charges on the nano-fibre and the negative image charges on the two grounded electrodes [149].

Furthermore, it was reported (see Figure 2.2.6a and b) that parallel electrodes constructed with high dielectric constants (ferrite materials with dielectric constant = 12) tend to form more aligned fibres than materials with low dielectric constants (epoxy resin with dielectric constant = 4) [186]. This may be because materials with high dielectric constants are

concentrating the electrostatic lines more efficiently and hence creating a denser electric field. Referring to the alignment mechanism shown in Figure 2.2.5c, parallel electrodes with low electrical conductivity, were possibly less efficient in attracting and dissipating residual charges on the fibre, which in turn led to low fibre alignment. However, low-conductivity dielectric materials can also be used to align fibres; this will be reviewed further in Section 2.2.4.1.

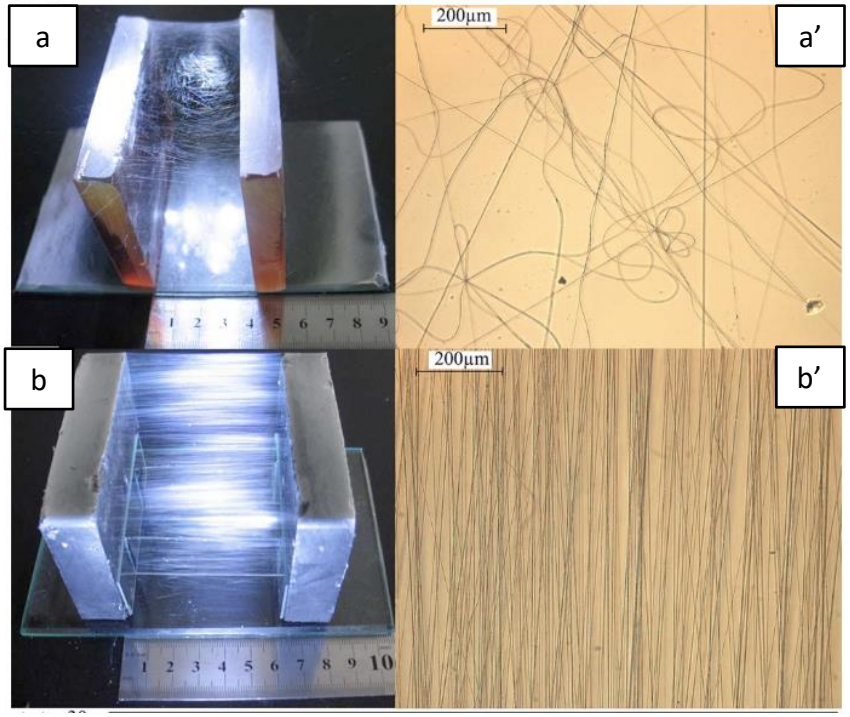

Figure 2.2.6 (a) and (b) Digital camera images of prepared nano-fibre mesh using epoxy and ferrite as the collectors, respectively. (a', b') Optical micrographs of (a, b), respectively. [186]

Secasanu *et al.* [187] computed the electric fields of parallel electrodes with different edge geometries as shown in Figure 2.2.7a, b and c, representing standard parallel electrodes, a single pointed electrode and sharpened electrodes, respectively. In the case of the sharp electrode tips with a chamfer angle of 26.6°, the electric field strength is higher and there is a

larger local voltage drop. This results in a higher possibility of fibres being deposited across the two tips. Compared to flat electrodes, sharpened electrodes can gather four times more aligned fibres.

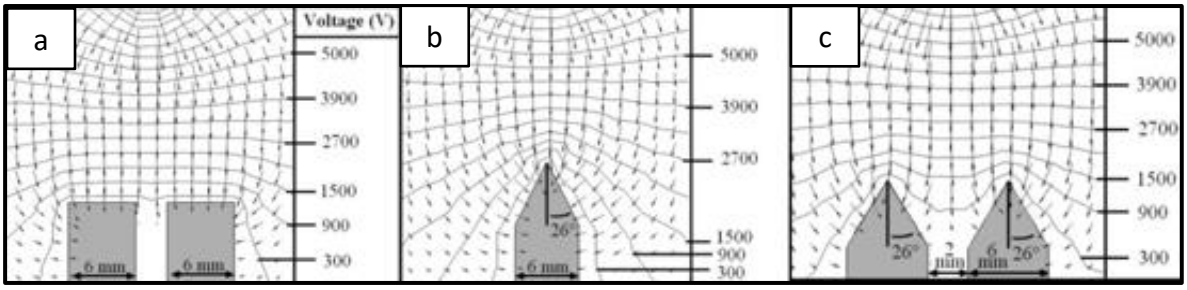

Figure 2.2.7 Electric fields simulated for (a) standard parallel electrodes, (b) single sharpened electrode and (c) a pair of sharpened parallel electrodes [187].

Although the parallel-plate electrode design offers a practical method to produce fibres with a high degree of alignment, with more than 80% of the fibres aligned, the length of the resultant fibre is generally limited to between 10 mm and 80 mm [186]. One possible explanation is that the diameter of the fibre whipping area is generally limited to this range, and the whipping diameter needs to be similar to, or larger than, the gap distance of the parallel electrodes [150, 188]. By adding another electrode between the parallel electrode with an opposite charge, the fibre length can be increased using a three-electrode set-up, as shown in Figure 2.2.8 [189]. Haseeb [189] created a triple parallel electrode array collector with two side electrodes of different polarity to that of the middle electrode, which had the same polarity as the needle. The purpose of this additional electrode was to repel and stretch the fibre during deposition. However, it was reported that the downside of the set-up was that a large number of fibres were either lost or deposited directly onto the negative electrodes [189].

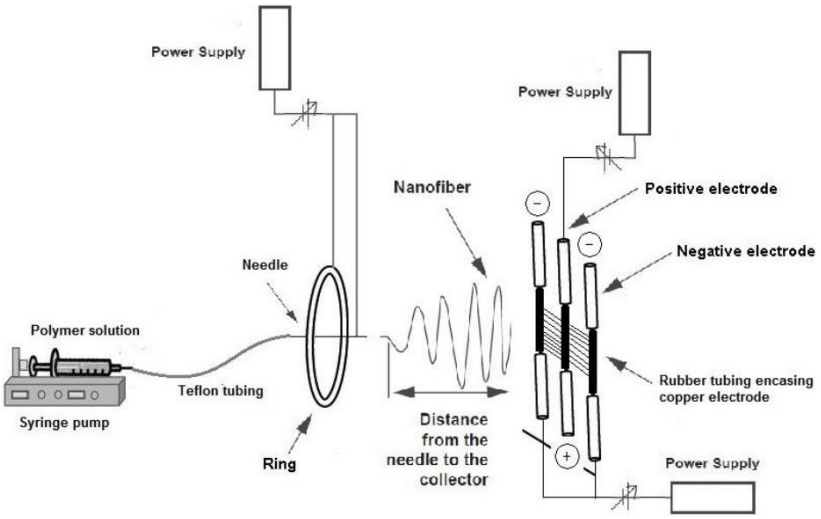

Figure 2.2.8 Schematic illustration of the triple parallel electrode grounded electrode configuration [189].

Park *et al.* [190] showed that parallel electrodes with an inclined spacing (see Figure 2.2.9a) could increase the fibre alignment across the gap compared with parallel electrodes arranged on the same plane. Hsu *et al.* [191] modified Park's set-up by replacing the clean edge collector with a serrated tooth-edge collector (see Figure 2.2.9b). Hsu *et al.* studied the influence of the collector parameters such as gap length, pitch length and notch angle on fibre alignment. Using 3D COMSOL model simulations (see Figure 2.2.9c and c'), they demonstrated that a sharp tooth angle, short pitch distance and short gap distance resulted in the formation of multiple independent fibre bundles. Moreover, they also showed that the pitch length must be smaller than the gap distance in order to produce fibre bundles.

Cai *et al.* [188] produced highly aligned electro-spun PVDF fibres with a maximum length of 60 cm; they used a *U*-shaped parallel electrode collector when electro-spinning with a solution of PVDF/DMF/acetone. A schematic illustration of their set-up is shown in Figure 2.2.10a. The main difference in the approach used by Cai *et al.* [188] was to apply a negative voltage to the

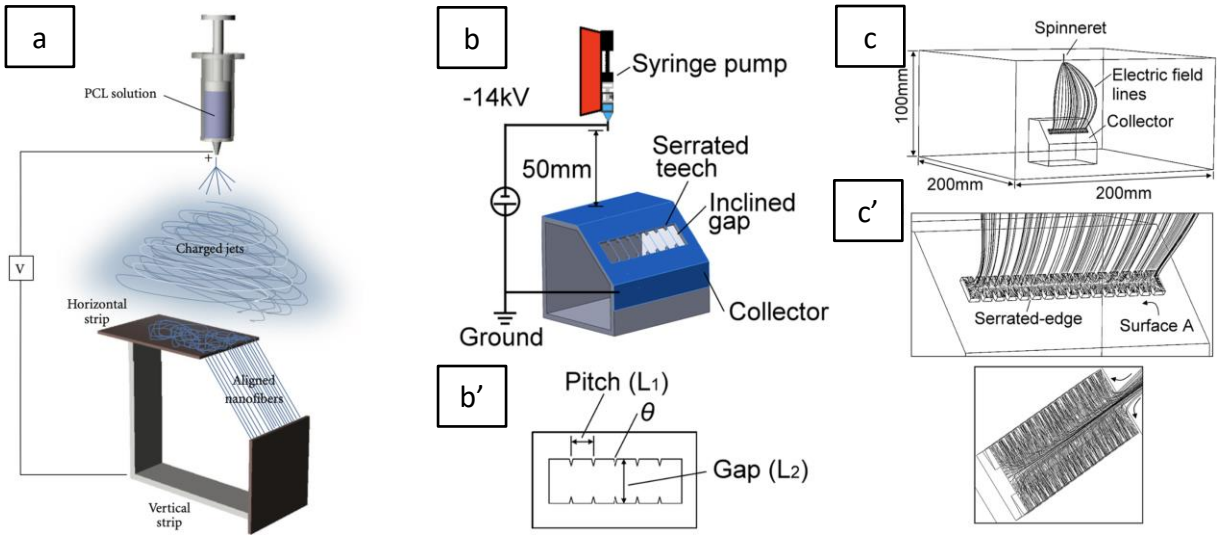

Figure 2.2.9 (a) Schematic diagram of the electro-spinning set-up for the inclined gap method designed by Park et al. [190]. (b) Illustrations of the experimental set-up for the serrated-edge incline gap collector designed by Hsu et al. [191]. (b') Three design parameters used for the serrated-tooth set-up (b). (c) 3D finite-element simulation with COMSOL showing the overall set-up. (c') Close-up view of the 3D electric field profile around the serrated-edge incline gap [191].

collector rather than ground it; they postulated that the discharge mechanism of the grounded electrode was to create an image charge on the surface of the electrodes and neutralise it when charged fibres were deposited onto it. Since the Coulomb interactions are inversely proportional to the square of the separation between two charges (refer to Equation (*2.11*)), only the jet adjacent to the electrode would be affected and stretched. Although the electric field lines simulated were similar, applying a negative voltage to the collector was shown to effectively attract the charges on the fibre jet and force it to move back and forth [188]. However, the SEM micrograph they presented showed a relatively low fibre density compared to that of the other parallel electrode methods.

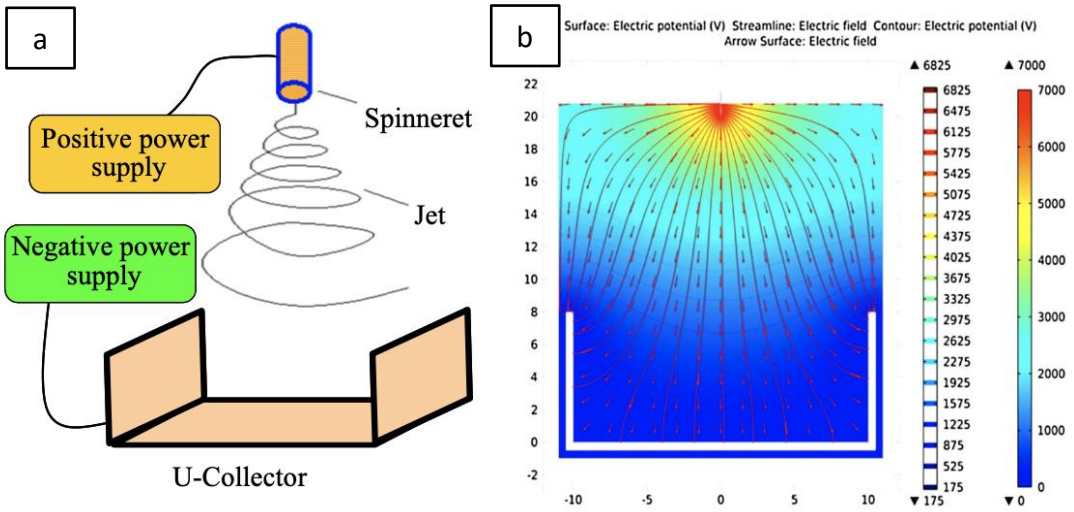

Figure 2.2.10 (a) Schematic illustration of the electro-spinning set-up of the U-shaped collector. (b) COMSOL simulation of the set-up [188].

2.2.2.2. Auxiliary Electrodes

Based on the parallel-plate electrode alignment method, multiple electrodes, such as 'steering' or auxiliary electrodes, have also been used to improve the alignment of the electro-spun fibres; steering electrodes are usually placed between the needle and the grounded collector. The basic function of the auxiliary electrodes is to modify the electric field between the spinneret and the grounded electrode. Such electrodes may be one or more ring-shaped electrodes placed in a row, as shown in Figure 2.2.11a and b [152], or parallel electrodes facing each other (see Figure 2.2.12a) [192].

The effect of these auxiliary electrode rings on the electric field has been simulated by Deitzel *et al.* [152] (see Figure 2.2.11b). Eight auxiliary copper ring electrodes were separated evenly across the 20 cm working distance from the tip of the needle to the target. The needle was charged at +9 kV, the collector was charged at –11 kV, and all the copper rings were set at +5 kV. In contrast with the electric field simulation of the conventional set-up (from the same

group) demonstrated in Figure 2.2.1b, the arrowed field lines show that the ring-electrodes suppress the field lines into the centre of the geometry, thereby reducing the whipping radius as well as the diameter of the deposition area. They observed that the fibre deposition changed from 7 cm to 1 cm, when the ring-electrodes were introduced.

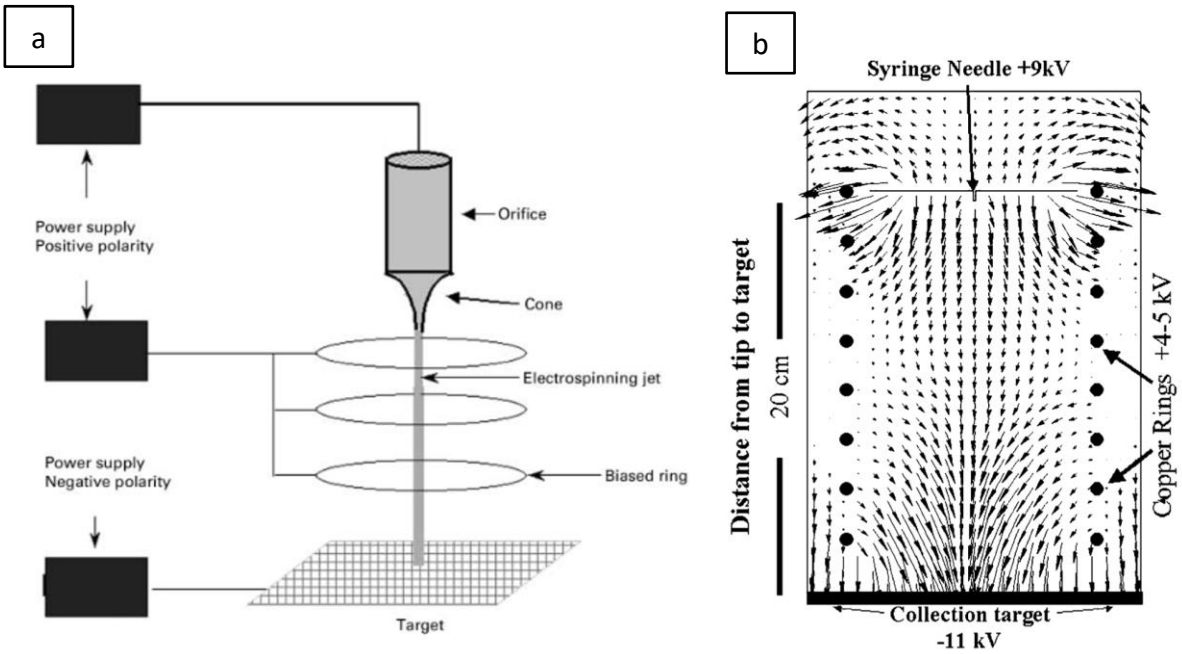

Figure 2.2.11 (a) Schematic illustration of multiple-ring auxiliary electrode configuration to produce aligned electro-spun fibres. (b) Electric field simulation of the auxiliary ring electrode set-up [152].

The shape of the auxiliary electrodes can also be a pair of parallel rectangular electrodes facing each other. Arras *et al.* [192] used a pair of rectangular 'steering' electrodes to influence the trajectory of the polymer jet. Their experimental setup is shown in Figure 2.2.12a. The fibre deposition area was suppressed when auxiliary electrodes were activated (see Figure 2.2.12b). Acharya *et al.* [18] used a similar design to that illustrated in Figure 2.2.12a and showed improved fibre alignment when using parallel plates in addition to a pair of positively charged steering electrodes.

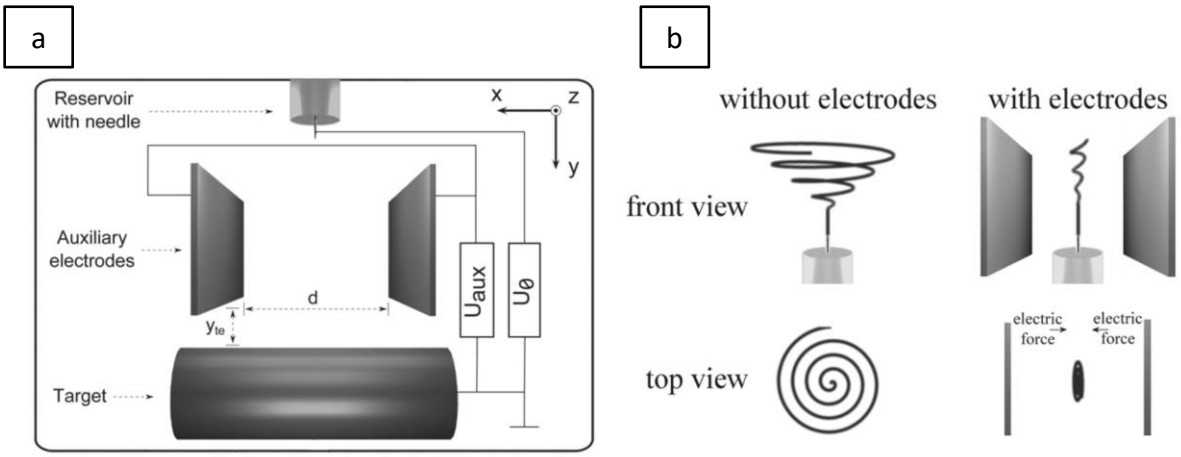

Figure 2.2.12 Schematic illustration showing: (a) the set-up for the auxilary parallel electrode and primary electrode configuration. U_{aux} and U_0 refer to the voltage on the auxiliary and primary electrodes; and (b) the effect of the electrodes on the trajectory of the jet and the deposition area [192].

An auxiliary electrode need not be placed between the needle and the collector. Kiselev *et al.* [193] demonstrated a way to reduce or even eliminate fibre bending instability: a 100 cm^2 conductive metal guard plate electrode with a hole in the centre was added to the set-up, with the needle inserted through the hole so that it is protruded by 20 or 30 mm. Schematic illustration of their experimental set-up is shown in Figure 2.2.13. They reported that aligned fibres could be produced with a relatively low mandrel collector rotation speed (4.71 m/s). Moreover, the method was reported to be capable of producing 100% highly aligned fibres that were distributed within 4°. This was achieved when the surface rotation speed of the mandrel was around 3.5 m/s for PEO and between 4.0 m/s and 6.1 m/s for PS/DMF. Unfortunately, Kiselev *et al.* [193] offered no explanation as to the reason for this phenomenon or the simulation.

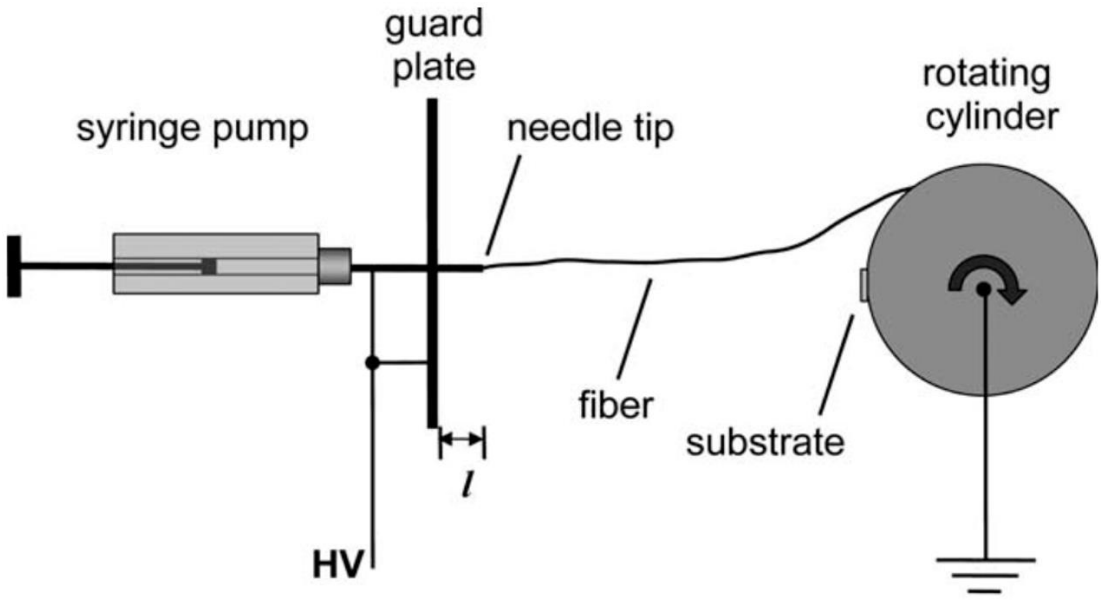

Figure 2.2.13 Schematic illustration of guard-plate auxiliary electrode fibre alignment set-up [193].

A simulation of the set-up shown in Figure 2.2.13 was completed by Yang *et al.* [194], who reported that the electric field lines became more uniform when a guard plate of dimensions 295 mm x 185 mm as introduced. As can be seen in Figure 2.2.14, unlike auxiliary electrodes, guard plates share the same electric potential as the needle, and the field uniformity increases as the position of the plate comes nearer to the needle tip. However, Yang *et al.* found that higher field uniformity near the needle tip required a higher electric potential to emit the jet from the Taylor cone. Furthermore, although the potential applied was higher, due to the electrostatic force along the *X*- and *Y*-component at the bending point (where bending instability starts), the bending instability was significantly reduced by the guard plate. The stable region of the jet was found to increase and the whipping area decreased, when the potential was increased.

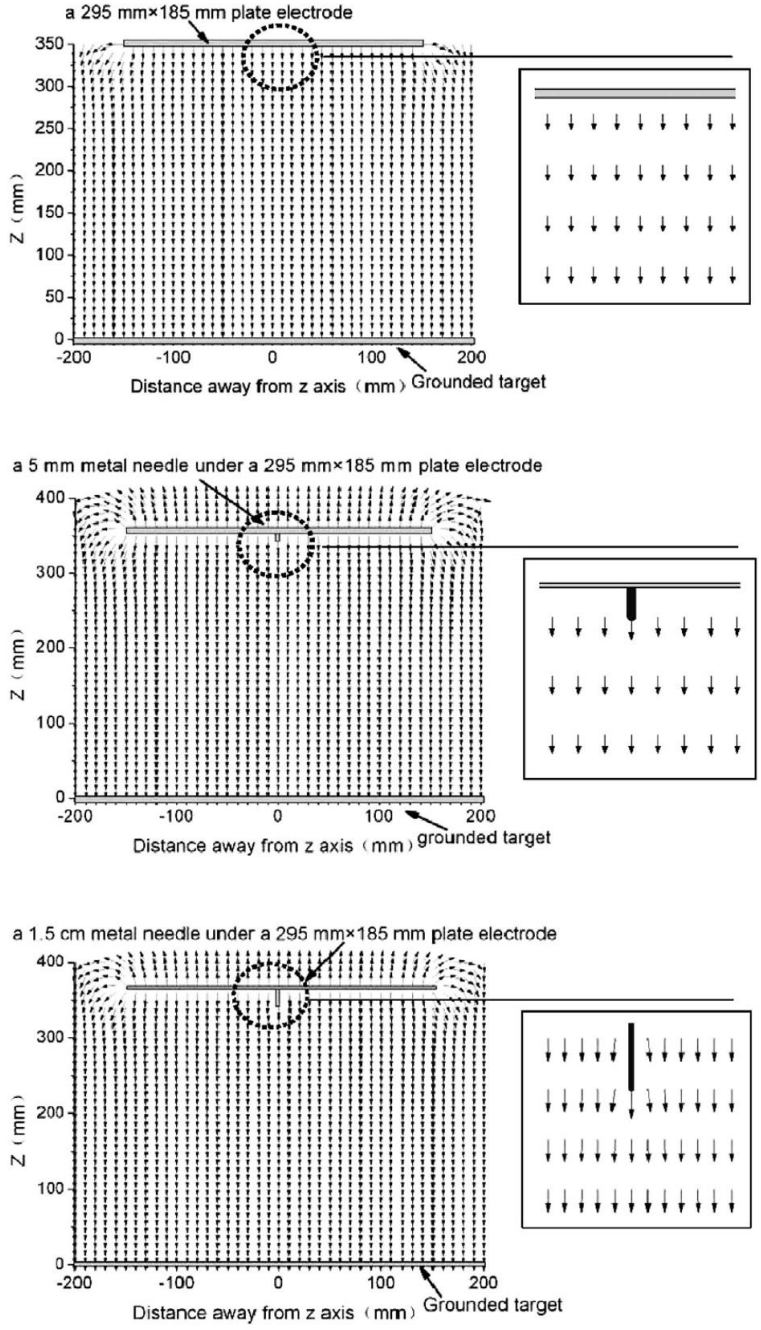

Figure 2.2.14 Electric field simulation of guard plate electro-spinning set-up with different plate positions reported by Yang et al. [194].

Cui *et al.* [195] and Ravichandran *et al.* [196] modified the electric field even further by combining the guard-plate and auxiliary-ring set-ups. Using COMSOL software, Cui *et al.* [195] established the electric field lines and the plot of the horizontal components of the electric

field strength (see Figure 2.2.15d) along the vertical cut line (lines 1, 2 and 3 in Figure 2.2.15a–c) through the centre of the whole geometry. They showed that the combined electrode configuration exhibited advantages from both methods, namely that the electric field strength of the horizontal components is uniform at the tip of the needle and becomes convergent at approximately 23 cm below the needle tip. In other words, the jets are initially less divergent but begin converging towards the centre of the field, where most of the electric force acts vertically towards the collector. Cui *et al.* further reported that this set-up significantly reduced the bending instability when electro-spinning PVP in ethanol. They elaborated that fibres could be aligned on the rotating collector with a linear velocity of 0.89 m/s; But, helical fibres were found at this velocity. However, they found that this could be eliminated when the linear velocity was increased to 6.7 m/s [195]. As a comparison, the minimum linear speed required to produce highly aligned fibre using the rotating mandrel set-up was 2.0 m/s when spinning PEO in water [14] and 5.3 m/s when spinning PEO in water and ethanol using the rotating disc method [151]. Referring to the alignment mechanism of the rotating collectors described in Section 2.2.1.1, it appears that the guard plates and auxiliary electrodes suppress only the whipping radius; they do not appear to suppress the whipping frequency. The whipping rate and extension rate of the jet are affected predominantly by polymer and solution parameters [171, 193].

Based on the papers mentioned above, the presence of the auxiliary electrodes significantly reduced the whipping of the polymer jet. However, collectors such as rotating mandrels must still be used to achieve the alignment. The previously described limitations of the rotating method still apply here.

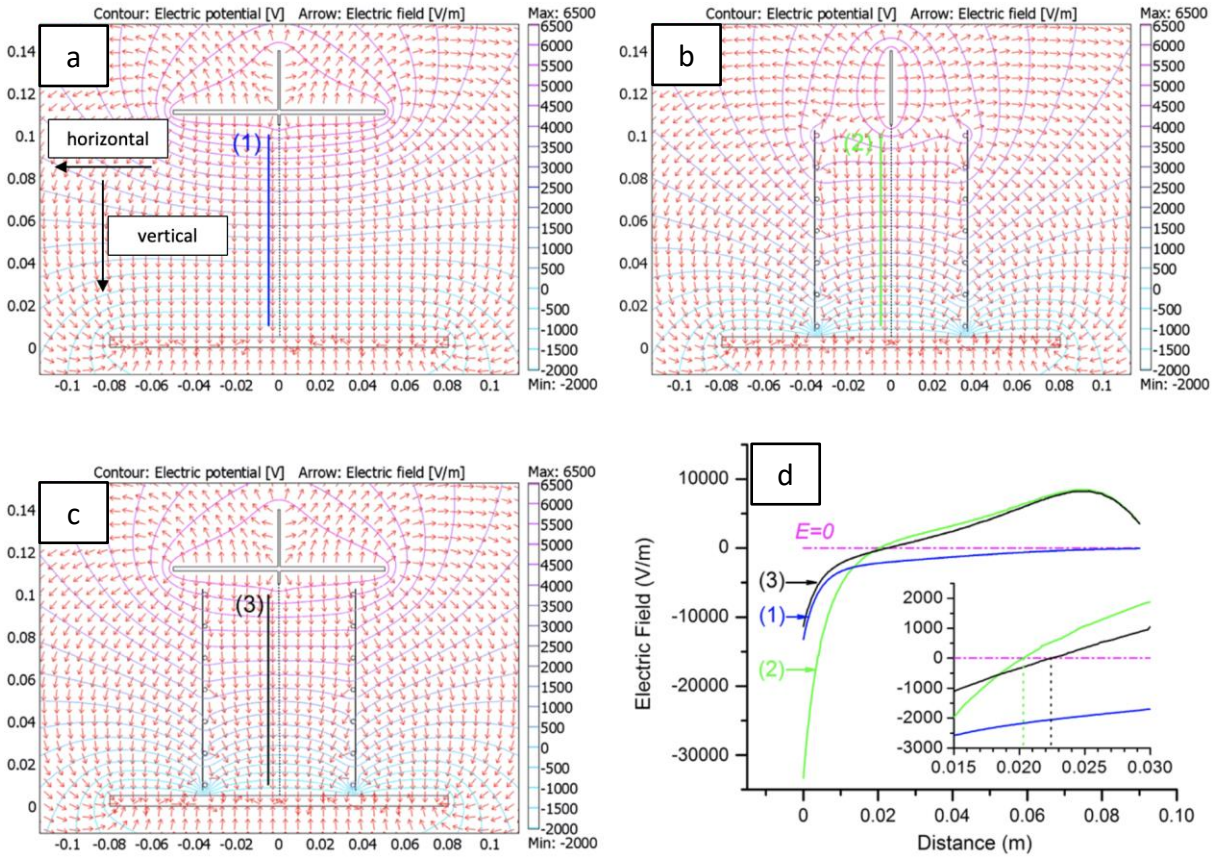

Figure 2.2.15 Simulation of the electric field distributions and the electric potential contours when (a) the guard electrode, (b) the auxiliary ring electrodes, and (c) both the guard electrode and auxiliary ring electrodes are introduced to the electro-spinning set-up. (d) The plot of the horizontal components of the electric field strength along the centre line [195].

2.2.3. Hybrid Alignment Methods

2.2.3.1. Variants of the Rotating Mandrel

In order to capitalise on the advantages of the rotating mandrel and parallel electrode fibre alignment methods mentioned in Sections 2.2.1 and 2.2.2, researchers have used hybrid systems that combine both methods to create longer and oriented electro-spun fibres. The simplest way to combine these two concepts is to change the surface of the rotating mandrel

into bars [178] or fins [197]. These bars and fins act as parallel electrodes that can 'steer' the movement of the whipping jet path into the direction of the rotation. Schematic illustrations of these two hybrid methods are shown in Figure 2.2.16a and b, respectively.

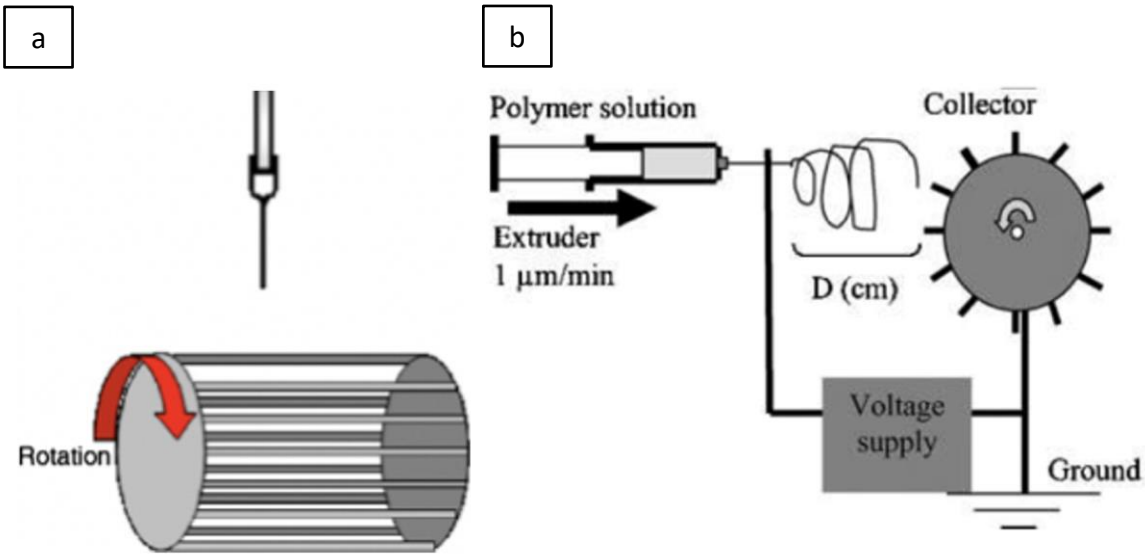

Figure 2.2.16 Schematic illustrations of (a) the rotating bar mandrel [178], and (b) the rotating fin mandrel [22].

Although these two set-ups apply the same concept, the resultant fibre alignment differs. Afifi *et al.* [22] report that, using the fin mandrel, 60% of the fibres were aligned within ± 5°, whereas the bar-based mandrel achieved 75% alignment. One potential explanation for this result may be that the fin collector generates more air turbulence than the bar collector. However, the degree of fibre alignment obtained from the bar mandrel decreased as spinning time increased; this trend is similar to that observed in the conventional rotating mandrel set-up in Section 2.2.1.1. Both papers [178, 197] reported that highly aligned fibres could be obtained with a lower drum rotation rate of ~1 rpm compared to the conventional mandrel design which operates at around 3,000 rpm. This is likely due to the fin and bar electrodes

acting as parallel electrodes, which helps to improve the alignment at low rotation speeds.

Changing the shape of the rotating mandrel to a disc (see Figure 2.2.17a) is another way to change the electric field lines. This concept was first demonstrated by Theron *et al.* [151]; by changing the conventional collector to a 26.6° sharp-edged rotating disc. The sharp edge provides a high localised electric field strength, and the fibres are attracted to this sharp rotating contour. In this method, the whipping movement of the fibre changes from that of a cone to that of an oval. This is because the sharp-edged collector guides the electric field lines to the edge of the collector (see Figure 2.2.17b), thereby causing the whipping radius to diminish as it reaches the edge of the disc. This can be seen in the high-speed photograph shown in Figure 2.2.17c [151].

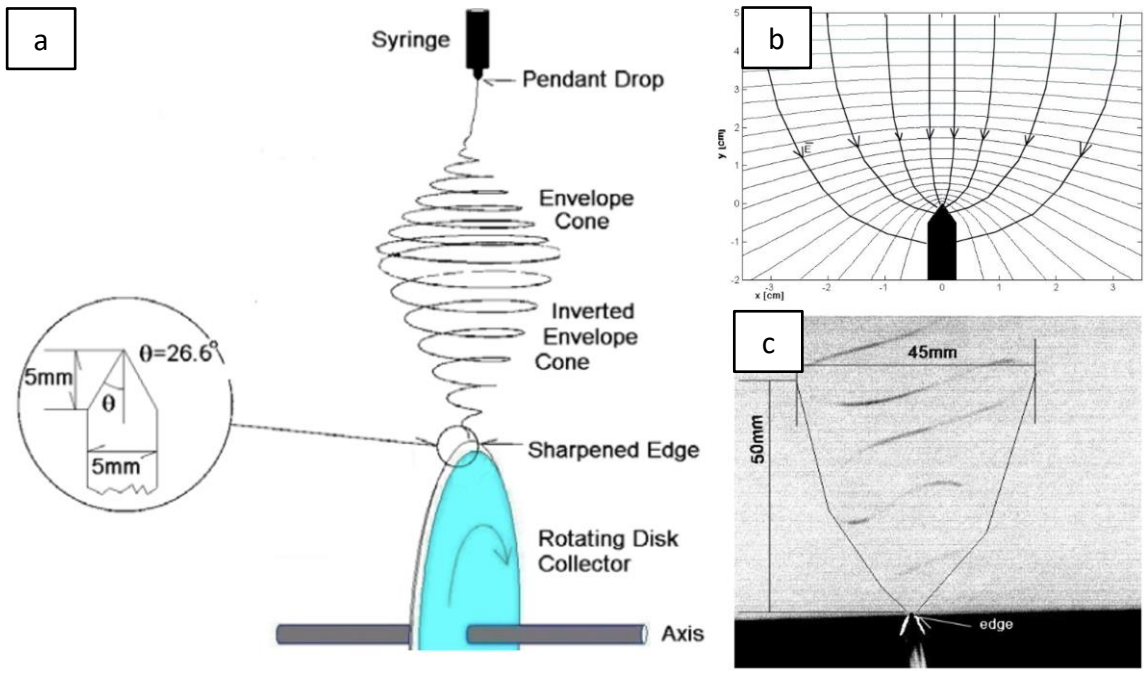

Figure 2.2.17 (a) Schematic illustration of the sharp-edged rotating disc set-up. (b) electric field simulation at the tip of the collector. (c) Photograph captured at the tip of the collector [151].

The disc design significantly reduces air turbulence during rotation when compared to the mandrel-based collector. This concept has been transformed into numerous designs, such as guiding electrodes [198, 199] and the end-point control method [200]. Sections 2.2.3.2 and Section 2.2.4.1, respectively, will describe these two designs in further detail.

2.2.3.2. Guiding Electrodes

The guiding electrodes can be understood as a variant of the sharp rotating disc electrodes set-up (see Figure 2.2.17a), with the difference being that the guiding electrodes are generally placed outside the area between the needle and the collector surface. The guiding electrodes are typically metal parts containing sharp-tipped metal, which is used to significantly increase the electric field strength at its tip and to guide the trajectory of the polymer jet. Furthermore, the collector in this set-up is neither grounded nor a conductor.

A typical set-up using a guiding electrode as demonstrated by Sundaray *et al.* [198] is illustrated in Figure 2.2.18. With reference to Figure 2.2.18, a sharp stainless-steel pin was mounted vertically on a traversing arm, and pointed towards the needle. A thin polystyrene sheet was used to collect the fibres by wrapping it around a cylindrical frame. Using this method, fibres of PS in tetrahydrofuran with 25 w/w% and PMMA in chloroform with 20 w/w% were obtained. Sundaray *et al.* [198] reported that a high degree of fibre alignment was achieved for both polymers when the rotation speed reached 2.5–3.0 m/s with only 4.8 kV applied. Furthermore, they showed that manually rotating the substrate could produce cross-ply patterns in two mutually perpendicular directions on the same substrate [198].

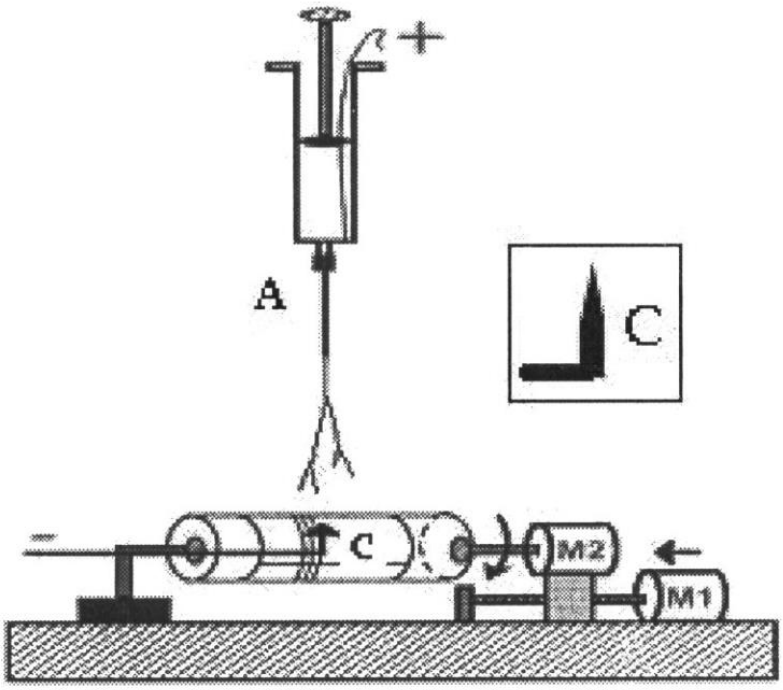

Figure 2.2.18 Schematic illustration of the guiding electrode alignment method proposed by Sundaray et al. [198]. The polymer solution is taken in a syringe with a fine wire inserted as electrode (A). A steel pin aligned exactly with the needle of the syringe is used as counter electrode (C). A view of the pin (C) is shown in the inset. A 1-mm-thick flexible plastic film wrapped around an insulating cylinder attached to the axle of a dc motor (M2) is used as the substrate. The dc motor assembly is mounted on a plastic block. This block along with M2 and substrate can be moved linearly parallel to the axis of the cylinder using a step-motor lead-screw arrangement [198].

Instead of inserting the electrode inside the mandrel, Teo *et al.* [201], reduced the diameter of the mandrel, changed the mandrel material to Teflon, and placed grounded aluminium flat strips or knife-edged aluminium strips below the rotating Teflon mandrel (see Figure 2.2.19a and b). They found that the fibres collected on the Teflon tube, when using the knife-edged aluminium strips, showed greater circumferential alignment when compared to the case when

the aluminium flat strips were used. The percentage of fibre aligned to within less than 4° increased from around 15% for the flat strips to 37% for the knife-edged strips. Once again, this demonstrates that sharp edges have the ability to concentrate and attract the field lines [201].

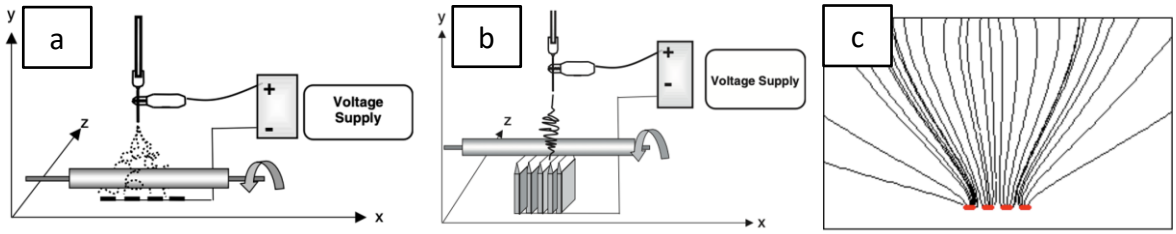

Figure 2.2.19 Schematic illustration of the electro-spinning set-up for: (a) counter-electrodes consisting of flat aluminium strips; and (b) knife-edged aluminium strips; and (c) showing the simulated electric field lines for set-up (a) [201].

Wu *et al.* [202] replaced the knife-edged aluminium strips (shown in Figure 2.2.19b) with three rod-like guiding electrodes that were placed parallel to each other with a set distance in-between (see Figure 2.2.20a), and located behind the rotating collector. However, instead of being grounded, these electrodes were connected to high-voltage power supplies, with the centre electrode charged positively and the two on either side charged negatively. The percentage of fibre aligned between 80–90° increased from 19.6%, without guiding electrodes, to 72.5% with guiding electrodes. Additionally, Wu *et al.* found that fibre density and degree of alignment increased when the gap between these guiding electrodes decreased. In their electric field line simulation, as the gap decreased, the field lines became more focused towards the centre electrode [202].

The use of guiding electrodes can be used to separate the role of collector and electrodes, which allows the aligned electro-spun fibre to be collected onto a non-conducting substrate. In some cases, this can prevent fibres from adhering onto the substrate, thereby enabling easy removal and reducing loss during transfer. However, in this case, due to the guiding electrodes being placed at a certain distance from the collector, the residual charge on the fibre surface can dissipate only through the air. The amount of fibre and the thickness of the mat that can be collected onto the substrate depends on the charge dissipation rate, which is in turn controlled by the humidity of the processing environment.

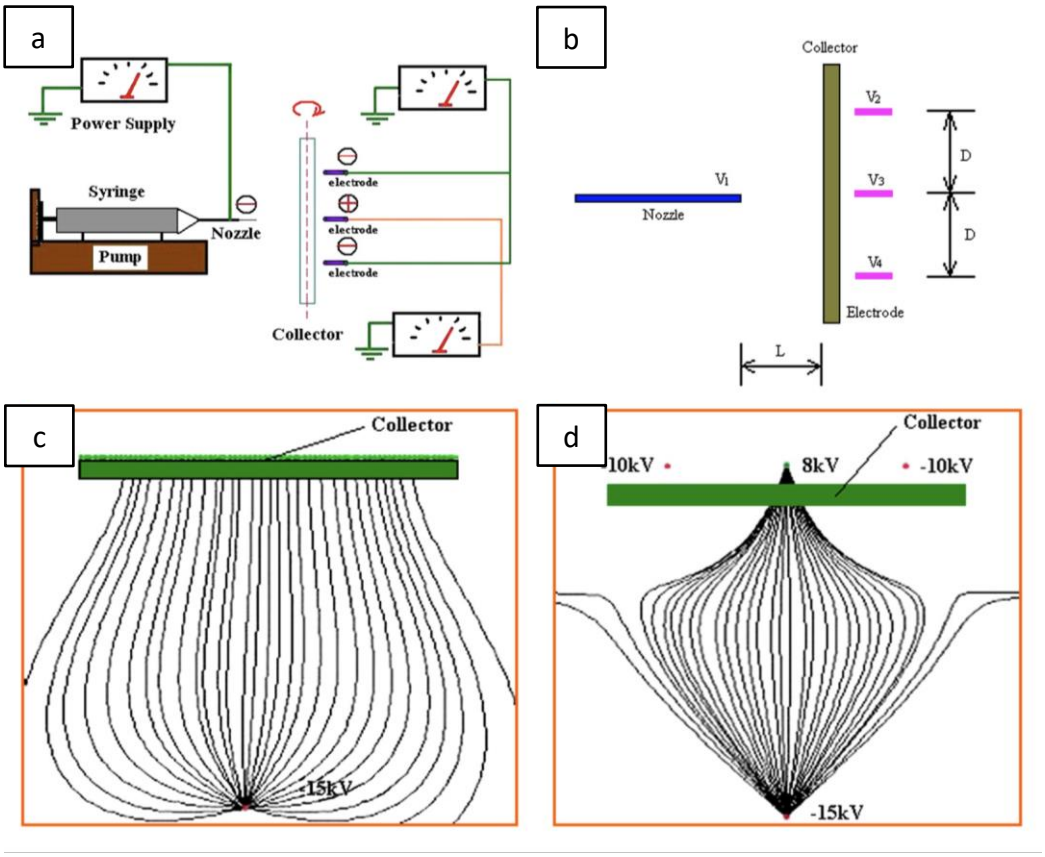

Figure 2.2.20 (a) Schematic illustration of the focused electro-spinning set-up with three auxiliary electrodes. (b) Design parameters of the set-up (a). Electric field line simulation of (c) conventional set-up and (d) focused electro-spinning set-up [202].

2.2.4. Other Nano-fibre Alignment Methods

2.2.4.1. Dielectric Insulating Materials

During electro-spinning, due to the fact that electro-spinning is the effect of the movement of charged particles [203], several researchers have shown that although the current in the polymer jet is minimal, it could nevertheless be detected using the set-up illustrated in Figure 2.2.21 [10, 203-205]. Deitzel *et al.* [10] found that the current value in their experiment was in the range of 7–11 nA. Therefore, low electrically conductive dielectric insulating materials can be introduced to modify the moving path of charged jets and thereby produce aligned fibres by controlling the jet trajectory.

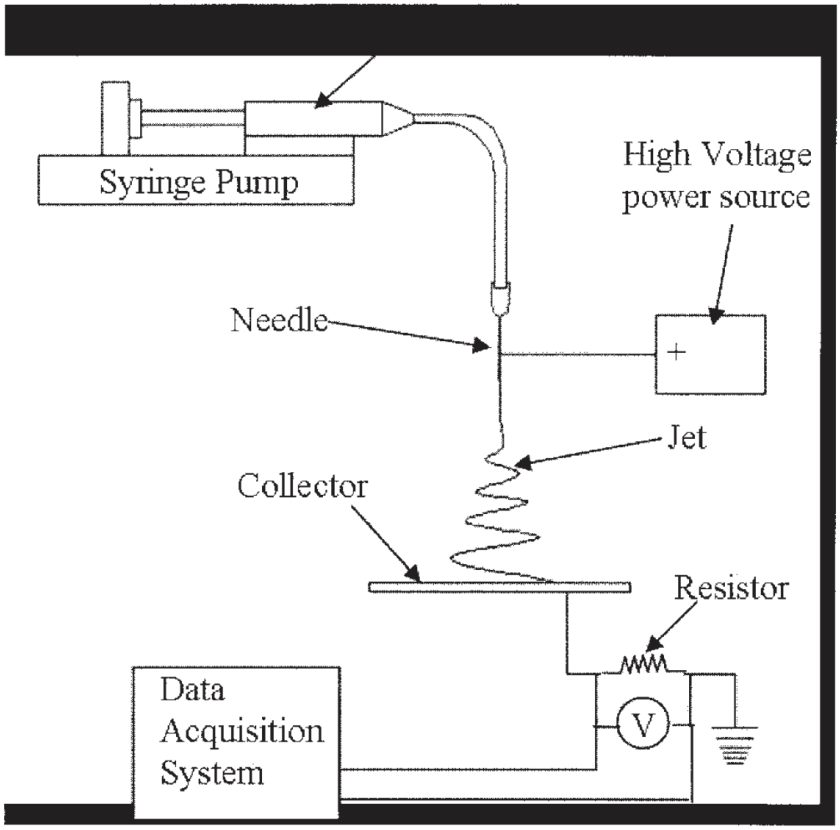

Figure 2.2.21 Electro-spinning current measurement set-up [203].

The concept of the rotating disc fibre alignment set-up (see Figure 2.2.17a) was modified by Nguyen *et al.* [200]. Unlike the rotating disc electrodes, the set-up of the end-point controlling method (as shown in Figure 2.2.22a) retains the rotating metal mandrel. Instead of changing the shape of the rotating mandrel to a disc, Nguyen *et al.* used two pieces of polyimide film on the top with a variable gap distance at the centre. A gap of 5 mm in the centre of the mandrel was set and examined in their study; the fibres were deposited within the gap. 80% of the fibres were said to be aligned to within 3° when the mandrel rotation rate was 3500 rpm [200]. They simulated the set-up using COMSOL (see Figure 2.2.22a'–d') and presented results of the electric field strength rainbow graph, the electric potential rainbow contour graph, and the electric current density graph. Due to the presence of the dielectric material in the system, the current vector graph was introduced into the simulation. Nguyen *et al.* concluded that applying the dielectric film has the same convergent effect on the field as that of the rotating disc collector [200].

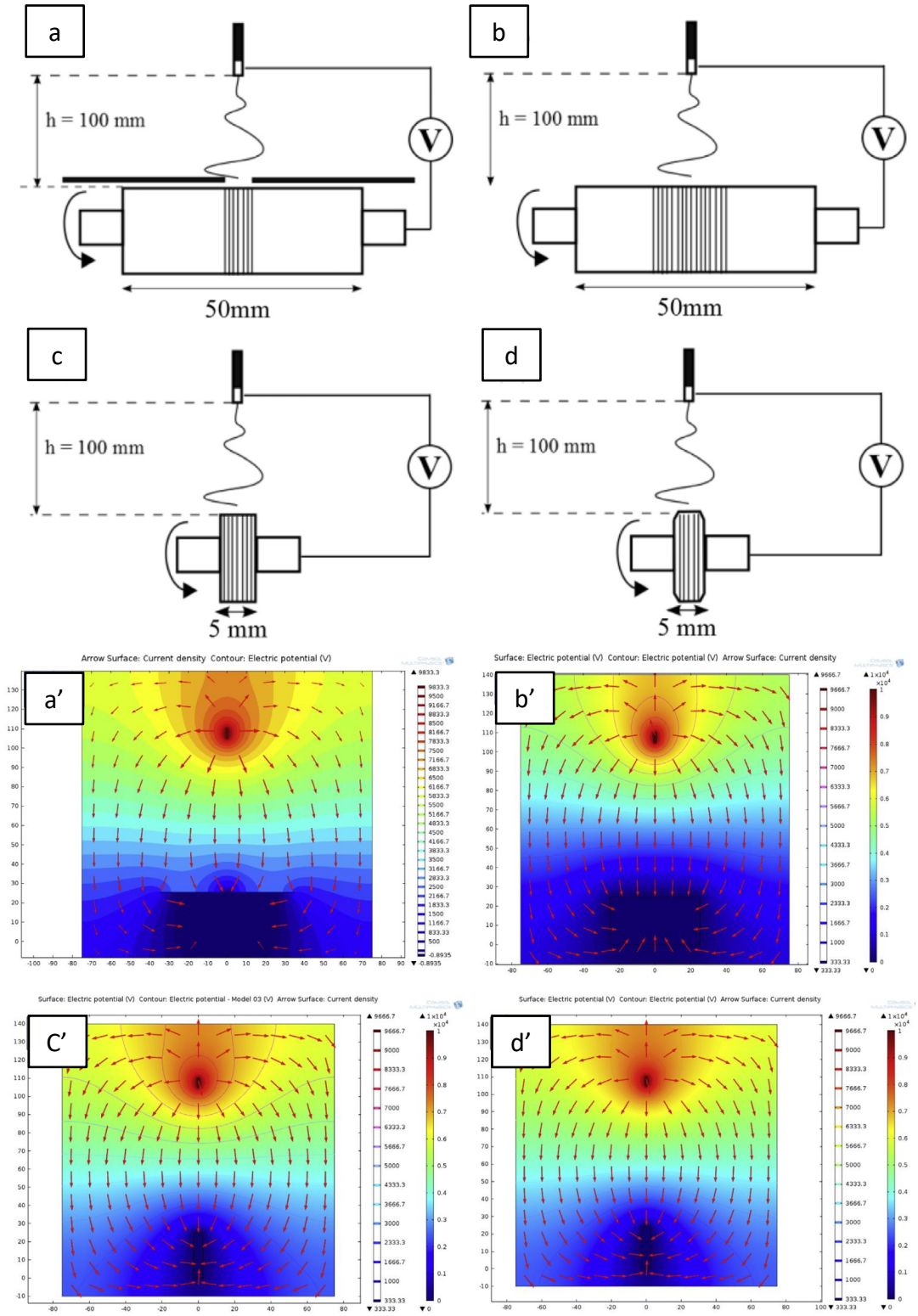

Figure 2.2.22 Schematic illustrations of various fibre alignment methods proposed by Nguyen et al. [200] and their corresponding simulation results.

A dielectric material was also introduced by Hwang *et al.* [206] in their experimental set-up. They place two identical insulating blocks 14 mm above the conventional collector. The dimension of the blocks were 50 mm × 30 mm × 50 mm with relative permittivity of 4. Unlike the traditional auxiliary electrode alignment set-up illustrated in Figure 2.2.12a, no external potential was applied to these insulating blocks. They found that the fibre trajectory was controlled, and the whipping was suppressed. The polymer jet moved back and forth along the gaps between these blocks (see Figure 2.2.23c). Aligned fibre arrays were produced by shifting the position of the collector perpendicular to the alignment direction under a certain speed. Unfortunately, the degree of fibre alignment was not reported [206].

Using the COMSOL simulation software, Hwang *et al.* [206] examined the electric field strength of all three axes separately from the tip of the needle to the centre of the collector. They found that the difference between electric field intensities at the centre and the edge was more significant when insulating blocks were employed (see Figure 2.2.23d). Therefore, this shows that the electrified polymer jet can be confined in the region between the insulating blocks, causing the direction of the jet motion to change from 3D to 2D. They also proved the concept using high-speed imaging [206].

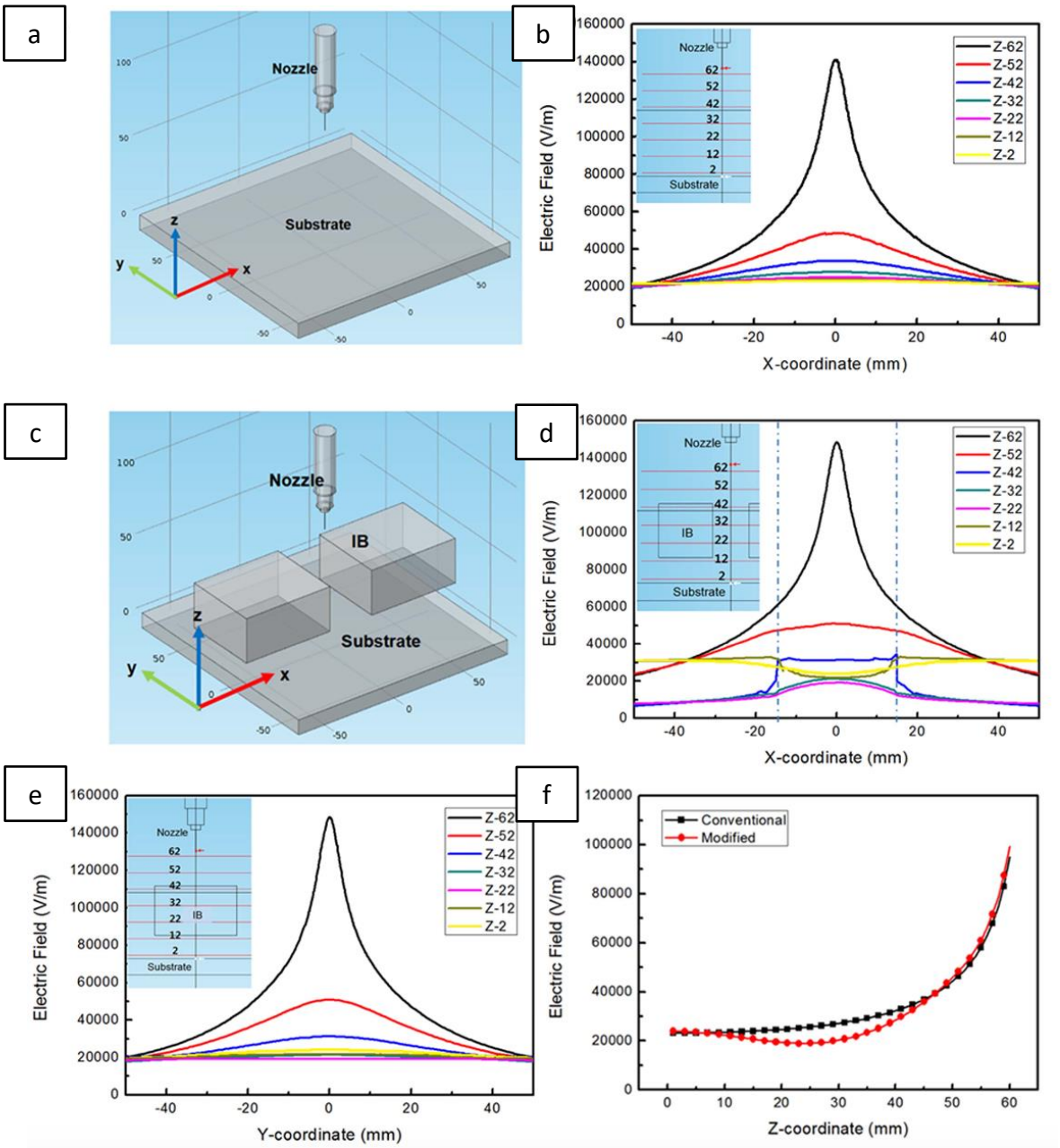

Figure 2.2.23 3D schematic diagrams of (a) conventional electro-spinning set-up and (c) insulating block method. Electric field simulation result of (b) conventional set-up, (d-e) insulating block method along X- and Y-axis. (f) Comparison of the electric field strength of the conventional and the modified set-up at the centre position [206].

2.2.4.2. Magnetic Field-assisted Alignment Method

Some researchers introduce magnets instead of using positively charged auxiliary electrodes to influence the electric field between the spinneret and the grounded electrode [20, 23, 207-210]; magnets with opposite poles facing each other were placed between the spinneret and the grounded collector. The results of the above-referenced studies indicate that the charged polymer jet experienced a radial Lorentz force as it travelled through the magnetic field. The force can be estimated using Equation (2.13) [211]:

$$F = qE + qv \times B \tag{2.13}$$

where *F* is the Lorentz force, *q* is the charged particle (C), *E* stands for the electric field (V/m), *v* stands for the velocity of charged particle (m/s), and *B* is the magnetic field (T). If the directions of the magnetic field and charged particle movement are known, the direction in which the Lorentz force is acting can be determined using the right-hand rule [211]. Higher applied voltage and solution conductivity can result in increased electric field strength and charge density, which results result in higher Lorentz force.

Liu *et al.* [23] placed two magnets with opposite poles facing each other to the left- and right-hand sides of the grounded collector (see Figure 2.2.24). Their results when spinning PVP/ethanol and PLGA/1,1,1,3,3,3-hexafluoro-2-propanol showed that no magnetic nanoparticles were required to align the fibre. The charged fibres were said to be attracted onto the collector and stretched across the gap of two opposite magnetic poles along the direction normal to the magnets' surface [23]. Using the same set-up, Mei *et al.* [80] also illustrated that PAN/DMF fibres could be aligned without the use of magnetic particles. They found that using optimal processing parameters, 40% of the fibres were aligned to within 5°.

The main processing parameter affecting the degree of alignment was the distance between magnets; the optimal distance was found to be 2.58 cm [80]. However, Yang *et al.* [20] claimed that the polymer solution must be magnetised by adding a small number of magnetic nanoparticles (0.22 wt% of Fe_3O_4) to achieve alignment [20]. Similar requirements were also reported by Ajo *et al.* [208] and Wang *et al.* [207]. The electro-spun PVP nano-fibre produced by Wang *et al.* [207] shows a relatively poor surface morphology in the presence of Fe_3O_4 due to the agglomeration of ferrite nanoparticles.

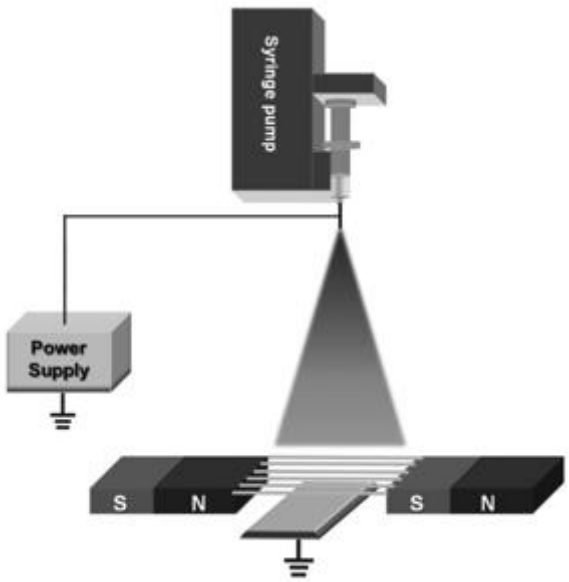

Figure 2.2.24 Schematic illustration of the magnetic field assisted electro-spinning set-up used for producing aligned nano-fibres [23].

Thus far, only a limited number of papers have studied the magnetic field's effect on the trajectory of electro-spun fibre jets. It is worth pointing out that the magnets are also metallic components. Of the various researchers' alignment techniques described in this section, none offered evidence to indicate that the existing electric field lines were not changed when the

magnets were introduced. Considering that the magnetic field is the dominant factor in these experiments, further explanation should have been offered.

2.2.4.3. Near Field Electro-spinning

In addition to changing the set-up of the electro-spinning rig, changing the process parameter is another way to lower the extent of whipping. In conventional electro-spinning, the intrinsic bending instability resulting in the polymer jet whipping after a short distance from the spinneret is the major barrier to producing aligned nano-fibres. Here, an elegant approach is used whereby the working distance is reduced to within the straight section of the polymer jet [212]. The concept of near-field or precise electro-spinning was demonstrated by Kameoka and Craighead [213]. The distance between the needle and collector was reduced from 10–20 cm to 0.5–3 mm; this is just before the occurrence of bending instability [213]. Since the whipping area increases as the working distance increases [13, 119], reducing the working distance will result in the width of the whipping area decreasing [214]. Moving the collector along the *X* and *Y* axis, with speed matching or higher than whipping speed, Ye *et al.* [215] were able to control the position and morphology of the fibre when it was deposited on the substrate. In this case, single nano-fibres can be produced [216, 217]. A number of authors have demonstrated near field electro-spinning [171, 212, 213, 215-218]. However, the process is not suitable for solvents with low volatility due to the lack of a whipping process. The relaxation of the polymer chains in the solvent-rich jet is likely to be an issue if the intention is to manufacture reinforcing fibres with a high degree of molecular orientation [40]. Furthermore, the production speed is significantly lower than other alignment techniques, with a few nano-fibres been produced per second.

2.3. Tensile Testing of Electro-spun Nano-fibre

2.3.1. Techniques to Determine the Tensile Properties of Electro-spun Nano-fibres

Tensile testing is a common, well-developed method used to determine the mechanical properties of materials [219]. A number of test standards have been specified by the American Society for Testing and Materials (ASTM) for characterising the tensile properties of various materials and forms. However, there appears to be no standard method for tensile testing electro-spun polymer nano-fibres. A number of distinctive experimental set-ups have been designed and used by various researchers to characterise the tensile properties of various kinds of electro-spun polymer nano-fibres, as summarised in Appendix B. In this section, the methodology and tensile test equipment used to characterise the tensile properties of electro-spun nano-fibres are reviewed briefly.

2.3.1.1. Universal Tensile Tester

Referring to Appendix B, the universal tensile tester is a common method that has been used to determine the tensile properties of electro-spun random and aligned nano-fibre mats, arrays or bundles. Balan *et al.* [38] used an Instron 3369 universal tensile tester with a 100 N load-cell and a sample grip, with a gripping area of 1 cm^2, to test 10 wt% PAN/DMF as-spun random oriented nano-fibres. They prepared the sample with a gauge length of 20–40 mm and use adhesive cushion tape as end-tabs. Due to the low density of the electro-spun fibre mat, the porosity of the mat was calculated using Equations (2.14) and (2.15) below:

$$Porosity = (1 - \frac{Apparent\ density\ of\ mat}{bulk\ density\ of\ mat}) \times 100 \quad (2.14)$$

$$Apparent\ density\ of\ mat = \frac{Mass\ of\ mat\ (g)}{Mat\ area\ (cm^2) \times mat\ thickness(cm)} \quad (2.15)$$

The porosity of samples produced from three different thicknesses of PAN nano-fibre mat was in the range 90 ± 5%. The effect of three test variables: gauge length (20, 30 and 40 mm); thickness (114, 198 and 298 μm) and cross-head speeds (1, 5 and 10 mm/minute) were studied. It was found that altering the thickness had the greatest effect, whereas the cross-head speed had the least [38].

The tensile properties of 10 wt% PAN/MWCNT/DMF randomly oriented electro-spun nano-fibre mat was determined by Karim *et al.* [220] using a universal tensile tester. In accordance with ASTM D3039 (Standard Test Method for Tensile Properties of Polymer Matrix Composite Materials), the test speed was set to 5 mm/minute, with a 20 mm gauge length. Karim *et al.* found that the highest Young's modulus (400 ± 20 MPa) and tensile strength (122 ± 4.8 MPa) were achieved when the sample contained 0.1 wt% MWCNT, which is approximately two times higher than that obtained for the neat PAN. However, the tensile sample preparation method was not described by Karim *et al.* [220].

Since the randomly oriented fibre mat exhibits complex fibre-fibre interactions during testing, Alexeev *et al.* [221] argued that the tensile properties of the mat cannot accurately represent the properties of a single nano-fibre. Tensile testing aligned fibre arrays or bundles, obtained by the fibre alignment techniques described in Section 2.2, can significantly reduce fibre-fibre interactions. This can help achieve more accurate results, so as to demonstrate the mechanical properties of electro-spun nano-fibres. Wang *et al.* [35] reported that the tensile strength,

tensile modulus and elongation at break of 10 wt% PAN/DMF for a non-woven membrane and aligned fibre yarn was 14 ± 2.4 MPa, 0.03 ± 0.01 GPa, 34.1 ± 6.4 % and 45 ± 2.5 MPa, 0.80 ± 0.11 GPa, 88.6 ± 8.4 %, respectively. Moon *et al.* [39] used an Instron 5564 universal tensile tester to assess 10 wt% PAN/DMF aligned fibre array that was fabricated using a rotating mandrel with a linear speed of 9.8 m/s. The aligned fibre specimen was mounted onto Manila paper tabs with gauge lengths of 20 mm; no end-tab adhesive information was given. The test was carried out at room temperature, with a cross-head displacement of 2 mm/minutes. The cross-sectional area of the aligned fibre specimen was obtained from the measured electro-spun nano-fibre denier and the density (1.18 g/mL) of the PAN fibres. The ultimate tensile strength obtained from their experiment was 78.5 ± 2.2 MPa, which is approximately two times higher than that achieved by Wang *et al.* [35].

It was found from the papers reviewed and presented in Appendix B that the test parameters (such as load-cell, cross-head speed, temperature and humidity) and specimen preparation methods (gauge length, width, end-tabbing method) differ from paper to paper, as there are no definitive test standards for tensile testing nano-fibre mats or bundles. Although preparing test specimens in the form of a fibre mat or an array is much less problematic. Compared to extracting single fibres, factors such as end-tabbing design need to be considered more carefully. A bad end-tab design may cause stress concentration, thus impacting the test results [222, 223]. End-tabs such as epoxy glue [224], double-sided tape [225] and cushion tape [38] have been used, but most papers leave the end-tab method unspecified. Load-cell selection has been based on the dimensions and material of the test specimen, generally ranging from 2–250 N [38, 84, 147, 224-228]. All the above-mentioned parameters may significantly influence the test results. Furthermore, the methodology for calculating porosity, density,

thickness and cross-sectional area also have not been standardised [35, 36, 39, 84, 220, 229]; thus, comparing the results from different sources is very difficult.

2.3.1.2. Micro/Nano Tensile Tester

For accurate determination of the tensile properties of a single fibre, it must be tested, regardless of the difficulties of this process. One method to achieve this is through a micro/nano tensile tester. This section presents a brief overview of micro- and nano-tensile test methods reported in the literature. A photograph of the nano tensile test equipment is shown in Figure 2.3.1a [31]. These tensile testers have the same working principle as the universal tensile tester, however, the load-cell is generally in the range of mN [29, 230, 231], μN [221] or nN [232-234]. Smaller load-cells have a higher resolution, which can be used to detect the tensile properties of nano-fibre mats [147] or even a single nano-fibre [235, 236]. A single nano-fibre can be extracted from a low-density array of aligned nano-fibre (see Figure 2.3.1b). This can be obtained by electro-spinning the polymer fibre onto a parallel electrode set-up for just a few seconds [230, 237]. The single nano-fibre is then transferred to a test frame (generally made of cardboard) and bonded using double-sided tape [29, 234] or epoxy adhesives [238] (see Figure 2.3.1b and c). The sides of the frame are cut before testing. This is similar to the procedure for tensile testing conventional reinforcing fibres.

Papkov *et al.* [239] fabricated aligned 8–10 wt% PAN in DMF, using a 5 cm gap width parallel electrode. A wire 'work' was used to pick up the individual nano-fibres, with gauge lengths of 5–10 mm, and they were transferred to the grips, where they were bonded using an epoxy adhesive. The authors determined the fibre cross-sectional area by measuring the diameter of fibre in the adjacent area, using SEM to avoid radiation damage to the testing

fibres. They found that the tensile properties of a single electro-spun fibre were significantly influenced by the diameter of the fibre. The highest elastic modulus (48 GPa), tensile strength (1750 MPa) and toughness (605 MPa) were obtained when the fibre diameter was approximately 100 nm. Detailed reasons for this are described in Section 2.3.2. The effect of relative humidity (0–60%) on the mechanical properties of randomly oriented PAN/DMF nano-fibre were studied by Huang *et al.* [147], using a rotating mandrel with a rotation rate of 70 rpm. They used a Tytron 250 microforce testing system (with no load-cell details stated). The test specimen had a dimension of 40 mm × 6.5 mm; it was cut from the mandrel substrate. However, Huang *et al.* did not mention their sample preparation method or how the cross-sectional area was determined. They report that the greatest tensile strength and Young's modulus, 6.25 MPa and 95 MPa, respectively, were achieved at 20% relative humidity. They suggest that the skin of the fibre forms faster, and fibre-fibre adhesion decreases, as the humidity increases.

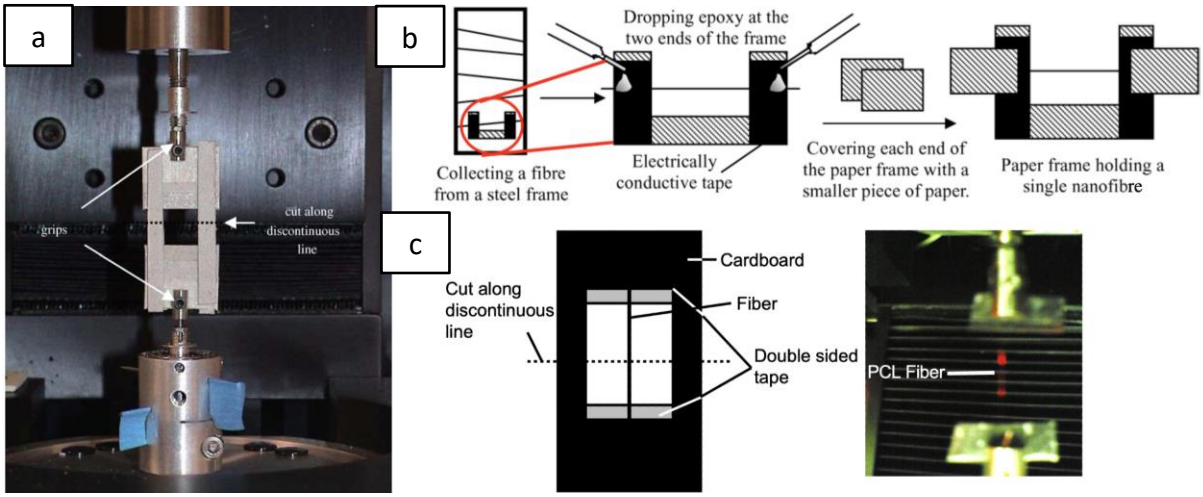

Figure 2.3.1 (a) Photograph of nano tensile tester [31]. (b) Schematic illustration of single fibre-extracting procedure proposed by Chen et al. [230]. (c) Schematic illustration and photograph of single nano-fibre mounting frame, as demonstrated by Wong et al. [234].

2.3.1.3. Other Mechanical Characterisation Methods

(i) AFM-based tensile testing methods: Atomic Force Microscopy (AFM) works by scanning a sharp tip (typically made of silicon or diamond) across a sample surface. The tip is mounted on a cantilever, which deflects as it interacts with the sample surface [240]. In addition to topography, AFM can also be used to identify the mechanical properties of a single nano-fibre. AFM has been used successfully to determine the mechanical properties of a single nano-fibre of PAN [241, 242], PEO [243], Nylon [227, 244, 245] and PCL [30, 32], through vibration method [227, 241, 242, 244, 245], to measure the force applied to the nano-fibre, in order to perform a tensile test [243] or a three-point bending test [30, 32, 33, 227, 244, 245]. Yuya *et al.* [241] measured the Young's modulus of PAN/DMF fibres using the non-contact vibration mode of AFM. A schematic illustration and a photograph of the set-up and the method of attaching the fibre to the AFM probes can be found in Figure 2.3.2a and b, respectively. The cantilever's spring constant was determined to be 0.1 N/m. They recorded the maximum cantilever resonance peaks with (19.4 kHz) and without (10.0 kHz) the fibre, by using finite element analysis modelling software (ANSYS). The Young's modulus of a 200 nm diameter PAN nano-fibre was calculated to be ~26.7 GPa, which is of the same level of magnitude as that reported by Papkov *et al.* [239] using a nano tensile tester. Zussman *et al.* [242] also used the vibration mode of the AFM cantilever to determine the Young's modulus of PAN/DMF nano-fibres that were carbonised at 1100 °C. Their experiment applied electron beam-induced deposition, to secure the fibre between the AFM probe and a tungsten wire (see Figure 2.3.2c). Fibres of various diameters (105–200 nm) and gauge lengths (11.5–78.3 μm) were measured, with the highest Young's modulus being 69.8 GPa. However, the fibre mounting method

mentioned in this set-up cannot be used for bonding polymer nano-fibres, as the electron beam will cause damage to the nano-fibres [235].

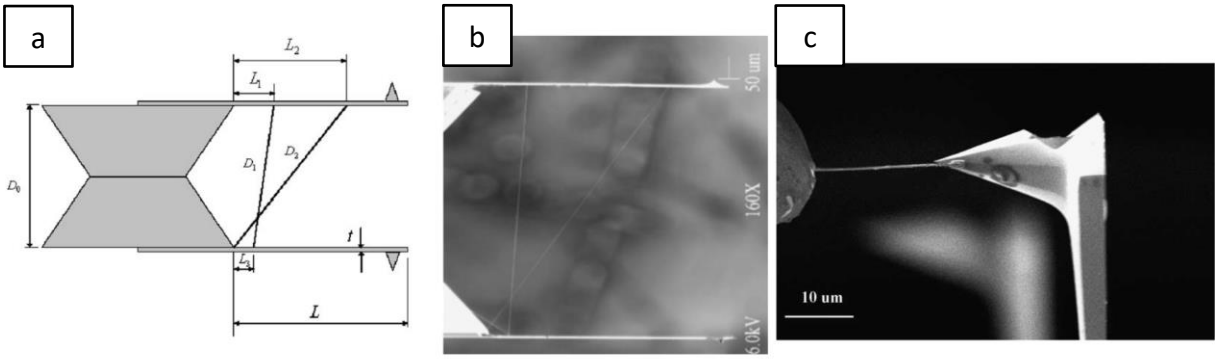

Figure 2.3.2 (a) Schematic showing the nano-fibres attached to two similar AFM cantilever probes. (b) Scanning electron microscope image showing nano-fibres attached to the AFM cantilever probes [241]. (c) SEM micrograph of a carbonised nano-fibre mounted between an AFM tip and a tungsten wire [242].

(ii) Microelectromechanical systems (MEMS): In 2005, Zhu [246] developed a MEMS device with an on-chip force sensor for material testing purposes. The MEMS device was generally embedded or used *in situ* with an electron-microscope. As shown in Figure 2.3.3a, this MEMS device consists of an electrostatic actuator [246], a thermal actuator [28], or both [247], shuttles (known as the specimen stage) and a load-cell fabricated by surface micromachining. These actuators provide displacement to the shuttle as the current is introduced and allow the test rate to be controlled.

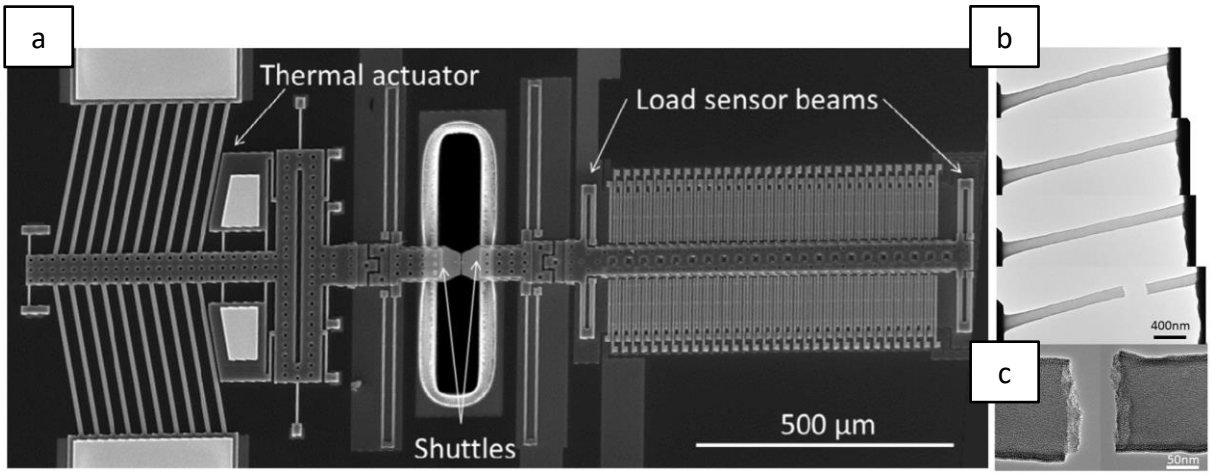

Figure 2.3.3 (a) Image of a MEMS device used for in situ TEM mechanical testing. (b) Sequential TEM images during a tensile test. (c) High-resolution image of the fracture surface in (b) [28].

Beese *et al.* [28] used MEMS devices for *in situ* TEM mechanical testing (with a load sensor stiffness of 1623 N/m) to determine the tensile property of single carbonised (800 °C) PAN/DMF electro-spun carbon nano-fibres. Both ends of the fibres were secured on each side of the shuttle using electron beam-induced deposition, which deposits a platinum weld of dimensions 250 x 500 nm. The diameter of the fibre was in the range of 100–300 nm and had a gauge length of 2.5 μm. They obtained tensile strength and Young's modulus values of 7.3 GPa and 262 GPa, respectively. Similar devices have also been reported by Chawla *et al.* [37] and Arshad *et al.* [248] to characterise the tensile strength and Young's modulus of carbonised electro-spun PAN/DMF nano-fibres. In these devices, the load-cell and actuator were located on the same side (See Figure 2.3.4a and b). The Young's modulus and tensile strength reported by Chawla *et al.* [37] was 3.8 ± 1.0 GPa and 209 ± 47.7 GPa, respectively (carbonisation temperature of 1100 °C), and values of 3.5 ± 0.6 GPa and 172 ± 40 GPa were reported by

Arshad *et al.* [248] (carbonisation temperature of 1400 °C). As will be explained in Section 2.4.2.2, higher carbonisation temperature typically leads to high strength and modulus.

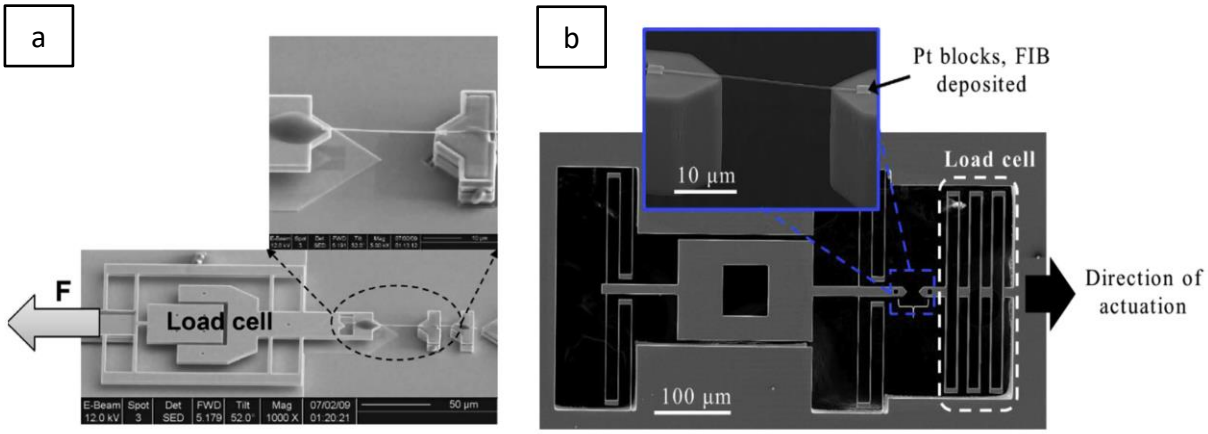

Figure 2.3.4 Image of the MEMS devices designed by (a) Arshad et al. [248] and (b) Chawla et al. [37]

The main benefit of the MEMS *in situ* SEM/TEM system is that it facilitates visualisation of the deformation mechanism during the tensile testing of single nano-fibres (see Figure 2.3.3b and c). However, due to the size and design of the device, the force is typically in the range of micro-Newtons (µN) to a few milli-Newtons (mN), and the displacement was limited to several micro-meters [249], where the gauge length of the sample was approximately 10 µm [250]. This is not suitable for testing a material that has a large stretch ratio. Furthermore, only materials such as pyrolysed PAN-based carbon nano-fibres [28, 37, 248], pyrolysed poly-furfuryl alcohol [250], polysilicon nanowire [249] and carbon nanotubes [251, 252] have been tested using MEMS. This is probably because FIB-deposited Pt block end-tabs are not suitable for typical polymer nano-fibres, due to the damage caused by electro-beam radiation, which may affect tensile properties [253].

(iii) Dynamic mechanical analyser (DMA): Researchers have also used the DMA to determine the mechanical properties of random [254] or aligned [255, 256] nano-fibre mats. Properties were characterised by cyclic loading of the sample over a range of frequencies, typically between 0.01 Hz and 1000 Hz. The benefit of using a DMA is the ability to analyse the mechanical properties of materials as a function of temperature [254], humidity [255], frequency [257] and time [256] without damaging the specimen [258].

Barua and Saha [259] used DMA to study the changed in the storage modulus, loss modulus and tan(δ) of electro-spun PAN nano-fibre yarn during the stabilisation process (between 50–400 °C) with a heating rate of 5 K/minute. A frequency of 2 Hz with a constant tension of 3 MPa was applied throughout the experiment. Aligned fibre yarns are obtained from electro-spinning 10 w/v% PAN in DMF with a disc collector rotating with a surface velocity of 13 cm/s. The DMA sample preparation was not described. Barua and Saha reported that the tensile strength of the nano-fibre yarn obtained was 157.2 ± 6.1 MPa, with an average fibre diameter of 284 ± 50 nm. Furthermore, three tan(δ) peaks were found at 120, 160 and 329 °C, which they said was due to the molecular movement in the ordered paracrystalline (120 °C), glass transition of amorphous regions (160 °C) and chemical changes during stabilisation (329 °C). The researchers also confirmed the conclusion drawn by Liu *et al.* [260], that both crystallisation and cross-linking increase storage modulus, whereas loss modulus was decreased during the cross-linking reaction. The time to reach maximum storage modulus decreased with increasing isothermal temperature (from 240 °C to 300 °C). Alarifi *et al.* [261] performed similar experiments and came to the same conclusions. Figure 2.3.5 presents the three-point bending method, sample mounting set-up and the dimension of the specimen, as used by the group.

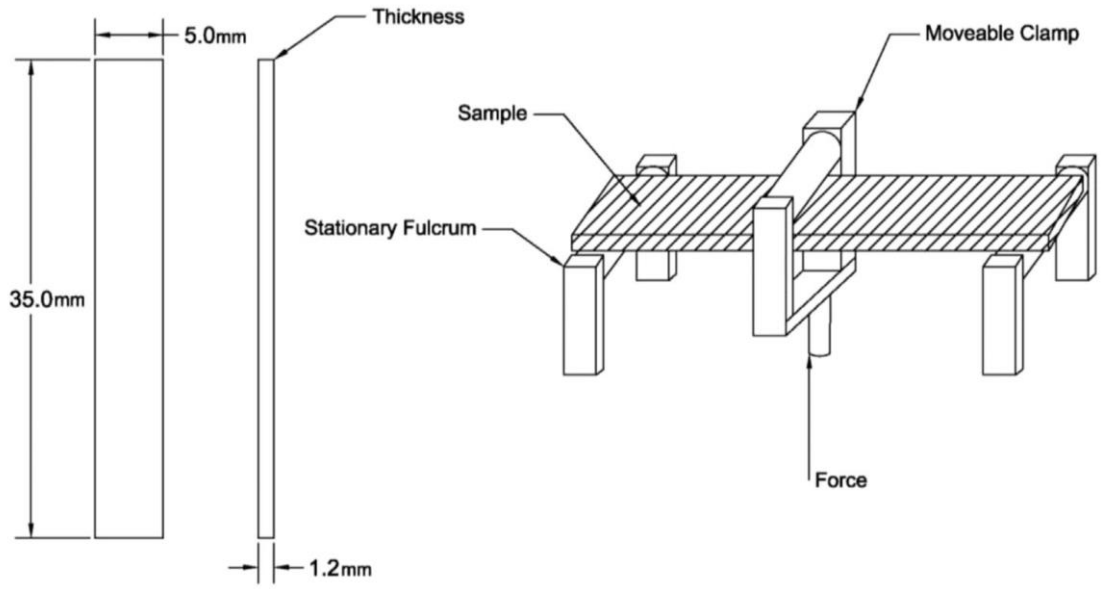

Figure 2.3.5 Schematic of a specimen mounted in a DMA three-point bending fixture [261].

2.3.2. Improving the Tensile Properties of Nano-fibres through Drawing

The mechanical properties of electro-spun polymer nano-fibres can be affected by various factors, such as the molecular weight [262-264], polymer solution concentration [231, 265, 266], solvent [267, 268], applied voltage [269, 270] and environmental conditions [147, 271]. This is because these parameters can affect fibre formation during the electro-spinning process. A contributing factor is the fact that the polymer on the surface of the jet solidifies faster than at the centre, which can lead to a core and shell structure [272-274]. It has been established that electro-spun polymer fibres have lower molecular orientation and crystallinity than those obtained from wet-spinning or melt-spinning [35, 275]. They are reported also to have lower mechanical properties than bulk polymers [40]. The degree of crystallinity of the polymer chains within the fibres influences the tensile strength and elastic modulus of the fibres. Improving the crystallinity and molecular orientation of electro-spun polymer fibres significantly enhances the mechanical behaviour of the fibres [31, 234, 242].

2.3.2.1. Stretching the Nano-fibre while Spinning

The tensile properties of polymer fibres can be improved by drawing the fibre [276]. During electro-spinning, the whipping created by the bending instability causes the polymer jet to undergo significant stretching which in turn significantly reduces the fibre diameter. A number of researchers have reported that by changing the electro-spinning parameters the whipping process and fibre diameter can be altered. It has been reported widely that the tensile properties of electro-spun nano-fibres increase as fibre diameter decreases [31, 221, 234, 238, 239, 265, 274, 277]. An AFM phase image generated by Lim *et al.* [265], shown in Figure 2.3.6a and b, demonstrated that the fibre with a higher diameter had more misaligned lamellae. The TEM shown in Figure 2.3.6c illustrates chain orientation in the skin region of the electro-spun Nylon-6,6 fibre [273]. Moreover, it was found that the tensile properties increase significantly when the fibre diameter drops below a certain threshold [238, 239, 278, 279].

Stachewicz *et al.* [274] have shown that electro-spun PVA fibres have a core-shell structure. Due to the higher solvent evaporation rate at the surface of the polymer jet, the molecular orientation in the shell is higher than it is at the core, which dominates the tensile properties of the fibre. Moreover, using AFM, the thickness of the shell was found to be consistent at approximately 30 nm and independent of the change in fibre diameter. As a result, the finer fibres had a higher skin:core ratio and therefore a higher Young's modulus than thicker fibres. Similar findings were also reported by Curgul *et al.* [280].

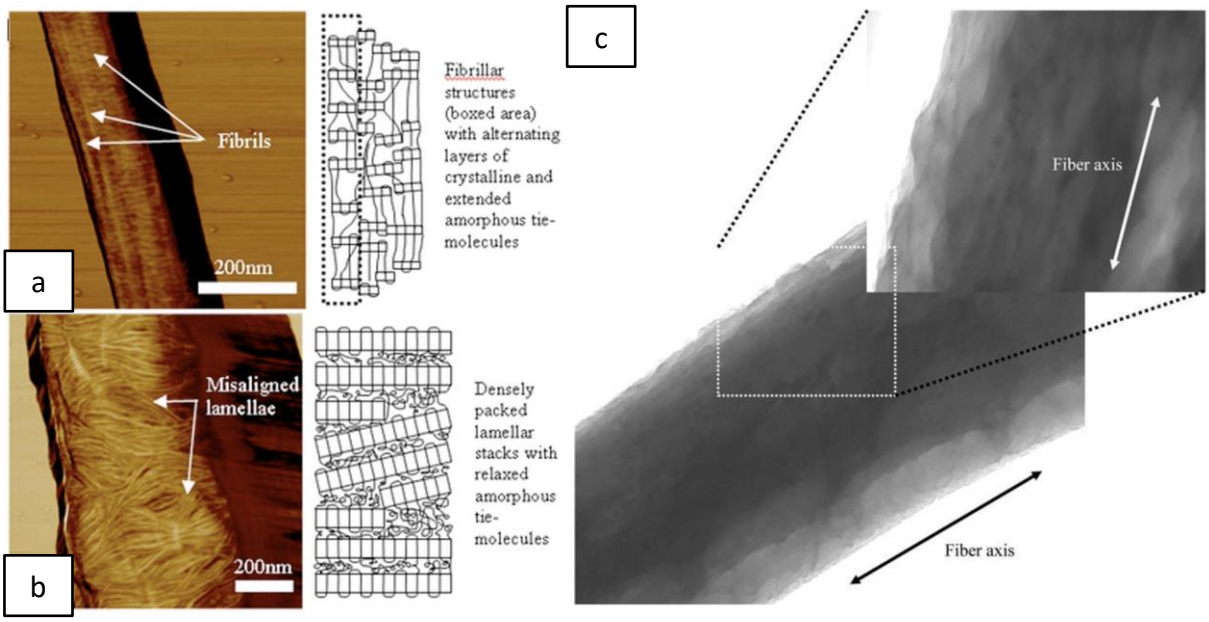

Figure 2.3.6 AFM phase images showing the surface morphology of PCL nano-fibres with diameters of (a) 150 nm and (b) 450 nm, with corresponding schematic diagrams of the nanostructure [265]. (c) A TEM micrograph of Nylon-6,6 fibre displaying the preferred orientation of the polymer chains [273].

Naraghi *et al.* [279] found that the Young's modulus of electro-spun PAN nano-fibres was increased when the fibre diameter decreased from 300 nm to 100 nm. Using polarised FTIR, by calculating from the relative strength of the transmission peak at 2240 cm^{-1}, corresponding to the nitrile group, they found an increase in the orientation factor from 21% to 50% and the degree of crystallinity from 7.3% to 16.8% with an increase in the electro-spinning distance from 15 to 25 cm and applied voltage from 15 kV to 25 kV. The crystallinity of the material was estimated from the XRD spectra of the material using Equation (2.16) [281]:

$$W\% = \frac{\sum I_c}{\sum I_a + \sum I_c} \tag{2.16}$$

where *W* is the crystallinity, *Ic* the diffracted intensity of the crystalline region and *Ia* the diffracted intensity of the amorphous region. Naraghi *et al.* [279] suggest that a longer spinning distance helps the fibre to stretch; it also increases the spinning time, which improves solvent evaporation, resulting in reduced chain relaxation when the fibre is deposited on the collector. However, because the mobility of the polymer chain is limited by the chain entanglement, they found that increments in crystallinity are reduced once the working distance reaches 20 cm. It was concluded that the increase in Young's modulus for fibres with diameters below 300 nm is predominantly due to the chain orientation and not crystallinity.

Papkov *et al.* [239] also found that tensile strength and Young's modulus increased significantly when the diameter of the electro-spun PAN fibre was reduced below 300 nm. However, unlike traditional high-performance fibre, a decrease in failure strain was not found. It has been claimed that fibres with low diameter can be simultaneously stiff and ductile [239]. Furthermore, the XRD spectra of various fibre diameters suggest that the crystallinity of PAN decreases as fibre diameter is decreased. This suggests that polymer crystallisation may be prevented by fast solvent evaporation-induced solidification. A primary attribute which increases the mechanical properties is the molecular orientation of the amorphous region [238, 278, 282].

2.3.2.2. Post-drawing the Nano-fibres

Although the stretching caused by the electro-spinning process can affect the molecular orientation and crystallinity of a polymer [283], the magnitude of effect has been shown to be low [40]. In addition to drawing the fibre during production, post-drawing the nano-fibre can further improve the mechanical properties of polymer nano-fibres [35-37, 84, 234, 237, 284].

Cold-drawing along the fibre axis favours the crystal orientation of the polymer fibre, which in turn increases the mechanical properties [164]. Coleman *et al.* [285] have demonstrated that the FWHM of $2\theta = 17°$ of PAN/DMF nano-fibre produced by 'touch-spinning' (see Figure 2.3.7) is 22% lower than that of the nano-fibre generated by electro-spinning, which shows that the fibre obtained using touch-spinning has a higher crystallinity. Colemen *et al.* claimed that the nano-fibre produced by touch-spinning was forcibly pulled along the longitudinal direction during the fibre formation [285].

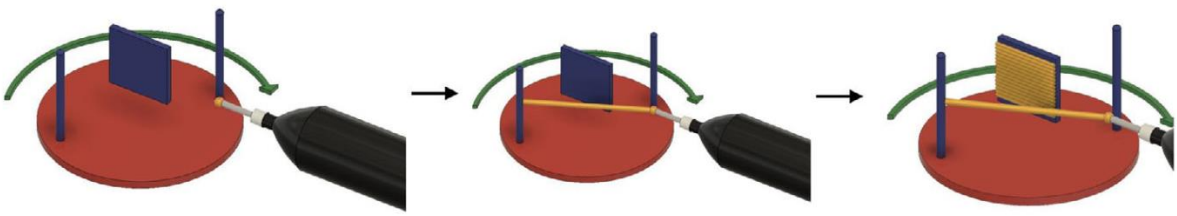

Figure 2.3.7 Schematic illustration of fibre formation through the 'touch-spinning' process [285].

A number of researchers have shown that the tensile properties of electro-spun fibre can be improved by increasing the take-up speed of the rotating mandrel [164, 166, 231, 233, 286, 287]. In general, the electro-spun fibre has been found to solidify prior to reaching the collector. Changing the take-up speed can be understood as a cold-drawing process. Jose *et al.* [286] increased the take-up speed of the rotating mandrel from 3000 rpm to 6000 rpm when collecting Nylon-6 electro-spun fibre; they reported that the Young's modulus increased from 58 MPa to 202 MPa. The 2θ peaks of 24° showed that the intensity increased as the take-up speed increased [286].

Chan *et al.* [233] have reported similar results from electro-spinning PHBV nano-fibre onto a disc. Increasing the take-up speed from 470 to 940 m/minute resulted in significant improvement in the elastic modulus and tensile strength, by two and three times, respectively. Kongkhlang *et al.* [287] used a 2D WAXD pattern and Herman's orientation function obtained from the azimuthal scan profile to study the molecular orientation of the electro-spun fibre. The Herman's orientation factor (*f*) is defined in Equation (2.17):

$$f = \frac{3\langle cos^2 \phi \rangle - 1}{2} \tag{2.17}$$

where $cos^2\phi$ represents a square averaged cosine of angle ϕ between the fibre axis and the crystallographic axis. When the value of f is 1, the polymer chains align perfectly along the fibre axis; when $f = -0.5$, the polymer chains align perfectly perpendicular to the fibre axis; $f = 0$ means the orientation is random. Their results indicate that the orientation function can reach 0.93 when the rotating speed of the disc collector increases from 630 m/minute to 1890 m/minute. Fennessey *et al.* [166] report that Herman's orientation function increased from 0 to 0.23 ± 0.01 when the take-up speed increased from 0 m/s to 8.61 m/s. However, this value decreased to 0.21 ± 0.07 when the rotation speed increased further (12.3 m/s).

The effect of the drawing on Herman's orientation factor has also been studied by Brennan *et al.* [84], though their results show that the electro-spun PAN nano-fibre has a negative orientation factor. A higher drawing ratio increases the orientation factor from –0.377 (2.8 mm/s) to –0.054 (7.7 mm/s). Brennan *et al.* contend that the negative orientation factor indicates that the PAN chain of their electro-spun nano-fibre shows a kinked lamellar structure (see Figure 2.3.8) obtained by the steric and dipolar repulsions of the nitrile group in the polymer [84]. This folded lamellar structure caused the chain to be oriented perpendicularly

to the fibre axis. Drawing the fibre can unfold the chain and align it along the fibre drawing direction. So far, most results show that the PAN fibre produced has a positive Herman's orientation factor [166, 279, 288, 289]. More experiments are needed to prove this conclusively.

Fiber type	Orientation factor	Related backbone angle
Draw ratio 1	–0.377 ± 0.063	73°
Draw ratio 2	–0.301 ± 0.156	69°
Draw ratio 3	–0.191 ± 0.132	63°
Draw ratio 4	–0.054 ± 0.158	57°
Conventional microfiber	0.372 ± 0.042	40.5°

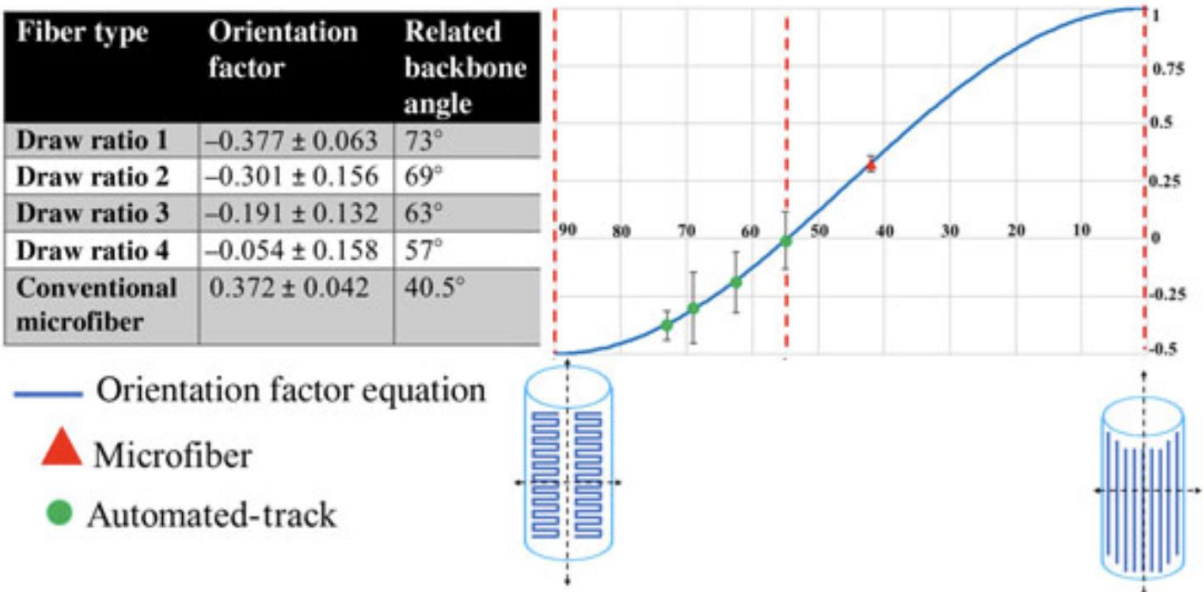

Figure 2.3.8 The table shows Herman's orientation factor values for PAN nano-fibres collected at different draw ratios. Herman's orientation factor for automated-track nano-fibre and conventional microfibres plotted against the predicted backbone angle from fibre axis. Herman's orientation factor equation is plotted against the changing angle between the polymer chain backbone and the fibre axis [84].

Wu *et al.* [229] produced aligned PAN nano-fibres using a high-speed rotating mandrel. A fibre sheet 4 cm wide and 10 cm long, with a thickness of 17 μm, was made. The samples were also hot-stretched using a metal weight (75 g) above the glass transition temperature (Tg) of PAN (approximately 95 °C) at 135 °C for 5 minutes along the fibre alignment direction. In contrast with as-spun fibre, hot-stretched fibre has higher crystallinity (from 7.92% to 31.8%) and

orientation factor (from 45.6% to 55.4%), with a smaller crystallite size (from 2.51 Å to 2.26 Å). Wu *et al.* used a universal testing machine to characterise aligned electro-spun PAN nano-fibre yarn; the dimensions of the tensile specimen were 5 mm x 20 mm. Comparing the tensile test results of as-spun with hot-stretched fibres, they observed that hot-stretched fibres exhibited a Young's modulus that was five times higher and that the ultimate tensile strength doubled [229]. Similar results were reported by Wang *et al.* [35]. They stretched the aligned PAN nano-fibre yarn by 100%, 200% and 300% of its original length. They reported that the tensile strength and modulus increased to 372 MPa and 11.8 GPa, respectively. The elongation at break decreased dramatically when comparing the drawn and as-prepared fibre yarn, where it dropped from 88.6% for as-prepared to 12.6% for the post-drawn specimen. Increasing the drawing ratio from 100% to 300% only lowered the elongation at break by 1%. The degree of crystallinity for the as-prepared and post-treated samples were 16.93% and 49.20%, respectively [35]. Similar findings have been reported by Liu *et al.* [290]

As reviewed above, both crystallinity and molecular orientation have been reported to improve after post-drawing of the fibre. As is common knowledge, a semicrystalline polymer (such as PAN) contains both crystalline and amorphous regions [291]. The fraction and the orientation of these two phases influence the strength and stiffness of the polymer material [234, 239, 278, 282]. The high tensile properties achieved by PAN fibres can be attributed to the planar-zigzag conformation in crystalline chains. Drawing the fibre increases the uniformity of the chain across the fibre axis, and the chain mobility is confined as the fibre diameter reduces [288]. Lopez-Barroń *et al.* [292] showed that cold-drawing the semi-crystalline fibre can extend the distance of the amorphous region between two adjacent crystalline regions. As is shown in Figure 2.3.9, only tie-chains in the amorphous region were

stretched and remained aligned without significant relaxation after being drawn. Based on computer simulations, Petrov *et al.* [293] have argued that semi-crystalline polymer chains align themselves when undergoing cold-drawing. Overdrawing results in chain slippage, which causes failure. The degree of polymer chain entanglement in relation to fibre length is crucial for improving the mechanical properties through drawing. Petrov *et al.* report that the optimal ratio between the total polymer length (N) and the entanglement length (Ne) necessary to obtain fibres with the highest degree of chain orientation is 2/5.

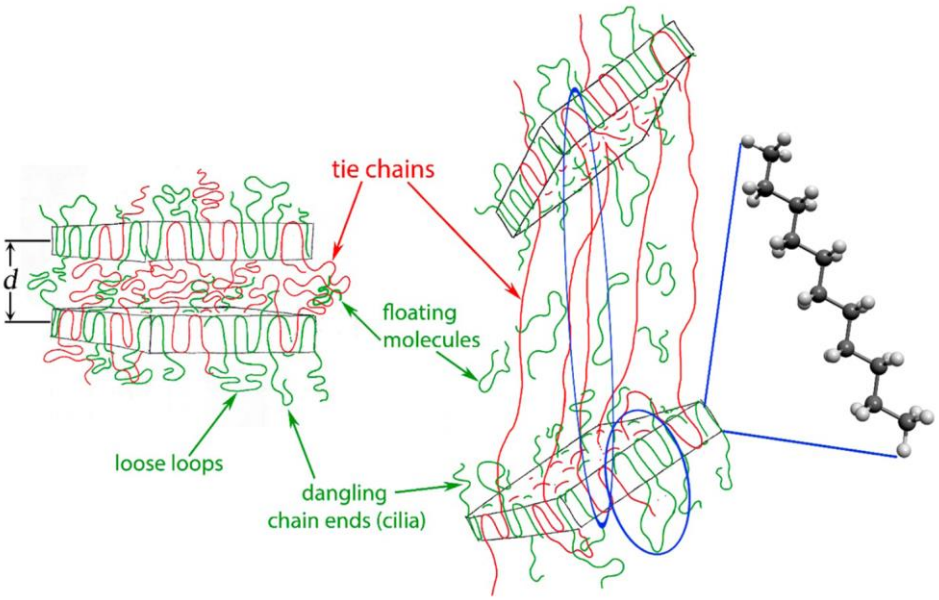

Figure 2.3.9 Schematic of the molecular alignment during cold-drawing of a semicrystalline polymer, as proposed by Lopez-Barroń et al. [292].

It should be noted that the studies mentioned above also report that the polymer fibre produced from electro-spinning has relatively low strength and Young's modulus, compared to commercially available micro-fibres. Arinstein *et al.* [278] have suggested that, when the fibre diameter is low, the mechanical properties may be entirely dependent on the amorphous region in the fibre. Using XRD, Zussman *et al.* [242] showed that Herman's orientation factor

of electro-spun PAN nano-fibre is 0.34, almost half the values of fibres fabricated by melt-spinning and wet-spinning (0.6 and 0.66, respectively). To maintain a high degree of molecular orientation during electro-spinning, the relationships between strain rate, chain relaxation time and solvent evaporation rate need to be controlled carefully. The relaxation time and strain rate are reported to be 0.1–0.01 s and 10^3–10^5 s^{-1}, respectively [119, 294]. Although the polymer chain can be stretched and oriented in such conditions, the residual solvent trapped inside the fibre core could significantly increase the relaxation speed [295], resulting in lower polymer chain orientation compared to those of other spinning methods [40].

2.4. PAN-based Carbon Nano-fibres

Fibrous carbon materials have long attracted the attention of scientists and engineers. Over the last 50 years, carbon fibres have become an essential industrial material due to their superior specific strength and modulus, chemical resistance, and low density, which are ideal for high-performance applications [296]. They have been applied in various fields, especially as a reinforcing material for resin composites. Carbon nano-fibres are carbon fibres with a diameter in the micron to nanometre range. They are typically produced by either chemical vapour deposition (CVD) or through the pyrolysis of organic precursor fibres. Because of the slow processing rate, CVD has generally been used to produce carbon nanotubes or to synthesise carbon fibres with diameters ranging from several microns down to 10 nm [242]. However, CVD cannot produce continuous fibres, only short lengths of around 150 mm [297]. Longer fibres can be made by pyrolysis from a precursor. The precursor materials can be isotropic and anisotropic mesophase pitches [298, 299], polyacrylonitrile (PAN) [248, 300, 301], polyimides (PIs) [302], poly(vinyl alcohol) (PVA) [303], polybenzi-midazole (PBI) [304],

poly(vinylidene fluoride) (PVDF) [305] and phenolic resins [306], or even biological precursors such as cellulose [307] and lignin [308]. PAN co-polymer is commonly used due to its high carbon yield, high tensile strength, and ease of processing. Dissolving the polymer into an appropriate solvent system makes it possible to use a variety of polymer fibre manufacturing processes, such as wet spinning to produce conventional fibres, and electro-spinning to create nano-fibres. After that, the precursor fibres are treated at elevated temperatures to convert them into graphitic carbon [309]. This section reviews the manufacturing process of carbon nano-fibres (CNFs) based on electro-spun PAN. The chemistry of the pyrolysis process and influences on the CNF tensility will be summarised briefly in the following section.

2.4.1. Manufacture and Pyrolysis of PAN-based CNFs

PAN-based nano-fibres are generally produced using electro-spinning [308-310]. PAN polymer powders are typically dissolved in polar solvents such as DMF, DMAc, or DMSO to a concentration around 10 wt% [43, 84, 242, 311, 312]. The dissolution process is carried out at temperatures between 60 °C and 80 °C to reduce viscosity for easier mixing [15]. A detailed summary of literature-reported electro-spinning conditions using a PAN-based precursor can be found in the first part of Appendix B.

2.4.1.1. Stabilisation

In order to convert PAN nano-fibre into CNFs, the precursor fibre is treated at high temperature (250–3000 °C) to obtain a graphitic structure [313]. This process involves two distinct stages: stabilisation (or oxidisation) and carbonisation [314].

Stabilisation is carried out at 180–350 °C in air. During stabilisation, PAN undergoes cyclisation, partly dehydrogenation, aromatisation, oxidation and cross-linking, forming a ladder structure that makes it denser and more stable [315]. Lee *et al.* [314] reported a dramatic weight loss of the PAN fibre from 295–325 °C, where the cyclisation occurs. Cyclisation of the nitrile groups in the acrylic molecule influences the fibre's thermal stability. The chemical reaction path suggested by Donnet *et al.* [316] shown in Figure 2.4.1.

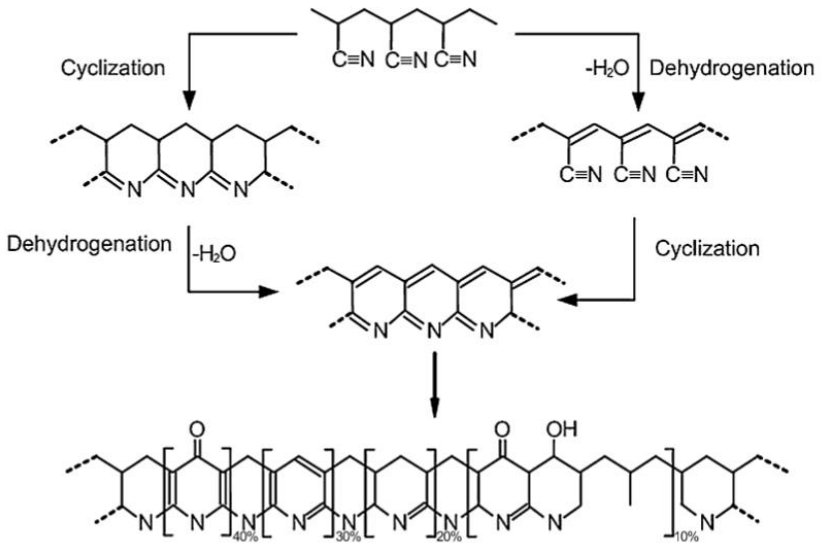

Figure 2.4.1 Proposed reaction pathways for PAN during stabilization [316].

However, Frank *et al.* [296] suggested that the stabilisation process is more complex. Multiple chemical models have been proposed in recent decades, such as those shown in Figure 2.4.2 [317-320]. Furthermore, the intermolecular cross-linking reactions during stabilisation can occur even without intermolecular cyclisation being completed. This means that intra- and inter-molecular stabilisation reactions can occur simultaneously. During this stage, the decomposition of organic compounds and the formation of denser structures results in a gross colour change from white to brown, or even black [310, 321]. Parameters such as heating rate and end-temperature holding time are also crucial for stabilisation: because PAN undergoes a

thermally induced cyclic reaction before its melting point, a slow heating rate is needed for the process to complete [296]. The fibres can fuse or even burn off when the temperature or heating rate is too high. However, if the stabilisation temperature is too low, the reactions will be slow and incomplete, leading to a fibre with poor mechanical properties [311].

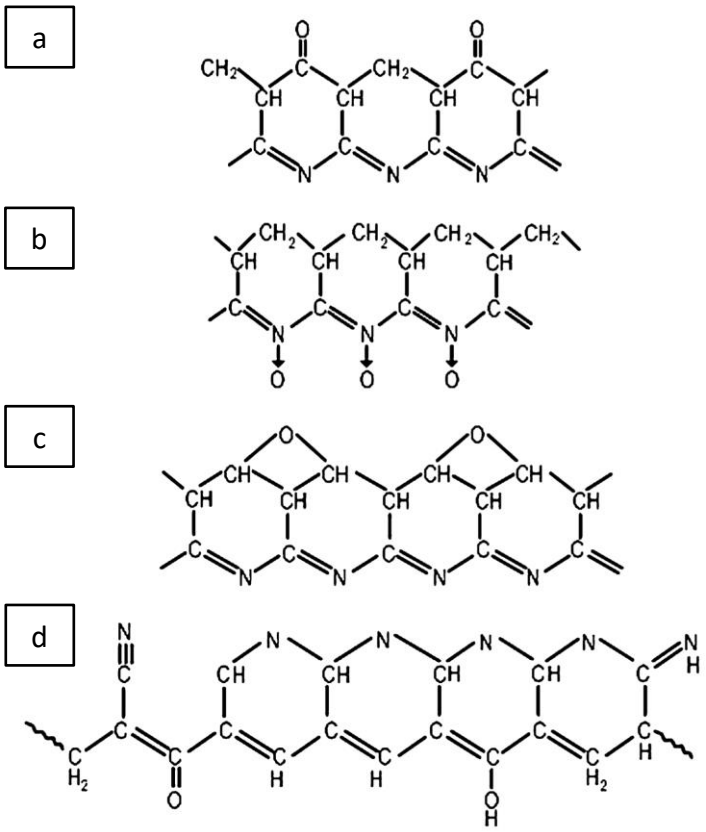

Figure 2.4.2 Proposed structures of oxidised PAN: (a) bridging ether links; (b) carbonyl groups; (c) donation of lone pair electron to an oxygen atom; (d) hydroxyl and carbonyl groups [315].

Various ideal stabilisation temperatures are identified, between 270 °C and 400 °C [242, 322-327]. Stabilisation can take place in both air and nitrogen [309]. Stabilising PAN-based precursor fibre in air can result in a skin-and-core structure, due to the diffusion of oxygen from the skin into the core [328]. In this case, the higher oxygen content at the surface can

result in more crystallinity in the skin. The skin–core structure has not been detected in fibres stabilised in a pure nitrogen atmosphere [329]. Bashir [317] indicated that oxygen initiates the cyclisation reaction because its lower activation energy makes the process easier than in the pure nitrogen atmosphere [317]. The presence of oxygen also helps dehydrogenation, forming double bonds that stabilise the carbon chain [330]. However, evidence shows that the dehydrogenation reaction can also occur after cyclisation. Oxygen is not involved in this reaction. The cyclisation reaction converts the C≡N bonds into C=N bonds to cross-link between PAN molecules. The chemical structure changes result in thermally stability, so that melting does not occur [331].

2.4.1.2. Carbonisation and Graphitisation

Carbonisation involves multiple changes, and the degree of carbonisation is usually measured by aromatic growth and polymerisation, which occurs from 400 °C to 3000 °C in an inert atmosphere, typically nitrogen or argon [330]. Carbonisation usually entails two steps. The first step occurs between 400–600 °C with a low heating rate to minimise mass transfer due to unstable structure, such as through the loss of low molecular weight components and gaseous by-products [315, 332]. Dramatic shrinkage occurs at this stage. The second step takes place above 600 °C [310]. However, an excessive heating rate can result in greater shrinkage [333]. To control the shrinkage, progressive and multi-stage heating procedures were developed [333], another option is to introduce tension during pyrolysis [334-336]. Low-modulus carbon fibre is produced at around 1,000–1500 °C, where the polymer starts to cross-link and form a structure called 'turbostratic' carbon [337]. The tensile strength also increases as the processing temperature increases due to increased carbon content. Fitzer *et al.* [332]

observed volatilisation during heat-treatment. They report that HCN was the main by-product below 700 °C, alongside CO_2, CO, and H_2O. Above 700 °C, N_2 was the main by-product [332]. Maximum strength is typically achieved around 1500–1700 °C [248]. Figure 2.4.3 illustrates the structural change for PAN during carbonisation [338].

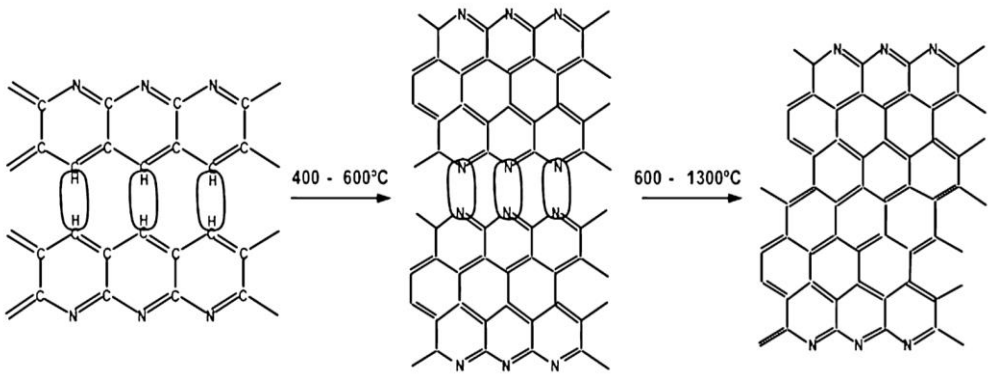

Figure 2.4.3 Chemical changes for PAN precursor during carbonisation [338].

Graphitisation is a high-temperature process, typically taking place around 1,600–3,000 °C. During this stage, the preform is converted from carbon to a graphitic structure, with a large number of small molecules being released, and the gaps between turbostratic carbon are reduced [339]. Higher graphitisation temperature can result in larger clusters of carbon rings, which act as initiating points for generating larger crystalline graphitic structures. Zhu *et al.* [340], show that the fibre shrank gradually over this temperature range, reducing in diameter from 8.0 μm at 1800 K to 6.6 μm at 2800 K, while the density increased from 1.746 g/cm^3 up to 1.858 g/cm^3. The carbon content, measured by XPS, was 98.55%. Meanwhile, changes in the molecular structure result in axially oriented graphitic layers with increased crystalline extension, and the obtained carbon fibres have substantially improved mechanical properties. Due to the loss of molecular interaction between graphitic layers, graphitisation will reduce the tensile strength but improve the fibre's Young's modulus and electrical conductivity [341].

2.4.2. Factors that Influence the Tensile Properties of CFs and CNFs

CNFs fabricated from PAN precursor nano-fibres through stabilisation and carbonisation have been studied over the past decade. A typical way to demonstrate how well the fibres have been heat treated is through their mechanical properties. Commercial carbon fibres typically have a tensile strength of around 5–7 GPa and a Young's modulus of 230–440 GPa [315]. Theoretically, a thinner fibre generally has better mechanical properties. However, the tensile test results (summarised in Appendix C), show that none of the reported PAN-based CNFs displays mechanical properties similar to those of commercial CFs, even those CNFs reinforced with carbon nanotubes. The diameter and tensile properties are ten times lower than the commercial ones.

2.4.2.1. Chain Orientation in Precursor Fibres

One factor influencing the tensile properties could be the chain orientation of PAN precursor fibre. The carbon structure becomes more ordered in the precursor fibre, with a higher orientation after inter-chain cyclisation and dehydrogenation. This helps form a larger area of aromatic lamellar structure [342]. As described in Section 2.3.2.1, the orientation of the polymer chain can be affected by production parameters and the drawing process. The orientation of the polymer chains during pyrolysis is preserved by strong intermolecular hydrogen bonding and by the rigidity of the ladder structure [296]. When preparing the PAN-based precursor fibre under different drawing ratios, Chen *et al.* [343] realised that the polymer chain orientation determined the mechanical properties of the resultant CFs in the skin regions of precursor fibres. They also illustrated that the chain orientation in the skin region increases when the draw ratio increases. However, an excessive drawing ratio could

lead to lower crystallinity, and a sharp drop in crystal size in the skin. They suggest that the skin region may be replaced by other kinds of deformation that result in disorientation. Applying tension to the precursor fibre during pyrolysis is crucial. The mechanical properties of both low-temperature and high-temperature carbonised samples show an increasing trend when the applied tension increases [344].

Gutmann *et al.* [345], studied the shrinkage of the PAN precursor material under heat-treatment, finding that the length change can be distinguished into two temperature ranges: 250–450 °C and 450–1,000 °C. The shrinkage rate reaches 0.028% /°C at 300 °C in the first region and 0.039% /°C at 730 °C in the second region. They also showed that applying stress during heat-treatment can reduce shrinkage, with the sample length reduced by 11.8% under 3 MPa, in contrast to 16.8% when 0.5 MPa was applied. Their results also demonstrate that loading the material during pyrolysis can improve its overall mechanical properties. However, the tensile properties were maximised when a stress of 1 MPa was applied [345]. Therefore, from the result reported above, it can be seen that obtaining a high orientation of the polymer chains within the precursor material and maintaining the chain orientation during heat-treatment is crucial for manufacturing CFs with desirable mechanical properties.

However, no papers were found that described tensioning during the pyrolysis of PAN nano-fibre, and this, therefore, was investigated in the current study.

2.4.2.2. Heat-treatment Conditions for CFs and CNFs

The mechanical performance of CFs and CNFs may also be affected by the heat-treatment conditions. Many researchers have confirmed that the mechanical properties of PAN-based CFs are highly dependent on the large number of processing parameters involved in the

stabilisation and carbonisation process such as heating rate [346], stabilisation temperature [332], stabilisation time [347], carbonisation time [348] and carbonisation temperature [342]. Furthermore, controlling the tensile holding time as well as temperature during stabilisation could also affect the density of the CFs due to cyclisation reactions [349]. Increasing the stabilisation temperature can result in higher tensile performance. The tensile strength is generally higher at a heat-treatment temperature of around 1,600 °C. Yang *et al.* [350], investigate the effect of amorphous carbon on the tensile behaviour of PAN-based carbon fibres. The tensile behaviour depended highly on the microstructural development of amorphous carbons containing sp^2 carbon structures. They stated that It cross-linked the larger crystalline graphitic planes, making it difficult for cracks to propagate [350].

Tensile strength and moduli can also be affected by the heat-treatment duration. Excessive holding time leads to lower tensile properties [314]. Xiao *et al.* [348], investigate the effect of heat-treatment temperature and time on tensile properties during high-temperature carbonisation. As they increased the carbonisation temperature from 1400 °C to 2840 °C, they observed a significant decrease in tensile strength and an increase in tensile modulus. The strength dropped from 4.6 GPa to 2.6 GPa, and Young's modulus increased from 238 GPa to 390 GPa. However, increasing the holding time from 1.2 minutes to 6.0 minutes at 2500 °C leads to a decrease in tensile strength from 3.71 GPa to 3.64 GPa, and an increase in Young's modulus from 316 MPa to 380 MPa. They suggest that the reason could be that the degree of covalent cross-linking between the graphitic planes in the carbon fibres decreases as temperature increases, but remains almost constant with heat-treatment time [348]. Liu *et al.* [308] similarly point out that larger crystalline graphitic structures were formed along the fibre directions when temperature increased above 1600 °C [308]. Due to the lower level of

amorphous sp^2 carbon, these graphitic structures become mobile under tensile load. Any defect-induced failure can propagate quickly through the grain boundaries, reducing the tensile strength [327].

The mechanical properties of CNFs follow a similar trend to those of CFs during heat-treatment. Arshad *et al.* [248], stabilised the PAN precursor nano-fibre at 300 °C for 1 hour in air and carbonised at 800, 1100, 1400 and 1700 °C in nitrogen, then evaluated single fibres using a MEMS testing platform. They report an increasing trend in Young's modulus as the carbonisation temperature increased. The tensile strength peaked at 3.52 GPa at 1400 °C, then decreased to 2.05 GPa when the temperature reached 1700 °C [248]. However, a different result has been reported by Zhou *et al.* [312], who carbonised the aligned electro-spun PAN-based nano-fibre precursor bundles up to 1000, 1400, 1800 and 2200 °C in a nitrogen atmosphere. The tensile properties of aligned CNF bundles were investigated using a nano-tensile testing machine. They reported that both tensile strength and Young's modulus increased with increasing carbonisation temperature. However, the highest tensile strength and Young's modulus obtained at 2200 °C, were 542 MPa and 58 GPa, respectively [312], significantly lower than reported by Arshad *et al.* [248] when testing a single CNF. This could be due to the fact that they tested fibre bundles, which may result in friction and interactions between adjacent fibres, causing damage during testing [351]. Moreover, heat-treating nano-fibre bundles at a higher temperature may result in stronger binding at fibre contact points among entangled nano-fibres, thus preventing the nano-fibres from separating and slipping with each other. Therefore, the properties of individual fibres may be higher than the fibre-bundle results reported.

Summary of the Key Findings and Issues in the Literature Review

- In general, the majority of the researchers use solvents that are toxic to dissolve and electro-spin PAN. A number of innovative and elegant electro-spinning methods have been used to produce aligned nano-fibres. However, these techniques do not permit the aligned fibres to be extracted continuously. The extraction of the nano-fibre in an efficient manner is necessary to use them in manufacturing techniques where they are used as reinforcements. In the future, it may be possible to weave the aligned fibres into fabrics or subject them to operations such as filament windings or pultrusion.

- The preparation of electro-spun fibres and their evaluation is not standardised. Therefore, comparing data from different sources is not practical. Moreover, sample preparation methods for tensile testing, are also not standardised, in particular, the end-tabbing of tensile specimens.

- The issue of measuring the cross-sectional area of electro-spun nano-fibre arrays remains to be a major problem. This is because any measurement technique that applies a force or pressure to the sample will distort it and give erroneous data. Until such a time that a method is developed to measure the cross-section area of electro-spun nano-fibres, pragmatic way forward is to obtain the measurements using conventional means, such as a digital micrometre and image analysis.

- The another significant issue that was identified in the literature was that the fibre volume fraction of the randomly oriented nano-fibre mats or aligned fibre bundles were not a addressed. The fibre volume fraction will have to be quantified when the nano-fibres are used as reinforcements in composites. Information on tensile test

sample preparation and end-tabbing methods were not addressed in any detail in the literature.

- Whilst the use of nano-reinforcements were covered in some depth in the literature, the post-processing of aligned electro-spun fibres, with a view to increasing the tensile properties was not addressed. A key issues that remains unsolved is the observation that the mechanical properties of electro-spun fibres and the associated crystallinity are significantly lower when compared to melt and solution-spun fibres.

The following chapter gives a detailed account of the experimental procedures that were used to address some of the above-mentioned issues.

3. EXPERIMENTAL

3.1. Materials

(i) Polymer: Polyacrylonitrile (PAN) used in this study was sourced from two suppliers. The first one, in powder form, with a weight average molecular weight of 230,000 g/mol, was purchased from Goodfellow (GF), UK. The second one was also supplied in powder form, with a molecular weight of 150,000 g/mol, and was purchased from Sigma-Aldrich (SA), UK. In order to ascertain the effect of molecular weight on fibre formation, both PANs were electro-spun into nano-fibres. Carbon nano-fibres (CNFs) were produced through pyrolysis of the electro-spun PAN supplied by GF.

(ii) Solvent: The solvent selected to dissolve the PAN was 99% purity anhydrous dimethyl sulfoxide (DMSO) from Fisher Scientific, UK. DMSO with a purity of 99.9%, was purchased from Sigma-Aldrich, UK and used for some of the experiments when the product from Fisher Scientific was discontinued. The solvents from the two suppliers were used without further purification. Due to the hygroscopic nature of DMSO, a silicone rubber septum was used to cap the container and the solution was withdrawn using a hypodermic needle and syringe.

(iii) Sample preparation for infrared spectroscopy: Potassium bromide (KBr) was used as-received (FTIR grade, ≥99% trace metals basis), and it was obtained from Sigma-Aldrich, UK. The KBr was dried at 80 °C for 4 hours prior to grinding it with the required material (as-received polymer, and electro-spun, oxidised and carbonised fibres) using a ceramic pestle and mortar. 200 mg of KBr was ground with 2 mg of the required material. Approximately 202 mg of the ground material was transferred to a 13 mm die set (Specac 3000, UK) and pressed

into a disk under an applied pressure of 10 tons. The analysis of the material was carried out using a transmission infrared spectrometer (Section 3.5.12). A 4-digit analytical balance (Analytical Plus, OHAUS, UK) was used to weigh all the samples used in this study.

(iv) Electrical conductivity of the calibration solution: Sodium chloride solution (HI7033), which was a calibration solution for the electrical conductivity measurements, had a conductivity of 84 µS/cm at 25 °C. This solution was purchased from HANNA Instruments, UK. The details of the equipment are described in Section 3.5.2.

(v) Silica gel: This item was purchased from Bluestar Packaging Suppliers Ltd, UK, and it was supplied in the form of 2–5 mm beads where the colour changed from yellow to green when it absorbed moisture. A batch size of 1 kg was purchased, and 50 g of the dried material was used in the electro-spinning chamber.

(vi) High-temperature adhesive: A high-temperature adhesive, Resbond™ 931, was used to bond the graphite components in the rig during pyrolysis (covered in Section 3.3.2). The product was manufactured by COTRONICS Co-op, USA and distributed in the UK by FINAL Materials. The adhesive (product code 931) was a two-component system that consisted of a powder and a binder. Each heat-treatment batch consisted of three samples. The total weight of the two components was approximately 1 g, and they were transferred to a 3 mm polypropylene (PP) cup (Wordmo, UK) using a 1 ml disposable pipette and spatula (Philip-Harris, UK) for the binder and powder, respectively. They were mixed manually for five minutes using a disposal wooden spatula until a thick and homogeneous paste was observed. The adhesive was applied to desired locations of the graphite rig and fibres (see Section 3.3.2) using a polytetrafluoroethylene (PTFE) spatula provided by the supplier. The adhesive was

cross-linked at 100 °C for four hours in an air-circulating oven (Memmert, UK) before it was placed in the tube furnace for subsequent heat-treatment.

(vii) Silicone oil: The silicone oil that was used in the liquid trap was obtained from Sigma-Aldrich, UK (product code 1003261003). This product had a viscosity of 20 Pa.s at 25 °C, with an operating temperature range from –40 °C to 200 °C. 300 ml was used in the liquid trap (see Section 3.3.3), and it was replaced when it discoloured.

(viii) Sodium carbonate: The outlet from the silicone oil liquid trap (see Section 3.3.3) was connected to a sodium carbonate liquid trap. This chemical was purchased from Sigma-Aldrich, UK, in powder form with ≥ 99.5% purity. It was dissolved in 300 ml water to form a 23 wt% concentrated solution. The solution was used in the liquid trap located at the outlet of the tube furnace to trap gaseous by-products generated during the pyrolysis of PAN fibres, such as CO, CO_2, HCN, H_2 and NH_3.

(ix) Furnace tube: The tube was made from high-purity alumina (99.9%), and it was supplied by Almath Crucibles Ltd, UK. The dimension of the tube was 46 mm (OD) x 38 mm (ID) x 1200 mm (Length). The alumina tube was rated to operate to a maximum of 1750 °C. The maximum heat-treatment used in the current study was 1200 °C.

(x) Graphite: The rig for securing the tensile test specimens for heat-treatment experiments was made using high-density graphite (1.77 g/cm^3) and they were provided by Rongxing Carbon, China. They offered a cut-to-size service, and the detailed dimension of the rig are presented in Section 3.3.2. The thermal expansion coefficient of the graphite used was 4.3×10^{-6} /°C. The material was rated to 427 °C in the air and 2760 °C in an inert atmosphere without

degrading or decomposing. In the current study, the operating temperatures in air and a nitrogen atmosphere were 300 °C and 1200 °C, respectively.

(xi) Grounded electrode for electro-spinning: The grounded electrode was crafted from copper sheet obtained from Metals4U LTD., UK, with a diameter of 10 cm and 0.9 mm thickness. The electrical wire that connected the grounded electrode to the ground terminal of the high-voltage power supply was soldered to the centre of the grounded copper sheet; this was done by the University Workshop.

(xii) Needles and syringes for electro-spinning: The syringes (SS05SE1) were supplied by Terumo, UK. It was made of PP and had a male Lure-lock tip with a capacity of 5 ml. The needles (AD725025) were purchased from Adhesive Dispensing Ltd, UK. The size of the needle was 25 gauge (0.515 mm OD, 0.26 mm ID) with a length of 6.35 mm, and it had a flat tip with a female Lure-lock base. This was the smallest size needle that was found to be suitable for the 14 w/v% PAN/DMSO solution (the viscosity at 55 °C was 18 Pa.s) used for electro-spinning.

(xiii) Aluminium foil: The foil was obtained from Kirkland, UK, in a roll of 300 mm width x 200 m length with an 18-micrometre thickness. The foil was used as the substrate to collect the randomly oriented electro-spun nano-fibres when using the rotating mandrel. Rectangular strips with a dimension of 12 cm x 25 cm were sectioned using a rotary cutter (18 mm diameter, Olfa, UK). The foil was wrapped tightly around the mandrel and secured using masking tape (2090, 3M, UK).

3.2. Electro-spinning Polyacrylonitrile/DMSO Solutions

PAN nano-fibres were fabricated via electro-spinning. PAN powders were used in the as-received state from the supplier. The following sub-section details the procedures that were developed to produce carbonised PAN nano-fibres in both random and aligned forms.

PAN with two different molecular weights was dissolved in DMSO separately. The PAN solutions were prepared in a 250 cm^3 3-neck round bottom flask under reflux. The polymer concentrations made were 2, 4, 6, 8, 10, 12, and 14 wt/vol% (w/v%) in DMSO. A schematic illustration and photograph of the experimental set-up are shown in Figure 3.2.1a and b, respectively.

In addition to using a magnetic stirrer to agitate the polymer solution, dry nitrogen gas bubbled into the liquid. The top centre neck of the round-bottom flask was attached to a condenser, and the other two were used to accommodate a digital thermometer probe (Dostmann electronic, NTC thermometer P300, UK) and a needle to introduce the nitrogen gas to the solution at 10 ml/hour. The refluxing was carried out for 6 hours at 60 °C. After the refluxing period, the solution was permitted to cool to room temperature naturally whilst the flask was purged with nitrogen gas. The solution was filtered using a 1 µm pore size disposable syringe filter (Xtra PTFE-100/25, CHROMAFIL, UK). The filtered solution was transferred to four individual glass vials, labelled and sealed with Parafilm (M996, Bemis, UK). The sealed glass vials were stored in a cabinet with silica gel. The solutions in the vials were used within three days of production, and a vial each was used for conductivity, viscosity, and surface tension measurements, and one was reserved for electro-spinning.

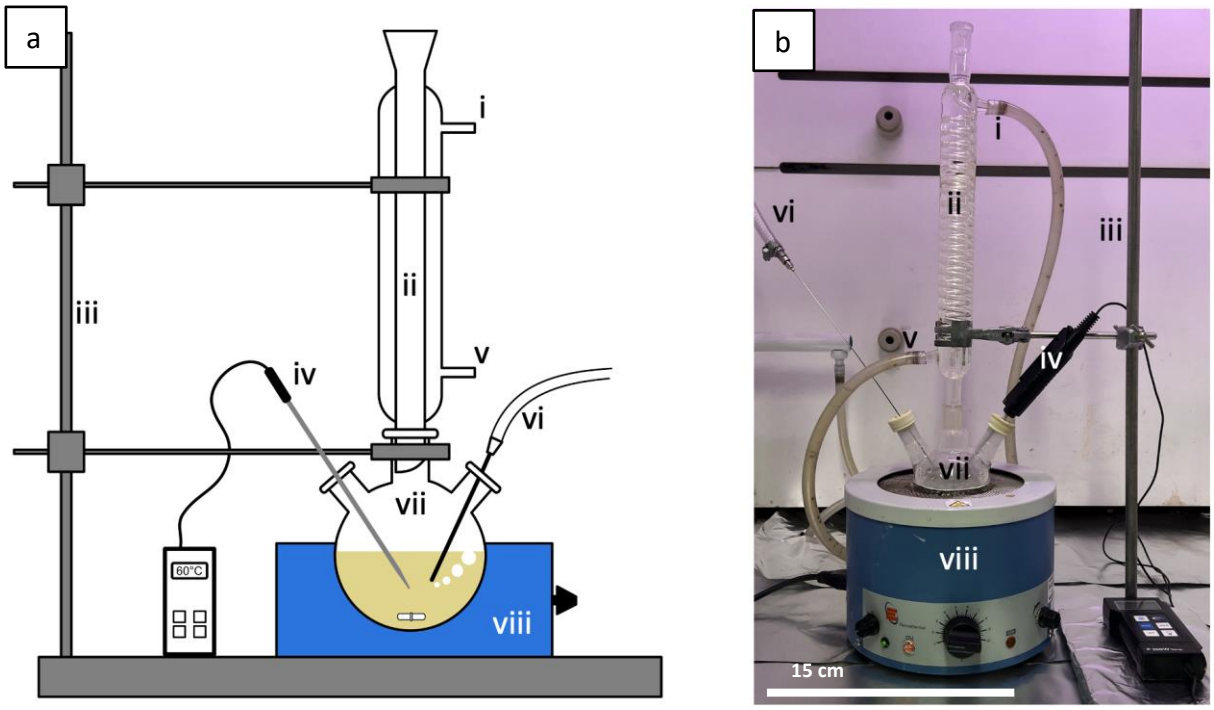

Figure 3.2.1 (a) Schematic illustration and (b) photograph of the reflux system that was used to dissolve PAN in DMSO: (i) water inlet; (ii) water condenser; (iii) metal stand; (iv) digital thermometer; (v) water outlet; (vii) nitrogen gas inlet; and (viii) magnetic stirrer heating mantle.

3.2.1. Electro-spinning PAN Nano-fibres

3.2.1.1. Electro-spinning of Randomly Oriented PAN Nano-fibre Using a Static and Rotational Electrode

(i) Electro-spinning apparatus: A schematic illustration and photograph of the custom-built conventional electro-spinning set-up are shown in Figure 3.2.2a and b, respectively. Figure 3.2.2c shows a schematic illustration of the electro-spinning rig with the door closed, and the routing of the positive and negative wires can be found in Figure 3.2.2d. The custom-built electro-spinning apparatus consisted of a polymethylmethacrylate (PMMA) chamber of

dimensions 400 mm (width) × 400 mm (length) × 400 mm (height); the thickness of the PMMA sheet was 5 mm. In order to improve the thermal insulation, the inner wall of the chamber was lined with black cardboard paper with a thickness of 4 mm (Ryman, UK), and it was secured in position using 5 cm wide black polyvinylchloride (PVC) electrical insulating tapes (GTSE, China).

The diameter and thickness of the circular grounded copper electrode were 10 cm and 0.9 mm, respectively. Aluminium foil (Kirkland, UK) with a 10 cm diameter was placed on the grounded copper electrode. The foil was cut using a rotary blade. Due care was taken to ensure that it was wrinkle-free and in intimate contact with the copper electrode. In the first set of experiments, this experimental set-up and electrode configuration were used to collect the randomly oriented fibre mats. However, it was established that this method of producing the nano-fibres was not suitable for producing the tensile test specimens because the thickness, for a given electro-spinning time, was not uniform from the centre (directly below the needle) to the outer perimeter. Instead, a slowly rotating mandrel was used to produce tensile test specimens. In this case, the sample was produced using the slow-rotating mode (50 rpm) (see Figure 3.2.3), which resulted in randomly oriented nano-fibres with relatively even thickness across the rotation direction within a certain width. A detailed analysis of the variation in thickness is presented in Section 4.3.1. The grounded aluminium mandrel had a diameter of 10 cm and a length of 25 cm, and its rotation rate was computer-controlled. The mandrel was grounded using a copper wire that touched the inner surface of the mandrel.

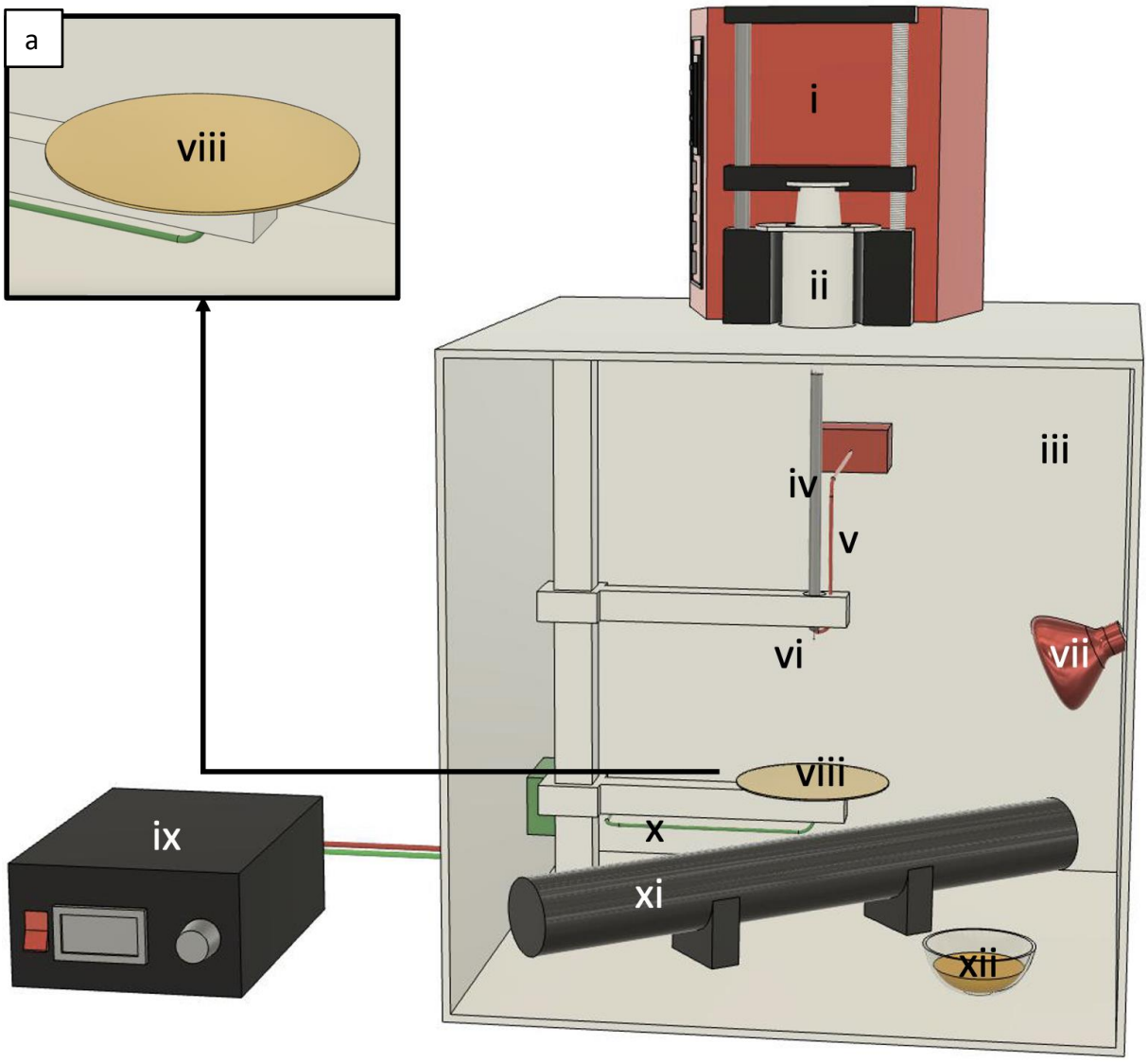

Figure 3.2.2 Cont.

Figure 3.2.2 Cont.

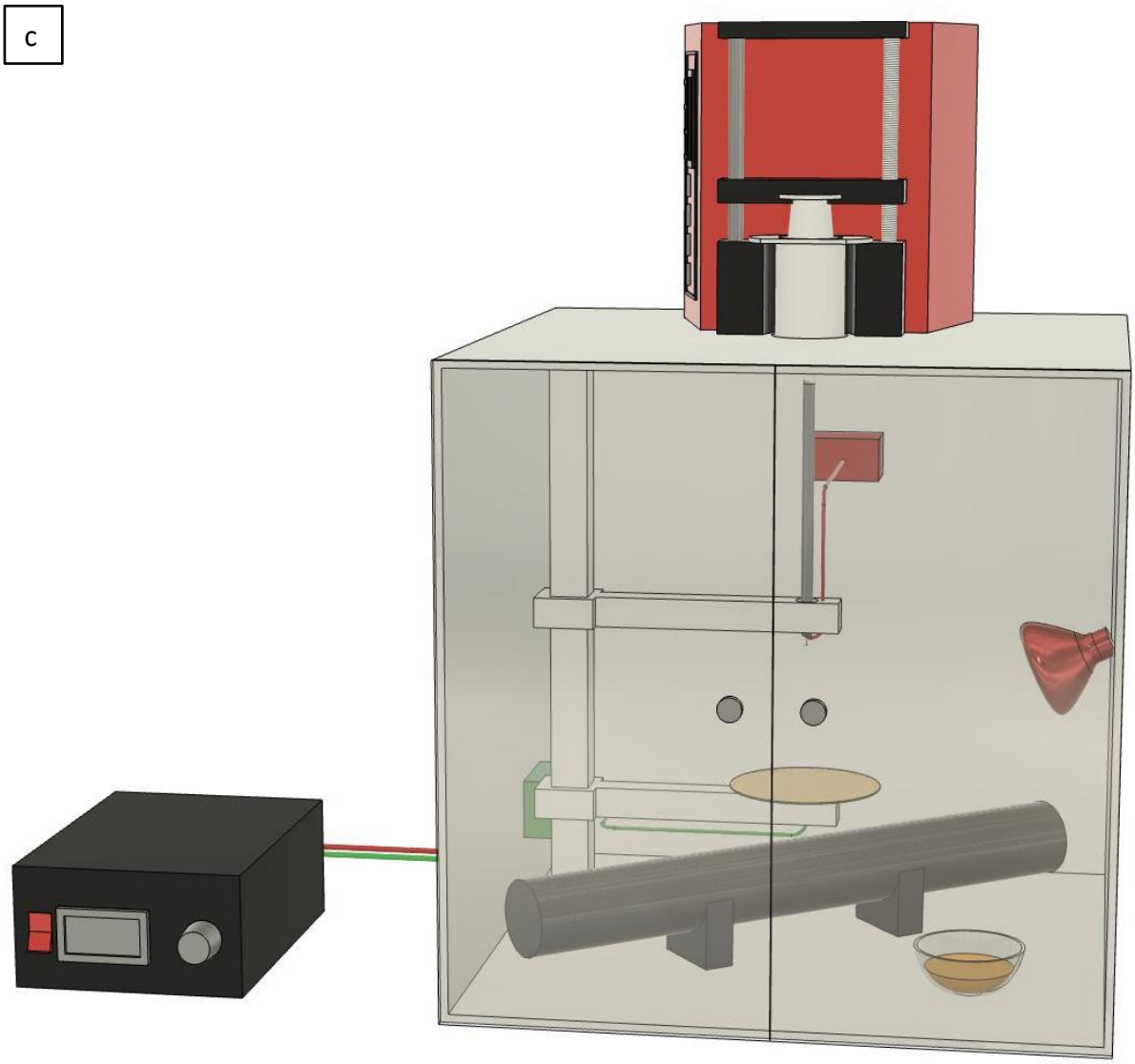

Figure 3.2.2 Cont.

d

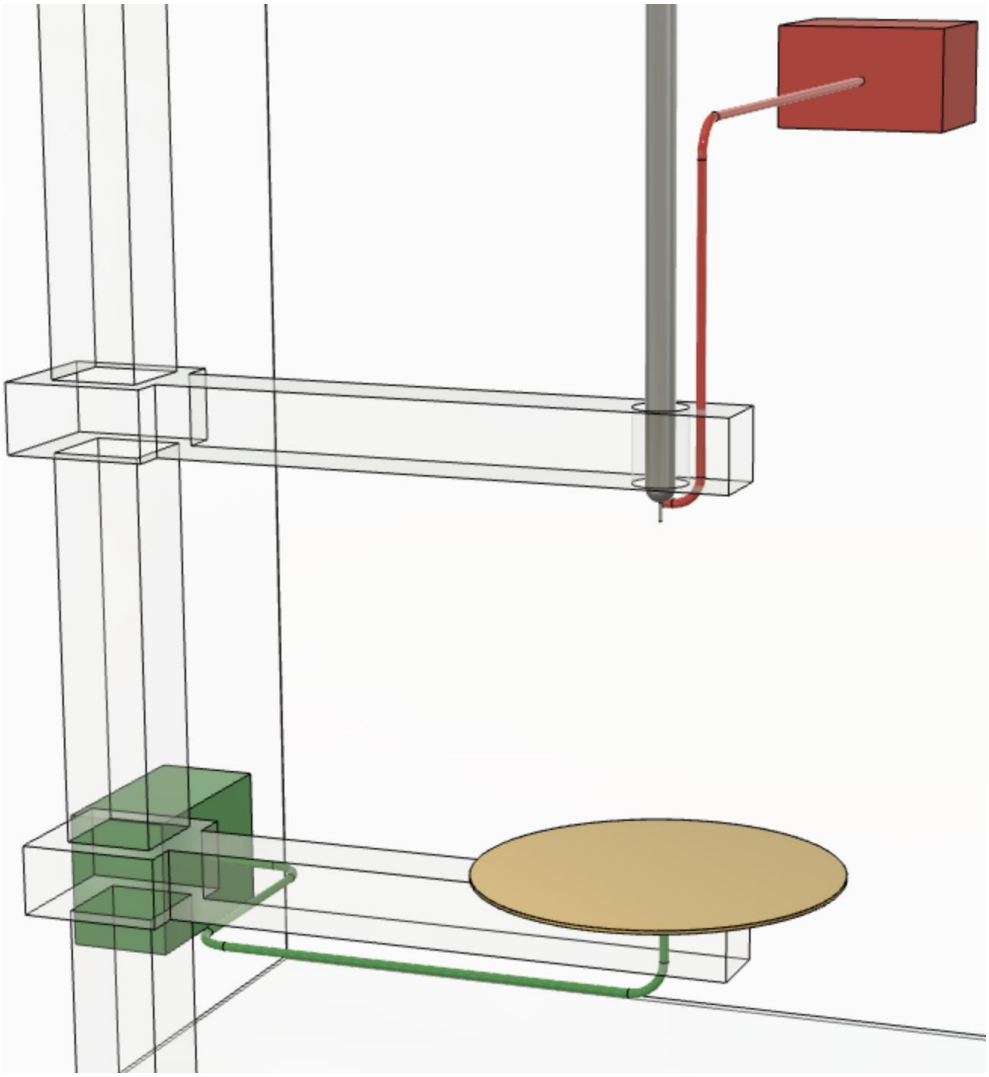

Figure 3.2.2 (a) Schematic illustration and (b) photograph of the conventional electro-spinning set-up: (i) solution dispensing unit; (ii) syringe; (iii) electro-spinning chamber; (iv) PTFE tube; (v) positive terminal; (vii) IR heating lamp; (viii) conventional collector; (ix) high-voltage power supply; (x) ground wire; (xi) static storage heater; (xii) silica gel. The insert in Figure 3.2.2 (a) shows a magnified view of the circular grounded collector. The insert in Figure 3.2.2 (b) shows a magnified view of the connection between the needle and the positive terminal of the power supply. (c) Schematic illustration of the set-up (a) once the door is closed. (d) Schematic illustration of the wire routing used to produce both positive (red) and grounded terminals (green) inside the electro-spinning chamber.

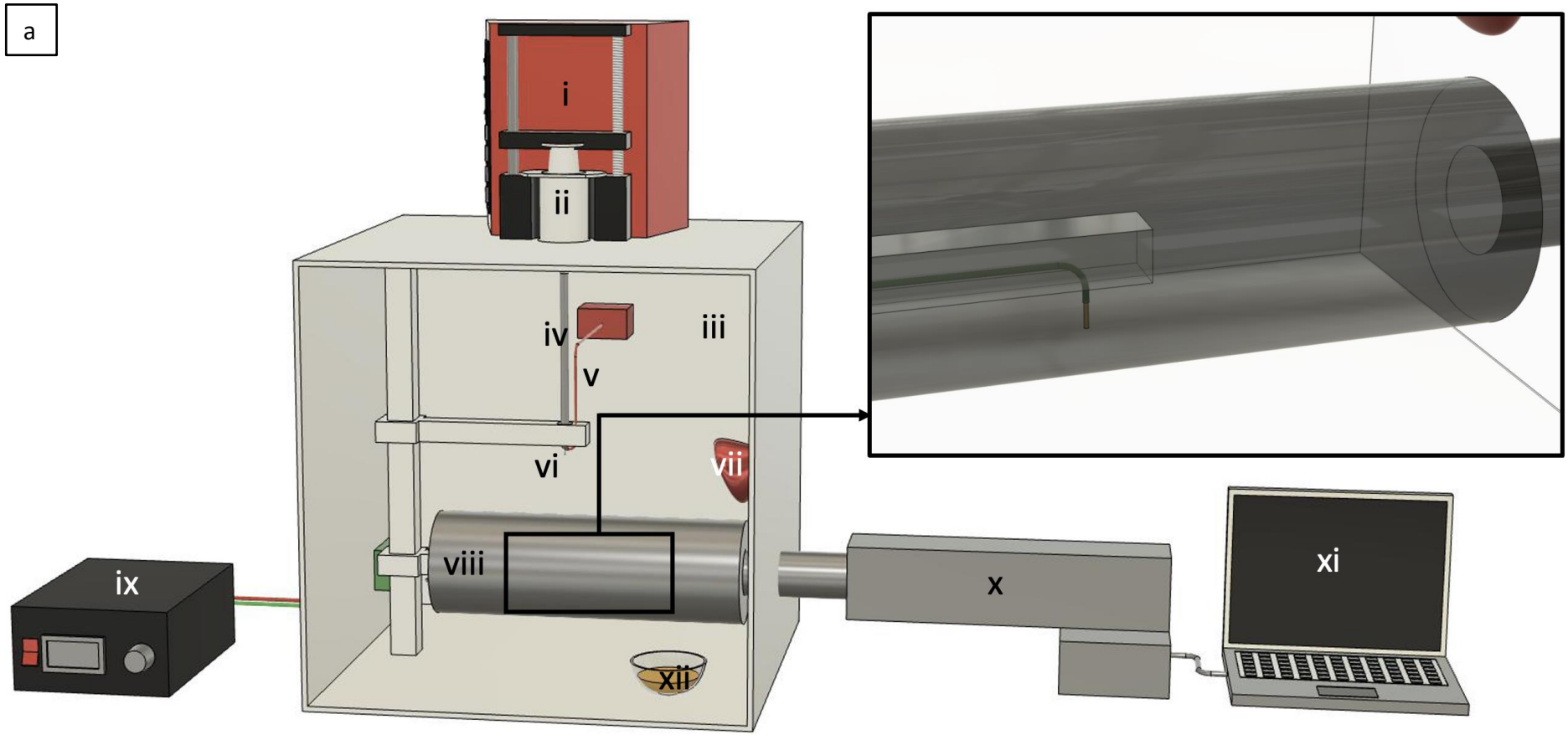

Figure 3.2.3 Cont.

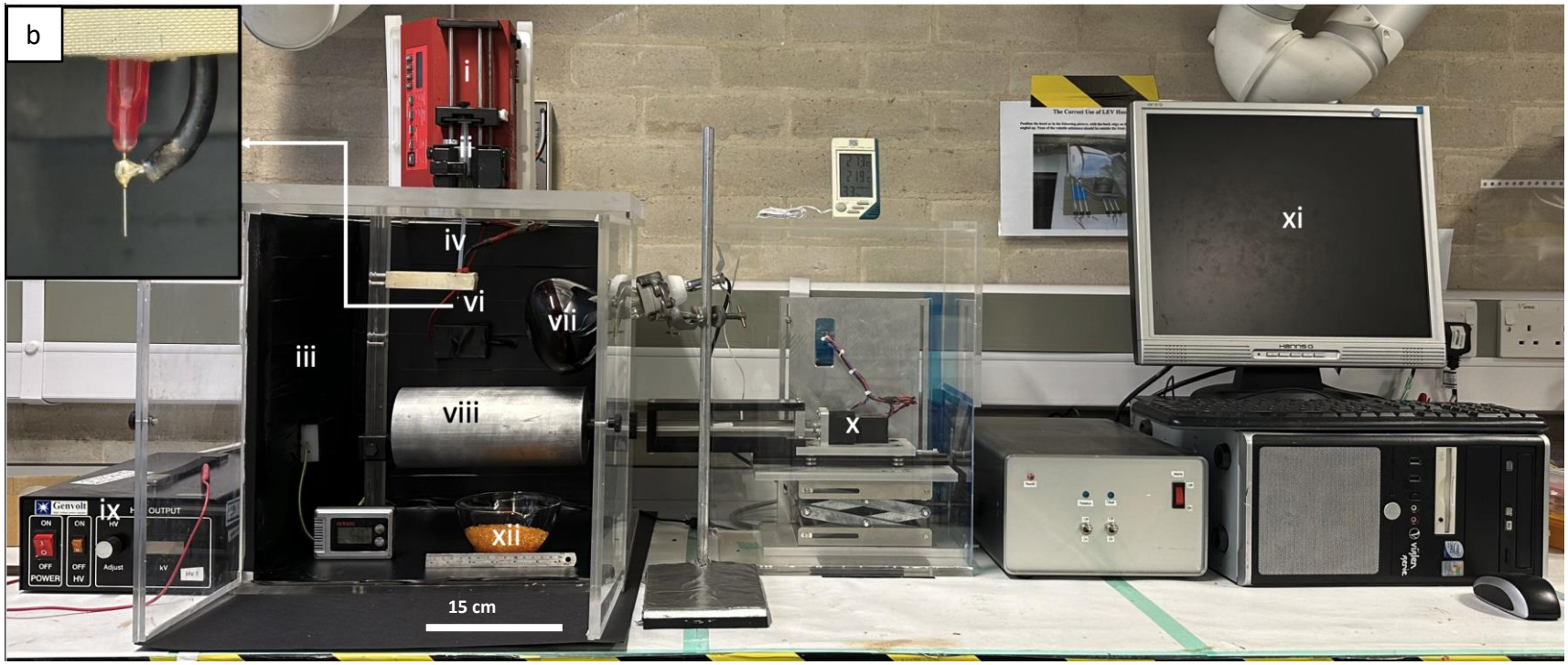

Figure 3.2.3 (a) Schematic illustration and (b) photograph of the rotating mandrel set-up for producing randomly oriented PAN nano-fibres: (i) solution dispensing unit; (ii) syringe; (iii) electro-spinning chamber; (iv) PTFE tube; (v) positive terminal; (vi) needle; (vii) IR lamp; (viii) rotating mandrel; (ix) high-voltage power supply; (x) electric motor; (xi) computer; and (xii) silica gel. The insert in Figure 3.2.3 (a) shows a transparent view of the ground connection between the wire (green) and the inner surface of the mandrel. The insert in Figure 3.2.3 (b) shows a magnified view of the connection between the needle and the positive terminal of the power supply.

(ii) Electro-spinning: The PAN/DMSO solution was transferred to a 5 ml syringe (Terumo, UK), and it was secured to the liquid dispenser (NE-300, World Precision Instruments, UK). The liquid was dispensed at 0.3 ml/hour. A flat tip 25-gauge needle (AD725025, Adhesive Dispensing Ltd, UK) with a bore and outer diameters of 0.3 mm and 0.5 mm, respectively and a length of 20 mm was attached to the syringe via a PTFE tube (Masterflex transfer tubing, Cole-Parmer, UK). The connection used between the syringe and the tubing was a PP female Lure lock adapter to a 1/8" hose barb fitting (Cole-Parmer Item # UY-45508-34, UK); and the connection used between the needle and the tubing was a PP male lure adapter to 1/8" ID hose barb fitting (Cole-Parmer Item # WZ-45518-26, UK). A 1 mm metal ring of dimensions 0.5 mm ID, 0.8 mm OD and thickness of 1 mm was attached to the needle, which in turn was connected to the positive output of the high-voltage DC power supply (73030, Genvolt, UK). The routing of the positive terminal and the grounded wires are illustrated in Figure 3.2.2d; the cables were secured with the PTFE tubing using a red zip-tie during electro-spinning. The applied voltage was in the range of 11–13 kV. The distance between the tip of the needle and the centre point of the collector was set at 100 mm. The electro-spinning operation was carried out in air where the air temperature within the chamber could be controlled between 25 °C and 55 °C. The temperature inside the chamber was regulated using a 175 W infrared lamp (IR 175R E27 Infrared Bulb, Phillips, UK). The infrared lamp was situated on one side of the chamber, and it switched on during electro-spinning. A 40 cm portable storage heater (Dimplex, UK) was used to pre-heat the chamber before the electro-spinning experiments; it was removed from the chamber just prior to electro-spinning. Silica gel was placed inside the chamber to lower the relative humidity (RH) to within 20 ± 2%. During the electro-spinning of PAN/DMSO solutions, the temperature within the chamber was maintained at 55 ± 2 °C. The

temperature and RH were monitored using a digital thermometer-hygrometer (RS Pro, RS Components, UK). The RH during electro-spinning was kept between 8–20%. The randomly oriented electro-spun fibres were collected for 10 minutes using the experimental set-up shown in Figure 3.2.2.

With regard to the fibre produced using the rotating mandrel, aluminium foil (Kirkland, UK) was wrapped tightly around the mandrel, and it was secured in position using masking tape. The rotation rate was set at 50 rpm. The rotation rate was measured using a digital camera by checking the rotation frequency of a marker on the mandrel. The working distance between the tip of the needle and the surface of the mandrel was 10 cm. All the other parameters were kept the same as the flat-plate collector. The experimental set-up is shown in Figure 3.2.3.

(iii) Background to the design of the Electro-spinning rig for producing aligned PAN nano-fibres: As mentioned in the literature review Section 2.2, the main issue for producing oriented electro-spun nano-fibres was continuous production of highly aligned electro-spun fibres that could be spooled and post-processed. The post-processing aspect refers to axial stretching during spooling to enhance the degree of molecular orientation of the polymer chains. The aligned fibres also allow a relatively uniform tension to be applied to the electro-spun fibre bundles during heat-treatment for precursors such as polyacrylonitrile (PAN) in order to compensate for shrinkage [345]. Applying uniform tension to the fibres will be simpler if they are oriented in one direction and plane. Moreover, aligned nano-fibre stacks can be subjected to axial stretching to control the residual fabrication stresses [352]. The mechanical testing of carbonised nano-fibres using conventional bundle-testing [35] will be significantly more straightforward if the filaments are aligned in one direction (described in Section 2.3.1).

With all the benefits mentioned above, an electro-spinning set-up that can hall-off aligned nano-fibres along the alignment direction is required. The design of such an electro-spinning set-up needed to meet the following requirements:

(a) Ability to produce highly aligned electro-spun fibres with a controlled trajectory during electro-spinning.

(b) A simple set-up that can be retrofitted to any existing conventional electro-spinning set-up.

(c) A facility to spool the aligned nano-fibre array continuously along the fibre alignment direction.

(d) Ability to apply tension whilst spooling.

The rationale for the electro-spinning rig that was designed was as follows. Previous researchers [10, 353] had shown that the flow of current was detected during electro-spinning. This was considered as the movement of charged species from a positively or negatively charged terminal to the grounded collector. Therefore, it was assumed by the author that using insulating materials could be used to shield and control the movement of the charged species, thus controlling the trajectory of the fibre jet. Another benefit of using the insulating dielectric material is that no secondary electric field (power supply and auxillary electrodes) is required to control the fibre trajectory. The proposed set-up is significantly simpler and practical when compared to other methods that have been reported in the literature for producing aligned electro-spun fibres. Furthermore, the proposed method enables the fibres to be extracted for post-processing. The following section describes the design and construction of the proposed fibre alignment technique.

3.2.1.2. Electro-spinning of Oriented PAN Nano-fibre Using the Vee-shield Collector

A custom-designed grounded collector, referred to as the Vee-shield collector, was used to produce aligned PAN nano-fibres. The primary difference between the conventional flat-plate electro-spinning (Figure 3.2.2), and the Vee-shield methods (Figure 3.2.4) is the presence of a Vee-shaped fixture on the grounded electrode. The insert in Figure 3.2.4a shows a magnified view of the Vee-fixture. The Vee-shield was constructed from a sheet of PTFE (Direct Plastic, UK) with dimensions of 10 cm width, 25 cm length and 3 mm thickness; the angles of the Vee-shield were varied as required, but they generally ranged from 45° to 75° about the vertical plane. The flat section of the Vee-shield was generally 6 mm wide and 100 mm long. A black craft paper (80 gsm, Ryman, UK) strip with dimensions of 0.6 cm x 10 cm x 0.1 mm was used as the static substrate for collecting aligned nano-fibres. The fibre alignment direction is shown by the arrow in the insert of Figure 3.2.4. The solution feed rate when using the Vee-shield was maintained at 0.01 ml/hour, and the applied voltage was kept at 14 kV, and the chamber temperature and RH were maintained at 55 ± 4 °C and 13 ± 4%, respectively.

The static Vee-shield grounded collector shown in Figure 3.2.4 was modified to enable continuous spooling of the electro-spun nano-fibres. The spooling (tape winding) rig was custom-built with a length and width of 350 mm and 150 mm, respectively. A schematic illustration of this continuous spooling rig is shown in Figure 3.2.6. The chassis of the rig is made of PMMA, and all rollers were made of PTFE. The rollers had a 0.65 mm gap width to fit 6 mm craft paper tape width. The inner surface of all rollers was covered with rubber to maintain the friction between the roller and the paper substrate. The take-up roller was driven by a speed-adjustable step motor (Charged Labs, UK) which was capable of a linear speed from

0.01–1 mm/minute. Figure 3.2.5 shows how the craft paper was threaded through the two slots in the flat section of the PTFE Vee-shield. The main purpose of this rig was to feed the paper substrate continuously to the Vee-shield collector and to collect the aligned nano-fibre preformed in one direction. A video of the spooling can be seen from the link provided (https://www.nature.com/articles/s41598-021-99890-w).

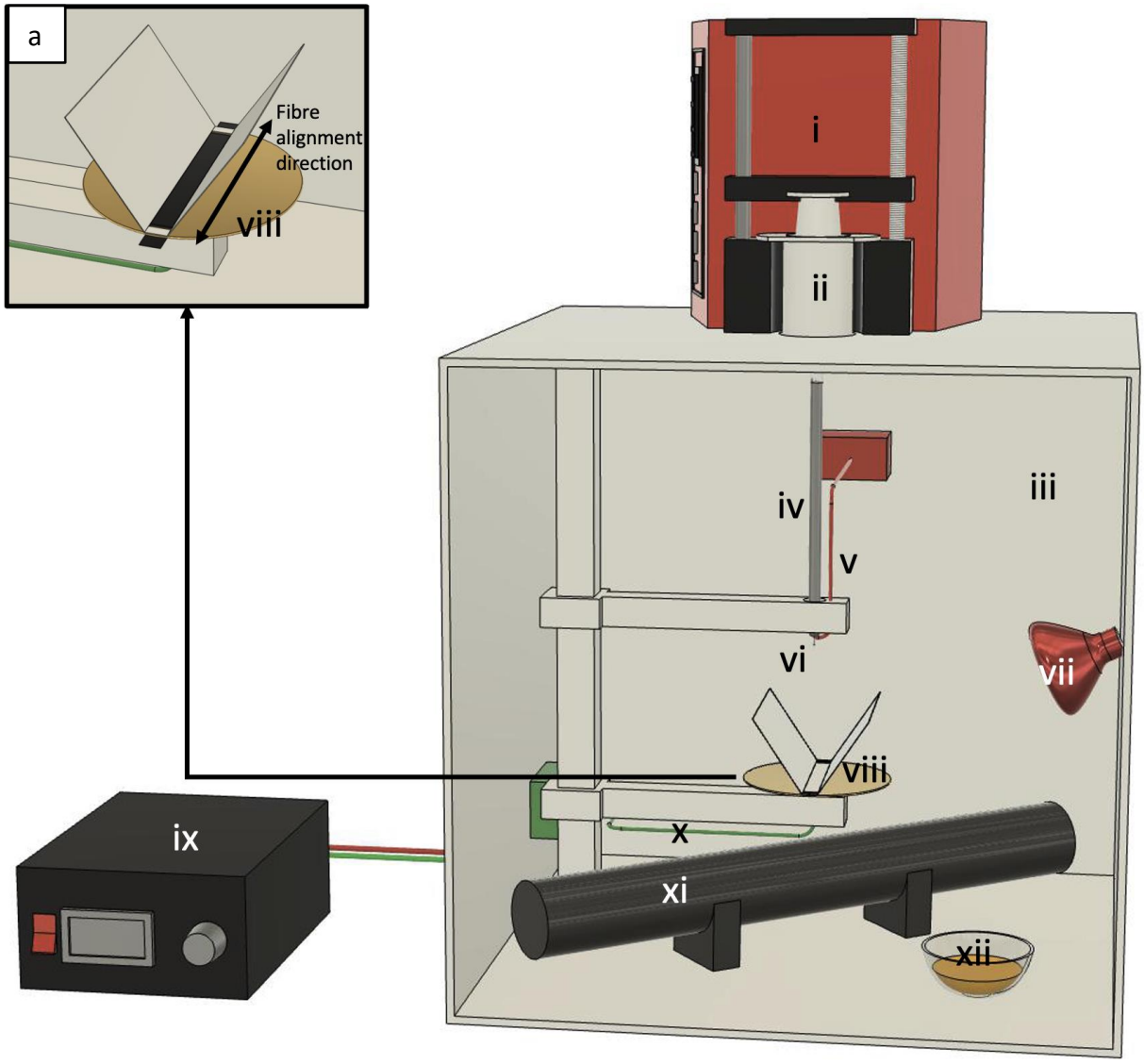

Figure 3.2.4 Cont.

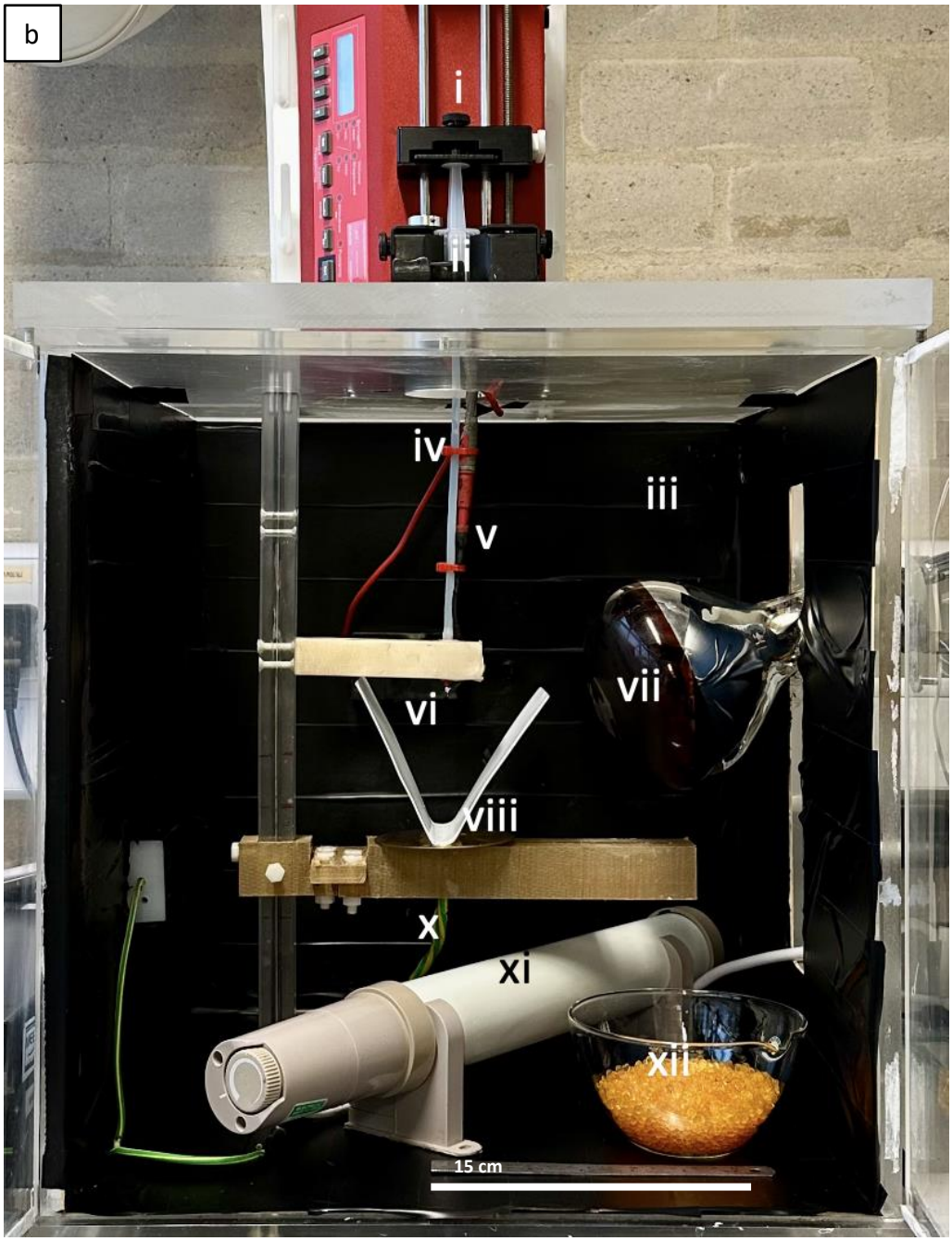

Figure 3.2.4 (a) Schematic illustrations and (b) photographs of the custom-designed Vee-shield grounded electrode configuration for producing aligned nano-fibres: (i) solution dispensing unit; (ii) syringe; (iii) electro-spinning chamber; (iv) PTFE tube; (v) positive terminal; (vii) IR lamp; (viii) Vee-shield collector; (ix) high-voltage power supply; (x) ground wire; (xi) static storage heater; and (xii) silica gel. The insert in Figure 3.2.4 (a) shows a magnified view of the Vee-shield collector and the fibre alignment direction.

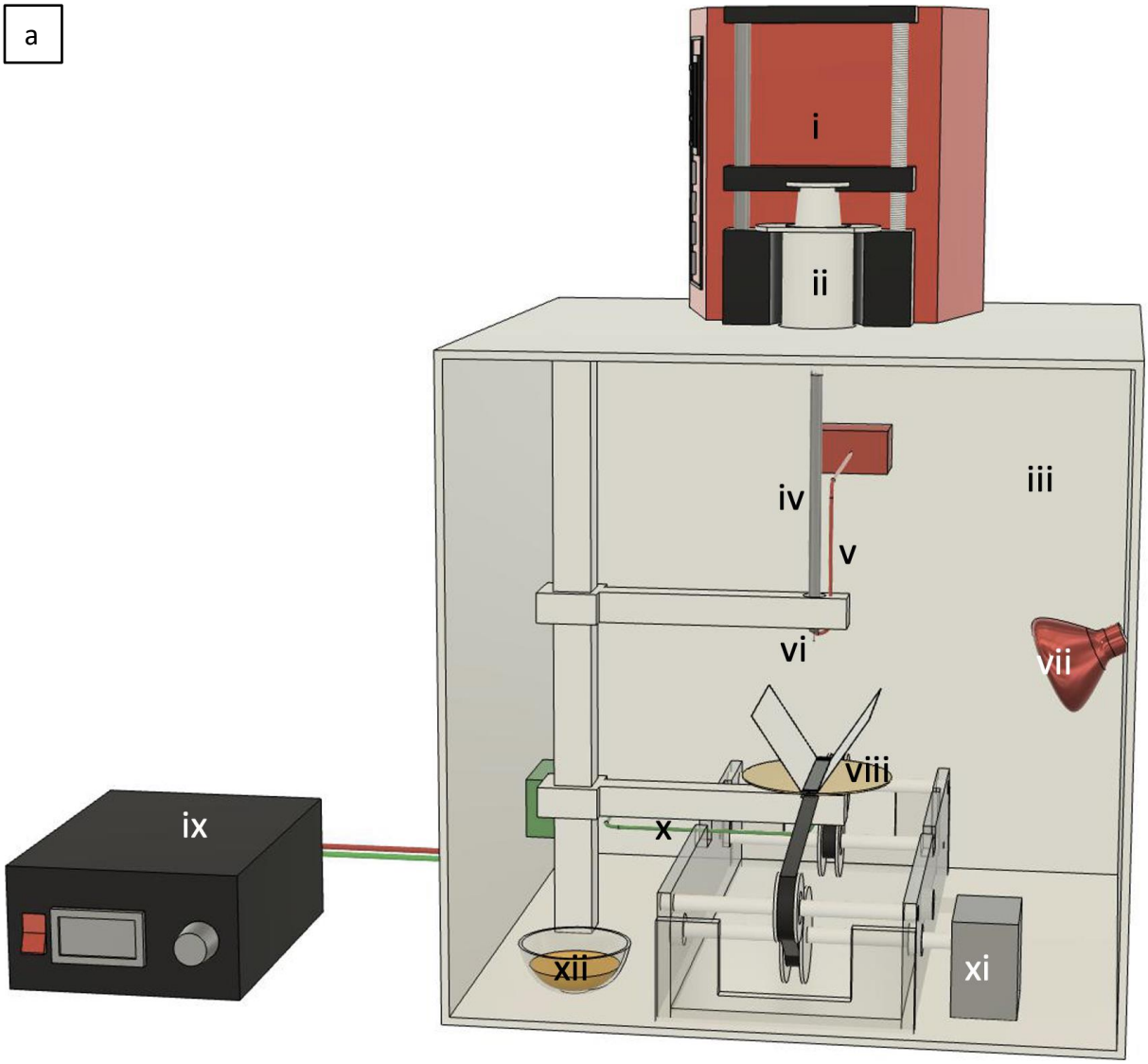

Figure 3.2.5 Cont.

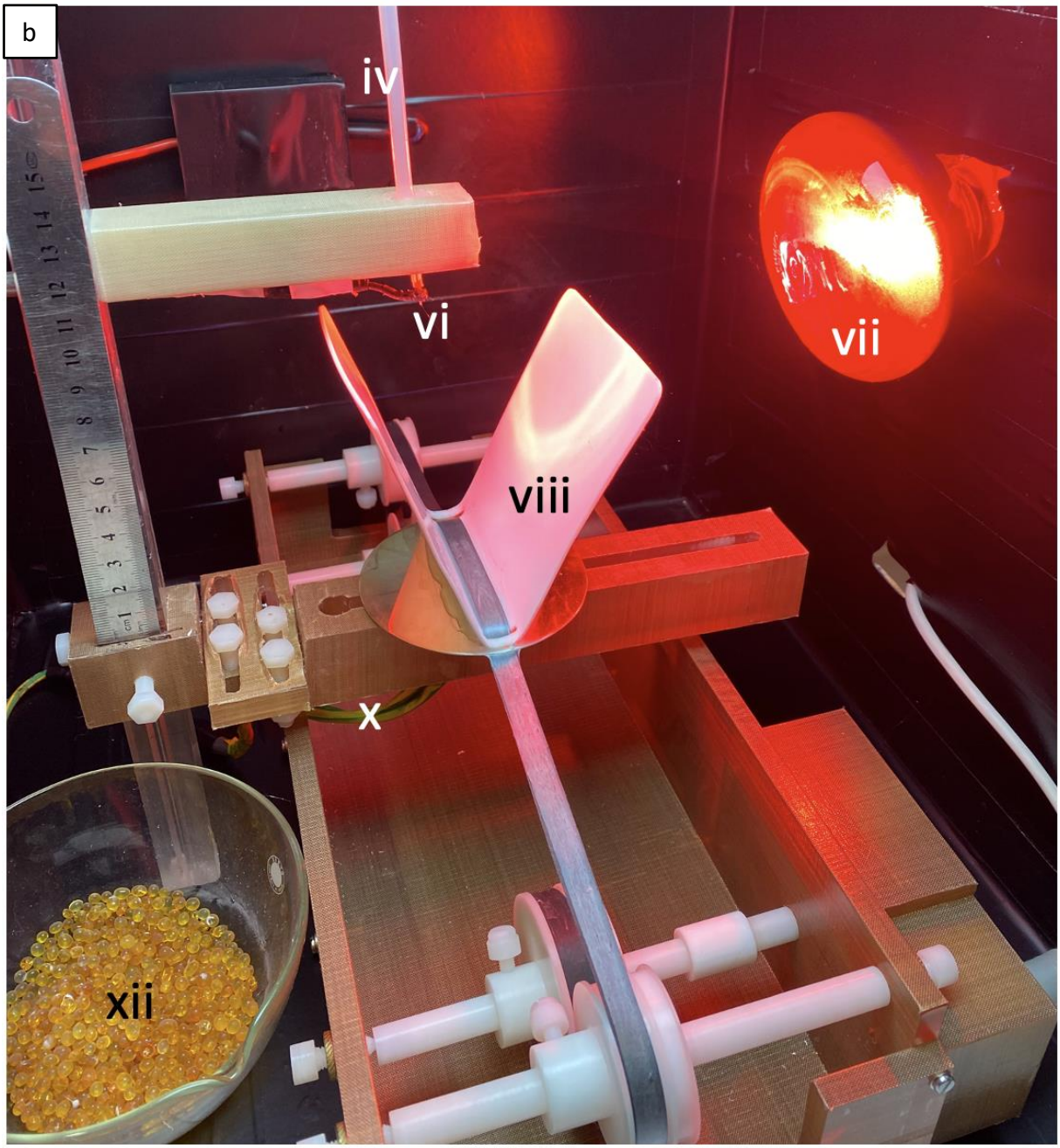

Figure 3.2.5 (a) Schematic illustration and (b) photograph of the custom-designed spooling set-up for continuous producing aligned nano-fibres using a Vee-shield collector: (i) solution dispensing unit; (ii) syringe; (iii) electro-spinning chamber; (iv) PTFE tube; (v) positive terminal; (vii) IR lamp; (viii) Vee-shield collector; (ix) high-voltage power supply; (x) ground wire; (xi) winding motor; (xii) silica gel; and (xiii) tape winding rig.

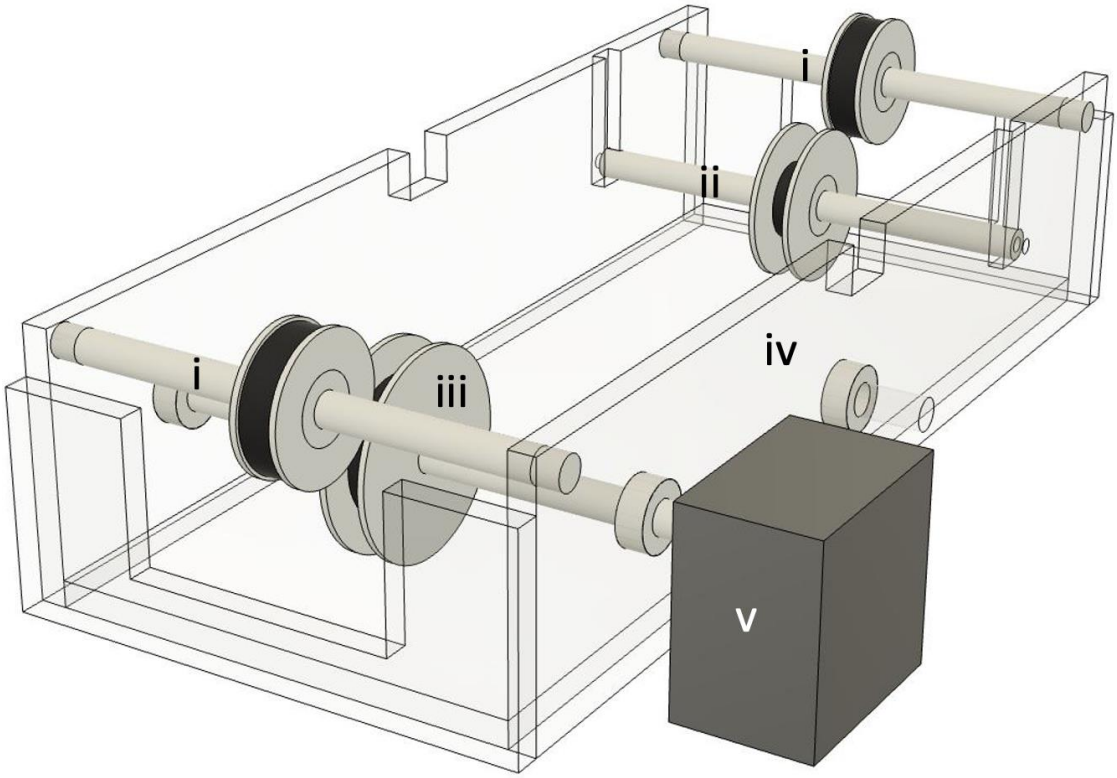

Figure 3.2.6 Schematic illustration of the custom-designed continuous spooling set-up: (i) levelling roller; (ii) feeding roller; (iii) take-up roller; (iv) main chassis; (v) winding motor.

3.2.2. Recovery and Storage of the As-spun Fibres

(i) Randomly oriented PAN nano-fibres: As discussed in Section 3.2.1.1, the conventional static grounded plate electrode was not used for producing the tensile test specimens because the thickness was not uniform across the area where the fibres were deposited. Instead, the randomly oriented fibres were manufactured using a rotating mandrel collector to produce the tensile test specimens and for further characterisation. After electro-spinning, the aluminium foil substrate was removed from the mandrel. A strip with dimensions of 6 mm x 315 mm was cut from the centre of the foil using an 18 mm rotary cutter (Olfa, UK). A photograph of the electro-spun PAN nano-fibres on the aluminium foil is shown in Figure 3.2.7,

where the length inscribed (315 mm) represents a width of 6 mm around the circumference of the mandrel that was directly below the needle (spinneret). The rotary cutter for sectioning was adopted as normal blades and scissors caused significant crinkling of the aluminium foil. It was also observed to reduce the deformation that was induced on the PAN fibres. The 6 mm x 315 mm strip was cut into four individual lengths with lengths and widths of 65 mm x 6 mm, respectively.

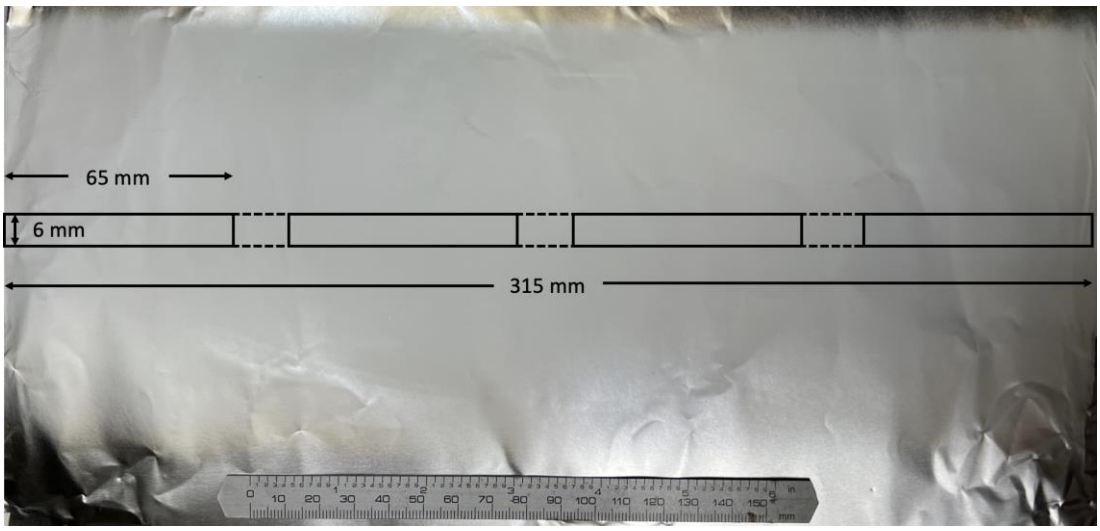

Figure 3.2.7 Photograph showing the randomly oriented PAN nano-fibres that were deposited on an aluminium foil substrate that was wrapped around the mandrel. The rectangle shows the location where the strip was cut out for preparing the tensile specimens.

(ii) Aligned PAN nano-fibres: The aligned nano-fibres were prepared using the Vee-shield as the collector during electro-spinning. Before removing the nano-fibres and paper substrate from the collector, an 18 mm rotary cutter was used to cut along the edge of the 6 mm × 65 mm paper substrate. Removing the substrate without this step was observed to cause the degree of alignment of the nano-fibre to be interfered with by those that were deposited outside the area of the substrate.

Both the as-spun random and aligned nano-fibre strips/bundles with dimensions 65 mm x 6 mm were delaminated from their substrates and transferred to a paper frame (see Figure 3.2.8b) with dimensions shown in Figure 3.2.8a prepared in advance. In order to enable alignment of the strip/bundle and easy sectioning, a 20 mm grided paper (100 gsm, VIZAL, UK) was used. The outer frame was sectioned with a steel craft knife (Olfa, UK). The inner frame was cut using a hand-held cutter punch (CUT50-18, My-Accessories, UK) that enabled reproducible dimensions of the frame to be produced. Next, two 24 mm x 8 mm double-sided tapes (GTSE, China) were placed on the top and bottom of the paper frame. The as-spun nano-fibre sample was attached to the frame with the fibre-side down and the craft paper on the surface, as shown in Figure 3.2.8d. Then, the craft paper substrate was peeled carefully off the nano-fibre bundle (see Figure 3.2.8e). A 20 mm wide sellotape (Ryman, UK) was placed at the top and bottom of the frame and gentle manual tension was applied to the fibre bundle as it was adhered to the sellotape (see Figure 3.2.8f). After that, another paper frame of the same dimensions but with double-sided tape was placed on top of the original frame to form a sandwich structure (see Figure 3.2.8g). Finally, the excess sellotape outside the frame was cut, and the sample with frame assembly was stored in a desiccator until required. The paper frame was observed to keep the tension in the aligned fibre bundle during storage and it also prevented it from curling during subsequent operations.

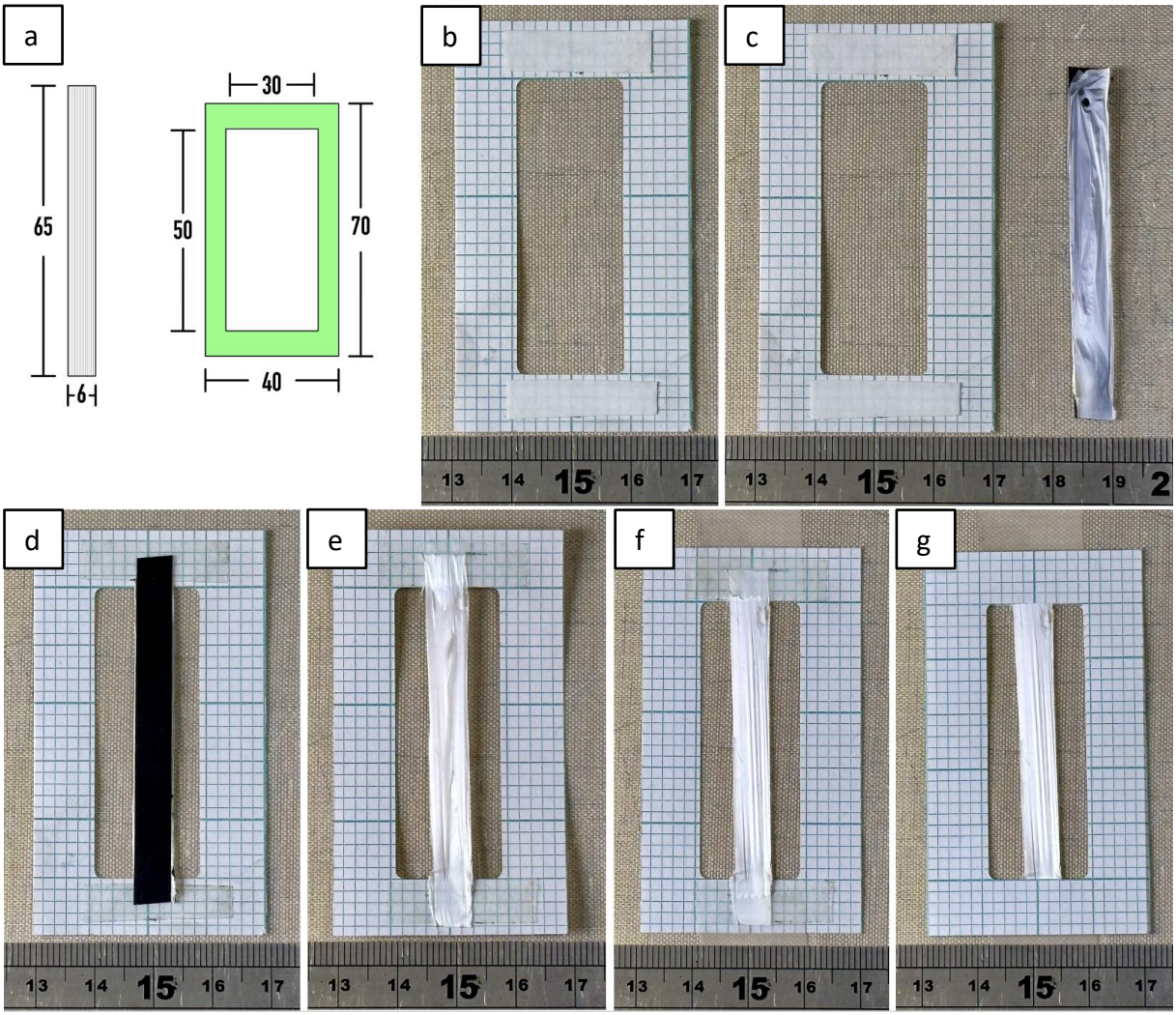

Figure 3.2.8 (a) Sechmatic diagram showing the dimensions of the nano-fibre strip/bundle (grey) and the paper frame (green); the dimensions are in mm, and (b–g) photographs of the sample transfer procedure of the as-spun random and aligned nano-fibres (see text for details).

3.2.3. Drying Regime for the Electro-spun Nano-fibres

It was necessary to remove any residual solvent in the electro-spun fibres prior to subsequent heat-treatment and characterisation. The random and aligned fibres were cut, sectioned and then transferred onto a paper frame before drying as described in Section 3.2.2. The electro-spun nano-fibres were placed on a non-stick Teflon-coated baking tray (ProChef, UK) and transferred into a vacuum oven (Gallenkamp, UK) (see Figure 3.2.9) that was operated at 1 bar. Light manual tension was applied to the fibre bundle in the paper frame, and it was fixed onto the tray using a heat-resistant tape (3M, 8992, UK), see Figure 3.2.10a. Photographs of the nano-fibre before and after heating are presented in Figure 3.2.10b and c, respectively. The samples were heated from ambient temperature at 10 K/minute to 100, 120 or 140 °C with a dwell time of 6 hours, after which the vacuum oven was permitted to cool naturally to ambient temperature. The fibre samples with the paper frame were stored in a desiccator until required.

Figure 3.2.9 Photograph of the vacuum oven set-up for drying the electro-spun nano-fibre: (i) vacuum pump; (ii) silica gel bottle; (iii) liquid nitrogen container; (iv) set temperature switch; (v) cut-off temperature switch; (vi) main switch; (vii) pressure gauge; (viii) gas inlet; (ix) gas outlet; (x) vacuum oven; and (xi) thermometer.

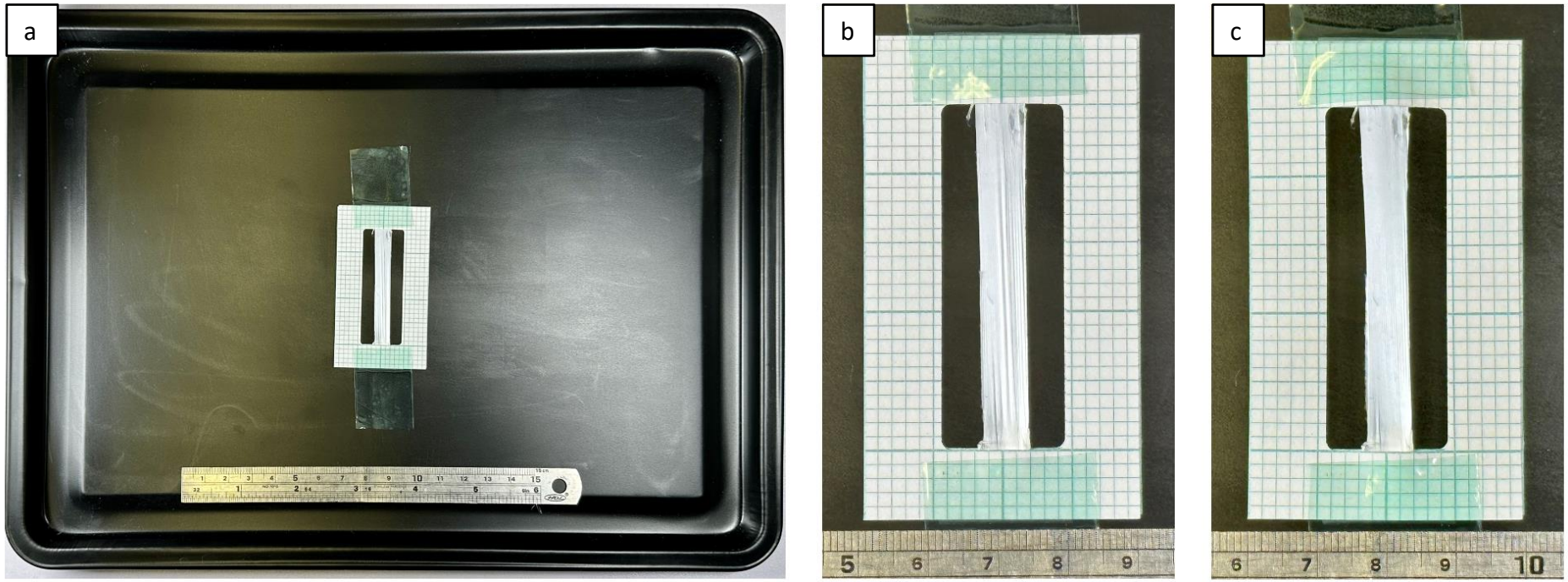

Figure 3.2.10 Photograph of (a) the nano-fibre bundles with the paper frame been adhered on a tray for drying. (b) A magnified photograph of electro-spun nano-fibres before drying. (c) A magnified photograph of electro-spun nano-fibres after drying in the vacuum oven.

3.3. Pyrolysis of the Electro-spun PAN Nano-fibres

3.3.1. Temperature Gradient Within the Tube Furnace

The pyrolysis experiments were conducted in an alumina tube furnace (PYRO THERM Furnaces, UK). An alumina tube (ALM4638, Almath Crucibles Ltd., UK) with inner and outer diameters of 38 mm and 46 mm, respectively and a length of 1,200 mm, was inserted into the tube furnace. A schematic illustration of the experimental set-up for the gas inlet and furnace assembly is presented in Figure 3.3.1. Two adjustable aluminium stands were manufactured by the University Workshop, and they were used to support, level and position the alumina tube at the centre of the furnace tube. Nitrogen gas or dried compressed air was supplied to the alumina tube via a flange that was bonded to the gas inlet side of the furnace using a high-temperature resistant adhesive (CIA, Technicqll silicate 1200, UK). The gas flow rate was regulated by a gas flowmeter (PLATON, UK). The temperature gradient profile within the alumina furnace tube was determined using a Pico TC-08 datalogger (Pico Technology, UK). The temperature was measured using an 80 cm long platinum-rhodium thermocouple (R-Type) and recorded using Pico TC-08 and Picolog Data Logging Software (Pico Technology, UK). The centre of the furnace tube was defined as the reference position '0'. In order to determine the effective heating length of the tube from the centre of the tube, the temperature gradient was measured from the centre in 5 cm increments as the tip of the thermocouple was withdrawn. The flow rate for the nitrogen gas (BOC, UK) through the furnace was set as 50 ml/minute. The temperature controller was programmed to heat from room temperature to 300 °C at 2 K/minute, then to 1,200 °C at 5 K/minute, and the heating rate curve was also obtained. The temperature was recorded after a dwell of 5 minutes at each desired position

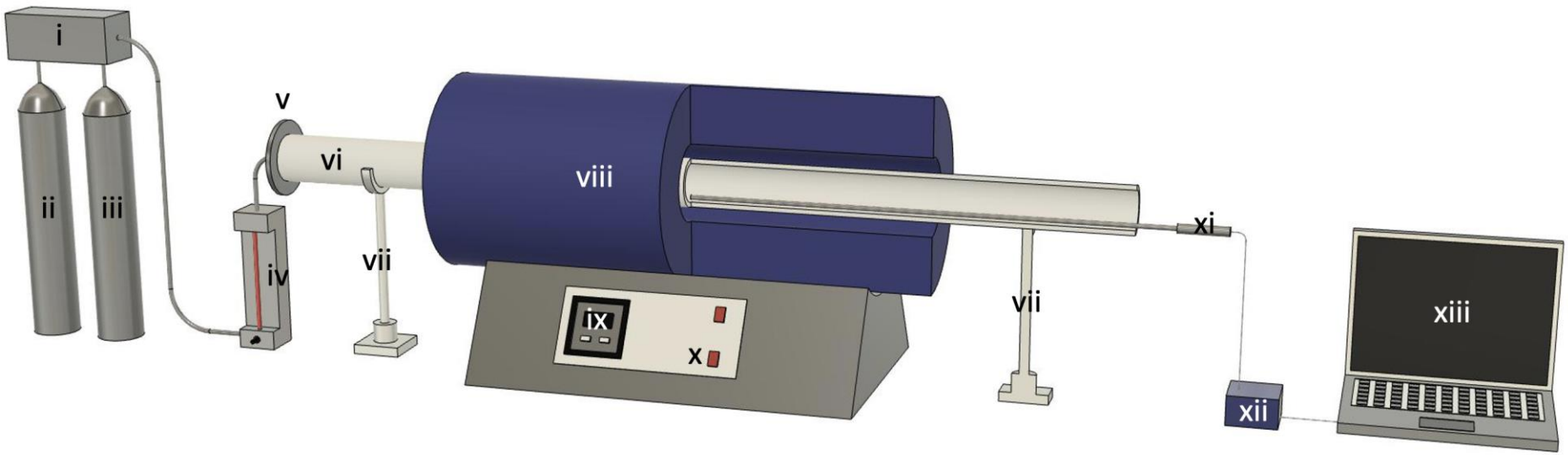

Figure 3.3.1 Schematic illustration of the experimental set-up for the furnace, nitrogen and dry compressed air supply: (i) gas regulator and switches; (ii) compressed nitrogen cylinder; (iii) compressed air cylinder; (iv) gas flow meter; (v) inter steel flange; (vi) alumina tube; (vii) tube stand; (viii) tube Furnace; (ix) temperature program display; (x) main switches; (xi) thermocouple; (xii) datalogger; and (xiii) computer.

along the alumina tube. In these experiments, the flange at the gas output-end was not used to enable the withdrawal of the thermocouple. The data from these experiments are presented in the Result and Discussion Section 4.2.1.

3.3.2. Custom-designed Rig and Sample Preparation for the Thermal Treatment of the Electro-spun PAN Nano-fibres

The inner bore diameter of the alumina furnace tube that was available for this research was 38 mm. A rig was custom-designed and manufactured to fulfil the following requirements:

(i) To apply tension, minimising the shrinkage of the nano-fibres during oxidation and subsequent carbonisation.

(ii) To simplify the loading and unloading of the rig with the samples into and out of the alumina furnace tube.

(iii) To apply a uniform temperature over the length of the samples in the rig.

(iv) To provide a simple method for weight-control that could be applied to each specimen.

(v) To allow for heat-treatment of multiple specimens where each specimen is loaded independently.

A photograph and schematic illustration of the various components of the custom-designed rig is shown in Figure 3.3.2a and b, respectively, along with their relevant dimensions. Figure 3.3.3 shows the sequence of practical steps that were involved in attaching and loading the electro-spun samples in the rig. A photograph of the assembled rig with the electro-spun fibres attached (without weights (rods)) is presented in Figure 3.3.2a.

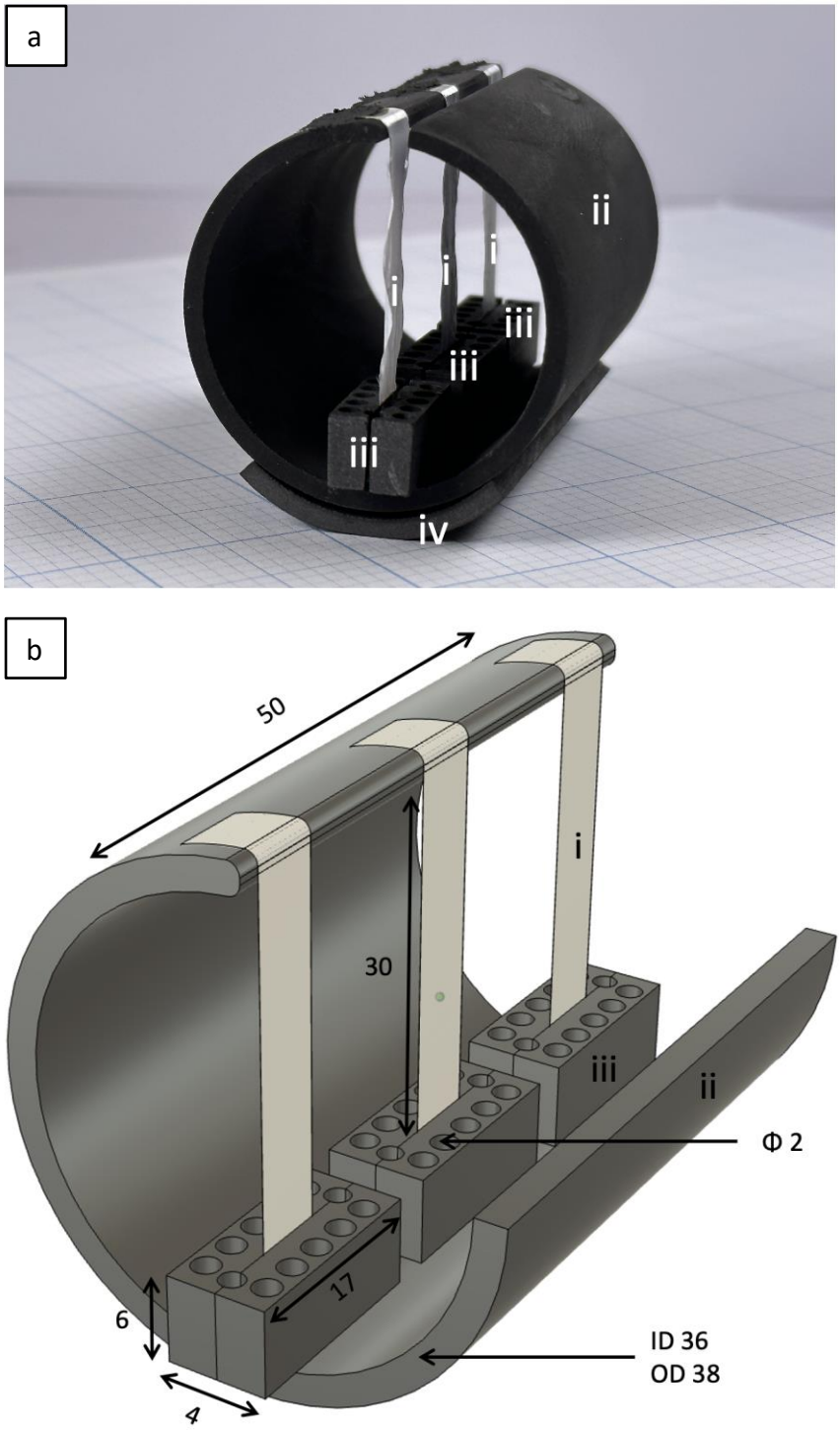

Figure 3.3.2 (a) Photograph and (b) schematic illustration of various components of the custom-designed heat-treatment rig. The dimensions are in mm. (i) Nano-fibre bundle; (ii) graphite fixture; and (iii) graphite weight holder.

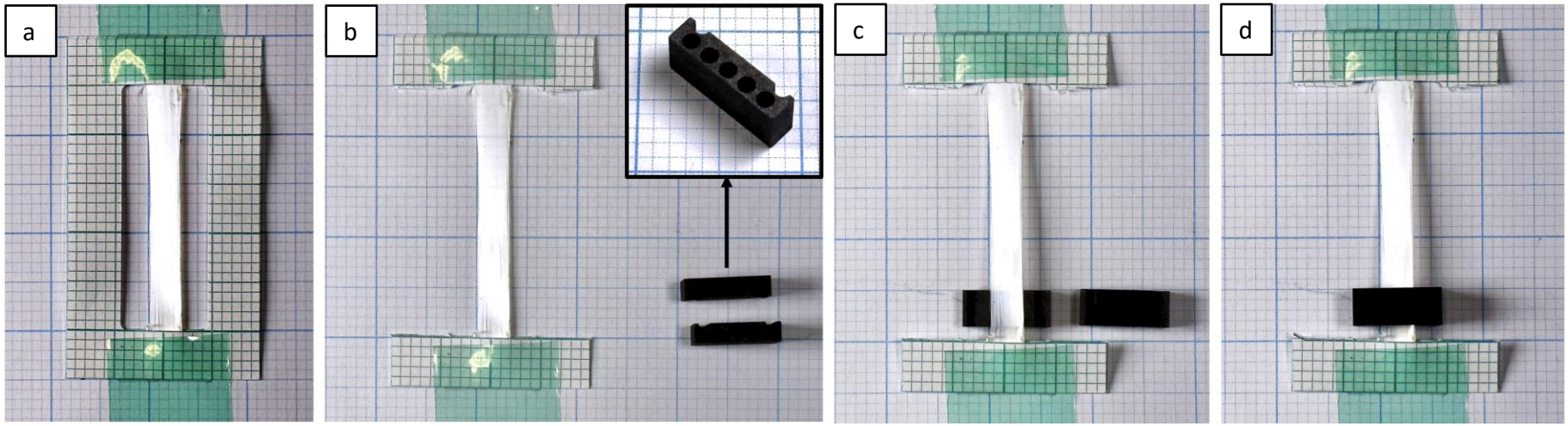

Figure 3.3.3 (a–d) Illustration of the sequential steps that were taken in attaching and loading the electro-spun fibres on the heat-treatment rig.

The insert in Figure 3.3.3 (b) shows a magnified view of the graphite weight.

After the fibres were dried and removed from the vacuum oven as described in Section 3.2.3, they were transferred to an A4 graph paper. The tension of the fibres was observed to be maintained where heat-resistant tape was used (see Figure 3.3.3a). Figure 3.3.3b shows the process where the left and right side of the vertical portion of the paper frame was cut for easier operation of the following steps. Two high-density graphite 'weights' of dimensions 40 mm x 70 mm x 170 mm were bonded to the bottom sides of the fibre bundles using the high-temperature graphite adhesive mentioned in Section 3.1. This was carried out in two stages, where Figure 3.3.3c and d show the graphite weights being positioned and bonded on the fibre bundle, respectively. The adhesive was cross-linked in an air-circulating oven at 100 °C for 4 hours. The sample was placed horizontally, and a 5 g weight was placed on top of the graphite weight to create a relatively uniform bond-line. The protruding fibre bundle below the graphite weights was removed carefully using a rotary cutter.

From the remaining sample, a section 30 mm long, was cut and removed. As shown in Figure 3.3.2a, the fibre bundle with the graphite weight was transferred to the 38 mm diameter graphite fibre holding rig with a length of 50 mm and a wall thickness of 1 mm. A thin layer of the high-temperature adhesive was applied to the outer surface of one wall of the slot. The fibre bundle with the graphite weight was fastened to the slotted graphite tube using a piece of adhesive tape; the width of the fibre bundle was positioned to coincide with where the adhesive was applied. The fibre bundle was impregnated with the adhesive by massaging the fibres carefully and gently. Another layer of high-temperature adhesive was placed on top to ensure all fibres were fully impregnated and secured. The base of the pre-bonded graphite weights was positioned to be suspended a fraction above the inner bore of the graphite tube. The high-temperature adhesive was cross-linked at 100 °C for four hours. The excess fibre

bundle that was secured to the top surface of the graphite tube was cut carefully and removed. The graphite tube could accommodate three individual fibre bundles, with a pair of graphite weights on each. A photograph and schematic illustration of the assembly (without weights (rods)) are shown in Figure 3.3.2a and b, respectively.

The graphite weights, where the thickness was 2 mm (see the insert in Figure 3.3.3b), were manufactured with five 5 mm deep cavities with a diameter of 2 mm. The weight of each graphite block was approximately 0.5 g, and the function of the cavities was to enable additional weight to be added using rods manufactured from zirconia, tungsten carbide or alumina. The rods were supplied in lengths of 20 mm each, which give weights corresponding to approximately 0.42 g, 1 g and 0.13 g for each zirconia, tungsten carbide and alumina rod, respectively. The additional weights were intended to be used to compensate for the shrinkage of the PAN during oxidation and carbonisation. The fixture support was necessary to maintain the spatial orientation of the graphite rig when it was loaded into the tube furnace. A photograph of the final assembly (with weights (rods)) is shown in Figure 3.3.4b.

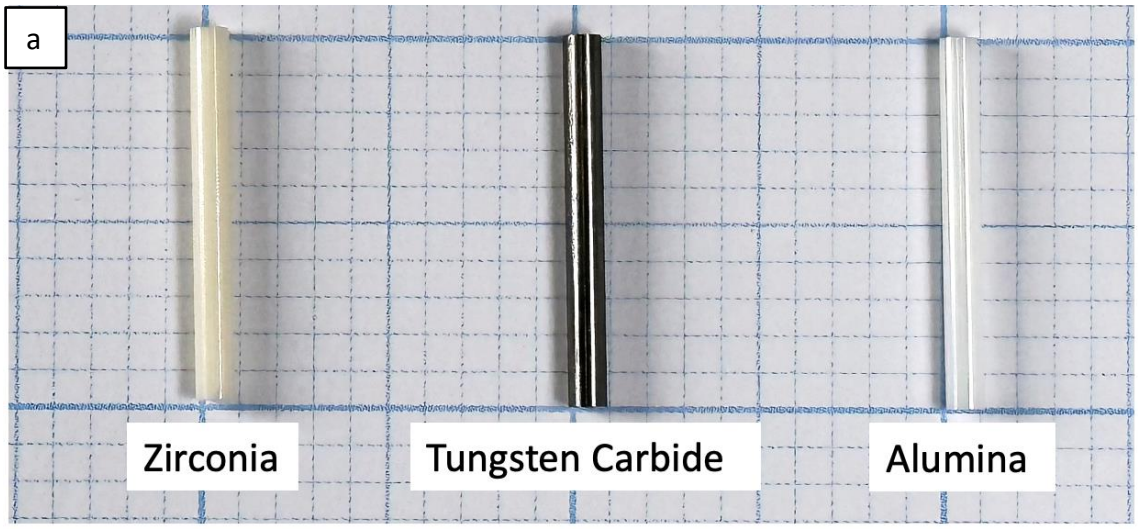

Figure 3.3.4 Cont.

Figure 3.3.4 Photograph of (a) weight rods made of zirconia, tungsten carbide and alumina and (b) the assembly of nano-fibre loaded on the graphite fixture with four alumina weights.

3.3.3. Oxidation of the Electro-spun PAN Fibres

The oxidation of the dried PAN fibres (discussed in Section 3.2.3) was carried out using the furnace set-up that was discussed in Section 3.3.1 for establishing the temperature gradient within the furnace tube. However, in this instance, after the graphite heat-treatment rig with the sample was positioned at the centre of the alumina furnace tube, a pair of porous alumina disks of dimensions 33 mm OD, 5 mm ID and 50 mm length were inserted into the gas outlet-end of the alumina furnace tube. A steel flange with a gas outlet was attached to the alumina tube. The temperature at the gas outlet of the flange when the furnace was operated at 600, 900 and 1200 °C was 45, 53 and 61 °C, respectively. The flanges were connected to a silicon rubber tube with outer and wall thickness of 10 mm and 2 mm, respectively, and attached to the gas outlet, this, in turn, was secured to a liquid trap (BS2461, Pyrex Quickfit, UK) that was

part-filled with Silicone oil (1003261003, Sigma-Aldrich, UK). The gas from the furnace tube was bubbled into the silicone oil and the effluent gas was directed to a second liquid trap that was filled with a 22 wt% of sodium carbonate (Sigma-Aldrich, UK). The outlet from the second liquid-trap was directed to a fixed air extractor system. The function of the calcium carbonate was to trap gaseous by-products produced during heat-treatment. The silicone oil was replaced when discolouration was detected visually. The calcium carbonate was replaced after every 10 experiments. Both ends of the alumina tube were sealed with high-temperature-resistant seals, and the flanges were tightened and fixed with metal screws. The presence of any leaks around the seal was checked using a detergent spray (Teepol, UK). This was done every time the gas outlet-ends of the furnace tube were disassembled and resealed. A schematic diagram and photograph of the PYRO THERM furnaces assembly with the metal flanges are presented in Figure 3.3.5a and b, respectively.

The oxidation of the electro-spun fibres was carried out in a dry compressed air environment where the flow rate was 50 ml/minute. The gas flow was switched on 5 minutes before the furnace was turned on. The sample was heated from room temperature to 100 °C with a dwell of one hour, and then the temperature was increased to 300 °C and held for one hour. The heating rate was 2 K/minute for both cases. A schematic illustration of the heating and dwell regimes is shown in Figure 3.3.6. After the final dwell period, the sample was cooled to ambient temperature naturally and the rig with the sample was removed carefully from the furnace. In order to remove the graphite rig with the sample, both flanges were disassembled from both ends of the tube. A 1.3 m long metal rod with a diameter of 2 mm was inserted from one end of the tube to push the graphite fixture out gently. The oxidised PAN nano-fibre samples were disassembled from the rig by cutting the top and bottom end of the nano-fibre

bundle using a rotary blade, the cut-lines are indicated by the dotted lines in Figure 3.3.7a. It was observed that the nano-fibre array remained straight without any curvature in the length or width directions when the tension was released (Figure 3.3.7b). Each sample was weighed using an analytical weighing balance described in Section 3.5.7. Samples were stored in a capped glass vial and labelled (see Figure 3.3.7c) until required for further characterisation. With regard to the carbonisation of the oxidised fibre bundles, the sample was not removed from the graphite fixture.

Figure 3.3.5 Cont.

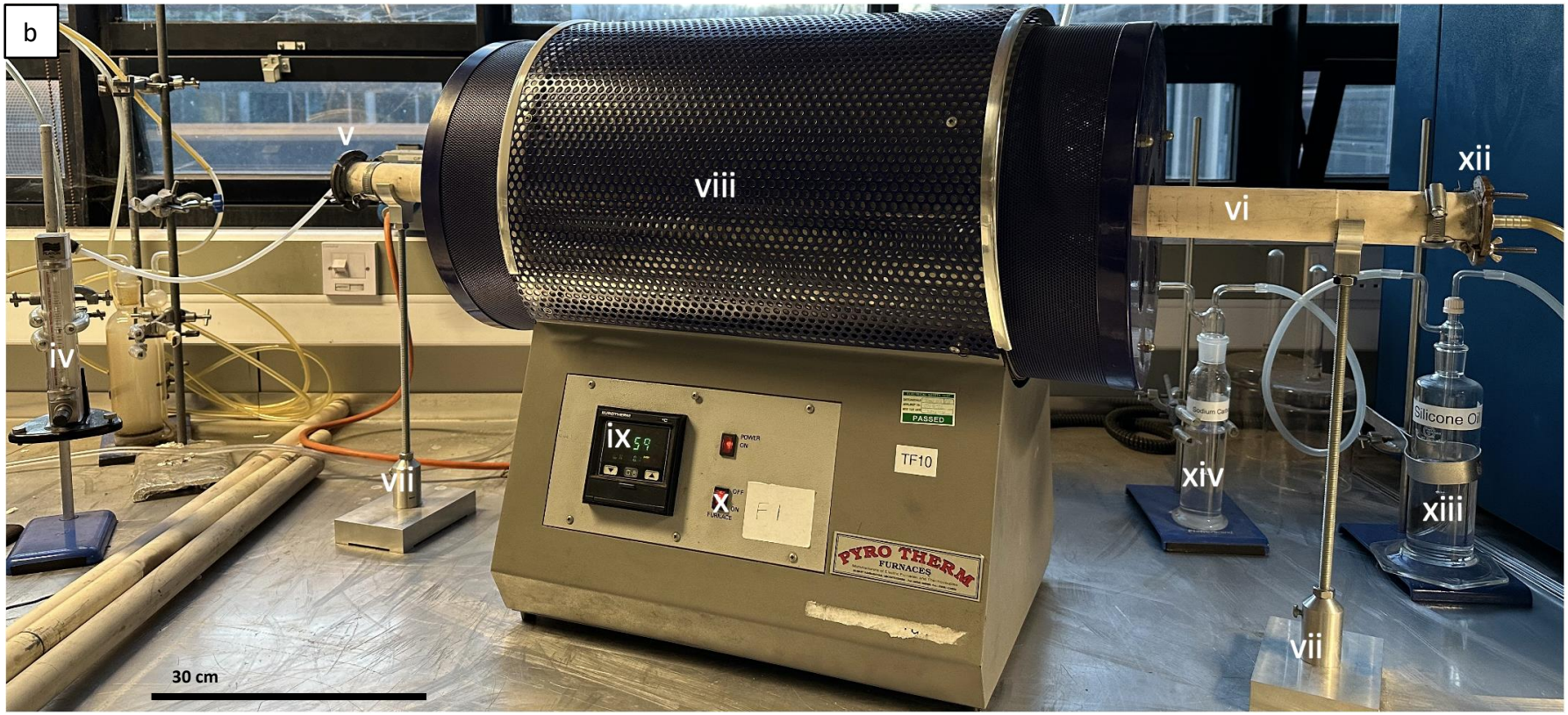

Figure 3.3.5 (a) Schematic illustration and (b) photograph of the gas supply cylinders, flow controller, furnace and liquid-trap bottles: (i) gas regulator and switches; (ii) compressed nitrogen cylinder; (iii) compressed air cylinder; (iv) gas flow meter; (v) inter steel flange; (vi) alumina tube; (vii) tube stand; (viii) tube furnace; (ix) temperature program display; (x) main switch; (xi) porous alumina brick; (xii) outlet steel flange; (xiii) silicon oil liquid trap; and (xiv) sodium carbonate liquid trap.

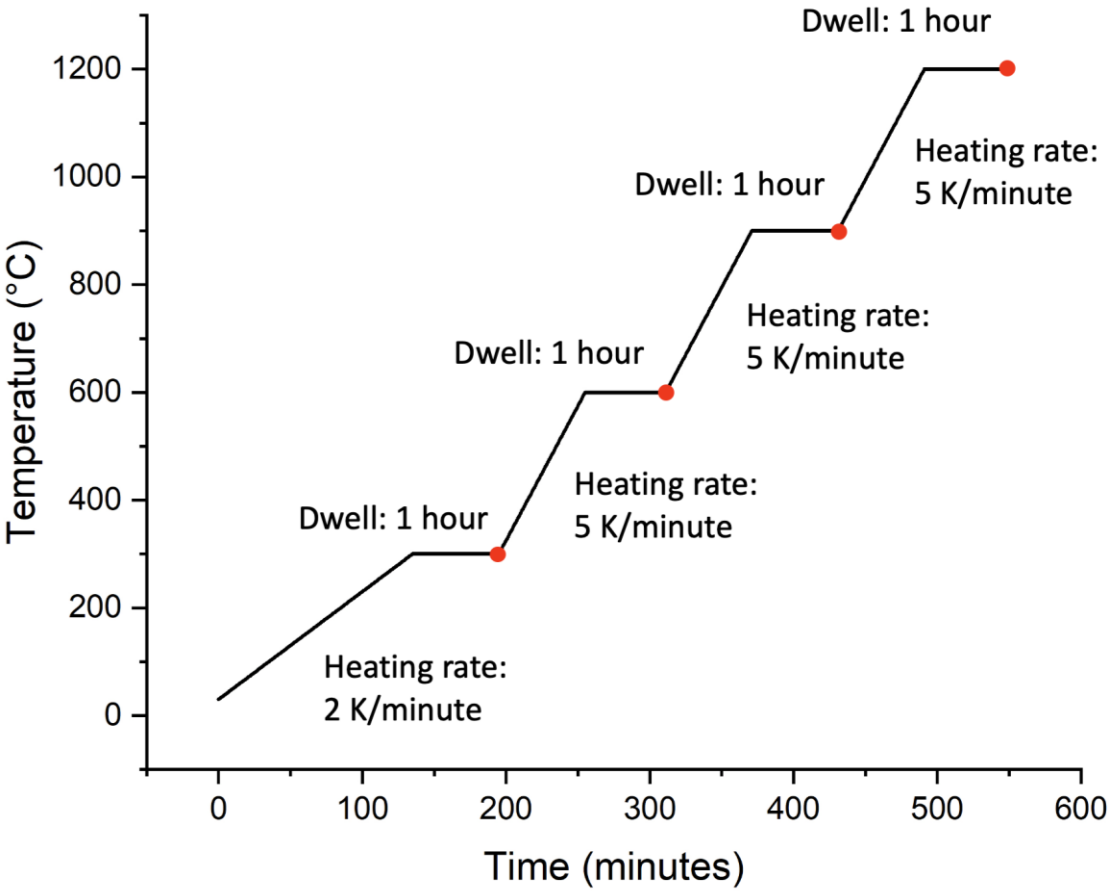

Figure 3.3.6 Illustration of the heating rate and dwell periods that were used for the stabilisation and carbonisation processes. The red circles represent the time when samples were removed for characterisation.

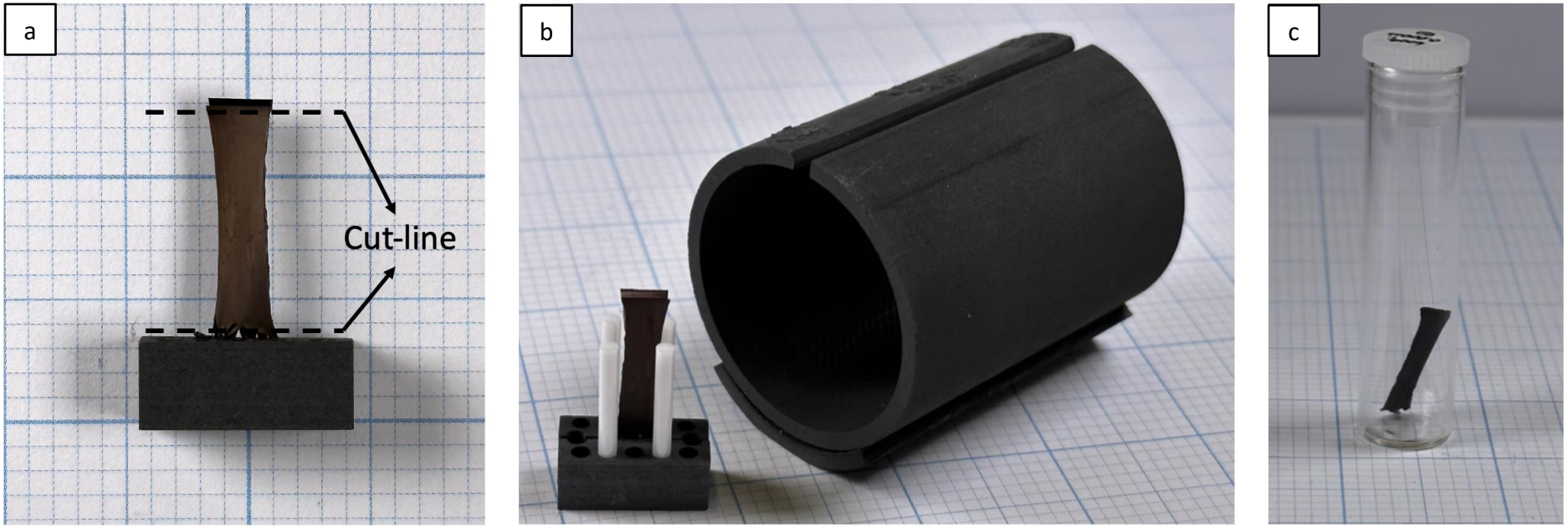

Figure 3.3.7 Photograph of (a) an oxidised sample where the dotted lines indicate the cut-line for removal of the fibre from the fixture. (b) Graphite fixture and nano-fibre assembly after stabilisation. (c) The stabilised nano-fibre sample was stored in the capped glass vial.

3.3.4. Carbonisation of the Oxidised PAN Nano-fibres

The carbonisation of the fibre bundles was carried out directly after the stabilisation process without taking the sample from the tube furnace. After the nano-fibre bundles were stabilised at 300 °C for one hour, the gas was switched from compressed air to nitrogen, where the gas flow was maintained at 50 ml/minute. The tube furnace was programmed to heat at 5 K/minute from 300 °C to 600, 900 or 1200 °C as required, with one hour of dwell at those temperatures. After the final dwell period, the sample was cooled to ambient temperature naturally, and the rig with the sample was removed carefully from the furnace using the same method as described in Section 3.3.3. Six samples were prepared from each carbonisation temperature. The pyrolysed samples were characterised using SEM, XRD and Raman spectroscopy. The details of the characterisation tests are described in Section 3.5.

It was observed that fibres carbonised at 1200 °C were not able to sustain any imposed load from the graphite weight. Carbonisation of the fibre bundle at 1200 °C was obtained by heating the fibre carbonised previously at 900 °C in the fixture shown in Figure 3.3.7 and then transferring the sample to an 8 cm alumina boat crucible (SRX115, Almath Crucible Ltd., UK), see Figure 3.3.8a. In order to avoid the fibre been blow off by the nitrogen gas flow, a 38 mm OD 30 mm ID graphite fixture (Rongxing Carbon, China) was used to protect the fibre during carbonisation at 1200 °C. A photograph of this assembly is shown in Figure 3.3.8.

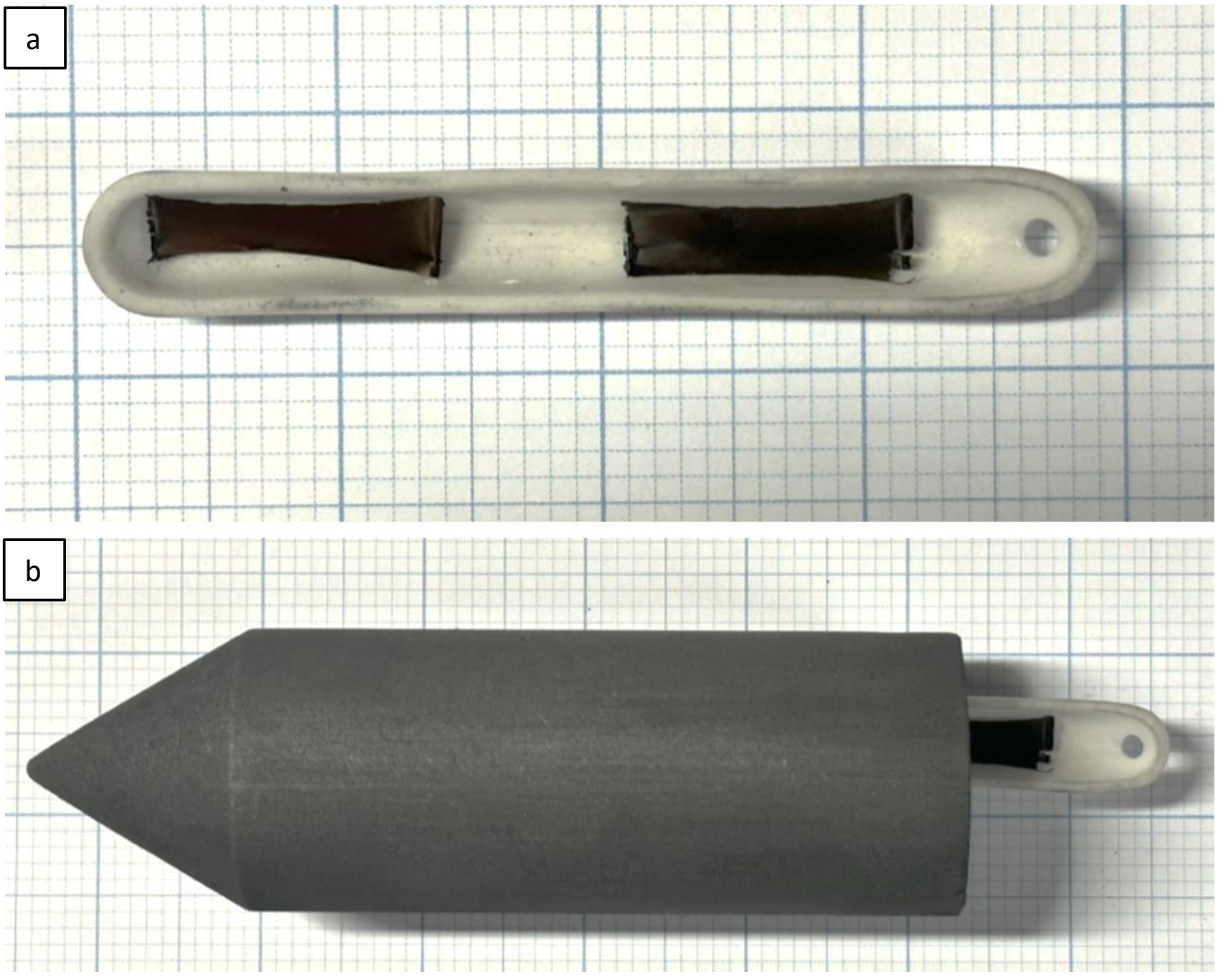

Figure 3.3.8 Photograph of: (a) an alumina boat crucible with two aligned PAN nano-fibre bundles that were pre-carbonised in the fixture shown in Figure 3.3.7; and (b) alumina boat crucible placed in the graphite fixture for carbonisation at 1200 °C. The pointed-end of the fixture faced the gas flow inlet.

3.4. Preparation of Tensile Test Specimens

Tensile tests were carried out on the as-spun, oxidised and carbonised PAN nano-fibre bundles where the orientation of the electro-spun fibres was either random or aligned. The following procedure was used to prepare the tensile test specimens.

3.4.1. End-tabbing the As-spun Nano-fibre Bundles

With reference to Figure 3.3.3a, the dried nano-fibre sample with the frame was removed from the desiccator and placed on 2 mm grid graph paper. The free-ends of the paper frame were secured to the graph paper using masking tape (Ryman, UK). A polyethylene terephthalate (PET) frame (dimensions shown in Figure 3.4.1e and g), was positioned carefully underneath the nano-fibre bundle such that the fibres were parallel to the left and right sides of the inner vertical edges of the PET frame (Figure 3.4.1a). The edges of the paper frame were lifted gently with a pair of plastic-tipped tweezers to ensure that the fibres did not rub against the plastic frame at any stage during sample preparation. After verifying the relative positions of the various items, approximately 28 μl of UV resin (Norland optical adhesive 68, USA) was evenly dispensed across the width and length of the intended end-tab bonding area at the top and bottom of the test frame using a micro-pipette (m100, Biohit, UK), (see Figure 3.4.1b). Due care and attention was paid to ensure that the impregnation was thorough and without any visual signs of under-impregnation or the presence of air bubbles. Special attention was also given to ensure that the adhesive did not wick into the gauge length of the test specimen. After the end-tab region was impregnated, another identical PET frame was placed on the top, precisely over the frame below, with the fibres sandwiched in between. Two thickness-gauges (spacers) of 0.3 mm were placed on either side of the paper frame, and a glass sheet (dimensions of 26 mm, 76 mm and 2 mm thickness with a weight of 2.4 g) was placed on top of the whole assembly, and two 100 g weights were placed on the top of the spacers; this assembly is shown in Figure 3.4.1c. This assembly was permitted to stand for one minute before a UV light with an intensity of 40 mW and wavelength between 300–425 nm (Thorlabs

560 UV-75, UK) was used to cross-link the adhesive. Due to the thickness of the UV resin, the UV irradiation was carried out in three cycles, with 30 seconds per cycle. After the adhesive had cross-linked, the fibres that were protruding outside the PET frame were cut using the rotary blade (Figure 3.4.1d). The samples were labelled and stored in a desiccator until required for testing.

3.4.2. End-tabbing the Oxidised and Carbonised Nano-fibres Bundles

As mentioned before, the shape and alignment of heat-treated nano-fibre samples could be maintained without the need for external tension. Therefore, a paper frame was not required to keep heat-treated nano-fibre bundles under tension during the preparation of the tensile test specimen. In other words, the heat-treated nano-fibre samples could be placed directly onto the PET frame. The end-tabbing method and the storage for the samples were the same as that described above. However, due to the fact that the sample shrinks as the heat-treatment temperature increase, the overall length of the carbonised fibres treated at 600 °C and 900 °C was approximately 17 mm and 16 mm, respectively. Therefore, a smaller sized frame with a smaller gauge length was used. The dimension of the small frame is shown in Figure 3.4.1g. In order to keep the consistency of the frame, the inner frame was cut using a 6.7 mm x 6.7 mm puncher (xs, Vaessen Creative, UK) and the outer frame was cut by a die puncher with 15 mm x 15 mm (CUT15-15, My-Accessories, UK). A photograph of an end-tabbed window assembly of the carbonised fibre bundle is shown in Figure 3.4.1h.

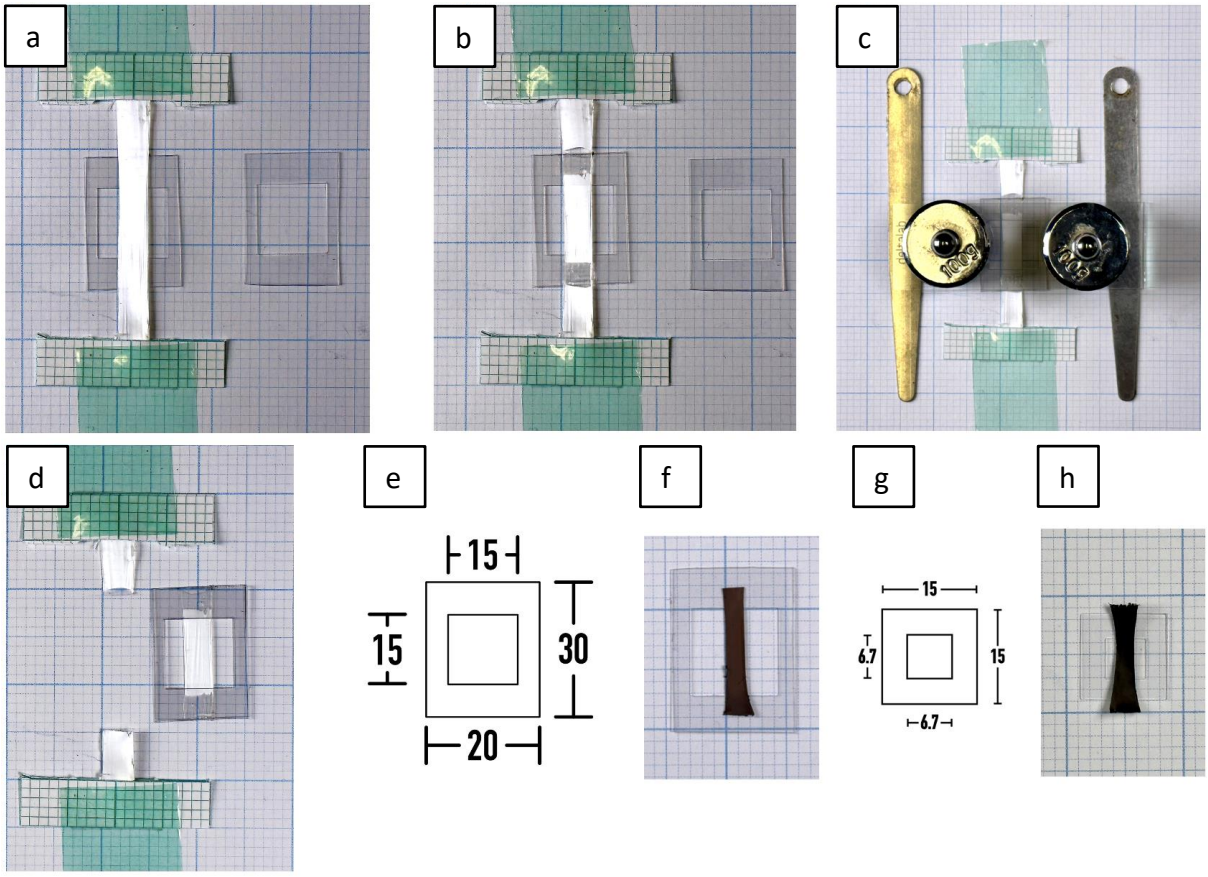

Figure 3.4.1 (a–d) Photographs showing the sequential steps that were taken to manufacture the tensile test specimens. (e) Schematic diagram of the dimension of the tensile test frame used for as-spun and stabilised nano-fibre specimen, units in mm. (f) Photographs showing the stabilised aligned fibre specimen on its test frame. (g) Schematic diagram of the dimension of the tensile test frame used for carbonised specimen, unit in mm. (h) Photographs showing the carbonised aligned nano-fibre specimen on its test frame.

3.5. Materials Characterisation

3.5.1. Rheometry

The rheological properties of the PAN/DMSO solutions were determined on a cone-and-plate rheometer (Discovery Hybrid Rheometer, model HR-1, TA instrument, UK). A photograph of the rheometer that was used is shown Figure 3.5.1. The diameter of the plates was 40 mm with a cone angle of 4°. The shear viscosity was determined using shear rates between 1–1000 s^{-1}, whereas, during the oscillation tests, the strain was kept at 25% whilst the angular frequency was changed from 0.1–500 rad/s^{-1}. Complex viscosity was obtained from the oscillation tests. The gap between the plates was set at 1.05 mm, and the experiments were carried out at 55 °C with a solvent evaporation-controlled function. The viscosity of each solution was measured three times using three fresh solutions. PAN/DMSO solution with concentrations of 2, 4, 6, 8, 10, 12, and 14 w/v% from the two PAN suppliers was characterised, including neat DMSO.

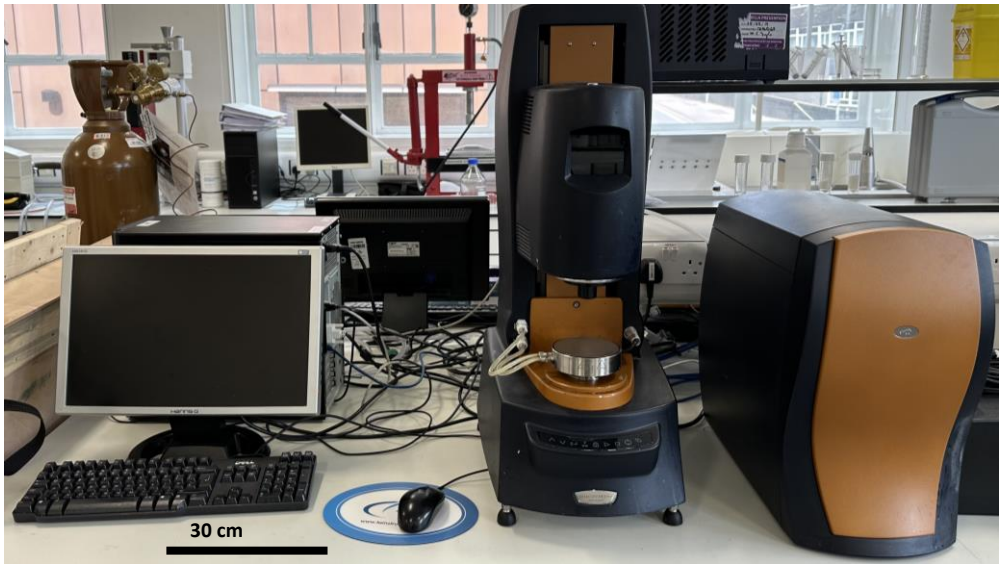

Figure 3.5.1 Photograph of the TA HR-1 Rheometer.

3.5.2. Electrical Conductivity

The following section is adapted from Section 'Characterising of polymer solution' of a co-authored paper published by the author; Shao *et al.* [15].

The electrical conductivity of the PAN/DMSO solutions was determined on a bench conductivity meter (Model 4510, Jenway, UK). A photograph of the electrical conductivity meter is shown in Figure 3.5.2. Before the measurements were taken, a sodium chloride conductivity standard solution (HI7033, Hanna Instrument) was used to calibrate the instrument at 25 °C. A temperature-controlled water bath (GD100, Grant, UK) was used to maintain the temperature during the measurements. The conductivity of each PAN/DMSO concentration was measured at 55 °C and repeated three times to obtain an average. Approximately 10 ml of each solution was used for each measurement. In order to prevent the sample from absorbing moisture during each measurement, the solution was placed in a 30 ml glass vial, and the top was sealed with a rubber stopper through which the measurement

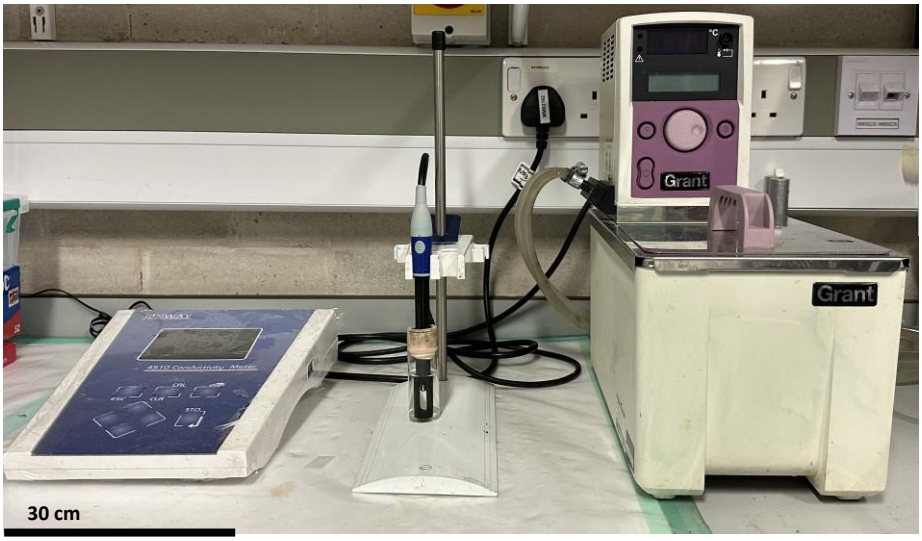

Figure 3.5.2 Photograph of the JENWAY 4510 liquid conductivity meter and a Grant GD 100 water bath that was used for temperature regulation.

probe was inserted. The conductivity data were recorded over five minutes after the set temperature was reached.

3.5.3. Surface Tension Measurements

The surface tension of the solutions were measured on a KRUSS K100 force tensiometer (Germany), as shown in Figure 3.5.3. Each experiment was repeated three times using the platinum Wilhelmy plate test geometry. 50 ml of the PAN/DMSO solution was required to maintain a minimum liquid height of 1 cm. In order to equilibrate the solution to 55 °C, it was placed in a capped glass vial and preheated in a water bath. Since the boiling point of DMSO is 189 °C, it was deemed safe to heat it in a capped glass vial. After 30 minutes, the solution was poured into a 20 cm diameter glass container and transferred into the equipment. The inbuilt heater controller of the tensiometer was used to maintain the PAN/DMSO solution at 55 °C. Three repeat experiments were conducted per solution and an average value was calculated.

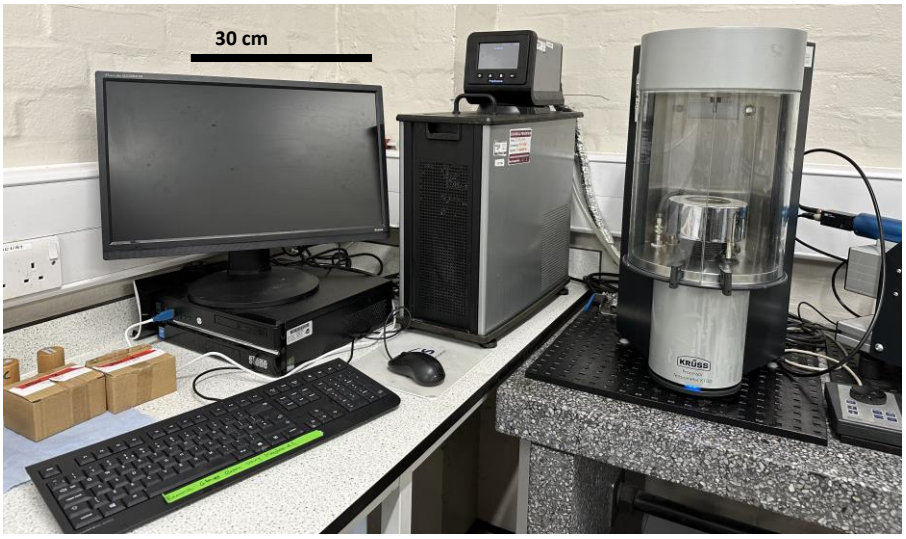

Figure 3.5.3 Photograph of the KRUSS K100 force tensiometer.

3.5.4. High-speed Camera

The following section is adapted from Section 'Characterisation of the electro-spun fibres' of a co-authored paper published by the author; Shao *et al.* [15].

A high-speed camera (Mini Ax 50, Photron, UK) was used to image the polymer jet during electro-spinning when using the conventional and Vee-shield set-ups. The equipment that was used is shown in Figure 3.5.4. The high-speed camera was operated at 100,000 frames/second with a resolution of 300 × 300 pixels.

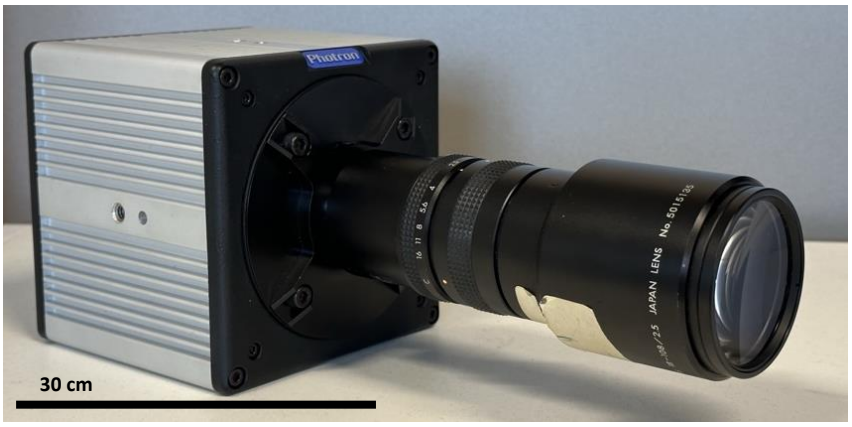

Figure 3.5.4 Photograph of the Photron Mini Ax 50 high-speed camera.

3.5.5. Differential Scanning Calorimetry

A Perkin-Elmer DSC 7 was used to characterise the as-received PAN powders, as-spun random PAN/DMSO fibres, as-spun aligned PAN/DMSO nano-fibres and cold-drawn aligned PAN/DMSO nano-fibres are shown in Figure 3.5.5. The weight of each sample was approximately 5 mg and placed in a 3 mm diameter aluminium pan (PerkinElmer, UK). Two 0.1 mm holes were punched on the 2.9 mm aluminium lid (PerkinElmer, UK) using a stainless-steel pin, and the lid and pan assembly were crimped using a standard sample pan crimper

press (Part number 02190048, PerkinElmer, UK). The experiments were conducted under a nitrogen environment where the gas flow rate was 10 ml/minute. An empty aluminium pan and lid were used in the reference compartment of the calorimeter. The temperature of the samples and reference was held isothermally at 20 °C for 1 minute and then increased to 350 °C at 10 K/minute. Calibration of the calorimeter was carried out using pure indium and tin at a heating rate of 10 K/minute from RT to 170 °C and 260 °C, respectively. The onset temperatures of these two materials were 156.61 °C and 231.90 °C, respectively. The baseline for the instrument was obtained by placing two near identical empty pans in the calorimeter, and it was programmed to perform the same heating routine as described above. The baseline was subtracted from the dataset for each batch of samples.

Figure 3.5.5 Photograph of the PerkinElmer differential scanning calorimeter 7.

3.5.6. Thermo-gravimetric Analysis

Thermo-gravimetric analyses (TGA) were used to determine the DMSO content in the PAN/DMSO nano-fibres. The TGA analyses were carried out on a NETXSCH STA 449C in an argon gas atmosphere where the gas flow rate was set at 50 ml/minute. A photograph of the equipment used is shown in Figure 3.5.6. Approximately 10 mg of the sample (as-received PAN powder, as-spun nano-fibres and dried electro-spun nano-fibres) was heated from room temperature up to 400 °C to determine the weight loss of DMSO, and to 1200 °C to study the high-temperature stability of the electro-spun fibres. The heating rate for both regimes was 10 K/minute.

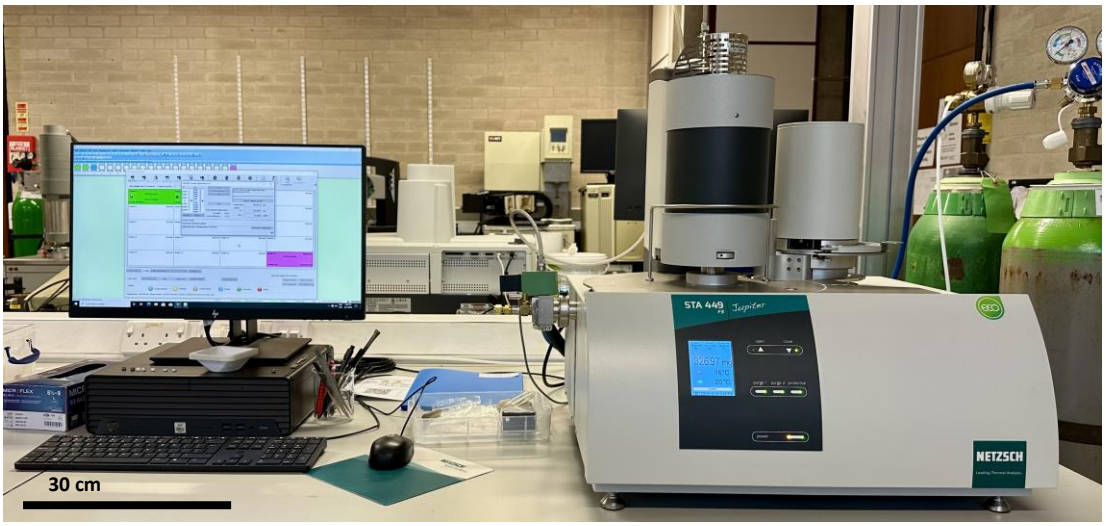

Figure 3.5.6 Photograph of the NETXSCH STA 449C.

3.5.7. Weight of the Electro-spun PAN Nano-fibres

The feasibility of using the density of the nano-fibre samples to normalise the fibre volume fraction for each of the tensile test samples was investigated. The density of each nano-fibre bundle was calculated using the bulk volume of the fibre sample and the weight of the nano-fibres. The weights of the electro-spun fibre bundles were measured individually using a Perkin-Elmer AD2Z Auto-balance, which has a measurement accuracy of 0.01 mg. A photograph of the auto-balance is shown in Figure 3.5.7.

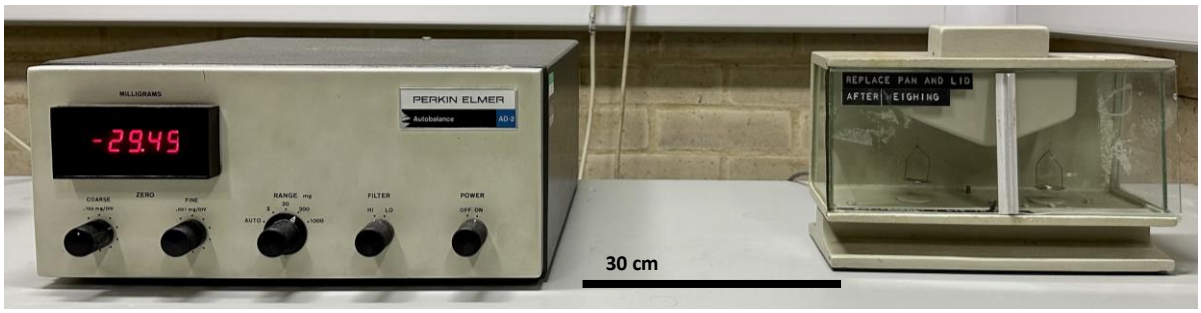

Figure 3.5.7 Photograph of the PerkinElmer AD2Z Auto-balance.

3.5.8. Scanning Electron Microscopy

The following section is adapted from Section 'Result and discussion' of a co-authored paper published by the author; Shao *et al.* [15].

The thickness, surface and cross-sectional morphology of aligned fibres were inspected using a Hitachi TM3030plus tabletop scanning electron microscope (SEM) (see Figure 3.5.8). The instrument was operated at 15 kV and the working distance was 8 µm. The electro-spun fibre mats were mounted onto a circular SEM aluminium stub using double-sided conductive carbon adhesive tape. The fibres were sputter-coated with gold/palladium alloy for 3 minutes

using an Emscope SC 500 vacuum sputter-coater to render the sample conductive. The thickness of aligned nano-fibre mats was measured from the SEM micrographs using Image-J software (NIH, USA). After electro-spinning of each batch of polymer solution, 3 out of the 10 samples were selected randomly from each batch to determine the sample thickness. Five micrographs were taken across the cross-section of the sample and 10 measurements were taken from each micrograph; this represents 50 individual measurements per sample. With regard to fibre diameter measurements after the electro-spinning of each polymer solution, one batch represents five individual samples. Two samples were selected randomly, and three micrographs were taken from three random spots from each of these samples. 100 measurements were taken from each micrograph; this represents 600 individual measurements per batch. The degree of fibre alignment for the PAN fibres obtained using the Vee-shield was also carried out using the Image-J software (Version: 2.1.0/1.53c Build: 5f23140693 Copyright 2010–2021 (https://imagej.nih.gov/ij/). The same protocol as that mentioned above for measuring the diameter of the fibres was used to quantify the relative orientation (600 measurements per batch of the sample). The micrographs were imported into the Image-J software to quantify the degree of alignment. The images were resliced to allow the border of the image to be parallel with the longitudinal edge of the substrate. A zero-degree reference line is drawn in the vertical plane that is parallel to the edge of the substrate. The orientation of the electro-spun fibre, in relation to the reference line, was obtained by drawing a line manually from one end of a fibre to the opposite end; this was performed for each of the randomly selected fibres, and the data are logged within the Image-J software.

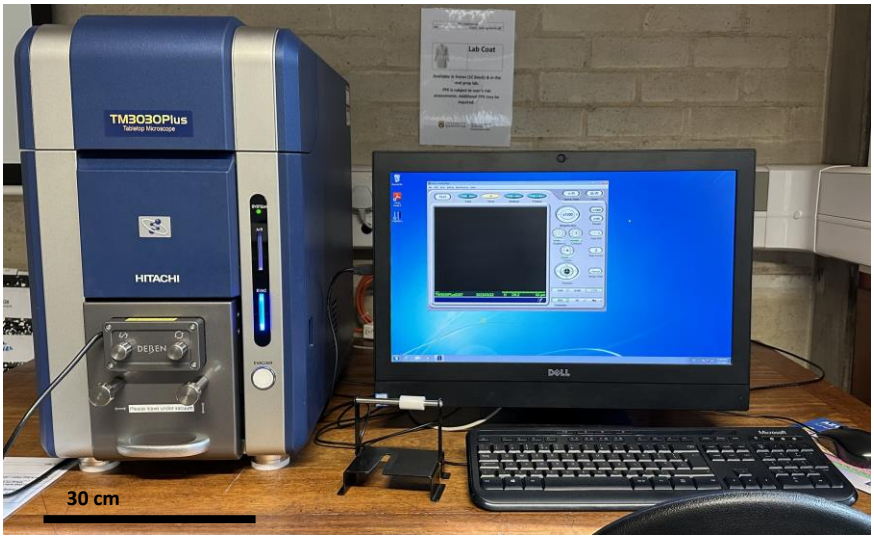

Figure 3.5.8 Photograph of the HITACHI TM3030plus tabletop SEM.

3.5.9. Transmission Electron Microscopy

A JEOL JEM-1400 transmission electron microscope (TEM), see Figure 3.5.9, was used to determine if the electro-spun fibres had a circular cross-section and to estimate the fibre volume fraction. The aligned nano-fibre samples in the tensile test frame were placed in a PTFE mould with dimensions of 25 mm x 32 mm x 20 mm. The fibres were impregnated using a mixture of 3 ml Araldite CY212 resin, 5 ml AGAR 100 (Epon substitute), 13 ml DDSA (hardener), 0.6 ml DBP (plasticiser) and 0.5 ml DMP 30 (Accelerator) to obtain a total of 22 ml of the liquid resin. The assembly was placed in a vacuum oven (Gallenkamp, UK) for 6 hours to degas the resin and to impregnate the fibres. Finally, the mould with the impregnated fibres and resin were cross-linked in an oven at 60 °C for twenty-four hours. The sample was microtomed (ULTRACUT, UK) into 100 nm sections using a diamond blade (Ultra 1436, DiATOME, Switzerland) with a 1 mm/s cutting speed. Each section was deposited onto a copper TEM grid (Agar scientific, UK) that has a 200 Mesh. 10 micrographs were captured per

sample, and thirty micrographs were recorded. Image-J software was used to measure the fibre volume fraction and the diameter of the fibres.

Figure 3.5.9 Photograph of the JEOL JEM-1400 TEM.

3.5.10. X-Ray Diffraction

X-ray diffraction was used to identify the crystal structure of the as-spun and carbonised electro-spun nano-fibres. The electro-spun fibre bundle of two cm in length was placed onto a twenty-five mm circular (shallow) sample holder (Proto, UK) and secured in the instrument. The holders were placed in an AXRD Benchtop diffractometer (Proto, UK) using Cu-Ka radiation (V = 30 kV, I = 20 mA, and λ = 1.541874 Å) with a 1 mm filter. The diffraction data 2θ were collected between 5–50°. Due to the fact that the sample was in a fibre form, the stage was not rotated. Two repeat experiments were performed on each sample. A photograph of the diffractometer is shown in Figure 3.5.10.

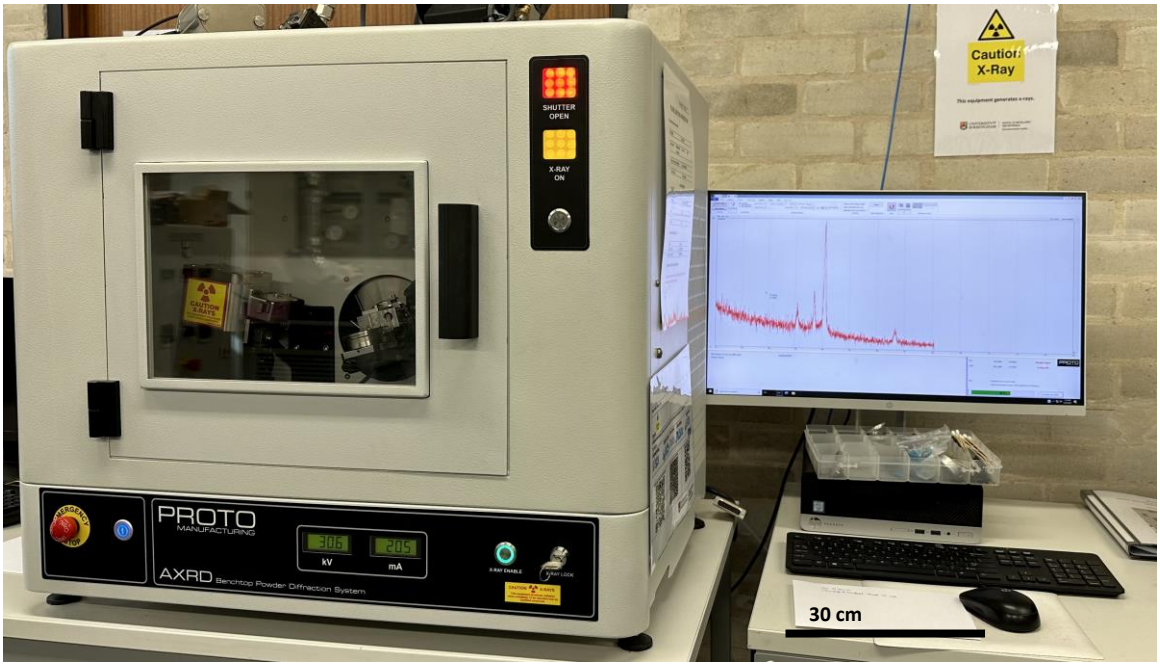

Figure 3.5.10 Photograph of the PROTO AXRD benchtop diffractometer.

3.5.11. Raman Spectroscopy

The degree of carbonisation of the pyrolysed PAN nano-fibres was measured using a Raman spectrometer (Renishaw RE-04, UK) that was equipped with a diode-pumped solid-state laser (532 nm) operating at 50 mW. A photograph of the RAMAN spectrometer is shown in Figure 3.5.11. The sample was transferred onto a glass slide and placed onto the optical microspore inside the chamber. The analysed area was observed and focused through an optical microscope at a magnification of 20x with a 1.15 mm working distance. A total of 10 accumulations per sample were collected at 10% laser power in the range of 500–2000 cm^{-1} over an exposure time of 10 seconds with a cosmic ray removal setting. Two tests were carried out on different positions for each carbonised sample. The intensity of two broad peaks around 1370 cm^{-1} (D-band) and 1590 cm^{-1} (G-band) was investigated.

Figure 3.5.11 Photograph of the RENISHAW RE-04 Raman spectrometer.

3.5.12. Fourier Transform Infrared Spectroscopy

Fourier Transform Infrared Spectroscopy (FTIR) was used to identify and analyse the functional groups present in the as-received PAN/DMSO solutions. It was also used to determine the presence of DMSO before and after the fibre bundles were dried in a vacuum oven under various temperatures. FTIR spectroscopy of the PAN/DMSO samples was carried out using a Thermo Scientific Nicolet 870 spectrometer, UK (see Figure 3.5.12a). 200 mg of pre-dried potassium bromide (KBr) and 2 mg of PAN/DMSO nano-fibre samples were ground and pressed into a disc with a diameter of 13 mm and a thickness of 0.6 mm under force of 10 tons using a desktop hydraulic press (Specac, UK). All the samples were analysed in the transmission mode. The FTIR spectra were acquired using an average of 100 scans at a resolution of 4 cm^{-1} in the wavelength range of 4,000–400 cm^{-1}. Omnic 8.1 software was used to analyse the spectra.

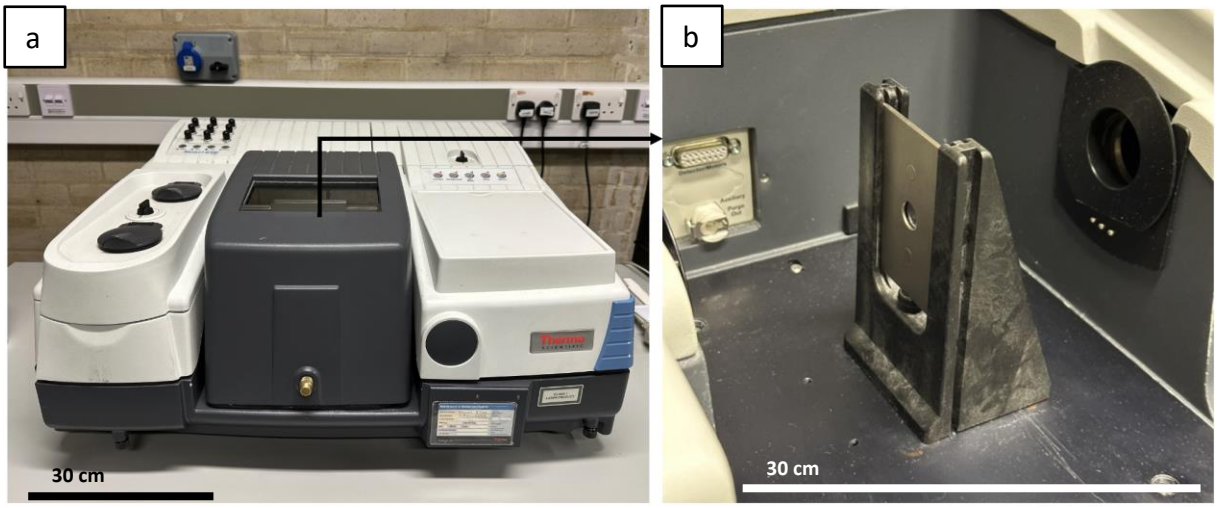

Figure 3.5.12 (a) Photograph of Thermo Scientific Nicolet 870 FTIR. (b) shows the transmission stage that was used.

3.5.13. Tensile Testing

The tensile properties of the nano-fibre bundles were evaluated using an Instron (US) 5566 universal testing machine with a 10 N load-cell. A photograph of the equipment is presented in Figure 3.5.13a. The grips used was a fibre filament micro tensile grip (2711-006 series, Instron, UK) to grip both ends of the tensile test sample. The gripped area was 36 mm^2 and it had an adjustable clamping force and self-aligning hard rubber-coated faces which had a maximum capacity of 5 N. The tests were carried out in an temperature regulated laboratory at 24 ± 2 °C and RH at 20 ± 4%. The rectangular and framed test specimen, described in Section 3.4, were used for the tensile tests. Before the tensile test, the length and width of each fibre sample were measured from photographs using Image-J. Each sample was measured five times and the data were averaged. Although the thickness was measured using the transverse sections on the SEM, a digital micrometre screw gauge was also used to measure the thickness of each test specimen. During the tensile test, attention was paid to ensuring that the fibres

were parallel to the principal loading direction. Before starting the tensile loading, the sides of the plastic frame were cut to ensure that only the fibres were held in the grips (as shown in Figure 3.5.13b). The load and the displacement were zeroed, and the cross-head displacement rate was set to 1 mm per minute with the load/displacement data were recorded. A limited number of experiments were also carried out to assess the effect of the rate of loading on the tensile strength. The gauge length for the tensile test specimen of as-spun and 300 °C stabilised fibres was 15 mm. Whereas the gauge length of the tensile specimen of 600 °C and 900 °C were 6.7 mm. Bluehill 3 software was used to record the load/displacement data.

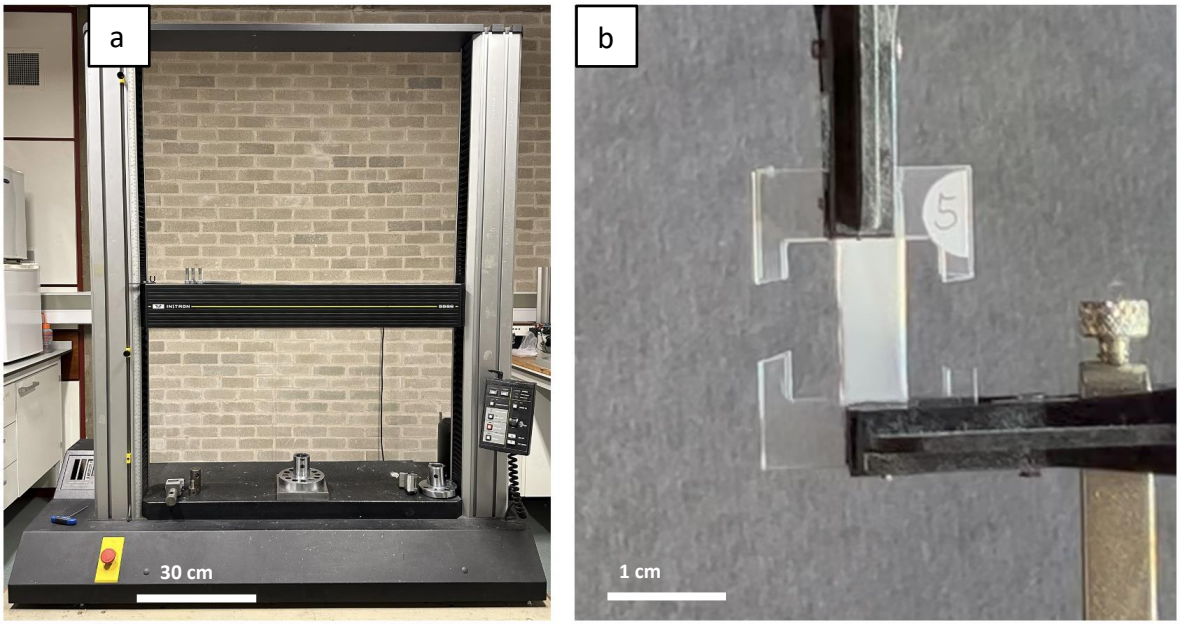

Figure 3.5.13 Photograph of (a) the Instron 5566 universal testing machine; and (b) tensile test sample mounted on the grips of the tensile tester.

3.5.13.1. Pre-stressing the Electro-spun Nano-fibre Specimens and Tensile Testing to Failure

The pre-stressing of the tensile test specimens to specified loads was carried out to investigate if it could increase the tensile properties of the electro-spun fibre bundles – this was deemed to be similar to cold-drawing of semi-crystalline polymers. In the first instance, the samples were loaded to a specified load, held at this load for 120 minutes, and unloaded prior to testing the sample to failure. In a second set of experiments, the sample was loaded to a specified load and held for 120 minutes prior to testing it to failure.

A typical load/displacement trace for an electro-spun and aligned PAN nano-fibre bundle is shown in Figure 3.5.14. The cross-head displacement rate was 0.1 mm/minute, and all the tests were carried out at ambient temperature 23 ± 2 °C. It was observed that the extension of the samples, without an increase in the load, commenced at approximately 4 mm, with failure initiating approximately after an extension of 6 mm, where the load decreased as a function of extension. It is worth mentioning at this stage that the purity of the DMSO was seen to have a significant effect on the tensile properties of the electro-spun PAN nano-fibre bundles. The bulk of the research in the current project was undertaken using DMSO from (Sigma-Aldrich, UK) where the purity was 99.9%. The supplier discontinued this solvent and 99% purity DMSO from (Fisher Scientific, UK) used for some of the tensile experiments. When this discrepancy was identified, a different supplier (Sigma-Aldrich, UK) was used for the majority of the experiments, as summarised in Table 3.1.

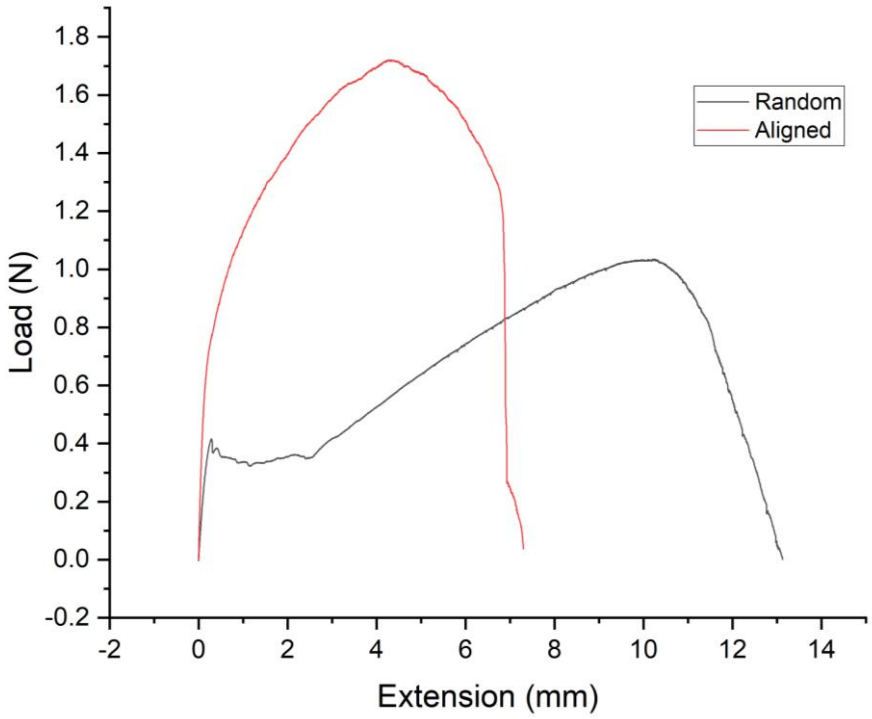

Figure 3.5.14 Typical load/displacement traces for electro-spun randomly oriented and aligned PAN nano-fibre specimens.

(i) Preloading to an extension of 4 mm, unload and reload to failure*:* With reference to the load/displacement trace shown in Figure 3.5.14, the first batch of tensile samples were extended to 4 mm and unloaded. The sample was reloaded to failure without removing it from the grips of the tensile test machine. A typical trace for of this loading, unloading and reloading to failure is shown in Figure 3.5.15.

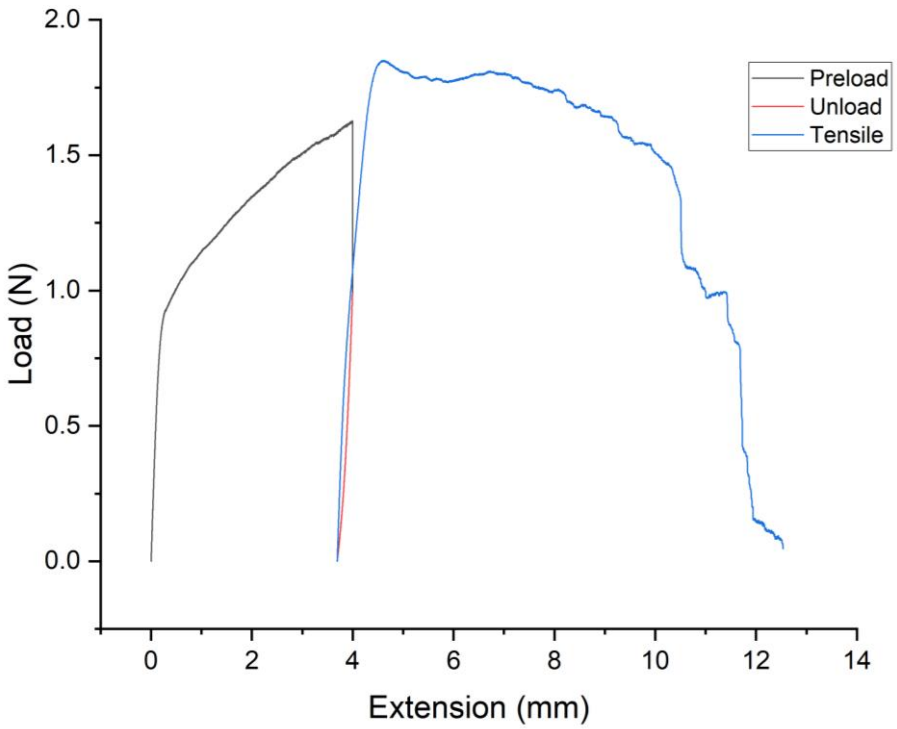

Figure 3.5.15 Example of a typical loading sequence where the aligned nano-fibre sample was loaded to an extension of 4 mm, unloaded completely and reloaded to failure.

(ii) Pre-loading to an extension of 2 mm followed by holding for 2, 4 and 6 hours prior to loading to failure: In this series of experiments, the electro-spun and aligned PAN fibre bundles were loaded to an extension of 2 mm and held for 2, 4 or 6 hours whilst the load-decay was monitored. The samples were loaded to failure after each load-hold period. This loading sequence is shown in Figure 3.5.16.

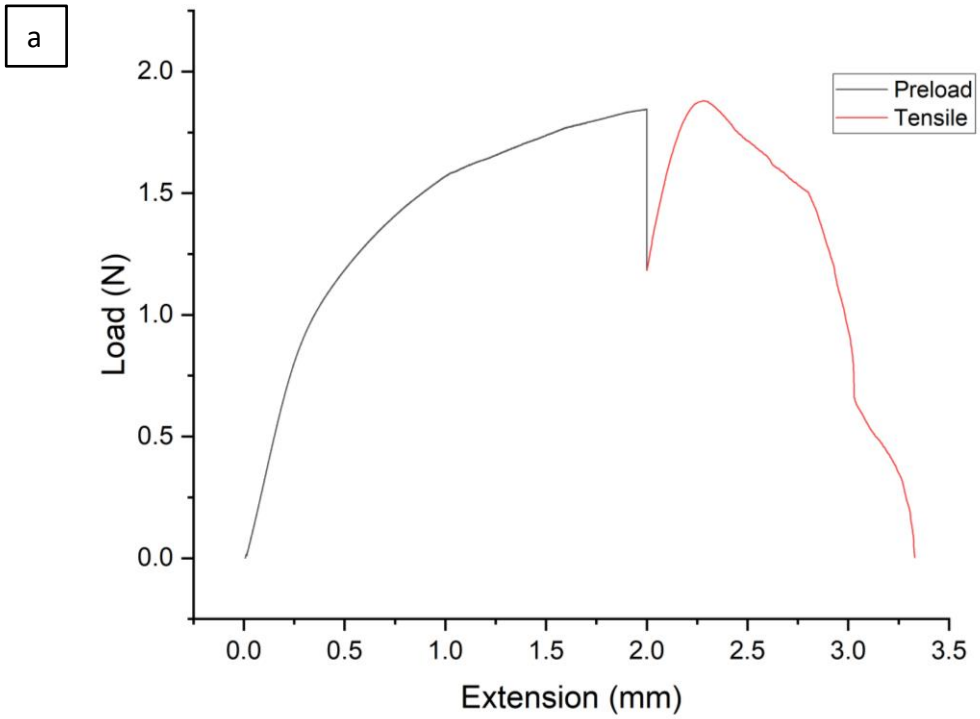

Figure 3.5.16 Cont.

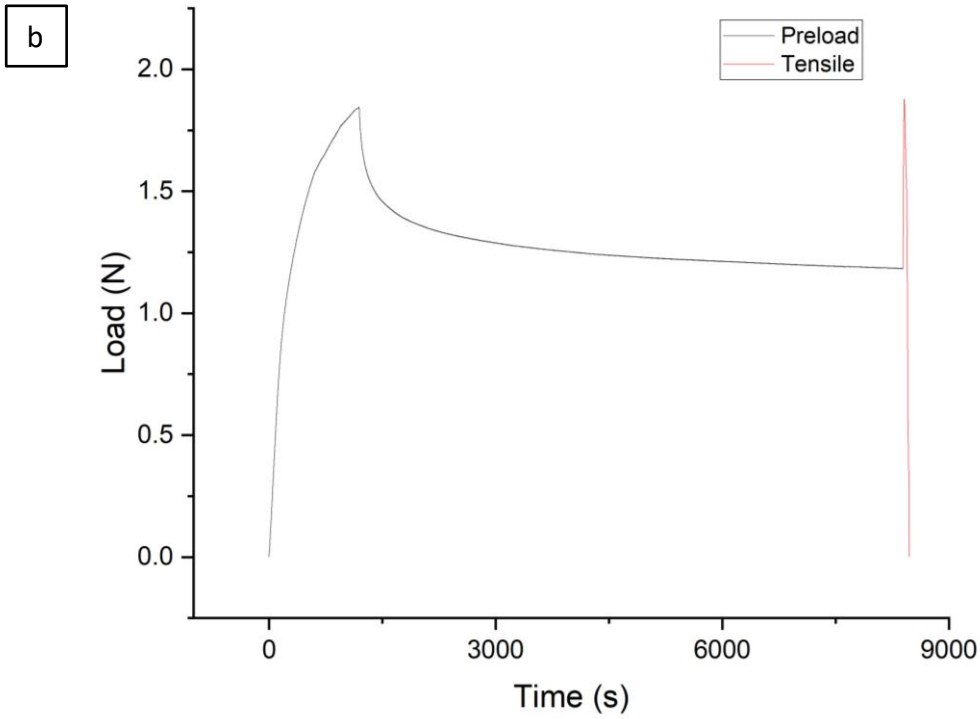

Figure 3.5.16 Example of loading sequences where the aligned nano-fibre sample was loaded to an extension of 2 mm, held for 2 hours and reloaded to failure. (a) Load-displacement graph and (b) Load-time graph.

3.5.13.2. Assessing the End-tabbing Methods

Prior to commencing the tensile tests, a series of experiments were undertaken to determine the best method to end-tab the fibre bundles. The methods investigated were double-sided tape, super-glue (Loctite 403, UK) and UV-cure resin (Norland optical adhesive 68, USA). The end-tabbing was carried out as described in Section 3.4. The use of double-sided tape was assessed as a number of the publications in the literature used this method to end-tab nano-fibre bundles.

Table 3.1 Summary of the tensile test specimens used in the current study. The RH and the spinning temperature were kept at 13 ± 4% and 55 ± 4 °C, respectively.

Sample Code	Alignment	Gauge Length (mm)	Heat-treatment Temperature (°C)	End-tab	DMSO Purity (%)	Test Rate (mm/minute)	Pre-Stretch rate	Holding Time (hour)	Stress Release
R1–10	Random	15	N/A	UV	99	1	N/A	N/A	N/A
A1–10	Aligned	15	N/A	UV	99	1	N/A	N/A	N/A
A21–23	Aligned	15	N/A	UV	99.9	1	N/A	N/A	N/A
A24–26	Aligned	15	N/A	Super-glue	99.9	1	N/A	N/A	N/A
A27–29	Aligned	15	N/A	Double-sided tape	99.9	1	N/A	N/A	N/A
AP1–10	Aligned	15	N/A	UV	99	1	0.1	2	Yes
AP11–13	Aligned	15	N/A	UV	99.9	1	0.1	1	No
AP14–16	Aligned	15	N/A	UV	99.9	1	0.1	2	No
AP17–19	Aligned	15	N/A	UV	99.9	1	0.1	4	No
A300 1–3	Aligned	15	300	UV	99.9	1	N/A	N/A	No
A600 1–3	Aligned	6.7	600	UV	99.9	1	N/A	N/A	No
A900 1–3	Aligned	6.7	900	UV	99.9	1	N/A	N/A	No

3.6. COMSOL Modelling

In order to investigate the mechanism responsible for fibre alignment when using the Vee-shield method, a COMSOL AC DC model with electric current physics was used (COMSOL Multiphysics, Version 5.3a, UK). All the simulations were conducted in stationary mode. The geometry of the modelling was completed using Fusion 360 education package. A three-dimensional drawing was generated using Fusion 360 (Autodesk, version 2.0, Education license, UK) using dimensions that were exactly the same as that in the set-up used in the practical work. The needle, Vee-shield fixture and metal collector were included in the geometry. The 3D geometry after importing it into COMSOL is shown in Figure 3.6.1.

All the sharp edges of the geometry were filleted by 1% to minimise the high density of meshing at sharp corners and edges. After the geometry was imported into the COMSOL software, a sphere with a radius of 40 cm was created where the centre of the sphere was positioned at the centre of the geometry. This sphere was identified as the boundary of the simulation, and the material of the sphere was designated as air. All other components in the geometry were set to be equivalent to the material used in the experimental set-up. A summary of these materials and their relevant properties is presented in Table 3.2. This information was imported from the COMSOL material database (Version 5.3a).

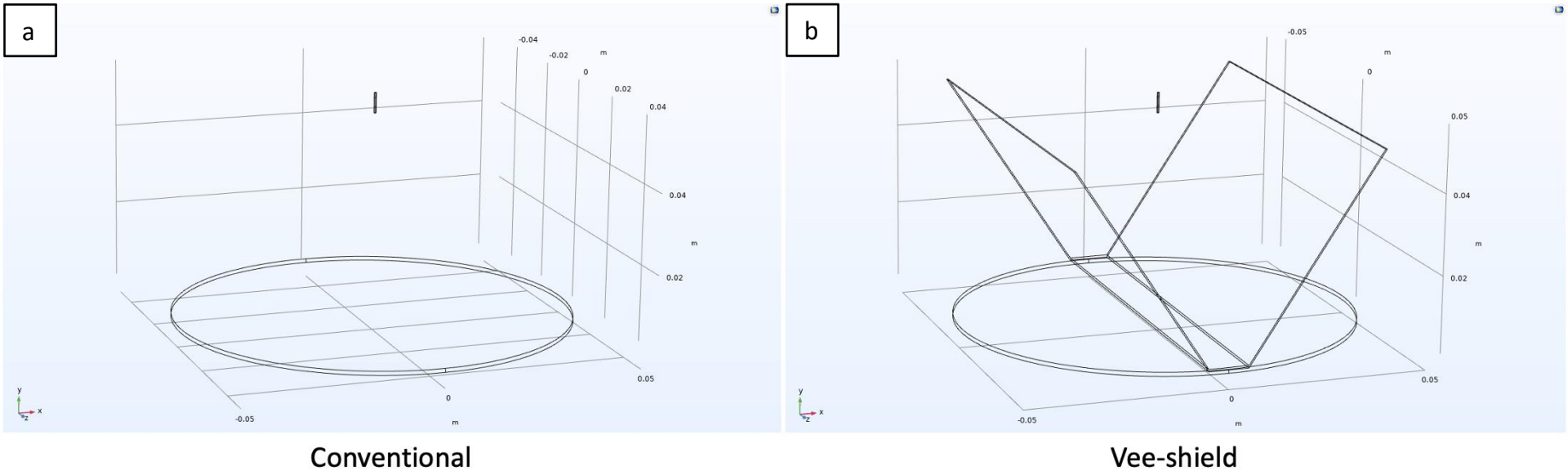

Figure 3.6.1 A screenshot of (a) conventional collector and (b) Vee-shield collector geometry imported into COMSOL.

Table 3.2 Summary of the relevant parameters that were used in the COMSOL simulations. These parameters were obtained from the COMSOL materials database, Version 5.3a.

Property	Variable	Value	Unit	Property group
Relative permittivity	epsilonr_iso ; epsilonrii = epsilonr_iso, epsilonrij = 0	1	1	Basic
Electrical conductivity	sigma_iso ; sigmaii = sigma_iso, sigmaij = 0	1e-4[S/m]	S/m	Basic
Coefficient of thermal expansion	alpha_iso ; alphaii = alpha_iso, alphaij = 0	alpha_p(pA,T)	1/K	Basic
Mean molar mass	Mn	0.02897	kg/mol	Basic
Bulk viscosity	muB	muB(T)	Pa·s	Basic
Relative permeability	mur_iso ; murii = mur_iso, murij = 0	1	1	Basic
Dynamic viscosity	mu	eta(T)	Pa·s	Basic
Ratio of specific heats	gamma	1.4	1	Basic
Heat capacity at constant pressure	Cp	Cp(T)	J/(kg·K)	Basic
Density	rho	rho(pA,T)	kg/m³	Basic
Thermal conductivity	k_iso ; kii = k_iso, kij = 0	k(T)	W/(m·K)	Basic
Speed of sound	c	cs(T)	m/s	Basic
Refractive index, real part	n_iso ; nii = n_iso, nij = 0	1	1	Refractive index
Refractive index, imaginary part	ki_iso ; kiii = ki_iso, kiij = 0	0	1	Refractive index
Parameter of nonlinearity	BA	(def.gamma+1)/2	1	Nonlinear model

Air

Property	Variable	Value	Unit	Property group
Relative permeability	mur_iso ; murii = mur_iso, murij = 0	1	1	Basic
Electrical conductivity	sigma_iso ; sigmaii = sigma_iso, sigmaij = 0	5.998e7[S/m]	S/m	Basic
Coefficient of thermal expansion	alpha_iso ; alphaii = alpha_iso, alphaij = 0	17e-6[1/K]	1/K	Basic
Heat capacity at constant pressure	Cp	385[J/(kg*K)]	J/(kg·K)	Basic
Relative permittivity	epsilonr_iso ; epsilonrii = epsilonr_iso, epsilonrij = 0	1	1	Basic
Density	rho	8960[kg/m^3]	kg/m³	Basic
Thermal conductivity	k_iso ; kii = k_iso, kij = 0	400[W/(m*K)]	W/(m·K)	Basic
Young's modulus	E	110e9[Pa]	Pa	Young's modulus and Poisson's ratio
Poisson's ratio	nu	0.35	1	Young's modulus and Poisson's ratio
Reference resistivity	rho0	1.72e-8[ohm*m]	Ω·m	Linearized resistivity
Resistivity temperature coefficient	alpha	0.0039[1/K]	1/K	Linearized resistivity
Reference temperature	Tref	298[K]	K	Linearized resistivity

Copper

Property	Variable	Value	Unit	Property group
Electrical conductivity	sigma_iso ; sigmaii = sigma_iso, sigmaij = 0	1e-23	S/m	Basic
Relative permittivity	epsilonr_iso ; epsilonrii = epsilonr_iso, epsilonrij = 0	2.55	1	Basic

PTFE

The applied electrical potential at the needle was set as 15 kV, and the collector terminal was set as the ground. In this study, a three-dimensional tetrahedral ultra-high meshing density was selected for all the simulations. The simulation results are mainly focused on a two-dimentional cut-plane along the YX and YZ directions, which can be seen in Figure 3.6.2a and b, respectively. The electrical potential, normalised electric field strength, normalised current density and current density vector plots were generated and compared between the Vee-shield set-up and the conventional set-up. The effect of the angle of PTFE was also modelled and compared using COMSOL.

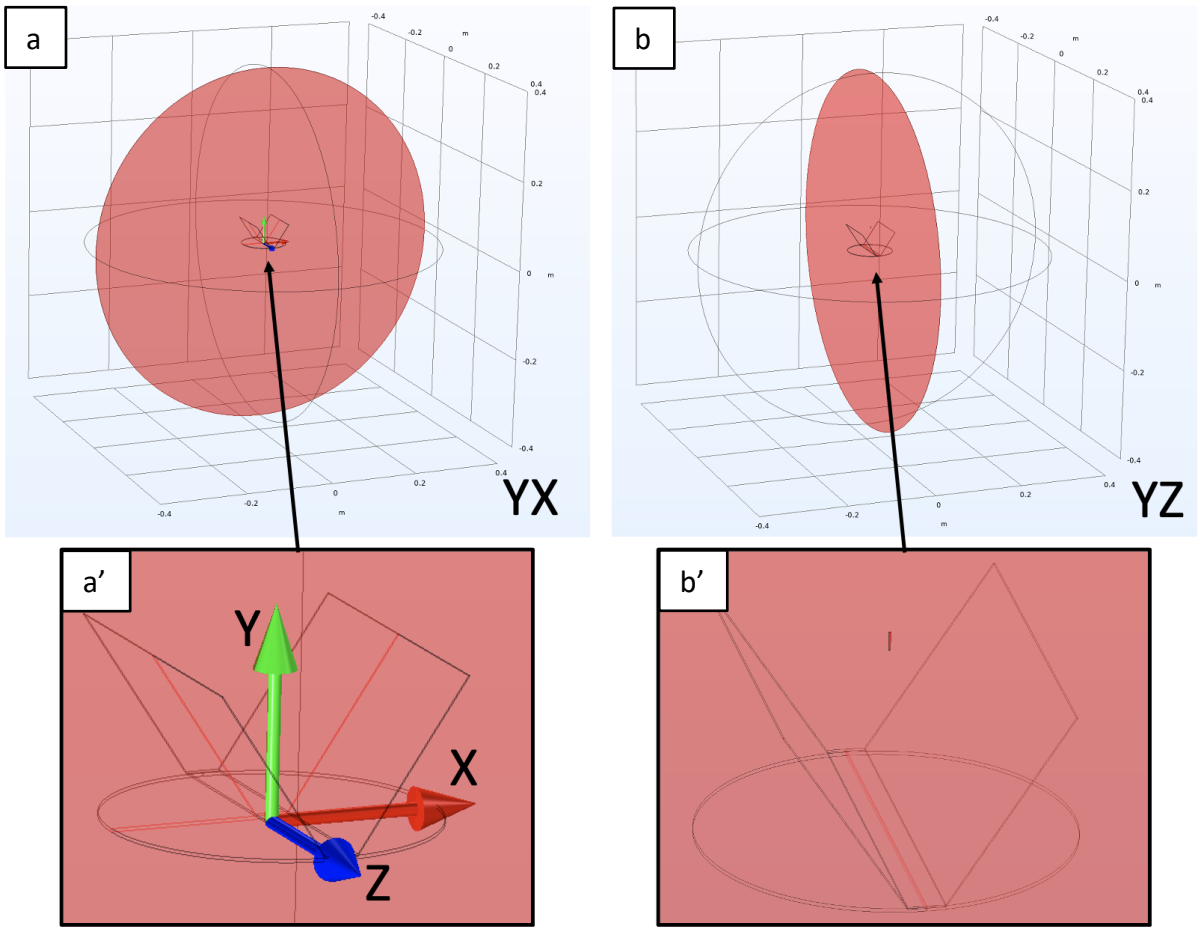

Figure 3.6.2 Schematic illustration showing the YX-(a) and YZ-(b) cut-plane used for the simulation. (a') and (b') showing a magnified image of (a) and (b), respectively.

4. RESULTS AND DISCUSSION

4.1. Electro-spinning of Highly Aligned PAN-based Carbon Nano-fibres

This chapter reports on a novel approach for producing highly aligned electro-spun polyacrylonitrile (PAN) nano-fibres using dimethyl sulfoxide (DMSO) as the solvent. The electro-spinning conditions and processing parameters for PAN/DMSO were optimised to produce bead-free fibres with a circular cross-section. A standardised method was established to dry the electro-spun fibres. A novel electro-spinning alignment rig, referred to as the 'Vee-shield' collector, was designed and built to allow the aligned fibre arrays to be produced continuously along the fibre alignment direction. The alignment mechanism was studied by investigating the electrode and electric field configurations using COMSOL simulation software. The electro-spun fibres were evaluated using scanning electron microscopy and image analysis to estimate the degree of fibre alignment and their diameters.

4.1.1. Reasons for Selecting PAN and DMSO

(i) PAN: The majority of carbon fibres produced globally use PAN as the precursor fibre. Whilst the parameters for extrusion, oxidation, carbonisation and graphitisation of PAN have been optimised in commercial production processes, the same cannot be said for electro-spinning. For example, at the time of writing, the author was not aware of any electro-spinning technique allowing aligned fibres to be hauled off and spooled continuously. In situations

where post-processes such as stretching or cold-drawing are required, it is essential for the fibres to be unidirectional. The fibre alignment technique described here could have been developed using any class of polymer but PAN was chosen because of its commercial importance in carbon fibre production. Since the target was to electro-spin unidirectional fibres continuously, the opportunity was taken to investigate whether post-processing could be used to improve its mechanical properties.

Two PAN suppliers, Sigma-Aldrich (SA) and Goodfellow (GF) were chosen as each offered a different molecular weight. Moreover, they have been used in previous studies [261, 321, 354-359]. GF PAN was chosen for the majority of the characterisation and tensile tests due to its higher molecular weight (230,000 g/mol) and its ability to withstand a higher draw ratio [360, 361].

(ii) Solvent: Solubility of a polymer depends on various factors such as the degree of polymerisation [362], molecular weight distribution [363], tacticity [364], and solvent properties [77]. Although binary solvent systems (generally DMF with acetone) have been used to dissolve PAN [365-368], a single-solvent system was considered here in order to reduce their complex behaviour during electro-spinning. For example, significantly different boiling points can result in void formation during drying [369], premature evaporation at the pendant drop (or Taylor cone when an electrical potential is applied), and clogging the needle [65]. Solvents with different dielectric constants may result in the formation of multiple jets and beaded fibres [370].

It is clear from Table 2.2 (Section 2.1.2) that a number of solvents can dissolve PAN. The primary reason as to why DMSO was selected is because the use of chlorinated and toxic

solvents were not permitted in the author's lab. This therefore ruled out DMF, THF and DMAc. A binary mixture of acetone and DMSO was not considered because of the low boiling point of acetone (56 °C). Furthermore, given that the boiling point of DMSO is 189 °C, it meant that the electro-spinning had to be carried out above room temperature to permit some of the DMSO to evaporate from the surface regions, thereby creating a 'skin' which contributes to the retention of circular cross-section. In the current study, the electro-spinning was carried out at 55 °C, and therefore this ruled out the use of acetone in DMSO as the binary solvent.

Awareness has grown, over recent years, of the environmental impact of many industrial chemicals and solvents, and cleaner and sustainable production methods have been sought. Whilst the majority of papers reviewed used DMF and DMAc for dissolving and electro-spinning PAN [354, 371-377], an increasing number of authors have switched to DMSO because it is currently classified as non-toxic [354, 371-377].

Overall Summary

- PAN was selected because of its commercial significance as a precursor for the production of reinforcing carbon fibres.
- The solvent, DMSO, was chosen as it is non-toxic whereas other suitable solvents for dissolving PAN are toxic.

4.1.2. Morphology of the As-received PAN and Dissolution in DMSO

The PAN powders were used as-received, without further purification or modification. The morphology of the as-received powder was examined using Scanning Electron Microscopy (SEM). Representative micrographs from the two suppliers (Goodfellow – coded as GF) and

(Sigma-Aldrich – coded as SA) are shown in Figure 4.1.1. On the whole, the GF PAN particles were elliptical and not agglomerated. On the other hand, the SA PAN was more irregular, and agglomerated. The micrographs in Figure 4.1.1a' and b' are magnified images representing the SA and GF PAN powers, respectively.

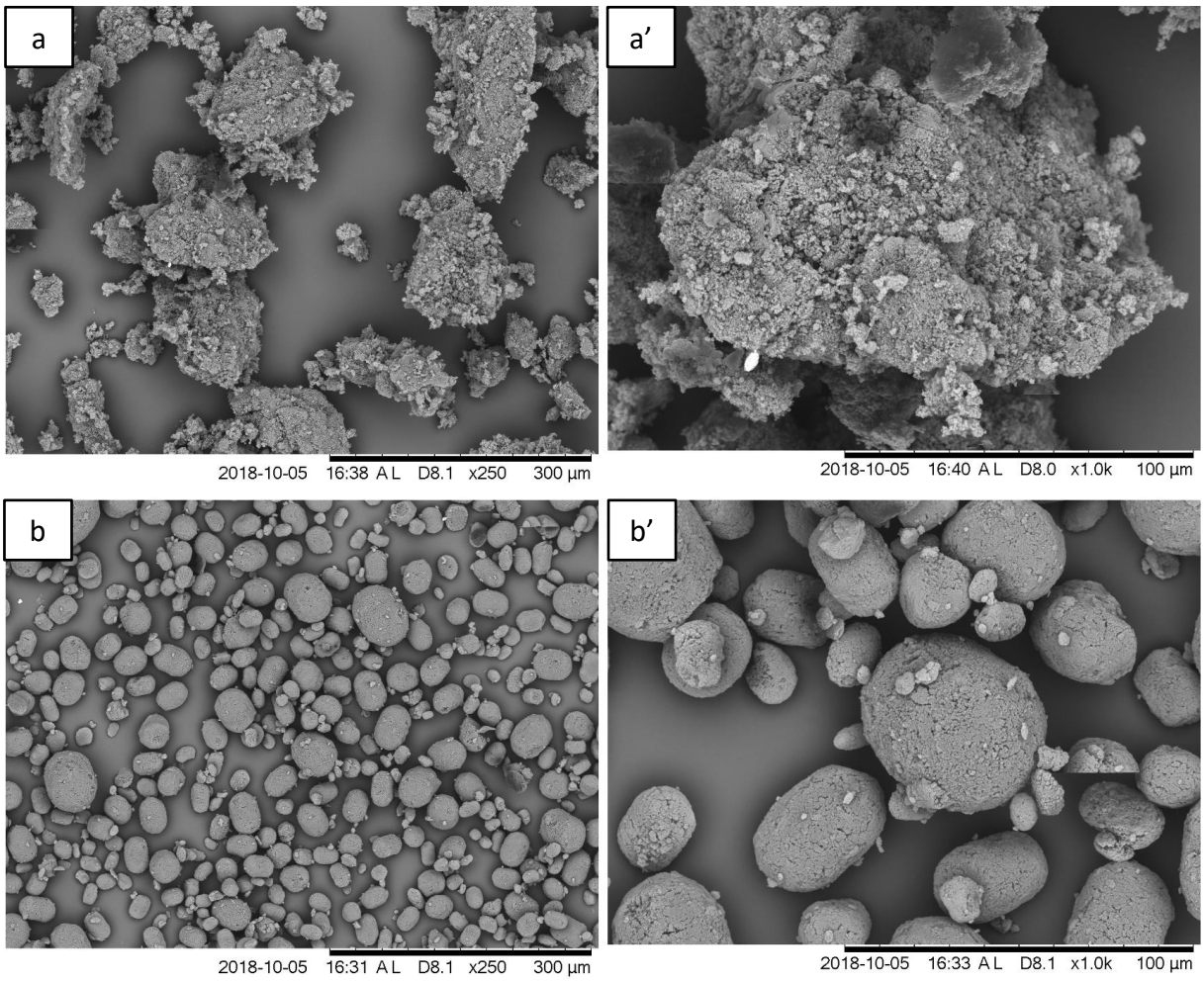

Figure 4.1.1 SEM micrographs of as-received PAN: (a) SA PAN; (b) GF PAN; and (a' & b') higher magnification images of SA and GF PANs, respectively.

As discussed in Section 3.2.1, PAN from the two suppliers was dissolved using DMSO at 60 °C for 6 hours. Visual inspection showed that both SA and GF PANs were dissolved fully under these conditions.

The molar masses of the SA and GF PANs were 150,000 g/mol and 230,000 g/mol, respectively. Solutions were made at concentrations of 2, 4, 6, 8, 10, 12, and 14 w/v% from both suppliers. 'w' represents the weight of PAN and 'v' is the volume of DMSO. The 16 w/v% GF PAN solution was too viscous, at room temperature, for electro-spinning. Solution parameters such as viscosity, conductivity and surface tension were characterised for the concentrations listed above. The fibre morphology after electro-spinning at each concentration was determined.

Overall Summary

- Whilst the morphology of the PAN supplied by two suppliers was different, it did not influence their dissolution in DMSO at 60 °C.

4.1.3. Viscosity

Figure 4.1.2a and b show plots of shear viscosity against shear rate for the SA and GF PANs as a function of polymer concentration. It is seen that the shear viscosities are similar at low concentration, but an order of magnitude greater for GF PAN at the higher concentrations. The complex viscosity was also measured using the same equipment under oscillation mode. As shown in Figure 4.1.3a and b, the complex viscosities are again comparable at low concentrations, and an order of magnitude higher for GF PAN at the higher concentrations. Shear thinning can be observed in Figure 4.1.2a and b, at higher polymer concentrations for both polymers. In addition, the onset points of shear thinning decreased with increasing concentration for both test methods. This is in agreement with that reported by Skvortsov *et al.* [368]. Furthermore, shear thinning becomes more obvious for the higher molar mass GF PAN, which can be attributed to the entangled chains tending to disentangle at a high shear

rate in the flow mode [109, 360, 378]. The polymer chains are oriented more or less parallel to the direction of the shear, resulting in elongation, which increases flowability, and therefore, decreases the bulk viscosity [109, 294, 360, 379-381]. Similar results were reported by Tan *et al.* [360] and Tenchurin *et al.* [381]. Tan *et al.* [360] reported that the shear viscosity of PAN/DMSO solution increases with increasing molecular weight due to higher chain entanglement. Shear-thinning behaviour was found with increasing shear rate (from 0.01–250 s^{-1}). Thus, a higher-molecular weight PAN will have an improved elasticity, which in turn can enable the polymer to withstand a high draw-ratio [360]. Tenchurin *et al.* [381] increased the molecular weight of 6 wt% PAN from 240,000 g/mol to 700,000 g/mol and reported that it resulted in an increase in the shear viscosity from 2.74 Pa.s to 11.4 Pa.s. The shear-thinning behaviour of the solution was also observed, where the shear rate offset point for shear-thinning became lower as the concentration and the molecular weight of the solution increased. This trend was also observed in the current study. Shear-thinning behaviour is more obvious when the solution is operated under shear mode than under oscillation mode. The complex viscosity shows a decrease when the angular frequency reaches 300 rad/s, at which point it begins to increase. Liu *et al.* [382] reported on the shear-thinning behaviour of PAN solution when the angular frequency was increased from 0.1 rad/s to 100 rad/s. The increase in the complex viscosity at angular frequencies above 300 rad/s has not been reported in the other papers reviewed. This may be due to the polymer chain becoming re-entangled at a higher angular frequency; more experiments are required to enable a definitive conclusion to be reached. During electro-spinning, the stretching of the polymer chains is unidirectional [171, 287, 383]. Therefore, the shear viscosity is more salient than the complex viscosity. In addition, the actual shear rate during electro-spinning is extremely high (approximately 10^3–

10^5 s^{-1}) [119, 171]. Such shear rates cannot be attained using conventional parallel-plate rheological equipment. The relevant literature on polymer rheological studies report on the relationship between viscosity and shear rate up to a maximum shear rate of only 1000 s^{-1} [360, 380-382, 384-386]. As the shear rate increases, a polymer solution with shear-thinning rheological properties typically exhibits three regions: a lower Newtonian region (low shear rate), a shear-thinning region (medium shear rate), and an upper Newtonian region (high shear rate). The solution will behave like a Newtonian fluid in both the lower and upper Newtonian regions [378, 387]. Due to the restrictions in the shear rate test range, the viscosity measured in this experiment shows a low Newtonian and partial shear-thinning region of the PAN/DMSO polymer solution, which can only indicate the level of chain entanglement, not the actual viscosity of the solution during electro-spinning. However, due to the fact that polymer chains cannot be elongated beyond the high Newtonian region [387], it can be anticipated that, although the shear thinning behaviour is more obvious when the polymer solution has higher molecular weight or concentration, the actual viscosities of polymer solutions at the electro-spinning shear rate may still exceed those of solutions with lower molecular weight or concentration [368, 388, 389].

Figure 4.1.4 a and b identify the turning points of the viscosity as approximately 10.9 w/v% for the SA PAN and 10.4 w/v% for the GF PAN, with the shear viscosity at those two concentrations being 0.77 Pa.s and 5.06 Pa.s, respectively. The gradient of the viscosity/concentration plot, after reaching the turning point, is significantly higher for the material with the higher-molecular weight GF polymer. This turning point in the

viscosity/concentration plot was explained previously in Section 2.1.3; it is known as the critical entanglement concentration (C*).

Varying the PAN/DMSO concentration, as reported by Grothe *et al.* [374] showed that the turning point was between 16 wt% to 18 wt% (the effects of molecular weight were not reported). Beadless fibres were formed at 18 wt% where the room-temperature shear viscosity was around 18 Pa.s [374]. Nasouri *et al.* [390] studied the viscosity (in mPa.s) of PAN (Mw = 100,000 g/mol) in DMF as a function of concentration (from 4 w/v% to 20 w/v%) at 22 °C. The concentration at the turning point is not reported, however, beadless nano-fibres could be spun from 10 w/v% where the viscosity at this concentration was 314.4 ± 13.2 mPa.s [390].

Kim *et al.* [391] used the same polymer–solvent combination and found the turning point to be around 544 cP (544 mPa.s), between 8–10 wt% polymer concentration. The molecular weight of the polymer was not given. Wang and Kumar [379] reported on entanglement the concentration of PAN/DMF solution, with PAN molecular weights of 100,000, 250,000, and 700,000 g/mol, and found them to be 5.1, 3.1, and 1.5 wt%, respectively.

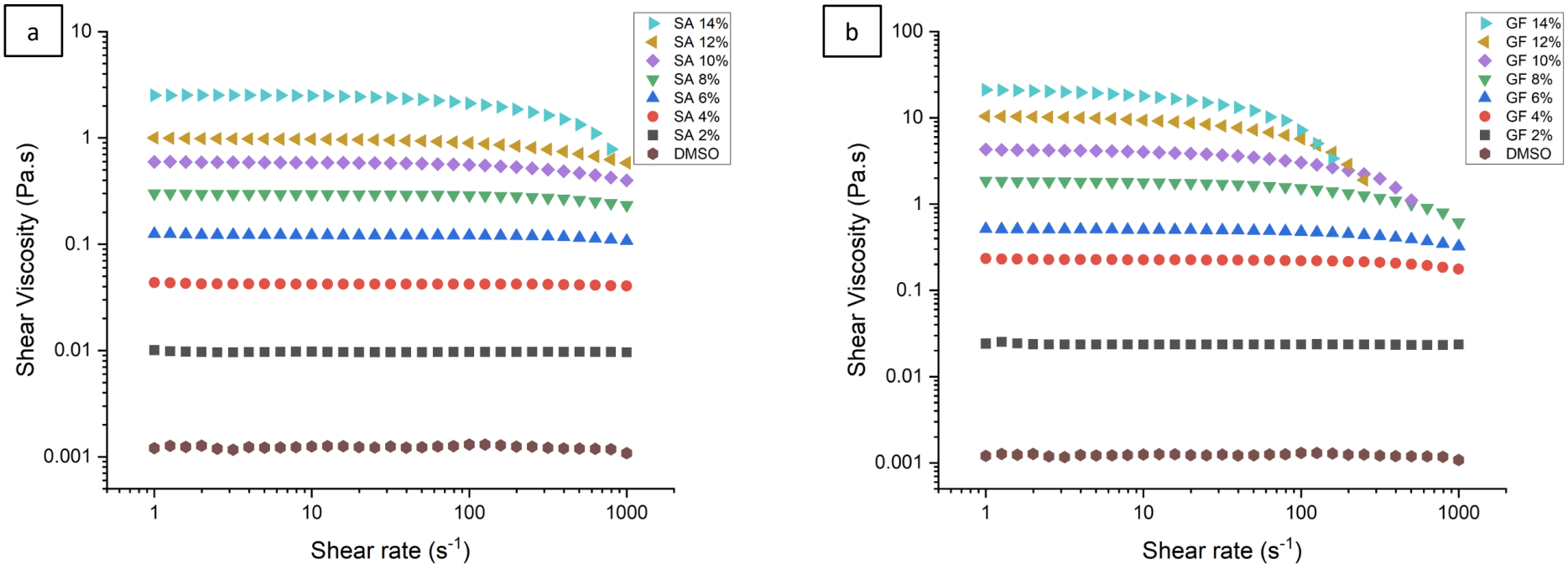

Figure 4.1.2 Shear viscosity against shear rate plot for specified (a) SA PAN and (b) GF PAN concentrations in DMSO. The experiments were conducted at 55 °C. Concentrations are in w/v%.

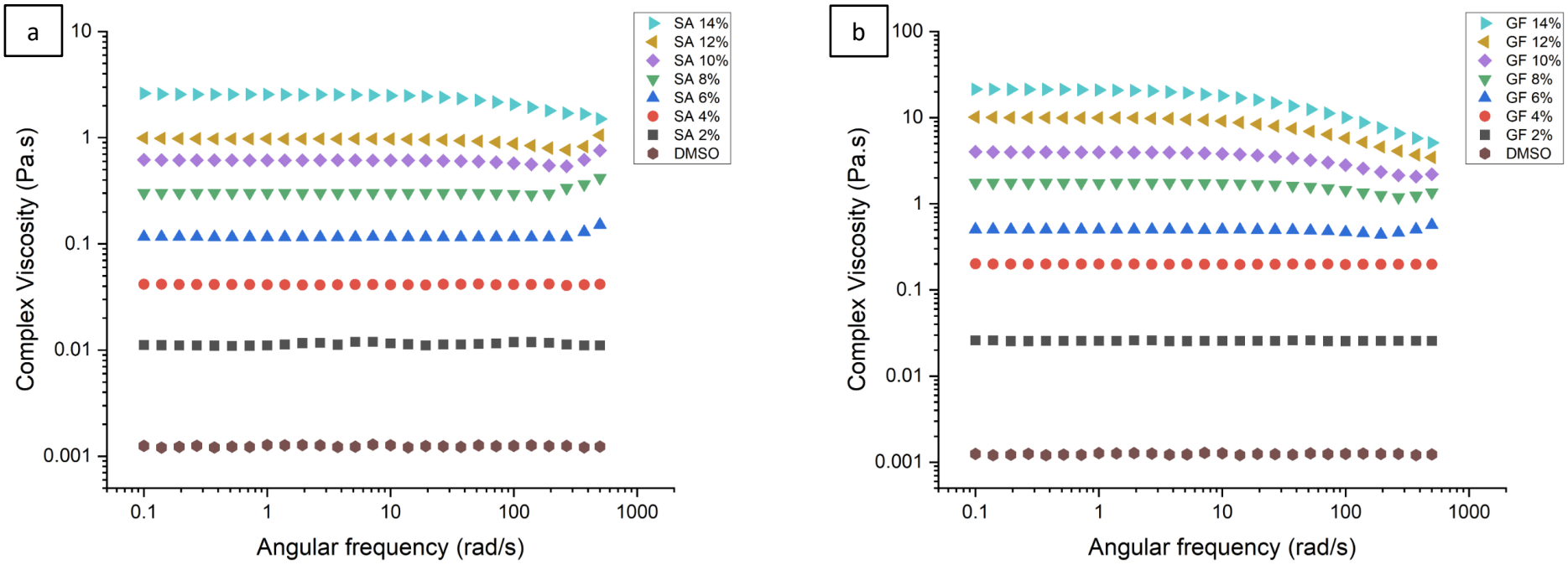

Figure 4.1.3 Complex viscosity against angular frequency plot for specified (a) SA PAN and (b) GF PAN concentrations in DMSO. The experiments were conducted at 55 °C. Concentrations are in w/v%.

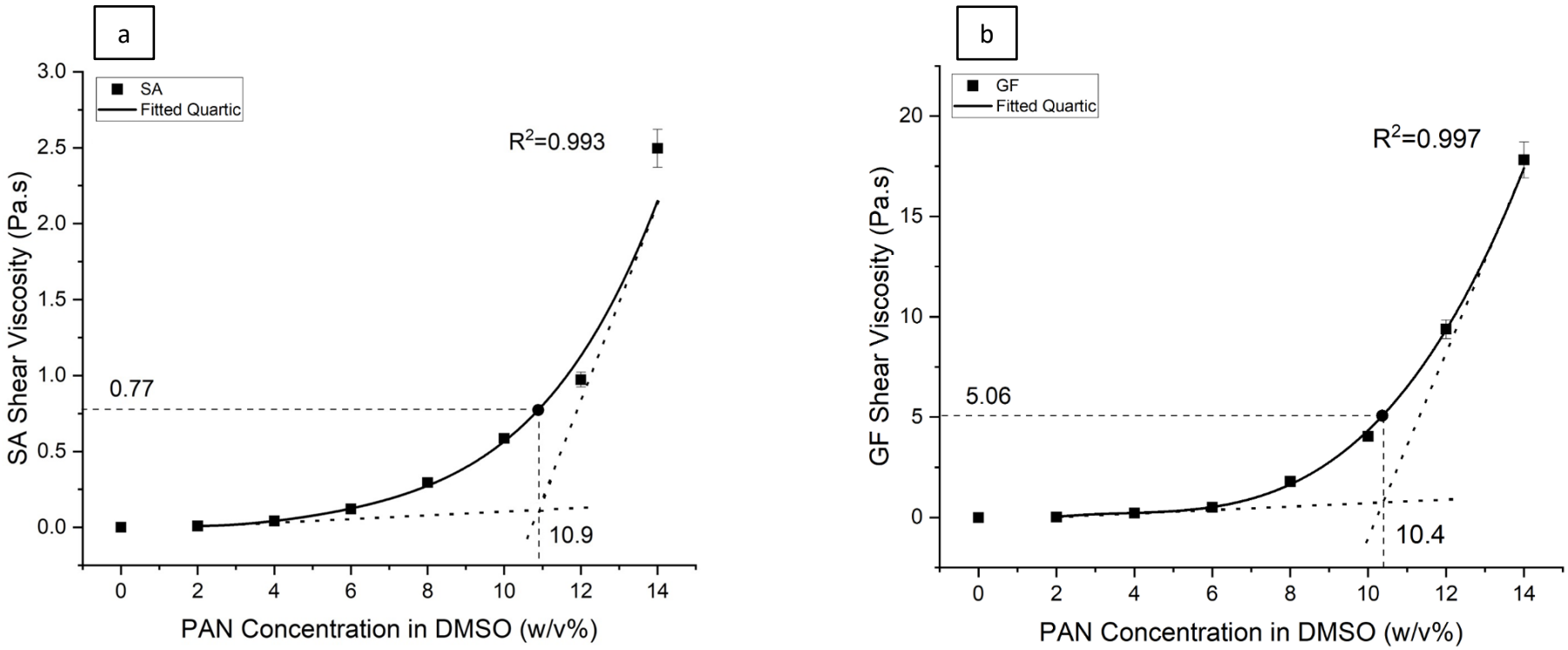

Figure 4.1.4 Shear viscosity versus concentration and polynomial fitted lines for (a) SA and (b) GF PANs in DMSO. The experiments were conducted at 55 °C.

Evidently, it can be observed that the entanglement concentration strongly depends on the polymer molecular weight. In this study, the lower-molecular weight SA PAN has a higher critical concentration than GF PAN, however the difference between these two concentrations appears to be negligible. It should be noted that this may be due to the experiments being carried out at 55 °C, whereas, as shown by Grothe *et al.* [374] PAN/DMSO solutions at room temperature show a greater shift in viscosity as the concentration is varied. Compared with the PAN/DMSO viscosity/concentration results reported by Grothe *et al.* [374] at room temperature, the low critical concentration difference obtained from this current study between SA and GF PANs is possibly due to the viscosity increment between each concentration having been reduced when the test was carried out at a higher temperature (55 °C). The relationship between fibre morphology and solution viscosity will be discussed further in Section 4.1.6.

Overall Summary

- The shear and complex viscosities for the SA and GF PAN/DMSO solutions were characterised as a function of polymer concentration and frequency.
- The viscosity for the GF PAN, with its higher molecular weight, was higher than that of SA PAN, which had a comparatively lower molecular weight.
- Shear thinning was observed for the two polymers at higher shear rates.
- The critical shear viscosity for the SA and GF PANs were 0.77 Pa.s and 5.06 Pa.s, respectively, where the data were obtained at 55 °C.

4.1.4. Electrical Conductivity

Since the electro-spinning process is initiated when the Coulomb force of the charged polymer exceeds the surface tension of the polymer solution, understanding the electrical conductivity of the solution is important. This was discussed in Section 2.1.4 of the literature review. As shown in Figure 4.1.5, at 55 °C, the electrical conductivity of the SA and GF PANs show an increase with increasing polymer concentration. Budtov [392], indicated that the conductivity of the polymer solution is proportional to the mobility of the charge carriers. From this conclusion, the polymer solution with higher molecular weight will tend to have lower ionic mobility [393, 394]. From the experimental results generated in the current study, the solution with the lower molecular weight polymer has a higher electrical conductivity; this follows the trend mentioned and observed by Budtov [392]. The electrical conductivity increases with the polymer concentration for the SA and GF polymers. The increase in the conductivity as a function of concentration is more obvious for the SA PAN. In Figure 4.1.5, the slope of the SA PAN is 3 times higher than that of the GF PAN. There are no turning points that can be seen in the conductivity results as the polymer concentration increases. This suggests that the electrical conductivity is not affected by the level of chain entanglement.

The effect of concentration of PAN/DMF solution on electrical conductivity as reported by Qin *et al.* [126] showed a slight increase in conductivity when concentration increases from 4−10 wt%. Kalayci *et al.* [395] reported that conductivity of 8 wt% and 13 wt% PAN/DMF were 39 μS/cm and 50 μS/cm, respectively. Lin *et al.* [396] suggested that conductivity increase is attributed to the higher content of polar nitrile groups in the PAN molecules. Similar findings were also described by Wang *et al.* [143].

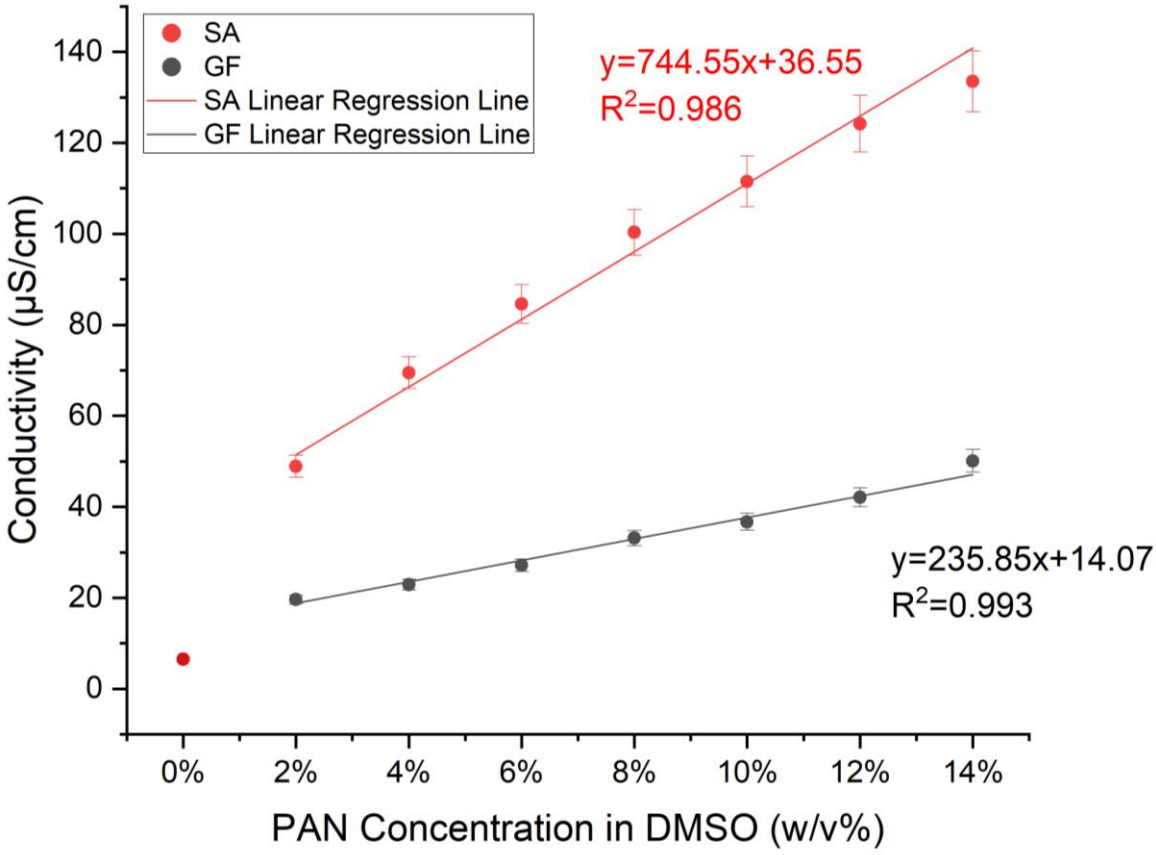

Figure 4.1.5 Relationship between conductivity and concentration for the SA and GF PANs in DMSO. The conductivity was measured at 55 °C.

Overall Summary

- The electrical conductivities for the SA and GF PAN polymers showed a linear relationship with polymer concentration.
- The electric conductivities of the SA and GF at 12 w/v% PAN/DMSO were 124.2 µS/cm and 42.1 µS/cm, respectively.
- The higher mobility of the SA PAN, with a lower molecular weight, may be one of the reasons for its higher electrical conductivity when compared to GF PAN.

4.1.5. Surface Tension

As stated previously, in addition to the influence of the polymer solution, the surface tension has a major influence on the ability of PAN solutions to be electro-spun. Figure 4.1.6 shows that increasing the polymer concentration results in a linear increase in the surface tension for the SA and GF PANs. The surface tension of GF PAN, with a higher molecular weight when compared to SA, has a higher value at all the concentrations investigated. The linear regression equations for the SA and GF PANs were y=8.57x+38.19 and y=11.75x+39.17, with corresponding R^2 values of 0.989 and 0.977, respectively. The surface tension of a polymer solution is mainly determined by hydrogen bonding, dipole–dipole forces and electrostatic interaction [397, 398]. The polar nitrile group in the PAN repeat unit, when increasing the concentration and the molecular weight of PAN, can provide higher inter-molecular attraction and result in higher cohesive energy, therefore increasing the surface tension of the solution. However, Wang *et al.* [143] reported that the change in the surface tension as a function of the polymer concentration for PAN/DMF solution was low and that is why relatively independent of the PAN concentration.

Overall Summary

- A linear relationship was observed between the surface tension and the concentration of PAN for the SA and GF polymers.
- The surface tension for the SA and GF PANs at 12 w/v% PAN/DMSO were 39.2 mN/m and 40.6 mN/m, respectively, at 55 °C.

- The GF PAN, with its higher molecular weight, had a higher surface tension when compared the SA PAN at all concentrations studied.

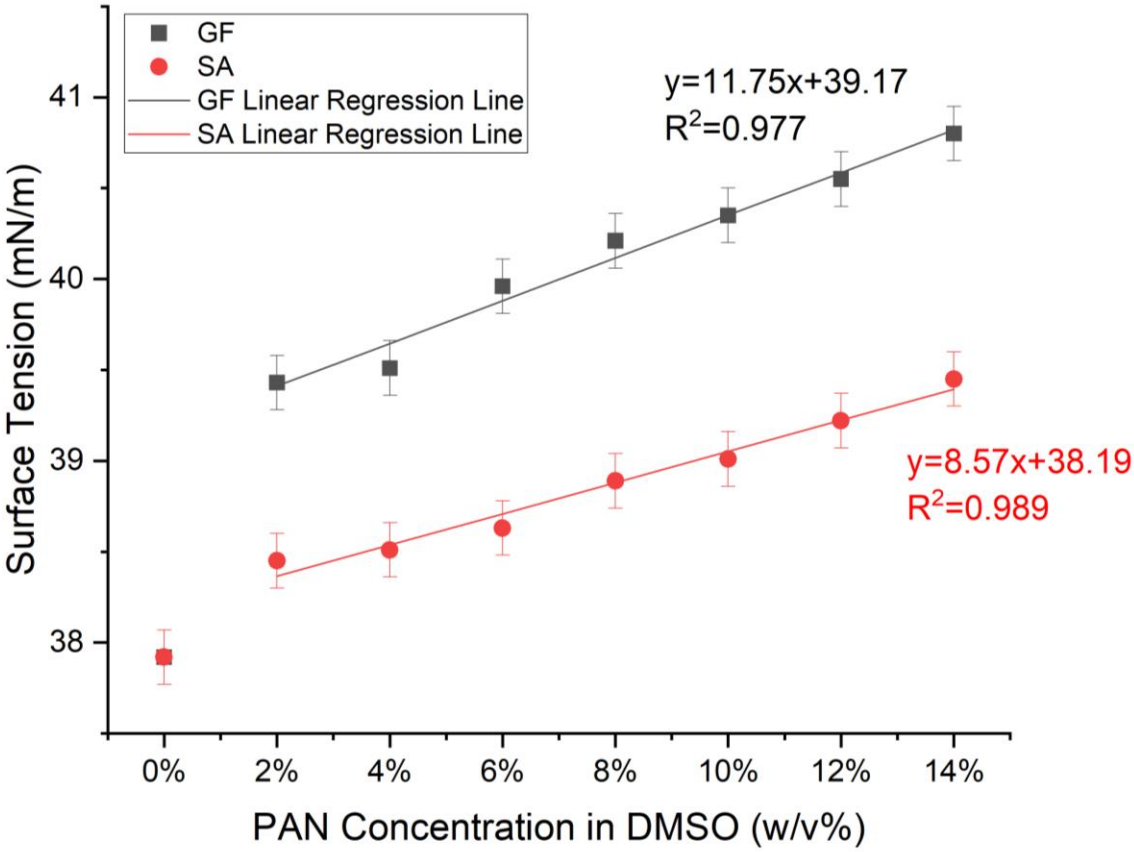

Figure 4.1.6 Relationship between surface tension and concentration for SA and GF PANs in DMSO as a function of concentration where the measurements were obtained at 55 °C.

4.1.6. Fibre Formation and Morphology of Electro-spun Fibres

The following section is adapted from Section 'Results and discussion' of a co-authored paper published by the author; Shao *et al.* [15].

In the first set of experiments, a conventional electro-spinning set-up using a static grounded electrode (Figure 3.2.2) was used to identify the optimum solution concentration and

processing parameters. The assessment and acceptance criteria were that the electro-spun fibres had to be unfused, be circular in cross-section, and be continuous and without beads. The vast majority of existing studies on PAN have been concerned with spinning at ambient temperature [36, 85, 87, 372, 374], but with two exceptions; Chen *et al.* [371] and Wang *et al.* [143] who conducted their experiments at 80 °C and 130 °C, respectively. They found that the fibre diameter decreased when the electro-spinning temperature increased. As noted in Section 4.1.1, the boiling points of DMSO and DMF are 189 °C and 153 °C, respectively, so DMSO requires a higher temperature to evaporate from the fibres within the electro-spinning chamber.

Controlling the chamber temperature was identified as a critical parameter for electro-spinning PAN/DMSO solutions. As seen in Figure 4.1.7a and b, fibres electro-spun using a 12 w/v% GF PAN/DMSO at 25 °C showed significantly more fibre fusion than those processed at 55 °C. This is because the boiling point of DMSO is 189 °C, and its volatilisation is a prerequisite for the formation of a 'skin' on the electro-spun fibre. The thickness of the outer skin on the fibres, as they are deposited on the grounded plate, and the overall solvent content will dictate whether the initially circular cross-section is retained. In instances where the temperature is below some critical level (as a function of the processing conditions and environment), electro-spun fibres will fuse. Therefore, the results shown in Figure 4.1.7a and b, demonstrate that electro-spinning PAN/DMSO cannot be conducted at room temperature because (a) the majority of the solvent is retained in the fibre when it is deposited on the grounded electrode; and (b) the lack of a polymer skin on the fibres make it difficult to maintain a circular cross-section.

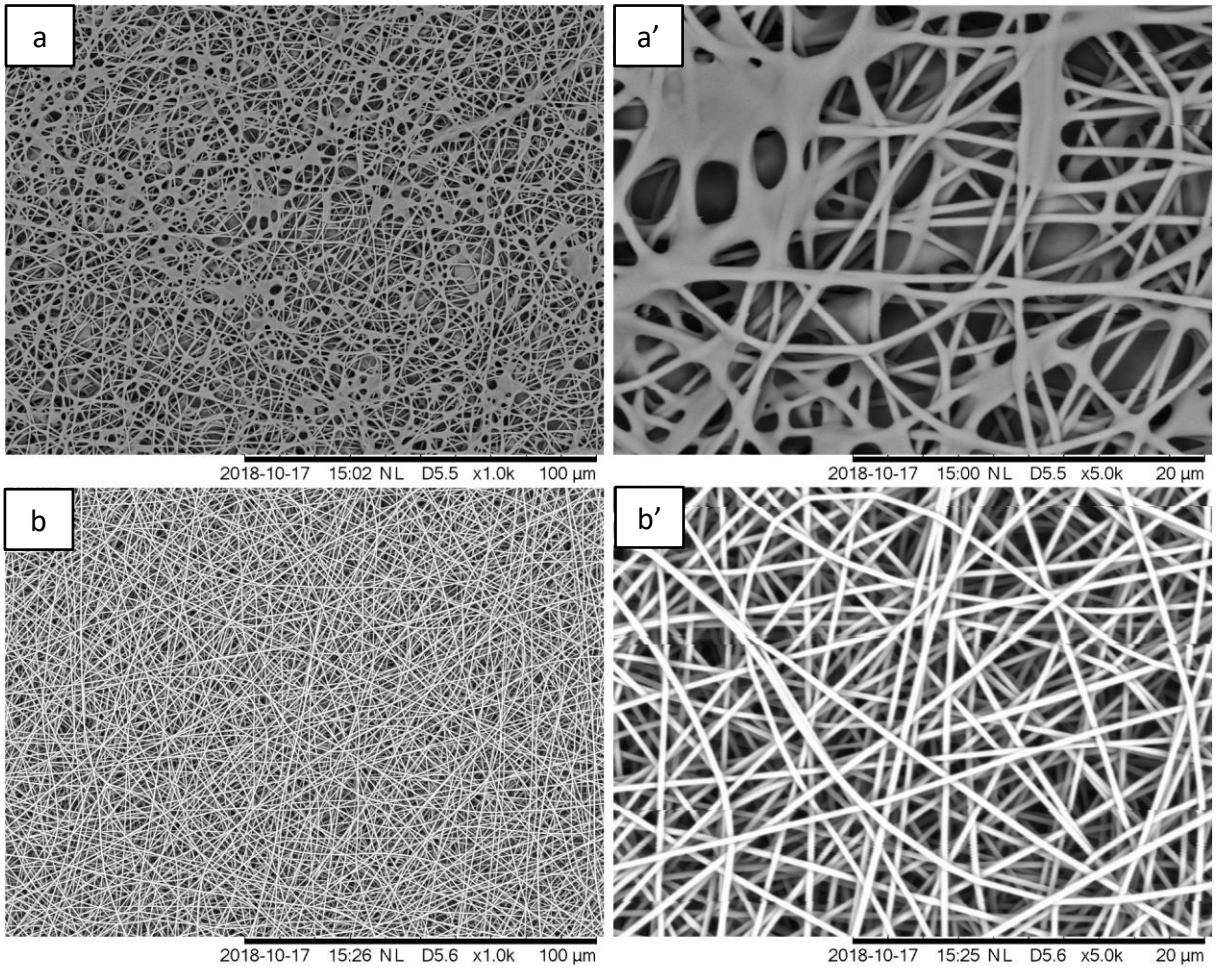

Figure 4.1.7 SEM micrographs of electro-spun GF PAN/DMSO fibres obtained at (a) ambient temperature (23 ± 3°C and 40% ± 3% RH) and (b) 55 °C and 13% ± 4% RH. (a') and (b') are the magnified images of (a) and (b), respectively.

The lowest voltages needed to electro-spin SA and GF PAN/DMSO solutions are shown in Table 4.1. With reference to the conductivity results in Figure 4.1.5, the effect of electrical conductivity of the solution on the critical applied voltage for electro-spinning is unclear. In addition, the minimum voltage required for electro-spinning was observed not to increase with increasing viscosity or surface tension. This finding is at odds with Lee *et al.* [399], who found that the critical voltage increased with increasing solution surface tension, and with

Yarin *et al.* [400], who reported that the critical voltage decreased with increasing solution conductivity. Other researchers [10, 51, 401, 402] have reported that the critical voltage increased with increasing viscosity. A detailed investigation will be required to determine the mechanics of this phenomenon. In the current study, the voltage was maintained at 13 kV as this was the minimum voltage required to maintain the shape of the Taylor cone when electro-spinning with a feed rate of 0.1 ml/hour. A larger Taylor cone was observed when applying a voltage below 13 kV, because the production speed is affected by the applied voltage. A higher applied voltage increases the electric field strength, increasing the force on the polymer solution towards the collector [130]. In the current study, it was concluded that the applied voltage and the solution dispensing rate had to be tuned and controlled carefully in order to produce uniform electro-spun fibre over a long period (more than 30 minutes).

The micro- and macroscopic appearances of the electro-spun fibres produced, as a function of the polymer concentration, are shown for the SA and GF PAN in Figure 4.1.8 and Figure 4.1.10. For SA PAN, Figure 4.1.8a and b represent cases where the polymer concentration was 2 w/v% and 4 w/v%. Evidence for electro-spraying can be seen in Figure 4.1.8a and b, where the electro-sprayed beads range in diameters from 20 nm to 1150 nm and 40 nm to 1000 nm, respectively. The bead features observed in this micrograph suggest conventional Plateau–Rayleigh instability [403]. The bead spacing makes it unlikely that they are due to intermittent overflow of the pendant drop from the needle tip. The 4 w/v% solution showed a larger average particle size and more obvious 'beads-on-string' phenomena [374, 379]. These features were also observed when the concentration reached 6 w/v% (Figure 4.1.10a), but a higher portion of strung beads was observed when compared to the 4 w/v% solution. Moreover, the beads were much smaller. Figure 4.1.10b shows that the number of beads

decreases significantly, and fibre formation was more obvious when the concentration reached 8 w/v%. Increasing the concentration of the polymer to 10 w/v% further reduced the number of beads and increased the number of electro-spun fibres; the average fibre diameter was also seen to increase as a function of the polymer concentration as seen in Figure 4.1.11. A similar trend was reported by previous researchers [36, 85, 283, 355].

Figure 4.1.8a' represents the case where the polymer concentration was 2 w/v% GF PAN in DMSO. Electro-spraying is seen in Figure 4.1.8a', with the diameters of the electro-sprayed beads ranging from 100–7000 nm. Both the bead size distribution and the bead size are greater than when using the lower-molecular weight SA PAN. Beads-on-string structures appeared when the concentration reached 4 w/v%; this is 2 w/v% lower than seen for the SA PAN. Figure 4.1.10a' shows that, as the concentration of the GF PAN is increased to 6 w/v% in DMSO, the number of beads is reduced significantly when compared to Figure 4.1.8b'. However, the bead diameter was not reduced. As before, increasing the concentration to 8 w/v% resulted in a significant reduction in the concentration of the beads and their relative diameters. The majority of the fibres observed in Figure 4.1.10b' range from 30–150 nm in diameter, and beads are rare. Table 4.2 shows that the average number of beads per frame for the 10 w/v% GF PAN was only 0.7. Similar to the case for SA PAN, a higher concentration of the polymer solution results in a higher average fibre diameter as presented in Figure 4.1.11 and Table 4.2.

Table 4.1 Processing conditions and results recorded when electro-spinning specified SA and GF PAN/DMSO concentrations.

PAN Supplier	Concentration (w/v%)	Minimum Voltage to Start Spinning (kV)	Chamber Temperature (°C)	Production Voltage (kV)	Feed Rate (ml/hour)	Working Distance (cm)	Result
SA	2%	7.5	55	13	0.1	10	Beads
	4%	7.0					Beads
	6%	6.4					Beads-on-strain
	8%	6.1					Fibre + Beads
	10%	5.9					Fibre
	12%	6.1					Fibre
	14%	6.9					Fibre
GF	2%	6.8					Beads
	4%	6.5					Beads-on-strain
	6%	6.3					Fibre + Beads
	8%	6.1					Fibre
	10%	6.2					Fibre
	12%	6.3					Fibre
	14%	6.6					Fibre

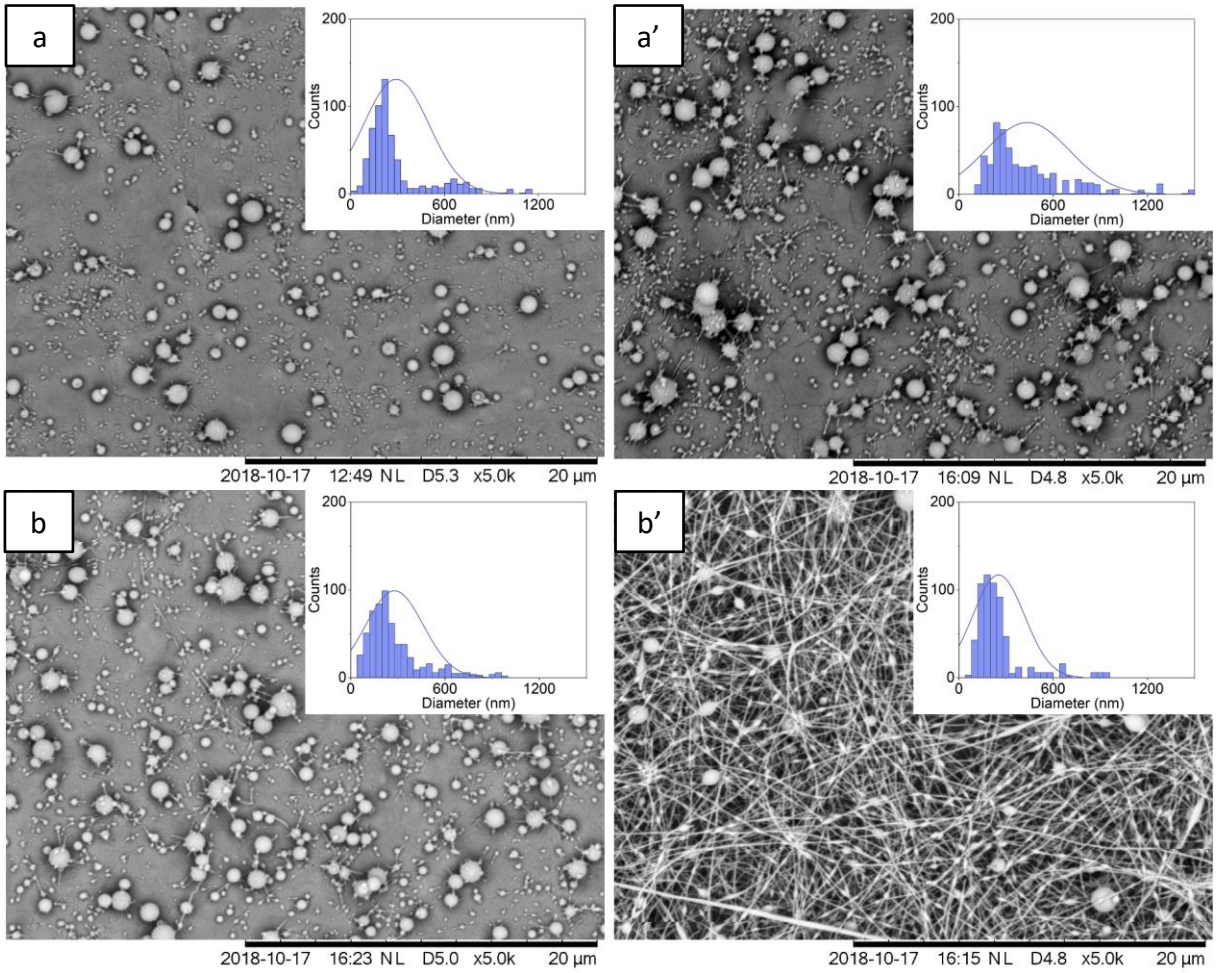

Figure 4.1.8 SEM micrographs overlaid with bead diameter distributions of electro-sprayed/electro-spun fibres produced by SA PAN at: (a) 2 w/v%; (b) 4 w/v%; and GF PAN at: (a') 2 w/v%; (b') 4 w/v% concentration.

With reference to the viscosity and the surface tension results in Figure 4.1.4 and Figure 4.1.6, the comparison of bead size distributions for SA PAN and GF PAN in Figure 4.1.8, as well as the average bead diameters summarised in Table 4.2, it can be seen that the average bead diameter for GF PAN initially decreases but then increases when the concentration is increased from 2 w/v% to 6 w/v%. The average bead diameter obtained from SA PAN decreased with increasing concentration. The bead diameter obtained at 6 w/v% was higher than for SA PAN at the same concentration. In general, increasing the molecular weight at the

same polymer concentration favours entanglement of the polymer chain, which improves fibre formation and results in smaller and fewer beads [404, 405]. Surface tension is the primary factor for bead formation, as it acts to minimise the surface-to-mass ratio. It can thus be said that high surface tension leads to the formation of large beads and a larger fibre diameter [111, 396], whereas a low surface tension will allow the polymer to stretch and flow without forming beads. However, in the current study, due to the high dipole moments, long solvent bridge and the low solvent evaporation rate of DMSO [77], larger beads were obtained at the higher molecular weight. Surface tension could have also contributed to the solvent remaining in the core of the fibre, allowing the polymer chains enough mobility to re-entangle after stretching [295, 406]. Polymer chain relaxation and surface tension dominate the formation of beads. With higher surface tension and molecular chain entanglements at higher molecular weight, GF PAN results in beads with larger diameters.

The SA and GF PANs show better fibre morphology with no obvious beads formed at a concentration of 8 w/v%. This is because chain entanglement is able to sustain the drawing during electro-spinning [95-97]. The correlation between the viscosity of the polymer solution and the shear viscosity agrees with previous findings that a critical viscosity is, indeed, required for fibre formation [98, 101, 102, 104]. In addition, the ejected polymer jet needs to have the appropriate 'strength' or viscoelastic properties to prevent the jet from fracturing as it undergoes whipping (bending instability) [12, 13].

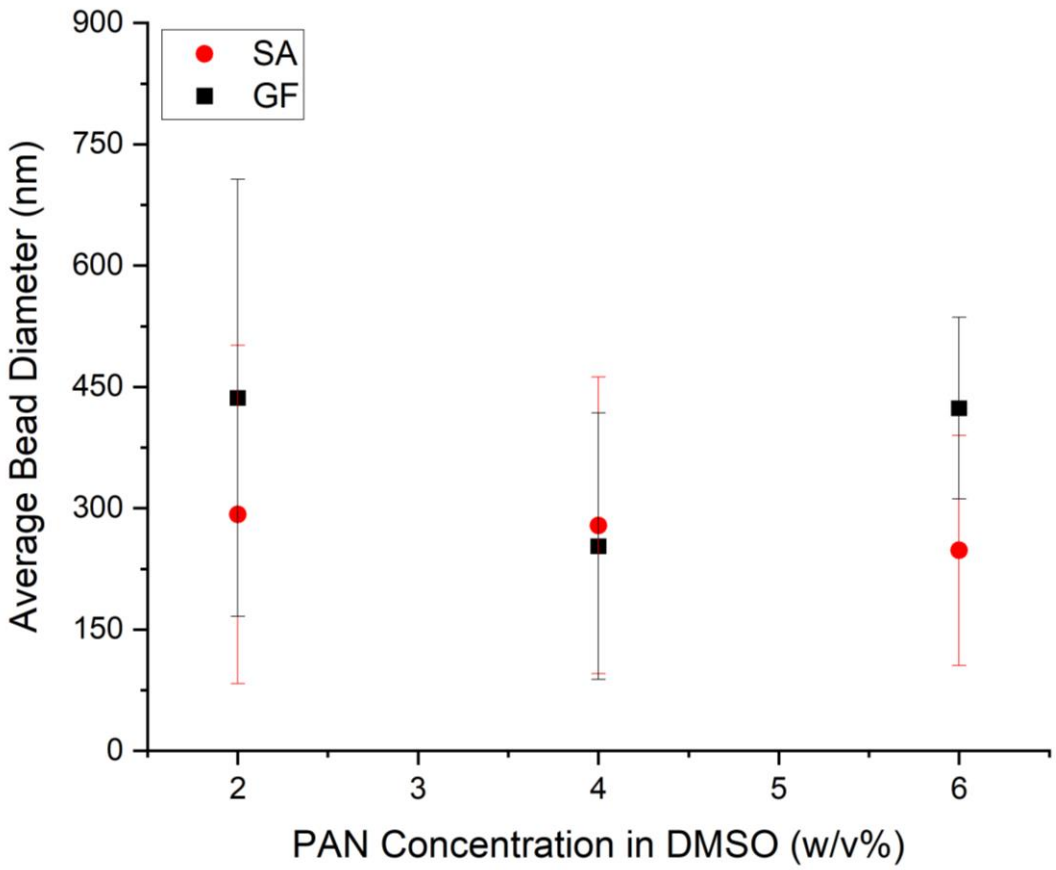

Figure 4.1.9 The average bead diameter obtained from different PAN concentrations in DMSO.

Figure 4.1.4a and b demonstrate how the increase in viscosity for the SA PAN and GF PAN commences above 10.9 w/v% and 10.4 w/v% in DMSO, respectively. SA PAN has a molecular weight of 150,000 g/mol, therefore, the critical polymer chain entanglement concentration will be higher than for GF PAN, which has a molecular weight of 230,000 g/mol. However, the SEM micrographs in Figure 4.1.8 and Figure 4.1.10 show beads-on-string morphology when the concentration reaches 6 w/v% and 4 w/v% for SA and GF PAN, respectively, with viscosities at those concentrations being 0.121 Pa.s and 0.226 Pa.s, respectively. The experimentally determined critical concentration is lower than that obtained from the shear viscosity-vs-

concentration graph in Figure 4.1.4. The data presented in Table 4.2 and Figure 4.1.4a corroborates the view that a critical polymer concentration is required for fibre formation during electro-spinning. One possible explanation is that the critical concentration was obtained from a curve fitted to a number of discrete points going up to a maximum concentration of 14 w/v%, and therefore does not demonstrate the critical concentration as taken from the full viscosity/concentration trace. Another possible reason could be use of a higher ambient temperature, hastening the solvent evaporation and fibre solidification rate, improving fibre formation at low concentrations [143].

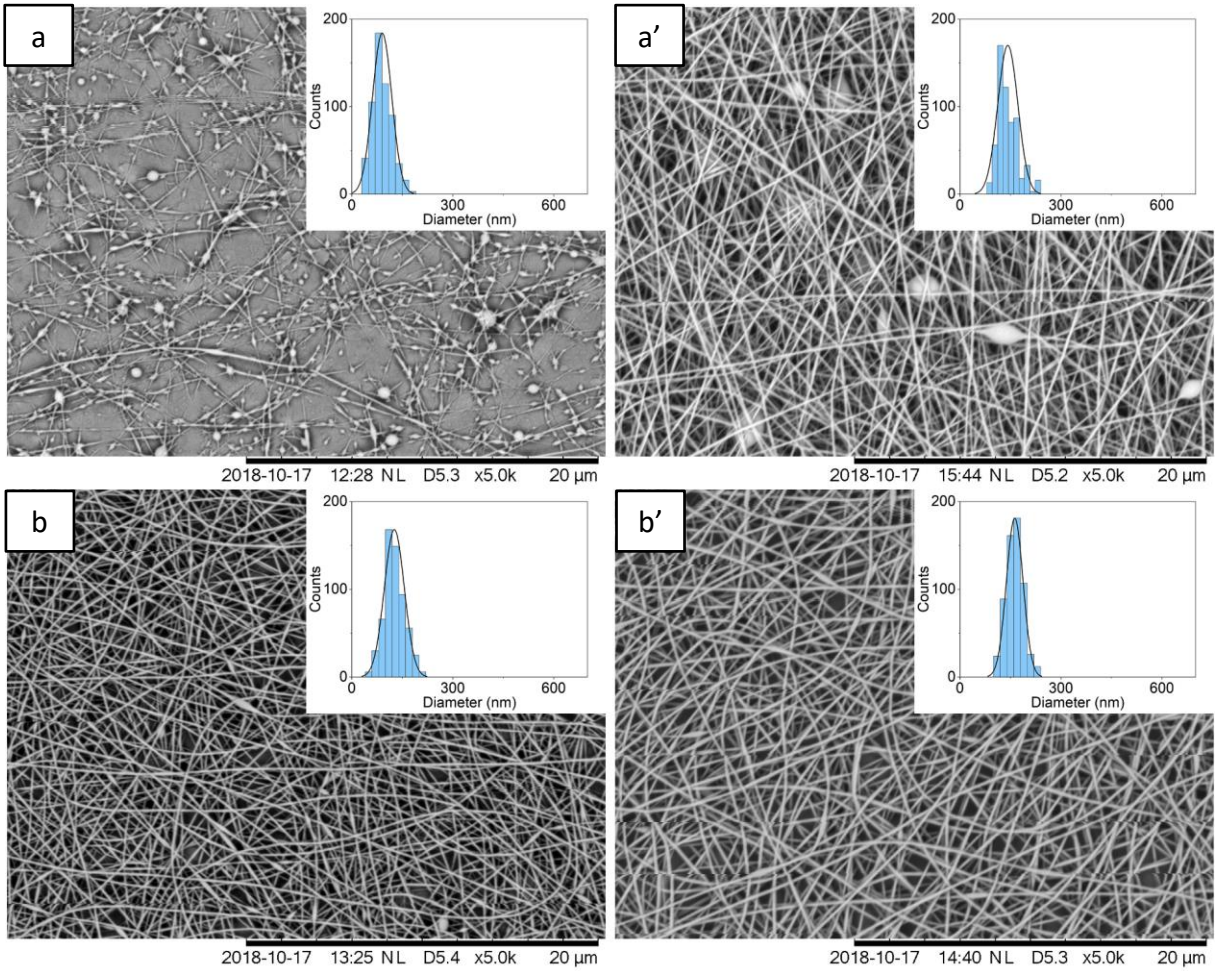

Figure 4.1.10 Cont.

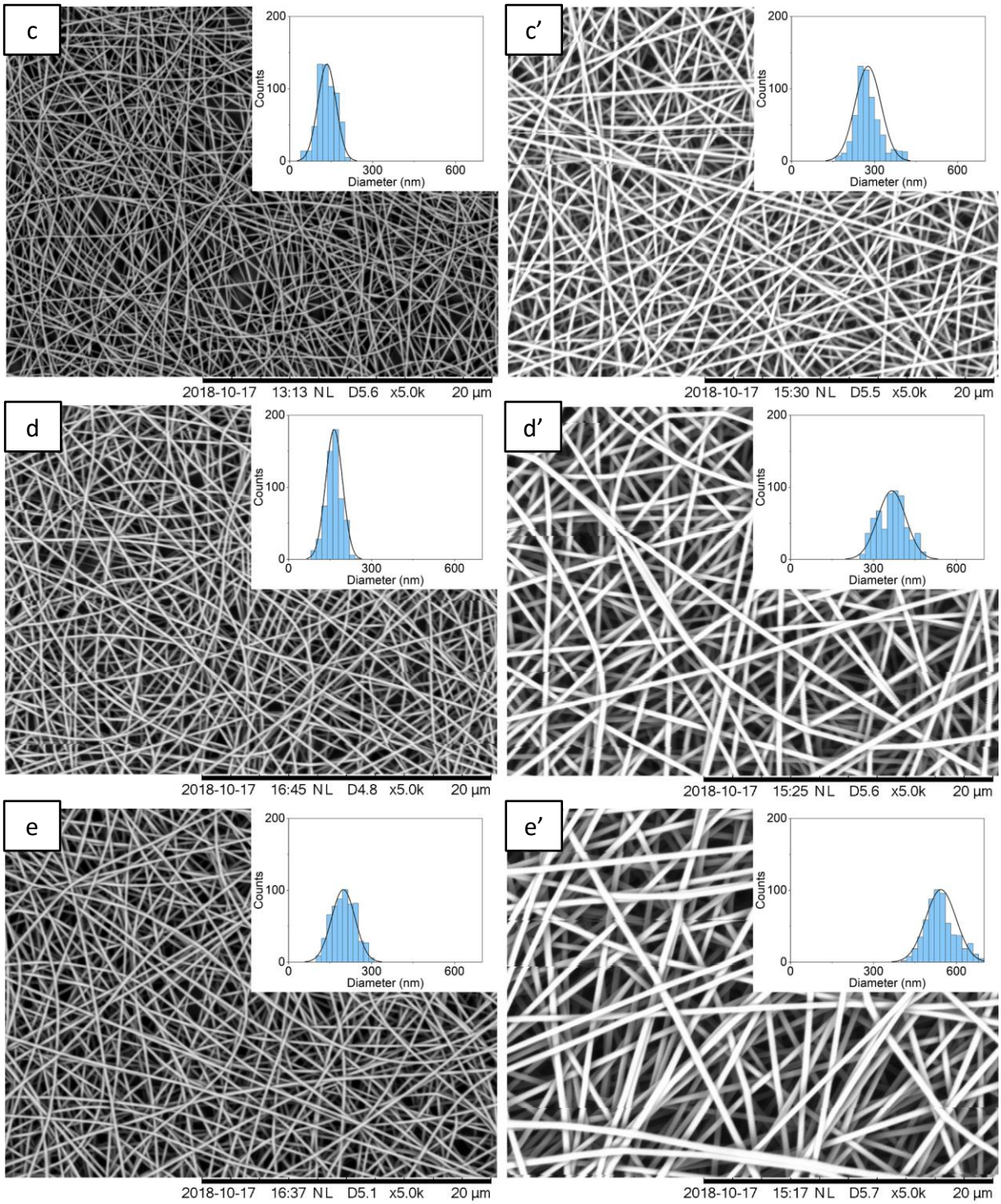

Figure 4.1.10 SEM micrographs overlaid with fibre diameter distributions of electro-spun fibres produced by SA PAN at: (a) 6; (b) 8; (c) 10; (d) 12; (e) 14 w/v%; and GF PAN at: (a') 6 (b') 8; (c') 10; (d') 12; (e') 14 w/v% concentration. Bead diameter was not included in the measurement of fibre diameter distribution for the 6 w/v% SA and GF PANs.

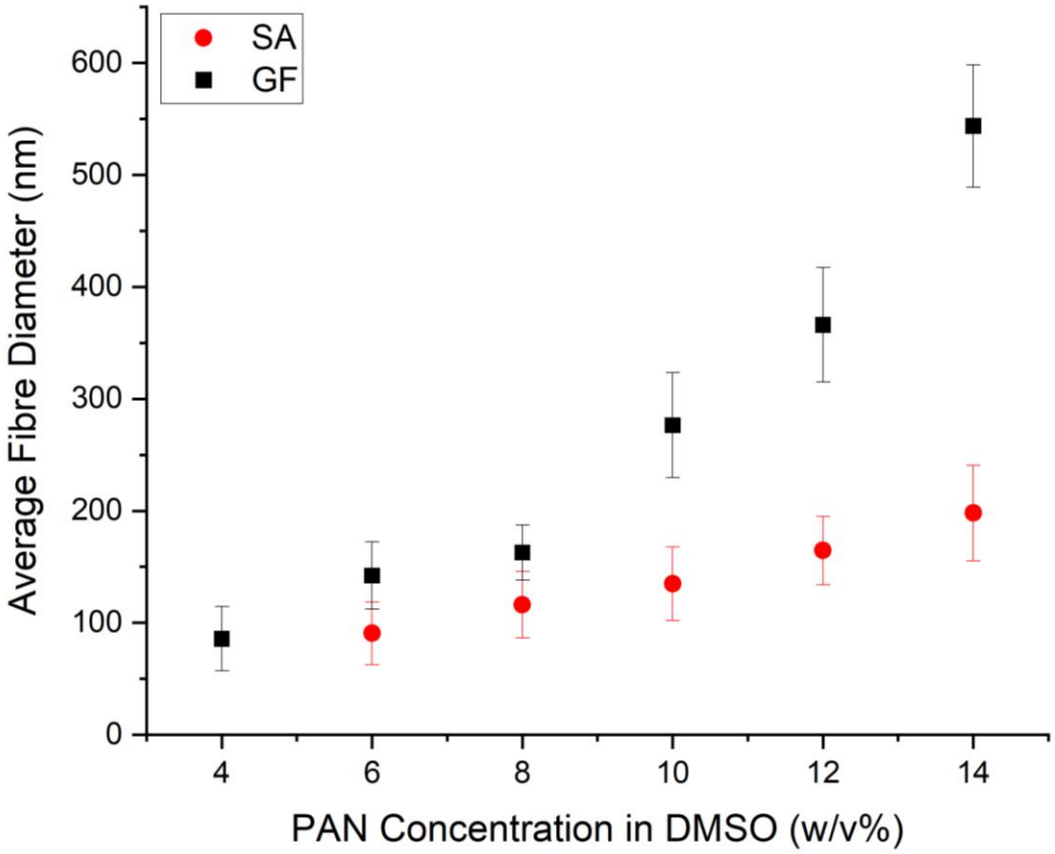

Figure 4.1.11 The average fibre diameter obtained from different PAN concentrations in DMSO. All other condition can be found in Table 4.1.

Table 4.2 Summary of bead diameter distribution, average bead diameter and average fibre diameter obtained from specified SA and GF PAN concentrations. The standard deviation is shown with square brackets.

Sample	Beads Density (beads/frame at x10000)	Average Bead Diameter (nm)	Average Fibre Diameter (nm)
SA 2%	1048	292.1 [209.0]	N/A
SA 4%	532	278.6 [183.3]	N/A
SA 6%	312	247.7 [142.0]	90.6 [28.1]
SA 8%	N/A	N/A	116.1 [29.5]
SA 10%	N/A	N/A	134.9 [32.9]
SA 12%	N/A	N/A	164.6 [30.5]
SA 14%	N/A	N/A	198.0 [42.6]
GF 2%	520	436.3 [270.3]	N/A
GF 4%	284	252.8 [164.8]	85.8 [28.7]
GF 6%	5	412.5 [112.2]	142.2 [29.9]
GF 8%	N/A	N/A	162.8 [24.6]
GF 10%	N/A	N/A	276.5 [46.8]
GF 12%	N/A	N/A	366.1 [51.3]
GF 14%	N/A	N/A	543.7 [54.7]

Overall Summary

- A series of experiments were carried out to establish the optimal electro-spinning conditions for the SA and GF PANs in DMSO.
- Bead-free electro-spun nano-fibres were produced from the SA and GF PANs at concentrations between 10–14 w/v% and 8–15 w/v% PAN/DMSO. At lower

concentrations, bead formation was observed. At concentrations greater than 14 w/v%, the viscosity was too high for electro-spinning.

- It was necessary to electro-spin at 55 °C as this was required to enable the DMSO to evaporate in the surface regions.
- The average fibre diameter was found to increase as the PAN concentration was increased. The average fibre diameters obtained from SEM micrographs for the SA and GF PANs at 12 w/v% were 164.6 nm and 366.1 nm, respectively.
- The average fibre diameter for the GF PAN shows an unexpected increase from 366.1 to 544.7 nm when the concentration was increased from 12 w/v% to 14 w/v%. The mechanism behind this requires further investigation.

4.1.7. The Effect of Drying Temperature on the Residual Solvent in PAN/DMSO Nano-fibres

Before oxidising and carbonising the electro-spun PAN/DMSO fibres, the DMSO had to be removed. This is because any residual solvent can lead to the formation of flaws during subsequent heat-treatment. Previous researchers have also noted that the presence of residual solvent during oxidation and carbonisation can lead to a reduction in the mechanical properties [407-410].

The drying experiments were carried out for six hours each at 100, 120 and 140 °C. The electro-spun 12 w/v% GF PAN/DMSO nano-fibres were heated in a vacuum oven as described in Section 3.2.3, Figure 3.2.9.

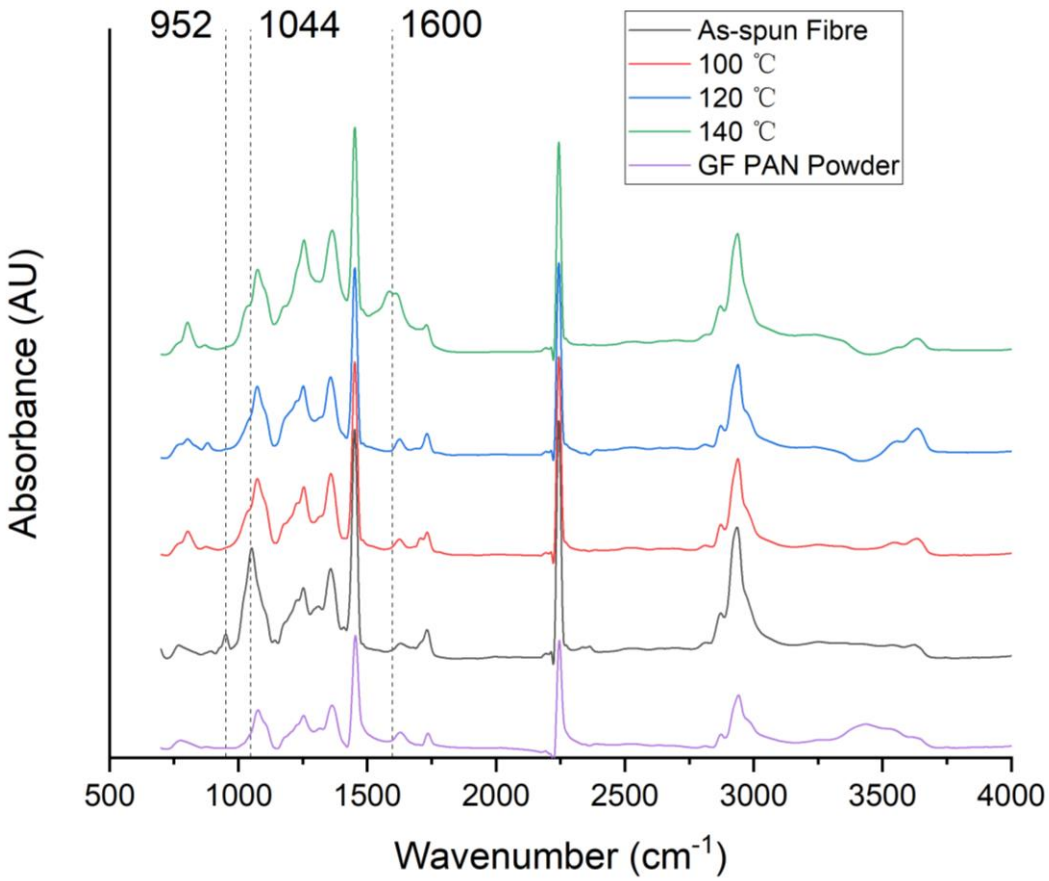

Figure 4.1.12 Overlaid FTIR spectra for PAN/DMSO fibres dried in a vacuum oven at various temperatures. The spectra of the as-received GF PAN powder are also provided as a baseline reference.

The overlaid FTIR spectra in Figure 4.1.12 above shows the changes in absorbance before and after drying the electro-spun fibres. The spectra of the as-spun nano-fibres show two peaks located at 952 cm^{-1} and 1044 cm^{-1}, neither of which is found in the spectra of as-received PAN power and vacuum oven-dried electron-spun fibre. These peaks correspond to C–H bending vibration and S=O stretching vibration, which is typical for DMSO [314, 361, 411-413]. Drying the nano-fibres in a vacuum oven at 100 °C and 120 °C for 6 hours was found to remove the remaining DMSO in the fibres. This was established by inspecting the spectra before and after

drying, and observing that the two peaks are absent. When the drying temperature was increased to 140 °C, peaks appeared at 1660 cm^{-1} and 1600 cm^{-1}; these relate to C=N stretching vibration and C=C stretching vibration [314, 414-417]. The rationale for this experiment was to maximise DMSO removal without oxidising the nano-fibres. Therefore, based on the FTIR spectroscopy results, drying the fibre at 120 °C for 6 hours was considered the optimal choice.

In order to demonstrate the effectiveness of the previously mentioned drying process; the TGA and DTG traces for the as-spun PAN/DMSO nano-fibres and the fibres that were dried at 120 °C for 6 hours in the vacuum oven are overlaid in Figure 4.1.13. It can be seen from the weight-loss curve for the as-spun fibres that there is a two-stage weight-loss behaviour beginning at 71.9 °C and 151.9 °C, respectively. The 2.7% weight-loss between 71.9 °C and 151.9 °C is probably due to the loss of absorbed moisture in the DMSO during electro-spinning and storage. As the boiling point of DMSO is 189 °C, the second weight-loss step of 1.5% (between 151.9 °C and 266.9 °C) can be attributed to the weight loss due to DMSO evaporation. This weight loss cannot be seen in the TGA trace for the vacuum oven-dried fibres, which demonstrates that drying the fibre at 120 °C in the vacuum oven sufficiently removes the remaining moisture and DMSO in the electro-spun fibres. A further discussion on the TGA traces for the PAN fibres is presented in Section 4.2.

The surface morphology of as-spun nano-fibres is displayed in Figure 4.1.14a, and that of vacuum oven dried nano-fibres can be seen in Figure 4.1.14b–d. The overlaid diameter distributions shown in Figure 4.1.14a–d for as-spun, 100, 120, and 140 °C vacuum oven dried fibre have standard deviations of 51.3, 50.7, 49.1 and 43.8 nm, respectively. The average fibre

diameter decreased slightly as temperature increased. The average fibre diameters were 366.1, 362.5, 361.1 and 361.7 nm, respectively. The fibre surface was not smooth, but appeared mottled. The surface morphology was not seen to change with increasing drying temperature. It is possible that the mottled appearance of the surface morphology could be due to localised shrinkage caused by irradiation under the SEM beam, which appears worse during image capturing. Another possibility is that the mottled appearance is caused by the gold coating. The gold coating used has an average particle size of 8 nm which can be visualised at such high magnification.

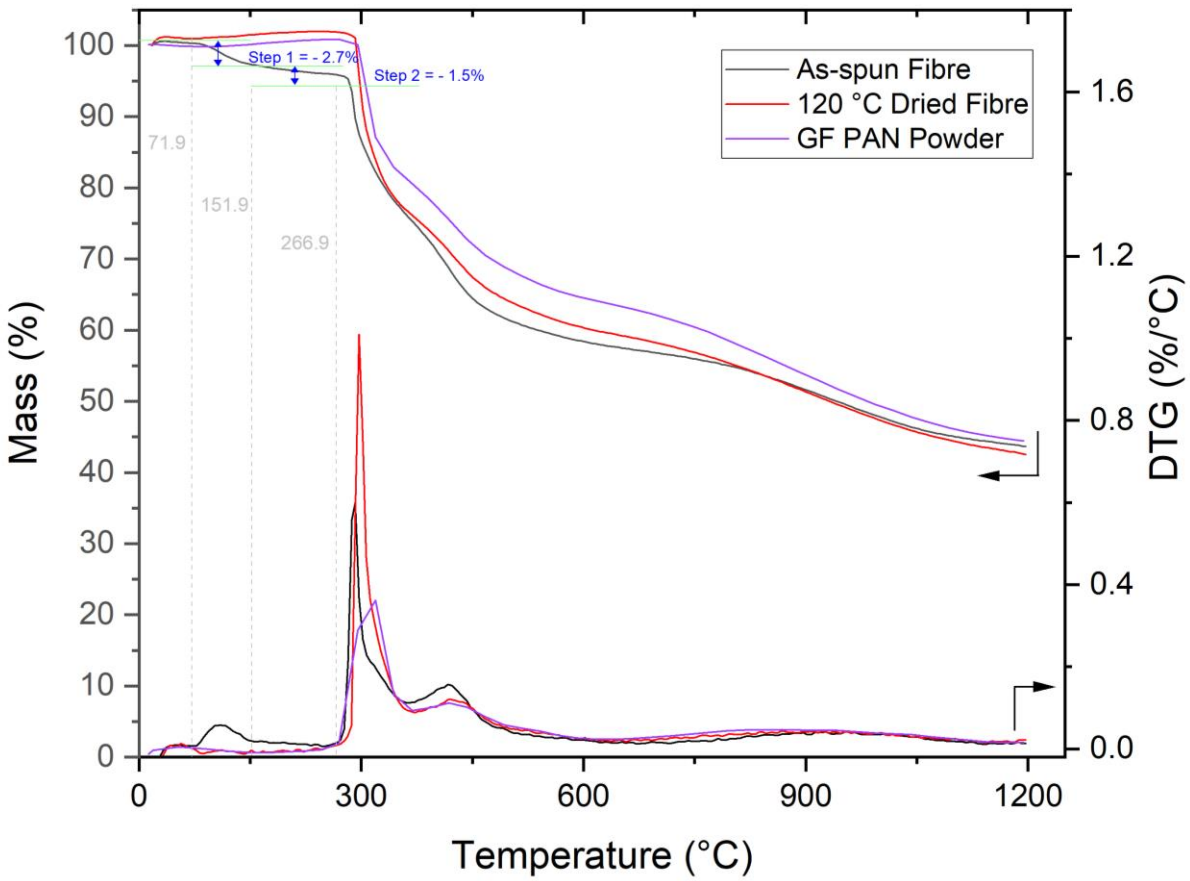

Figure 4.1.13 Comparison of the DTG and TGA curves of as-received GF PAN powder, as-spun fibre and the fibre dried at 120 °C for 6 hours in a vacuum oven.

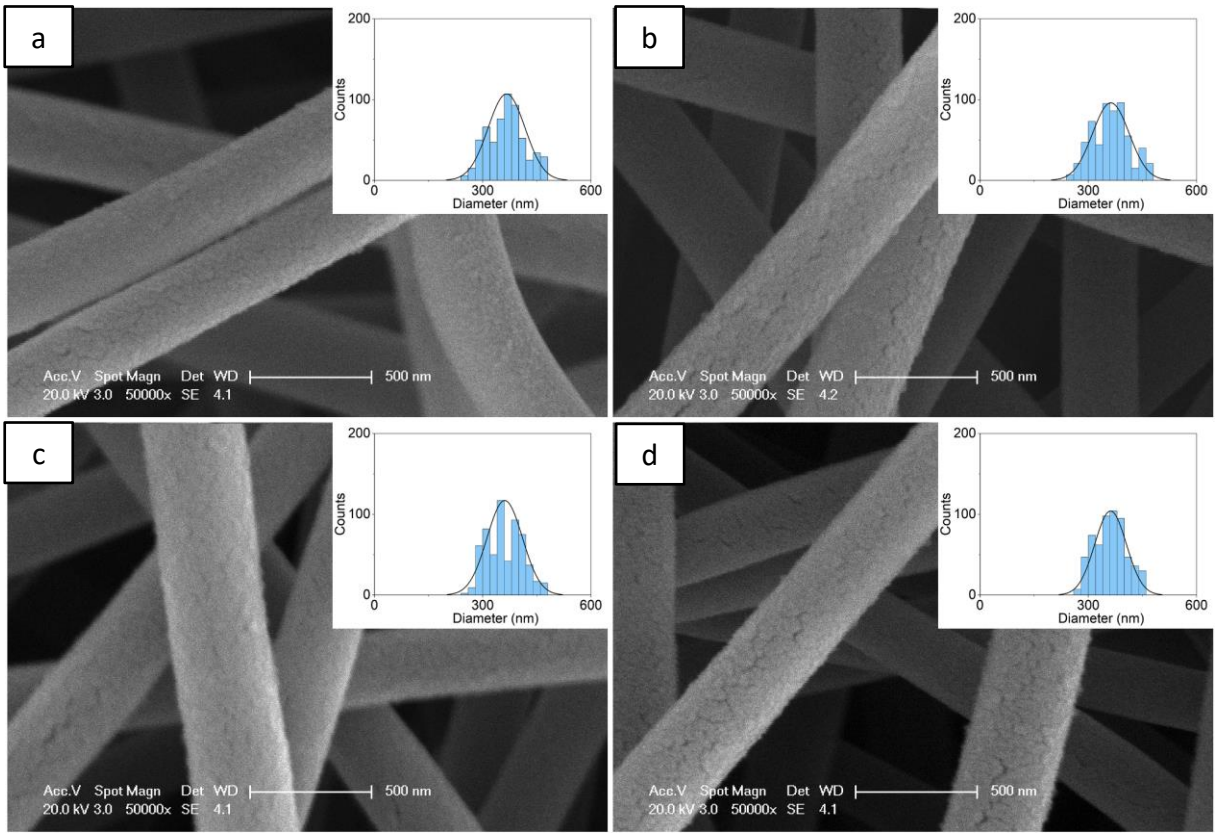

Figure 4.1.14 High magnification SEM micrograph overlaid with diameter distribution of: (a) as-spun; (b) 100 °C; (c) 120 °C; and (d) 140 °C 12 w/v% GF PAN nano-fibres dried in a vacuum oven.

Overall Summary

- Experiments were conducted to define a regime to remove any DMSO from the electro-spun PAN/DMSO nano-fibres.
- FTIR spectroscopy was used to detect the presence/absence of DMSO in the electro-spun nano-fibres.
- The drying temperature was of importantance, as the intention was to remove the DMSO, not to cross-link the PAN nano-fibres.

- TGA was also used to define the drying temperature required to remove the DMSO from the electro-spun PAN nano-fibres.
- The drying regime chosen consisted of heating the fibres in a vacuum oven at 120 °C for six hours.
- The dried nano-fibres were stored in a desiccator until required.

4.1.8. Electro-spinning of Aligned PAN/DMSO Nano-fibres

The following section is adapted from Section 'Results and discussion' of a co-authored paper published by the author; Shao *et al.* [15].

With reference to Section 2.2, a discussion on fibre alignment during electro-spinning was presented. The methods that control the shape of the electric field were seen to be more effective and applicable to most polymer solutions. However, none of the electro-spinning methods reported in the literature are capable of producing aligned nano-fibres in a continuous manner, where they can be extracted or spooled. The conventional static grounded electrode was modified by introducing a dielectric material (PTFE) to influence the electric field lines and the Vee-shield fibre alignment method was developed. In the following section, the detailed configuration and mode of operation of the Vee-shield set-up and the mechanism for fibre alignment is demonstrated using COMSOL Multiphysics simulation software. The degree of fibre alignment was also examined using SEM micrographs.

4.1.8.1. Effect of the Vee-shield Geometry on Fibre Alignment

Based on the schematic illustration of the Vee-shield configuration shown in Figure 4.1.15, a flat-based *V*-shaped PTFE dielectric (item i) was placed on the conventional electro-spinning

collector (item iv). The opposite edges of the copper disk (items ii and ii') act as the 'active' grounded electrodes. The role of the PTFE shield is discussed in the next section. With the aid of the high-speed camera, Shown in Figure 4.1.16a and b, it was observed that the length of the straight section of the jet (before whipping was observed) was 1.7 cm for conventional electro-spinning and 3.6 cm when the Vee-shield was used. Furthermore, the whipping speed and the trajectory were observed to be slowed and controlled when the Vee-shield was present. It will be shown later that the presence of the Vee-shield enables the polymer jet to oscillate between the ends of the grounded electrodes. Aligned electro-spun nano-fibres are deposited within the narrower rectangular bottom section of the Vee-shield (item iii) along its length. A cellulose paper strip was used as a substrate which is placed within the bottom area of the Vee-shield to ease the removal of the nano-fibres. The effect on the degree of alignment was studied and is explained in Section 4.1.8.2.

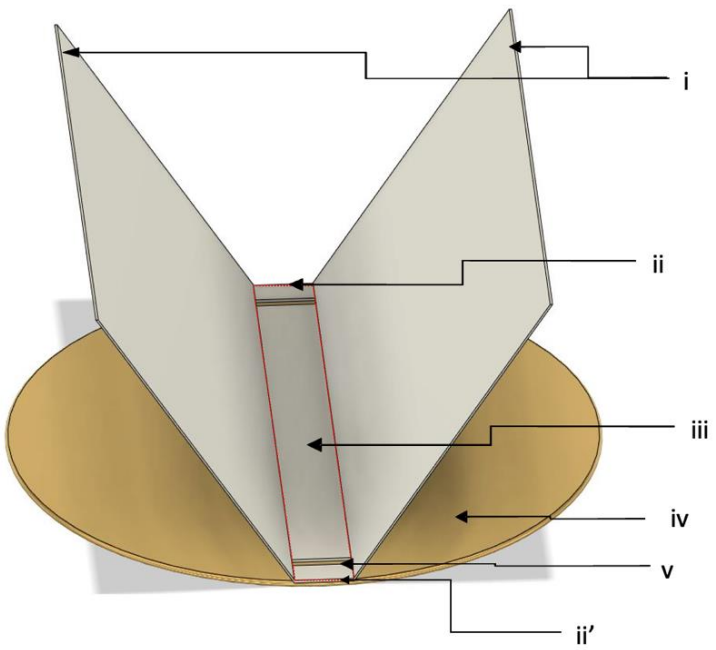

Figure 4.1.15 Schematic illustration of the Vee-shield collector.

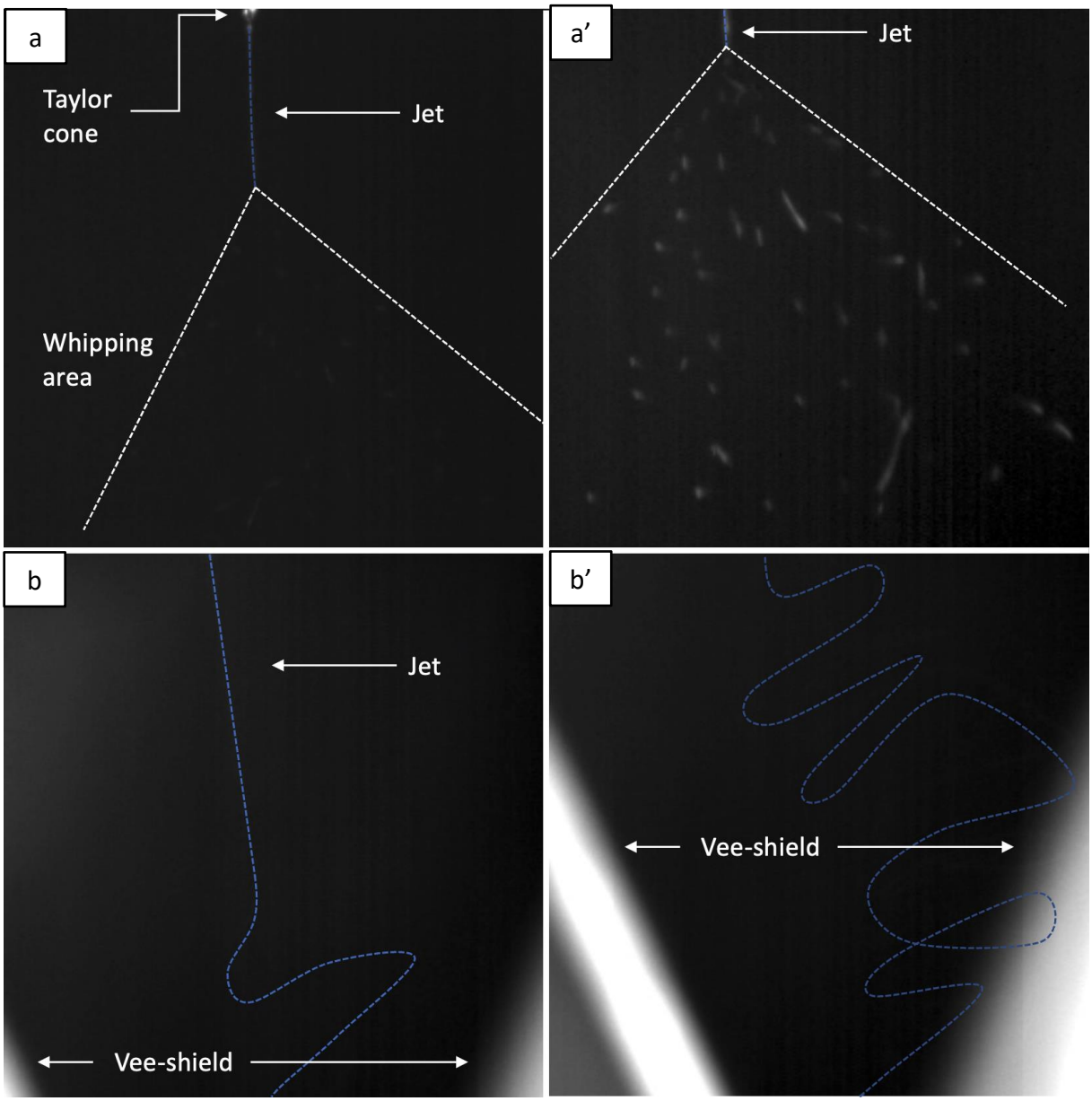

Figure 4.1.16 High-speed photographs of the electro-spinning process using: (a, a') conventional flat-plate collector showing the cone of the whipping area; and (b, b') Vee-shield collector. The blue dotted lines have been drawn to aid in visualisation of the jet's path. (a') and (b') are the lower areas of (a) and (b), respectively.

4.1.8.2. Effect of the Vee-shield on Fibre Alignment

In this section, the mechanism of the Vee-shield alignment technique will be illustrated by comparing the Vee-shield electrode set-up with the conventional set-up using the COMSOL simulation software. The study will focus on the YX and YZ cut-planes across the centre of these two geometries. A schematic illustration of the cut-planes for the conventional and the Vee-shield set-ups are shown in Figure 4.1.17a, Figure 4.1.18a and Figure 4.1.19a. It is worth mentioning that due to the symmetry of the conventional set-up, YX and YZ planes are identical during the simulation. Therefore, only one set of simulation results, along the YX plane, is reported for the conventional electro-spinning set-up.

Figure 4.1.17a–d shows the electrical potential, normalised electric field strength, electric field streamlines and current density vector simulation results for the YZ cut-plane of the conventional electro-spinning set-up. The applied potential was set at 15 kV. From the electrical field strength illustrated in Figure 4.1.17c, the electric field strength at the edge of the ground copper collector is higher than anywhere else around the collector. Since charge transport is required for electro-spinning, it is seen in Figure 4.1.17c and d that there is no preferential route for the charged electro-spun fibres to follow, which is similar to the results reported by Theron *et al.* [151] and Deitzel *et al.* [152]. The electric field leads to the bending instability and whipping action of the polymer jet, the fibres will be deposited randomly over a finite area, below the needle, on the grounded electrode [10, 13, 116, 151, 152]. For a conventional electro-spinning set-up where the dielectric material is not present, the path of the current density arrows in Figure 4.1.17d is similar to the electric field lines presented in Figure 4.1.17c.

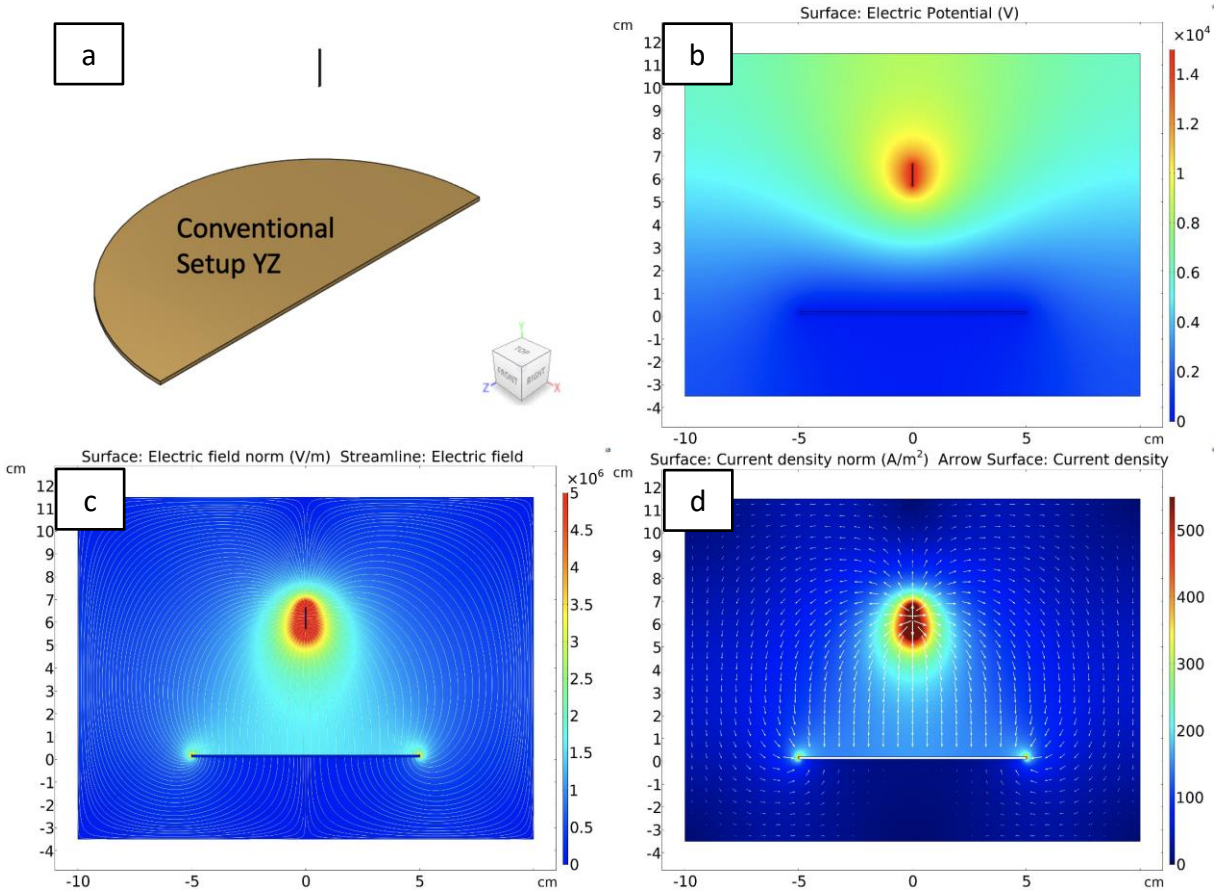

Figure 4.1.17 (a) A schematic diagram of the YZ cut-plane for the conventional electro-spinning set-up. The COMSOL simulation results showing the: (b) electric potential; (c) electric field; and (d) electric current density along the YZ plane.

When the insulating PTFE Vee-shield is introduced, the simulation results along both YZ and YX cut-planes are shown in Figure 4.1.18 and Figure 4.1.19, respectively. On comparing the electric field streamlines as well as the electric field strength of the conventional electro-spinning set-up (Figure 4.1.17c) and the Vee-shield set-up along the YX plane shown in Figure 4.1.19c, no significant changes can be seen when the Vee-shield is present. Figure 4.1.20a shows how the field streamline is changed when it passes through the Vee-shield, this is because the changing dielectric constants affect the configuration of the streamline. The

dielectric constant of air and PTFE are different, and this results in different directions of the field lines in the simulation. However, the resultant of electric field lines cannot explain the mechanism of alignment when a dielectric material is present.

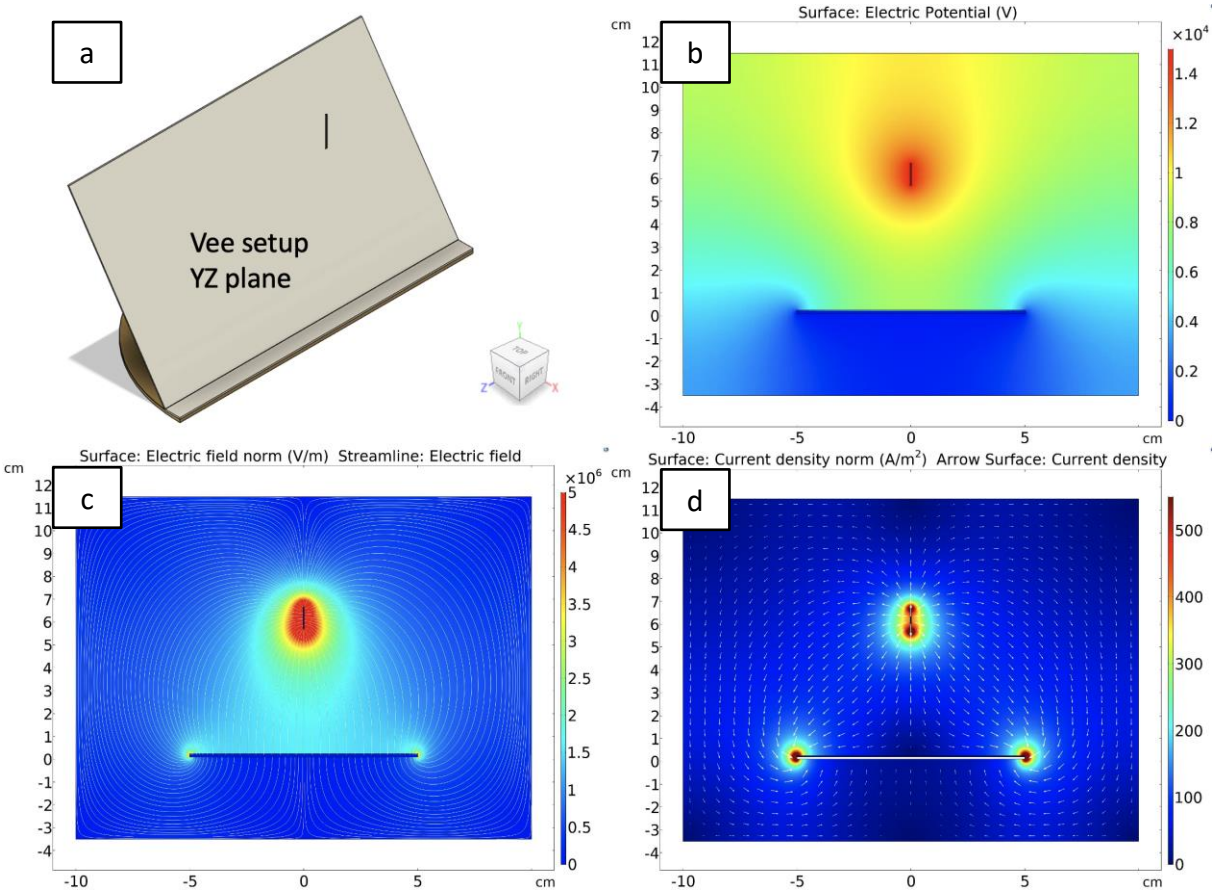

Figure 4.1.18 (a) Schematic illustration of the YZ cut-plane of the Vee-shield collector. The COMSOL simulation result showing the: (b) electric potential; (c) electric field; and (d) electric current density along the YZ plane.

Other than electric field streamlines and field strength, the simulation of electric potential and the current vector graph illustrate the difference when introducing a Vee-shield (dielectric material) to the system. Comparing the electric potential plots without and with the Vee-shield in Figure 4.1.17b, Figure 4.1.18b and Figure 4.1.19b, it can be seen that the PTFE Vee-

shield effectively decreases the electric potential between the needle and the collector. This decrease is smaller along the YX plane than the YZ plane. Since the movement of charge is more likely to flow along the direction with a higher potential difference, the charge carrier (charged polymer fibre jet in this case) will move along the YZ plane of the Vee-shield set-up. This is also verified by the current density plots, shown in Figure 4.1.18d and Figure 4.1.19d. When the Vee-shield is introduced, the current density at the edge of the grounded copper along the YX plane is lower than that observed in the YZ plane. The electric current density arrow vectors on the graph clearly show that the preferred direction for the movement of

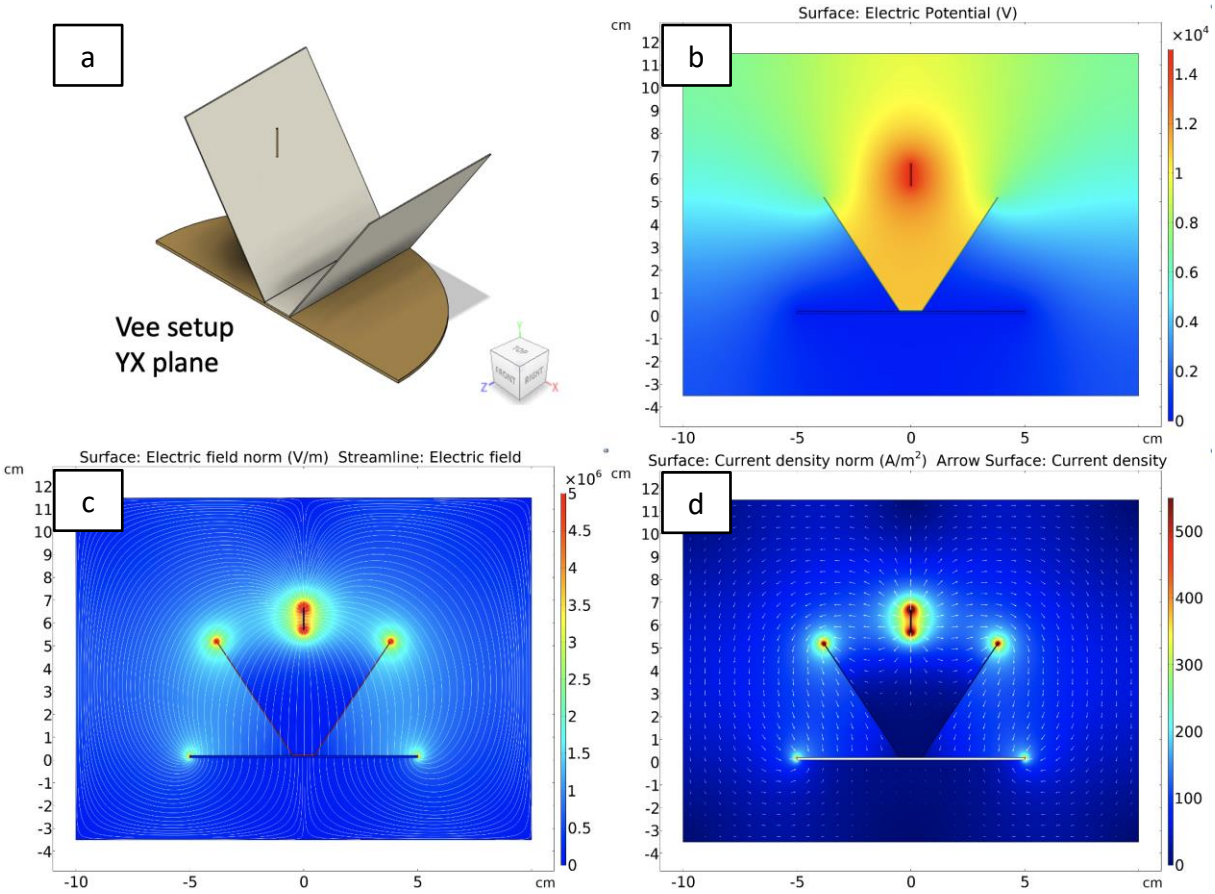

Figure 4.1.19 (a) A schematic illustration of the YX cut-plane of the Vee-shield collector. The COMSOL simulation result showing the: (b) electric potential; (c) electric field; and (d) electric current density along the YX plane.

charges is along the YZ plane. All these simulations support the observation that the electro-spun fibres will oscillate predominantly between the exposed ends of the grounded electrode. Magnified electric field streamlines and current density arrow plots in Figure 4.1.20a and b illustrate the difference when current density is considered in the simulation. This suggests that current density arrows and the electric potential plots are more suitable for predicting the movement of the polymer jet during electro-spinning.

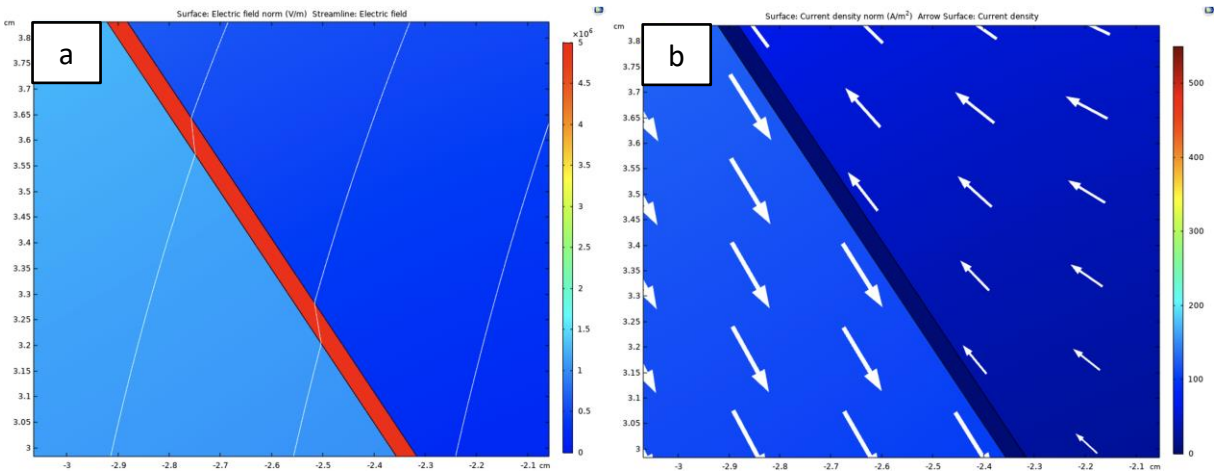

Figure 4.1.20 Magnified COMSOL simulation result for: (a) electric field strength; (b) electric current density arrows in the Vee-shield set-up along the YX plane. The diagonal red line in (a) and the dark blue line in (b) at the same position represents the Vee-shield.

A comparison of the electro-spun fibres produced with and without the Vee-shield is shown in Figure 4.1.21a and b, respectively. Both sets of fibres were produced under the optimal process parameters using the methods mentioned in Section 4.1.6. The spinning time was 10 minutes for each set-up. It can be seen that the fibres are aligned when the Vee-shield is introduced. The fibre diameter distributions are overlaid in Figure 4.1.21. The average fibre diameter for the randomly oriented and aligned nano-fibres were 366.1 and 410.7 nm, respectively, and the standard deviations were 51.3 nm and 105.9 nm, respectively. Although

the spinning time was kept constant, the fibre density for aligned fibres, when using the Vee-shield, was significantly lower in contrast with the randomly oriented fibres. Furthermore, during electro-spinning using the Vee-shield, the dimension of the Taylor cone was observed to be slightly larger, and some dripping of the polymer solution was observed. With the help of the simulation and the high-speed camera images presented in Figure 4.1.18d, Figure 4.1.19d and Figure 4.1.16b and b', it is proposed that under the same applied electric potential, due to the presence of the Vee-shield, the potential difference and the effective grounded area are reduced significantly. This slows the movement of the polymer jet, and it results in a reduced deposition rate and whipping of the polymer jet. This in turn, was seen to cause a 10% increase in the average fibre diameter and a doubling of the diameter distribution. The degree of fibre alignment was analysed using Image-J and the results are summarised in Table 4.3. The alignment distribution is shown as an overlay in Figure 4.1.21b.

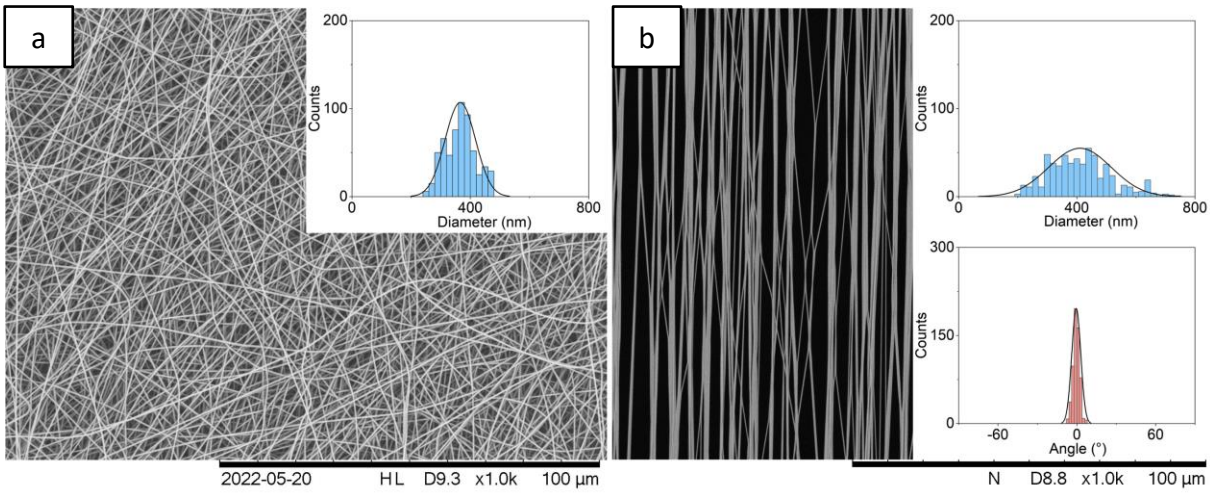

Figure 4.1.21 SEM micrographs, overlaid with fibre diameter distributions (top right) and alignment distribution (bottom right) of electro-spun PAN fibre obtained using: (a) conventional flat-plate electrode electro-spinning; and (b) Vee-shield set-ups.

Table 4.3 Distribution of fibre alignment achieved for PAN electro-spun fibre with and without the Vee-shield.

Degree of Fibre Alignment	**<1°**	**1–2°**	**2–3°**	**3–5°**	**5–10°**	**10–20°**	**20–45°**	**45–90°**
Percentage of Fibre Distribution (Vee-shield set-up without spooling)	42.0	35.1	13.6	7.4	1.1	0.3	0.3	0.2
Percentage of Fibre Distribution (Conventional set-up)	N/A							

4.1.8.3. Effect of Fibre Deposition (Electro-spinning) Time

As described in the literature review section, the degree of fibre alignment achieved when using parallel electrode-based electro-spinning can be affected by the deposition time. Due to the fact that the fibre alignment mechanism in the Vee-shield set-up shears similarities with the parallel electrode technique, the effect of spinning time on the degree of fibre alignment was investigated. The electro-spinning was carried out for 1, 5, 10 and 30 minutes to study the effect of the deposition time on the fibre diameter, aligned fibre density and degree of alignment. The fibre density was measured as the average number of fibres normal to the fibre alignment direction within a region of 50 x 50 µm, using SEM micrographs that were obtained at the same magnification.

It is apparent from the SEM micrographs presented in Figure 4.1.22a–d that when the electro-spinning time was increased from 1 minute to 30 minutes, the fibre density increased from 9 fibres to 288 fibres per 50 µm width. The degree of fibre alignment was found to increase with

the deposition time. Unlike the traditional parallel electrode electro-spinning methods, with the Vee-shield, a high level of alignment can be achieved even when spinning time is as low as 1 minute, where 91% of the fibres were aligned to within ± 5°. Nevertheless, from the fibre alignment distribution plot overlaid in Figure 4.1.22 and the results summarised in Table 4.4, the standard deviation of the distribution also increases. The main reason for these observations can be attributed to the residual charge that is carried on the surface of the electro-spun fibres and the rate of charge dissipation [15]. Charges retained on the fibre surface aid alignment by repelling the incoming fibres from occupying the same space [150]. Interestingly, from the fibre diameter distribution overlaid in Figure 4.1.22, the fibre diameter was decreased by 23% when the spinning time reached 30 minutes. Also, the distribution narrows as deposition time increases. One possible explanation for this is that the electro-spinning temperature inside the chamber was controlled manually using the IR lamp. The temperature was found to increase from 55 ± 2 °C to 57 ± 2 °C over the 30-minute spinning period. Higher temperatures will reduce the solution viscosity, resulting in a smaller diameter fibre [108, 142]. However, further investigations and a systematic set of experiments are required to investigate this hypothesis further.

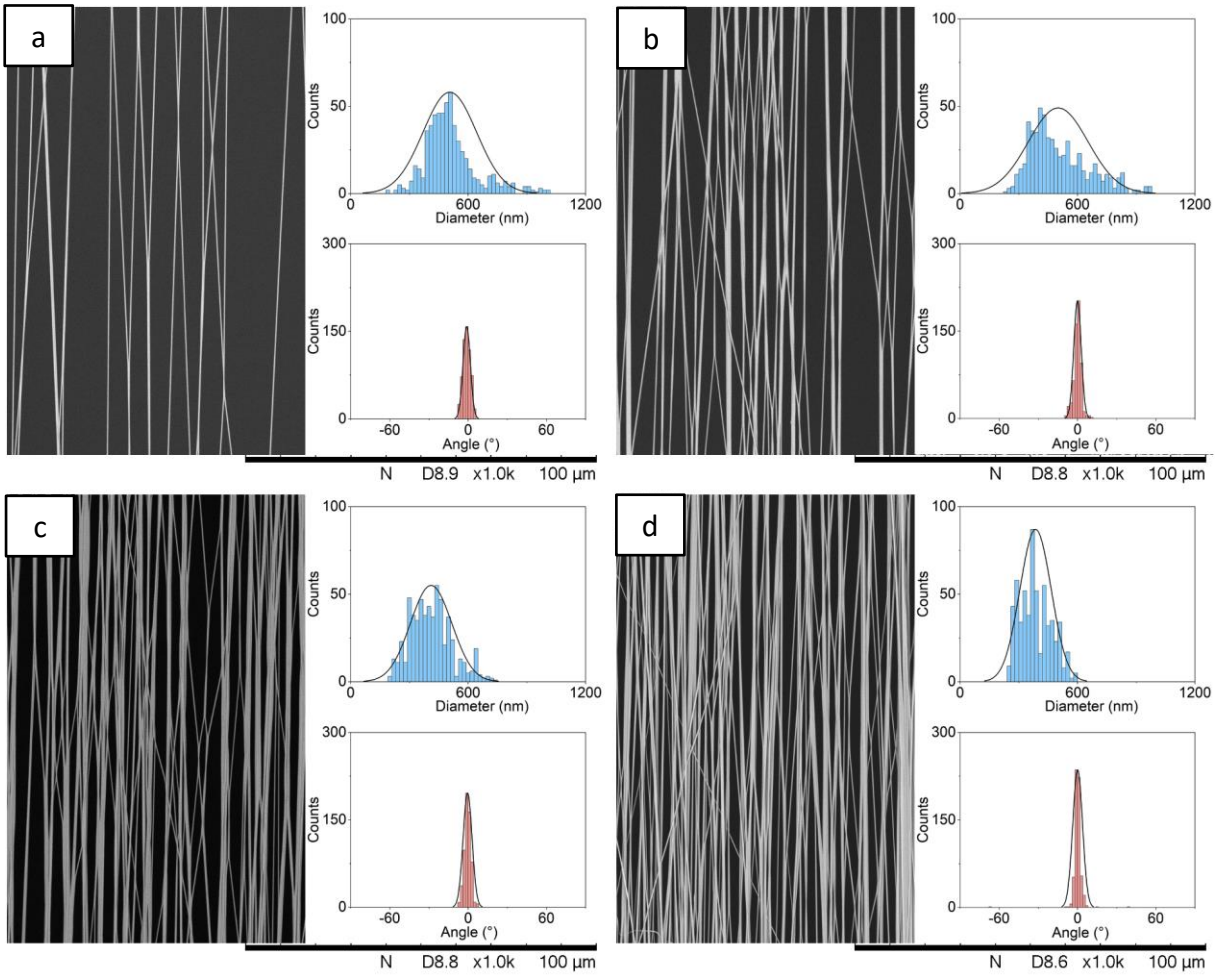

Figure 4.1.22 SEM micrographs, overlaid with distribution of fibre diameter (top right) and distribution of degree of fibre alignment (bottom right) of aligned 12 w/v% PAN/DMSO fibres obtained after electro-spinning for: (a) 1; (b) 5; (c) 10; and (d) 30 minutes using the Vee-shield set-up.

Table 4.4 Summary of the average fibre diameter, degree of alignment of the Vee-shield aligned 12 w/v% PAN/DMSO fibre with different spinning times. The values in parenthesis represent the standard deviation.

Spinning Time (min)	Number of Fibres (per 50 µm)	Average Fibre Diameter (nm)	% of Aligned Fibre Between 0-5°
1	9	506.2 [136.7]	91 [2.8]
5	63	501.4 [152.8]	92 [2.9]
10	125	410.7 [105.9]	94 [3.4]
30	288	385.5 [80.1]	98 [3.7]

4.1.8.4. Effect of the Angle of Vee-shield Geometry

It was observed that when the width of the bottom rectangular portion of the Vee-shield (see Figure 4.1.15) was maintained at 6 mm, changing the angle of the PTFE Vee-shield was seen to have a significant effect on the degree of alignment and fibre deposition location. When the angle between the PTFE Vee-shield is altered from 60° to 90°, using the grounded copper plate as the reference plane, under the same electro-spinning condition as mentioned previously, fibres were not observed on the cellulose substrate; instead, they were deposited randomly in between the inner faces of the PTFE shield. Based on the simulation results, the following explanation is offered. When the angle of the PTFE Vee-shield was 90° to the plane of the base, as shown in Figure 4.1.23b and Figure 4.1.24b, the electrical potential is confined further than when the PTFE Vee-shield was at 60°, as seen in Figure 4.1.18b and Figure 4.1.19b. On inspecting the current density vector plots (Figure 4.1.23d), it may be concluded that the fibres could be aligned along YZ plane. However, it is seen in Figure 4.1.24b that the electric potential profile is wider near the tip of the needle. This may explain the observation

where the whipping of the fibre jet was seen to start closer to the upper section of the Vee-shield. Furthermore, since the width of the rectangular section was only 6 mm, it led to an increase in the overall diameter of the whipping area and hence, the fibres (~99%) were deposited randomly in between the inner faces of the PTFE shield. No nano-fibres were collected on the substrate located at the bottom of the Vee-shield. Therefore, no SEM micrographs are presented.

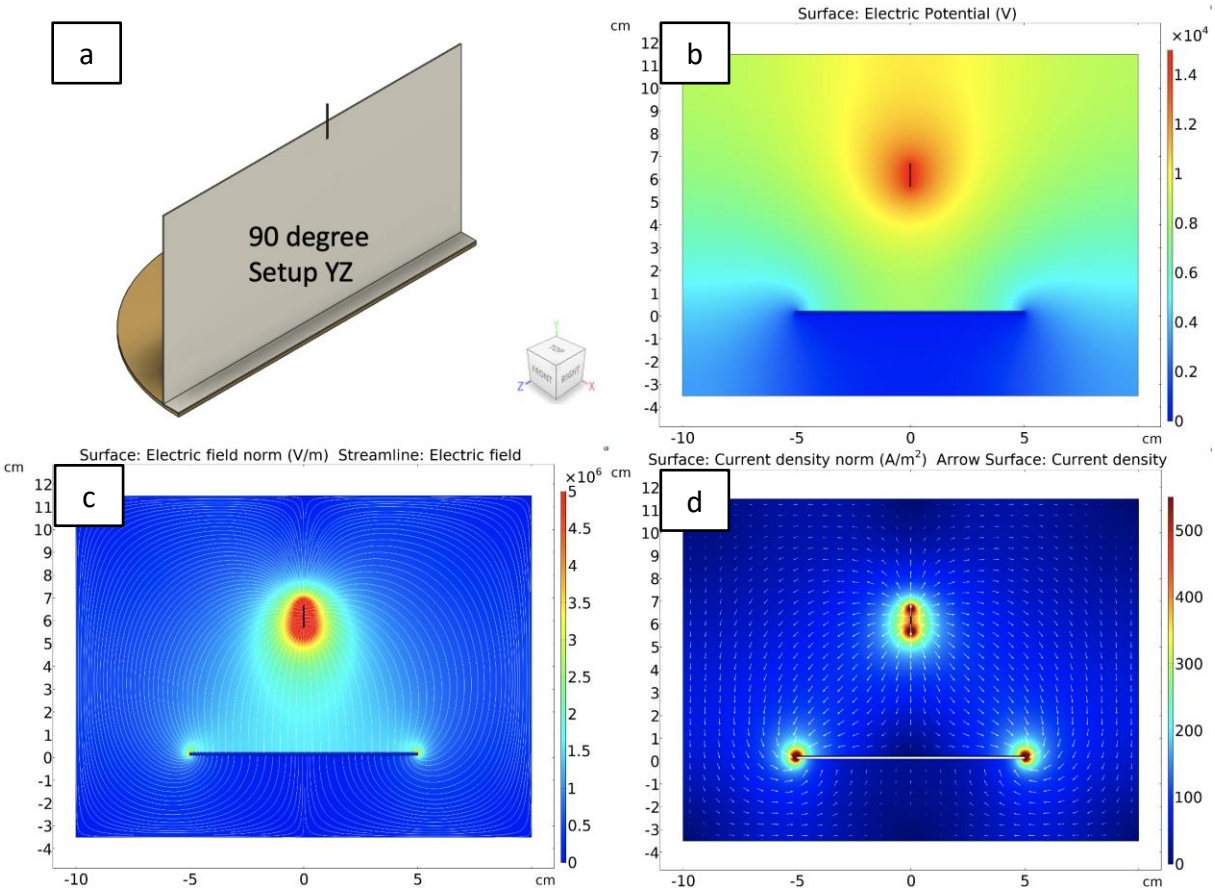

Figure 4.1.23 (a) Schematic illustration of the YZ cut-plane of the Vee-shield collector set at 90°. COMSOL simulation result for: (b) electric potential; (c) electric field; and (d) electric current density along the YZ plane.

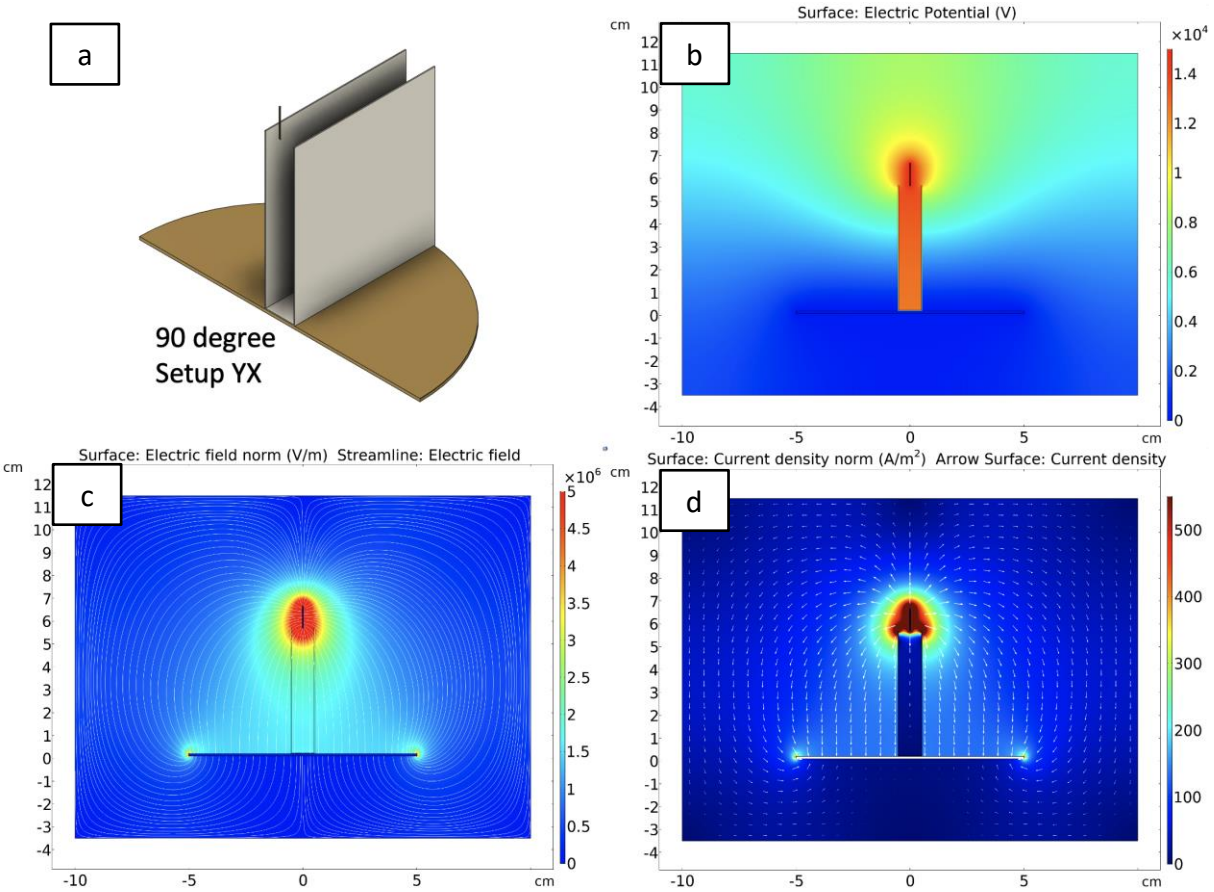

Figure 4.1.24 (a) Schematic illustration of the YX cut-plane of the Vee-shield collector set at 90°. COMSOL simulation result for: (b) electric potential; (c) electric field; and (d) electric current density along the YX plane.

When the Vee-shield angle is decreased to 0° as shown in Figure 4.1.25 and Figure 4.1.26, the current density vector plots (Figure 4.1.25d and Figure 4.1.26d) shows that the charge can flow to both ends. However, due to the presence of the PTFE sheet, and the fact that it is shorter along the YZ plane, the current density is higher in this direction. On inspecting the electrical potential plots (Figure 4.1.25b and Figure 4.1.26b), the difference between the YZ and YX planes can be identified. The electric potential was confined when the PTFE sheet covered the edge of the grounded electrode along the YX plane. Although the current vector

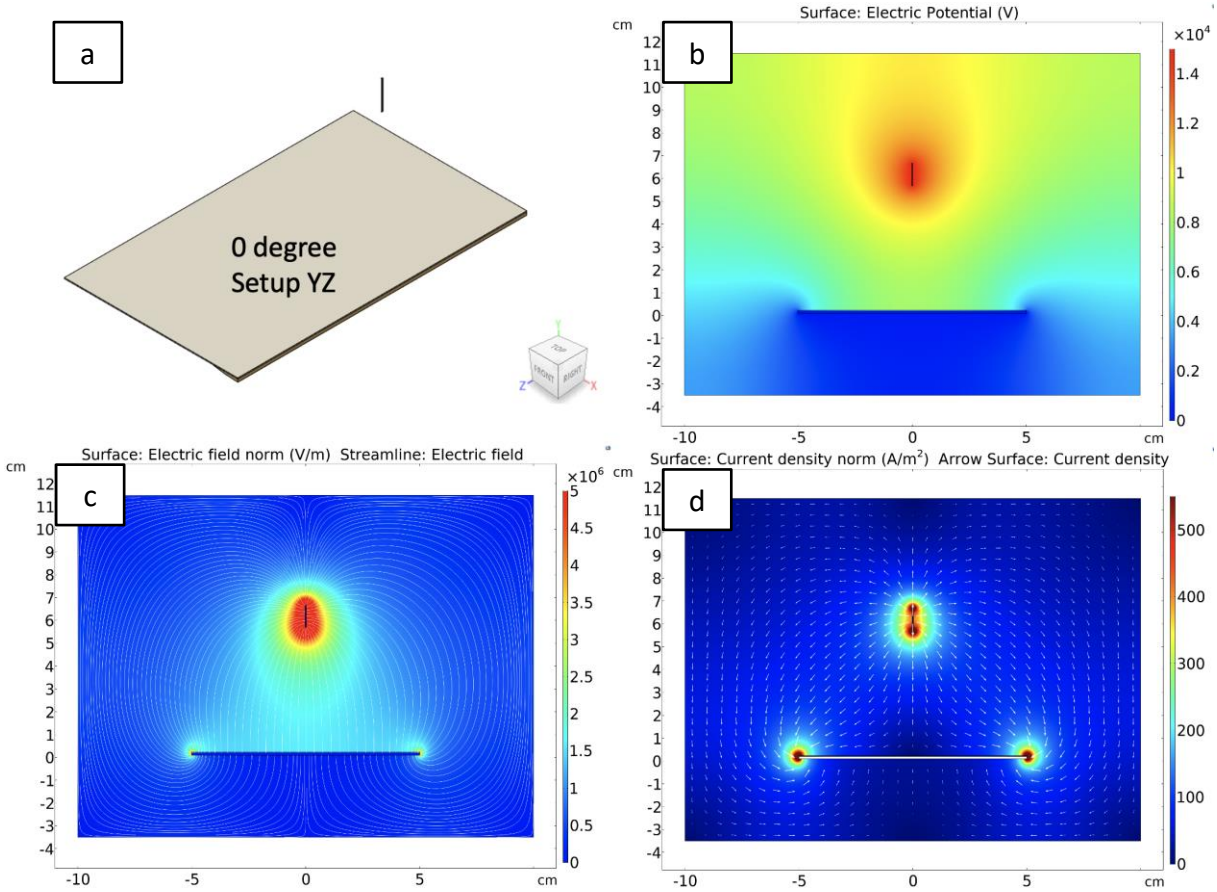

Figure 4.1.25 (a) Schematic illustration of the YZ cut-plane of the Vee-shield collector set at 0°. COMSOL simulation showing the: (b) electric potential; (c) electric field; and (d) electric current density along YZ the plane.

plots suggest that the charge can flow to both ends of the grounded plate, the density of the fibres that are deposited on the cellulose substrate (see Figure 4.1.27a) will be significantly lower when compared to the case where the Vee-shield is at 60° as shown in Figure 4.1.22d. Based on the result reported in Table 4.5, it is seen that more than 70% of the fibres were deposited on the surface of the PTFE shield as opposed to on the cellulose tape. After 30 minutes of electro-spinning, it is seen that the overall degree of fibre alignment was reduced significantly (Figure 4.1.27a). Moreover, the fibre density of the nano-fibre deposited on the

0° PTFE Vee-shield was also reduced. A summary of the fibre alignment distribution is shown in Table 4.5. Only 28% of the nano-fibre were aligned between 0−5° with the standard deviation of 2.9. The average fibre diameter also decreased.

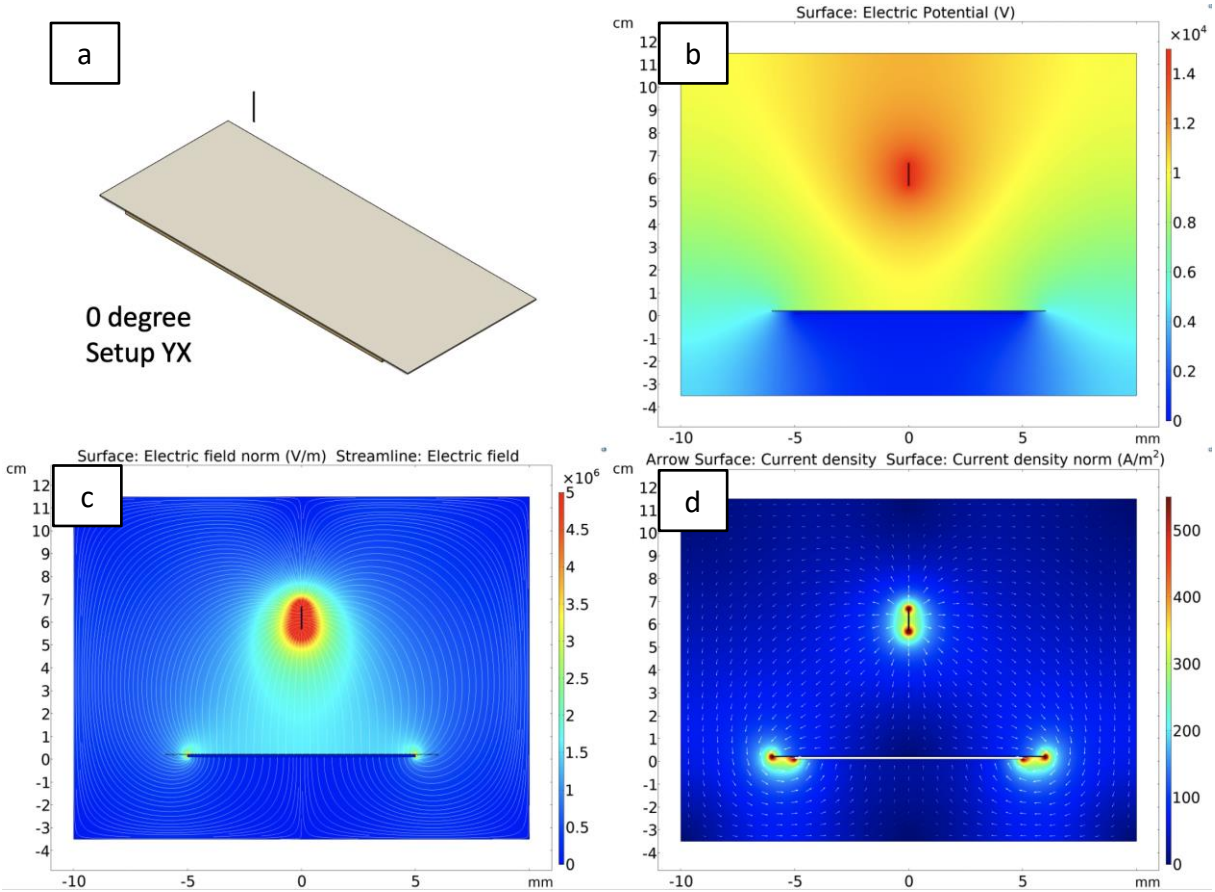

Figure 4.1.26 (a) Schematic illustration of the YX cut-plane of the Vee-shield collector set at 0°. COMSOL simulation result for: b) electric potential; (c) electric field; and (d) electric current density along the YX plane.

Reducing the Vee-shield angle to 0° can be assumed to be similar to increasing the deposition width of the rectangular section of the Vee-shield (see Figure 4.1.15). It was found that increasing the width of the substrate (flat section of the Vee-shield) leads to a decrease in the degree of fibre alignment along with the number of fibres that were deposited on the

substrate. Figure 4.1.28 shows an SEM micrograph of electro-spun fibres using a 1.5 cm deposition width. After spinning for 30 minutes, the percentage of nano-fibres that were aligned between 0−5° was reduced by 25%. A summary of the % of aligned fibres between 0−5° after 30 minutes and the average fibre diameter is shown in Table 4.5.

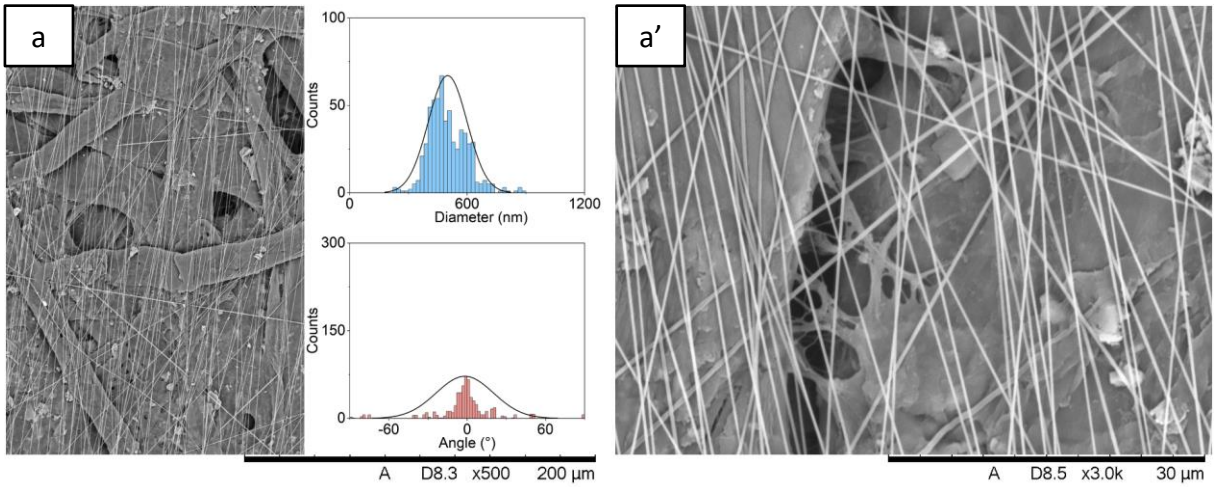

Figure 4.1.27 (a, a') SEM micrographs of electro-spun PAN/DMSO fibres with the PTFE sheet Vee-shield at 0°. The distribution of fibre diameter (top right) and distribution of degree of fibre alignment (bottom right) for the electro-spun fibres are overlaid in (a). The electro-spinning was carried out for 10 minutes. The substrate material visible below the fibres is cellulose (paper).

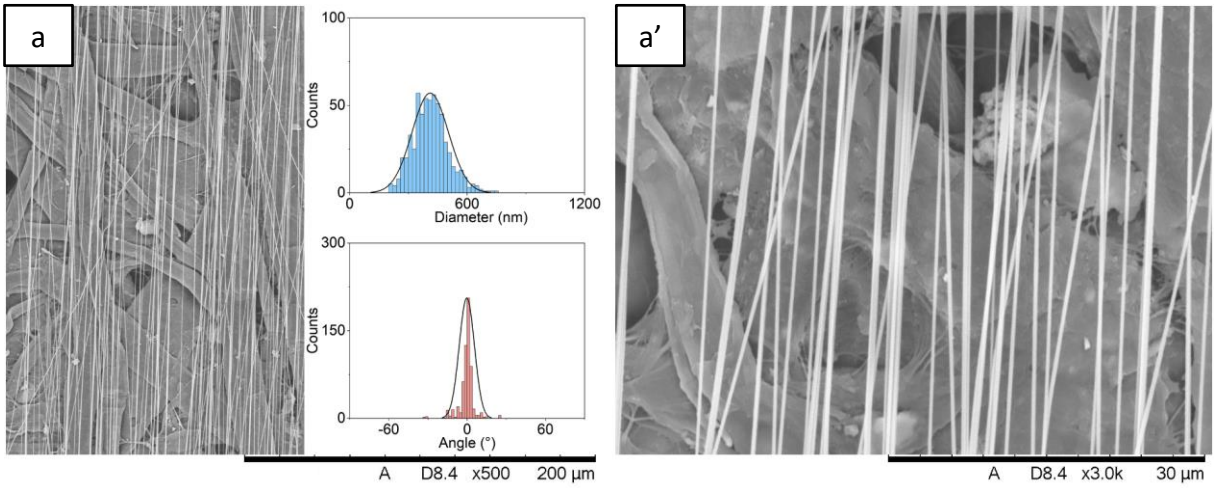

Figure 4.1.28 (a, a') SEM micrograph of electro-spun PAN/DMSO fibre with PTFE Vee-shield at 60°; the fibre deposition width was 1.5 cm. The distribution of fibre diameter (top right) and distribution of the degree of fibre alignment (bottom right) for the electro-spun fibres are overlaid in (a). The electro-spinning was carried out for 10 minutes. The substrate material visible below the fibres is cellulose (paper).

The data presented in Table 4.6 support the simulations where it is observed that as the Vee-shield is changed from 90° to 0°, the mass of the electro-spun fibres that are deposited on the cellulose substrates increases progressively and reaches a maximum around 60° and then it decreases along with a decrease in the degree of fibre alignment. It is envisaged that further optimisation and modification of the Vee-shield, including the introduction of auxiliary electrodes, will enable the majority of the electro-spun fibres to be deposited on the substrate.

Table 4.5 Summary of the average fibre diameter and degree of fibre alignment measured from the aligned PAN/DMSO nano-fibres with different PTFE shield angles and deposition widths. Standard deviation is indicated by square brackets. In all cases the electro-spinning was carried out for 10 minutes.

PTFE Shield Angle (°)	Deposition Width (cm)	% of Aligned Fibres Between 0–5° after 30 Minutes	Average Fibre Diameter (nm)
60	0.6	98 [3.7]	385.5 [80.1]
0	0.6	28 [2.9]	480.6 [99.0]
60	1.5	73 [2.6]	411.4 [93.3]

Table 4.6 Summary of the approximate weights of the electro-spun nano-fibres that were deposited on the cellulose substrate and on the Vee-shield over 30 minutes of electro-spinning. Values for standard deviation are indicated by square brackets.

PTFE Shield Angle (°)	Upper-section (near the needle) (wt%)	Mid-section (wt%)	Lower-section (near the substrate) (wt%)	On the Cellulose Substrate (wt%)
0	25 [0.71]	34 [1.30]	28 [0.84]	13 [1.14]
30	10 [1.30]	32 [0.89]	32 [1.67]	26 [1.51]
60	2 [0.55]	9 [1.14]	36 [1.10]	53 [0.55]
90	44 [1.14]	51 [2.77]	4 [1.79]	1 [0.55]

4.1.8.5. Effect of the Vee-shield Material

The results of experiments to demonstrate the Vee-shield concept using different types of materials for the shield is presented in Table 4.8. SEM micrographs of the electro-spun fibres aligned using Vee-shield materials corresponding to wood, glass and PS are shown in Figure 4.1.29a–c. It was found that the material used for the Vee-shield has a large effect on the degree of alignment. According to Table 4.8, although the volume resistivity of wood is higher than PS and glass, an increase in the degree of alignment was observed when changing the Vee-shield material from wood to PS. This is likely due to the specification of the wood used in the experiment not being characterised, which may have lower density and lower volume resistivity than the value assumed in Table 4.7. Despite this, materials with low relative permittivity and low volume resistivity are required to obtain the fibre alignment with the Vee-shield technique. It is clear from this dataset that the ideal material for the Vee-shield is PTFE. Li *et al.* [150], reached a similar conclusion with their parallel-plate design, where the introduction of insulators in between the parallel-plates aided fibre alignment. The experimentally derived conclusion is that since electro-spinning is associated with charge transport, using conductive materials such as a metal is not an option for the Vee-shield material. Budi *et al.* [418] used column-guided arrays to produce aligned fibres. Accepting that it is not simple to extract these fibres for post-processing, they stated that using highly insulating materials or materials with a high dielectric constant in the air gap would increase the degree of fibre alignment.

Table 4.7 Summary of the experimentally derived data for the average % of aligned fibres that were deposited on the substrate between 0–5°, and the wt% of the fibres that were deposited on the substrate after electro-spinning a 12 w/v% solution of PAN in DMSO for 10 minutes. The relative permittivity and the volume resistivity for the Vee-shield materials are reported. Values for standard deviation are indicated by square brackets [419-423].

Material Used as the Vee-shield	**% of Aligned Fibres Between 0–5° after 10 Minutes**	**Aligned Fibre deposited on the Substrate after 10 Minutes of Electro-spinning (wt%)**	**Relative Permittivity @ 1MHz**	**Volume Resistivity (Ohm.cm)**
No shield	0	0	1.0005	1×10^{18}
Wood (Species unknown)	51 [5.65]	22 [0.61]	2	$\sim 3 \times 10^{17}$
Polystyrene (PS)	69 [2.79]	42 [0.79]	2.7	1×10^{16}
PTFE	94 [3.4]	50 [0.51]	2.1	1×10^{19}
Borosilicate glass	54 [4.98]	32 [0.42]	4.8	1×10^{16}
Aluminium	0	0	N/A	2.65×10^{-8}

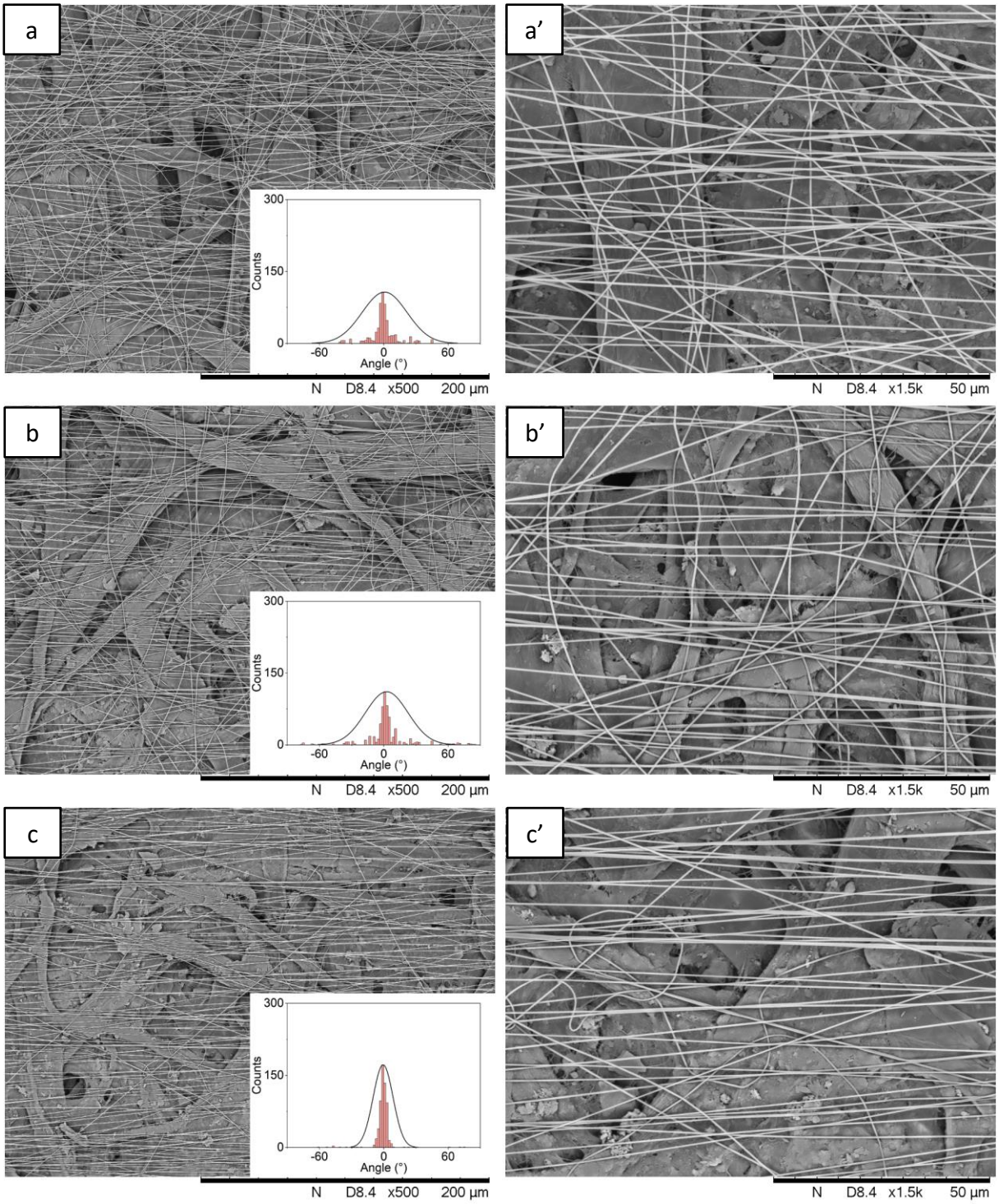

Figure 4.1.29 SEM micrographs overlaid with distribution of the degree of fibre alignment of electro-spun PAN/DMSO nano-fibre using different Vee-shield materials: (a, a') Wood; (b, b') Glass; and (c, c') PS. In all cases electro-spinning was carried out for 10 minutes. The substrate material visible below the fibres is cellulose (paper).

4.1.9. Aligned Nano-fibres Obtained with Other Polymer Solutions Using the Vee-shield Set-up

The following section is adapted from Section 'Results and discussion' of a co-authored paper published by the author; Shao *et al.* [15].

In order to demonstrate the versatility of Vee-shield alignment technique, in addition to electro-spinning PAN in DMSO, the following polymers were electro-spun using the Vee-shield method: (a) 30/70% PAN/lignin blend in DMSO; (b) 30% polyethylene oxide (PEO) in deionised (DI) water; (c) 13.5% poly-vinylpyrrolidone (PVP) in ethanol; (d) 14% polyvinylidene fluoride (PVDF) in acetone/DMSO; and (e) 20% polycaprolactone (PCL) in acetone/DMSO. The purpose of this study was to demonstrate that the Vee-shield electro-spinning method is not limited to PAN/DMSO and that it could be used with other classes of polymers and solvents. The SEM micrographs of aligned polymer nano-fibres can be found in Figure 4.1.30a–f. The effectiveness of the Vee-shield technique for producing aligned fibres was demonstrated conclusively with the above-mentioned polymers and the data are presented in Table 4.9. The properties of the polymers and the solvents used, and the solution properties are presented in Table 4.8. The outcome of these preliminary studies is discussed briefly.

With reference to Table 4.1, the electro-spinning parameters were similar for the polymers except for PAN, where the temperature of the chamber was 55 °C. The electro-spinning time was 10 minutes in all cases. The frequency plots for the diameter and degree of alignment for these combinations of polymers and solvents are overlaid in Figure 4.1.30a–f, respectively. With reference to Figure 4.1.30a–f, the diameter of the electro-spun fibres and their

respective standard deviations are shown in Table 4.9; the data for the 12 w/v% PAN in DMSO has been included to enable comparison. A notable feature is this dataset is that the range of diameters observed for PAN and PVDF is larger. It is not possible at this stage to assign a particular reason(s) for this observation as more detailed work is required. However, contributing factors could include the differences in the rate of charge dissipation, variations in the RH, the electrical conductivity of the solutions, the vapour pressure, the rate of evaporation of the solvent etc. However, the data presented does demonstrate that the Vee-shield method can be used with most classes of polymers, accepting that each will have to be optimised for the intended end-use application.

Table 4.8 Experimentally derived conductivity data for the polymer and solvent combinations investigated in this study.

Polymer	**Molecular Weight (g/mol)**	**Solvent**	**Concentration (w/v%)**	**Conductivity (µS/cm)**
PVP	1.3M	Ethanol	13.5%	12.5 ± 0.4
PCL	45k	Acetone/DMSO (2:1)	30%	0.55 ± 0.03
PEO	600k	DI water	7.5%	77.2 ± 0.8
Lignin/PAN	7,367/230k (7:3)	Acetone/DMSO (2:1)	24%	168 ± 2
PAN	230k	DMSO	12%	18.9 ± 0.3
PVDF	534k	Acetone/DMSO (3:7)	20%	4.7 ± 0.08

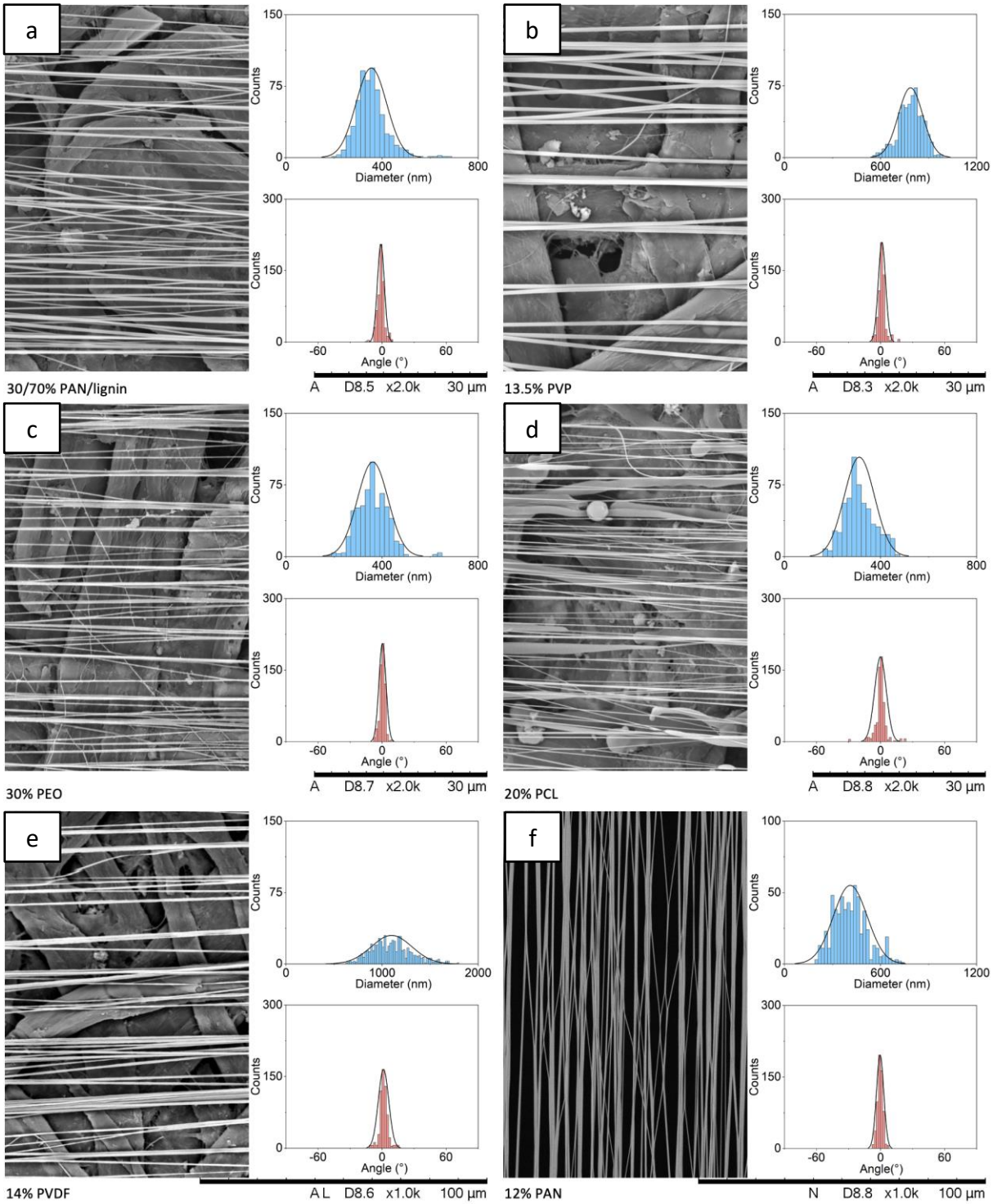

Figure 4.1.30 SEM micrographs overlaid with diameter distribution (top right) and distribution of the degree of alignment (bottom right) of aligned electro-spun fibre using the Vee-shield using: (a) 30/70% PAN/lignin; (b) 30% PEO; (c) 13.5% PVP; (d) 14% PVDF; (e) 20% PCL; and (f) 12% PAN.

Table 4.9 Experimentally derived data for the average fibre diameter and the % of fibre alignment achieved between 0–5° after 10 minutes of electro-spinning. Values for standard deviation are indicated by square brackets.

	30/70% PAN/Lignin	**30% PEO**	**14% PVDF**	**20% PCL**	**13.5% PVP**	**12% PAN**
Average Fibre Diameter (nm)	352 [59]	360 [64]	1100 [206]	311 [63]	787 [76]	367 [11]
% of Fibre Alignment between 0–5° after 10 Minutes	81 [2.03]	82 [1.43]	78 [1.68]	70 [1.77]	64 [2.09]	94 [3.4]

Overall Summary

- The main hypothesis was that modifying the grounded electrode, using an electrical insulating material, could alter the charged jet trajectory between the charged needle and the electrode, causing the electro-spun fibres to be deposited in an aligned manner.
- This was demonstrated using COMSOL modelling.
- The output from the model was used to construct and evaluate the 'Vee-shield' grounded electrode configuration.
- A high-speed camera was used to validate the COMSOL model and from the images, it could be observed that the presence of the Vee-shield altered the trajectory of the polymer jet that emanated from the Taylor cone.

- The COMSOL simulation indicated that a Vee-shield angle of 60° was the optimum angle to produce aligned nano-fibres.
- When using the Vee-shield, after electro-spinning for 30 minutes, 98% of the fibres were aligned between 0–5°. The average fibre diameter was 385.5 nm. The PAN/DMSO concentration was 12 w/v%.
- A range of materials were used to construct the Vee-shield. Materials with low relative permittivity resulted in a higher proportion of aligned fibres being deposited. PTFE and polystyrene Vee-shields resulted in 94% and 69% of aligned fibre being deposited, respectively.
- It was demonstrated that the Vee-shield grounded electrode could be used with all other polymers investigated (PVP, PCL, PEO, lignin and PVDF).
- The percentage of aligned fibres between 0–5° after 10 minutes of electro-spinning was 81, 82, 78, 70, 64 and 94 for PAN/lignin, PEO, PVDF, PCL, PVP and PAN respectively.
- Further detailed studies are required to understand the electro-spinning characteristics of the other polymers (other than PAN) and solvent combinations.

4.1.10. Demonstration of Continuous Spooling in Conjunction with the Vee-shield

The following section is adapted from Section 'Results and discussion' of a co-authored paper published by the author; Shao *et al.* [15].

The main purpose for designing the Vee-shield alignment rig was to produce aligned nano-fibre arrays along the fibre haul-off direction and enable continuous spooling. Based on the Vee-shield set-up, a motor-driven tape spooling rig was designed (Figure 3.2.6). The

experimental set-up shown in Figure 3.2.4 can be changed easily from a static and batch production method to one where the aligned fibres are produced continuously, as shown in Figure 3.2.5a where a motorised spooling rig was introduced. A photograph of the experimental set-up can be found in Figure 3.2.5b. Here, a 12 w/v% of GF PAN/DMSO was electro-spun continuously onto a creel consisting of 100 cm length cellulose tape which was drawn and spooled. Figure 4.1.31 shows a 12 w/v% of GF PAN/DMSO that was electro-spun continuously and spooled at 0.07 cm/s; the insert shows a magnified view of a section of the cellulose reel with the aligned PAN fibres. Figure 4.1.32 shows optical micrographs, and Figure 4.1.33a shows SEM micrographs illustrating the degree of fibre alignment achieved during electro-spinning using the Vee-shield in conjunction with continuous spooling. A closer inspection of Figure 4.1.33b shows the presence of some fractured and misaligned fibres. This is reflected in the frequency distribution plots for the dataset from Table 4.10 that are overlaid in Figure 4.1.33a, where it is seen that the diameter distribution is narrower for the static Vee-shield when compared to continuous spooling. The full-width at half maximum (FWHM) from the histogram for the static and spooling methods are 11 and 31, respectively. Possible reasons for this observation include: (a) since the electro-spun fibres whip from one end of the grounded electrode to the other, as the cellulose substrate is hauled off, some of the fibres are unable to stretch as they are spooled and they fracture; and (b) in order to prepare the electro-spun fibres for scanning electron microscopy, it was necessary to cut the cellulose substrate into smaller sections. This resulted in some of the fibres may have lost tension or fractured, leading to the observed bending and wavy miss-aligned fibres. It is envisaged that the number of fractured fibres and those that cause misalignment as a consequence may be

reduced by altering the manner in which the cellulose substrate is introduced to the slots in the copper electrode.

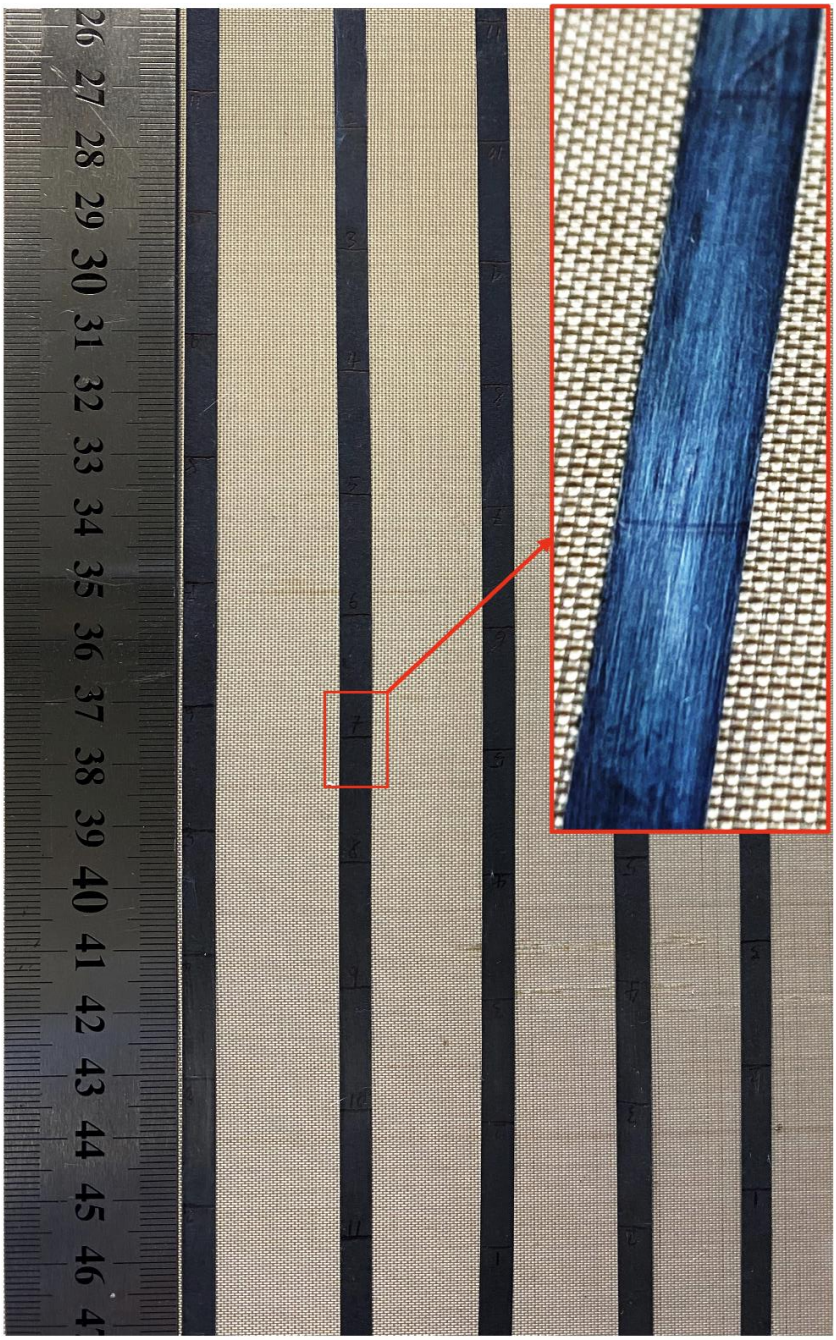

Figure 4.1.31 Photograph showing the five mm wide strips of cellulose paper that were cut into short sections after spooling. The insert shows the electro-spun PAN fibres that were deposited of the reel of cellulose paper.

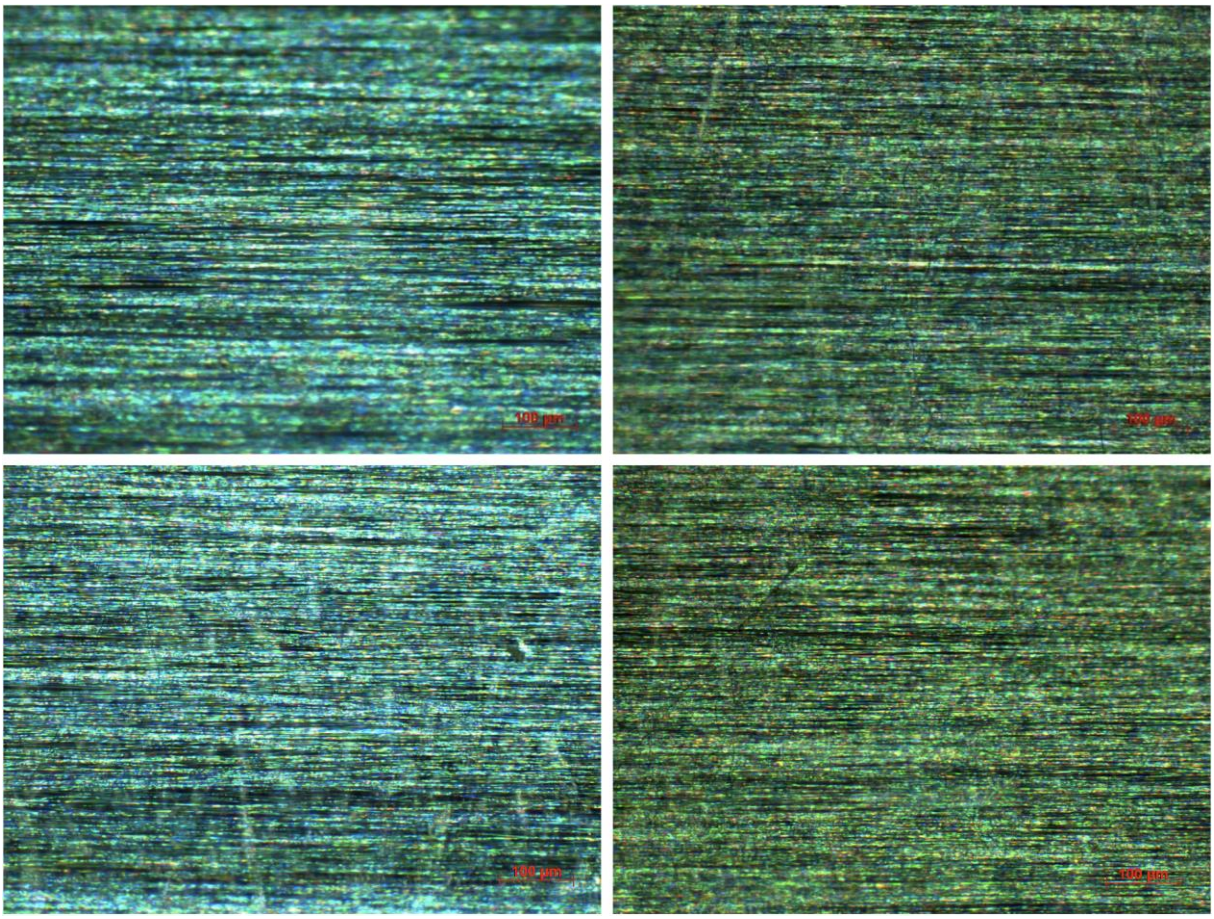

Figure 4.1.32 Optical microscope images of aligned nano-fibres on the cellulose substrate when spooling (the overall length of the substrate was 30 cm). The images were captured at 5 cm intervals.

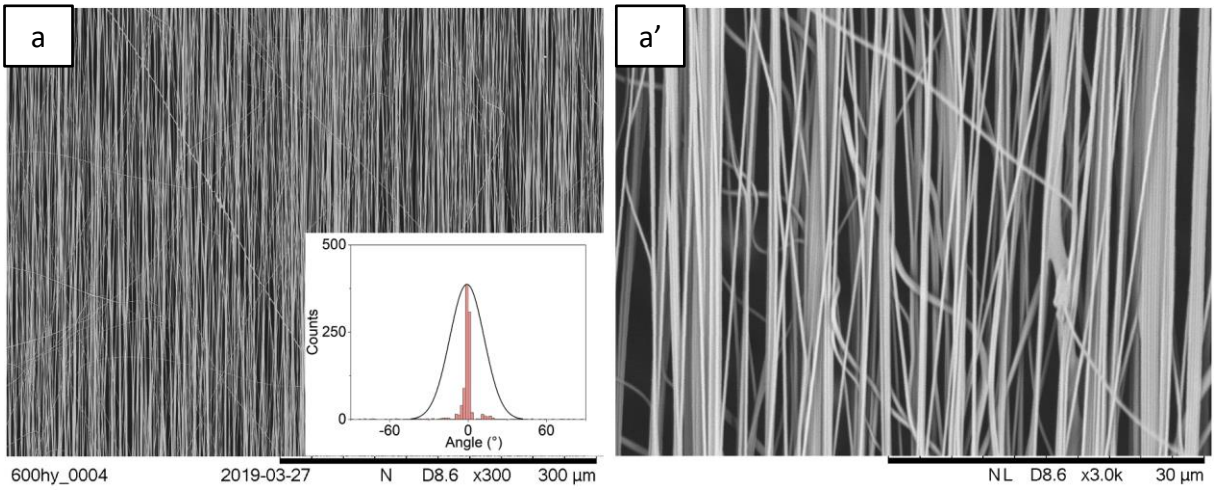

Figure 4.1.33 SEM micrograph overlaid with distribution of degree of alignment for GF PAN/DMSO nano-fibres obtained from spooling at (a) 0.07 cm/s. (a') shows a magnified SEM micrograph of (a).

Table 4.10 Distribution of fibre alignment achieved for 12 w/v% PAN in DMSO using the Vee-shield fixture, with and without spooling. The standard deviations for the whole datasets with and without spooling were 12.13 and 4.14, respectively.

Degree of Fibre Alignment	**<1°**	**1–2°**	**2–3°**	**3–5°**	**5–10°**	**10–20°**	**20–45°**	**45–90°**
% of fibre distribution (Vee-shield set-up without spooling)	42.0	35.1	13.6	7.4	1.1	0.3	0.3	0.2
% of fibre distribution (Vee-shield set-up with spooling)	39.4	30.1	8.1	6.5	3.7	6.4	3.2	2.6

In the spooling mode, it is apparent in Figure 4.1.34 that the fibre density can be increased by decreasing the spooling rate to 0.03 cm/s. However, more misaligned and fractured fibres were observed, resulting in a slightly decreased fibre alignment with 81.2% of the fibre aligned within 5°, with a standard deviation of 15.3. It is appreciated that reducing the spooling speed further may not be practical for continuous spooling operations. Low spooling speeds may cause thicker fibre layers to be formed and possibly increase the number of fibres that are deposited outside the substrate area; a greater force would be required to remove these fibres during spooling. If the force required is higher than the friction between the fibre layer and the cellulose paper substrate, the aligned fibre will separate from the substrate and would not be hauled-off by the roller. This issue could be addressed by changing the substrate material to a material with higher surface friction.

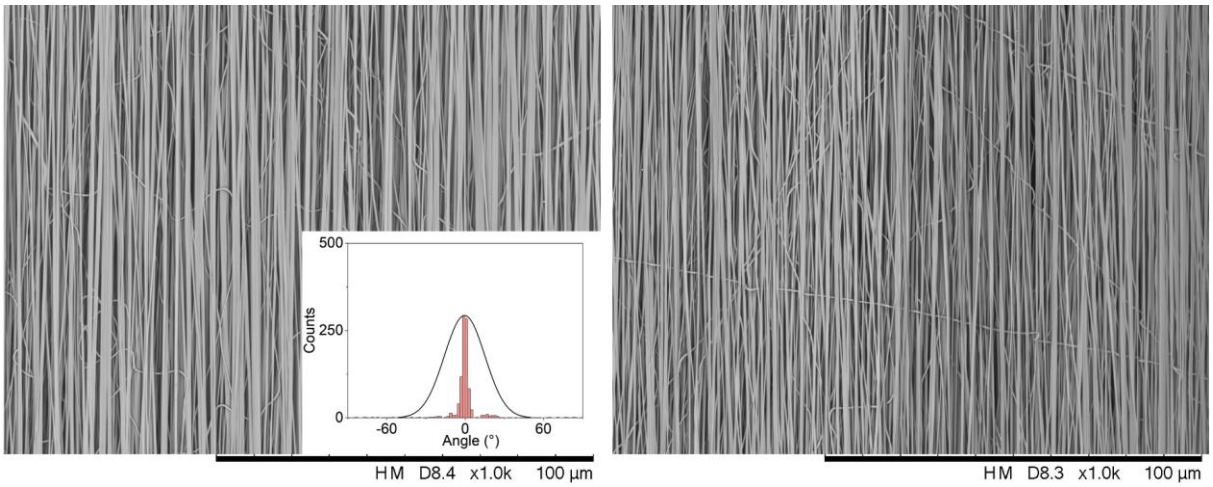

Figure 4.1.34 SEM micrographs overlaid with distribution of degree of alignment for GF PAN/DMSO aligned nano-fibres from two random locations within the fibre bundle, obtained from spooling at 0.03 cm/s.

4.1.11. Production of Layers of Electro-spun Fibres at Specified Angles

As described in the last section, the fibre alignment can be controlled by the direction of the Vee-shield in relation to the substrate material. The Vee-shield technique was applied to produce nano-fibre layers at specified angles. This was achieved by changing the angle between the substrate and the Vee-shield to produce *in situ* layers of nano-fibre that were stacked at − 45°, + 45°, 0°. SEM micrographs presented in Figure 4.1.35a−c show such a multi-angle *in situ* laminate stack of aligned fibre arrays. Here, the Vee-shield was rotated manually to the appropriate angle to achieve the desired fibre orientation in relation to the longitudinal axis of the cellulose substrate. The fibre alignment shown in Figure 4.1.35a−c demonstrates that unidirectional, cross-ply quasi-isotropic laminates and preforms for the production of composites can be manufactured using the Vee-shield technique. Moreover, as described in Section 4.1.8.3, the fibre density of each laminate can also be altered by the time of deposition. In other words, the spooling speed can be altered during production (described in the last section). A schematic illustration of the concept of continuous product cross-ply fibre arrays is shown in Figure 4.1.36, where multiple Vee-shield collectors can be connected in sequence to achieve the required fibre angle.

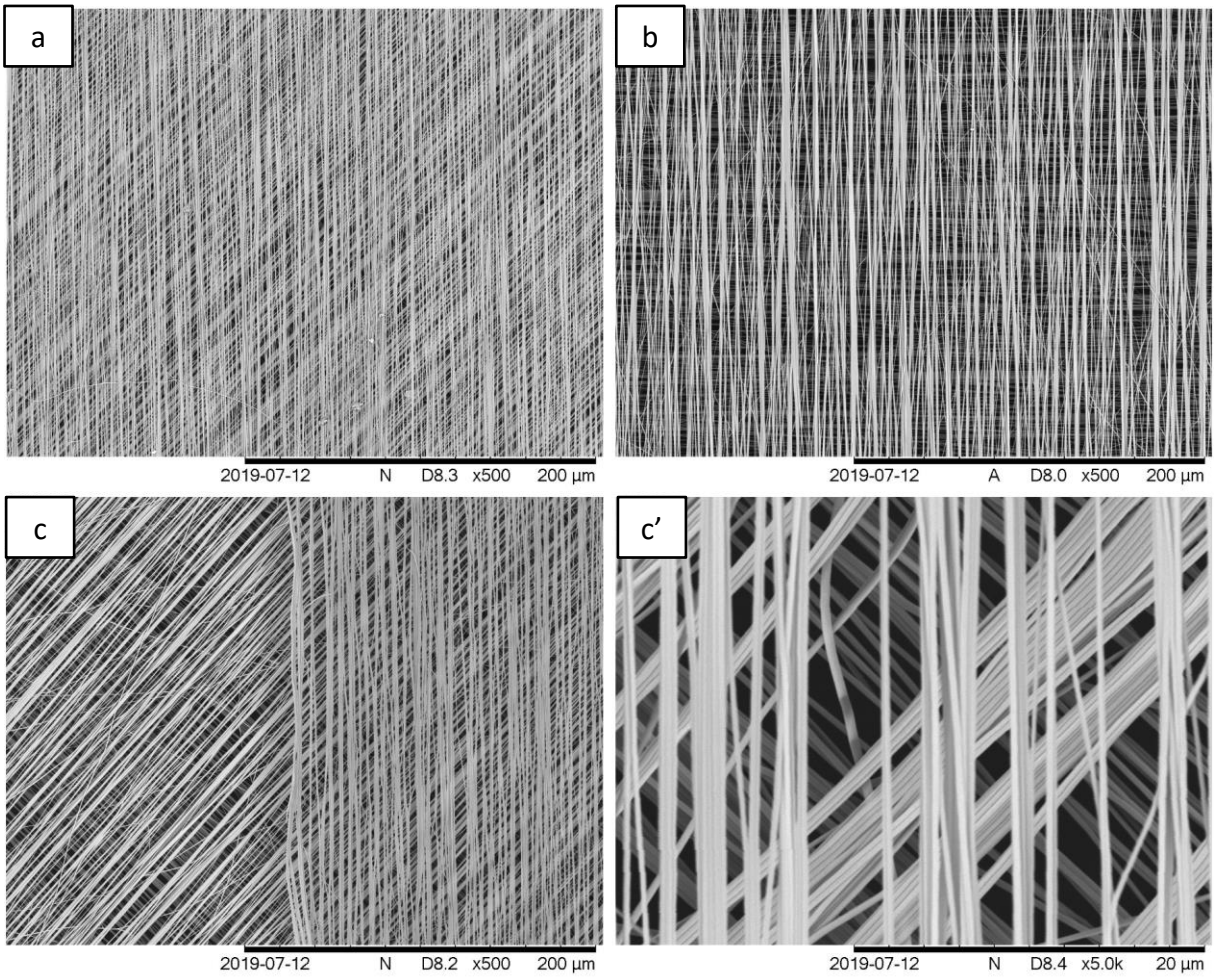

Figure 4.1.35 SEM micrographs of multilayer aligned fibre arrays stacked at: (a) 0°, 45°; (b) 0°, 90°; (c) 0°, 45°, 90°; and (c') magnified image of (c).

<u>Overall Summary</u>

- One of the goals of this research was to demonstrate that the Vee-shield could be retrofitted to existing electro-spinning equipment. For example, those based on flat plate electrodes. Such a rig was designed, constructed and evaluated.
- The feasibility of spooling or hauling off the electro-spun fibres was demonstrated.

- When the Vee-shield was used in conjunction with the spooling rig, the percentage of fibres that were deposited between 0–5° was 84%, whereas that for the Vee-shield alone was 98%.
- One possible reason for the reduction in the percentage of aligned fibres whilst spooling with the Vee-shield in place was that some fibres fractured during spooling.
- The feasibility of producing preforms where the fibres are aligned at 0, 45 and 90° was demonstrated. In future this will enable *in-situ* laminated fibres to be produced at different angles.

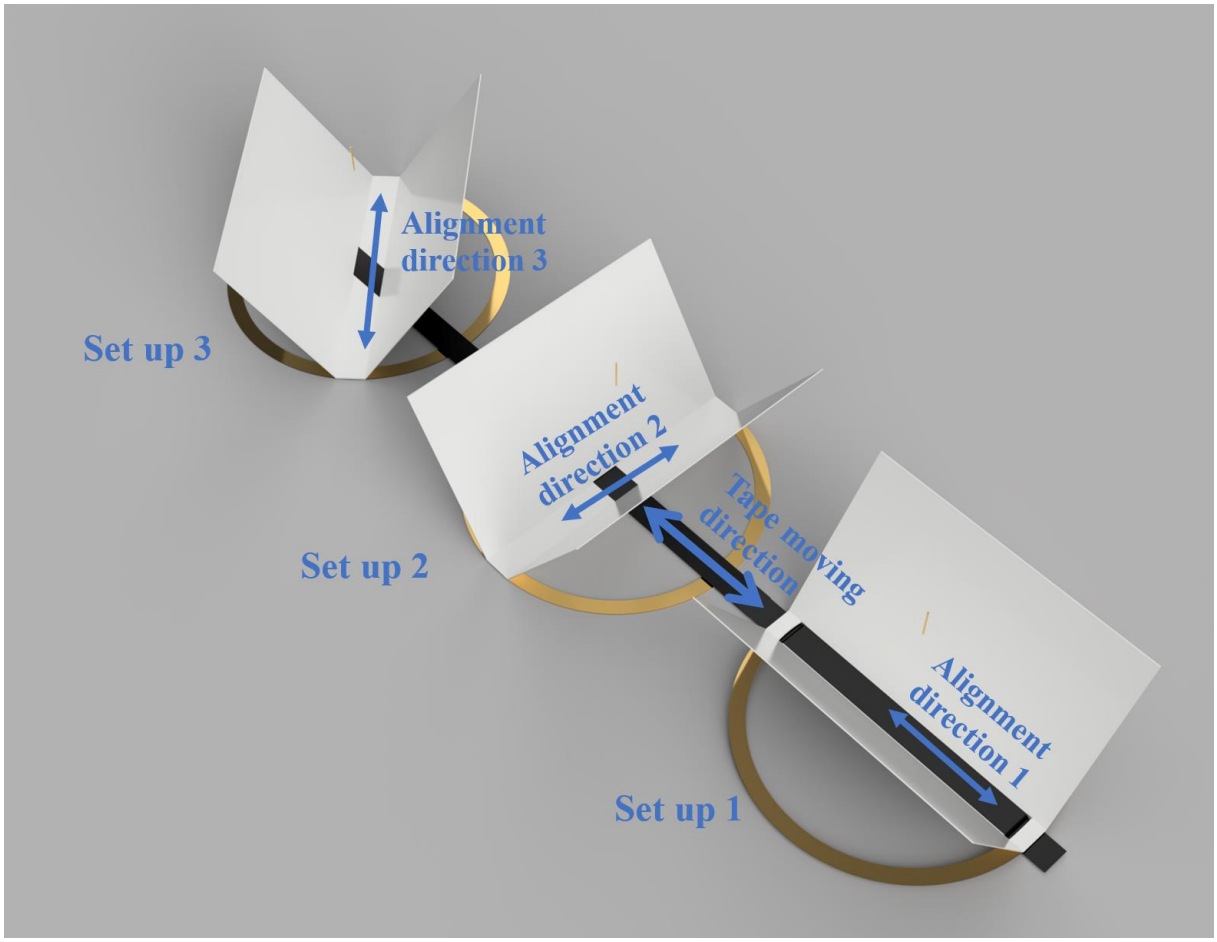

Figure 4.1.36 Schematic illustration of the concept for continuous production of angle-ply fibre arrays.

4.2. Stabilisation and Carbonisation of Aligned PAN Nano-fibres

After the aligned PAN nano-fibres were electro-spun and dried, they were oxidised and carbonised to produce carbon nano-fibres. The oxidation or thermo-stabilisation was conducted in air where the samples were heated from ambient temperature to 300 °C at 2 K/ minute. Carbonisation was then carried out, in nitrogen, at 5 K/minute with dwells at 600, 900 and 1200 °C as described in Figure 3.3.6. The end-tabbing procedures and the graphite rig that was used for mounting the samples were discussed in Section 3.3.2.

Fibres were removed from the furnace, cooled to ambient temperature (in a nitrogen atmosphere), and characterised after each of the dwell regions shown in Figure 3.3.6. In this section, the fibre morphology and crystallinity of the oxidised and carbonised aligned nano-fibres are discussed. The fixture used to tension the fibre arrays in the graphite rig was described in Section 3.3.2.

With reference to Figure 4.2.1, the TGA thermogram and the derivative (DTG) for the electro-spun dried GF PAN/DMSO can be divided into four regions. In region 1 (indicated by the black numbers), increasing the temperature from 20 °C to 281 °C results in a 1% increase in mass. However, previous studies show that a small amount of weight loss should be expected in this region [424, 425]. In the current study, referring to the TGA results for as-spun GF PAN fibre and vacuum oven-dried fibre shown in Figure 4.1.13 above, a weight increase was found in all samples. The underlying mechanisms for this phenomenon have not been identified, therefore, more work will be required to develop a better understanding of this behaviour.

However, it is possible that this may be associated with either the subtraction of the baseline, or permanent contamination of the sample holder. Nevertheless the % weight gain is of the order of approximately 1%. In region 2, between 281 °C and 372 °C, a 24.1% weight loss is observed. Cyclisation takes place with a maximum of 1.1% weight loss at 298 °C. This matches the exothermic peak found at 294.6 °C in a DSC thermogram, as shown in Figure 4.2.2. In the region 3, a further decrease in weight, from 75.9% to 62.8%, was observed as the temperature increased from 371.3 °C to 528.9 °C. In regions 2 and 3, ammonia, hydrogen cyanide, methane, water and carbon monoxide were typically said to be obtained as volatile by-product gases released from the material [426, 427], resulting in further weight loss. The dehydrogenation [425] and carbonisation processes occur up to 1200 °C [314, 414]. A continuous reduction in weight was observed, resulting in a weight-loss of approximately 20.3% [428]. The residual mass at 1200 °C was 42.5%. The purpose of this experiment was to compare the weight-loss characteristics for the as-received GF PAN powder and the as-spun fibre (after drying at 120 °C in a vacuum oven for 6 hours). Another motivation behind these experiments was to determine whether a correlation could be established between weight loss, temperature and shrinkage. The weight losses of 120 °C-dried PAN nano-fibres at 300, 600, 900 and 1200 °C were 8.9%, 39.9%, 48.8% and 57.5%, respectively.

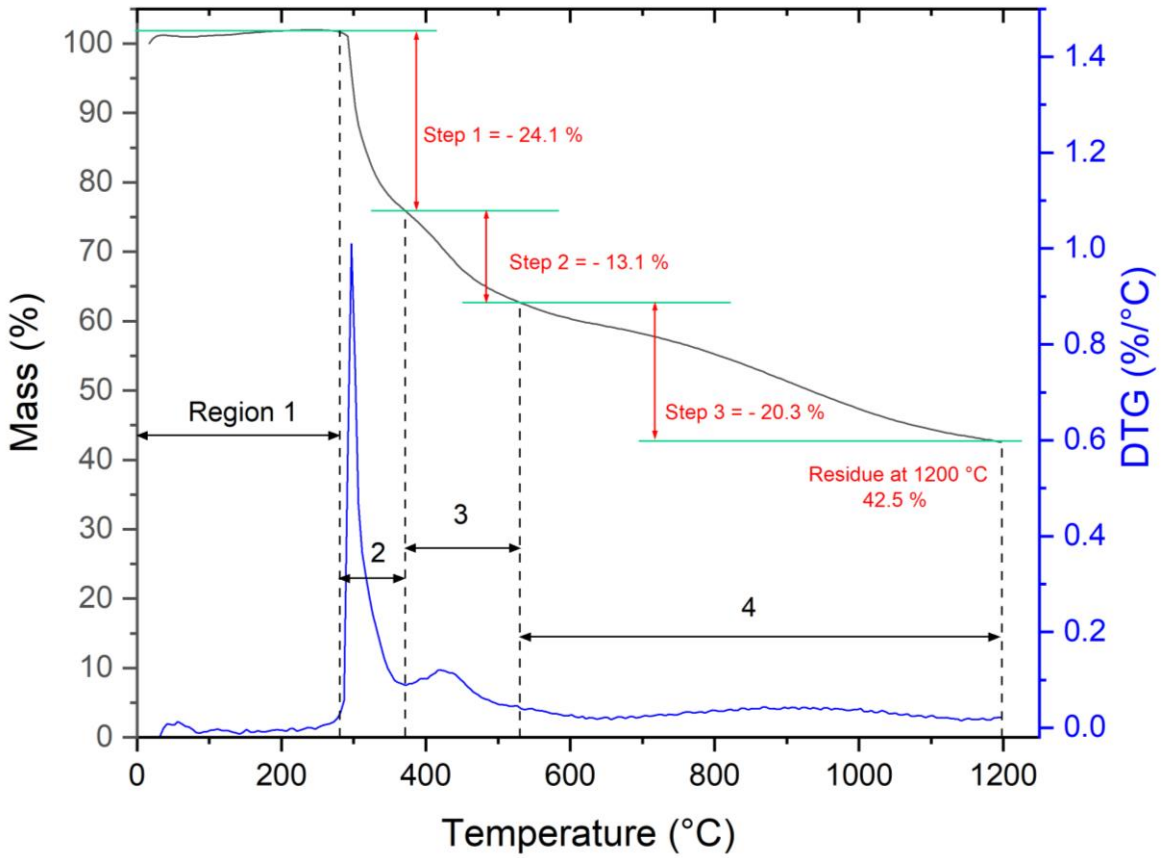

Figure 4.2.1 TGA and DTG traces for 120 °C vacuum dried GF PAN nano-fibre, heated from 20 °C to 1200 °C at 10 K/minute.

<u>Overall Summary</u>

- TGA was used to study the weight loss in the electro-spun PAN fibres as a function of temperature.
- DSC was used as a guide to identify the onset of the cyclisation exotherm, which was identified to be approximately 293.1 °C.

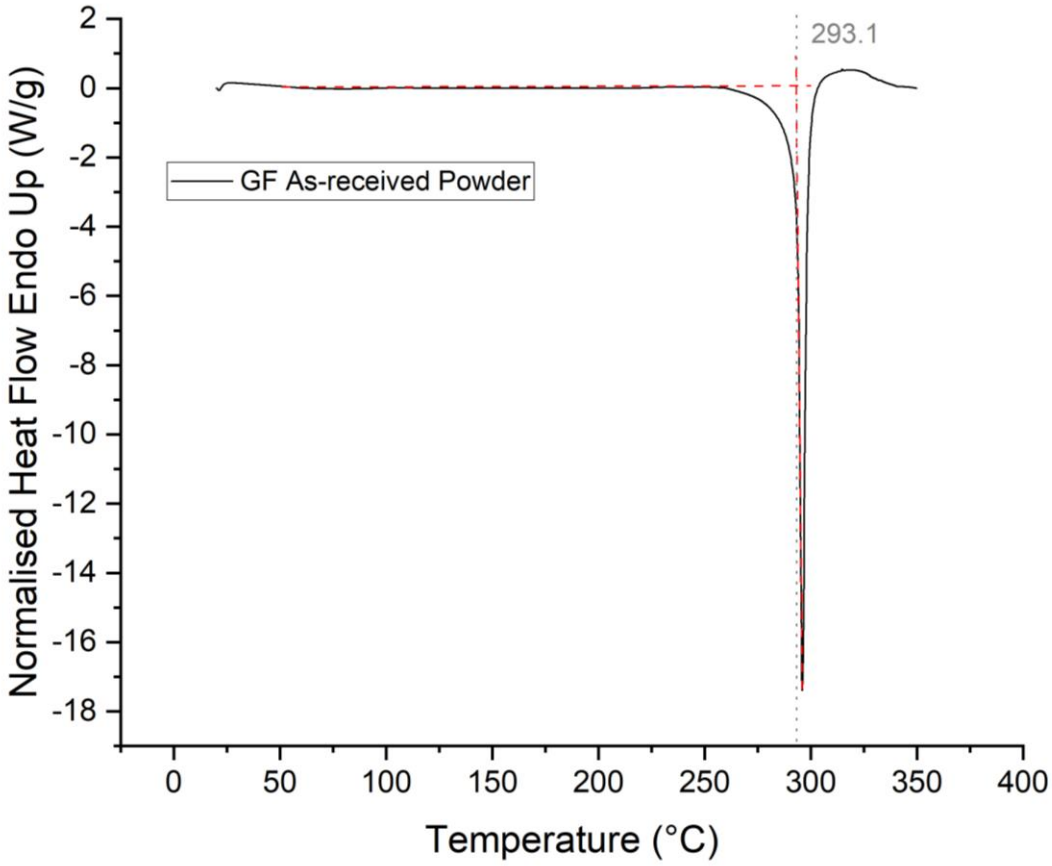

Figure 4.2.2 DSC trace of as-received GF PAN powder.

4.2.1. Establishing the Temperature Gradient within the Tube Furnace

The heating rate and the temperature gradient in the tube furnace were evaluated using an R-type thermocouple and data logger. The details of this set-up was described in Section 3.3.1. These measurements were taken at the centre of the furnace where the graphite rig would be located. Figure 4.2.3 and Figure 4.2.4 show the temperature/time traces when the furnace was programmed to heat from room temperature to 300 °C at 2 K/minute, and 5 K/minute from 300 °C to 1200 °C. However, the actual heating rate recorded using the thermocouple was 2.23 K/minute and 4.71 K/minute, respectively. This was possibly because the nitrogen gas was not heated as it was introduced to the furnace. It was necessary to establish the

temperature gradient in the furnace in order to design and specify the length of the graphite fibre mounting rig for oxidation and carbonisation (see Figure 3.3.2).

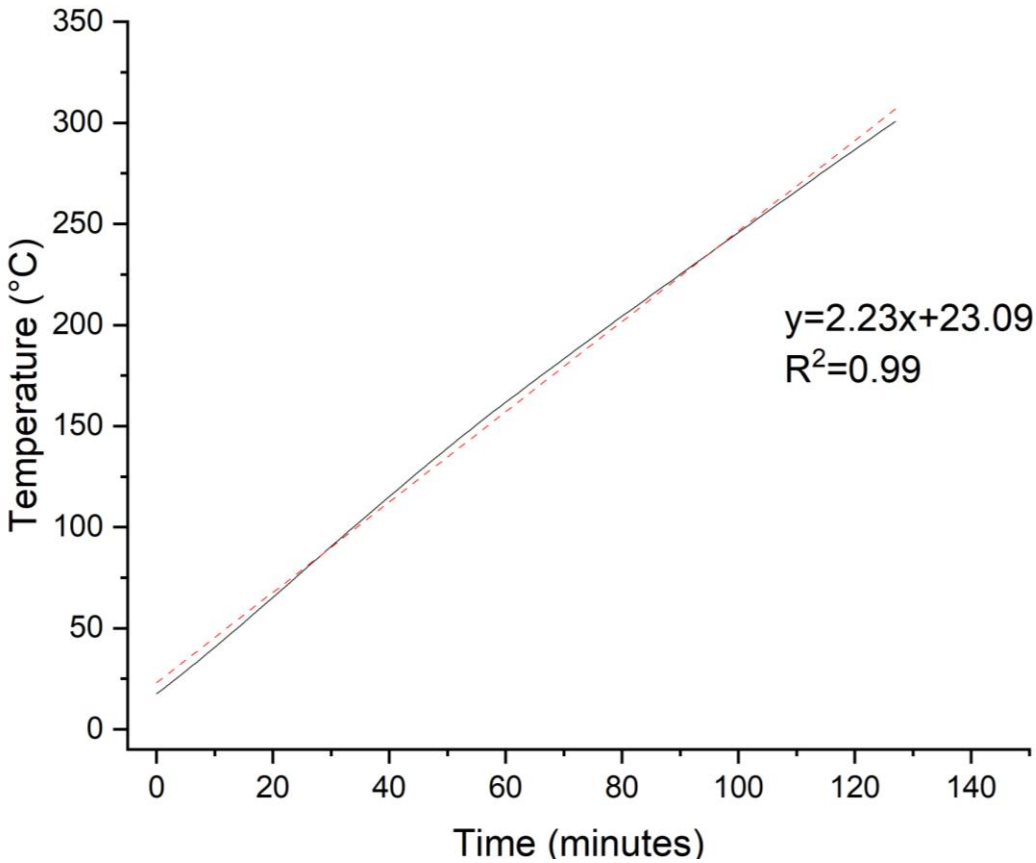

Figure 4.2.3 Temperature against time calibration trace for the PYRO THERM tube furnace at the centre of the furnace from ambient temperature to 300 °C (oxidation) using a heating rate of 2 K/minute. The air gas flow was set at 50 ml/minute. The dotted line represents the linear regression.

The temperature gradient with regard to the position about the centre of the tube furnace is shown in Figure 4.2.5. The temperature measurement was taken from the centre of the furnace, set as 0 cm, with 5 cm increments. It is apparent in Figure 4.2.5 that the temperature closer to the gas inlet-end of the tube furnace, marked with a negative distance, is slightly lower than the opposite end. Since the overall length of the thermocouple was 80 cm, the

temperature was measured between −20 cm and 60 cm about the centre point of the furnace. Since the temperature at positions −2.5 cm to +2.5 cm about the centre point was between 1197.2 °C and 1195.4 °C, the graphite fibre loading rig was made 5 cm in length.

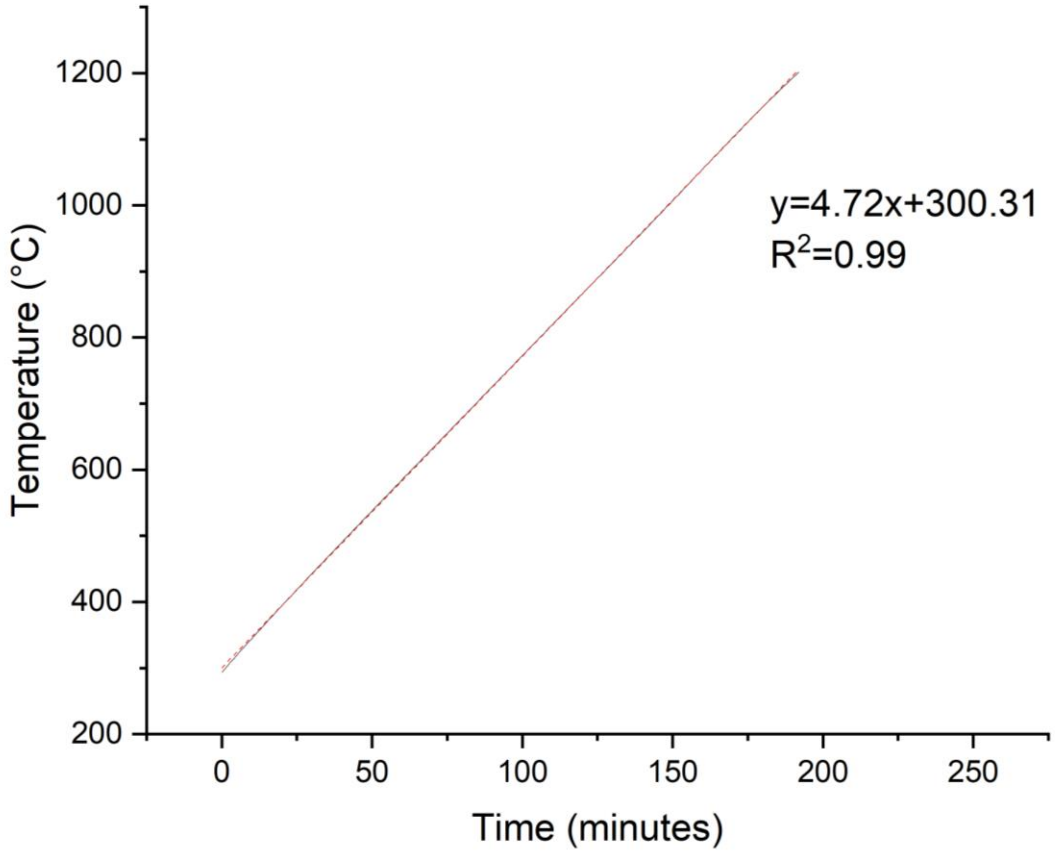

Figure 4.2.4 Temperature against time calibration trace for the PYRO THERM tube furnace at the centre of the furnace from 300 °C to 1200 °C (carbonisation) using a heating rate of 5 K/minute. The nitrogen gas flow was set at 50 ml/minute. The dotted line represents the linear regression.

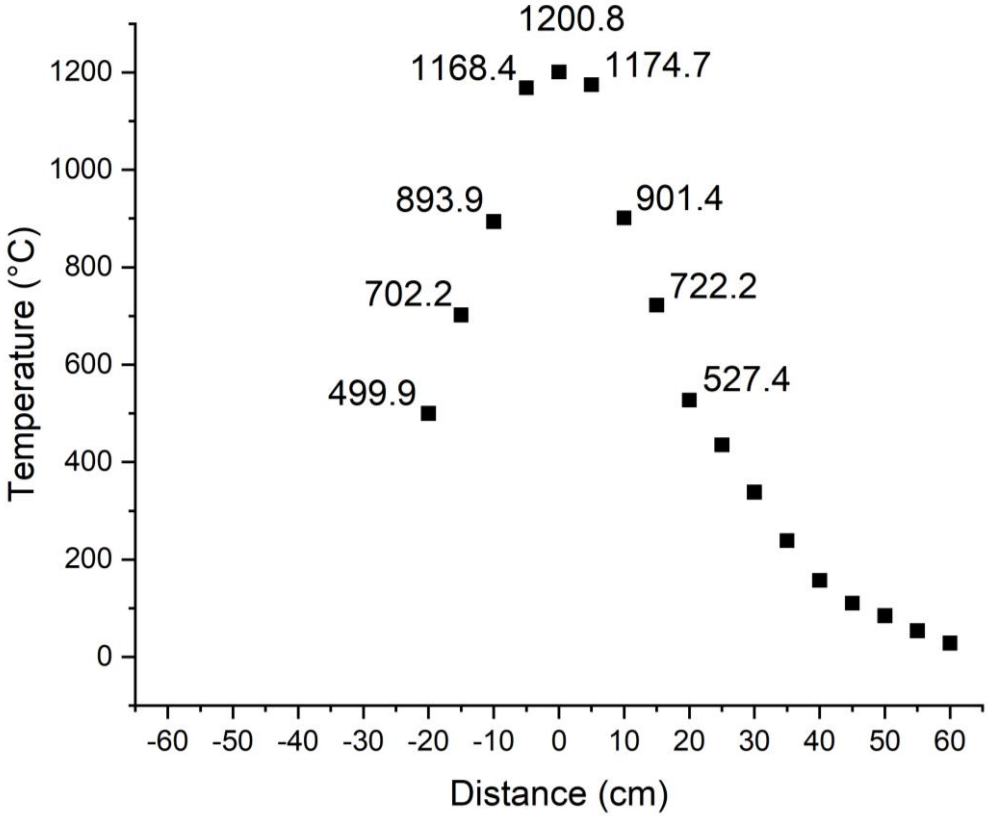

Figure 4.2.5 Temperature profile with regard to the position about the centre of the tube used for the oxidation and carbonisation experiments. Position '0' refers to the centre of the furnace.

<u>Overall Summary</u>

- An R-type thermocouple was used to determine the temperature gradient within the tube furnace.
- It was established that 1200 °C could be assured at ± 2.5 cm of the centre point (position '0') of the furnace.
- This dimension was important in ensuring that the rig for heat-treating the electro-spun PAN fibres was exposed to the same temperature. Three specimens were heat-treated in the rig.

4.2.2. Effect of Weight (tension) on the Stabilisation and Carbonisation of Aligned PAN Nano-fibres

From the TGA analysis, heat-treating PAN to 1200 °C resulted in a 57.5% weight loss. Other researchers reported that the PAN fibres would shrink along both the longitudinal and transverse (diameter) directions during pyrolysis [310, 333, 429], due to cross-linking reactions [332, 337]. Fixing both ends of the aligned fibres would likely result in fibre fractures at random positions at the bonding points or within the gauge length, making it unusable for tensile testing. Furthermore, it is known that restraining the shrinkage of PAN precursor by applying tension to the fibres can improve the mechanical properties of carbonised fibres [344, 345]. Therefore, the reason for designing and introducing the graphite fibre loading rig were to: (i) permit the aligned nano-fibres to shrink whilst under load (ii) maintain the tension on the aligned fibre array during heat-treatment; (iii) to constrain fibre shrinkage during pyrolysis; and (iv) increase the crystallinity of the carbon nano-fibres. A series of experiments were conducted to determine the optimum weight that could be added to the graphite weights (see Section 3.3.2 and Figure 3.3.2) without causing fibre fracture during the oxidation and carbonisation periods. Four rods made of either alumina, zirconia or tungsten carbide were paired and positioned on either side of the fibre array to balance the weight (see Figure 3.3.4). Table 4.11 shows a summary of the lengths of the oxidised and carbonised nano-fibre samples after specified heat-treatments using different weights. The percentage decrease in the length was calculated and it is apparent from Table 4.11 that applying a higher weight can restrain the shrinkage during oxidation.

Table 4.11 Summary of the length of the sample after heat-treatment using different static weights. Samples marked N/A represents the case where fibres that fractured after the heat-treatment.

Heat-treatment Temperature (°C)	**Graphite + Alumina x4 (1.75 g)**	**Graphite + Zirconia x4 (2.68 g)**	**Graphite + Tungsten Carbide x4 (5 g)**	**Weight Loss Obtained from TGA**
As-spun (dried at 120 °C for 6 hours)	(3.0 cm) 100%			0%
300	(2.2 cm) 26.7%	(2.3 cm) 23.3%	(2.6 cm) 13.3%	8.9%
600	(1.7 cm) 43.3%	N/A	N/A	39.9%
900	(1.6 cm) 46.7%	N/A	N/A	48.8%
1200	N/A	N/A	N/A	57.5%

SEM micrographs of the cross-sectional view and the surface view of oxidised fibres with different weights are presented in Figure 4.2.6 and Figure 4.2.7, respectively. Increasing the static weight significantly reduced the thickness of the aligned PAN nano-fibre bundle by: (i) eliminating the air gap between the fibres and (ii) fibres fracturing during the oxidisation process. From Figure 4.2.7, it is clear from the fibre diameter distribution plot that the higher the applied weight, the lower the average fibre diameter and narrower the distribution; the standard deviation was also reduced. However, the degree of fibre alignment measured from the SEM micrographs was found to decrease as the applied weight increased. The results from this part of the study are summarised in Table 4.12. During these experiments, it was found that although the fibres with the applied weight survived the oxidative heat-treatment, the weight on the fibres made them vulnerable to fracture when they were removed from the

furnace. Possible reasons for this may be that: (i) Whilst the weight constrains the shrinkage, it significantly reduces the average fibre diameter from 334 ± 83 nm to 258 ± 65 nm. (ii) Smaller diameter fibres in the distribution may not be able to support the tension applied, leading to fibre fracture (see Figure 4.2.7c and d). (iii) The fractured fibres reduce the tensile load that can be applied to the fibre bundle, and increases the difficulty in handling them. (iv) When bonding the fibre bundle to the graphite loading rig, it was not possible to ensure that each filament was aligned perfectly and that the tension and applied load was distributed uniformly. It is worth noting that at the time of writing, there were no publications on tensioning electro-spun nano-fibres during oxidation and carbonisation.

It can be seen from Table 4.11 that no sample survived when carbonising the aligned the PAN nano-fibre array under load at 1200 °C. The reasons for this are similar to that described in the section above. The fibres became extremely sensitive to handling when they were carbonised at 1200 °C. It was possible to obtain carbonised fibres at 1200 °C but only if a load was not applied (see Figure 4.2.8).

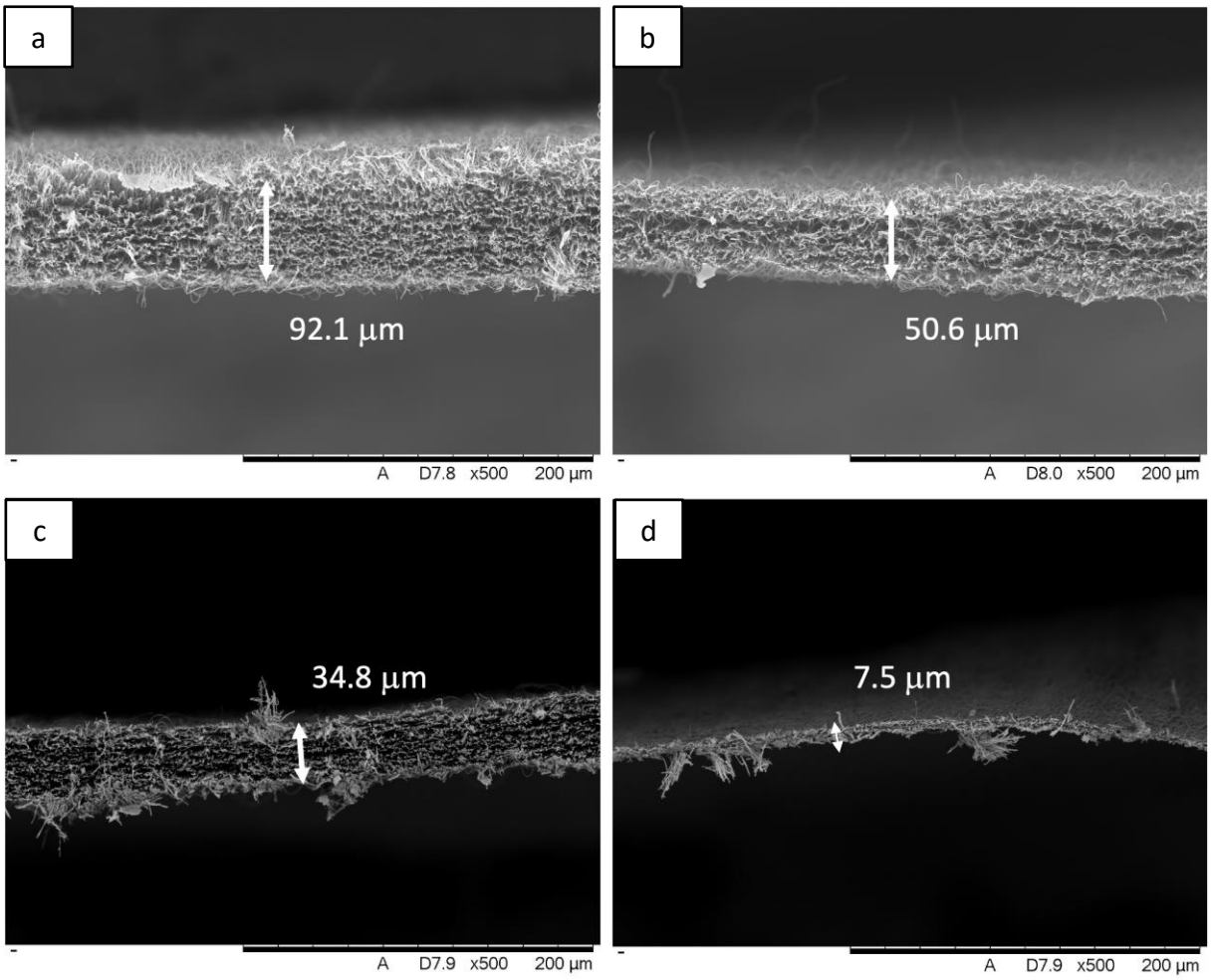

Figure 4.2.6 SEM micrographs of the cross-sectional view and measured average thickness of oxidised fibres with different static weights using: (a) graphite weight (no extra added weight); (b) alumina; (c) zirconia; and (d) tungsten carbide added weights.

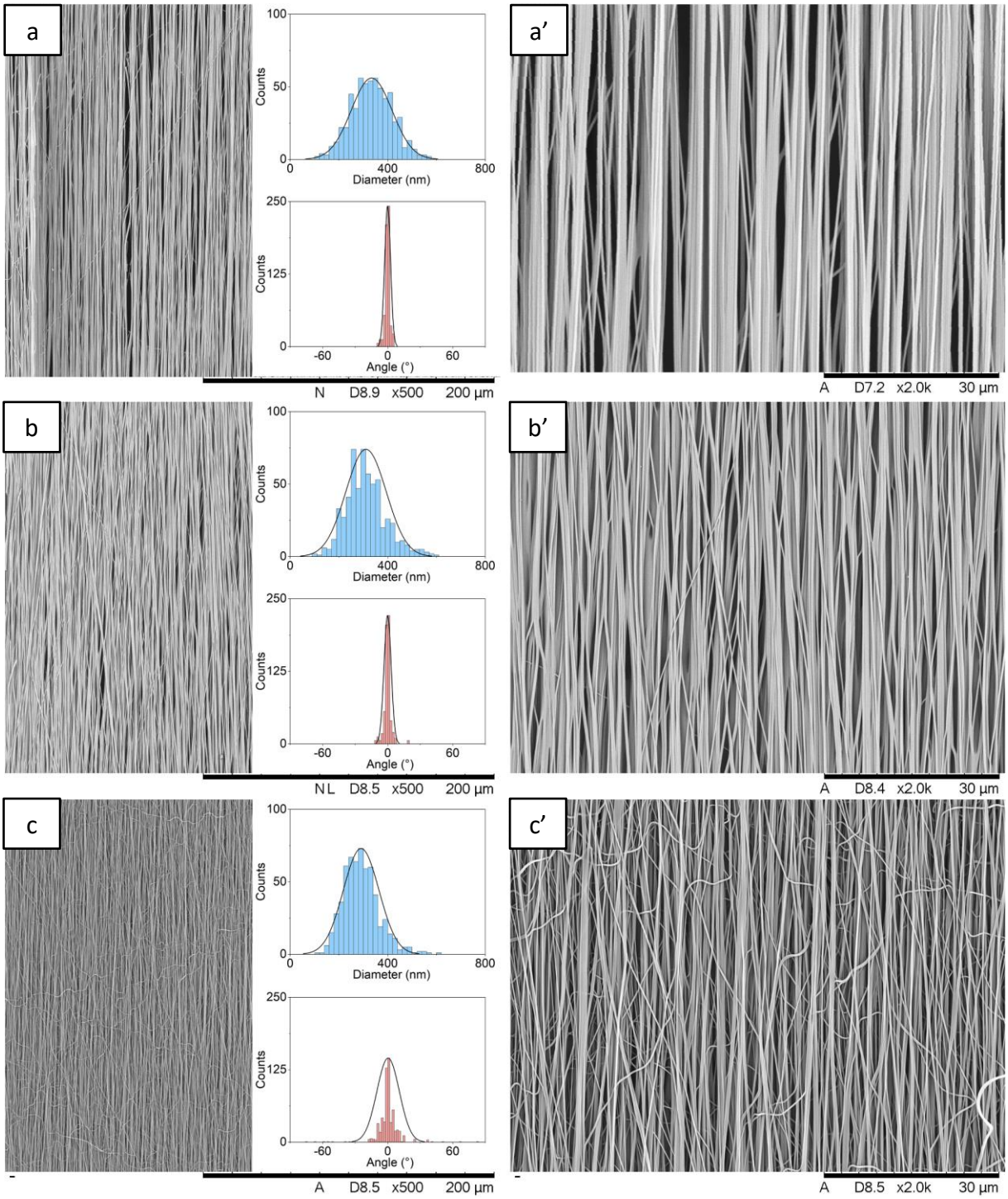

Figure 4.2.7 Cont.

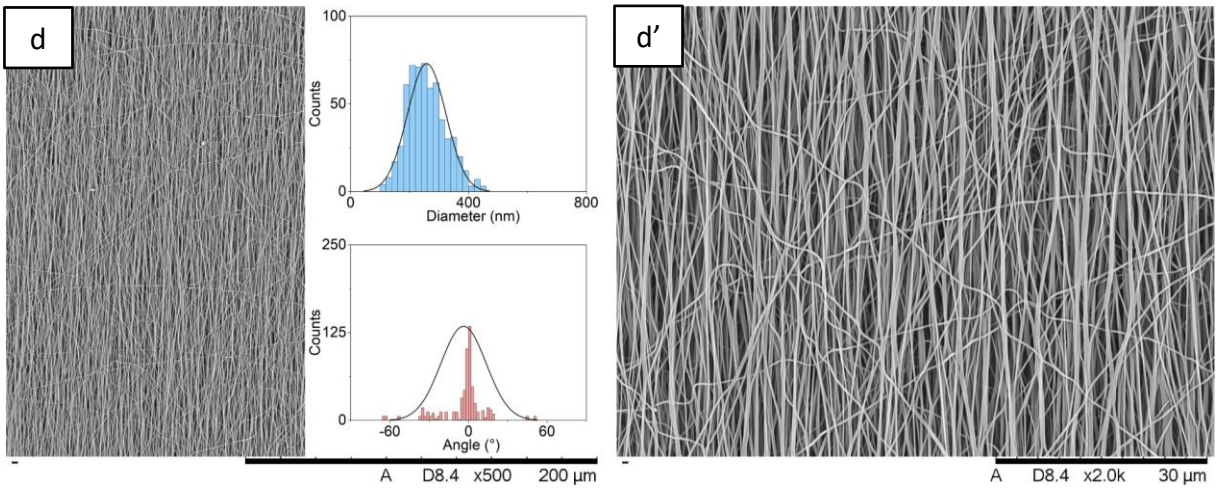

Figure 4.2.7 SEM micrographs overlaid with diameter distribution (top right) and distribution of the degree of alignment (bottom right) of oxidised fibres with different static weights using: (a, a') graphite bricks (no added weight); (b, b') alumina; (c, c') zirconia; and (d, d') tungsten carbide. The total weight for (a), (b) and (c) were 1.75, 2.68, and 5 g, respectively.

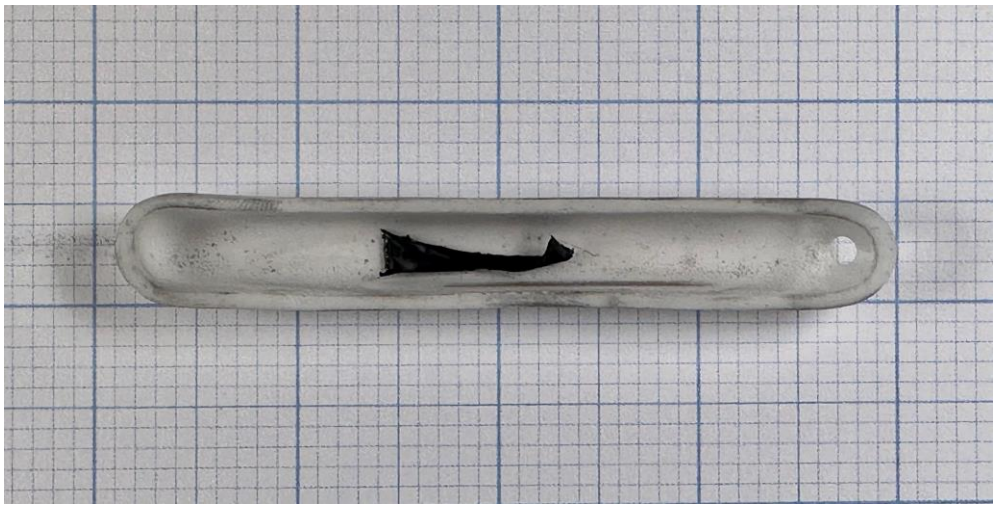

Figure 4.2.8 Macroscopic appearance on a PAN nano-fibre bundle obtained after carbonisation at 1200 °C in nitrogen.

Table 4.12 Result of average fibre diameter and average % of aligned fibres between 0–5° for the oxidised fibre with different static weights using: (a) graphite weight (no added weight); (b) lumina; (c) zirconia; and (d) tungsten carbide. Values for standard deviation are indicated by square brackets.

Weight Type and Total Weights	**Average Fibre Diameter (nm)**	**Average % of aligned fibres between 0–5°**
Graphite (No added weight) (1 g)	334.1 [83.3]	93 [2.8]
Graphite + Alumina (1.75 g)	311.2 [82.7]	91 [3.3]
Graphite + Zirconia (2.68 g)	291.1 [73.0]	67 [10.3]
Graphite + Tungsten Carbide (5 g)	258.2 [65.4]	64 [17.3]

Overall Summary

- A unique graphite rig was designed, built and evaluated. It was found that electro-spun PAN nano-fibres could be tensioned during oxidation and carbonisation.
- A graphite 'end-tab' was designed and bonded to the bottom-section of the sample. This end-tab had a facility to introduce weights to keep the fibres under tension. The top-section of the nano-fibre bundle was bonded to the top outer surface of the graphite rig.
- The heat-treatment of electro-spun fibres under weight has not been reported previously.
- The average thickness of the oxidised aligned fibres decreased significantly as a function of the magnitude of applied weight. For example, without the extra weight,

the thickness was 92 μm. It decreased to 51, 35 and 7.5 μm as the weight was increased from 0 g to 1.75, 2.68 and 5 g respectively.

- Controlling the tension during heat-treatment was shown to be an effective way to retain the orientation of the fibres, and also to reduce the thickness of the aligned fibre bundle.
- The average fibre diameter decreased from 334 nm to 331 nm, and from 291 nm to 258 nm as the weight was increased from 1 g to 1.75 g and from 2.68 g to 5 g respectively.
- Keeping the aligned fibres under tension led to a reduction in length by 27, 43 and 47% when the fibres were heat-treated with a weight of 1.75, 2.68 and 5 g respectively.
- Increasing weight during heat-treatment to 2.68 g and 5 g led to failure of the sample above 300 °C.

4.2.3. Effect of Heat-treatment Temperature on Aligned PAN Nano-fibres

In order to maintain a consistent applied load during oxidation, only alumina rods were used for carbonisation up to 900 °C (see Table 4.11). Photographs of the oxidised and carbonised aligned PAN nano-fibres are shown in Figure 4.2.9. During heat-treatment, both the width and length of the fibre bundle reduce. From the TGA result, the weight reductions at 300, 600 and 900 °C were 8.9%, 39.9% and 48.8%, respectively. The length of the fibre is reduced from 30 mm (as-spun) to 22 mm (300 °C), 17 mm (600 °C) and 16 mm (900 °C), respectively, which is a reduction of 26.7%, 43.3% and 46.7%, respectively. It can also be seen from the photographs shown in Figure 4.2.9 that the fibre bundle after oxidation and carbonisation was dumbbell-shaped. The width was measured at the narrowest region of the sample. The width was

reduced from 6.0 mm (as-spun) before heat-treatment to 3.6 mm (300 °C), 2.4 mm (600 °C) and 2.1 mm (900 °C), respectively. This corresponds to a reduction of 40%, 60% and 65%, respectively. The dumbbell shape formed because the ends of the aligned fibre bundle were bonded to the graphite rig and weight using high-temperature adhesives, preventing free-shrinkage. Unfortunately, as shown in Figure 4.2.8, the fibres that were carbonised at 1200 °C, without an applied dead-load, could not be compared with the fibres that were heat treated with a dead-load because they curled. Manually flattening the fibre array fractured the samples. Therefore, it was not possible to measure the length and width of the fibre samples that were carbonised at 1200 °C.

The average fibre diameter and the fibre diameter distributions are shown in Figure 4.2.10 and summarised in Table 4.13. The average fibre diameter was reduced from 382 nm (as-spun) to 311.2, 246.9, 182.9 and 145.5 nm when treated at 300, 600, 900 and 1200 °C, respectively. This represents a reduction of 19%, 35%, 52% and 62%, respectively. The diameter distribution narrows as the heat-treatment temperature increases. The above-mentioned observations imply that in addition to the intrinsic shrinkage during heat-treatment, the applied weight on the specimen contributes to a reduction in the fibre diameter due to stretching under load. The diameter distribution also reduced possibly because, as thinner fibres fracture, only the thicker fibres remain. Sabantina *et al.* [430] reported that the average fibre diameter of non-woven PAN nano-fibres before and after carbonisation (at 800 °C) was not changed (220 ± 60 nm and 222 ± 57 nm, respectively). A similar result was also reported by Panapoy *et al.* [431]. However, the reasoning behind the lack of change in the diameter was not explained in either case. A number of researchers report that the fibre diameter decreases with increasing heat-treatment temperature [242, 321, 322, 432-434], without a static load being applied.

Schierholz *et al.* [432] report that the fibre diameter of a single PAN-based electro-spun fibre at room temperature and heat-treated at 250, 600, 800 and 1000 °C was 320, 230, 212, 199 and 189 nm, respectively. Gu *et al.* [322] found that the average fibre diameter and the standard deviation of the 1000 °C carbonised PAN-based electro-spun fibre reduced from 206 nm to 156 nm and 41 nm to 38 nm, respectively. The diameter reduction reported by Gu *et al.* [322] was 41% and 24%, respectively, which is lower than the result obtained in the current study. The data generated in this current study confirms that the static weight can further reduce the diameter of the fibre through stretching, which can potentially improve the molecular orientation [344] and crystallinity [279].

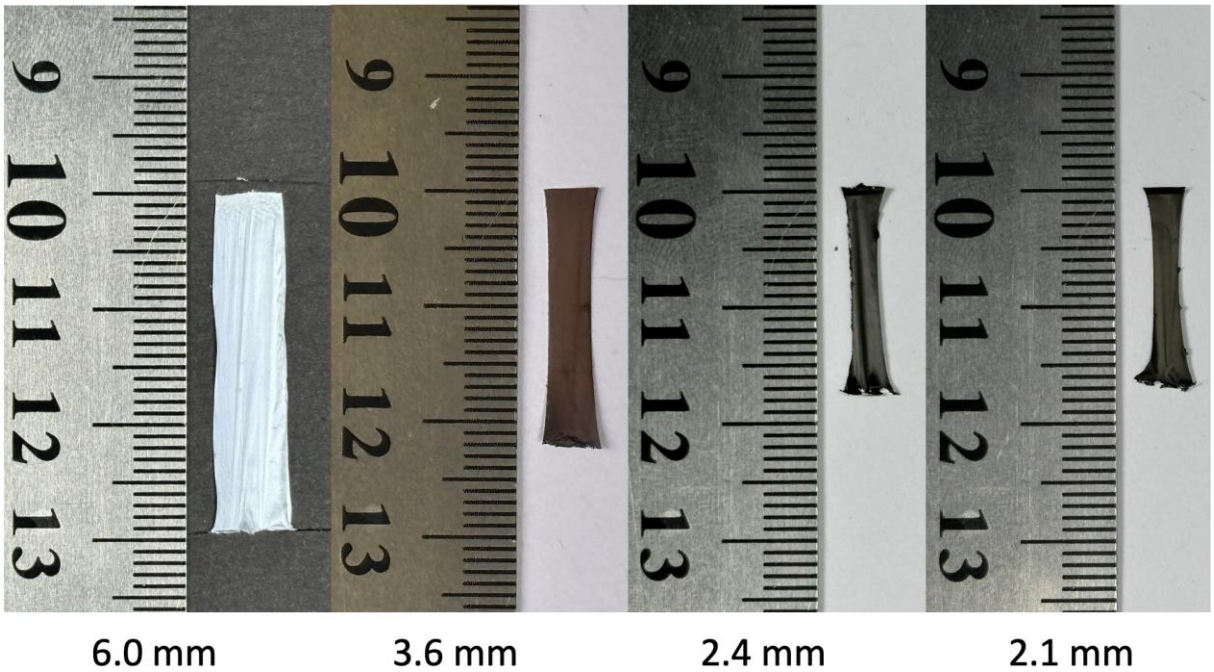

Figure 4.2.9 Photographs of (a) as-spun and samples heat treated at: (b) 300 °C; (c) 600 °C; and (d) 900 °C using alumina static weights. The number below the photograph represents the width of the narrowest section of the fibre sample, respectively.

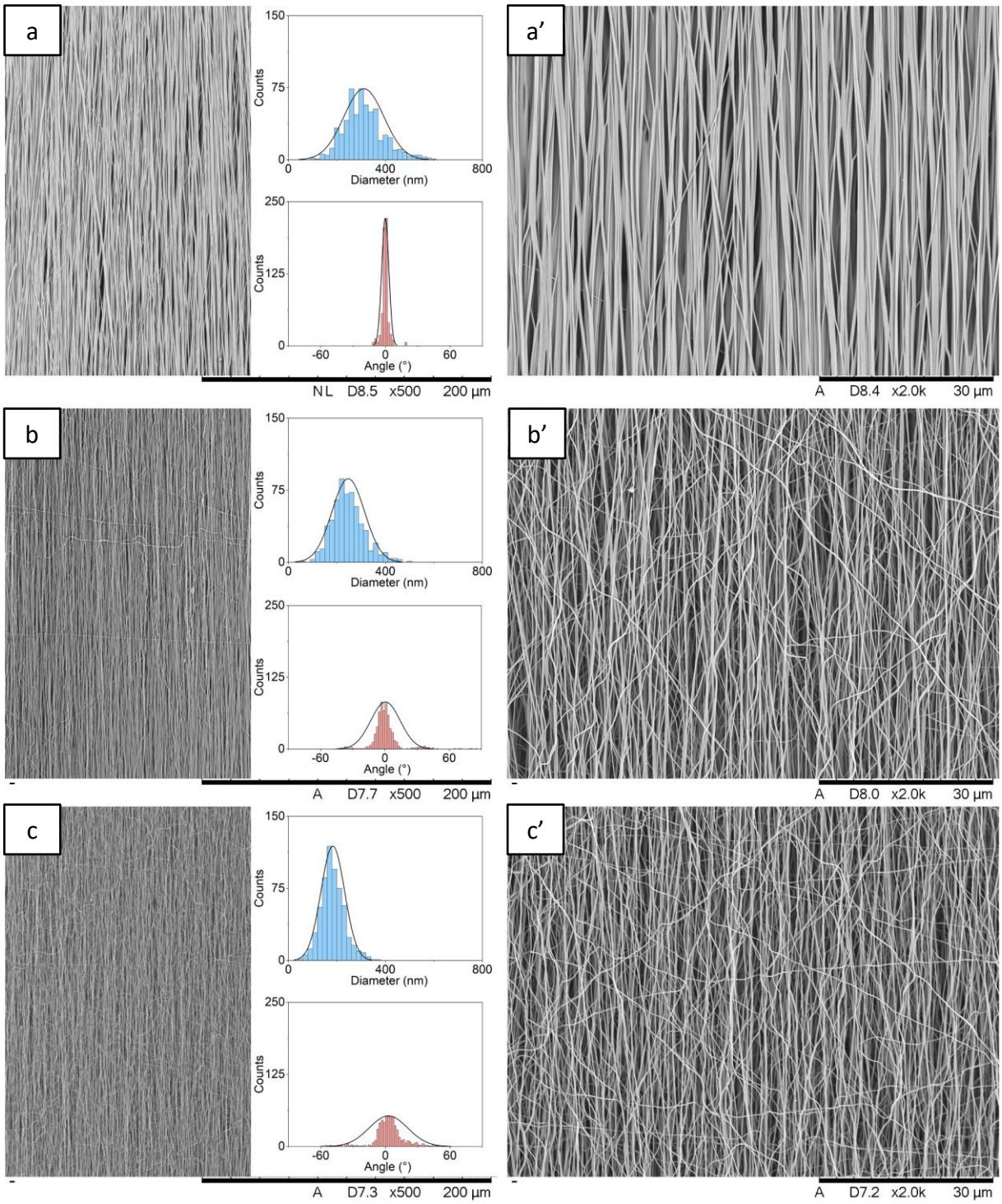

Figure 4.2.10 Cont.

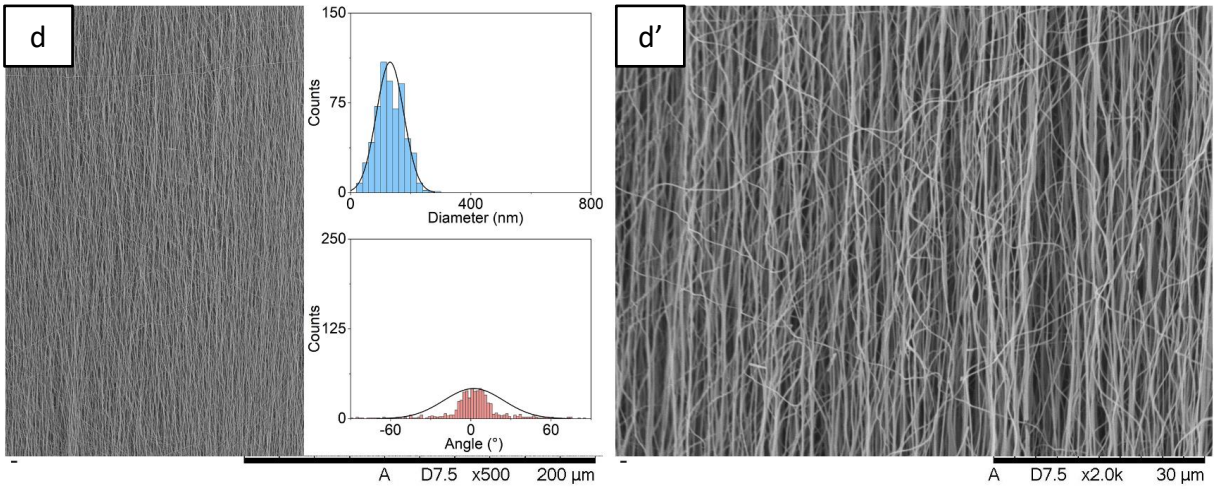

Figure 4.2.10 SEM micrographs overlaid with distributions of diameter (top right) and degree of alignment (bottom right) when alumina static weights were used on the fibre samples that were heat treated at: (a, a') 300 °C; (b, b') 600 °C; (c, c') 900 °C; and (d, d') 1200 °C.

Table 4.13 Average fibre diameter and average % of fibres aligned between 0–5° following heat-treatment at (a) 300 °C, (b) 600 °C, and (c) 900 °C using alumina static weights. Standard deviations are indicated by square brackets. (indicates values based on SEM micrographs that include fractured and misaligned fibres.)*

Heat-treatment Temperature (°C)	Average Fibre Diameter (nm)	Average % of Aligned Fibres between 0–5°
300	311.2 [82.7]	91 [3.3]
600	246.9 [67.4]	56.5* [13.7]
900	182.9 [48.9]	39.5* [17.9]
1200	131.5 [45.6]	31.5* [19.4]

Overall Summary

- The fibre alignment distribution broadened, and the degree of alignment was significantly reduced as heat-treatment time increased (See Table 4.13).
- The loss of alignment as observed from the SEM micrographs is likely due to fibre fracture caused by (i) manual handling; (ii) uneven bonding of the sample to the graphitic rig and weights, leading to an uneven loading of the sample; and (iii) non-uniform impregnation.
- The micrographs shown in Figure 4.2.10 were also used to determine the degree of fibre alignment after heat-treatment.

4.2.3.1. XRD Charcteristion of Oxidised and Carbonised Aligned PAN Nano-fibres

As mentioned in Section 3.5.10 X-ray diffraction (XRD) can be used to characterise the material's crystal structure and degree of crystallinity [435, 436]. Typical PAN XRD spectra show a strong peak at the 2θ angle of 16.8° (1 0 0) and a weak peak located at 28.6° (1 1 0) [242, 312, 437]. When the PAN precursor undergoes stabilisation, the (1 0 0) (2θ ≅ 17°) peak disappears while a broad diffraction peak centred at 2θ ≅ 25° appears. This new peak represents the X-ray reflections of (0 0 2), which indicate the formation of the crystallographic plane of graphite crystallites in the stabilised PAN [312]. Further carbonisation results in the (1 0 0) peak disappearing while a broad diffraction peak at 2θ ≅ 25°, representing (0 0 2), appears [323, 437].

Figure 4.2.11 shows overlaid XRD spectra of GF PAN heat-treated at 300, 600, 900 and 1200 °C. The as-spun aligned PAN nano-fibres show a sharp peak around 16.7° and a broad peak around

25°. After the fibres have been stabilised at 300 °C in air, a reduction in the intensity of the peaks located at 16.7° and 25° can be observed. This is because stabilisation leads to cross-linking and cyclisation of the polymer chains, which reduces the degree of disorder and the crystallinity in the fibre. Further temperature increases to 600 °C and 900 °C showed an increased intensity in the 2θ range between 17° to 25°. The two broad peaks located around 18° and 24° can barely be identified. The intensity of the broad peak at 24°, from fibres treated at 900 °C, is slightly more obvious than those that were treated at 600 °C. The peak intensity rises even higher at 1200 °C. This may be attributed to the formation of new crystal structures or to changes in the crystallographic orientation of the polymer chains, as reported by other researchers [323, 437]. The peak near 24° was expected to be more intense and to occur at a larger angle with increasing heat-treatment temperature [312], due to decreased the inter-layer spacing of the crystal, which can be calculated using the Bragg equation [242, 314]. However, due to the small number of samples prepared, the diffraction results are obscured by a low signal-to-noise ratio. The exact location of the 2θ angle was hard to determine. More experimental iterations would be required to improve upon this. The XRD results do, however, show the success of the heat-treatment and the formation of a graphitic structure.

Overall Summary

- XRD analysis confirmed that increasing the heat-treatment from 300 °C to 1200 °C increased the graphitic characteristics of the aligned PAN nano-fibres.

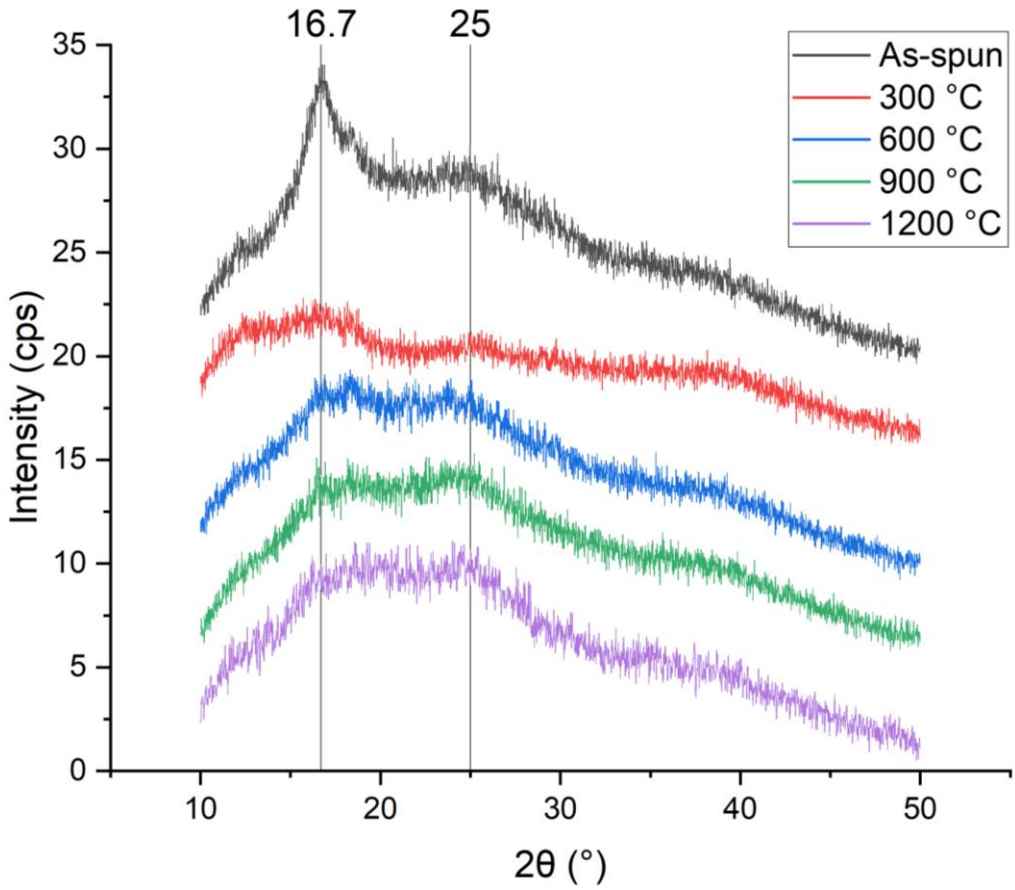

Figure 4.2.11 Overlaid XRD spectra of the electro-spun PAN/DMSO fibres heat treated at different temperatures.

4.2.3.2. Raman Spectroscopy of the Oxidised and Carbonised Aligned PAN Nano-fibres

Raman spectroscopy was performed to investigate the effect of heat-treatment on the graphitic character development as a function of temperature [324, 438]. Raman spectroscopy, with a laser wavelength of 516–532 nm, has commonly been used to identify the graphite structure in CNFs [324, 325]. Two typical peaks, located around 1350 cm^{-1} and 1580 cm^{-1}, represent the D-band and G-band, respectively [439]. The D-band is a disorder-induced vibrational mode that arises from the breathing mode of sp^2-bonded carbon atoms

in a graphitic lattice with topological defects such as vacancies or disordered edges [440, 441]. The G-band represents the Raman-active vibrational mode that arises from the in-plane stretching of C=C stretching vibrations due to sp^2-bonded carbon atoms in a graphitic lattice [442, 443]. The R-value is the ratio between I_D and I_G. The lower the R-value, the higher the number of sp^2 (graphite) clusters on the sample [325]. Other sub-bands, such as D_I (1200 cm^{-1}), D'' (1500 cm^{-1}) and D' (1600 cm^{-1}), are also used to indicate the presence of discorded graphitic structure [444, 445]. In order to visualise these peaks, the Raman spectra were deconvolved into the bands mentioned above using a Gaussian and Lorentzian peak-fitting routine. An example of the peak fitting outcome can be found in Figure 4.2.12. The band intensity, FWHM and area were obtained from the deconvoluted peaks. The Pearson's correlation coefficient of all the curve fittings exceeded 99%.

Raman spectra of the aligned GF PAN nano-fibre heat-treated at 300, 600, 900 and 1200 °C are presented in Figure 4.2.13. It is clear that, as the heat-treatment temperature increases, the intensity of the D-band declines, and the intensity of the G-band increases, consonant with trends reported elsewhere [325, 446-449]. The peak position of the D and G bands of the fibre heat-treated at 300 °C is narrower than at higher temperatures. This could contribute to the high intensity of the disordered amorphous graphitic structure of the D'' sub-band located around 1,500 cm^{-1} when the heat-treatment temperature is low [444, 445]. The peak position of the D and G bands, as well as the intensity ratio (I_D/I_G), full-width at half-maximum (FWHM) and the ratio of integrated intensity (A_D/A_G) are summarised in Table 4.14. It is seen that the position of the D and G bands does not change as heat-treatment temperature increases, which is similar to the result reported by Wang *et al.* [450]. The R-value (intensity ratio of D- and G-band) was found to decrease as heat-treatment temperature increases [325, 450]. On

comparing the data presented in Appendix C which summarises the R-values reported in literature, the results obtained from heat-treated aligned PAN nano-fibre in this current study at 900 °C are higher than any other reported values at the same temperature. This indicates that the carbonisation of the aligned fibre array under load can improve the formation of ordered graphitic structures [242, 439, 451].

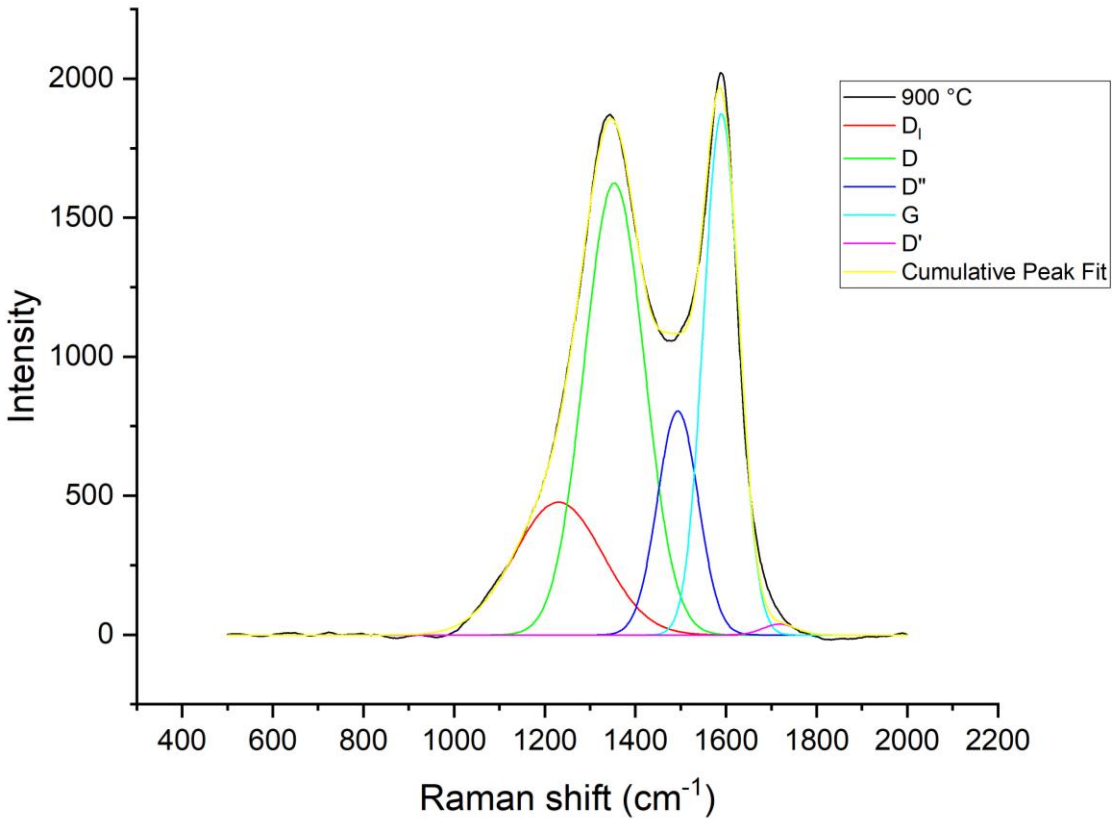

Figure 4.2.12 Deconvolved Raman spectra for electro-spun GF PAN/DMSO fibres carbonised at 900 °C.

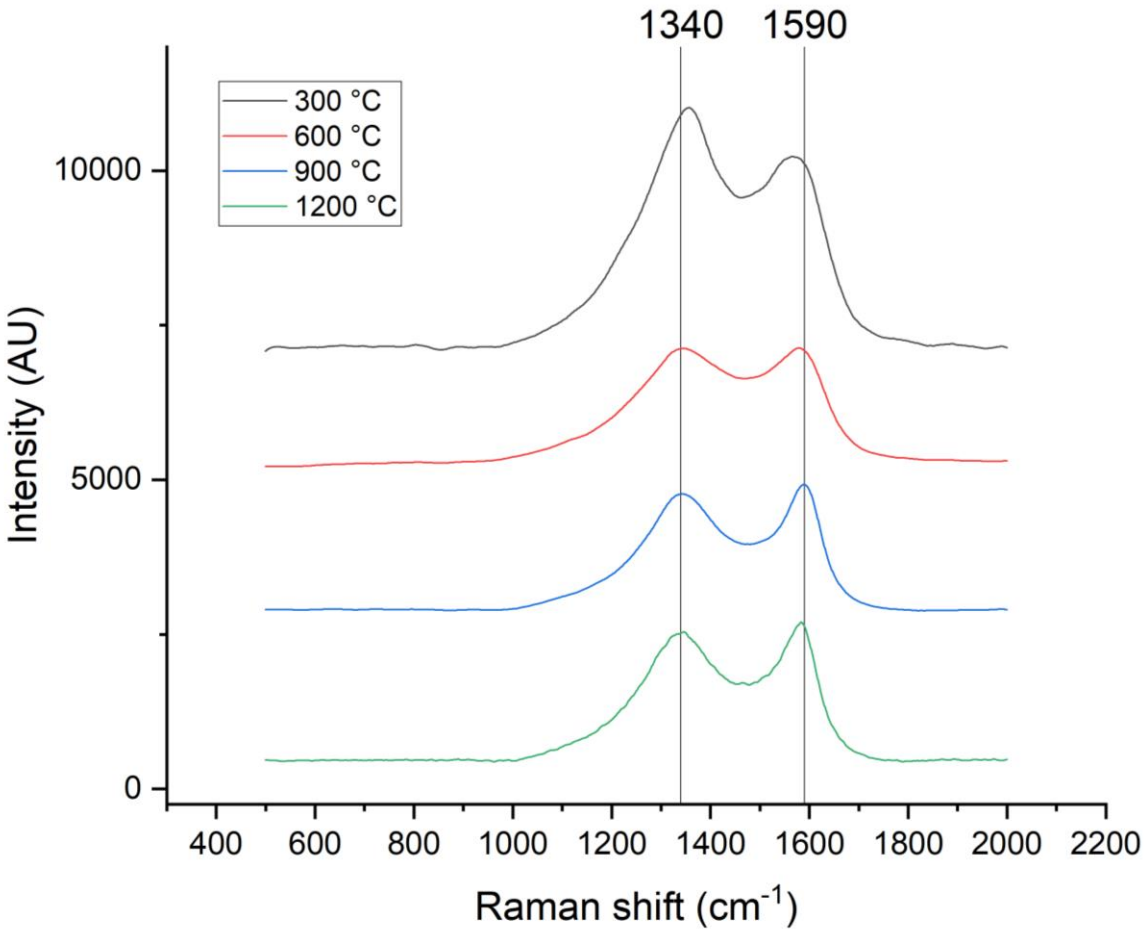

Figure 4.2.13 Overlaid Raman spectra for GF PAN/DMSO fibre heat treated at 300 °C, 600 °C 900 °C and 1200 °C.

<u>Overall Summary</u>

- Raman spectroscopy corroborated the conclusions reached through XRD analysis.
- The ratio of the I_D/I_G peaks (R-value) decreased from 1.16 to 0.94, 0.87 and 0.85 as the heat-treatment temperatures increased from 300 °C to 600, 900 and 1200 °C, respectively.

- The R-values reported in the current study represent the highest values reported in literature for fibres treated to 900 °C. This is attributed in part to the tensioning of the fibres during heat-treatment.

Table 4.14 Summary of the average peak position of D- and G-band, the intensity ratio (I_D/I_G), full-width at half-maximum (FWHM) and the ratio of integrated intensity (A_D/A_G) of aligned PAN-based electro-spun fibres heat-treat at different temperatures. Standard deviations are given in square brackets.

Heat-treatment Temperature (°C)	D-band Position	G-band Position	I_D/I_G (R-value)	FWHM of D-band	FWHM of G-band	A_D/A_G
300	1362 [2.4]	1575 [2.1]	1.16 [0.03]	162.6 [6.2]	125.7 [12.2]	0.7 [0.1]
600	1342 [1.1]	1578 [1.2]	0.99 [0.02]	166.8 [9.9]	119.7 [15.6]	1.4 [0.2]
900	1343 [0.8]	1589 [0.7]	0.87 [0.04]	155.6 [10.9]	92.6 [11.6]	1.5 [0.3]
1200	1345 [1.0]	1851 [0.5]	0.85 [0.03]	159.0 [9.2]	92.7 [10.7]	1.6 [0.2]

4.2.3.3. Characterising the Cross-sectional Morphology of Heat-treated PAN Nano-fibres using TEM

Due to specimen shrinkage as well as the fibre thinning after heat-treatment, the sample became very difficult to handle and prepare, especially when performing tensile tests. Critical information for generating tensile test results, such as measuring the thickness of the specimens using a micrometre screw gauge without destroying the sample, was very difficult. The same difficulties also apply to weighing the carbonised fibres.

It is worth pointing out that the micrometre screw gauge does apply pressure when measuring the thickness of a specimen, and this is problematic when dealing with intrinsically porous and brittle materials. The major problem in generating accurate tensile test results for the carbonised PAN nano-fibre bundles was determining the cross-sectional area and the fibre volume fraction. As mentioned in Section 2.3.1, the density of the randomly oriented and aligned electro-spun fibres has been reported to be extremely low [38, 452]. Stress and strain data cannot be calculated accurately using the bulk dimensions for the reasons mentioned above.

Therefore, finding a way to identify the cross-section of the aligned nano-fibre bundle is crucial. A variety of attempts were made to investigate ways to determine the cross-section of the aligned fibre bundles. Keeping the aligned nano-fibres vertical whilst imaging using SEM was difficult. The main reason was that, after sectioning in liquid nitrogen to inspect the cross-section, tension was lost and they curled at the tip. Electron beam damage was also prominent at high magnification.

The problem was part-solved in the later stage of the research using TEM. Out of a batch of ten specimen prepared, three were randomly selected to be impregnated and cross-linked in a thermosetting resin as outlined in Section 3.5.9. 100 nm thick cross-sections were obtained using a diamond-tipped microtome blade (Ultra 1436, DiATOME, Switzerland). This aspect of sample preparation was carried out by T. Morris of the Electron Microscopy Centre, University of Birmingham.

TEM micrographs of the cross-section of the heat-treated aligned GF PAN nano-fibres are presented in Figure 4.2.14a–d. Figure 4.2.14a shows that the as-spun fibres have a near-

circular cross-section. Previous publications have reported the cross-section of PAN fibres to be ‘kidney-’ or ‘ribbon-shaped’ [330, 337, 350, 453, 454]. Neither cross-section was observed in the electro-spun fibres produced in the current study. Fibre bundles with a small level of fusion at the contact point can be observed, and fibres without any fusion can also be seen when they are in intimate contact with each other. The fusion is probably due to the slow solidification of the fibre skin during fibre formation, the skin being too thin when the fibres come into contact. However, no clear evidence was found to show that fibres fused as the temperature is increased. The fibres inspected did not show any signs of porosity or internal flaws.

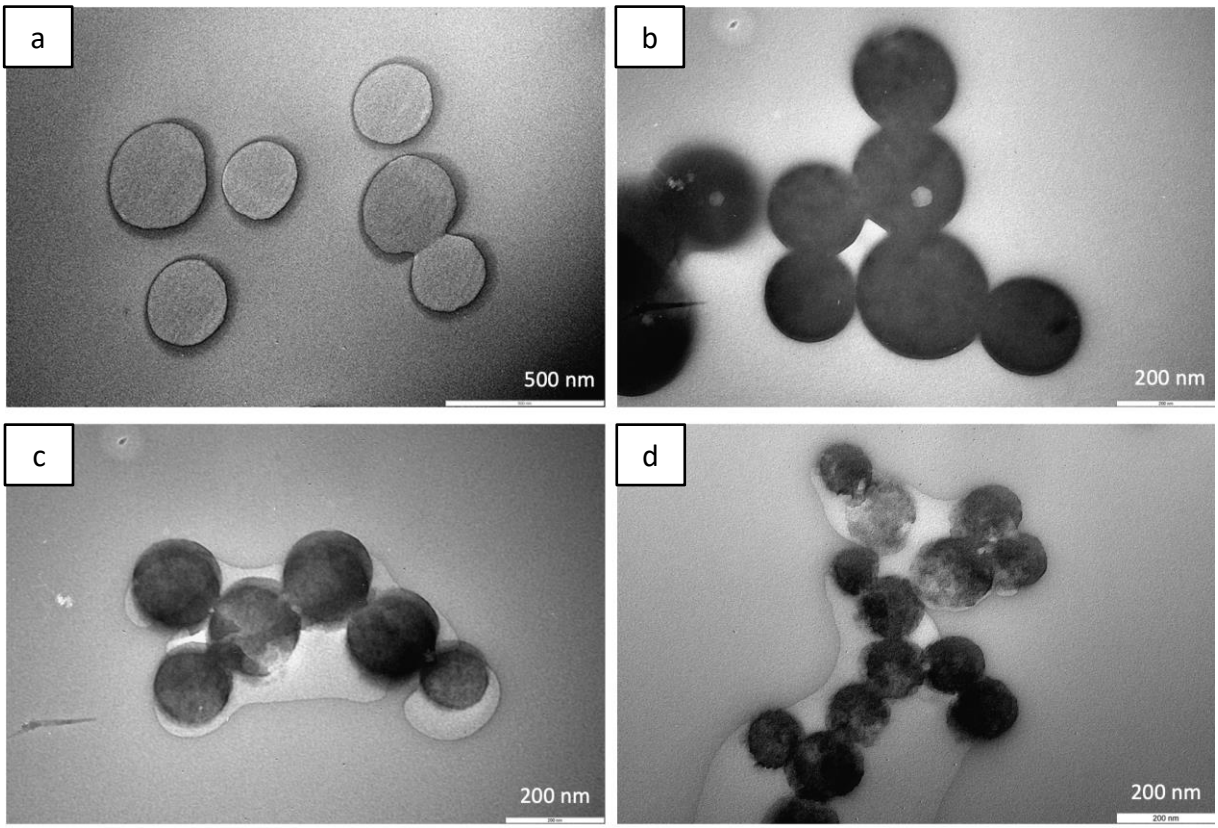

Figure 4.2.14 Cont.

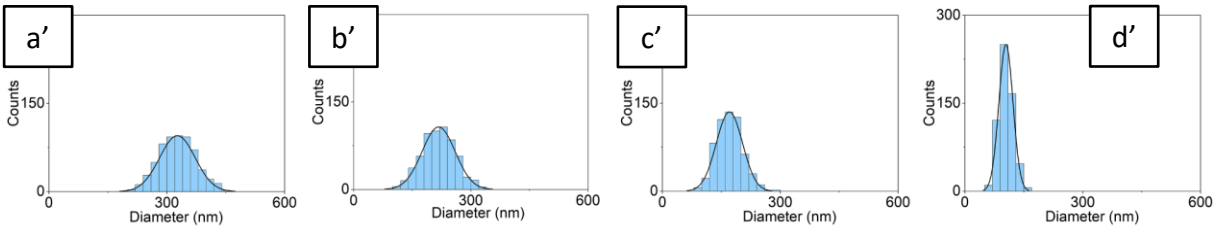

Figure 4.2.14 TEM micrographs and diameter distribution of the cross-section of the aligned GF PAN nano-fibre after heat-treatment at: (a) as-spun (dried at 120 °C for 6 hours); (b) 300 °C; (c) 600 °C and (d) 900 °C. (a'–d') where the fibre diameter distributions were obtained from TEM.

The ultra-thin TEM samples showed some microstructural features that warrant future investigation. Previous researchers have attempted to link the features observed in the TEM samples to the formation of the graphitic crystalline structures [37, 242, 301, 304, 340, 356, 432]. As the fibre diameter is reduced, as can been seen in Figure 4.2.14c and d, full impregnation of the fibre bundle (by the resin) becomes difficult. Compared with carbonised fibre, the shape of the fibre was less irregularity when stabilised at 300 °C. The fibre diameter distribution, measured from TEM micrographs, is shown in Figure 4.2.14a'–d' and summarised in Table 4.15. Compared with the fibre diameter obtained from the SEM, both methods show a decrease in average fibre diameter as heat-treatment temperature increases. However, the average fibre diameter obtained from TEM is a few nanometres less than obtained from SEM.

In addition, the distribution in Figure 4.2.14a'–d' exhibits a smaller standard deviation. The fibre diameters obtained from the cross-section using TEM is more representative, due to the fibre sample being at the same height. The cross-sectional image for the 1200 °C sample was not obtainable. The fibres were too brittle and fractured during resin impregnation. An alternative method is needed for sample preparation in future work.

The TEM images of the cross-section of the nano-fibre bundles are presented in Figure 4.2.15a. Due to the surface tension of resin, the fibres splayed out during impregnation. This was realised when the thickness of the as-spun fibre, measured using a TEM image, turned out to be three times higher than the thickness measured using SEM or a micrometer screw gauge. The supporting evidence for this can be found in Figure 4.2.15b, where the sample thicknesses visualised by TEM and SEM were approximately 19 μm and 5 μm, respectively.

The main conclusion from this section is that a reliable method needs to be developed to measure the cross-sectional area and fibre volume fraction for electro-spun nano-fibres.

Table 4.15 Comparison of the average fibre diameter of aligned PAN-based electro-spun fibres heat-treated at different temperatures measured using SEM and TEM. Values for standard deviation are indicated by square brackets.

Heat-treatment Temperature (°C)	**Average Fibre Diameter from TEM (nm)**	**Average Diameter Shrinkage in %**	**Average Fibre Diameter from SEM (nm)**	**Average Diameter shrinkage in %**
As-spun (dried at 120 °C for 6 hours)	326.9 [45.4]	0%	385.5 [80.1]	0%
300	217.6 [42.4]	33%	311.2 [82.7]	19%
600	170.7 [33.4]	48%	246.9 [67.4]	37%
900	104.5 [18.0]	68%	182.9 [48.9]	53%

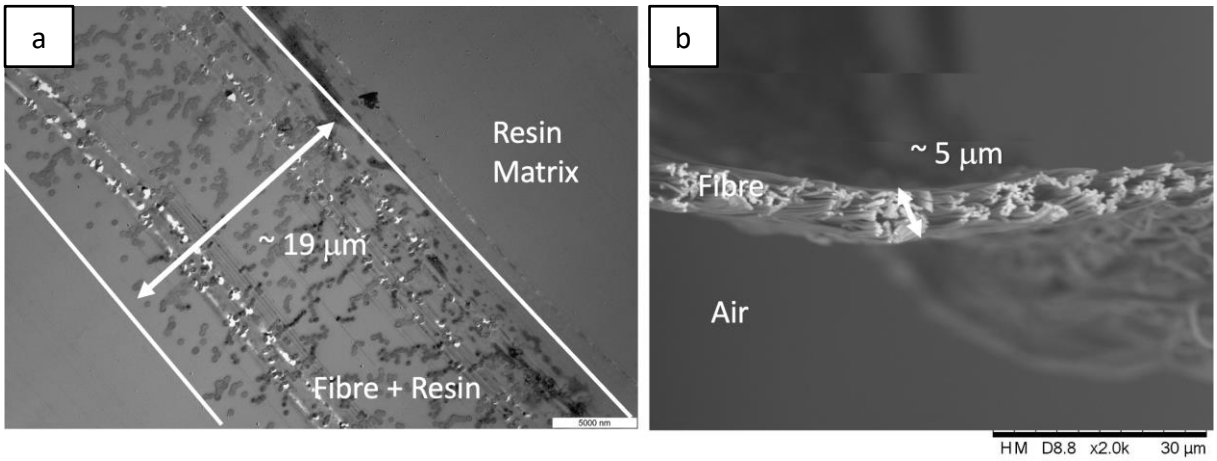

Figure 4.2.15 Cross-sectional views of aligned as-spun PAN nano-fibres obtained by (a) TEM and (b) SEM.

Overall Summary

- The practical problems associated with measuring the cross-section area of the electro-spun aligned nano-fibres was discussed previously. The same issues applied to determining the fibre volume fraction.
- Collaboration was sought with the Electron Microscopy Centre where a TEM-based method to inspect the cross section of individual electro-spun fibres was developed.
- The cross-section of the fibres was near circular.
- Only a limited number of fused fibres were observed. Even when the fibres were in intimated contact, a clear boundary between them was observed. This provides further evidence of the importance of the formation of the 'skin' on the fibres during electro-spinning.
- A discrepancy was observed between the average diameter measurements when using SEM and TEM.

- Unfortunately, it was not possible to quantify the fibre volume fraction using the TEM because the fibres splayed when the sample was impregnated, and the resin cross-linked in preparation for microtoming.

4.3. Tensile Testing of Randomly Oriented and Aligned PAN Nano-fibres

4.3.1. Preparation of Randomly Oriented PAN Nano-fibres

The randomly oriented electro-spun PAN fibres were initially produced using the conventional flat-plate electro-spinning set-up shown in Figure 3.2.1a. In order to produce the tensile test specimens, a thickness of around 4 µm is required, from a practical handling point of view. This thickness of the mat can be obtained by increasing the electro-spinning time. However, as shown in Figure 4.3.1a–c, it was found that, when using the flat-plate collector, the deposition area of the randomly oriented nano-fibres increased with the spinning time. This is because the electro-spun fibres are produced layer-by-layer, and as the thickness increases, the ability of the grounded electrode to dissipate charge decreases because the nano-fibre layers are not as conductive as the metal foil. Moreover, as the thickness of the nano-fibre layer increases, it makes it more difficult for the residual charges on the surface of the fibres to be dissipated. All these factors result in reduced electric field attraction from the tip of the needle to the centre of the collector. These issues increase the whipping area of the polymer jet, thereby increasing the fibre deposition area. This is illustrated in Figure 4.3.1a–c where the electro-spinning time was increased sequentially from 1, 5 and 10 minutes.

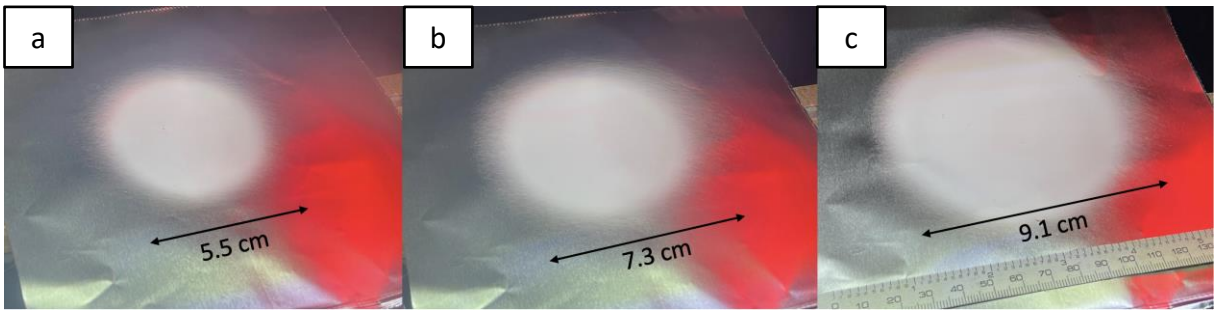

Figure 4.3.1 Photographs showing the increase in the fibre deposition area after electro-spinning for (a) 1, (b) 5 and (c) 10 minutes.

In this current study, the dimensions of the tensile test specimen had a length of 65 mm and a width of 6 mm. Figure 4.3.2a shows a schematic representation of the fibre deposition area when using a flat-plate grounded electrode. The intended perimeter of the tensile test specimen is superimposed on Figure 4.3.2a. After 30 minutes of electro-spinning, the thickness of the mat was measured at the centre and the edge (see Figure 4.3.2b) and it was 6 µm and 4.8 µm, respectively. This thickness variation between the centre and the edge was 1.2 ± 0.2 µm over ten independent measurements. Therefore, this geometry was deemed as not suitable for the test specimens as the thickness is not uniform. Therefore, in order to produce randomly aligned fibre samples for tensile testing with a relatively uniform thickness across the length of the specimen, a rotating mandrel was used.

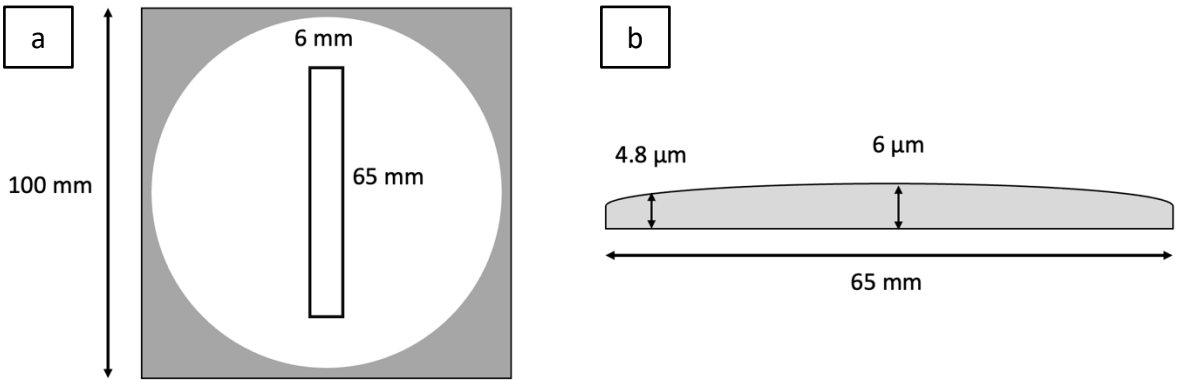

Figure 4.3.2 Schematic illustration of: (a) the dimension of the designated sectioning area of a tensile test specimen; (b) the cross-sectional view of the thickness of the specimen measured at the centre and the edge.

Randomly oriented fibres can be collected on a rotating mandrel when the rotation speed is significantly slower than the whipping speed of the jet [14]. In the current case, the slowest possible speed was 50 rpm. SEM micrographs of the fibre produced using the flat-plate collector and the low-speed rotating mandrel are shown in Figure 4.3.3a and b, respectively. The average diameter of the flat electrode and 50 rpm rotating mandrel were 366.1 and 367.4 nm, respectively, and the standard deviation was 51.3 nm and 50.3 nm, respectively.

The details of how the randomly oriented fibres were sectioned and removed from the aluminium foil was described in Section 3.3.2.

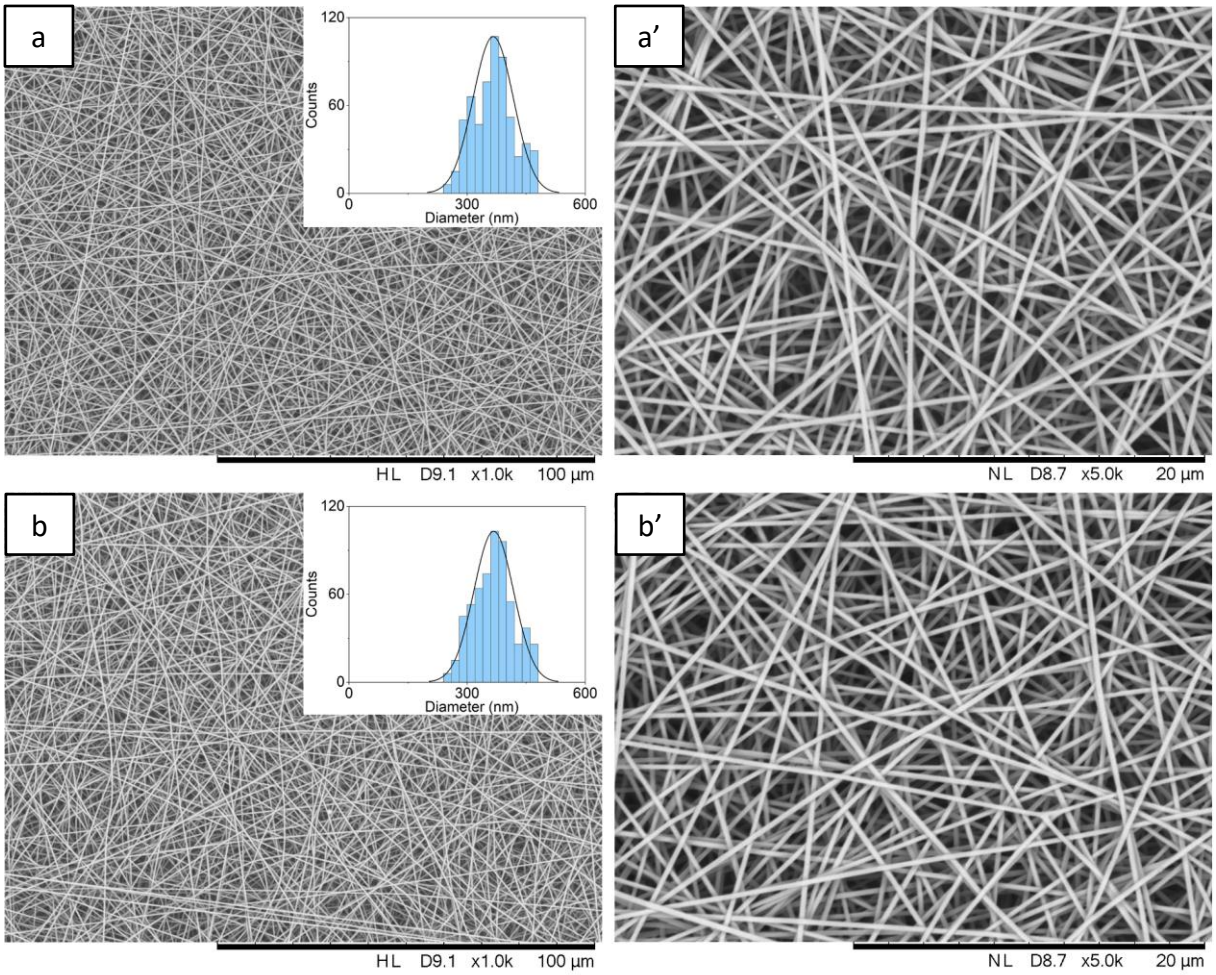

Figure 4.3.3 SEM micrographs overlaid with diameter distribution plots showing electro-spun PAN fibres produced using: (a, a') the conventional flat electrode set-up and (b, b') the rotating mandrel that was operated at 50 rpm.

<u>Overall Summary</u>

- In general, electro-spun nano-fibres mats are produced using a flat plate grounded collector.
- In the current study, it was established that samples produced on a flat plate grounded electrode had a variable thickness from the centre (directly below the needle) to the outer perimeter.

- A rotating mandrel of diameter 10 cm operating at 50 rpm was used to produce tensile test specimens with a relatively uniform thickness across the gauge length.

4.3.2. Assessment of the Tensile Test Specimen using SEM

A typical cross-sectional image of a tensile test frame and the end-tab region is shown in Figure 4.3.4a. A uniform bond-line thickness is seen where the average UV resin bonding thickness was 57 ± 6 µm. However, only one side of the test frame is shown due to the delamination of the other side when it was sectioned in liquid nitrogen. Figure 4.3.4b and c show the end-tab region of the randomly oriented and aligned tensile test specimens that were impregnated with the UV resin, respectively. A higher magnification micrograph of Figure 4.3.4c is shown in Figure 4.3.4d, where it can be seen that each nano-fibre in the bundle is impregnated by the UV resin.

In order to maintain the desired gauge length, it was important for the UV resin not to wick into the gauge length region. An example where the end-tab resin adhesive wicked into the gauge length and impregnated the fibres is presented in Figure 4.3.5a, where super-glue was used as the end-tab resin. In contrast, when the UV resin was used as the adhesive for the end-tab, the impregnated area could be controlled to prevent it from wicking into the gauge length region; this is shown in Figure 4.3.5b.

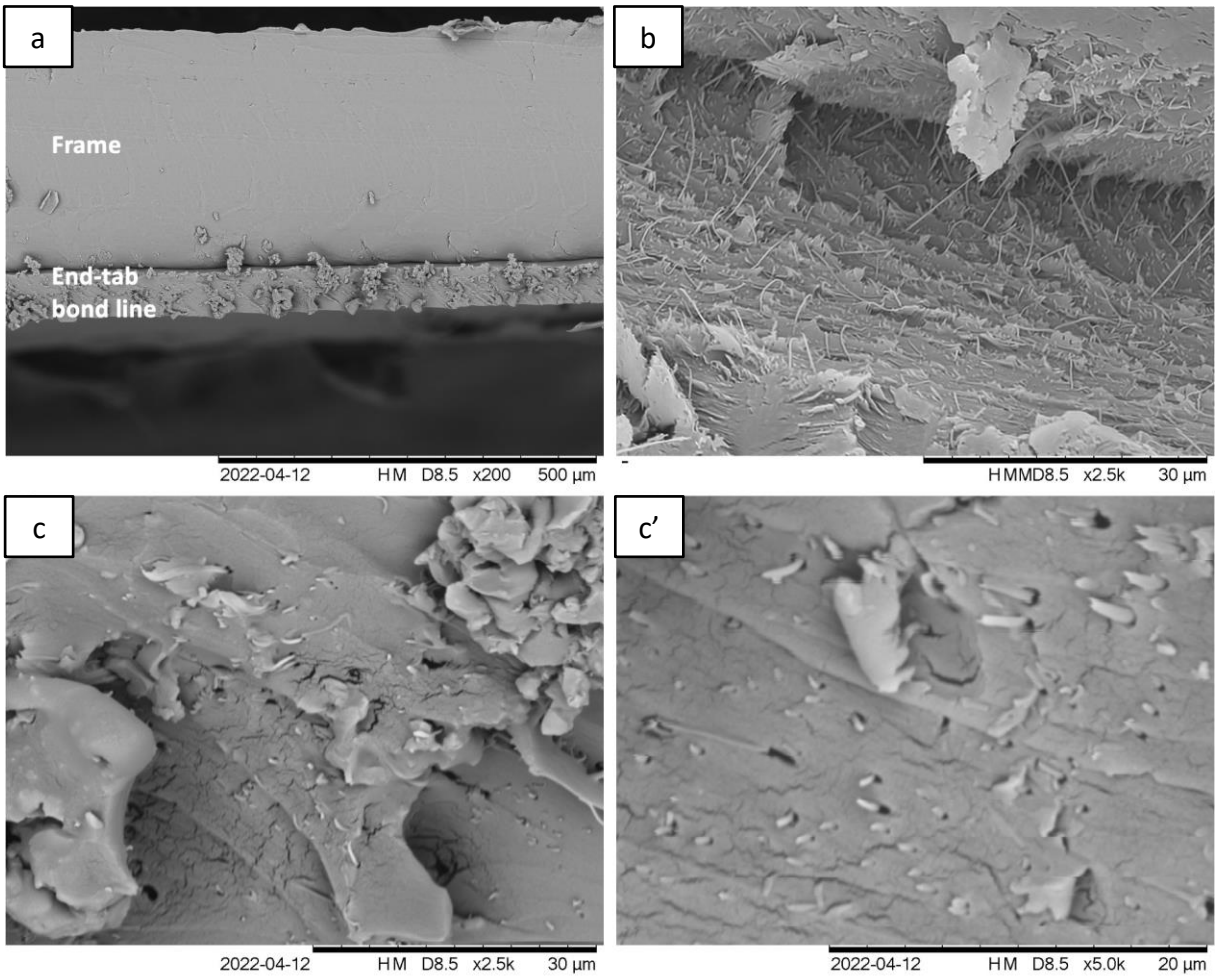

Figure 4.3.4 The SEM micrograph of: (a) the cross-section of the tensile test frame and the end-tab region; (b) fractured end-tab region of random nano-fibres; (c) fractured end-tab region of aligned nano-fibres; and (c') magnified image of (c).

The cut-edge of the specimen was also inspected using the SEM, where a rotary blade was used to minimise the damage along the cut-edge of the sample. The edges of the aligned, and randomly oriented tensile test specimen that were sectioned using the rotary blade are presented in Figure 4.3.6a and b, respectively. As the fibres in an aligned array are all orientated in one direction with gaps between fibres, the sample can be cut cleanly parallel to the direction of alignment, whereas cutting a randomly oriented fibre mat results in a

smeared edge along the cut axis. However, this sectioning method was developed through trial-and-error, and it was established that it was one of the most efficient ways of sectioning the nano-fibre arrays when preparing the test specimens. Figure 4.3.6b and c show that the level of damage to the edges of the tensile test specimens was significantly lower when the rotary cutter was used when compared to the use of a pair of scissors.

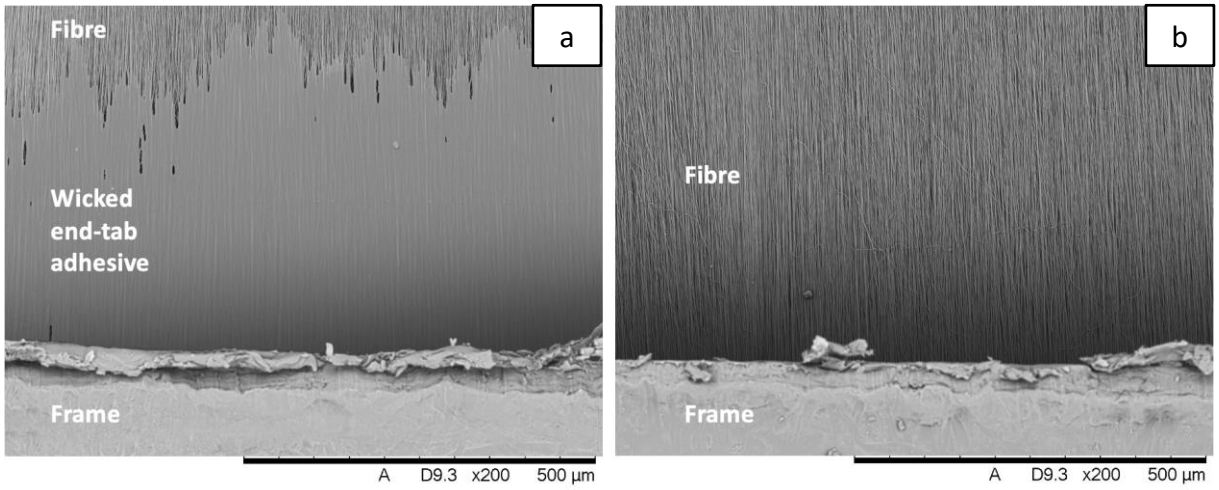

Figure 4.3.5 SEM micrographs showing an example of: (a) super-glued end-tab adhesive that had wicked through the gauge length region; and (b) UV resin end-tab without any evidence of wicking of the adhesive.

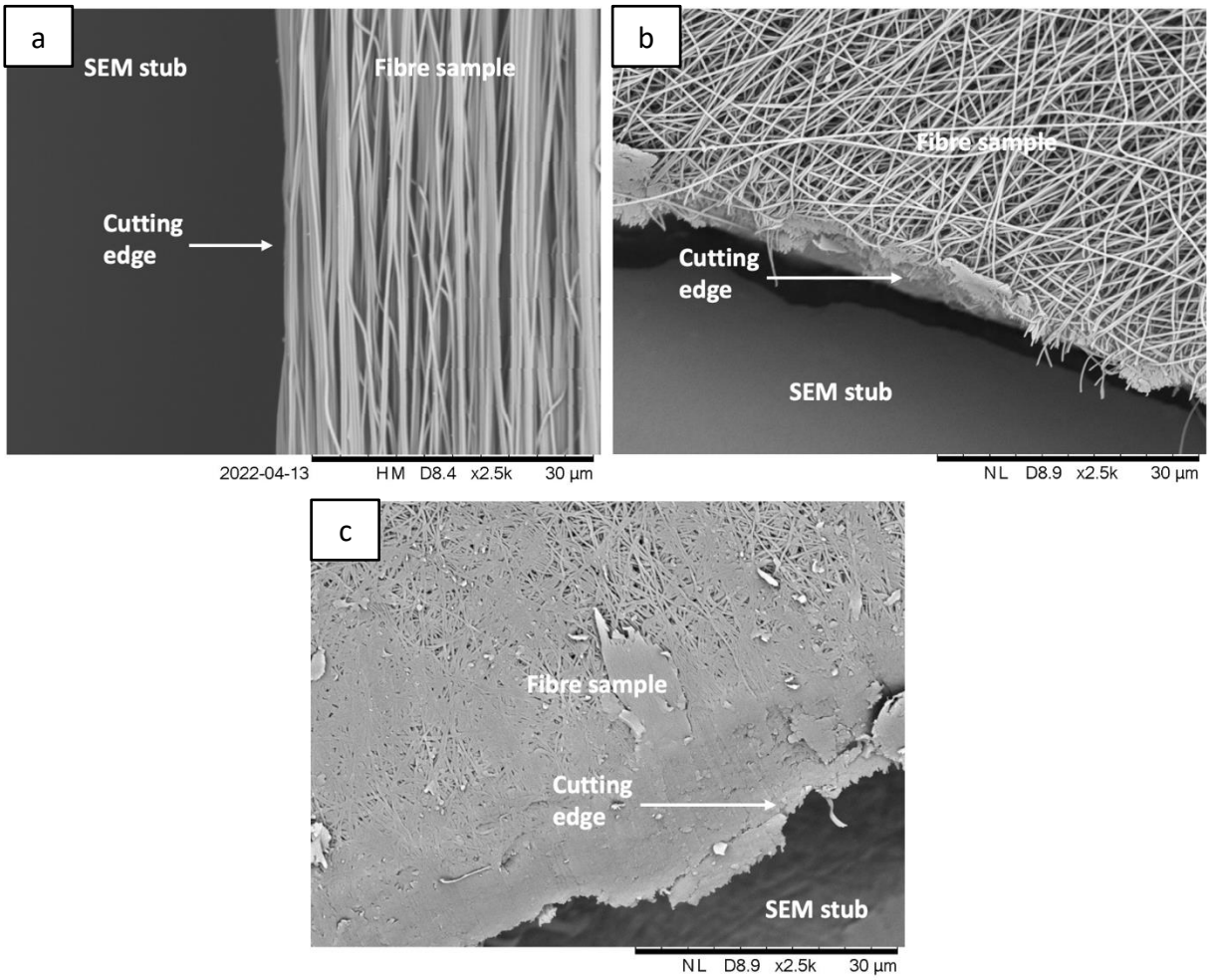

Figure 4.3.6 Appearance of the cut-edge of the tensile test specimen corresponding to: (a) aligned; (b) randomly oriented nano-fibres using a rotary blade; and (c) edge of a randomly oriented fibre specimen that was cut using a pair of scissors.

<u>Overall Summary</u>

- A rotary blade was found to be the ideal tool for cutting and sectioning the randomly oriented and aligned PAN nano-fibres.
- The fibres were fully impregnated into the UV resin end-tabs and examined using SEM.

4.3.3. Effect of the End-tabbing Method on the Tensile Test Results

As described in Section 2.3.1, the tensile test results can be significantly influenced by the end-tabbing method and quality [222, 223]. The effect of three types of end-tab adhesive (double--sided tape, super-glue and UV resin) on the tensile test results was investigated briefly. The sample preparation methods for the double-sided tape and super-glue are described in Section 3.4. The solvent used to dissolve the PAN in order to produce electro-spun fibres for the tensile test specimen in this set of experiments was 99.9% high-purity DMSO supplied by Sigma-Aldrich, and the effect of the solvent purity on the tensile test result is discussed in Section 0.

The purpose of the end-tabbed region is to evenly distribute the gripping force through the frame to the specimen to avoid stress concentrations. After the test specimens were produced, the thickness of the frame and fibre sandwich structure was measured using a micrometre screw gauge. As shown in Figure 4.3.7, the average thickness of the test specimen for the double-sided tape was 0.712 ± 0.05 mm, and the thicknesses of the specimen bonded with super-glue and UV resin were 0.650 ± 0.01 mm and 0.652 ± 0.01 mm, respectively. The higher thickness of the double-sided tape prevented it from fully impregnating each fibre. This causes the sample with the double-sided tape to be significantly thicker than the thickness (0.65 mm) across the gauge length.

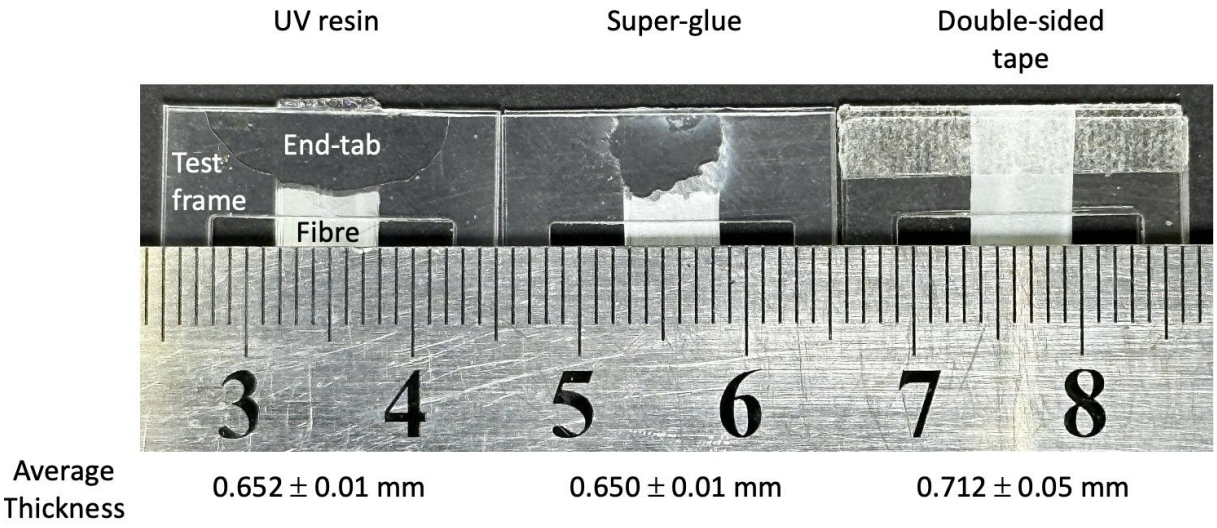

Figure 4.3.7 Photograph of the end-tab region using different end-tab adhesives.

The end-tab fabricated from super-glue showed an uneven bond-line. Although the super-glue selected had low viscosity, the curing time was fast, making the bond-line thickness difficult to control for each sample. A conventional two-part epoxy/amine resin was also evaluated. However, the curing time was around 20 hours, and preventing the resin from wicking into the gauge length region was challenging. Applying heat to accelerate the curing was considered, but it resulted in unacceptable shrinkage. After a detailed study using the above-mentioned bonding methods for the end-tab, the UV resin was found to be more controllable with regard to limiting the impregnation to within the end-tab region, and the shrinkage was negligible.

Figure 4.3.8 illustrates the stress–strain result for the aligned PAN/DMSO fibres with different end-tab bonding methods. Here, the cross-sectional area of the specimen was obtained according to the bulk dimensions measured from each specimen using a micrometre screw gauge. In addition, the width was determined from a photograph using Image-J software.

Detailed measurements, as well as the test results of each specimen, are presented in Table 4.16.

As shown in Figure 4.3.8b, In this study, Young's modulus was measured between 0 and 0.015 (1.5%) strain as the stresses caused some specimens to deform plastically at 0.02 (2%). Using the sample coded as A21 as an example, the linear fit was obtained at 0.015 strain with the following equation: y=2714.95x+0.26, and R^2=0.996. The Young's modulus was calculated to be 2652.45 MPa. The three types of end-tabbing methods are colour-coded.

The results show that the specimen tested with double-sided tape has the highest failure strain, with an average of 16 ± 2.5%. This end-tabbing method has the lowest ultimate tensile strength (UTS) of all three. The average UTSs of double-sided tape, super-glue and UV resin adhesive are 67.4 ± 2.3, 68.8 ± 4.4 and 76.7 ± 3.3 MPa, respectively. This is possibly due to the double-sided tape's inability to bond the aligned nano-fibre effectively throughout the thickness. In addition, Figure 4.3.8a illustrates that the tensile test for the specimen bonded using super-glue is variable, possibly because of the lack of bond-line control across the specimens, as described above. The lowest failure strain is 33%, one-fourth of the highest value within the same batch. The specimen bonded with the UV adhesive has the highest average UTS and Young's modulus and the lowest average failure strain of all three end-tab bonding methods. This end-tabbing method was selected for all the subsequent tensile test specimen preparations.

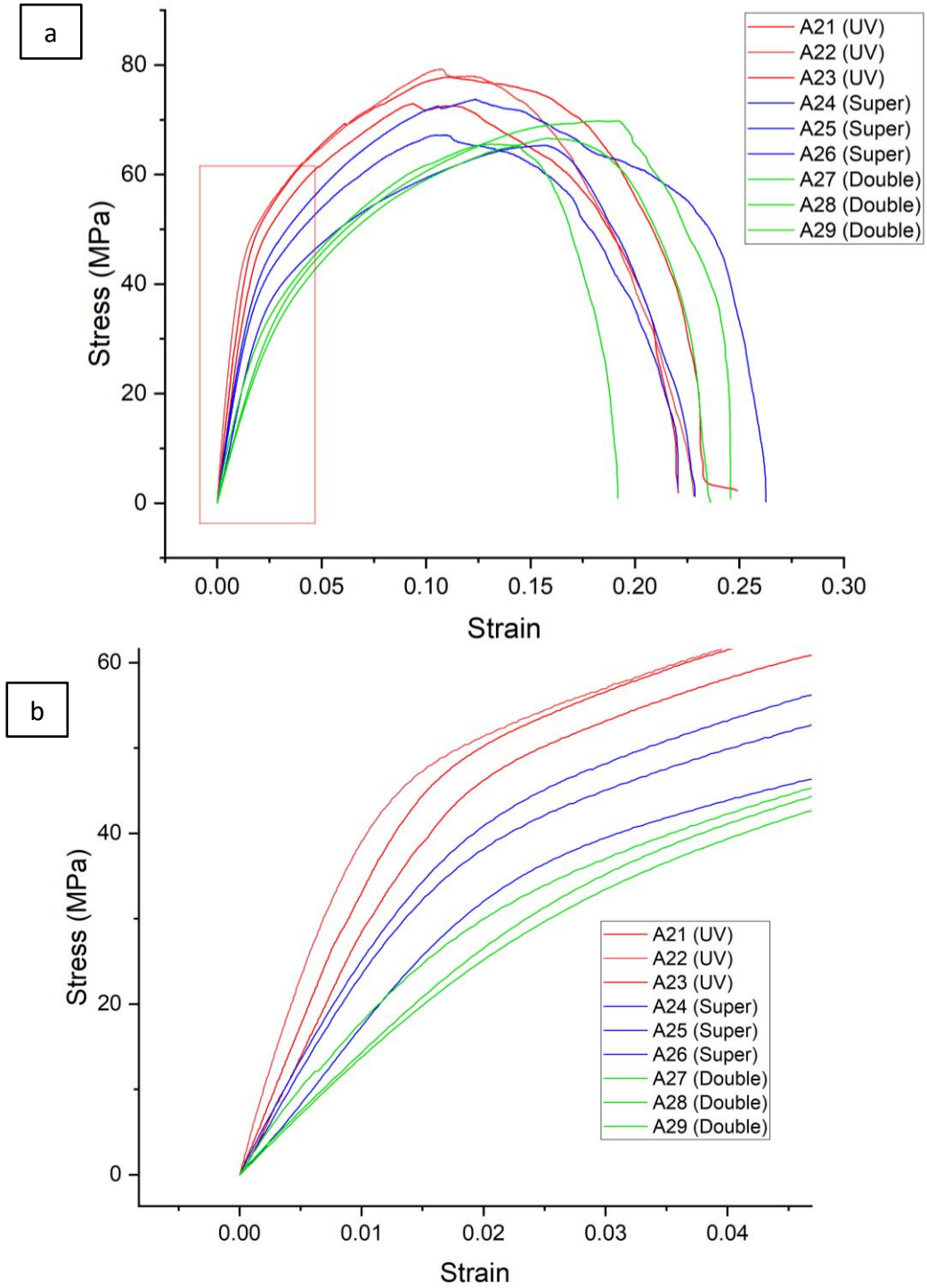

Figure 4.3.8 (a) Stress–strain plots for aligned electro-spun PAN nano-fibres that were end-tabbed using super-glue, double-sided adhesive tape and a photo-curable UV resin. (b) Zoomed in of the left part of the traces from (a).

Table 4.16 Summary of the tensile test results for the aligned electro-spun PAN nano-fibre bundles (see Figure 4.3.8) where three methods were used to end-tab the samples: super-glue, double-sided tape and photo-curable UV resin.

Aligned As-spun Fibres (Effect of End-tab) (Cross-head speed: 0.1 mm/min; 99.9% DMSO)										
Sample Number	**End-tab**	**Width (m)**	**Gauge Length (mm)**	**Thickness (m)**	**Area (m^2)**	**Weight (mg)**	**Max Load (N)**	**UTS (MPa)**	**Young's Modulus (GPa)**	**Failure Strain (%)**
A21	UV	0.00609	15	3.90E−06	2.38E−08	0.19	1.84913	77.9	2.96	11
A22	UV	0.00618	15	3.70E−06	2.29E−08	0.18	1.81388	79.3	3.15	11
A23	UV	0.00623	15	4.10E−06	2.55E−08	0.20	1.86353	73.0	2.65	9
Average (A21−A23)	UV	0.006168	15	3.90E−06	2.41E−08	0.19	1.84218	76.7	2.90	10
A24	Super-glue	0.00636	15	4.20E−06	2.67E−08	0.19	1.74610	65.4	1.71	16
A25	Super-glue	0.00601	15	3.90E−06	2.34E−08	0.18	1.72904	73.8	2.29	12
A26	Super-glue	0.00644	15	4.20E−06	2.70E−08	0.19	1.81932	67.3	2.15	11
Average (A24−A26)	Super-glue	0.00627	15	4.10E−06	2.57E−08	0.19	1.76482	68.8	2.05	13
A27	Double-sided tape	0.00655	15	4.10E−06	2.69E−08	0.18	1.79026	66.7	1.32	16
A28	Double-sided tape	0.00611	15	4.00E−06	2.44E−08	0.19	1.70723	69.9	1.39	18
A29	Double-sided tape	0.00632	15	4.20E−06	2.65E−08	0.18	1.74164	65.6	1.65	13
Average (A28−A29)	Double-sided tape	0.00633	15	4.10E−06	2.59E−08	0.18	1.74638	67.4	1.45	16

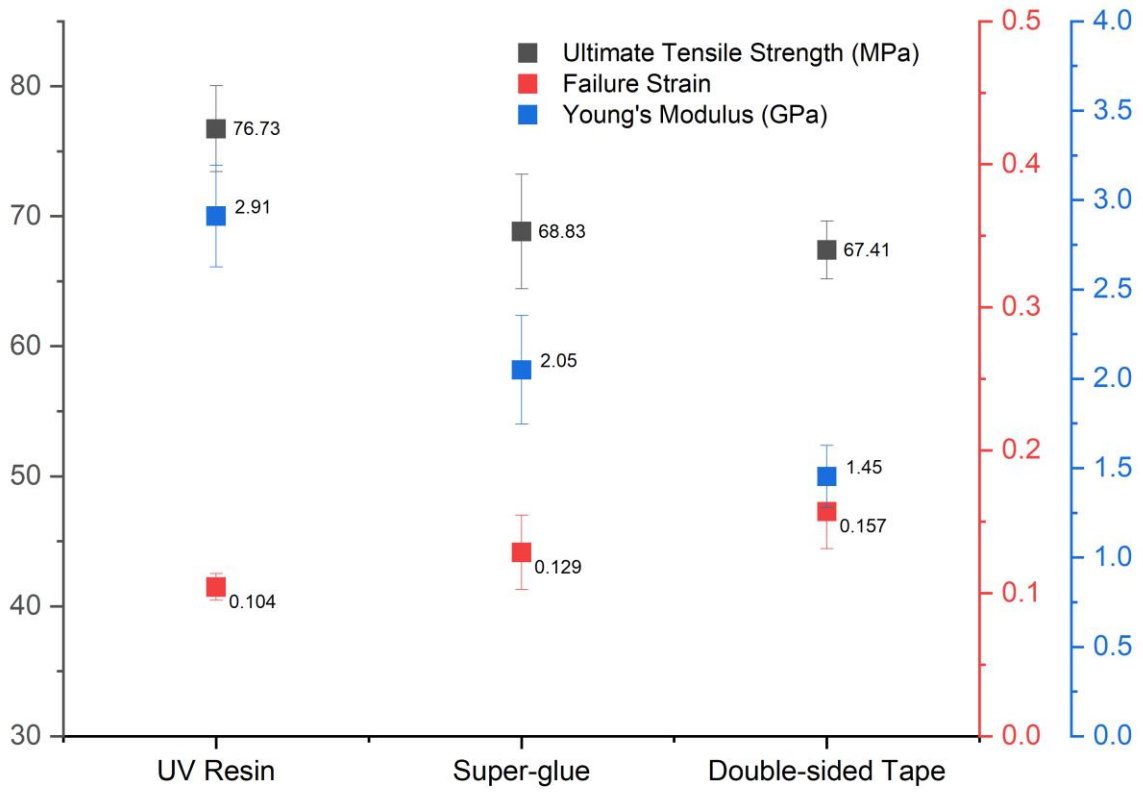

Figure 4.3.9 Summary of the tensile strength, Young's modulus and failure strain for aligned electro-spun PAN/DMSO nano-fibres with the end-tabs of super-glue, double-sided adhesive tape and a photo-curable UV resin.

<u>Overall Summary</u>

- Significant time and effort was dedicated to developing an end-tabbing method which was consistent and repeatable. A key requirement was to ensure that the resin did not wick into the gauge length section of the nano-fibre array.
- UV resin with PET end-tabs in the form of a conventional window frame-based fixture was used for the tensile tests.

- There were no indications of slippage during the test.
- A minimum of 3 tensile samples were tested per batch of 10 specimens produced.

4.3.4. Tensile Testing of Randomly Oriented Electro-spun PAN Nano-fibres

A set of ten (R1 to R10) as-spun randomly aligned PAN nano-fibre specimens were prepared and tested. The width, thickness and weight of the nano-fibre mat were measured prior to the test, as summarised in Table 4.17. The stress–strain curves for each test are shown in Figure 4.3.12. As in the previous section, Young's modulus was measured at 0.015 (1.5%) strain. Using R5 as an example, the linear fit is obtained at 0.015 strain with an equation of y=587.22x+0.66 with R^2=0.979. In addition, the Young's modulus was calculated to be 586.14 MPa.

Although the processing conditions of the electro-spun fibres was controlled as precisely as practically possible, the results show significant scatter. Still, the overall trends of most of the specimens are similar. From Figure 4.3.10, using specimen R5 as an example, the graph can be divided into four regions. In region 1, a relatively linear elastic behaviour up to 0.02 strain is followed by a slight drop in stress. The randomly oriented fibre strip starts to neck and elongate. As the displacement increases, Poisson's contraction becomes more prominent. The longitudinal extension and lateral contraction cause some 'wrinkles' to form on the specimen, as shown in Figure 4.3.10b. This was possibly due to one or more of the following: (i) Since the fibres were oriented randomly, as the loading increased, the off-axis fibres tried to rotate towards the vertical loading axis. As a result, a variable tension was imposed on the filaments, leading to non-uniform extension in the axial, lateral and through-thickness directions. (ii) While the application of the UV resin was controlled each time visually at a microscopic level,

the possibility of some of the resin wicking into the gauge length region cannot be ruled out completely, resulting in the non-uniform loading of the filaments.

In region 2, the stress increases slowly to 0.17 strain, where yielding is observed. The sample extends without an increase in the load. With conventional solid polymers (not electro-spun), the neck grows in this region. Upon inspection of Figure 4.3.10c, lateral contraction and extension of the sample occur over the whole gauge length, as opposed to the growth of the neck at the expense of the un-drawn regions (as seen in commercial polymers). Furthermore, in region 3, the stress continues to increase as a function of the displacement. The slopes in regions 1 and 3 are 0.59 and 0.04 GPa, respectively.

An interesting observation in region 3 was the disappearance of the so-called 'wrinkles' with increasing displacement, which is possible because of (i) the significant forced reorientation of the filaments with increasing displacement and (ii) a considerable reduction in the intrinsic porosity within the test specimen due to the realignment of the off-axis fibres and Poisson's contraction. Evidence for this reorientation of the randomly oriented fibres in a specimen with applied load in region 3 is presented in Figure 4.3.10d. The SEM micrographs illustrated in Figure 4.3.11d were obtained after stopping the tensile test at the desired load/displacement point and unloading the sample from the machine. Therefore, some relaxation could have taken place after the specimen was unloaded.

Region 4 represents the gradual fracture of the filaments, generally between 0.9 and 1.1 strain (see Figure 4.3.12a). This gradual decrease in the load with extension is characteristic when bundles of fibres are tested in tension where the failure is sequential. All specimens were fractured at either the top or bottom necking point (see Figure 4.3.10f). Throughout the

process, Figure 4.3.11a–f (which corresponds to Figure 4.3.10a–f) shows that the post-fractured specimens displayed a higher degree of oriented fibres when compared to as-spun fibres. Of note, the SEM micrographs taken at the fracture point of the random fibres show a relatively low degree of alignment. This could be due to some relaxation and recoiling of the fibres near the fracture point of the specimen.

An expanded graph of Figure 4.3.12a between −0.05 to 0.35 strain is shown in Figure 4.3.12b. Clearly, samples R9 and R10 do not follow the trend described in the last paragraph. Elastic behaviour in region 1 is not observed in R10, and a slow increase in stress, typically observed in region 2, does not occur in R9 or R10. These results may be due to variations in the humidity during fibre production between each batch. These two specimens (R9 and R10) were manufactured from the batch with 14–16% RH, whereas others were produced at around 10–12% RH (owing to weather conditions). Higher humidity has been reported to result in a poor fibre–fibre connection, causing lower moduli [147]. Furthermore, the low evaporation rate of DMSO makes it more sensitive to environmental conditions during production.

The average fibre diameter of the randomly oriented nano-fibre before (Figure 4.3.11a) and after tensile testing (Figure 4.3.11f) decreased from 367.4 nm to 334.0 nm. However, the standard deviation increased from 50.3 nm to 54.4 nm. Moreover, the median also reduced from 370.8 nm to 323.4 nm. These values, again, illustrate the uneven stretching of individual fibres when tensile testing randomly oriented nano-fibre mat.

Figure 4.3.12a shows that the randomly oriented fibre bundles can be stretched by 90–110% relative to their original length. The average UTS was 28.1 ± 3.5 MPa with an average failure strain of 83 ± 6%. The Young's modulus was also calculated at 0.015 strain. The average

Young's modulus recorded was 0.49 ± 0.14 GPa. This is similar to that reported by Karim *et al.* [220] when using 10 wt% PAN and 1 wt% MWCNT in DMF where the UTS was 122 MPa and the Young's modulus was 0.4 GPa. In addition, Huang *et al.* [147] reported maximum UTS and Young's modulus obtained were 6.25 MPa and 0.095 GPa, respectively, when spinning PAN/DMF at 20% RH. On the other hand, the maximum Young's modulus obtained by Balan *et al.* [38] for PAN/DMF was only 0.3 MPa, which is significantly lower than those reported by other researchers. The differences in tensile test results reported by various researchers, as well as the result obtained from this current study, particularly in Young's modulus, indicates the need for a standardised methods for material and solvent selection, nano-fibre production and the subsequent techniques used for sample preparation and testing. One possible reason can be a difference in packing density and porosity of the electro-spun nano-fibre mat due to processing [455, 456] and environmental conditions [147] during fibre production. Furthermore, because the tensile properties of the random fibre mat are predominantly affected by the friction and interaction between fibres when they re-orient themselves under tension [351], the low packing density may lead to lower fibre–fibre interaction and, therefore, lower tensile properties. Another reason may be the method used to determine the cross-sectional area, which is neither straightforward nor standardised throughout the literature reviewed [38, 147, 457, 458]. A detailed summary of the electro-spinning conditions and characterisation method of specimen density for nano-fibre bundle tensile testing obtained by various researchers can be found in Appendix B.

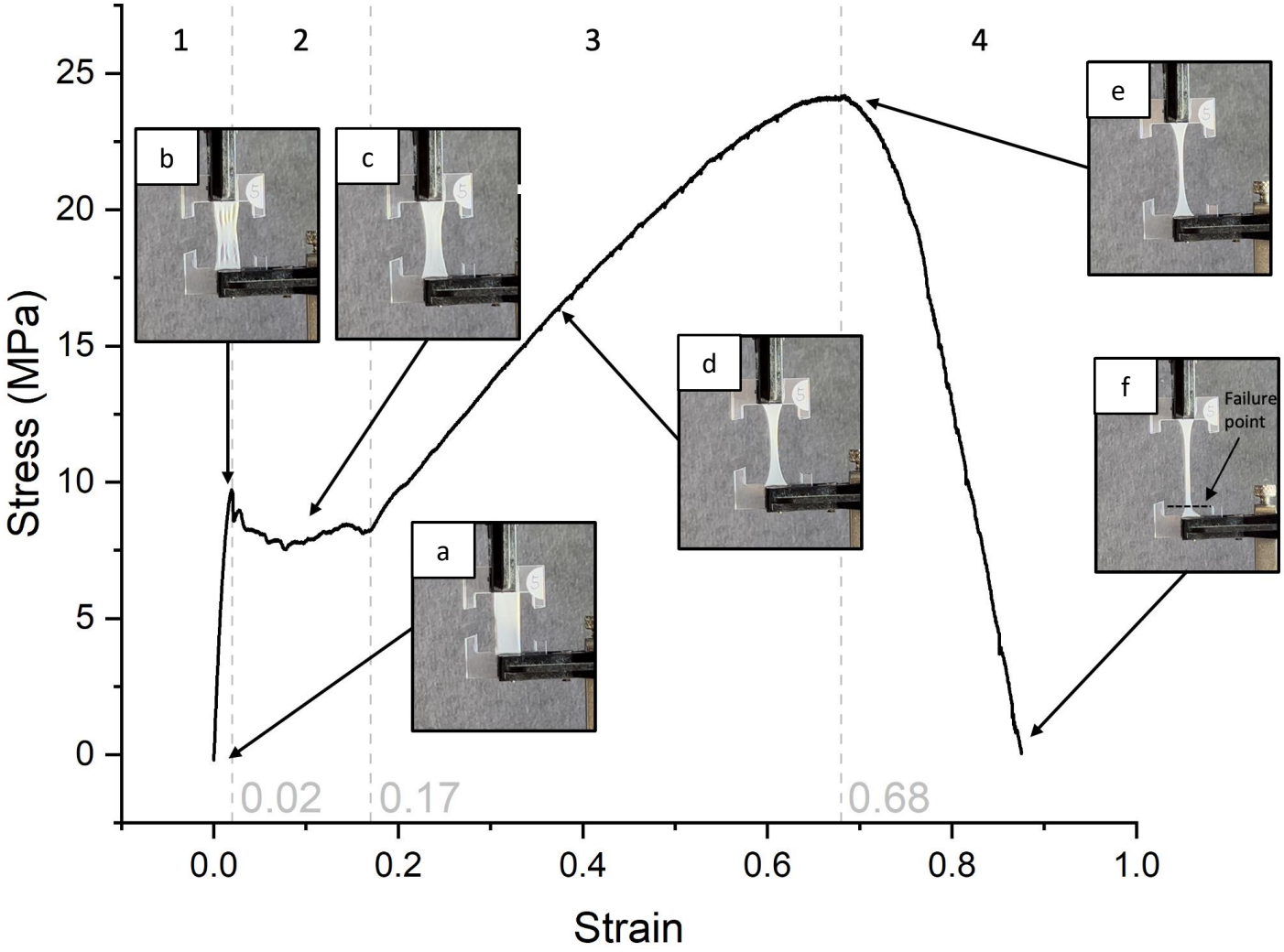

Figure 4.3.10 Stress−strain trace for sample R5. The coded items are described in the text.

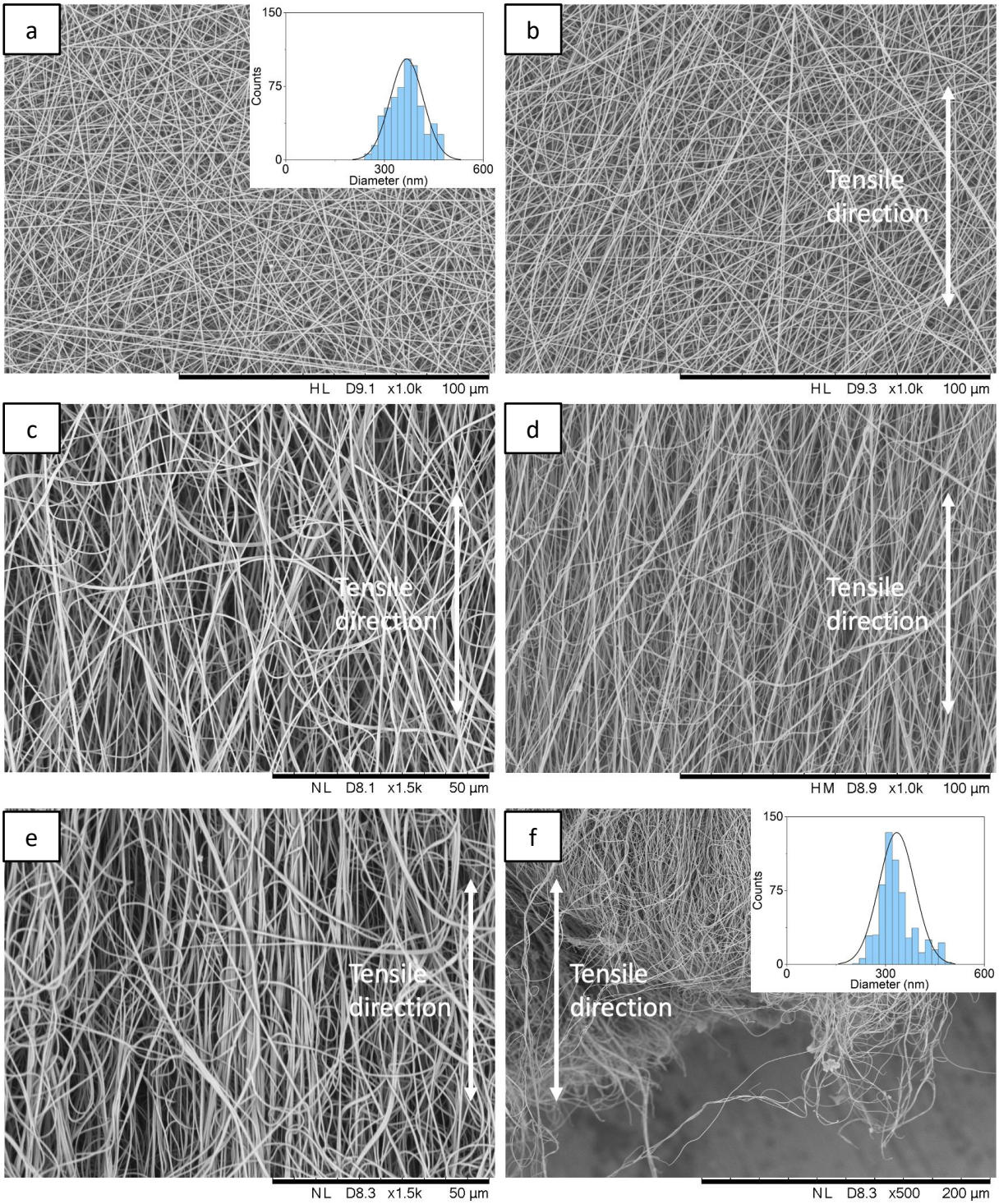

Figure 4.3.11 (a–f) SEM micrographs corresponding to photos (a–f) in Figure 4.3.10. Fibre diameter distribution of (a) and (f) are overlaid on the corresponding SEM micrograph.

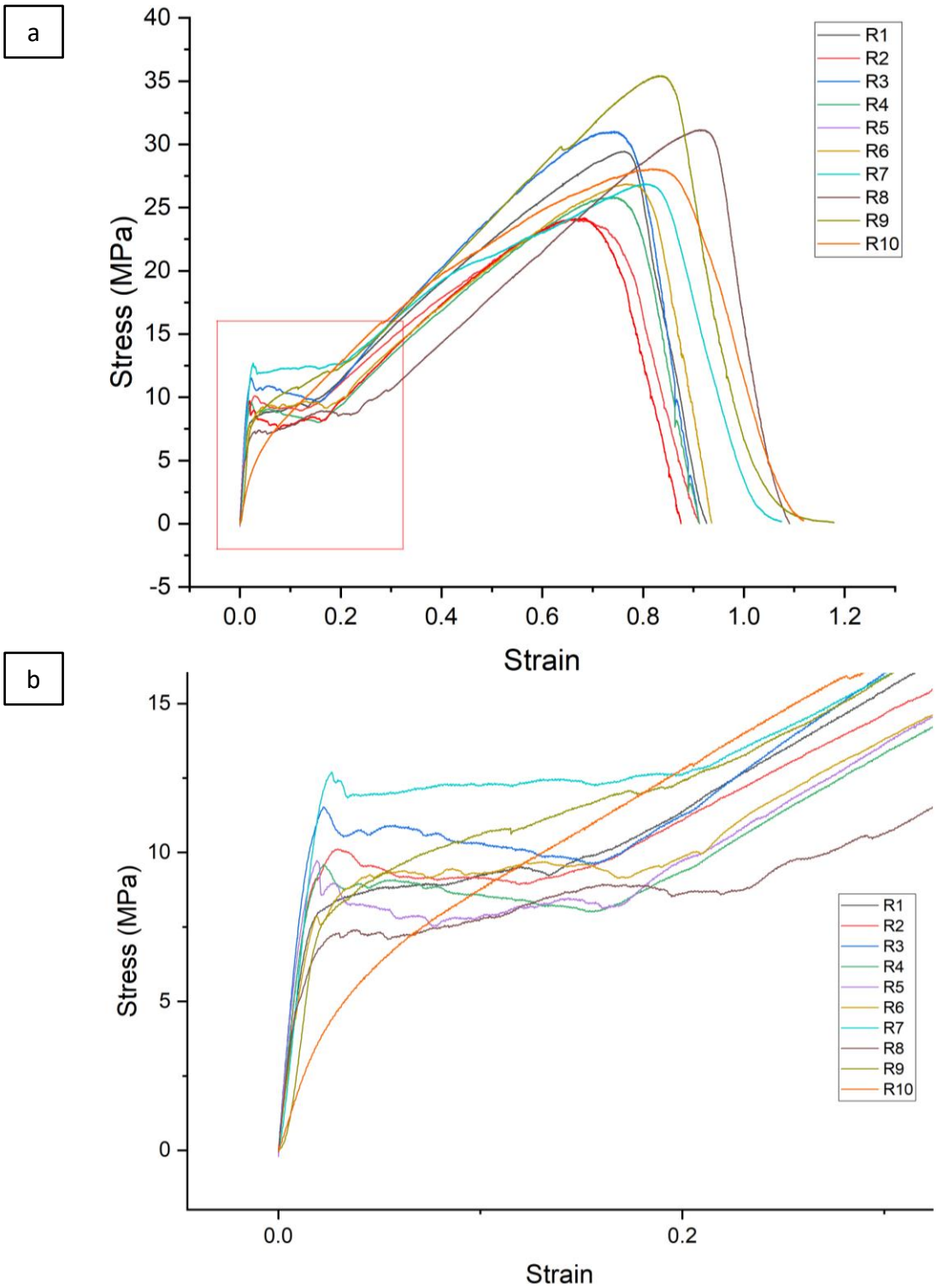

Figure 4.3.12 (a) Stress–strain traces for the randomly oriented fibre bundles. (b) Zoomed in of the left part of the traces from (a).

Table 4.17 Summary of the tensile test data for the randomly oriented electro-spun PAN/DMSO nano-fibre samples.

Random As-spun Fibres (Cross-head speed: 0.1 mm/minute; 99.0% DMSO)									
Sample Number	**Width (m)**	**Gauge Length (mm)**	**Thickness (m)**	**Cross-sectional Area (m^2)**	**Weight (mg)**	**Max Load (N)**	**UTS (MPa)**	**Young's Modulus (GPa)**	**Failure Strain**
R1	0.005780	15	5.90E−06	3.41E−08	0.18	1.00432	29.5	0.48	0.88
R2	0.006880	15	5.80E−06	3.99E−08	0.18	0.96124	24.1	0.55	0.95
R3	0.005954	15	5.90E−06	3.51E−08	0.16	1.08938	31.0	0.66	0.89
R4	0.006362	15	6.10E−06	3.88E−08	0.17	1.00223	25.8	0.54	0.86
R5	0.007010	15	6.10E−06	4.28E−08	0.17	1.03197	24.1	0.59	0.79
R6	0.006298	15	6.10E−06	3.84E−08	0.17	1.03536	27.0	0.46	0.79
R7	0.006402	15	5.80E−06	3.71E−08	0.17	0.99723	26.9	0.60	0.83
R8	0.005366	15	5.90E−06	3.17E−08	0.17	0.98789	31.2	0.40	0.80
R9	0.005168	15	6.00E−06	3.10E−08	0.17	1.09877	35.4	0.38	0.75
R10	0.005780	15	6.00E−06	3.47E−08	0.17	0.97392	28.1	0.18	0.78
Average (R1−R10)	0.006100	15	5.96E−06	3.67E−08	0.17	1.01823	28.3	0.48	0.83

Overall Summary

- The majority of the samples were photographed, and a video was taken during the tensile tests.
- In the case of the randomly oriented electro-spun samples, typical necking and extension was observed.
- An interesting observation was made in that the degree of fibre orientation was higher after testing the samples to failure. This is attributed to the randomly oriented fibres rotating and attempting to align themselves during tensile loading.

4.3.5. Tensile Testing of As-spun Aligned PAN Nano-fibres

This section reports the tensile testing of aligned as-spun PAN nano-fibres. All tensile test specimens were prepared using the procedures described in Section 3.4, with the Vee shield in place. The effect of solvent purity when producing the aligned electro-spun fibres and the cross-head displacement rate on the tensile properties are presented. Figure 4.3.13 shows the stress–strain traces of ten aligned electro-spun PAN nano-fibre specimens prepared using 99.0% purity DMSO supplied by Fisher Scientific. The experiments conducted with two classes of solvents are summarised in Table 3.1 in Section 3.5.13. As described in Section 4.3.3, the thickness and width of each nano-fibre specimen in this set of experiments were measured using a micrometre screw gauge and Image-J using micrographs, respectively. The dimensions and test results for each specimen are presented in Table 4.18. Again, Young's moduli were determined at 0.015 (1.5%) strain. The tensile results of the aligned fibres show significant

scatter with a similar overall trend to the random fibres, possibly caused by the fluctuation of environmental conditions inside the electro-spinning chamber during production.

As shown in Figure 4.3.13, using A8 as an example, the tensile test trace of the aligned PAN nano-fibre can be separated into four regions. Region 1 shows a relative linear elastic behaviour within 0.015 strain, typical behaviour for this. In region 2, the stress increases with strain, causing the fibre to begin plastic deformation with strain hardening. As described in Section 2.3.2, strain-hardening (cold-drawing) results in the polymer chains beginning to stretch and becoming more oriented along the direction of deformation [234, 239, 278, 282, 292].

The lateral contraction caused by longitudinal extension can be observed in Figure 4.3.13b. However, it is less evident than the contraction observed from random specimens in Figure 4.3.10. The corresponding SEM micrographs (Figure 4.3.14a–d) show that the gap between each fibre was reduced with fewer misaligned fibres. The likely reason for lateral contraction observed in this region (Figure 4.3.12b) is that off-axis fibres become reorientated when intersecting with other fibres. In region 3, as shown in Figure 4.3.13c, the lateral contraction becomes more evident. Although necking is typically observed in this region, this was not the case for this experiment, according to the SEM micrographs. Alternatively, fibres might have started to fail individually. Possible reasons include (i) fibres with small diameters failing sooner than those with larger diameters or (ii) uneven distribution of stress along the fibres. Therefore, the failure strain was determined at the UTS. After 0.45 strain, in region 4, most of the bundle starts to fail simultaneously, but at a random position inside the gauge length (see Figure 4.3.13d) within a short strain range of 0.4 and 0.6 strain (see Figure 4.3.15a).

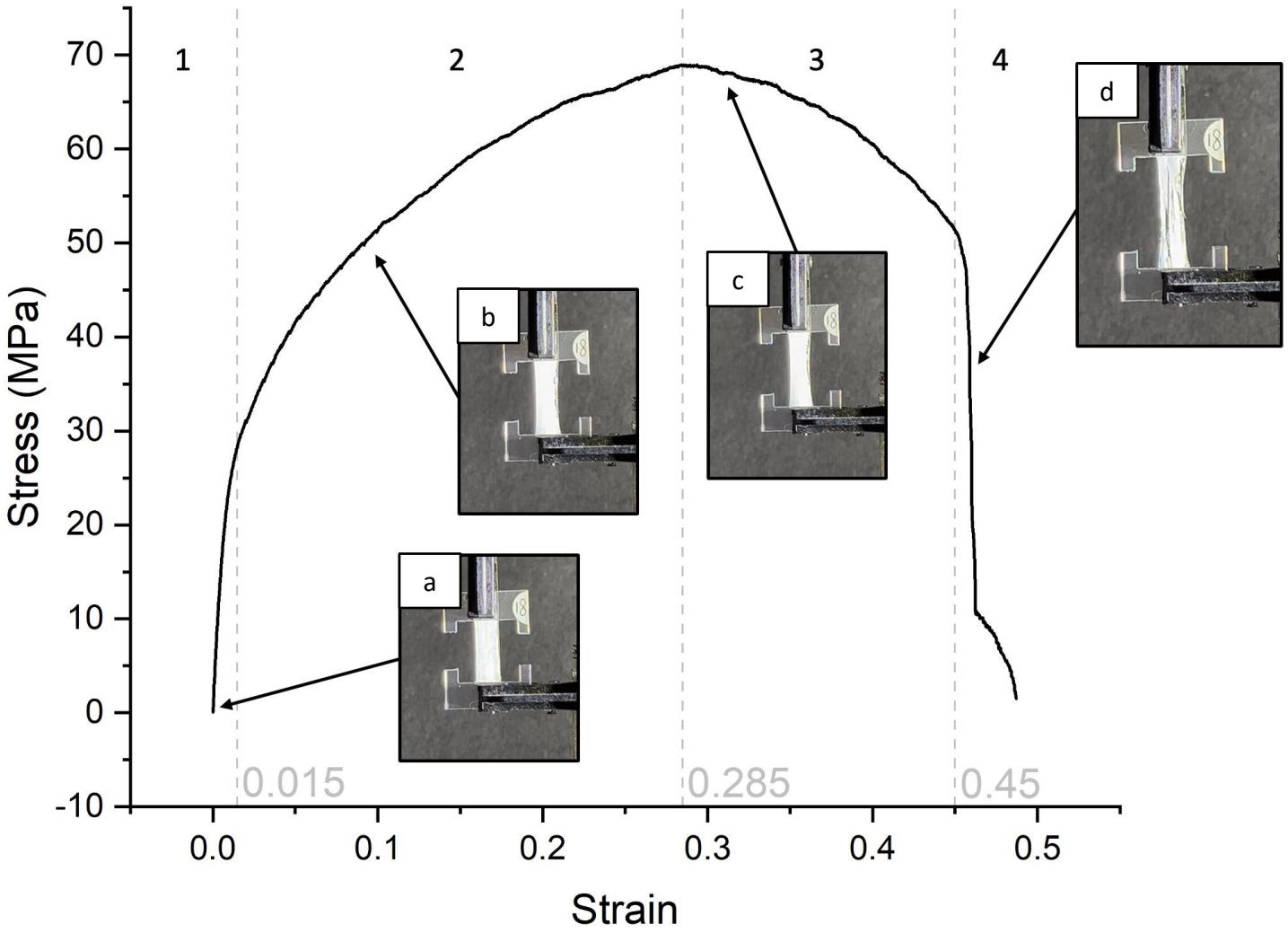

Figure 4.3.13 Stress−strain trace for sample A8. The coded items are described in the text.

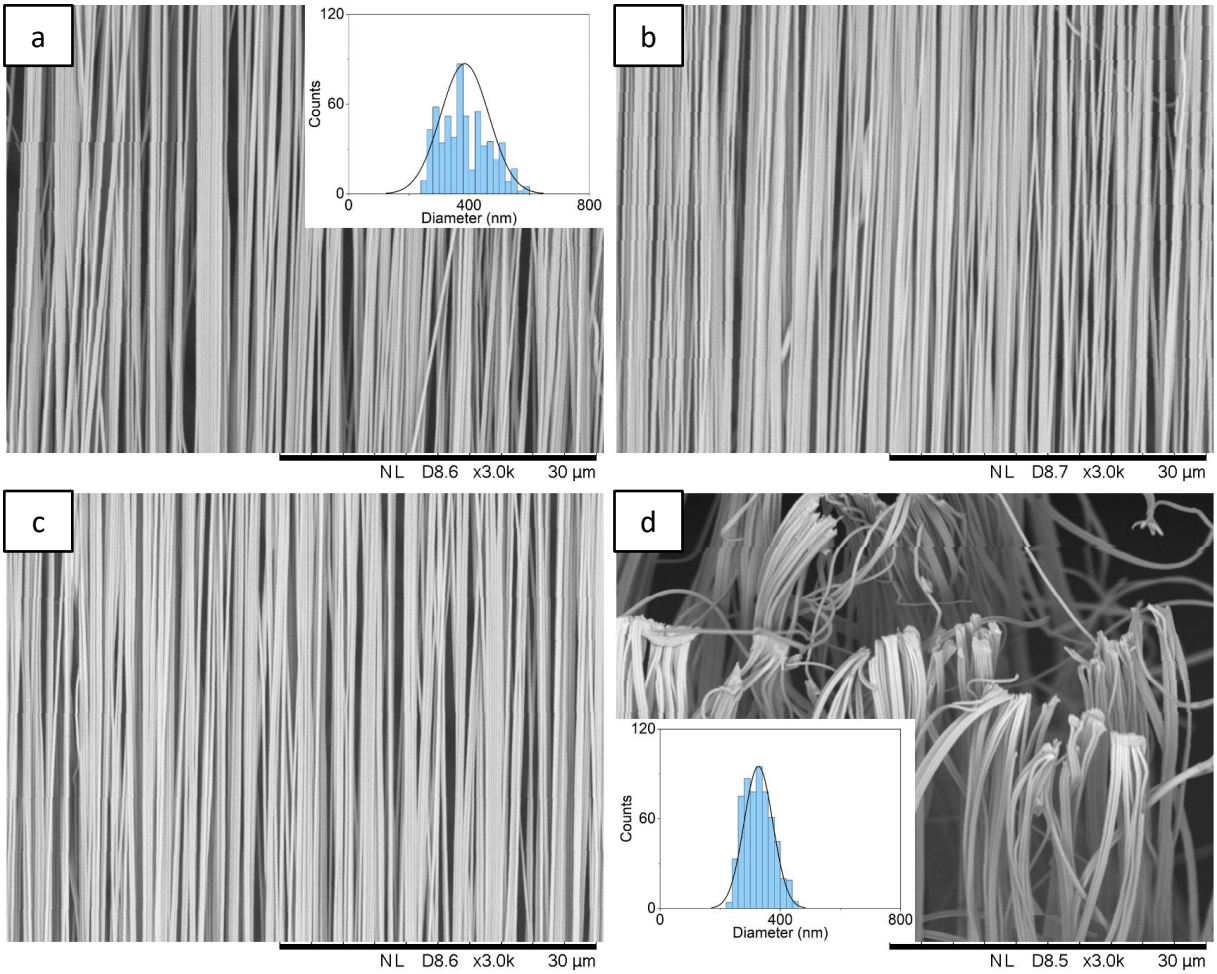

Figure 4.3.14 (a−d) SEM micrographs corresponding to the photo (a−d) in Figure 4.3.13. Fibre diameter distribution of (a) and (d) are overlaid on the corresponding SEM.

Furthermore, the SEM micrograph of the fractured fibre ends is shown in Figure 4.3.12d. The diameter distributions before (Figure 4.3.14a) and after (Figure 4.3.14d) tensile testing indicate a narrowing with standard deviations of 80.1 nm and 47.7 nm, respectively. The average fibre diameter decreases from 385.5 nm to 327.2 nm.

For equivalent weights of specimens, the thickness of the aligned fibre test specimens was an average of 30% thinner than the randomly oriented fibre bundles. This show that the intrinsic porosity in the aligned fibre bundles is reduced significantly. Figure 4.3.15b shows a relatively

linear elastic region for the aligned fibre bundles, followed by plastic deformation from approximately 3–30% strain. The stress of the fibre array increases gradually to a maximum value of around 70 MPa at about 0.3 strain. The average Young's modulus at 0.015 strain is 2.07 ± 0.14 GPa. The average tensile failure stress and strain for the aligned electro-spun PAN fibres are 69.2 ± 12.0 MPa and 0.26 ± 0.04, respectively. A summary of the tensile data for the aligned electro-spun PAN nano-fibre bundles is presented in Table 4.18. Referring to Figure 4.3.15, in two of the samples, intermittent load drops are observed, leading to their ultimate failure stresses. After the UTS is reached, the general trend is the stress decreasing gradually, but stepwise, as a function of the extension. The observed load drops are possibly due to variable tension in the specimen introduced at the end-tabbing stage.

The UTS and Young's modulus of the aligned PAN/DMF nano-fibre array using parallel electrodes reported by Jalili *et al.* [36] were 99 MPa and 2.79 GPa, respectively. Similar results were also represented by Moon *et al.* [39] when using a high-speed rotating mandrel at a linear velocity of 9.8 m/s, they reported a UTS of 78.5 MPa and Young's modulus of 4.3 GPa. The results reported in the literature show higher UTSs and Young's moduli than that reported in this current study but with the same magnitude. A likely reason for this is because of the different solvents used (DMF compared to DMSO used in this study). Recalling the results of higher-purity DMSO aligned electro-spun fibre (A21–A23) illustrated in Section 4.3.3, Figure 4.3.8a, the average tensile test result of the aligned fibre can be affected not only by the type of solvent but also the purity of the solvent. A higher-purity solvent yielded an 11% higher UTS, 40% higher Young's modulus and 40% lower failure strain, perhaps caused by the impurities in the solvent, which affect the fibre formation during electro-spinning. Further experiments are needed to verify this assumption.

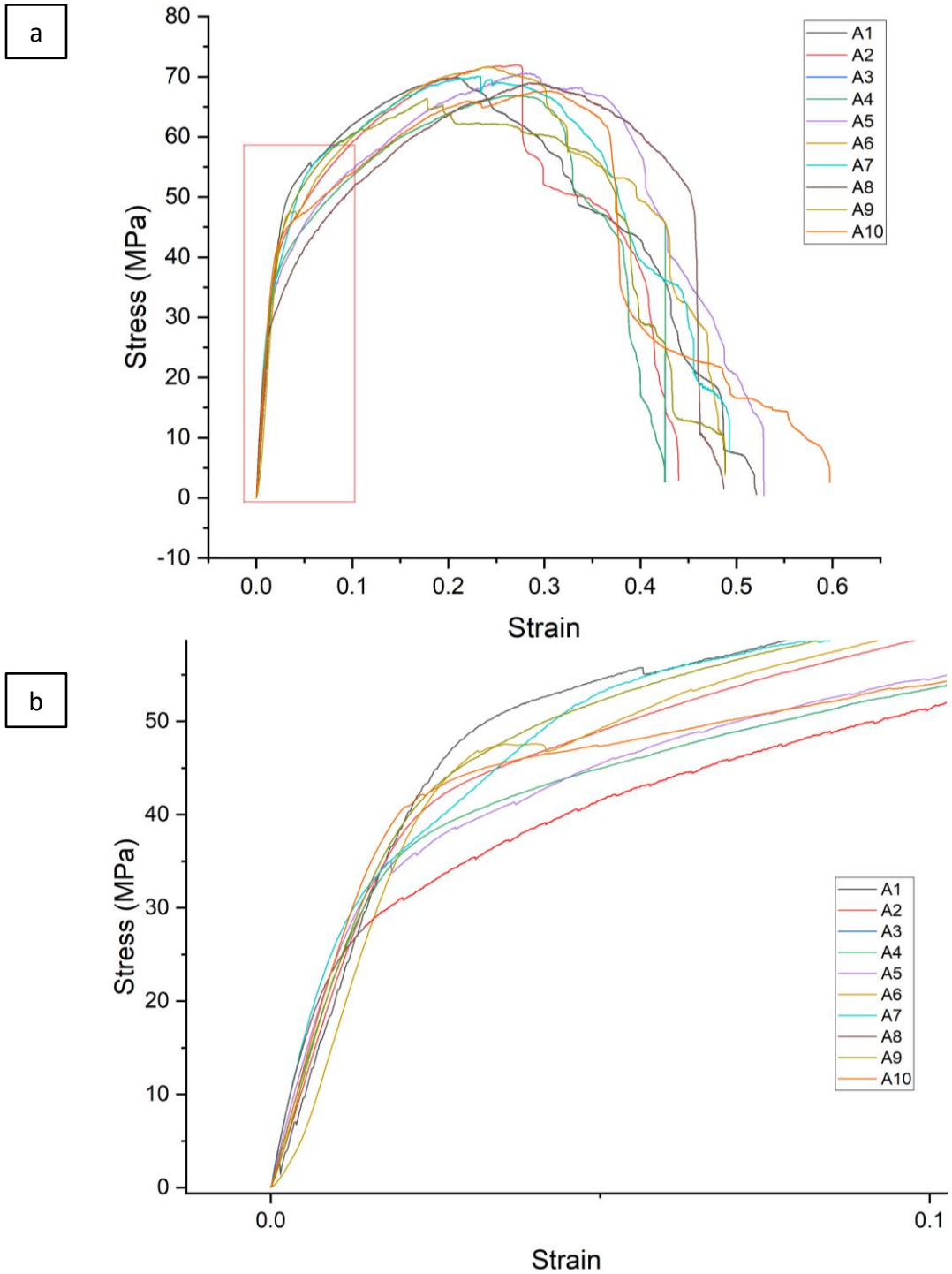

Figure 4.3.15 (a) Stress–strain plots for the aligned electro-spun PAN nano-fibre bundles. (b) Zoomed in of the left part of the traces from (a).

Table 4.18 Summary of the tensile test data and properties for the aligned electro-spun PAN nano-fibres.

Aligned as-spun fibres (Cross-head speed: 0.1 mm/minute; 99.0% DMSO)									
Sample Number	**Width (m)**	**Gauge Length (mm)**	**Thickness (m)**	**Cross-sectional Area (m^2)**	**Weight (mg)**	**Max Load (N)**	**UTS (MPa)**	**Young's Modulus (GPa)**	**Failure Strain (%)**
A1	0.006108	15	4.00E−06	2.44E−08	0.17	1.70816	69.9	2.06	21
A2	0.006018	15	3.90E−06	2.35E−08	0.18	1.68891	72.0	2.10	27
A3	0.005970	15	4.20E−06	2.51E−08	0.17	1.69917	67.8	1.90	28
A4	0.005970	15	4.10E−06	2.45E−08	0.17	1.63697	66.9	2.08	27
A5	0.006508	15	3.70E−06	2.41E−08	0.16	1.69998	70.6	2.14	28
A6	0.006310	15	4.10E−06	2.59E−08	0.18	1.85193	71.6	1.85	24
A7	0.005526	15	4.60E−06	2.54E−08	0.17	1.78227	70.1	2.17	23
A8	0.005802	15	4.30E−06	2.49E−08	0.18	1.72052	69.0	1.90	29
A9	0.005476	15	4.40E−06	2.41E−08	0.15	1.59942	66.4	2.16	18
A10	0.006158	15	4.10E−06	2.52E−08	0.17	1.70726	67.6	2.31	31
Average (A1−A10)	0.005985	15	4.14E−06	2.47E−08	0.17	1.70946	69.2	2.07	25

In contrast with the tensile test result of the randomly oriented PAN nano-fibre bundles reported in Section 4.3.4, the results of the aligned fibres are superior (see Figure 4.3.16 and Figure 4.3.17). The UTSs of the aligned fibres are 2.4 times higher, and Young's modulus is four times greater than the corresponding values for the randomly oriented fibre bundles. As a result, the failure strains for the aligned and randomly oriented bundles are 0.26 ± 0.04 and 0.83 ± 0.06, respectively. The failure strain, on the other hand, is higher for the randomly oriented specimens. This result is reasonable as off-axis fibres can rotate and realign towards the loading axis, enabling a higher extension to failure.

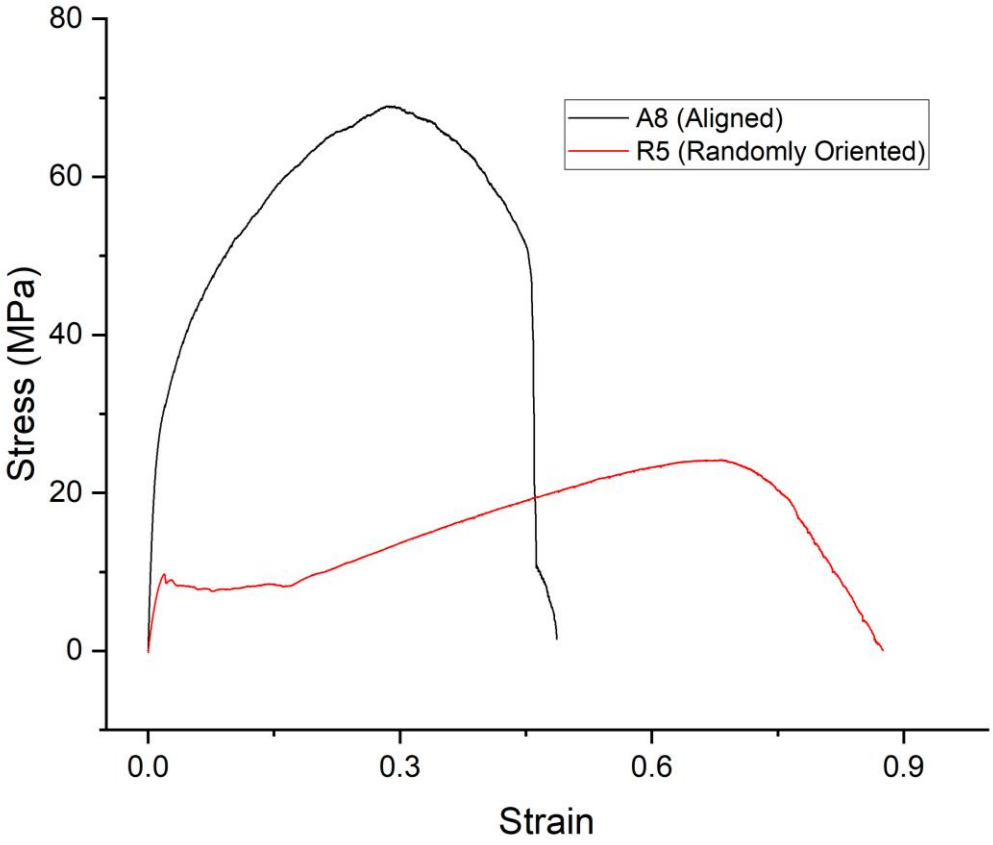

Figure 4.3.16 Comparison of the representative stress–strain trace of PAN-based electro-spun fibre specimens that were randomly oriented (R5) and aligned (A8).

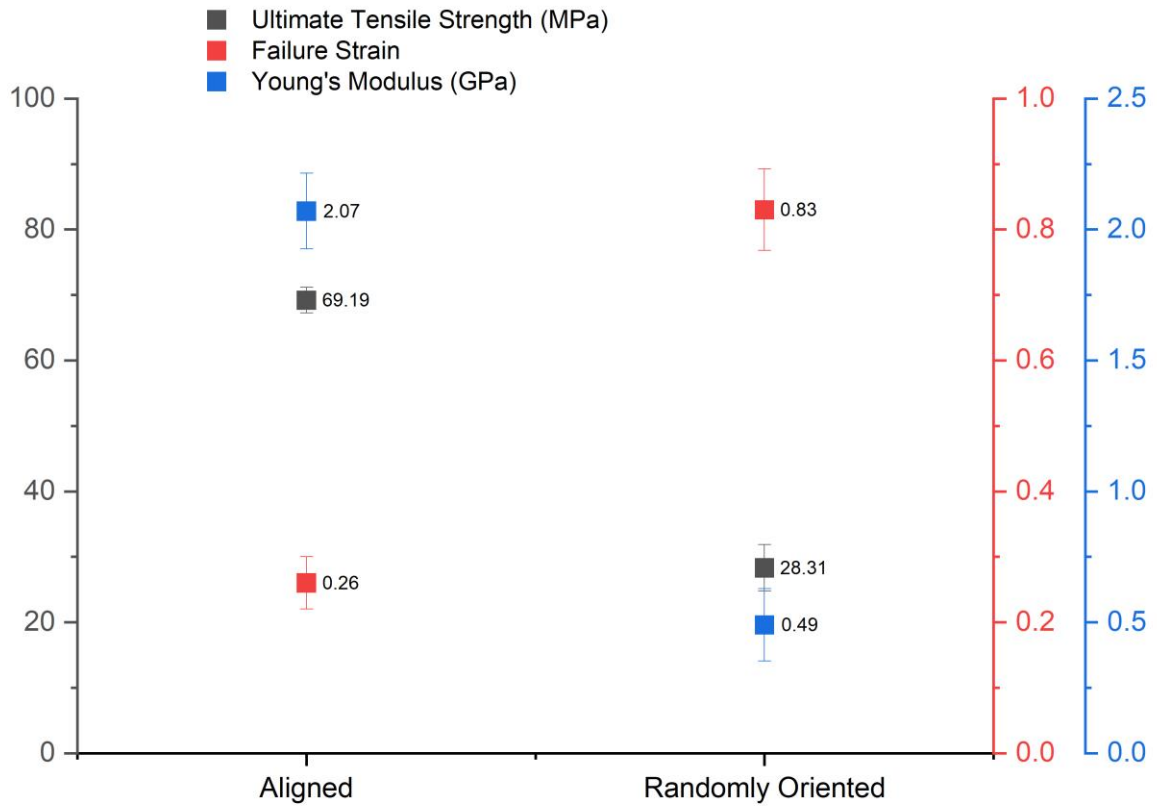

Figure 4.3.17 Comparison of the tensile properties of the aligned and randomly oriented fibre bundles.

<u>Overall Summary</u>

- It was demonstrated conclusively that the aligned electro-spun PAN fibres have superior Young's moduli and ultimate failure stress when compared to the randomly oriented fibre samples.

4.3.6. Improving the Tensile Properties of the Aligned Nano-fibres by Cold-Drawing

4.3.6.1. Effect of Pre-loading the Aligned PAN Nano-fibre Bundles on the Tensile Properties

As discussed in the literature review in Section 2.3.2, the mechanical properties of polymer fibres can be improved through cold-drawing [164, 276]. Drawing or pre-stretching the aligned fibre will increase the molecular alignment primarily in the amorphous regions [40, 285] within the polymer chain leading to an increase in the tensile properties [35-37, 84, 234, 237, 284]. Ten samples of the aligned nano-fibre were prepared using the lower purity (99.0%) DMSO. They were pre-stretched to 27% strain which corresponds to a displacement of approximately 4 mm. The cross-displacement rate was 0.1 mm/minute. The temperature and RH were 24 ± 2 °C and 2 ± 4%, respectively. The fibre bundle was held under these conditions for two hours. From the stress-relaxation traces shown in Figure 4.3.19, the stress-relaxation under a displacement of 4 mm was approximately 30% during the first ten minutes. The average total stress relaxation after two hours was 39 ± 6%. A summary of the relevant parameters for this series of pre-load tests are summarised in Table 4.19. Samples AP6 and AP4 show the highest and lowest stress relaxation (55% and 33%, respectively) during the hold-period. When the sample is loaded and the strain kept constant, stress relaxation occurs at a molecular level through molecule movement (segmental motion or viscous flow) [459-461], rotation and rearrangement of the molecule chain when stress is released [462]. The aligned PAN nano-fibres shows the characteristic of a viscoelastic material [463], and shows a similar trend to dry-spun and gel-spun PAN fibres as reported by Tan *et al.* [464].

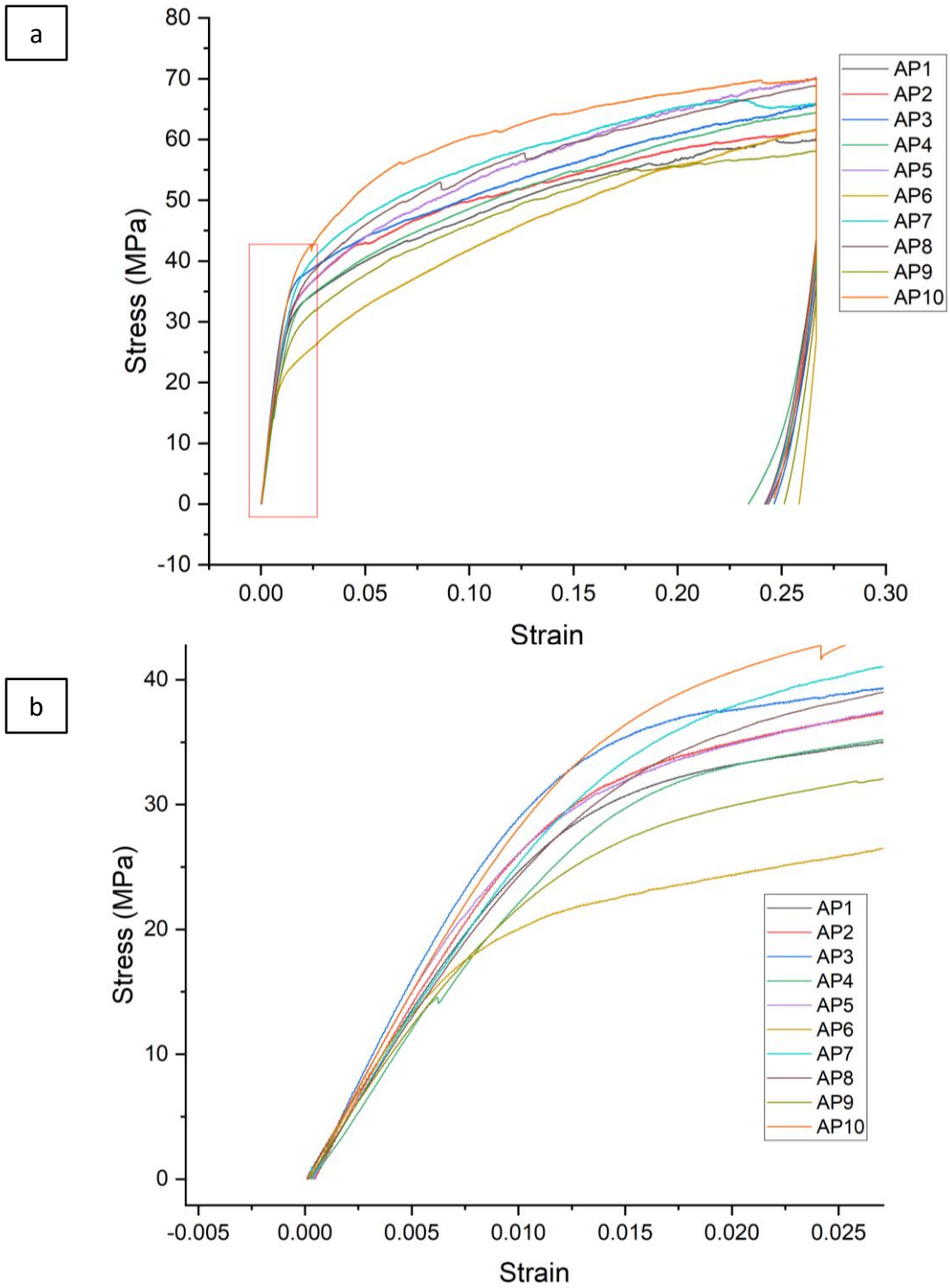

Figure 4.3.18 (a) Stress−strain traces for the aligned electro-spun PAN nano-fibre bundles that were loaded to a displacement of 4 mm and unloaded. The corresponding stress-relaxation traces are shown in Figure 4.3.19 (below). (b) Zoomed in of the left part of the traces from (a).

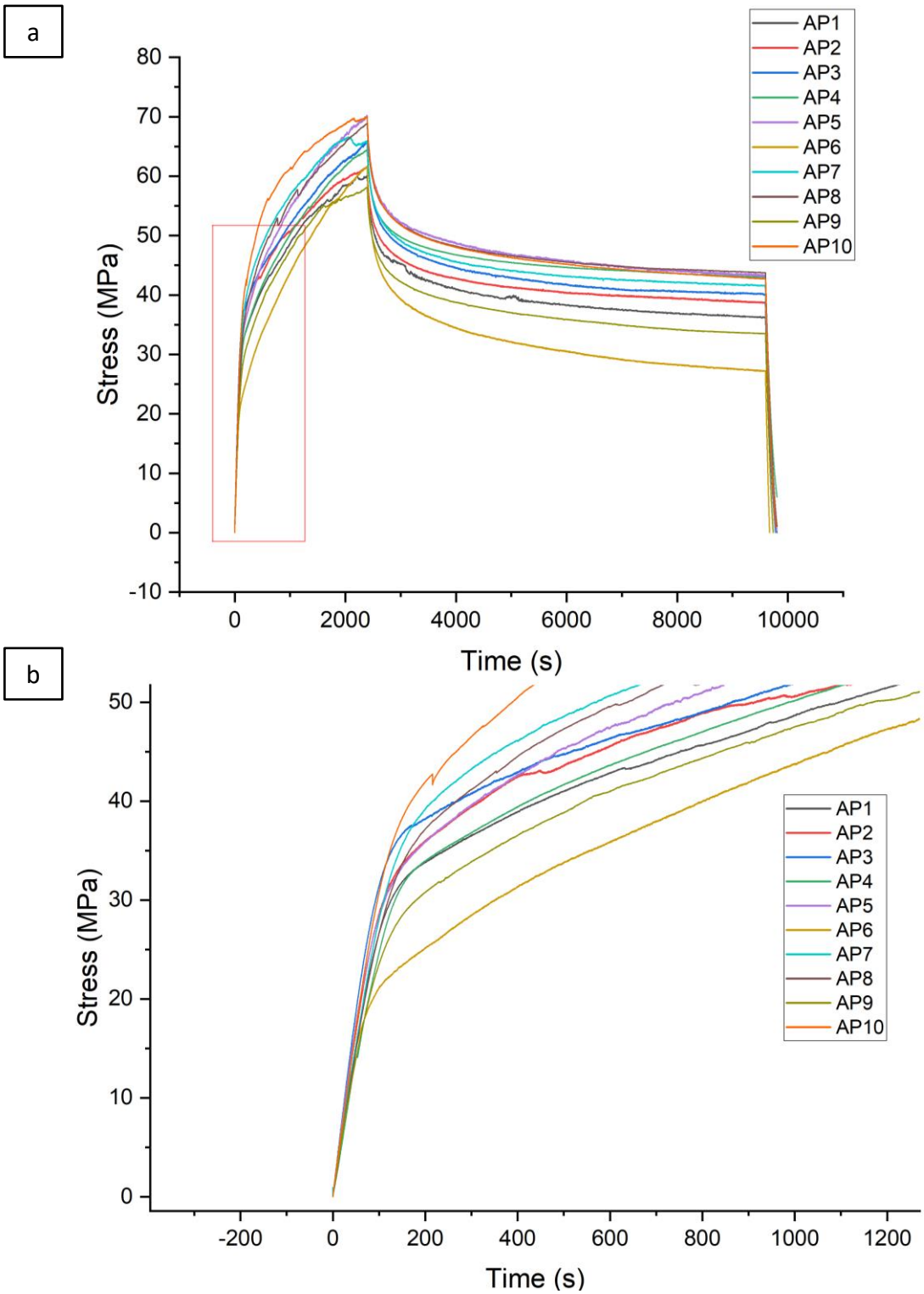

Figure 4.3.19 Stress-relaxation traces for the pre-loaded samples from Figure 4.3.18 (above).

(b) Zoomed in of the left part of the traces from (a).

Table 4.19 Summary of the test specimen details and the pre-loading conditions where the samples were loaded to a displacement of 4 mm, held at this displacement for two hours before unloading and re-loading to failure.

Preloading and Holding Aligned As-spun Fibres to 4 mm (Cross-head speed: 0.1 mm/minute; 2h holding time) (99.0% DMSO)										
Sample Number	**Width (m)**	**Gauge Length (mm)**	**Thickness (m)**	**Cross-sectional Area (m^2)**	**Weight (mg)**	**Max Load when Pre-load (N)**	**Load Drop when Holding (N)**	**UTS when Pre-load (MPa)**	**Stress Decay when Holding (MPa)**	**Stress Decay in %**
AP1	0.006666	15	4.30E−06	2.87E−08	0.17	1.72728	0.678	60.3	23.7	39%
AP2	0.006518	15	3.80E−06	2.48E−08	0.16	1.56632	0.570	63.2	23.0	36%
AP3	0.006028	15	4.10E−06	2.47E−08	0.17	1.65888	0.631	67.1	25.5	38%
AP4	0.006352	15	4.10E−06	2.60E−08	0.17	1.69914	0.559	65.2	21.5	33%
AP5	0.005462	15	4.20E−06	2.29E−08	0.16	1.64340	0.612	71.6	26.7	37%
AP6	0.006336	15	4.20E−06	2.66E−08	0.16	1.66818	0.916	62.7	34.4	55%
AP7	0.005758	15	4.00E−06	2.30E−08	0.17	1.55392	0.562	67.5	24.4	36%
AP8	0.005756	15	4.20E−06	2.42E−08	0.17	1.67617	0.606	69.3	25.1	36%
AP9	0.006358	15	4.20E−06	2.67E−08	0.16	1.56861	0.656	58.7	24.6	42%
AP10	0.005758	15	3.60E−06	2.07E−08	0.16	1.45086	0.566	70.0	27.3	39%
Average (AP1−AP10)	0.006099	15	4.07E−06	2.48E−08	0.17	1.62128	0.636	65.6	25.6	39%

Table 4.20 Summary of the extension for each specimen when the stress was released.

Stress Unload of Preloaded Aligned As-spun Fibres to 0 (Cross-head speed: 0.1 mm/minute)			
Number	**Stress Unload Distance (mm)**	**Stress Unload Distance in %**	**New Gauge Length (mm)**
AP1	0.34447	9%	18.66
AP2	0.39845	10%	18.60
AP3	0.32569	8%	18.67
AP4	0.50850	13%	18.49
AP5	0.36799	9%	18.63
AP6	0.12641	3%	18.87
AP7	0.35197	9%	18.65
AP8	0.37115	9%	18.63
AP9	0.26722	7%	18.73
AP10	0.30656	8%	18.69
Average (AP1−AP10)	0.33684	9%	18.66

At the end of the hold period, the load was returned to 'zero' by unloading the sample at 0.1 mm/minute. After the load was returned to zero, the pre-stretched specimens were subjected to the regular tensile test, where the sample was loaded to failure at 1 mm/minute.

Figure 4.3.20 illustrates the stress-strain traces for the aligned and pre-stretched nano-fibres. Specimens AP2, AP3, AP4 and AP10 show additional yielding after they were pre-stretched, unloaded and re-loaded to failure. Table 4.21 summarises the specimen dimensions and tensile test results for all the pre-loaded specimens after the stress was released. The average UTS, Young's modulus and failure strain are shown in Figure 4.3.21. In contrast with the samples that were not stretched, the average UTS increased by 6%, with the failure strain being 23% lower. The Young's modulus of the pre-stretched fibres attained an average of 2.74 ± 4.9 GPa, which is 24.4% higher than un-stretched fibre bundles and 2.25 GPa higher than the average Young's modulus of the randomly aligned fibre bundles. Similar findings have

been reported by a number of researchers, which has been reviewed in Section 2.3.2. They report that the tensile properties of electro-spun nanofibres can be improved either by increasing the take-up speed of the rotating mandrel or post-stretching [164, 166, 231, 233, 286, 287] the fibre mat after spinning [37, 84]. The improvement in the tensile test properties is a result of the increase in uniformity of the polymer chain [288] and molecular chain orientation during stretching [37, 84, 229, 292]. Thus it follows that pre-stretching the aligned nano-fibre can improve the tensile properties. However, further work is needed to optimise this process.

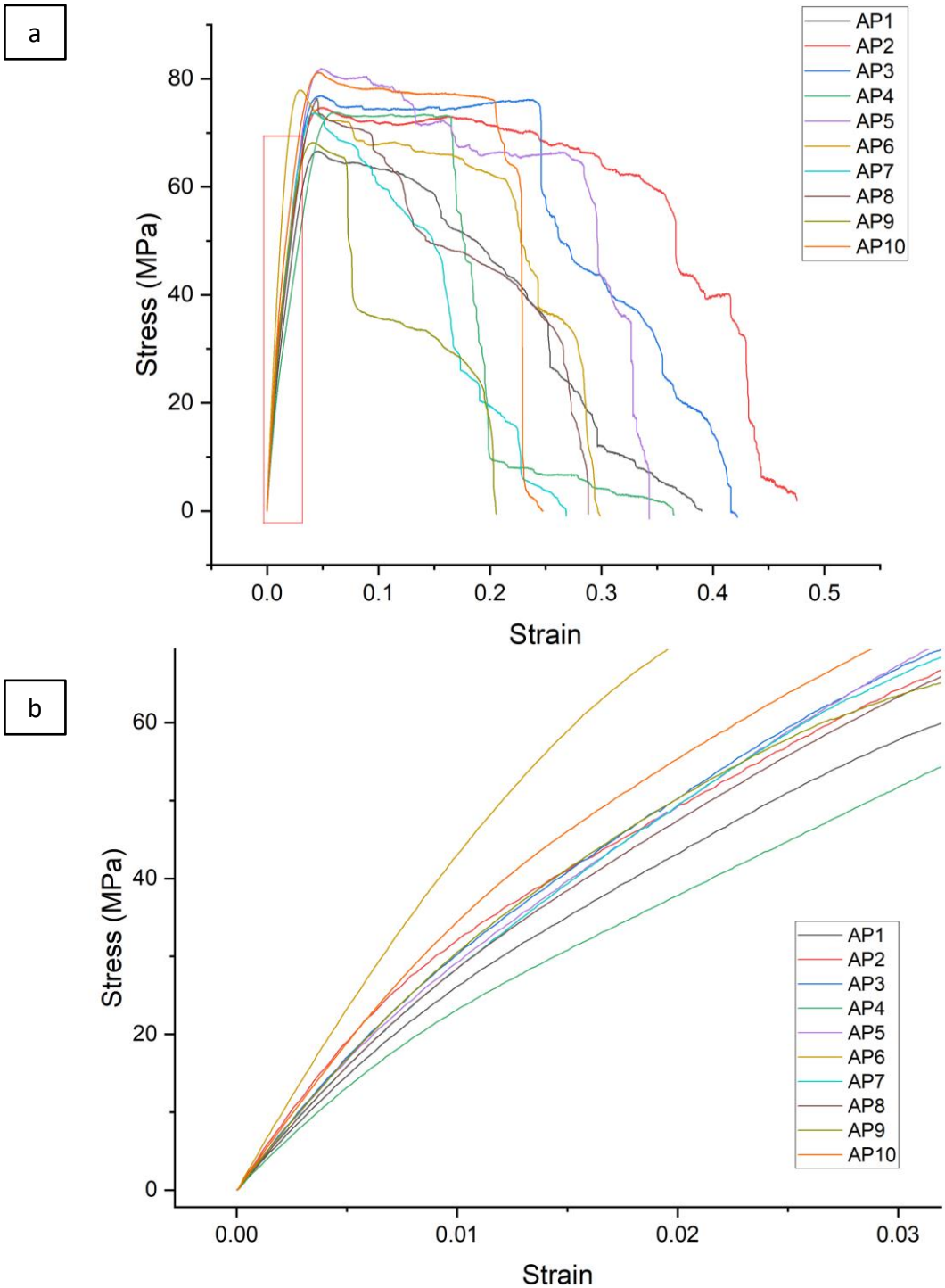

Figure 4.3.20 Stress−strain traces for the samples from Figure 4.3.18 that were loaded to a displacement of 4 mm, held for two hours, unloaded (see Figure 4.3.19) and re-loaded to failure (current Figure). (b) Zoomed in of the left part of the traces from (a).

Table 4.21 Summary of the relevant data and mechanical properties for the samples that were loaded to a displacement of 4 mm and held for two hours (see Figure 4.3.20), unloaded and reloaded to failure.

Tensile Test of Preloaded Aligned as-spun fibres (Cross-head speed: 1 mm/minute) (99.0% DMSO)									
Sample Number	**Width (m)**	**Gauge Length (mm)**	**Thickness (m)**	**Cross-sectional Area (m^2)**	**Weight (mg)**	**Max Load (N)**	**UTS (MPa)**	**Young's Modulus (GPa)**	**Failure Strain (%)**
AP1	0.006666	18.65553	4.30E−06	2.87E−08	0.17	1.90924	66.6	2.34	28
AP2	0.006518	18.60155	3.80E−06	2.48E−08	0.16	1.85010	74.7	2.74	36
AP3	0.006028	18.67431	4.10E−06	2.47E−08	0.17	1.89978	76.9	2.72	25
AP4	0.006352	18.4915	4.10E−06	2.60E−08	0.17	1.92255	73.8	2.05	17
AP5	0.005462	18.63201	4.20E−06	2.29E−08	0.16	1.87890	81.9	2.65	28
AP6	0.006336	18.87359	4.20E−06	2.66E−08	0.16	2.07383	77.9	3.93	17
AP7	0.005758	18.64803	4.00E−06	2.30E−08	0.17	1.69648	73.7	2.62	15
AP8	0.005756	18.62885	4.20E−06	2.42E−08	0.17	1.84515	76.3	2.56	9
AP9	0.006358	18.73278	4.20E−06	2.67E−08	0.16	1.82168	68.2	2.75	7
AP10	0.005758	18.69344	3.60E−06	2.07E−08	0.16	1.68246	81.2	3.07	21
Average (AP1−AP10)	0.006099	18.66315	4.07E−06	2.48E−08	0.17	1.85801	75.1	2.74	20

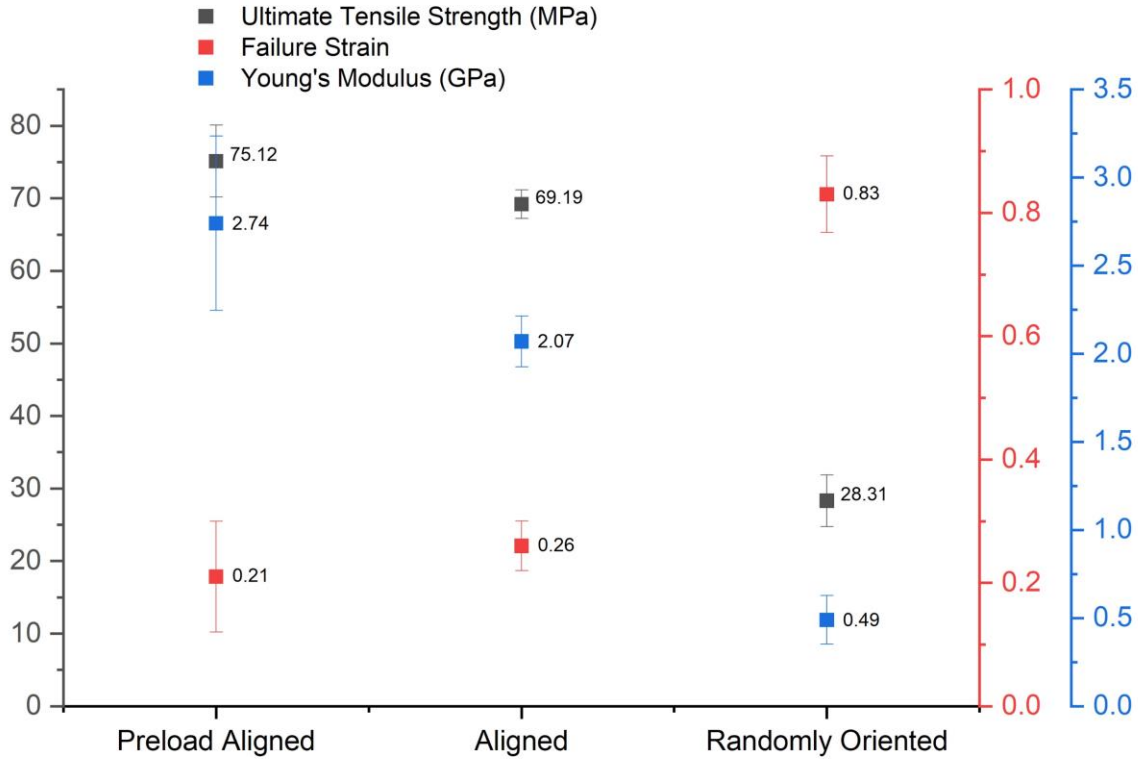

Figure 4.3.21 Comparison of the tensile properties of the pre-loaded and aligned, aligned without pre-load and the randomly oriented electro-spun PAN nano-fibre bundles.

4.3.6.2. Effect of the Pre-load Time on the Tensile Properties

In this set of experiments, due to the discontinuation of the low-purity DMSO solvent, the electro-spun nano-fibre were produced using higher purity DMSO (99.9%). As described in Section 0, the nano-fibres made with the higher purity DMSO had a higher Young's modulus with lower failure strain. On this occasion, with reference to the result reported in Table 4.16 and Figure 4.3.8 (Sample number A21−A23), the fibre prepared with high purity DMSO generally reached their UTS around 13.3% strain. Therefore, the pre-stretch displacement was altered from 4 mm to 2 mm as it was not possible to guarantee that all the test specimens would survive a displacement of 4 mm. The hold-periods for this set of experiments at a displacement of 2 mm were 1, 2 and 4 hours.

A further change was made to the test procedure in relation to the previous case where the load was released before reloading to failure. Here, the sample was not unloaded after the hold-period. Instead, it was loaded to failure immediately after the hold-period. This was done to minimise any further relaxation of the pre-stretched samples during the unloading phase.

Figure 4.3.23 illustrates the stress-relaxation during the hold-period at a displacement of 2 mm, which can be used to characterise the viscoelastic properties of the material [464, 465]. The dimensions of each test specimen and the corresponding data are presented in Table 4.22. As expected, the magnitude of the stress relaxation was higher with increasing time. The stress relaxation was significant in the first hour, where the average relaxation was 33 ± 2% when compared with corresponding starting values. It dropped a further 2.5%, 1.8% and 1.3% in the second, third and fourth hour, respectively.

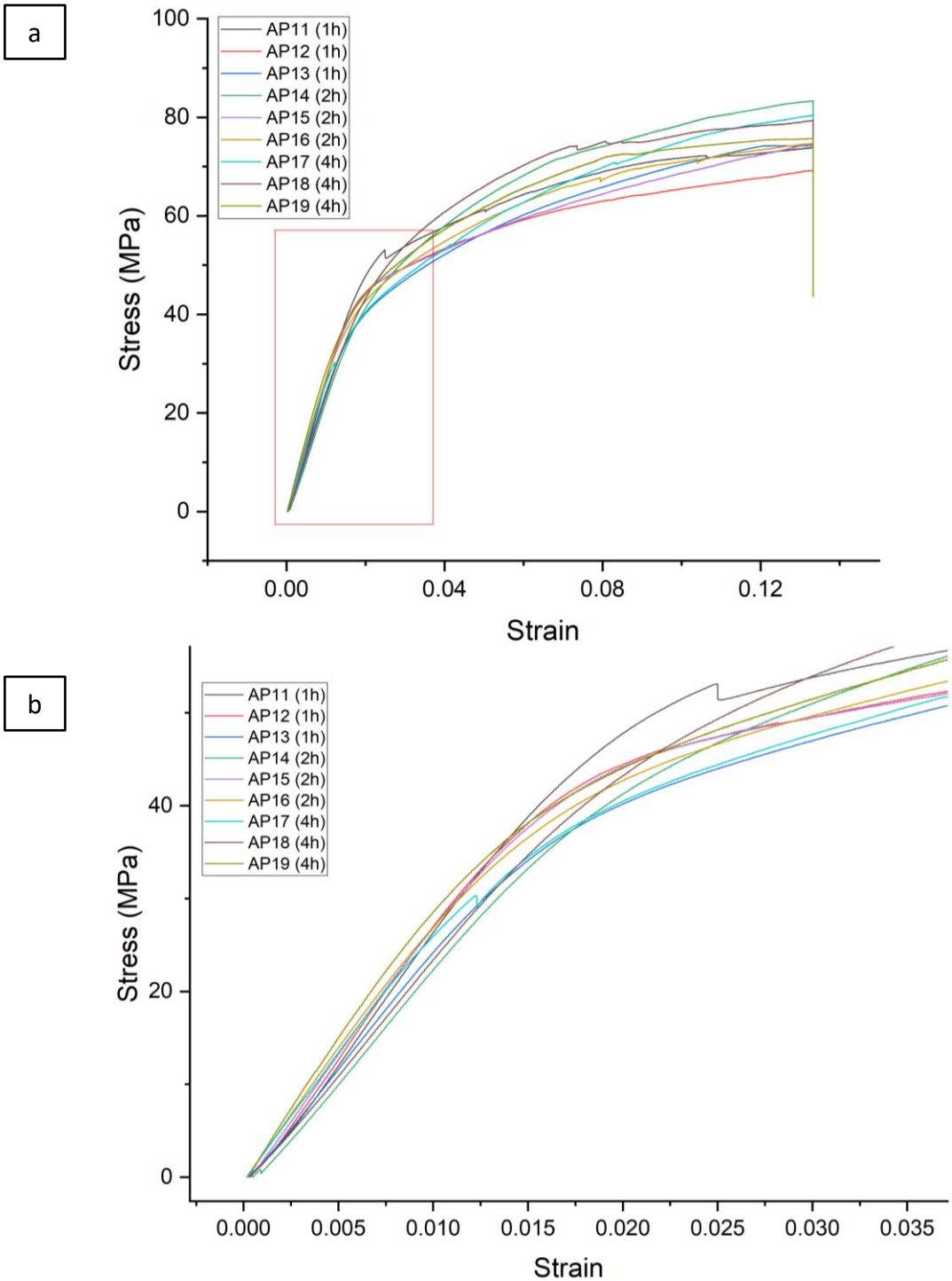

Figure 4.3.22 Stress−strain traces for the aligned electro-spun PAN nano-fibre bundles that were loaded to a displacement of 2 mm and held for 1, 2 and 4 hours from Figure 4.3.23 (below). (b) Zoomed in of the left part of the traces from (a).

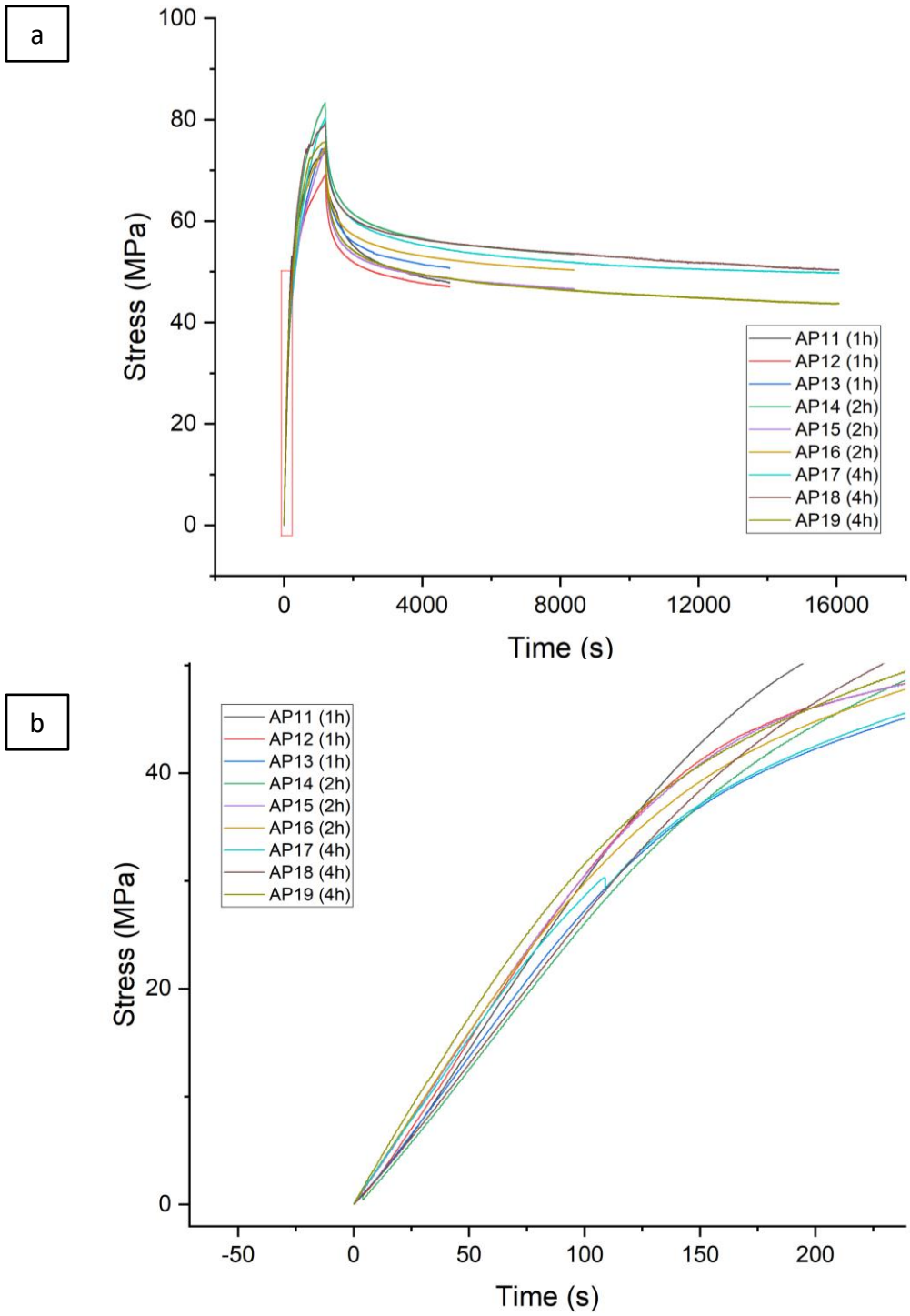

Figure 4.3.23 Stress-relaxation traces for the pre-loaded samples from Figure 4.3.22 (above).

(b) Zoomed in of the left part of the traces from (a).

Table 4.22 Summary of the test specimen details and the pre-loading conditions where the samples were loaded to a displacement of 2 mm, held at this displacement for 1, 2, and 4 hours and re-loading to failure.

Preloading and Holding Aligned as-spun fibres to 2 mm (different holding time) (Cross-head speed: 0.1 mm/minute) (99.9% DMSO)												
Sample Number	**Holding Time (hour)**	**Width (m)**	**Gauge Length (mm)**	**Thickness (m)**	**Cross-sectional Area (m^2)**	**Weight (mg)**	**Max Load when pre-load (N)**	**Load drop when holding (N)**	**UTS when Pre-load (MPa)**	**Stress Decay when Holding (MPa)**	**Stress Decay in %**	**Young's Modulus (GPa)**
AP11	1	0.00626	15	3.90E−06	2.44E−08	0.19	1.80386	0.63575	73.9	26.0	35%	2.67
AP12	1	0.00632	15	4.00E−06	2.53E−08	0.18	1.74890	0.55909	69.2	22.1	32%	2.70
AP13	1	0.00612	15	3.80E−06	2.33E−08	0.18	1.72915	0.54920	74.4	23.6	32%	2.52
Average (AP11−AP13)	1	0.00623	15	3.90E−06	2.43E−08	0.18	1.76063	0.58135	72.5	23.9	33%	2.63
AP14	2	0.00615	15	3.60E−06	2.21E−08	0.17	1.84575	0.66066	83.4	29.8	36%	2.21
AP15	2	0.00611	15	4.00E−06	2.44E−08	0.19	1.82078	0.68166	74.5	27.9	37%	2.50
AP16	2	0.00626	15	4.10E−06	2.57E−08	0.19	1.91669	0.62507	74.7	24.4	33%	2.44
Average (AP14−AP16)	2	0.00617	15	3.90E−06	2.41E−08	0.18	1.86107	0.65579	77.5	27.4	35%	2.38
AP17	4	0.00607	15	3.70E−06	2.25E−08	0.18	1.80603	0.68764	80.4	30.6	38%	2.30
AP18	4	0.00636	15	3.80E−06	2.42E−08	0.19	1.91817	0.6995	79.4	28.9	36%	2.31
AP19	4	0.00624	15	4.00E−06	2.50E−08	0.18	1.88870	0.79828	75.7	32.0	42%	2.55
Average (AP17−AP19)	4	0.00622	15	3.83E−06	2.39E−08	0.18	1.87097	0.72847	78.5	30.5	39%	2.39

Stress−strain plots for pre-stretched aligned fibre specimens at different holding periods are shown in Figure 4.3.24. The dimensions, test conditions and test results for each of the samples are summarised in Table 4.23. The tensile test without releasing the stress shows a significantly lower failure strain when compared to the previous case. Unlike the stress-strain traces seen in Figure 4.3.25 (reported in the last section), the behaviour seen in Figure 4.3.24 is different where the load drops off after the peak stress is reached. Increasing the hold-period did not show a clear effect on the failure strain. The failure strain can be influenced by the environmental conditions during fibre formation. Since the range of failure strains is low, and all samples show similar behaviour, it is reasonable to assume that this small variation is due to environmental conditions. Samples A21−A23 were not pre-stretched, and they are represented in Figure 4.3.26 as 0 hours on the X-axis. Cold-drawing of the fibres and holding them at a displacement of 2 mm for 1 hour showed a small increase in the UTS. However, the average value of Young's modulus was increased from 2.91 ± 0.28 GPa to 5.15 ± 0.05 GPa. This represents an increase of 77%. The average value for the UTS and Young's modulus increase with holding time to a maximum of 88.97 ± 4.22 MPa and 5.80 ± 0.31 GPa, respectively, after 4 hours of holding.

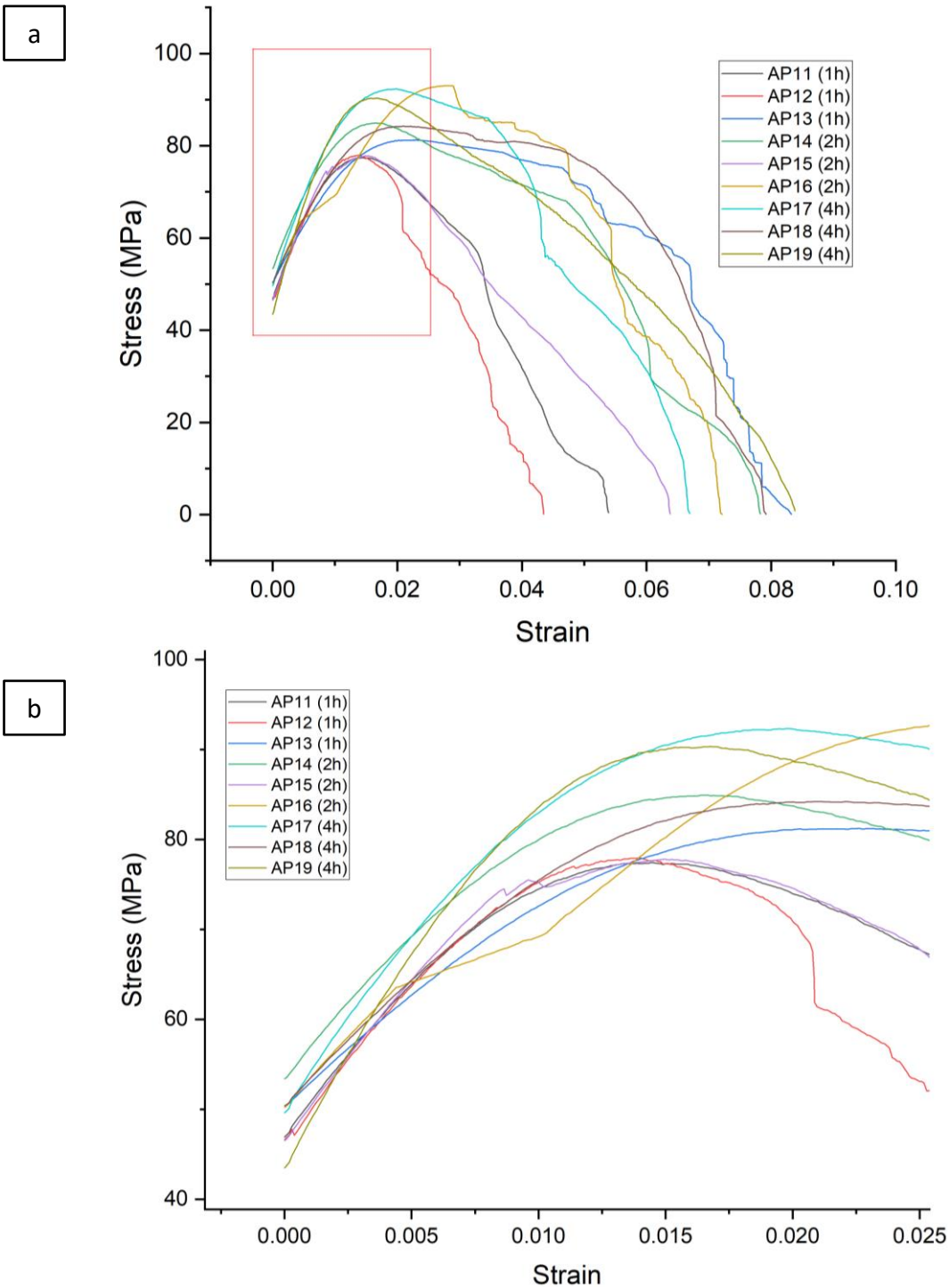

Figure 4.3.24 Stress−strain traces for the samples from Figure 4.3.22 that were loaded to a displacement of 2 mm, held for 1, 2 and 4 hours (see Figure 4.3.23), and re-loaded to failure (current Figure). (b) Zoomed in of the left part of the traces from (a).

Table 4.23 Summary of the relevant data and mechanical properties for the samples that were loaded to a displacement of 2 mm with different holding time, loaded to failure immediately after the hold-period (see Figure 4.3.24).

Preloaded Aligned as-spun fibres (different Holding time study) (Cross-head speed: 1 mm/minute) (99.9% DMSO)											
Sample Number	**Holding Time (hour)**	**Width (m)**	**Gauge Length (mm)**	**Thickness (m)**	**Area (m^2)**	**Weight (mg)**	**Max Load (N)**	**Starting Stress (MPa)**	**UTS (MPa)**	**Young's Modulus (GPa)**	**Failure Strain (%)**
AP11	1	0.00626	17	3.90E−06	2.44E−08	0.19	1.89025	46.9	77.4	5.12	1.5
AP12	1	0.00632	17	4.00E−06	2.53E−08	0.18	1.96944	46.6	77.9	5.12	1.3
AP13	1	0.00612	17	3.80E−06	2.33E−08	0.18	1.8886	50.2	81.2	5.21	2.0
Average (AP11−AP13)	1	0.00623	17	3.90E−06	2.43E−08	0.18	1.91609	47.9	78.8	5.15	1.6
AP14	2	0.00615	17	3.60E−06	2.21E−08	0.17	1.88023	53.4	84.9	5.59	1.7
AP15	2	0.00611	17	4.00E−06	2.44E−08	0.19	1.90079	46.5	77.8	5.15	1.5
AP16	2	0.00626	17	4.10E−06	2.57E−08	0.19	2.38629	50.2	93.0	5.33	2.9
Average (AP14−AP16)	2	0.00617	17	3.90E−06	2.41E−08	0.18	2.05577	50.0	85.2	5.36	2.0
AP17	4	0.00607	17	3.70E−06	2.25E−08	0.18	2.07381	49.6	92.3	6.00	2.0
AP18	4	0.00636	17	3.80E−06	2.42E−08	0.19	2.03572	50.4	84.2	5.44	2.0
AP19	4	0.00624	17	4.00E−06	2.50E−08	0.18	2.25493	43.5	90.3	5.97	1.6
Average (AP17−AP19)	4	0.006223	17	3.83E−06	2.39E−08	0.18	2.12	47.8	88.93	5.80	1.9

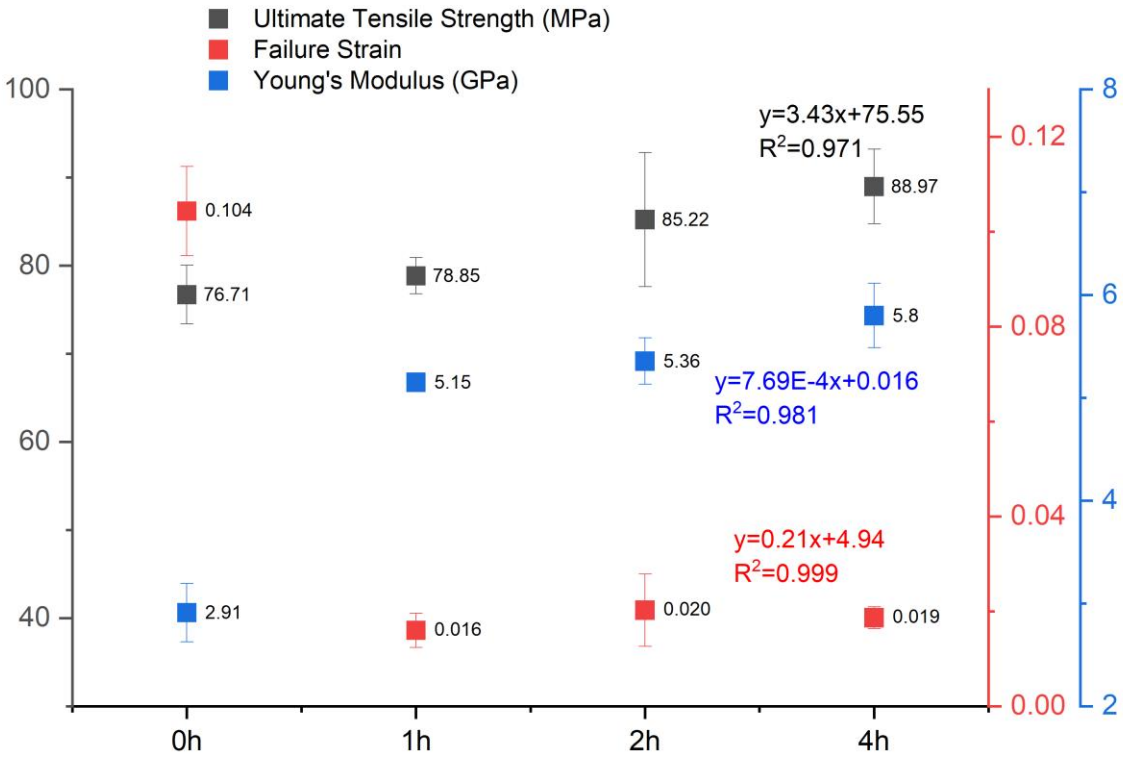

Figure 4.3.25 Comparison of the tensile properties of the fibre were loaded to a displacement of 2 mm, held for 1, 2 and 4 hours. 0h stands for the fibres that were not pre-loaded (sample A21−A23). The colours of the best-fit line equation and R^2 values between 1 and 4h correspond to those indicated in the legend.

<u>Overall Summary</u>

- With reference to one of the original research hypotheses, it was shown that post-treating the electro-spun PAN nano-fibres by stretching is a viable method to increase Young's modulus and ultimate tensile strength.

4.3.7. Tensile Testing of Aligned Heat-treated Nano-fibres

4.3.7.1. Determining the Fibre Cross-sectional Area Using TEM

As described in Section 4.2.3.3, the cross-sectional area of the fibre bundle can be obtained using TEM. Using these TEM micrographs, the actual cross-sectional area of the fibre bundle is estimated by multiplying the average cross-sectional area of the fibre by the number of fibres. Figure 4.3.26 shows a pair of solid lines that represent the thickness boundary of the test specimen. The two perpendicular dotted lines represent an 8500 nm width boundary. By counting the number of fibres over a certain distance along the width of the sample and multiplying the average cross-sectional area of a single nano-fibre, the total cross-sectional area of the test specimen can be estimated. An average of ten TEM images was evaluated from each test specimen, as summarised in Table 4.24 and Table 4.25.

To compare the tensile test results of heat-treated fibres to as-spun fibres, the cross-sectional areas of aligned as-spun fibres A21–A23 were recalculated using the TEM method (T, which stands for TEM, is added to the sample code). The cross-sectional area measured using the TEM method was 2.5 times lower than that calculated from the thickness obtained from the micrometre screw gauge. The UTS and Young's results show significant increases, reaching 195.1 ± 10.4 MPa and 7.4 ± 0.7 GPa, respectively.

However, Young's modulus obtained using the TEM method was still 72% lower than that of a single PAN/DMF nano-fibre obtained by AFM cantilever, as reported by Yuya *et al.* [241]. The accuracy of the TEM method for determining the fibre volume fraction needs to be improved in future work.

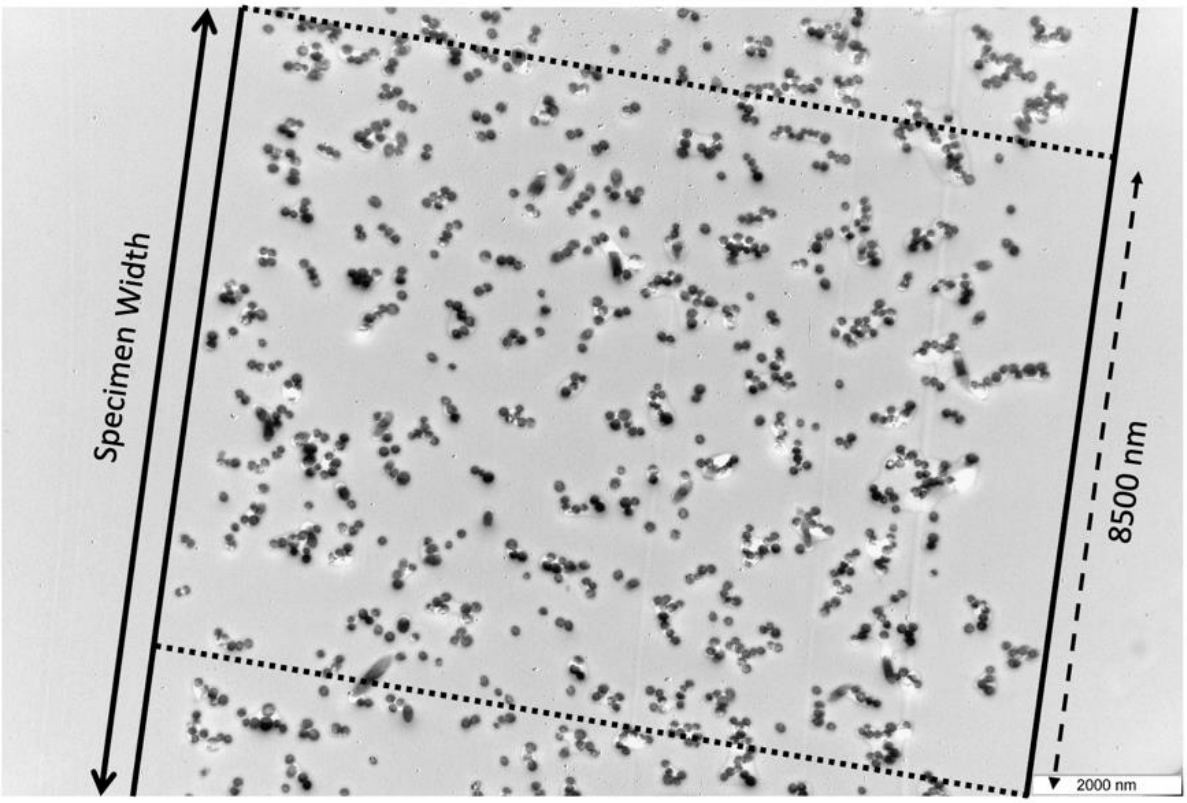

Figure 4.3.26 Example showing the fibre counting method, where the desired area is drawn on the TEM micrograph to determine the fibre volume fraction and cross-sectional area of the sample.

Table 4.24 Summary of the specimen details obtained by TEM, the mechanical property results and tensile test data for the samples A21T–A23T.

Tensile Test of Aligned PAN Nano-fibre (Cross-head speed: 1 mm/minute) (99.9% DMSO)												
Sample Number	**Width (µm)**	**Gauge Length (mm)**	**Thickness Obtained from TEM (µm)**	**Bulk Area of Specimen (µm²)**	**Average Number of Fibres per 25 µm²**	**Total Number of Fibres per Sample**	**Average Fibre Area (nm²)**	**Cross-sectional Area (m²)**	**Max Load (N)**	**UTS (MPa)**	**Young's Modulus (GPa)**	**Failure Strain (%)**
A21T	609	15	19.2	11692.8	246	115057	86517.6	9.95E−09	1.84913	185.8	7.06	10
A22T	618	15	18.6	11494.8	240	110350	79672.6	8.79E−09	1.81388	206.3	8.19	11
A23T	623	15	18.9	11774.7	251	118218	81686.3	9.66E−09	1.86353	193.0	6.85	9
Average (A21T−A23T)	617	15	18.9	11654.1	246	114542	82625.5	9.47E−09	1.84218	195.0	7.37	10
A21	609	15	N/A					2.38E−08	1.84913	77.9	2.96	10
A22	618	15						2.29E−08	1.81388	79.3	3.15	11
A23	623	15						2.55E−08	1.86353	73.0	2.59	9
Average (A21−A23)	617	15						2.41E−08	1.84218	76.7	2.90	10

4.3.7.2. Tensile Properties of Oxidised and Carbonised Aligned PAN Nano-fibres

The stress–strain traces for the heat-treated aligned PAN nano-fibres are shown in Figure 4.3.27. Compared to the stress–strain traces obtained for the as-spun fibres, the yielding region is no longer observed, and the fibre exhibits brittle fracture. In this case, the Young's modulus was measured at 0.009 strain. As shown in the result reported in Table 4.25, the average failure strain is significantly reduced from 0.1 ± 0.01 for the as-spun aligned fibres to 0.02 ± 0.002 when fibres were oxidised at 300 °C. Moreover, the samples carbonised at 600 and 900 °C show load drops prior to catastrophic failure. This type of failure is typical of the weaker fibres failing and the load being imposed on the surviving fibres.

Figure 4.3.27 shows that increasing the carbonisation temperature reduces the failure strain and improves Young's modulus from 7.4 ± 0.7 GPa (as-spun fibre) to 37.2 ± 1.1 GPa (carbonised at 900 °C). With reference to the TEM and Raman spectroscopy results reported in Section 4.2.3.2, the formation of ordered graphitic structures is the main reason for this improvement. Compared with others reported in the literature summarised in Appendix C, this is the highest value reported at this temperature when the tensile properties are assessed using a universal tensile test machine. Again, this demonstrates that applying load during stabilisation and carbonisation can improve the formation of graphitic carbon.

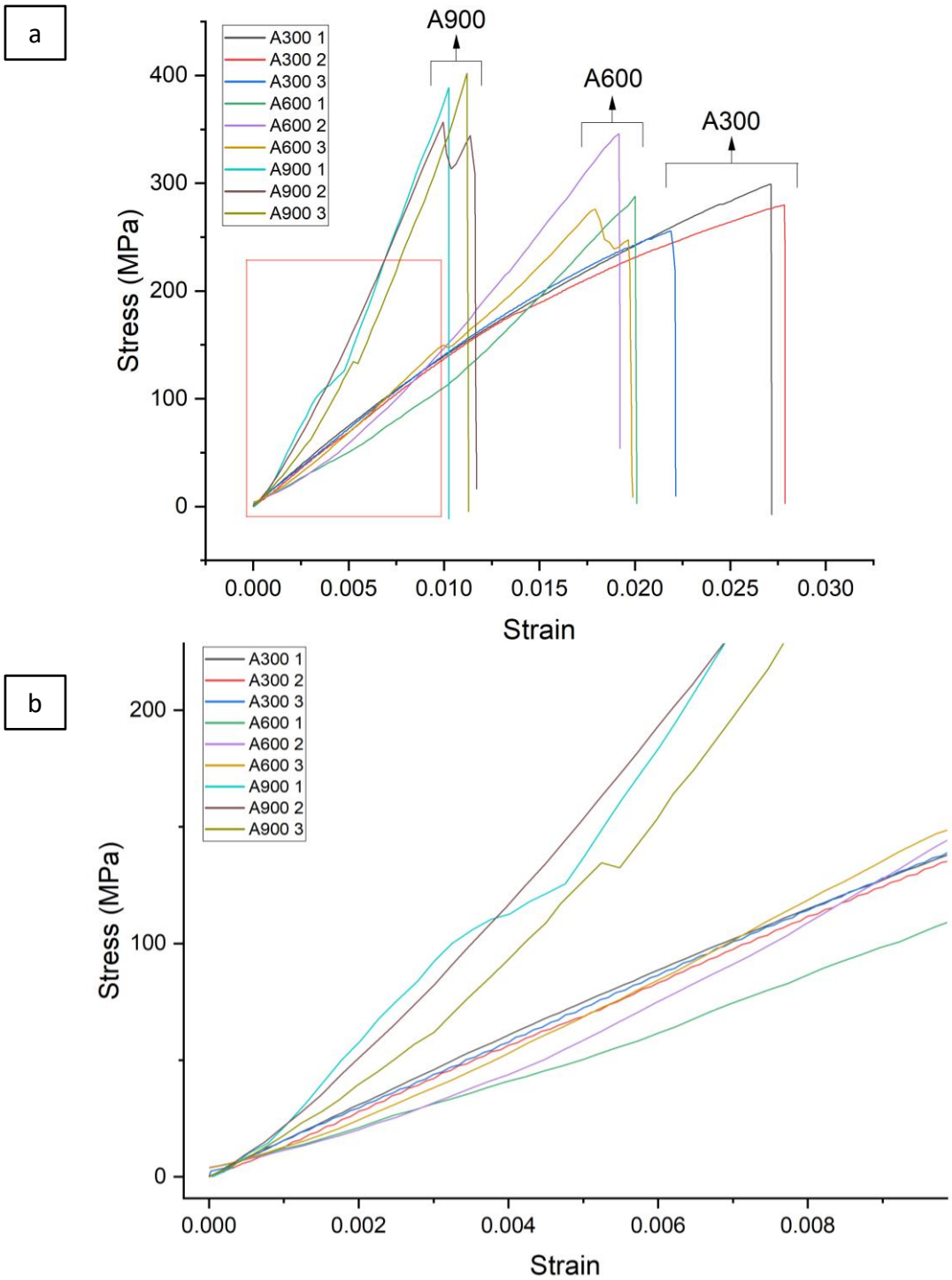

Figure 4.3.27 Stress–strain traces for aligned PAN nano-fibre samples heat-treated at different temperatures. The cross-sectional areas of the samples were measured using the relevant TEM micrographs. (b) Zoomed in of the left part of the traces from (a).

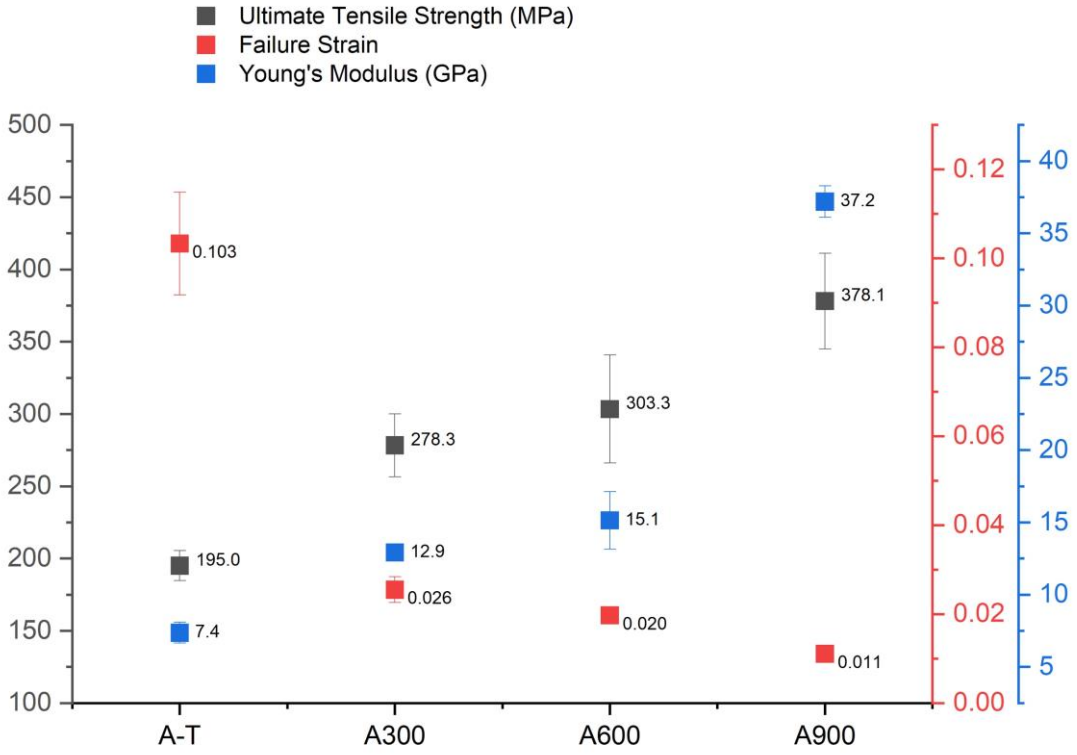

Figure 4.3.28 Comparison of the tensile properties of aligned PAN nano-fibre samples heat-treated at different temperatures. The cross-sectional areas of the samples were measured using the relevant TEM micrographs.

The UTS of the sample was also found to increase with the heat-treatment temperature. The average UTS, failure strain and Young's modulus are summarised in Table 4.25. The UTS and Young's modulus of aligned PAN-base carbon nano-fibre bundle heat-treated at 1000 °C reported by Zhou *et al.* [312] were 325 ± 15 MPa and 40 ± 4 GPa, respectively, which are similar to those obtained from heat-treatment at 900 °C in this study. However, the values are still one-half to one-third of the results obtained from tensile testing of single carbon nano-fibre [242, 248], as reviewed in Section 2.3.

The SEM micrograph of the failure point of stabilised and carbonised PAN nano-fibres is illustrated in Figure 4.3.29a−c. In contrast with the fracture point of as-spun fibres shown in Figure 4.3.14d, the fracture surface of the fibre stabilised at 300 °C is relatively flat and clean, with small sectioned broken fibres visible. An increasing amount of smaller broken fibres are seen along the fracture surface as the temperature increases to 600 °C and 900 °C, which indicates that the fibre becomes increasingly fragile at increased temperatures.

Overall Summary

- Conclusive proof can be found in Figure 4.3.28 that heat-treating the aligned electro-spun nano-fibre under tension increases the tensile strength and the Young's modulus. These properties increased as a function of the heat-treatment temperature from 300–900 °C.

Table 4.25 Summary of the specimen details obtained by TEM and the mechanical properties result for the samples with different heat-treat temperatures.

Tensile Test of Heat-treated Aligned PAN Nano-fibre (Cross-head speed: 1 mm/minute) (99.9% DMSO)														
Sample Number	**Heat-treatment Temp (°C)**	**Width (um)**	**Weight (mg)**	**Gauge Length (mm)**	**Thickness Obtained from TEM (µm)**	**Bulk Area of Specimen (µm²)**	**Average Number of Fibres per 25 µm²**	**Total Number of Fibres per Sample**	**Average Fibre Area (nm²)**	**Cross-sectional Area (m²)**	**Max Load (N)**	**UTS (MPa)**	**Young's Modulus (GPa)**	**Failure Strain (%)**
A300 1	300	359	0.11	15	16.5	5923.5	427	101173	64963.2	6.57E−09	2.0	299.2	13.0	2.7
A300 2	300	362	0.11	15	16.1	5828.2	441	102809	64242.4	6.60E−09	1.8	280.0	12.6	2.7
A300 3	300	356	0.12	15	15.9	5660.4	455	103019	67886.7	6.99E−09	1.8	255.7	13.2	2.2
Average (A300 1-3)	300	359	0.11	15	16.2	5804.0	441	102334	65697.4	6.72E−09	1.9	278.3	12.9	2.5
A600 1	600	244	0.10	6.7	13.5	3294.1	883	116344	22885.3	2.66E−09	0.8	287.8	13.2	2.0
A600 2	600	241	0.09	6.7	13.7	3301.7	891	117673	21382.5	2.52E−09	0.9	346.0	17.2	1.9
A600 3	600	237	0.09	6.7	13.4	3175.8	902	114583	23778.7	2.72E−09	0.8	276.2	15.0	2.0
Average (A600 1-3)	600	241	0.09	6.7	13.5	3257.2	892	116200	22682.1	2.63E−09	0.8	303.3	15.1	2.0
A900 1	900	207	0.07	6.7	12.5	2587.5	1011	104639	8576.7	8.97E−10	0.4	401.0	38.4	1.0
A900 2	900	214	0.08	6.7	12.1	2589.4	1054	109169	7697.7	8.40E−10	0.3	393.1	36.8	1.2
A900 3	900	218	0.07	6.7	12.2	2659.6	1004	106810	10207.0	1.09E−09	0.4	340.2	36.4	1.1
Average (A900 1-3)	900	213	0.07	6.7	12.2	2612.2	1023	106873	8827.1	9.42E−10	0.4	378.1	37.2	1.1

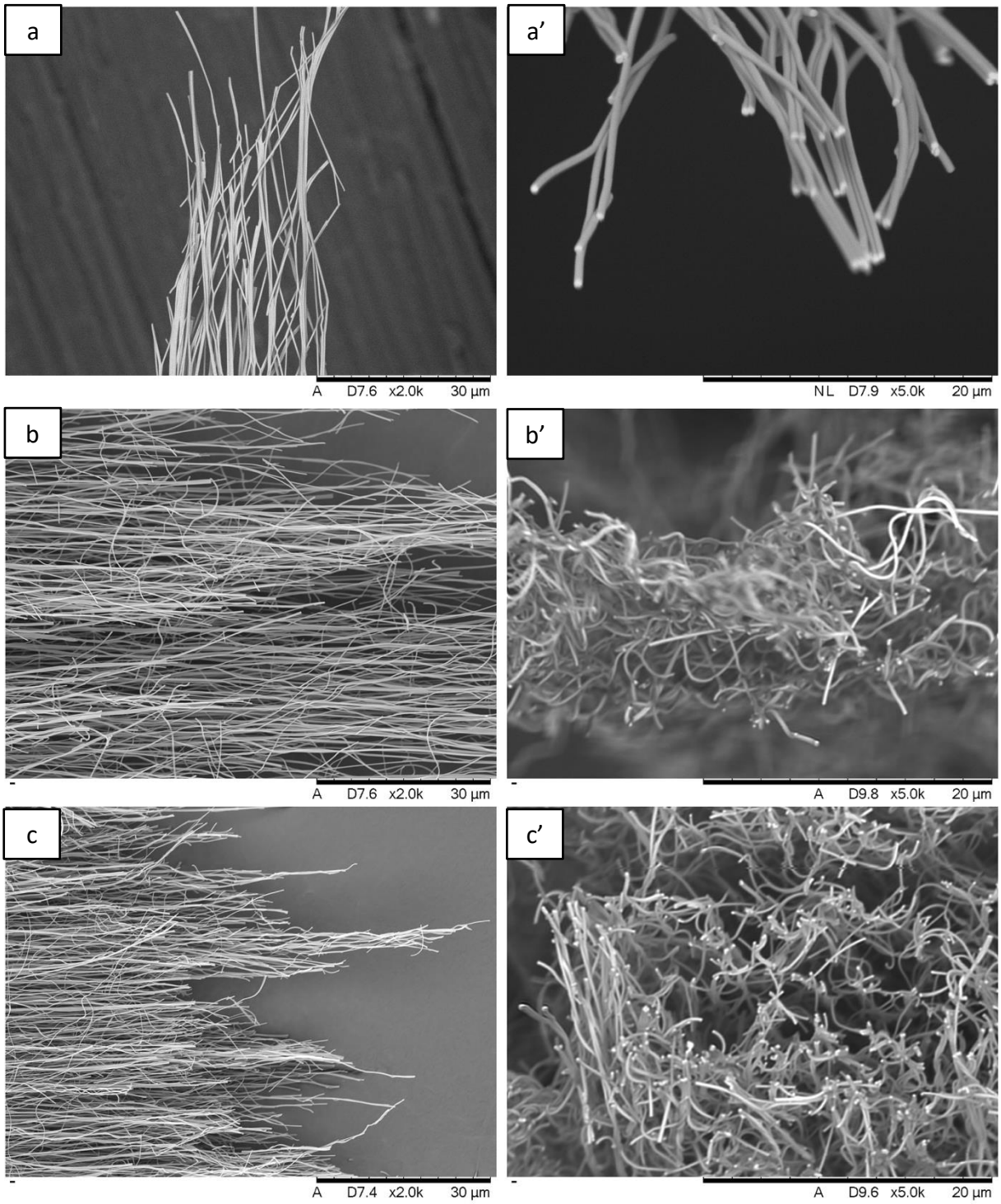

Figure 4.3.29 SEM micrographs of the fracture surface of aligned PAN nano-fibre array heat-treated at (a) 300 °C, (b) 600 °C and (c) 900 °C. (a'–c') Magnified cross-sectional view of (a–c), respectively.

5. CONCLUSIONS AND RECOMMENDATIONS FOR FUTURE WORK

5.1. Conclusions

(i) Electro-spinning: A new electrode configuration was modelled, designed and constructed to enable the production of aligned PAN nano-fibre bundles. PAN was selected because it is the primary precursor for the manufacture of carbon fibres. Unlike the majority of the research reported in the literature, the solvent that was used in the current study was DMSO. It was selected because it is non-toxic when compared to other commonly used solvents such as DMF and DMAc. The current study is the first reported electro-spinning technique where aligned fibres can be extracted and spooled continuously. This is an important development because post-processing the aligned fibres is possible. This includes cold-stretching to increase the degree of molecular alignment of the polymer chains.

(ii) Degree of fibre alignment: The degree of fibre alignment was established using image analysis where approximately 91% of the fibres were deposited to within 3°. This is one of the highest reported to-date but with an added unique advantage that the aligned fibres can be extracted continuously in a practical and efficient manner. When the spooling rig was used, 78% of the fibres were aligned to within 3°.

(iii) Enhancing the tensile strength and Young's modulus of the electro-spun fibres: In the past, it was assumed that the extensive whipping and resultant stretching of the electro-spun polymer should enhance significantly the molecular alignment of the polymer chains.

However, it is now established that the mechanical properties of the electro-spun fibres are significantly lower than expected. Therefore, in the current study, experiments were designed to identify techniques for post-processing the aligned electro-spun fibres with a view to increase their mechanical properties. The post-processing technique used including three forms of cold-drawing: (i) the specimen was strained to a constant value and the stress relaxation was monitored for a specified time, the samples were unloaded and reloaded and tested to failure; and (ii) the specimen was strained to a specific value, held for a specified time and then loaded to failure; and (iii) the specimen was strained to a specified value, the hold period was varied and each was tested to failure. The Young's modulus and the ultimate tensile strength of the as-spun and cold-drawn fibres were 2.9 ± 0.28 GPa and 76.7 ± 3.3 MPa, and 8.5 ± 0.3 GPa and 88.9 ± 4.2 MPa, respectively.

(iv) End-tabbing the tensile test specimens: The tensile testing of the electro-spun fibres was made possible by the extensive trials that were carried out to establish the optimum way to end-tab the specimens. Reports in literature generally use superglue or double-sided adhesive tape to tensile test bundles of randomly oriented and aligned fibres. In the current study it was demonstrated that photo-curable UV resin was the ideal end-tab material because: (i) it was possible to prevent the resin from seeping into the fibres in the gauge length region; (ii) the viscosity was such that it could be applied precisely over the end-tab region; and (iii) the shrinkage upon UV irradiation to cross-link the resin was minimal.

(v) Custom-designed rig for heat-treatment and the application of a load during oxidation and carbonisation: The oxidation and carbonisation of the electro-spun PAN samples was a challenge for many reasons. A rig was required to enable the specimens to be secured and a

defined load applied during oxidation and carbonisation. The load was required to compensate for the shrinkage that occurs when PAN is oxidised and carbonised. The rig is best described as a slotted graphite tube where the aligned fibres were bonded to it at one end using a high-temperature adhesive. The opposite end of the fibre was bonded to two graphite loading blocks with a series of partially drilled holes. Sections of alumina rods were positioned in the holes to provide the required load for the electro-spun fibre bundles. This was used for the oxidation at 300 °C in air and 600 °C and 900 °C in nitrogen. The rig was designed for use up to 1200 °C but the fibres proved to be too fragile for manual handling at this temperature. Nevertheless, the rig design was unique.

(vi) Tensile properties of the heat-treated fibres: The Young's modulus and the ultimate failure stress increased as a function of the heat-treatment temperature. For example, Young's modulus increased from 7.4 ± 0.7 GPa (as-spun fibre) up to 37.2 ± 1.1 GPa (carbonised at 900 °C). In the case of the ultimate tensile failure stress, it increased from 195.0 ± 10.2 MPa to 378.1 ± 33.1 MPa for the as-spun and carbonised samples at 900 °C. These values represent one of the highest reported in the literature.

(vii) Conventional analytical characterisation: Raman spectroscopy and XRD were used to characterise the graphitic and sp^2 characterised of the carbonised PAN fibres. Both techniques verified that the graphitic characteristic increased as a function of processing temperature.

(viii) Versatility of the Vee-shield technique to produce aligned nano-fibres: The technique was used with a number of common synthetic and a natural polymer to produce highly-aligned nano-fibres.

(ix) In-situ production of unidirectional and angle-ply layers: The feasibility of producing angle-ply preforms was demonstrated by rotating the Vee-shield manually.

(x) Scale-up: The technology developed on the custom-designed laboratory electro-spinner can be scaled up to an industrial scale machine that was co-designed with an industrial company.

5.2. Recommendations for Future Work.

(i) Appropriate advanced analytical techniques, such as 2D WAXD as well as polarised FTIR, should be used to study the microstructure and to establish the degree of molecular orientation in the skin and the core of electro-spun fibres. Such a study will also enable the effects of processing parameters on the subsequent properties of the oxidised, carbonised and graphitised nano-fibres to be studied. Optical fibre sensors can also be used to enable *in situ* spectroscopic analysis to be undertaken to establish as to why the overall crystallinity and mechanical properties of electro-spun fibres are inferior to those manufactured using conventional melt and solvent spinning.

(ii) A furnace should be designed to enable continuous spooling and *in situ* heat-treatment of the electro-spun fibres in a nitrogen/inert atmosphere under controllable tension. Since the elimination of oxygen is a prerequisite for carbonisation and graphitisation, a chamber should be constructed to house a spooling unit. The chamber should be designed to enable easy loading and unloading of the spools containing the electro-spun fibres. Conventional fibre tension-controllers can be used to maintain the required tension. The furnace can be

instrumented with non-contact optical fibres to enable real-time near infrared and Raman spectroscopy to study the chemical conversion processes.

(iii) A suitable technique needs to be developed to measure the thickness and width of electro-spun strips where the intrinsic porosity does not interfere with the measurements. This is a fundamental problem that needs to be addressed because any technique that applies a mechanical force to an array of the nano-fibres will induce compaction of the as-spun PAN fibres. The problem after carbonisation is that the fibres become extremely sensitive to handling. The weight and density of the nano-fibre bundles should be measured, per batch, and this should be used to normalise the tensile data. Other techniques that should be considered include gas pycnometry and mercury porosimetry. These conventional techniques should be used to develop a technique where the sample is vacuum-bagged and where interferometry is used to compute the thickness as a function of the applied vacuum.

(iv) A practical technique needs to be developed to quantify the fibre volume fraction within an electro-spun nano-fibre strip. This can potentially be done by creating nano-fibre composites with fibres pre-loaded under tension and vacuum infusion used to create a composite. The TEM-based technique developed in this current study can be used to measure the fibre volume fraction.

(v) Catalysts need to be developed to reduce the carbonisation, and eventually, the graphitisation temperatures, for example: nickel acetate tetrahydrate (NiAc) [466]. Components such as graphene [467] and multi-walled carbon nanotubes (MWCNTs) [272, 468] have been used previously to increase the carbon yield and to increase the crystallinity and the mechanical properties of carbon fibres. Alternatively, microwave heating can be used to

reduce the overall energy consumption during oxidation, carbonisation and graphitisation. Sensors can also be integrated to study the chemical changes in real-time.

(vi) The Vee-shield technique should be applied to natural polymers, such as lignin and cellulose as petroleum is a finite resource, and there is a global drive to develop bio-based precursors for the production of carbon fibres. However, there are issues with natural polymers such as as-received lignin such as: (a) their polymer dispersion index (PDI) is too large when compared to synthetic polymers, and this needs to be addressed; (b) the effect of the inorganic content on electro-spinning needs to be studied; and (c) the intrinsic variability, depending on the source of the lignin, needs to be addressed. The Vee-shield method is versatile in that the processing parameters can be optimised to produce nano-fibres continuously. Furthermore, multiple spinnerets can be used to produce fibre arrays in the required volume.

REFERENCE

1. Sill, T.J. and H.A. Von Recum, *Electrospinning: applications in drug delivery and tissue engineering.* Biomaterials, 2008. **29**(13): p. 1989-2006.
2. Hu, X., et al., *Electrospinning of polymeric nanofibers for drug delivery applications.* Journal of controlled release, 2014. **185**: p. 12-21.
3. Fang, J., et al., *Applications of electrospun nanofibers.* Chinese science bulletin, 2008. **53**: p. 2265-2286.
4. Mirjalili, M. and S. Zohoori, *Review for application of electrospinning and electrospun nanofibers technology in textile industry.* Journal of Nanostructure in Chemistry, 2016. **6**: p. 207-213.
5. Mercante, L.A., et al., *Electrospinning-based (bio) sensors for food and agricultural applications: A review.* TrAC Trends in Analytical Chemistry, 2017. **91**: p. 91-103.
6. Dai, Y., et al., *Ceramic nanofibers fabricated by electrospinning and their applications in catalysis, environmental science, and energy technology.* Polymers for Advanced Technologies, 2011. **22**(3): p. 326-338.
7. Pan, H., et al., *Continuous aligned polymer fibers produced by a modified electrospinning method.* Polymer, 2006. **47**(14): p. 4901-4904.
8. Doshi, J. and D.H. Reneker, *Electrospinning process and applications of electrospun fibers.* Journal of electrostatics, 1995. **35**(2-3): p. 151-160.
9. Taylor, G.I., *Disintegration of water drops in an electric field.* Proceedings of the Royal Society of London. Series A. Mathematical and Physical Sciences, 1964. **280**(1382): p. 383-397.
10. Deitzel, J.M., et al., *The effect of processing variables on the morphology of electrospun nanofibers and textiles.* Polymer, 2001. **42**(1): p. 261-272.
11. Hohman, M.M., et al., *Electrospinning and electrically forced jets. I. Stability theory.* Physics of fluids, 2001. **13**(8): p. 2201-2220.
12. Shin, Y., et al., *Electrospinning: A whipping fluid jet generates submicron polymer fibers.* Applied physics letters, 2001. **78**(8): p. 1149-1151.
13. Yarin, A.L., S. Koombhongse, and D.H. Reneker, *Bending instability in electrospinning of nanofibers.* Journal of applied physics, 2001. **89**(5): p. 3018-3026.
14. Sun, Z., et al., *The effect of solvent dielectric properties on the collection of oriented electrospun fibers.* Journal of Applied Polymer Science, 2012. **125**(4): p. 2585-2594.
15. Shao, S., T. Ma, and G.F. Fernando, *Electro-spinning of highly-aligned polyacrylonitrile nano-fibres with continuous spooling.* Sci Rep, 2021. **11**(1): p. 21713.
16. Mortimer, C.J. and C.J. Wright, *The fabrication of iron oxide nanoparticle‐nanofiber composites by electrospinning and their applications in tissue engineering.* Biotechnology journal, 2017. **12**(7): p. 1600693.
17. Xue, J., et al., *Electrospinning and electrospun nanofibers: Methods, materials, and applications.* Chemical reviews, 2019. **119**(8): p. 5298-5415.
18. Acharya, M., G.K. Arumugam, and P.A. Heiden, *Dual Electric Field Induced Alignment of Electrospun Nanofibers.* Macromolecular Materials and Engineering, 2008. **293**(8): p. 666-674.
19. Yuan, H., et al., *Stable jet electrospinning for easy fabrication of aligned ultrafine fibers.* Journal of Materials Chemistry, 2012. **22**(37).
20. Yang, D., et al., *Fabrication of Aligned Fibrous Arrays by Magnetic Electrospinning.* Advanced Materials, 2007. **19**(21): p. 3702-3706.

21. Park, S.H. and D.-Y. Yang, *Fabrication of aligned electrospun nanofibers by inclined gap method.* Journal of Applied Polymer Science, 2011. **120**(3): p. 1800-1807.
22. Afifi, A.M., et al., *Fabrication of Aligned Poly(L-lactide) Fibers by Electrospinning and Drawing.* Macromolecular Materials and Engineering, 2009. **294**(10): p. 658-665.
23. Liu, Y., et al., *Magnetic-field-assisted electrospinning of aligned straight and wavy polymeric nanofibers.* Adv Mater, 2010. **22**(22): p. 2454-7.
24. Khamforoush, M. and M. Mahjob, *Modification of the rotating jet method to generate highly aligned electrospun nanofibers.* Materials Letters, 2011. **65**(3): p. 453-455.
25. Mittal, J., R. Mathur, and O. Bahl, *Post spinning modification of PAN fibres—a review.* Carbon, 1997. **35**(12): p. 1713-1721.
26. Luo, C., et al., *Electrospinning versus fibre production methods: from specifics to technological convergence.* Chemical Society Reviews, 2012. **41**(13): p. 4708-4735.
27. Lawrence, C.A., *Advances in yarn spinning technology*. 2010: Elsevier.
28. Beese, A.M., et al., *In situ transmission electron microscope tensile testing reveals structure–property relationships in carbon nanofibers.* Carbon, 2013. **60**: p. 246-253.
29. Tanaka, K., et al., *Development of an electrospinning method for the tensile testing of single nanofibers*, in *High Performance Structures and Materials V*. 2010. p. 177-185.
30. Croisier, F., et al., *Mechanical testing of electrospun PCL fibers.* Acta Biomater, 2012. **8**(1): p. 218-24.
31. Tan, E.P., S.Y. Ng, and C.T. Lim, *Tensile testing of a single ultrafine polymeric fiber.* Biomaterials, 2005. **26**(13): p. 1453-6.
32. Baker, S.R., et al., *Determining the mechanical properties of electrospun poly-epsilon-caprolactone (PCL) nanofibers using AFM and a novel fiber anchoring technique.* Mater Sci Eng C Mater Biol Appl, 2016. **59**: p. 203-212.
33. Hang, F., et al., *In situ tensile testing of nanofibers by combining atomic force microscopy and scanning electron microscopy.* Nanotechnology, 2011. **22**(36): p. 365708.
34. Namazu, T., Y. Isono, and T. Tanaka, *Evaluation of size effect on mechanical properties of single crystal silicon by nanoscale bending test using AFM.* Journal of Microelectromechanical systems, 2000. **9**(4): p. 450-459.
35. Wang, X., et al., *Enhanced Mechanical Performance of Self-Bundled Electrospun Fiber Yarns via Post-Treatments.* Macromolecular Rapid Communications, 2008. **29**(10): p. 826-831.
36. Jalili, R., M. Morshed, and S.A.H. Ravandi, *Fundamental parameters affecting electrospinning of PAN nanofibers as uniaxially aligned fibers.* Journal of Applied Polymer Science, 2006. **101**(6): p. 4350-4357.
37. Chawla, S., J. Cai, and M. Naraghi, *Mechanical tests on individual carbon nanofibers reveals the strong effect of graphitic alignment achieved via precursor hot-drawing.* Carbon, 2017. **117**: p. 208-219.
38. Balan, K.K., et al., *Effect of thickness of mat and testing parameters on tensile strength variability of electrospun nanofibrous mat.* Materials Today: Proceedings, 2016. **3**(6): p. 1320-1329.
39. Moon, S. and T. Emrick, *High flame resistant and strong electrospun polyacrylonitrile–carbon nanotubes–ochre nanofibers.* Polymer, 2013. **54**(7): p. 1813-1819.
40. Yao, J., C. Bastiaansen, and T. Peijs, *High Strength and High Modulus Electrospun Nanofibers.* Fibers, 2014. **2**(2): p. 158-186.
41. Chen, J., et al., *Study on the coagulation mechanism of wet-spinning PAN fibers.* Journal of Polymer Research, 2006. **13**: p. 515-519.
42. Al Faruque, M.A., et al., *Impact of the wet spinning parameters on the alpaca -based polyacrylonitrile composite fibers: Morphology and enhanced mechanical properties study.* Journal of Applied Polymer Science, 2020. **137**(41): p. 49264.

43. Zhang, B., et al., *Recent advances in electrospun carbon nanofibers and their application in electrochemical energy storage.* Progress in Materials Science, 2016. **76**: p. 319-380.
44. Miao, J., et al., *Electrospinning of nanomaterials and applications in electronic components and devices.* Journal of nanoscience and nanotechnology, 2010. **10**(9): p. 5507-5519.
45. Wendorff, J.H., S. Agarwal, and A. Greiner, *Electrospinning: materials, processing, and applications*. 2012: John Wiley & Sons.
46. Stanger, J., et al., *Effect of charge density on the Taylor cone in electrospinning.* International Journal of Modern Physics B, 2009. **23**(06n07): p. 1956-1961.
47. Bhardwaj, N. and S.C. Kundu, *Electrospinning: A fascinating fiber fabrication technique.* Biotechnology advances, 2010. **28**(3): p. 325-347.
48. Hutmacher, D.W. and P.D. Dalton, *Melt electrospinning.* Chemistry–An Asian Journal, 2011. **6**(1): p. 44-56.
49. Huang, Z.-M., et al., *A review on polymer nanofibers by electrospinning and their applications in nanocomposites.* Composites science and technology, 2003. **63**(15): p. 2223-2253.
50. Lannutti, J., et al., *Electrospinning for tissue engineering scaffolds.* Materials Science and Engineering: C, 2007. **27**(3): p. 504-509.
51. Li, Z., et al., *Effects of working parameters on electrospinning.* One-dimensional nanostructures: Electrospinning technique and unique nanofibers, 2013: p. 15-28.
52. Nayak, R., et al., *Melt-electrospinning of polypropylene with conductive additives.* Journal of Materials Science, 2012. **47**: p. 6387-6396.
53. Lian, H. and Z. Meng, *Melt electrospinning vs. solution electrospinning: A comparative study of drug-loaded poly (ε-caprolactone) fibres.* Materials Science and Engineering: C, 2017. **74**: p. 117-123.
54. Boland, E.D., et al., *Utilizing acid pretreatment and electrospinning to improve biocompatibility of poly (glycolic acid) for tissue engineering.* Journal of Biomedical Materials Research Part B: Applied Biomaterials: An Official Journal of The Society for Biomaterials, The Japanese Society for Biomaterials, and The Australian Society for Biomaterials and the Korean Society for Biomaterials, 2004. **71**(1): p. 144-152.
55. Lee, K., et al., *Characterization of nano-structured poly (ε-caprolactone) nonwoven mats via electrospinning.* polymer, 2003. **44**(4): p. 1287-1294.
56. Zeng, J., et al., *Poly-L-lactide nanofibers by electrospinning–Influence of solution viscosity and electrical conductivity on fiber diameter and fiber morphology.* e-Polymers, 2003. **3**(1).
57. Wan, Y.Q., et al., *Electrospinning of high-molecule PEO solution.* Journal of applied polymer science, 2007. **103**(6): p. 3840-3843.
58. Uyar, T. and F. Besenbacher, *Electrospinning of uniform polystyrene fibers: The effect of solvent conductivity.* Polymer, 2008. **49**(24): p. 5336-5343.
59. Liu, H. and Y.L. Hsieh, *Ultrafine fibrous cellulose membranes from electrospinning of cellulose acetate.* Journal of Polymer Science Part B: Polymer Physics, 2002. **40**(18): p. 2119-2129.
60. Zhang, X., M.R. Reagan, and D.L. Kaplan, *Electrospun silk biomaterial scaffolds for regenerative medicine.* Advanced drug delivery reviews, 2009. **61**(12): p. 988-1006.
61. Ohkawa, K., et al., *Electrospinning of chitosan.* Macromolecular rapid communications, 2004. **25**(18): p. 1600-1605.
62. Huang, Z.-M., et al., *Electrospinning and mechanical characterization of gelatin nanofibers.* Polymer, 2004. **45**(15): p. 5361-5368.
63. Matthews, J.A., et al., *Electrospinning of collagen nanofibers.* Biomacromolecules, 2002. **3**(2): p. 232-238.
64. Cozza, E.S., et al., *On the electrospinning of PVDF: Influence of the experimental conditions on the nanofiber properties.* Polymer International, 2013. **62**(1): p. 41-48.

65. Khan, I., B. Hararak, and G.F. Fernando, *Improved procedure for electro-spinning and carbonisation of neat solvent-fractionated softwood Kraft lignin.* Scientific Reports, 2021. **11**(1): p. 1-13.
66. Koski, A., K. Yim, and S. Shivkumar, *Effect of molecular weight on fibrous PVA produced by electrospinning.* Materials Letters, 2004. **58**(3-4): p. 493-497.
67. Kalimuldina, G., et al., *A review of piezoelectric PVDF film by electrospinning and its applications.* Sensors, 2020. **20**(18): p. 5214.
68. Tenhaeff, W.E., et al., *Highly robust lithium ion battery anodes from lignin: an abundant, renewable, and low-cost material.* Advanced Functional Materials, 2014. **24**(1): p. 86-94.
69. Chen, R., et al., *Facile fabrication of foldable electrospun polyacrylonitrile-based carbon nanofibers for flexible lithium-ion batteries.* Journal of Materials Chemistry A, 2017. **5**(25): p. 12914-12921.
70. Brown, T.D., P.D. Dalton, and D.W. Hutmacher, *Melt electrospinning today: An opportune time for an emerging polymer process.* Progress in Polymer Science, 2016. **56**: p. 116-166.
71. Leach, M.K., et al., *Electrospinning fundamentals: optimizing solution and apparatus parameters.* JoVE (Journal of Visualized Experiments), 2011(47): p. e2494.
72. Zhang, H., et al., *Thermal analysis and crystal structure of poly (acrylonitrile-co-itaconic acid) copolymers synthesized in water.* Polymers, 2020. **12**(1): p. 221.
73. Tan, L., et al., *Investigating the spinnability in the dry-jet wet spinning of PAN precursor fiber.* Journal of applied polymer science, 2008. **110**(4): p. 1997-2000.
74. Miller-Chou, B.A. and J.L. Koenig, *A review of polymer dissolution.* Progress in polymer science, 2003. **28**(8): p. 1223-1270.
75. Kong, C.S., et al., *Electrospinning mechanism for producing nanoscale polymer fibers.* Journal of Macromolecular Science®, Part B: Physics, 2010. **49**(1): p. 122-131.
76. Hansen, C.M., *Hansen solubility parameters: a user's handbook*. 2007: CRC press.
77. Eom, Y. and B.C. Kim, *Solubility parameter-based analysis of polyacrylonitrile solutions in N, N-dimethyl formamide and dimethyl sulfoxide.* Polymer, 2014. **55**(10): p. 2570-2577.
78. Cole, K.S. and R.H. Cole, *Dispersion and absorption in dielectrics I. Alternating current characteristics.* The Journal of chemical physics, 1941. **9**(4): p. 341-351.
79. Lindvig, T., M.L. Michelsen, and G.M. Kontogeorgis, *A Flory–Huggins model based on the Hansen solubility parameters.* Fluid Phase Equilibria, 2002. **203**(1-2): p. 247-260.
80. Mei, L., et al., *Solvent selection for polyacrylonitrile using molecular dynamic simulation and the effect of process parameters of magnetic-field-assisted electrospinning on fiber alignment.* High Performance Polymers, 2014. **27**(4): p. 439-448.
81. Smallwood, I., *Handbook of organic solvent properties*. 2012: Butterworth-Heinemann.
82. Weaver, J. and H. Frederikse, *Crc handbook of chemistry and physics.* CRC Press, Boca Raton, 1977. **76**: p. 12-156.
83. Vogel, A.I., *Practical organic chemistry.* Long Man Group Lted, London, 1974.
84. Brennan, D.A., et al., *Electrospinning and post-drawn processing effects on the molecular organization and mechanical properties of polyacrylonitrile (PAN) nanofibers.* MRS Communications, 2019. **9**(2): p. 764-772.
85. Gomes, D.S., et al., *Characterization of an electrospinning process using different PAN/DMF concentrations.* Polímeros, 2007. **17**: p. 206-211.
86. Heikkila, P. and A. Harlin, *Electrospinning of polyacrylonitrile (PAN) solution: Effect of conductive additive and filler on the process.* Express Polymer Letters, 2009. **3**(7): p. 437-445.
87. Qin, X.H., et al., *Effect of different salts on electrospinning of polyacrylonitrile (PAN) polymer solution.* Journal of applied polymer science, 2007. **103**(6): p. 3865-3870.

88. Peng, G.-q., et al., *Effect of coagulation bath DMSO concentration on the structure and properties of polyacrylonitrile (PAN) nascent fibers during wet-spinning.* Journal of Macromolecular Science, Part B, 2008. **47**(6): p. 1130-1141.
89. Yi, K., et al., *Diffusion coefficients of dimethyl sulphoxide (DMSO) and H2O in PAN wet spinning and its influence on morphology of nascent polyacrylonitrile (PAN) fiber.* Journal of Engineered Fibers and Fabrics, 2013. **8**(1): p. 155892501300800113.
90. Wang, Y., et al., *Formation of surface morphology in polyacrylonitrile (PAN) fibers during wet-spinning.* Journal of Engineered Fibers and Fabrics, 2018. **13**(2): p. 155892501801300208.
91. Zeng, X., et al., *Investigation the jet stretch in PAN fiber dry-jet wet spinning for PAN-DMSO-H2O system.* Journal of applied polymer science, 2009. **114**(6): p. 3621-3625.
92. Zhou, P., et al., *Effect of bath concentration on coagulation kinetics at the early stage during wet spinning of PAN copolymer nascent fibers.* Journal of Macromolecular Science, Part B, 2011. **50**(6): p. 1215-1225.
93. Singh, M., *Surface tension and viscosity measurements of liquids with the survismeter: a single instrumental unit.* Physics and Chemistry of Liquids, 2006. **44**(5): p. 579-584.
94. Haghi, A. and M. Akbari, *Trends in electrospinning of natural nanofibers.* physica status solidi (a), 2007. **204**(6): p. 1830-1834.
95. Porter, R.S. and J.F. Johnson, *The entanglement concept in polymer systems.* Chemical Reviews, 1966. **66**(1): p. 1-27.
96. De Gennes, P., *Dynamics of entangled polymer solutions. I. The Rouse model.* Macromolecules, 1976. **9**(4): p. 587-593.
97. Huang, Q., et al., *Concentrated polymer solutions are different from melts: Role of entanglement molecular weight.* Macromolecules, 2013. **46**(12): p. 5026-5035.
98. Shenoy, S.L., et al., *Role of chain entanglements on fiber formation during electrospinning of polymer solutions: good solvent, non-specific polymer–polymer interaction limit.* Polymer, 2005. **46**(10): p. 3372-3384.
99. Gupta, P., et al., *Electrospinning of linear homopolymers of poly (methyl methacrylate): exploring relationships between fiber formation, viscosity, molecular weight and concentration in a good solvent.* Polymer, 2005. **46**(13): p. 4799-4810.
100. Mit-uppatham, C., M. Nithitanakul, and P. Supaphol, *Ultrafine electrospun polyamide-6 fibers: effect of solution conditions on morphology and average fiber diameter.* Macromolecular Chemistry and Physics, 2004. **205**(17): p. 2327-2338.
101. McKee, M.G., et al., *Correlations of solution rheology with electrospun fiber formation of linear and branched polyesters.* Macromolecules, 2004. **37**(5): p. 1760-1767.
102. Colby, R.H. and M. Rubinstein, *Two-parameter scaling for polymers in ϑ solvents.* Macromolecules, 1990. **23**(10): p. 2753-2757.
103. Fetters, L., et al., *Connection between polymer molecular weight, density, chain dimensions, and melt viscoelastic properties.* Macromolecules, 1994. **27**(17): p. 4639-4647.
104. McKee, M.G., et al., *Solution rheological behavior and electrospinning of cationic polyelectrolytes.* Macromolecules, 2006. **39**(2): p. 575-583.
105. Liu, Y., et al., *Controlling numbers and sizes of beads in electrospun nanofibers.* Polymer International, 2008. **57**(4): p. 632-636.
106. Zhu, S., et al., *Study on the Morphologies and Formational Mechanism of Poly(hydroxybutyrate-co-hydroxyvalerate) Ultrafine Fibers by Dry-Jet-Wet-Electrospinning.* Journal of Nanomaterials, 2012. **2012**: p. 1-8.
107. Fridrikh, S.V., et al., *Controlling the fiber diameter during electrospinning.* Phys Rev Lett, 2003. **90**(14): p. 144502.
108. Demir, M.M., et al., *Electrospinning of polyurethane fibers.* Polymer, 2002. **43**(11): p. 3303-3309.

109. Rošic, R., et al., *The role of rheology of polymer solutions in predicting nanofiber formation by electrospinning.* European Polymer Journal, 2012. **48**(8): p. 1374-1384.
110. Salas, C., *Solution electrospinning of nanofibers*, in *Electrospun nanofibers*. 2017, Elsevier. p. 73-108.
111. Fong, H., I. Chun, and D.H. Reneker, *Beaded nanofibers formed during electrospinning.* Polymer, 1999. **40**(16): p. 4585-4592.
112. Fridrikh, S.V., et al., *Controlling the fiber diameter during electrospinning.* Physical review letters, 2003. **90**(14): p. 144502.
113. Kim, K., H. Shim, and J. Kim, *Fiber formation model for electrospinning. III. Critical fiber formation.* Fibers and Polymers, 2016. **17**(10): p. 1641-1645.
114. Kim, K., J. Kim, and H. Shim, *Fiber formation model for PVP (polyvinyl pyrrolidone) electrospinning. I. Critical voltage.* Fibers and Polymers, 2017. **18**(3): p. 493-501.
115. Kim, K., H. Shim, and J. Kim, *Fiber formation model for electrospinning. II. Stable jet voltage.* Fibers and Polymers, 2016. **17**(10): p. 1634-1640.
116. Rutledge, G.C. and S.V. Fridrikh, *Formation of fibers by electrospinning.* Adv Drug Deliv Rev, 2007. **59**(14): p. 1384-91.
117. Liu, H. and G. Cao, *Effectiveness of the Young-Laplace equation at nanoscale.* Scientific reports, 2016. **6**(1): p. 1-10.
118. Yousefzadeh, M., *Modeling and simulation of the electrospinning process*, in *Electrospun nanofibers*. 2017, Elsevier. p. 277-301.
119. Reneker, D.H., et al., *Bending instability of electrically charged liquid jets of polymer solutions in electrospinning.* Journal of Applied Physics, 2000. **87**(9): p. 4531-4547.
120. Jaeger, R., et al. *Electrospinning of ultra-thin polymer fibers*. in *Macromolecular symposia*. 1998. Wiley Online Library.
121. Jarusuwannapoom, T., et al., *Effect of solvents on electro-spinnability of polystyrene solutions and morphological appearance of resulting electrospun polystyrene fibers.* European polymer journal, 2005. **41**(3): p. 409-421.
122. Tan, S.-H., et al., *Systematic parameter study for ultra-fine fiber fabrication via electrospinning process.* Polymer, 2005. **46**(16): p. 6128-6134.
123. Zong, X., et al., *Structure and process relationship of electrospun bioabsorbable nanofiber membranes.* polymer, 2002. **43**(16): p. 4403-4412.
124. Kim, G.-T., et al., *Investigation of pore formation for polystyrene electrospun fiber: effect of relative humidity.* Korean Journal of Chemical Engineering, 2005. **22**: p. 783-788.
125. Angammana, C.J. and S.H. Jayaram, *Analysis of the effects of solution conductivity on electrospinning process and fiber morphology.* IEEE Transactions on industry applications, 2011. **47**(3): p. 1109-1117.
126. Qin, X.-H., et al., *Effect of different salts on electrospinning of polyacrylonitrile (PAN) polymer solution.* Journal of Applied Polymer Science, 2007. **103**(6): p. 3865-3870.
127. Guo, L., K.C. Tam, and R.D. Jenkins, *Effects of salt on the intrinsic viscosity of model alkali-soluble associative polymers.* Macromolecular Chemistry and Physics, 1998. **199**(6): p. 1175-1184.
128. Li, Y., et al., *Developments of advanced electrospinning techniques: A critical review.* Advanced Materials Technologies, 2021. **6**(11): p. 2100410.
129. Dhanalakshmi, M., A.K. Lele, and J.P. Jog, *Electrospinning of Nylon11: Effect of processing parameters on morphology and microstructure.* Materials Today Communications, 2015. **3**: p. 141-148.
130. Bakar, S., et al. *Effect of voltage and flow rate electrospinning parameters on polyacrylonitrile electrospun fibers*. in *IOP Conference Series: Materials Science and Engineering*. 2018. IOP Publishing.

131. Katti, D.S., et al., *Bioresorbable nanofiber -based systems for wound healing and drug delivery: Optimization of fabrication parameters.* Journal of Biomedical Materials Research Part B: Applied Biomaterials: An Official Journal of The Society for Biomaterials, The Japanese Society for Biomaterials, and The Australian Society for Biomaterials and the Korean Society for Biomaterials, 2004. **70**(2): p. 286-296.
132. Wannatong, L., A. Sirivat, and P. Supaphol, *Effects of solvents on electrospun polymeric fibers: preliminary study on polystyrene.* Polymer International, 2004. **53**(11): p. 1851-1859.
133. Khajavi, R. and M. Abbasipour, *Controlling nanofiber morphology by the electrospinning process*, in *Electrospun nanofibers*. 2017, Elsevier. p. 109-123.
134. Zargham, S., et al., *The effect of flow rate on morphology and deposition area of electrospun nylon 6 nanofiber.* Journal of Engineered Fibers and Fabrics, 2012. **7**(4): p. 155892501200700414.
135. Fallahi, D., et al., *Effect of applied voltage on jet electric current and flow rate in electrospinning of polyacrylonitrile solutions.* Polymer international, 2008. **57**(12): p. 1363-1368.
136. Beachley, V. and X. Wen, *Effect of electrospinning parameters on the nanofiber diameter and length.* Materials Science and Engineering: C, 2009. **29**(3): p. 663-668.
137. Ki, C.S., et al., *Characterization of gelatin nanofiber prepared from gelatin–formic acid solution.* Polymer, 2005. **46**(14): p. 5094-5102.
138. Zhou, F.L., R.H. Gong, and I. Porat, *Polymeric nanofibers via flat spinneret electrospinning.* Polymer Engineering & Science, 2009. **49**(12): p. 2475-2481.
139. Long, F., et al., *The influence of electrospinning distances on fibre diameter of poly (vinyl alcohol) electrospun nanofibres.* Proc. MERD, 2017. **2017**: p. 377-378.
140. Jalili, R., S.A.A. HOSSEINI, and M. Morshed, *The effects of operating parameters on the morphology of electrospun polyacrilonitrile nanofibres.* 2005.
141. Kim, C.H., et al., *Effect of collector temperature on the porous structure of electrospun fibers.* Macromolecular Research, 2006. **14**: p. 59-65.
142. De Vrieze, S., et al., *The effect of temperature and humidity on electrospinning.* Journal of materials science, 2009. **44**: p. 1357-1362.
143. Wang, C., et al., *Electrospinning of polyacrylonitrile solutions at elevated temperatures.* Macromolecules, 2007. **40**(22): p. 7973-7983.
144. Amiraliyan, N., M. Nouri, and M.H. Kish, *Effects of some electrospinning parameters on morphology of natural silk -based nanofibers.* Journal of Applied Polymer Science, 2009. **113**(1): p. 226-234.
145. Mailley, D., A. Hébraud, and G. Schlatter, *A Review on the Impact of Humidity during Electrospinning: From the Nanofiber Structure Engineering to the Applications.* Macromolecular Materials and Engineering, 2021. **306**(7).
146. Cai, Y. and M. Gevelber, *The effect of relative humidity and evaporation rate on electrospinning: fiber diameter and measurement for control implications.* Journal of Materials Science, 2013. **48**: p. 7812-7826.
147. Huang, L., et al., *Controlling electrospun nanofiber morphology and mechanical properties using humidity.* Journal of Polymer Science Part B: Polymer Physics, 2011. **49**(24): p. 1734-1744.
148. Medeiros, E.S., et al., *Effect of relative humidity on the morphology of electrospun polymer fibers.* Canadian Journal of Chemistry, 2008. **86**(6): p. 590-599.
149. Li, D., Y. Wang, and Y. Xia, *Electrospinning of polymeric and ceramic nanofibers as uniaxially aligned arrays.* Nano letters, 2003. **3**(8): p. 1167-1171.
150. Li, D., Y. Wang, and Y. Xia, *Electrospinning Nanofibers as Uniaxially Aligned Arrays and Layer-by-Layer Stacked Films.* Advanced Materials, 2004. **16**(4): p. 361-366.

151. Theron, A., E. Zussman, and A. Yarin, *Electrostatic field-assisted alignment of electrospun nanofibres.* Nanotechnology, 2001. **12**(3): p. 384.
152. Deitzel, J.M., et al., *Controlled deposition of electrospun poly (ethylene oxide) fibers.* Polymer, 2001. **42**(19): p. 8163-8170.
153. Teo, W.E. and S. Ramakrishna, *A review on electrospinning design and nanofibre assemblies.* Nanotechnology, 2006. **17**(14): p. R89-R106.
154. O'Connor, R.A. and G.B. McGuinness, *Electrospun nanofibre bundles and yarns for tissue engineering applications: A review.* Proceedings of the Institution of Mechanical Engineers, Part H: Journal of Engineering in Medicine, 2016. **230**(11): p. 987-998.
155. Kessick, R. and G. Tepper, *Electrospun polymer composite fiber arrays for the detection and identification of volatile organic compounds.* Sensors and Actuators B: Chemical, 2006. **117**(1): p. 205-210.
156. Tian, L., M.P. Prabhakaran, and S. Ramakrishna, *Strategies for regeneration of components of nervous system: scaffolds, cells and biomolecules.* Regenerative biomaterials, 2015. **2**(1): p. 31-45.
157. Corey, J.M., et al., *Aligned electrospun nanofibers specify the direction of dorsal root ganglia neurite growth.* Journal of Biomedical Materials Research Part A: An Official Journal of The Society for Biomaterials, The Japanese Society for Biomaterials, and The Australian Society for Biomaterials and the Korean Society for Biomaterials, 2007. **83**(3): p. 636-645.
158. Chew, S.Y., et al., *The effect of the alignment of electrospun fibrous scaffolds on Schwann cell maturation.* Biomaterials, 2008. **29**(6): p. 653-661.
159. Zhong, S., et al., *An aligned nanofibrous collagen scaffold by electrospinning and its effects on in vitro fibroblast culture.* Journal of Biomedical Materials Research Part A: An Official Journal of The Society for Biomaterials, The Japanese Society for Biomaterials, and The Australian Society for Biomaterials and the Korean Society for Biomaterials, 2006. **79**(3): p. 456-463.
160. Ma, Z., et al., *Grafting of gelatin on electrospun poly (caprolactone) nanofibers to improve endothelial cell spreading and proliferation and to control cell orientation.* Tissue engineering, 2005. **11**(7-8): p. 1149-1158.
161. Tamura, T. and H. Kawakami, *Aligned electrospun nanofiber composite membranes for fuel cell electrolytes.* Nano letters, 2010. **10**(4): p. 1324-1328.
162. Thavasi, V., G. Singh, and S. Ramakrishna, *Electrospun nanofibers in energy and environmental applications.* Energy & Environmental Science, 2008. **1**(2): p. 205-221.
163. Matthews, J.A., et al., *Electrospinning of collagen type II: a feasibility study.* Journal of bioactive and compatible polymers, 2003. **18**(2): p. 125-134.
164. Kim, K.-W., et al., *The effect of molecular weight and the linear velocity of drum surface on the properties of electrospun poly (ethylene terephthalate) nonwovens.* Fibers and Polymers, 2004. **5**(2): p. 122-127.
165. Chew, S.Y., et al., *Mechanical properties of single electrospun drug-encapsulated nanofibres.* Nanotechnology, 2006. **17**(15): p. 3880-3891.
166. Fennessey, S.F. and R.J. Farris, *Fabrication of aligned and molecularly oriented electrospun polyacrylonitrile nanofibers and the mechanical behavior of their twisted yarns.* Polymer, 2004. **45**(12): p. 4217-4225.
167. Sarkar, S., S. Deevi, and G. Tepper, *Biased AC Electrospinning of Aligned Polymer Nanofibers.* Macromolecular Rapid Communications, 2007. **28**(9): p. 1034-1039.
168. Wang, H.B., et al., *Creation of highly aligned electrospun poly-L-lactic acid fibers for nerve regeneration applications.* J Neural Eng, 2009. **6**(1): p. 016001.
169. Persano, L., et al., *High performance piezoelectric devices based on aligned arrays of nanofibers of poly(vinylidenefluoride-co-trifluoroethylene).* Nat Commun, 2013. **4**: p. 1633.
170. Xu, J. and Y. Zhang, *Uniaxially well-aligned nanofiber arrays fabricated by electrospinning with a stable and low moving velocity jet.* Fibers and Polymers, 2017. **18**(11): p. 2146-2152.

171. Wang, C., T. Hashimoto, and Y. Wang, *Extension Rate and Bending Instability of Electrospinning Jets: the Role of the Electric Field.* Macromolecules, 2021. **54**(15): p. 7193-7209.
172. Liu, H., et al., *Electrospinning of nanofibers for tissue engineering applications.* Journal of Nanomaterials, 2013. **2013**: p. 3-3.
173. Greenfeld, I., et al., *Fast X-ray phase-contrast imaging of electrospinning polymer jets: measurements of radius, velocity, and concentration.* Macromolecules, 2012. **45**(8): p. 3616-3626.
174. Milleret, V., et al., *Tuning electrospinning parameters for production of 3D-fiber-fleeces with increased porosity for soft tissue engineering applications.* Eur Cell Mater, 2011. **21**(1473-2262): p. 286-303.
175. Tuck, S.J., et al., *Critical variables in the alignment of electrospun PLLA nanofibers.* Mater Sci Eng C Mater Biol Appl, 2012. **32**(7): p. 1779-1784.
176. Krishnamoorthy, T., et al., *Direct Deposition of Micron-Thick Aligned CeramicTiO2Nanofibrous Film on FTOs by Double-Needle Electrospinning Using Air-Turbulence Shielded Disc Collector.* Journal of Nanomaterials, 2011. **2011**: p. 1-7.
177. Yuan, H., Q. Zhou, and Y. Zhang, *Improving fiber alignment during electrospinning*, in *Electrospun Nanofibers*. 2017. p. 125-147.
178. Katta, P., et al., *Continuous electrospinning of aligned polymer nanofibers onto a wire drum collector.* Nano letters, 2004. **4**(11): p. 2215-2218.
179. Kessick, R., J. Fenn, and G. Tepper, *The use of AC potentials in electrospraying and electrospinning processes.* Polymer, 2004. **45**(9): p. 2981-2984.
180. Liu, S.-L., et al., *Assembly of Oriented Ultrafine Polymer Fibers by Centrifugal Electrospinning.* Journal of Nanomaterials, 2013. **2013**: p. 1-9.
181. Badrossamay, M.R., et al., *Nanofiber assembly by rotary jet-spinning.* Nano Lett, 2010. **10**(6): p. 2257-61.
182. Edmondson, D., et al., *Centrifugal electrospinning of highly aligned polymer nanofibers over a large area.* Journal of Materials Chemistry, 2012. **22**(35): p. 18646-18652.
183. Kancheva, M., et al., *Advanced centrifugal electrospinning setup.* Materials Letters, 2014. **136**: p. 150-152.
184. Liu, L. and Y.A. Dzenis, *Analysis of the effects of the residual charge and gap size on electrospun nanofiber alignment in a gap method.* Nanotechnology, 2008. **19**(35): p. 355307.
185. Yusuf, Y., et al., *Study of parallel oriented electrospun polyvinyl alcohol (PVA) nanofibers using modified electrospinning method*. 2016.
186. Yan, H., L. Liu, and Z. Zhang, *Alignment of electrospun nanofibers using dielectric materials.* Applied Physics Letters, 2009. **95**(14).
187. Secasanu, V.P., C.K. Giardina, and Y. Wang, *A novel electrospinning target to improve the yield of uniaxially aligned fibers.* Biotechnology progress, 2009. **25**(4): p. 1169-1175.
188. Cai, X., et al., *Electrospinning of very long and highly aligned fibers.* Journal of Materials Science, 2017. **52**(24): p. 14004-14010.
189. Haseeb, B., *Controlled deposition and alignment of electrospun PMMA-g-PDMS nanofibers by novel electrospinning setups*. 2011.
190. Park, S.H., et al., *Quantitatively Controlled Fabrication of Uniaxially Aligned Nanofibrous Scaffold for Cell Adhesion.* Journal of Nanomaterials, 2011. **2011**: p. 1-9.
191. Hsu, Y.H., C.H. Chan, and W.C. Tang, *Alignment of Multiple Electrospun Piezoelectric Fiber Bundles Across Serrated Gaps at an Incline: A Method to Generate Textile Strain Sensors.* Sci Rep, 2017. **7**(1): p. 15436.
192. Arras, M.M., et al., *Electrospinning of aligned fibers with adjustable orientation using auxiliary electrodes.* Science and technology of advanced materials, 2012.

193. Kiselev, P. and J. Rosell-Llompart, *Highly aligned electrospun nanofibers by elimination of the whipping motion.* Journal of Applied Polymer Science, 2012. **125**(3): p. 2433-2441.
194. Yang, Y., et al., *Effect of electric field distribution uniformity on electrospinning.* Journal of applied physics, 2008. **103**(10): p. 104307.
195. Cui, X., L. Li, and F. Xu, *Controlled assembly of poly(vinyl pyrrolidone) fibers through an electric-field-assisted electrospinning method.* Applied Physics A, 2010. **103**(1): p. 167-172.
196. Ravichandran, R., et al., *Biomimetic surface modification of titanium surfaces for early cell capture by advanced electrospinning.* Biomed Mater, 2012. **7**(1): p. 015001.
197. Afifi, A.M., et al., *Fabrication of Aligned Poly (l-lactide) Fibers by Electrospinning and Drawing.* Macromolecular materials and engineering, 2009. **294**(10): p. 658-665.
198. Sundaray, B., et al., *Electrospinning of continuous aligned polymer fibers.* Applied physics letters, 2004. **84**(7): p. 1222-1224.
199. Vimal, S.K., N. Ahamad, and D.S. Katti, *A simple method for fabrication of electrospun fibers with controlled degree of alignment having potential for nerve regeneration applications.* Mater Sci Eng C Mater Biol Appl, 2016. **63**: p. 616-27.
200. Nguyen, D.-N., Y. Hwang, and W. Moon, *Electrospinning of well-aligned fiber bundles using an End-point Control Assembly method.* European Polymer Journal, 2016. **77**: p. 54-64.
201. Teo, W.E., et al., *Porous tubular structures with controlled fibre orientation using a modified electrospinning method.* Nanotechnology, 2005. **16**(6): p. 918-924.
202. Wu, Y., L.A. Carnell, and R.L. Clark, *Control of electrospun mat width through the use of parallel auxiliary electrodes.* Polymer, 2007. **48**(19): p. 5653-5661.
203. Yalcinkaya, B., et al., *On the Nature of Electric Current in the Electrospinning Process.* Journal of Nanomaterials, 2013. **2013**: p. 1-10.
204. Pokorny, M., K. Niedoba, and V. Velebny, *Transversal electrostatic strength of patterned collector affecting alignment of electrospun nanofibers.* Applied Physics Letters, 2010. **96**(19): p. 193111.
205. Lien, C.K., *Current measurements in electrospinning.* 2013.
206. Hwang, W., C. Pang, and H. Chae, *Fabrication of aligned nanofibers by electric-field-controlled electrospinning: insulating-block method.* Nanotechnology, 2016. **27**(43): p. 435301.
207. Wang, H., et al., *Fabrication of aligned ferrite nanofibers by magnetic-field-assisted electrospinning coupled with oxygen plasma treatment.* Materials Research Bulletin, 2009. **44**(8): p. 1676-1680.
208. Ajao, J.A., et al., *Electric-magnetic field-induced aligned electrospun poly (ethylene oxide) (PEO) nanofibers.* Journal of Materials Science, 2010. **45**(9): p. 2324-2329.
209. Hu, H., et al., *Synergic effect of magnetic nanoparticles on the electrospun aligned superparamagnetic nanofibers as a potential tissue engineering scaffold.* RSC Adv., 2013. **3**(3): p. 879-886.
210. Huang, W., et al., *Effect of Magnetic Field on Stability of Jet Motion in Electrospinning.* Materials and Manufacturing Processes, 2016. **31**(12): p. 1603-1607.
211. Kovetz, A., *Electromagnetic theory*. Vol. 975. 2000: Oxford University Press Oxford.
212. He, X.-X., et al., *Near-Field Electrospinning: Progress and Applications.* The Journal of Physical Chemistry C, 2017. **121**(16): p. 8663-8678.
213. Kameoka, J. and H.G. Craighead, *Fabrication of oriented polymeric nanofibers on planar surfaces by electrospinning.* Applied Physics Letters, 2003. **83**(2): p. 371-373.
214. Bisht, G.S., et al., *Controlled continuous patterning of polymeric nanofibers on three-dimensional substrates using low-voltage near-field electrospinning.* Nano Lett, 2011. **11**(4): p. 1831-7.

215. Ye, D., et al., *Large-Scale Direct-Writing of Aligned Nanofibers for Flexible Electronics.* Small, 2018. **14**(21): p. e1703521.
216. Sun, D., et al., *Near-field electrospinning.* Nano letters, 2006. **6**(4): p. 839-842.
217. Hellmann, C., et al., *High Precision Deposition Electrospinning of nanofibers and nanofiber nonwovens.* Polymer, 2009. **50**(5): p. 1197-1205.
218. Chang, C., K. Limkrailassiri, and L. Lin, *Continuous near-field electrospinning for large area deposition of orderly nanofiber patterns.* Applied Physics Letters, 2008. **93**(12): p. 123111.
219. Davis, J.R., *Tensile testing*. 2004: ASM international.
220. Karim, S.A., et al., *Mechanical Properties and the Characterization of Polyacrylonitrile/Carbon Nanotube Composite Nanofiber.* Arabian Journal for Science and Engineering, 2018. **43**(9): p. 4697-4702.
221. Alexeev, D., et al., *Mechanical evaluation of electrospun poly(ε-caprolactone) single fibers.* Materials Today Communications, 2020. **24**.
222. Stoner, E., D. Edie, and S. Durham, *An end-effect model for the single-filament tensile test.* Journal of Materials Science, 1994. **29**: p. 6561-6574.
223. Cunningham, M.E., S.V. Schoultz, and J. Toth, *Effect of end-tab design on tension specimen stress concentrations*. 1985: ASTM International.
224. Lee, D.Y., et al., *Characteristics of chemo-mechanically driven polyacrylonitrile fiber gel actuators.* Materials Science and Engineering: C, 2008. **28**(2): p. 294-298.
225. Molnar, K., L.M. Vas, and T. Czigany, *Determination of tensile strength of electrospun single nanofibers through modeling tensile behavior of the nanofibrous mat.* Composites Part B: Engineering, 2012. **43**(1): p. 15-21.
226. Haji, A., et al., *Relationship between Single Walled Carbon Nanotubes Individual Dispersion Behavior and Properties of Electrospun Nanofibers*. 2013, Sumy State University.
227. Li, L., et al., *Formation and properties of nylon-6 and nylon-6/montmorillonite composite nanofibers.* Polymer, 2006. **47**(17): p. 6208-6217.
228. Yeum, J.H., S.B. Yang, and Y. Sabina, *Fabrication of Highly Aligned Poly(Vinyl Alcohol) Nanofibers and its Yarn by Electrospinning*, in *Electrospinning - Material, Techniques, and Biomedical Applications*. 2016.
229. Wu, S., et al., *Preparation of PAN-based carbon nanofibers by hot-stretching.* Composite Interfaces, 2008. **15**(7-9): p. 671-677.
230. Chen, F., et al., *Mechanical characterization of single high-strength electrospun polyimide nanofibres.* Journal of Physics D: Applied Physics, 2008. **41**(2).
231. Inai, R., M. Kotaki, and S. Ramakrishna, *Structure and properties of electrospun PLLA single nanofibres.* Nanotechnology, 2005. **16**(2): p. 208-13.
232. Tan, E. and C. Lim, *Mechanical characterization of nanofibers–a review.* Composites Science and Technology, 2006. **66**(9): p. 1102-1111.
233. Chan, K.H.K., et al., *Effect of molecular orientation on mechanical property of single electrospun fiber of poly [(R)-3-hydroxybutyrate-co-(R)-3-hydroxyvalerate].* The Journal of Physical Chemistry B, 2009. **113**(40): p. 13179-13185.
234. Wong, S.-C., A. Baji, and S. Leng, *Effect of fiber diameter on tensile properties of electrospun poly(ε-caprolactone).* Polymer, 2008. **49**(21): p. 4713-4722.
235. Tan, E.P.S. and C.T. Lim, *Mechanical characterization of nanofibers – A review.* Composites Science and Technology, 2006. **66**(9): p. 1102-1111.
236. Chong, E.J., et al., *Evaluation of electrospun PCL/gelatin nanofibrous scaffold for wound healing and layered dermal reconstitution.* Acta biomaterialia, 2007. **3**(3): p. 321-330.
237. Tan, E.P. and C.T. Lim, *Effects of annealing on the structural and mechanical properties of electrospun polymeric nanofibres.* Nanotechnology, 2006. **17**(10): p. 2649-54.
238. Pai, C.-L., M.C. Boyce, and G.C. Rutledge, *Mechanical properties of individual electrospun PA 6 (3) T fibers and their variation with fiber diameter.* Polymer, 2011. **52**(10): p. 2295-2301.

239. Papkov, D., et al., *Simultaneously strong and tough ultrafine continuous nanofibers.* ACS nano, 2013. **7**(4): p. 3324-3331.
240. Binnig, G., C.F. Quate, and C. Gerber, *Atomic force microscope.* Physical review letters, 1986. **56**(9): p. 930.
241. Yuya, P.A., et al., *Determination of Young's modulus of individual electrospun nanofibers by microcantilever vibration method.* Applied Physics Letters, 2007. **90**(11): p. 111909.
242. Zussman, E., et al., *Mechanical and structural characterization of electrospun PAN-derived carbon nanofibers.* Carbon, 2005. **43**(10): p. 2175-2185.
243. Tan, E., et al., *Tensile test of a single nanofiber using an atomic force microscope tip.* Applied Physics Letters, 2005. **86**(7): p. 073115.
244. Zussman, E., et al., *Tensile deformation of electrospun nylon-6,6 nanofibers.* Journal of Polymer Science Part B: Polymer Physics, 2006. **44**(10): p. 1482-1489.
245. Hang, F., et al., *In situ tensile testing of nanofibers by combining atomic force microscopy and scanning electron microscopy.* Nanotechnology, 2011. **22**(36): p. 365708.
246. Zhu, Y. and H.D. Espinosa, *An electromechanical material testing system for in situ electron microscopy and applications.* Proceedings of the National Academy of Sciences, 2005. **102**(41): p. 14503-14508.
247. Bhowmick, S., et al., *Advanced microelectromechanical systems-based nanomechanical testing: beyond stress and strain measurements.* Mrs Bulletin, 2019. **44**(6): p. 487-493.
248. Arshad, S.N., M. Naraghi, and I. Chasiotis, *Strong carbon nanofibers from electrospun polyacrylonitrile.* Carbon, 2011. **49**(5): p. 1710-1719.
249. Kahn, H., et al., *Electrostatically actuated failure of microfabricated polysilicon fracture mechanics specimens.* Proceedings of the Royal Society of London. Series A: Mathematical, Physical and Engineering Sciences, 1999. **455**(1990): p. 3807-3823.
250. Samuel, B., et al., *Mechanical testing of pyrolysed poly-furfuryl alcohol nanofibres.* Nanotechnology, 2007. **18**(11): p. 115704.
251. Lu, S., et al., *Analysis of a microelectromechanical system testing stage for tensile loading of nanostructures.* Review of Scientific Instruments, 2006. **77**(5): p. 056103.
252. Takakura, A., et al., *Strength of carbon nanotubes depends on their chemical structures.* Nature communications, 2019. **10**(1): p. 3040.
253. Reimer, L. and A. Schmidt, *The shrinkage of bulk polymers by radiation damage in an SEM.* Scanning, 1985. **7**(1): p. 47-53.
254. Chen, S., et al., *Electrospun nanofiber belts made from high performance copolyimide.* Nanotechnology, 2008. **19**(1): p. 015604.
255. Peresin, M.S., et al., *Crosslinked PVA nanofibers reinforced with cellulose nanocrystals: Water interactions and thermomechanical properties.* Journal of Applied Polymer Science, 2014. **131**(11).
256. Hwang, K.Y. and W.-R. Yu, *Measuring tensile strength of nanofibers using conductive substrates and dynamic mechanical analyzer.* Fibers and Polymers, 2009. **10**: p. 703-708.
257. Saba, N., et al., *A review on dynamic mechanical properties of natural fibre reinforced polymer composites.* Construction and Building Materials, 2016. **106**: p. 149-159.
258. Menard, K.P. and N. Menard, *Dynamic mechanical analysis*. 2020: CRC press.
259. Barua, B. and M.C. Saha, *Studies of reaction mechanisms during stabilization of electrospun polyacrylonitrile carbon nanofibers.* Polymer Engineering & Science, 2018. **58**(8): p. 1315-1321.
260. Liu, Y., H.G. Chae, and S. Kumar, *Gel-spun carbon nanotubes/polyacrylonitrile composite fibers. Part II: Stabilization reaction kinetics and effect of gas environment.* Carbon, 2011. **49**(13): p. 4477-4486.

261. Alarifi, I.M., et al. *Mechanical and thermal properties of carbonized PAN nanofibers cohesively attached to surface of carbon fiber reinforced composites*. in *Macromolecular Symposia*. 2016. Wiley Online Library.
262. Smith, P., P.J. Lemstra, and J.P. Pijpers, *Tensile strength of highly oriented polyethylene. II. Effect of molecular weight distribution.* Journal of Polymer Science: Polymer Physics Edition, 1982. **20**(12): p. 2229-2241.
263. Perkins, W.G., N.J. Capiati, and R.S. Porter, *The effect of molecular weight on the physical and mechanical properties of ultra-drawn high density polyethylene.* Polymer Engineering & Science, 1976. **16**(3): p. 200-203.
264. Termonia, Y., P. Meakin, and P. Smith, *Theoretical study of the influence of the molecular weight on the maximum tensile strength of polymer fibers.* Macromolecules, 1985. **18**(11): p. 2246-2252.
265. Lim, C., E. Tan, and S. Ng, *Effects of crystalline morphology on the tensile properties of electrospun polymer nanofibers.* Applied Physics Letters, 2008. **92**(14): p. 141908.
266. Tarus, B., et al., *Effect of polymer concentration on the morphology and mechanical characteristics of electrospun cellulose acetate and poly (vinyl chloride) nanofiber mats.* Alexandria Engineering Journal, 2016. **55**(3): p. 2975-2984.
267. Mahmud, M.M., et al., *Effects of binary solvent mixtures on the electrospinning behavior of poly (vinyl alcohol).* Materials Research Express, 2018. **5**(11): p. 115407.
268. Cai, J., et al., *Effect of solvent treatment on morphology, crystallinity and tensile properties of cellulose acetate nanofiber mats.* The Journal of The Textile Institute, 2017. **108**(4): p. 555-561.
269. Can-Herrera, L., et al., *Morphological and mechanical properties of electrospun polycaprolactone scaffolds: Effect of applied voltage.* Polymers, 2021. **13**(4): p. 662.
270. Huan, S., et al., *Effect of experimental parameters on morphological, mechanical and hydrophobic properties of electrospun polystyrene fibers.* Materials, 2015. **8**(5): p. 2718-2734.
271. Al-Abduljabbar, A. and I. Farooq, *Electrospun Polymer Nanofibers: Processing, Properties, and Applications.* Polymers (Basel), 2022. **15**(1).
272. Prilutsky, S., E. Zussman, and Y. Cohen, *The effect of embedded carbon nanotubes on the morphological evolution during the carbonization of poly (acrylonitrile) nanofibers.* Nanotechnology, 2008. **19**(16): p. 165603.
273. Baji, A., et al., *Electrospinning of polymer nanofibers: Effects on oriented morphology, structures and tensile properties.* Composites Science and Technology, 2010. **70**(5): p. 703-718.
274. Stachewicz, U., et al., *Size dependent mechanical properties of electrospun polymer fibers from a composite structure.* Polymer, 2012. **53**(22): p. 5132-5137.
275. Catalani, L.H., G. Collins, and M. Jaffe, *Evidence for molecular orientation and residual charge in the electrospinning of poly (butylene terephthalate) nanofibers.* Macromolecules, 2007. **40**(5): p. 1693-1697.
276. Rein, D., et al., *Electrospinning of ultrahigh-molecular-weight polyethylene nanofibers.* Journal of Polymer Science Part B: Polymer Physics, 2007. **45**(7): p. 766-773.
277. Hwang, K.Y., et al., *Mechanical characterization of nanofibers using a nanomanipulator and atomic force microscope cantilever in a scanning electron microscope.* Polymer Testing, 2010. **29**(3): p. 375-380.
278. Arinstein, A. and E. Zussman, *Electrospun polymer nanofibers: mechanical and thermodynamic perspectives.* Journal of Polymer Science Part B: Polymer Physics, 2011. **49**(10): p. 691-707.
279. Naraghi, M., S. Arshad, and I. Chasiotis, *Molecular orientation and mechanical property size effects in electrospun polyacrylonitrile nanofibers.* Polymer, 2011. **52**(7): p. 1612-1618.

280. Curgul, S., K.J. Van Vliet, and G.C. Rutledge, *Molecular dynamics simulation of size-dependent structural and thermal properties of polymer nanofibers.* Macromolecules, 2007. **40**(23): p. 8483-8489.
281. Tan, L., et al., *Investigation into the gelation and crystallization of polyacrylonitrile.* European Polymer Journal, 2009. **45**(5): p. 1617-1624.
282. Arinstein, A., et al., *Effect of supramolecular structure on polymer nanofibre elasticity.* Nature nanotechnology, 2007. **2**(1): p. 59-62.
283. Mottaghitalab, V. and A.K. Haghi, *A study on electrospinning of polyacrylonitrile nanofibers.* Korean Journal of Chemical Engineering, 2010. **28**(1): p. 114-118.
284. Bao, J., L.I. Clarke, and R.E. Gorga, *Effect of constrained annealing on the mechanical properties of electrospun poly(ethylene oxide) webs containing multiwalled carbon nanotubes.* Journal of Polymer Science Part B: Polymer Physics, 2015. **54**(8): p. 787-796.
285. Coleman, B.F., et al., *Touchspinning: Mechanically drawing polyacrylonitrile nanofibers.* Journal of Applied Polymer Science, 2022. **139**(24).
286. Jose, M.V., et al., *Morphology and mechanical properties of Nylon 6/MWNT nanofibers.* Polymer, 2007. **48**(4): p. 1096-1104.
287. Kongkhlang, T., et al., *Electrospinning as a new technique to control the crystal morphology and molecular orientation of polyoxymethylene nanofibers.* Journal of the American Chemical Society, 2008. **130**(46): p. 15460-15466.
288. Sawai, D., Y. Fujii, and T. Kanamoto, *Development of oriented morphology and tensile properties upon superdawing of solution-spun fibers of ultra-high molecular weight poly (acrylonitrile).* Polymer, 2006. **47**(12): p. 4445-4453.
289. Chen, J. and I. Harrison, *Modification of polyacrylonitrile (PAN) carbon fiber precursor via post-spinning plasticization and stretching in dimethyl formamide (DMF).* Carbon, 2002. **40**(1): p. 25-45.
290. Liu, H.-Y., L. Xu, and Q.-L. Sun, *Highly aligned electrospun nanofibers by hot-drawing.* Thermal Science, 2015. **19**(4): p. 1357-1360.
291. Flory, P.J. and D.Y. Yoon, *Molecular morphology in semicrystalline polymers.* Nature, 1978. **272**(5650): p. 226-229.
292. López-Barrón, C.R., et al., *Molecular alignment in polyethylene during cold drawing using in-situ SANS and Raman spectroscopy.* Macromolecules, 2017. **50**(9): p. 3627-3636.
293. Petrov, A., V.Y. Rudyak, and A. Chertovich, *Optimal Entanglement of Polymers Promotes the Formation of Highly Oriented Fibers.* Macromolecules, 2022. **55**(15): p. 6493-6504.
294. Theron, S., E. Zussman, and A. Yarin, *Experimental investigation of the governing parameters in the electrospinning of polymer solutions.* Polymer, 2004. **45**(6): p. 2017-2030.
295. Greiner, A. and J.H. Wendorff, *Electrospinning: a fascinating method for the preparation of ultrathin fibers.* Angewandte Chemie International Edition, 2007. **46**(30): p. 5670-5703.
296. Frank, E., F. Hermanutz, and M.R. Buchmeiser, *Carbon Fibers: Precursors, Manufacturing, and Properties.* Macromolecular Materials and Engineering, 2012. **297**(6): p. 493-501.
297. Melechko, A.V., et al., *Vertically aligned carbon nanofibers and related structures: Controlled synthesis and directed assembly.* Journal of applied physics, 2005. **97**(4): p. 3.
298. Wazir, A.H. and L. Kakakhel, *Preparation and characterization of pitch-based carbon fibers.* New carbon materials, 2009. **24**(1): p. 83-88.
299. Liu, J., et al., *Development of pitch-based carbon fibers: a review.* Energy Sources, Part A: Recovery, Utilization, and Environmental Effects, 2020: p. 1-21.
300. Yusof, N. and A. Ismail, *Post spinning and pyrolysis processes of polyacrylonitrile (PAN)-based carbon fiber and activated carbon fiber: A review.* Journal of Analytical and Applied Pyrolysis, 2012. **93**: p. 1-13.
301. Jang, D., et al., *Strategies for the production of PAN-Based carbon fibers with high tensile strength.* Carbon, 2022. **186**: p. 644-677.

302. Bürger, A., et al., *Polyimides as precursors for artificial carbon.* Carbon, 1975. **13**(3): p. 149-157.
303. Zhang, S.-J., H.-Q. Yu, and H.-M. Feng, *PVA-based activated carbon fibers with lotus root-like axially porous structure.* Carbon, 2006. **44**(10): p. 2059-2068.
304. Jiao, Y., et al., *Coordination enhancement of hydrogen and helium recovery in polybenzimidazole-based carbon molecular sieve membranes.* Separation and Purification Technology, 2023: p. 123691.
305. Yang, Y., et al., *Highly porous electrospun polyvinylidene fluoride (PVDF)-based carbon fiber.* Carbon, 2011. **49**(11): p. 3395-3403.
306. Tzeng, S.-S. and Y.-G. Chr, *Evolution of microstructure and properties of phenolic resin-based carbon/carbon composites during pyrolysis.* Materials Chemistry and Physics, 2002. **73**(2-3): p. 162-169.
307. Wu, Q. and D. Pan, *A new cellulose based carbon fiber from a lyocell precursor.* Textile research journal, 2002. **72**(5): p. 405-410.
308. Liu, C.-K., et al., *Preparation of carbon nanofibres through electrospinning and thermal treatment.* Polymer International, 2009. **58**(12): p. 1341-1349.
309. Feng, L., N. Xie, and J. Zhong, *Carbon Nanofibers and Their Composites: A Review of Synthesizing, Properties and Applications.* Materials (Basel), 2014. **7**(5): p. 3919-3945.
310. Inagaki, M., Y. Yang, and F. Kang, *Carbon nanofibers prepared via electrospinning.* Adv Mater, 2012. **24**(19): p. 2547-66.
311. Yamashita, Y., et al., *Carbonization conditions for electrospun nanofibre of polyacylonitrile copolymer.* 2008.
312. Zhou, Z., et al., *Development of carbon nanofibers from aligned electrospun polyacrylonitrile nanofiber bundles and characterization of their microstructural, electrical, and mechanical properties.* Polymer, 2009. **50**(13): p. 2999-3006.
313. De Oliveira, J.B., et al., *Carbon nanofibers obtained from electrospinning process.* Materials Research Express, 2018. **5**(2): p. 025602.
314. Lee, S., et al., *Structural Evolution of Polyacrylonitrile Fibers in Stabilization and Carbonization.* Advances in Chemical Engineering and Science, 2012. **02**(02): p. 275-282.
315. Rahaman, M.S.A., A.F. Ismail, and A. Mustafa, *A review of heat treatment on polyacrylonitrile fiber.* Polymer degradation and Stability, 2007. **92**(8): p. 1421-1432.
316. Donnet, J.-B. and R.C. Bansal, *Carbon fibers*. 1998: Crc Press.
317. Bashir, Z., *A critical review of the stabilisation of polyacrylonitrile.* Carbon, 1991. **29**(8): p. 1081-1090.
318. Houtz, R., " *Orlon" Acrylic Fiber: Chemistry and Properties.* Textile Research Journal, 1950. **20**(11): p. 786-801.
319. Burlant, W. and J. Parsons, *Pyrolysis of polyacrylonitrile.* Journal of Polymer Science, 1956. **22**(101): p. 249-256.
320. Lubin, G., *Handbook of composites*. 2013: Springer Science & Business Media.
321. Munajat, N.A., et al., *The effects of different carbonization temperatures on the properties of electrospun carbon nanofibre from polyacrylonitrile (PAN) precursor.* Journal of Advanced Research in Fluid Mechanics and Thermal Sciences, 2018. **49**(2): p. 85-91.
322. Gu, S.-Y., Q.-L. Wu, and R. Jie, *Preparation and surface structures of carbon nanofibers produced from electrospun PAN precursors.* New Carbon Materials, 2008. **23**(2): p. 171-176.
323. Sutasinpromprae, J., et al., *Preparation and characterization of ultrafine electrospun polyacrylonitrile fibers and their subsequent pyrolysis to carbon fibers.* Polymer International, 2006. **55**(8): p. 825-833.
324. Wang, Y., S. Serrano, and J.J. Santiago-Avilés, *Raman characterization of carbon nanofibers prepared using electrospinning.* Synthetic Metals, 2003. **138**(3): p. 423-427.

325. Kim, C., et al., *Raman spectroscopic evaluation of polyacrylonitrile-based carbon nanofibers prepared by electrospinning.* Journal of Raman Spectroscopy, 2004. **35**(11): p. 928-933.
326. Agend, F., N. Naderi, and R. Fareghi-Alamdari, *Fabrication and electrical characterization of electrospun polyacrylonitrile-derived carbon nanofibers.* Journal of Applied Polymer Science, 2007. **106**(1): p. 255-259.
327. Gao, A., et al., *Correlation between graphite crystallite distribution morphology and the mechanical properties of carbon fiber during heat treatment.* Materials Letters, 2011. **65**(23-24): p. 3444-3446.
328. Sun, T., Y. Hou, and H. Wang, *Effect of Atmospheres on Stabilization of Polyacrylonitrile Fibers.* Journal of Macromolecular Science, Part A, 2009. **46**(8): p. 807-815.
329. Choi, J., et al., *Evolution of structural inhomogeneity in polyacrylonitrile fibers by oxidative stabilization.* Carbon, 2020. **165**: p. 225-237.
330. Khayyam, H., et al., *PAN precursor fabrication, applications and thermal stabilization process in carbon fiber production: Experimental and mathematical modelling.* Progress in Materials Science, 2020. **107**: p. 100575.
331. Kim, C., et al., *Fabrications and structural characterization of ultra-fine carbon fibres by electrospinning of polymer blends.* Solid State Communications, 2007. **142**(1-2): p. 20-23.
332. Fitzer, E., W. Frohs, and M. Heine, *Optimization of stabilization and carbonization treatment of PAN fibres and structural characterization of the resulting carbon fibres.* Carbon, 1986. **24**(4): p. 387-395.
333. Zhang, L., et al., *A review: carbon nanofibers from electrospun polyacrylonitrile and their applications.* Journal of Materials Science, 2013. **49**(2): p. 463-480.
334. Edie, D., *The effect of processing on the structure and properties of carbon fibers.* Carbon, 1998. **36**(4): p. 345-362.
335. Ozbek, S. and D. Isaac, *Strain-induced density changes in PAN-based carbon fibres.* Carbon, 2000. **38**(14): p. 2007-2016.
336. Tsai, J.S. and C.H. Lin, *The effect of the side chain of acrylate comonomers on the orientation, pore‐size distribution, and properties of polyacrylonitrile precursor and resulting carbon fiber.* Journal of applied polymer science, 1991. **42**(11): p. 3039-3044.
337. Lu, J., et al., *Microstructure and properties of polyacrylonitrile based carbon fibers.* Polymer Testing, 2020. **81**.
338. Zhu, D., et al., *Study of carbon films from PAN/VGCF composites by gelation/crystallization from solution.* Carbon, 2002. **40**(3): p. 363-373.
339. Kaburagi, M., et al., *Small angle X-ray scattering from voids within fibers during the stabilization and carbonization stages.* Carbon, 2003. **41**(5): p. 915-926.
340. Zhu, J., et al., *Unveiling Carbon Ring Structure Formation Mechanisms in Polyacrylonitrile-Derived Carbon Fibers.* ACS Appl Mater Interfaces, 2019. **11**(45): p. 42288-42297.
341. Saha, B. and G.C. Schatz, *Carbonization in polyacrylonitrile (PAN) based carbon fibers studied by ReaxFF molecular dynamics simulations.* The Journal of Physical Chemistry B, 2012. **116**(15): p. 4684-4692.
342. Wang, Y.-f., et al., *Regulating the radial structure of polyacrylonitrile fibers during pre-oxidation and its effect on the mechanical properties of the resulting carbon fibers.* New Carbon Materials, 2021. **36**(4): p. 827-834.
343. Chen, L., et al., *New insights into orientation differences between skin and core regions of polyacrylonitrile fibers during pre-stabilization with the stretching process.* Polymer, 2020. **210**.
344. Salim, N.V., et al., *The Role of Tension and Temperature for Efficient Carbonization of Polyacrylonitrile Fibers: Toward Low Cost Carbon Fibers.* Industrial & Engineering Chemistry Research, 2018. **57**(12): p. 4268-4276.

345. Gutmann, P., et al., *Carbonization of polyacrylonitrile-based fibers under defined tensile load: Influence on shrinkage behavior, microstructure, and mechanical properties.* Polymer Degradation and Stability, 2019. **163**: p. 174-184.
346. Kim, M.-A., et al., *Strengthened PAN-based carbon fibers obtained by slow heating rate carbonization.* Scientific reports, 2016. **6**(1): p. 1-7.
347. Wang, S., et al., *Influence of heat treatment on physical–chemical properties of PAN-based carbon fiber.* Ceramics International, 2006. **32**(3): p. 291-295.
348. Xiao, H., et al., *The effect of heat treatment temperature and time on the microstructure and mechanical properties of PAN-based carbon fibers.* Journal of Materials Science, 2014. **49**: p. 794-804.
349. Buckley, J.D. and D.D. Edie, *Carbon-carbon materials and composites*. 1993: William Andrew.
350. Yang, F., et al., *Effect of amorphous carbon on the tensile behavior of polyacrylonitrile (PAN)-based carbon fibers.* Journal of Materials Science, 2019. **54**(11): p. 8800-8813.
351. Bazbouz, M.B. and G.K. Stylios, *The tensile properties of electrospun nylon 6 single nanofibers.* Journal of Polymer Science Part B: Polymer Physics, 2010. **48**(15): p. 1719-1731.
352. Rashid, T.U., R.E. Gorga, and W.E. Krause, *Mechanical Properties of Electrospun Fibers—A Critical Review.* Advanced Engineering Materials, 2021. **23**(9).
353. Samatham, R. and K.J. Kim, *Electric current as a control variable in the electrospinning process.* Polymer Engineering & Science, 2006. **46**(7): p. 954-959.
354. Kurban, Z., et al., *Turbostratic graphite nanofibres from electrospun solutions of PAN in dimethylsulphoxide.* European polymer journal, 2010. **46**(6): p. 1194-1202.
355. Khan, Z., et al., *Morphology, mechanical properties and surface characteristics of electrospun polyacrylonitrile (PAN) nanofiber mats.* Int. J. Adv. Eng. Nano Technol, 2015. **2**: p. 15-22.
356. Kaerkitcha, N., S. Chuangchote, and T. Sagawa, *Control of physical properties of carbon nanofibers obtained from coaxial electrospinning of PMMA and PAN with adjustable inner/outer nozzle-ends.* Nanoscale research letters, 2016. **11**: p. 1-9.
357. Mohamed, A., et al., *Photocatalytic degradation of organic dyes and enhanced mechanical properties of PAN/CNTs composite nanofibers.* Separation and Purification Technology, 2017. **182**: p. 219-223.
358. Isaac, B., R.M. Taylor, and K. Reifsnider, *Anisotropic Characterizations of Electrospun PAN Nanofiber Mats Using Design of Experiments.* Nanomaterials (Basel), 2020. **10**(11).
359. Ahn, H., et al., *Microstructure Analysis of Drawing Effect and Mechanical Properties of Polyacrylonitrile Precursor Fiber According to Molecular Weight.* Polymers (Basel), 2022. **14**(13).
360. Tan, L., J. Pan, and A. Wan, *Shear and extensional rheology of polyacrylonitrile solution: effect of ultrahigh molecular weight polyacrylonitrile.* Colloid and Polymer Science, 2012. **290**: p. 289-295.
361. Cowie, J.M.G. and V. Arrighi, *Polymers: chemistry and physics of modern materials*. 2007: CRC press.
362. Hou, C., et al., *High-molecular-weight polyacrylonitrile by atom transfer radical polymerization.* Journal of applied polymer science, 2006. **100**(4): p. 3372-3376.
363. Iovleva, M., V. Smirnova, and G. Budnitskii, *The solubility of polyacrylonitrile.* Fibre Chemistry, 2001. **33**(4): p. 262-264.
364. Ghorpade, R.V., D.W. Cho, and S.C. Hong, *Effect of controlled tacticity of polyacrylonitrile (co) polymers on their thermal oxidative stabilization behaviors and the properties of resulting carbon films.* Carbon, 2017. **121**: p. 502-511.
365. Wang, W., et al., *Unexpectedly high piezoelectricity of electrospun polyacrylonitrile nanofiber membranes.* Nano energy, 2019. **56**: p. 588-594.

366. Yushkin, A., et al., *Fabrication of Polyacrylonitrile UF Membranes by VIPS Method with Acetone as Co-Solvent.* Membranes, 2022. **12**(5): p. 523.
367. Gao, Q., et al., *Effect of drying method on the microstructures and mechanical strength of polyacrylonitrile nascent fibers.* Drying Technology, 2022. **40**(7): p. 1329-1337.
368. Skvortsov, I.Y., et al., *Rheology and molecular interactions in polyacrylonitrile solutions: Role of a solvent.* Journal of Molecular Liquids, 2022. **364**: p. 119938.
369. Bognitzki, M., et al., *Nanostructured fibers via electrospinning.* Advanced materials, 2001. **13**(1): p. 70-72.
370. Yoon, J.W., et al., *Multi-jet electrospinning of polystyrene/polyamide 6 blend: thermal and mechanical properties.* Fashion and Textiles, 2017. **4**: p. 1-12.
371. Chen, H.-M. and D.-G. Yu, *An elevated temperature electrospinning process for preparing acyclovir-loaded PAN ultrafine fibers.* Journal of Materials Processing Technology, 2010. **210**(12): p. 1551-1555.
372. Sabantina, L., et al. *Investigation of needleless electrospun PAN nanofiber mats*. in *AIP Conference Proceedings*. 2018. AIP Publishing LLC.
373. Sabantina, L., et al., *Stabilization of polyacrylonitrile nanofiber mats obtained by needleless electrospinning using dimethyl sulfoxide as solvent.* Journal of Industrial Textiles, 2020. **50**(2): p. 224-239.
374. Grothe, T., et al., *Impact of solid content in the electrospinning solution on the physical and chemical properties of polyacrylonitrile (PAN) nanofibrous mats.* Tekstilec, 2020. **63**(3).
375. Wortmann, M., et al., *New polymers for needleless electrospinning from low-toxic solvents.* Nanomaterials, 2019. **9**(1): p. 52.
376. Yan, G., et al., *Self-assembly of electrospun polymer nanofibers: A general phenomenon generating honeycomb-patterned nanofibrous structures.* Langmuir, 2011. **27**(8): p. 4285-4289.
377. Grothe, T., et al., *Needleless Electrospinning of PAN Nanofibre Mats.* Tekstilec, 2017. **60**(4).
378. Muhammed, N.S., et al., *Comparative study of green and synthetic polymers for enhanced oil recovery.* Polymers, 2020. **12**(10): p. 2429.
379. Wang, T. and S. Kumar, *Electrospinning of polyacrylonitrile nanofibers.* Journal of applied polymer science, 2006. **102**(2): p. 1023-1029.
380. Yang, T., et al., *Rheological behaviour of polyacrylonitrile in an ionic liquid solution.* 2010.
381. Tenchurin, T.K., et al., *Rheological features of fiber spinning from polyacrylonitrile solutions in an electric field. Structure and properties.* Fibre Chemistry, 2014. **46**: p. 151-160.
382. Liu, H.C., et al., *Rheological behavior of polyacrylonitrile and polyacrylonitrile/lignin blends.* Polymer, 2017. **111**: p. 177-182.
383. Feng, J., *The stretching of an electrified non-Newtonian jet: A model for electrospinning.* Physics of fluids, 2002. **14**(11): p. 3912-3926.
384. Brunchi, C.-E., M. Bercea, and S. Morariu, *Viscometric and rheological study of polyacrylonitrile solutions.* e-Polymers, 2009. **9**(1).
385. Huang, S., et al., *Preparation and Properties of Electrospun Poly (Vinyl Pyrrolidone)/Cellulose Nanocrystal/Silver Nanoparticle Composite Fibers.* Materials (Basel), 2016. **9**(7).
386. Morariu, S., et al., *Influence of Temperature on the Rheological Behavior of Polymer Mixtures in Solution.* Industrial & Engineering Chemistry Research, 2011. **50**(15): p. 9451-9455.
387. Cooke, M.E. and D.H. Rosenzweig, *The rheology of direct and suspended extrusion bioprinting.* APL bioengineering, 2021. **5**(1): p. 011502.
388. Zhang, D., et al., *The effect of ultrahigh shear rate on the physical characteristics of xanthan gum.* Polymer Bulletin, 2022: p. 1-21.
389. Cross, M.M., *Rheology of non-Newtonian fluids: a new flow equation for pseudoplastic systems.* Journal of colloid science, 1965. **20**(5): p. 417-437.

390. Nasouri, K., A. Shoushtari, and A. Kaflou, *Investigation of polyacrylonitrile electrospun nanofibres morphology as a function of polymer concentration, viscosity and Berry number.* Micro & Nano Letters, 2012. **7**(5): p. 423-426.
391. Kim, Y.-N., et al., *Effect of Viscosity on the Morphology of Electrospun Polyacrylonitrile Fibers as a Linear Actuator and Artificial Muscles.* Journal of the Korean Ceramic Society, 2006. **43**(4): p. 203-206.
392. Budtov, V., *Study of the concentration dependence of the viscosity of dilute polymer solutions. Compression of polymer chains.* Polymer Science USSR, 1967. **9**(4): p. 854-862.
393. Raicu, V., et al., *Electrical conductivity of aqueous polymer solutions: 1. Theory and experimental verification.* Colloid and Polymer Science, 1997. **275**: p. 372-377.
394. Prins, P., et al., *Charge transport along coiled conjugated polymer chains.* The Journal of Physical Chemistry C, 2007. **111**(29): p. 11104-11112.
395. Kalayci, V.E., et al., *Charge consequences in electrospun polyacrylonitrile (PAN) nanofibers.* Polymer, 2005. **46**(18): p. 7191-7200.
396. Lin, T., et al., *Effects of polymer concentration and cationic surfactant on the morphology of electrospun polyacrylonitrile nanofibres.* 2005.
397. Wu, W., R.J. Giese, and C. Van Oss, *Evaluation of the Lifshitz-van der Waals/acid-base approach to determine surface tension components.* Langmuir, 1995. **11**(1): p. 379-382.
398. Qun, G. and W. Ajun, *Effects of molecular weight, degree of acetylation and ionic strength on surface tension of chitosan in dilute solution.* Carbohydrate Polymers, 2006. **64**(1): p. 29-36.
399. Lee, K.H., et al., *The change of bead morphology formed on electrospun polystyrene fibers.* Polymer, 2003. **44**(14): p. 4029-4034.
400. Yarin, A.L., B. Pourdeyhimi, and S. Ramakrishna, *Fundamentals and applications of micro-and nanofibers*. 2014: Cambridge University Press.
401. Mazoochi, T., et al., *Investigation on the morphological characteristics of nanofiberous membrane as electrospun in the different processing parameters.* International Journal of Industrial Chemistry, 2012. **3**: p. 1-8.
402. Subbiah, T., et al., *Electrospinning of nanofibers.* Journal of applied polymer science, 2005. **96**(2): p. 557-569.
403. Bodnár, E., J. Grifoll, and J. Rosell-Llompart, *Polymer solution electrospraying: A tool for engineering particles and films with controlled morphology.* Journal of Aerosol Science, 2018. **125**: p. 93-118.
404. Jacobs, V., R.D. Anandjiwala, and M. Maaza, *The influence of electrospinning parameters on the structural morphology and diameter of electrospun nanofibers.* Journal of applied polymer science, 2010. **115**(5): p. 3130-3136.
405. Ojha, S.S., et al., *Morphology of electrospun nylon‐6 nanofibers as a function of molecular weight and processing parameters.* Journal of applied polymer science, 2008. **108**(1): p. 308-319.
406. Lu, C., et al., *Computer simulation of electrospinning. Part I. Effect of solvent in electrospinning.* Polymer, 2006. **47**(3): p. 915-921.
407. Park, O.-K., et al., *Effects of functional group of carbon nanotubes on mechanical properties of carbon fibers.* Composites Part B: Engineering, 2015. **76**: p. 159-166.
408. Liu, H., et al., *Preparation, stabilization and carbonization of a novel polyacrylonitrile-based carbon fiber precursor.* Polymers, 2019. **11**(7): p. 1150.
409. Ahn, H., et al., *Microstructure and Mechanical Properties of Polyacrylonitrile Precursor Fiber with Dry and Wet Drawing Process.* Polymers, 2021. **13**(10): p. 1613.
410. Goodhew, P., A. Clarke, and J. Bailey, *A review of the fabrication and properties of carbon fibres.* Materials Science and Engineering, 1975. **17**(1): p. 3-30.

411. Fawcett, W.R. and A.A. Kloss, *Solvent-induced frequency shifts in the infrared spectrum of dimethyl sulfoxide in organic solvents.* The Journal of Physical Chemistry, 1996. **100**(6): p. 2019-2024.
412. Ravi, J., et al., *FTIR markers of methionine oxidation for early detection of oxidized protein therapeutics.* European Biophysics Journal, 2011. **40**: p. 339-345.
413. Wallace, V.M., et al., *Revisiting the aqueous solutions of dimethyl sulfoxide by spectroscopy in the mid-and near-infrared: experiments and Car–Parrinello simulations.* The Journal of Physical Chemistry B, 2015. **119**(46): p. 14780-14789.
414. Coleman, M. and R. Petcavich, *Fourier transform infrared studies on the thermal degradation of polyacrylonitrile.* Journal of Polymer Science: Polymer Physics Edition, 1978. **16**(5): p. 821-832.
415. Surianarayanan, M., R. Vijayaraghavan, and K. Raghavan, *Spectroscopic investigations of polyacrylonitrile thermal degradation.* Journal of Polymer Science Part A: Polymer Chemistry, 1998. **36**(14): p. 2503-2512.
416. Ouyang, Q., et al., *Mechanism and kinetics of the stabilization reactions of itaconic acid-modified polyacrylonitrile.* Polymer Degradation and Stability, 2008. **93**(8): p. 1415-1421.
417. Duan, Q., B. Wang, and H. Wang, *Effects of stabilization temperature on structures and properties of polyacrylonitrile (PAN)-based stabilized electrospun nanofiber mats.* Journal of Macromolecular Science, Part B, 2012. **51**(12): p. 2428-2437.
418. Budi, M.A., A. Kubart, and J.S. Andrew, *Guide column array: a versatile approach to aligning and patterning ceramic nanofibers.* Nanoscale, 2018. **10**(44): p. 20681-20688.
419. Pawar, S., P. Murugavel, and D. Lal, *Effect of relative humidity and sea level pressure on electrical conductivity of air over Indian Ocean.* Journal of Geophysical Research: Atmospheres, 2009. **114**(D2).
420. Brandrup, J., et al., *Polymer handbook*. Vol. 89. 1999: Wiley New York.
421. Serway, R.A. and J.W. Jewett, *Principles of Physics: A Calculus-Based Text, Volume 2*. Vol. 2. 2012: Cengage Learning.
422. Tropf, W.J., M.E. Thomas, and T.J. Harris, *Properties of crystals and glasses.* Handbook of optics, 1995. **2**: p. 33.1-33.101.
423. Weatherwax, R.C. and A.J. Stamm, *The electrical resistivity of resin-treated wood and laminated hydrolyzed-wood and paper-base plastics.* Electrical Engineering, 1945. **64**(12): p. 833-838.
424. Moafi, H.F., A. Fallah Shojaie, and M. Ali Zanjanchi, *Photoactive polyacrylonitrile fibers coated by nano-sized titanium dioxide: synthesis, characterization, thermal investigation.* Journal of the Chilean Chemical Society, 2011. **56**(1): p. 610-615.
425. Bajaj, P., T. Sreekumar, and K. Sen, *Thermal behaviour of acrylonitrile copolymers having methacrylic and itaconic acid comonomers.* Polymer, 2001. **42**(4): p. 1707-1718.
426. Xue, T.J., M.A. McKinney, and C.A. Wilkie, *The thermal degradation of polyacrylonitrile.* Polymer Degradation and Stability, 1997. **58**(1-2): p. 193-202.
427. Chatterjee, N., et al., *An XRD characterization of the thermal degradation of polyacrylonitrile.* Journal of Polymer Science Part B: Polymer Physics, 1995. **33**(12): p. 1705-1712.
428. Karacan, I. and G. Erdoğan, *A study on structural characterization of thermal stabilization stage of polyacrylonitrile fibers prior to carbonization.* Fibers and Polymers, 2012. **13**: p. 329-338.
429. Manocha, L., O. Bahl, and G. Jain, *Length changes in PAN fibres during their pyrolysis to carbon fibres.* Die Angewandte Makromolekulare Chemie: Applied Macromolecular Chemistry and Physics, 1978. **67**(1): p. 11-29.
430. Sabantina, L., et al., *Fixing PAN nanofiber mats during stabilization for carbonization and creating novel metal/carbon composites.* Polymers, 2018. **10**(7): p. 735.

431. Panapoy, M., A. Dankeaw, and B. Ksapabutr, *Electrical conductivity of PAN-based carbon nanofibers prepared by electrospinning method.* Thammasat Int. J. Sc. Tech, 2008. **13**(January 2008): p. 11-17.
432. Schierholz, R., et al., *The carbonization of polyacrylonitrile-derived electrospun carbon nanofibers studied by in situ transmission electron microscopy.* RSC advances, 2019. **9**(11): p. 6267-6277.
433. Hoffmann, A. and A.J. Kuehne, *High throughput centrifugal electrospinning of polyacrylonitrile nanofibers for carbon fiber nonwovens.* Polymers, 2021. **13**(8): p. 1313.
434. Dhakate, S.R., et al., *Morphology and thermal properties of PAN copolymer based electrospun nanofibers.* Synthetic Metals, 2011. **161**(5-6): p. 411-419.
435. Epp, J., *X-ray diffraction (XRD) techniques for materials characterization*, in *Materials characterization using nondestructive evaluation (NDE) methods*. 2016, Elsevier. p. 81-124.
436. Khan, H., et al., *Experimental methods in chemical engineering: X-ray diffraction spectroscopy—XRD.* The Canadian journal of chemical engineering, 2020. **98**(6): p. 1255-1266.
437. Yang, Y., et al., *Polyacrylonitrile-based electrospun carbon paper for electrode applications.* Journal of Applied Polymer Science, 2012. **124**(5): p. 3861-3870.
438. Dresselhaus, M.S., et al., *Raman spectroscopy of carbon nanotubes.* Physics reports, 2005. **409**(2): p. 47-99.
439. Mirzaei, E., et al., *Functionalization of PAN-Based Electrospun Carbon Nanofibers by Acid Oxidation: Study of Structural,Electrical and Mechanical Properties.* Fullerenes, Nanotubes and Carbon Nanostructures, 2015. **23**(11): p. 930-937.
440. Matthews, M.J., et al., *Origin of dispersive effects of the Raman D band in carbon materials.* Physical review B, 1999. **59**(10): p. R6585.
441. Osswald, S., et al., *Elimination of D-band in Raman spectra of double-wall carbon nanotubes by oxidation.* Chemical Physics Letters, 2005. **402**(4-6): p. 422-427.
442. Jawhari, T., A. Roid, and J. Casado, *Raman spectroscopic characterization of some commercially available carbon black materials.* Carbon, 1995. **33**(11): p. 1561-1565.
443. Ferrari, A.C. and D.M. Basko, *Raman spectroscopy as a versatile tool for studying the properties of graphene.* Nature nanotechnology, 2013. **8**(4): p. 235-246.
444. Boudou, J.-P., et al., *Oxygen plasma modification of pitch-based isotropic carbon fibres.* Carbon, 2003. **41**(1): p. 41-56.
445. Schwan, J., et al., *Raman spectroscopy on amorphous carbon films.* Journal of Applied Physics, 1996. **80**(1): p. 440-447.
446. Kim, C., et al., *Fabrication of Electrospinning-Derived Carbon Nanofiber Webs for the Anode Material of Lithium-Ion Secondary Batteries.* Advanced Functional Materials, 2006. **16**(18): p. 2393-2397.
447. Wang, Y. and J.J. Santiago-Avilés, *Large negative magnetoresistance and two-dimensional weak localization in carbon nanofiber fabricated using electrospinning.* Journal of applied physics, 2003. **94**(3): p. 1721-1727.
448. Chen, T., et al., *Electrospun carbon nanofibers as anode materials for sodium ion batteries with excellent cycle performance.* Journal of Materials Chemistry A, 2014. **2**(12).
449. Wang, G., et al., *Activated carbon nanofiber webs made by electrospinning for capacitive deionization.* Electrochimica Acta, 2012. **69**: p. 65-70.
450. Wang, Z., et al., *The structural basis for giant enhancement enabling single-molecule Raman scattering.* Proceedings of the National Academy of Sciences, 2003. **100**(15): p. 8638-8643.
451. Huang, Y. and R. Young, *Effect of fibre microstructure upon the modulus of PAN-and pitch-based carbon fibres.* Carbon, 1995. **33**(2): p. 97-107.

452. Wan, L.Y., et al., *An analysis of the tensile properties of nanofiber mats.* Polymer, 2015. **73**: p. 62-67.
453. Kim, S., et al., *Preparation and characterization of PAN-based superfined carbon fibers for carbon-paper applications.* Bulletin of the Korean Chemical Society, 2013. **34**(12): p. 3733-3737.
454. Franklin, R., et al., *Reinforcing carbonized polyacrylonitrile fibers with nanoscale graphitic interface-layers.* Journal of Materials Science & Technology, 2021. **95**: p. 78-87.
455. Soliman, S., et al., *Controlling the porosity of fibrous scaffolds by modulating the fiber diameter and packing density.* Journal of Biomedical Materials Research Part A, 2011. **96**(3): p. 566-574.
456. Bian, Y., et al., *Influence of fiber diameter, filter thickness, and packing density on PM2. 5 removal efficiency of electrospun nanofiber air filters for indoor applications.* Building and Environment, 2020. **170**: p. 106628.
457. Isaac, B., R.M. Taylor, and K. Reifsnider, *Mechanical and Dielectric Properties of Aligned Electrospun Fibers.* Fibers, 2021. **9**(1).
458. Lee, M.W., et al., *Self-Healing Nanofiber-Reinforced Polymer Composites. 1. Tensile Testing and Recovery of Mechanical Properties.* ACS Appl Mater Interfaces, 2015. **7**(35): p. 19546-54.
459. Hua, C.C. and J.D. Schieber, *Segment connectivity, chain-length breathing, segmental stretch, and constraint release in reptation models. I. Theory and single-step strain predictions.* The Journal of chemical physics, 1998. **109**(22): p. 10018-10027.
460. Nguyen, T.D., et al., *A thermoviscoelastic model for amorphous shape memory polymers: incorporating structural and stress relaxation.* Journal of the Mechanics and Physics of Solids, 2008. **56**(9): p. 2792-2814.
461. Fancey, K.S., *A mechanical model for creep, recovery and stress relaxation in polymeric materials.* Journal of materials science, 2005. **40**(18): p. 4827-4831.
462. Kapnistos, M., et al., *Unexpected power-law stress relaxation of entangled ring polymers.* Nature materials, 2008. **7**(12): p. 997-1002.
463. Tobolsky, A.V., *Stress relaxation studies of the viscoelastic properties of polymers.* Rubber Chemistry and Technology, 1957. **30**(2): p. 427-448.
464. Tan, L., A. Wan, and D. Pan, *Pregelled gel spinning of polyacrylonitrile precursor fiber.* Materials Letters, 2011. **65**(5): p. 887-890.
465. Tobolsky, A.V., *Stress relaxation studies of the viscoelastic properties of polymers.* Journal of Applied Physics, 1956. **27**(7): p. 673-685.
466. Araga, R., S. Kali, and C.S. Sharma, *Low temperature catalyst-assisted pyrolysis of polymer precursors to carbon.* Bulletin of Materials Science, 2017. **40**(7): p. 1519-1527.
467. Rajabpour, S., et al., *Low-temperature carbonization of polyacrylonitrile/graphene carbon fibers: A combined ReaxFF molecular dynamics and experimental study.* Carbon, 2021. **174**: p. 345-356.
468. Prilutsky, S., E. Zussman, and Y. Cohen, *Carbonization of electrospun poly (acrylonitrile) nanofibers containing multiwalled carbon nanotubes observed by transmission electron microscope with in situ heating.* Journal of Polymer Science Part B: Polymer Physics, 2010. **48**(20): p. 2121-2128.
469. Smit, E., U. Bűttner, and R.D. Sanderson, *Continuous yarns from electrospun fibers.* Polymer, 2005. **46**(8): p. 2419-2423.
470. Shang, S., et al., *The effect of electrospun fibre alignment on the behaviour of rat periodontal ligament cells.* Eur Cell Mater, 2010. **19**: p. 180-92.
471. Bajaj, B., et al., *Coiled Fibers of Poly (Amide-Co-Imide) PAI and Poly (Trimellitic Anhydride Chloride-Co-4, 4'-Methylene Dianiline)(PTACM) by Using Mechano-Electrospinning.* Journal of Engineered Fibers and Fabrics, 2012. **7**(2_suppl): p. 155892501200702S06.

472. Teo, W.-E., et al., *A dynamic liquid support system for continuous electrospun yarn fabrication.* Polymer, 2007. **48**(12): p. 3400-3405.
473. Liao, C.-C., C.-C. Wang, and C.-Y. Chen, *Stretching-induced crystallinity and orientation of polylactic acid nanofibers with improved mechanical properties using an electrically charged rotating viscoelastic jet.* Polymer, 2011. **52**(19): p. 4303-4318.
474. Shehata, N., et al., *Static-Aligned Piezoelectric Poly (Vinylidene Fluoride) Electrospun Nanofibers/MWCNT Composite Membrane: Facile Method.* Polymers (Basel), 2018. **10**(9).
475. Teo, W.E. and S. Ramakrishna, *Electrospun fibre bundle made of aligned nanofibres over two fixed points.* Nanotechnology, 2005. **16**(9): p. 1878-1884.
476. Dalton, P.D., D. Klee, and M. Möller, *Electrospinning with dual collection rings.* Polymer, 2005. **46**(3): p. 611-614.
477. Shi, R., Y. Bin, and X. Jian, *Study of the structural orientation and mechanical strength of the electrospun nanofibers from polymers with different chain rigidity and geometry.* Polymer Bulletin, 2017. **75**(3): p. 947-962.
478. Rafique, J., et al., *Electrospinning highly aligned long polymer nanofibers on large scale by using a tip collector.* Applied Physics Letters, 2007. **91**(6): p. 063126.
479. Arras, M.M., et al., *Electrospinning of aligned fibers with adjustable orientation using auxiliary electrodes.* Sci Technol Adv Mater, 2012. **13**(3): p. 035008.
480. Zussman, E., A. Theron, and A. Yarin. *Assembly of electrospun nanofibers into crossbars*. in *Proceedings of the 2nd IEEE Conference on Nanotechnology*. 2002. IEEE.
481. Chen, D., et al., *High performance polyimide composite films prepared by homogeneity reinforcement of electrospun nanofibers.* Composites Science and Technology, 2011. **71**(13): p. 1556-1562.
482. Lei, T., et al., *Alignment of electrospun fibers using the whipping instability.* Materials Letters, 2017. **193**: p. 248-250.
483. Dabirian, F. and S. Hosseini, *Novel method for nanofibre yarn production using two differently charged nozzles.* Fibres Text. East. Eur, 2009. **17**(3): p. 45-47.
484. Laudenslager, M.J. and W.M. Sigmund, *A continuous process to align electrospun nanofibers into parallel and crossed arrays.* Journal of Nanoparticle Research, 2013. **15**(4).
485. Zheng, J., et al., *Electrospun Aligned Fibrous Arrays and Twisted Ropes: Fabrication, Mechanical and Electrical Properties, and Application in Strain Sensors.* Nanoscale Res Lett, 2015. **10**(1): p. 475.
486. Seo, D.K., et al., *Preparation and characterization of the carbon nanofiber mat produced from electrospun PAN/lignin precursors by electron beam irradiation.* Rev. Adv. Mater. Sci, 2011. **28**(1): p. 31-34.
487. Lin, Y., et al., *Mechanical properties of polymer nanofibers revealed by interaction with streams of air.* Polymer, 2012. **53**(3): p. 782-790.
488. Lu, P. and Y.L. Hsieh, *Multiwalled carbon nanotube (MWCNT) reinforced cellulose fibers by electrospinning.* ACS Appl Mater Interfaces, 2010. **2**(8): p. 2413-20.
489. McCullen, S.D., et al., *Morphological, electrical, and mechanical characterization of electrospun nanofiber mats containing multiwalled carbon nanotubes.* Macromolecules, 2007. **40**(4): p. 997-1003.
490. Kwon, I.K., S. Kidoaki, and T. Matsuda, *Electrospun nano- to microfiber fabrics made of biodegradable copolyesters: structural characteristics, mechanical properties and cell adhesion potential.* Biomaterials, 2005. **26**(18): p. 3929-39.
491. Li, Y.-P., et al., *PEGylated PLGA nanoparticles as protein carriers: synthesis, preparation and biodistribution in rats.* Journal of controlled release, 2001. **71**(2): p. 203-211.
492. Asvar, Z., et al., *Evaluation of electrospinning parameters on the tensile strength and suture retention strength of polycaprolactone nanofibrous scaffolds through surface response methodology.* J Mech Behav Biomed Mater, 2017. **75**: p. 369-378.

493. Yao, J., et al., *High-performance electrospun co-polyimide nanofibers.* Polymer, 2015. **76**: p. 105-112.
494. Maccaferri, E., et al., *How Nanofibers Carry the Load: Toward a Universal and Reliable Approach for Tensile Testing of Polymeric Nanofibrous Membranes.* Macromolecular Materials and Engineering, 2021. **306**(7).
495. Lee, K.H., et al., *Influence of a mixing solvent with tetrahydrofuran andN,N-dimethylformamide on electrospun poly(vinyl chloride) nonwoven mats.* Journal of Polymer Science Part B: Polymer Physics, 2002. **40**(19): p. 2259-2268.
496. Mannarino, M.M. and G.C. Rutledge, *Mechanical and tribological properties of electrospun PA 6(3)T fiber mats.* Polymer, 2012. **53**(14): p. 3017-3025.
497. Veleirinho, B., M.F. Rei, and J.A. Lopes-Da-Silva, *Solvent and concentration effects on the properties of electrospun poly(ethylene terephthalate) nanofiber mats.* Journal of Polymer Science Part B: Polymer Physics, 2008. **46**(5): p. 460-471.
498. Jiang, S., et al., *Temperature-induced molecular orientation and mechanical properties of single electrospun polyimide nanofiber.* Materials Letters, 2018. **216**: p. 81-83.
499. Patlolla, A., G. Collins, and T.L. Arinzeh, *Solvent-dependent properties of electrospun fibrous composites for bone tissue regeneration.* Acta Biomater, 2010. **6**(1): p. 90-101.

APPENDIX A

Table A Summary of the main techniques that have been reported in the literature for producing aligned fibres during electro-spinning.

Set-up	Material	Solvent	Feed rate (ml/hour)	Potential (kV)	WD (cm)	Collector Parameter	SEM	Reference
Mechanical Based Fibre Alignment								
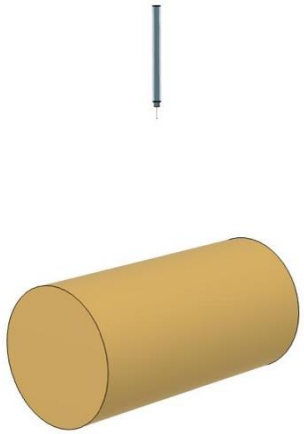	Collagen	HFP	0–25	15–30	10–15	Rotating speed: 500–2500 rpm	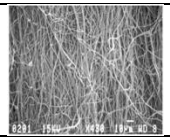	[63]
	10 w/v% PS	DMF	6–78	10–30	10	Rotating speed: 500–2500 rpm	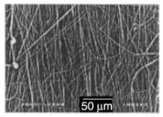	[132]
	15 wt% PAN	DMF	N/A	8–16	13 and 16	Rotating speed: 3.5–12.3 m/s	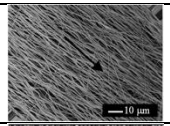	[166]
	5 wt% PLLA	TFE	0.1–0.7	5–15	15	Rotating speed: 100–800 rpm	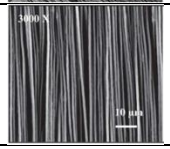	[19]
	3 wt % PEO	Chloroform	0.3	15	12	Rotating speed: 8 m/s	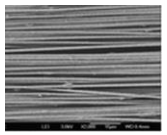	[14]
	12–21 wt% PVDF	DMF/acetone	1	25–30	20	Rotating speed: 16 m/s	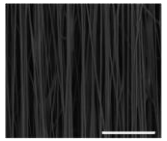	[169]

	7.27 g/L PLA	Dioxane	0.1–0.5	11	30–70	Rotating speed: 400–1000 rpm	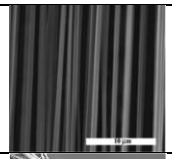	[170]
	15–20 wt% PVDF	DMAc	1	20	20	Take-up speed: 0.05 m/s		[469]
	18 wt % PVA	DMF		15			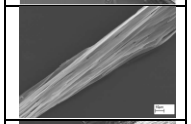	
	5 wt% PAN	DMF		15			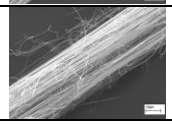	
	20 wt% PLGA	DMF/acetone	3	21	20	Take-up speed: 50–700 mm/minute	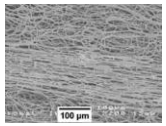	[470]
	26–30 wt% PAI/PTACM	DMSO/THF	6000–9000	8–15	N/A	Take up speed: 1000–1500 rpm	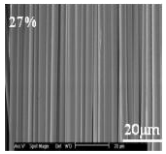	[471]
	0.08–0.1 g/ml PVDF	DMAc/acetone	1–15	12	10–20	Vortex hole diameter: 5 mm Take up speed: N/A	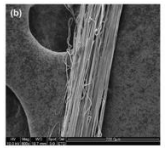	[472]
	8 wt% PLA	chloroform	0	0	N/A	Spinneret Rotating	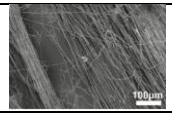	[181]

	5 wt% PEO	Distilled water				speed: 4000–12000 rpm		
	8 wt% PAA	Distilled water					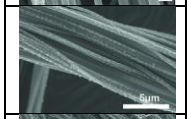	
	14 wt% gelatin	Acetic acid					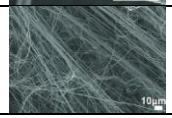	
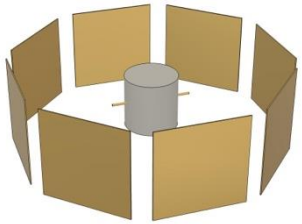	5–6 wt% PLA	chloroform/ DMF	0.25	5–30	34	Spinneret Rotating speed: 1800 rpm	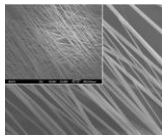	[473]
	20–27.5 wt% PVDF	DMF/acetone	N/A	12–15	25–50	Spinneret Rotating speed: 100–400 rpm	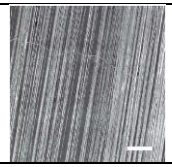	[182]
	17 wt% PAN	DMF	N/A	40	13–17	Spinneret Rotating speed: 1900 rpm	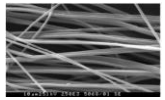	[183]
	PS	THF	N/A	3	2.5	Spinneret Rotating speed: 420 rpm	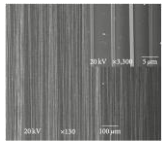	[180]
Electro–spinning Under a Controlled Electric Field								
	0.41 g/ml PVP	Ethanol	0.2	5	7.6	Gap width: 1 cm	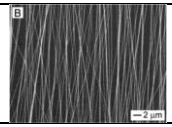	[149, 150]

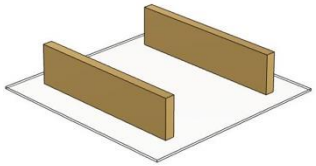	4.5 wt% PEO	Distilled water	N/A	12	40	Gap width: 3–18 cm	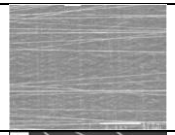	[184]
	50 v/v% PEG:PEO		1.5	10	35	Gap width: 2 mm		[187]
	9 wt% PVA	Distilled water	N/A	15	10	Gap width: 5–6 cm		[186]
	16 w/v% PVA	Distilled water	N/A	20–25	1.6	Gap width: 1–45 mm	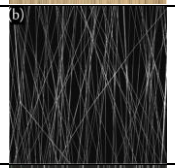	[204]
	11–19 wt% PVA	Distilled water	N/A	5–15	9	Gap width 5–20 mm	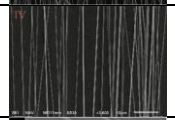	[185]
	15 wt% PVDF	DMF	1.5	25	10	Gap width: 2 cm	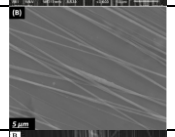	[474]
	0.12 g/ml PCL	Chloroform/ methanol	1	15	5–15		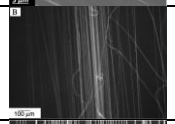	[475]
	12 wt% PVDF	DMF/aceton e	0.3	5.5–16	10–30	Gap width: 1–60 cm	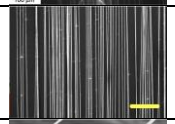	[188]
	9 wt% PCL	Chloroform: Methanol	0.1	15	N/A	Ring gap width: 4–10 cm	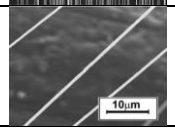	[476]

	20 wt% PCL	DMF/MC	0.6	14	1.6	Use of inclined gap configuration		[190]
	15 wt% PPEK	NMP	2, 6, 10, 20	8–18	30	60° inclined gap electrode	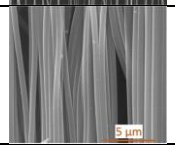	[477]
	20 wt% PVDF	DMF	0.6	–14	0.5	45° inclined gap with serrated-edge collector	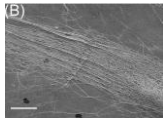	[191]
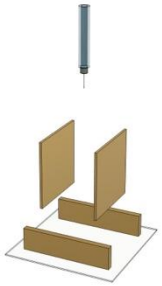	8 wt% PLLA	Chloroform	5	15–25	N/A	Gap width: 1–3 cm Auxiliary electrodes had 6–15kV potential	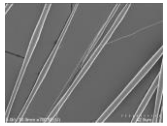	[18]
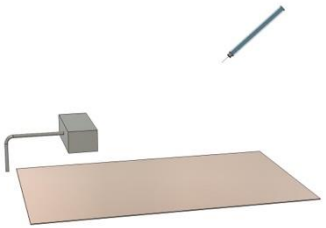	7–15 w/v% PAN	DMF	N/A	N/A	N/A	68 cm long metal sheet	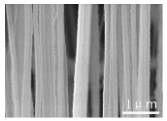	[478]

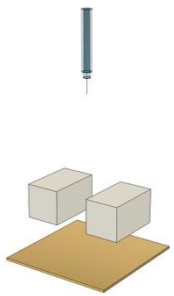	2.5 wt% PEO	DIistilled water/ethanol	0.12–0.3	4–7	10	Moveable flat plate collector	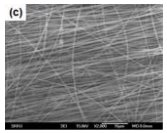	[206]
Hybrid Alignment Methods								
	10 wt% PEO	Distilled water	N/A	5–15	20	Flat plate collector	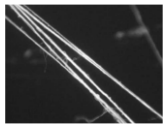	[152]
	15 wt% PVP	ethanol	0.48	15	N/A	Rotatingal flat plate collector. Take-up speed: 0.5–2 mm/s	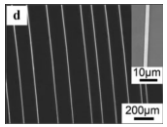	[195]

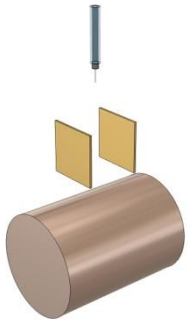	5 wt% PU	2-propanol	0.6	–15	12	Take-up speed 0.9 m/s	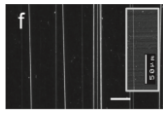	[479]
	6 wt% PEO	Distilled water/ethanol	0.025	9	10.5	Take-up speed: 1100–4000 rpm with 3, 5 and 7 cm drum diameter.	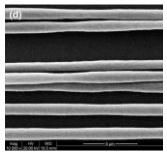	[193]
	4 wt% PLLA	Chloroform/ DMF	0.6	7–25	5–30	Rotating diec. Take-up speed 8 m/s.	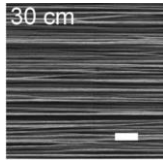	[175]
	4 wt% PEO	Distilled water/ethanol	N/A	8.5	15	Take-up speed 22 m/s.	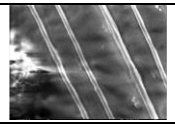	[151, 480]

	10 wt% PAN	DMF	1.5	22	22	Take-up speed 24 m/s.		[312]
	25 wt% poly(amic acid) (PAA)	DMAc	0.25	18–25	20	Take-up speed 20 m/s.	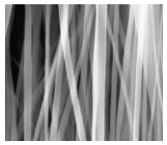	[481]
	15, 20, 25 wt% PS	Tetrahydrofuran	N/A	5	15–30	Take-up speed 2.5–4.2 m/s.	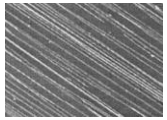	[198]
	15, 20, 25 wt% PMMA	Chloroform						
	15 wt% PS	THF/DMF	0.2	5–14	4–5	Circular disc collector. Take-up speed 9.4–23.4 m/s.	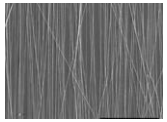	[199]
	10 wt% PCL	Chloroform/ methanol	1.2–1.5	20	7	4 mm diameter teflon tube. Take-up speed: 838 rpm	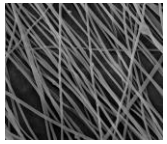	[201]

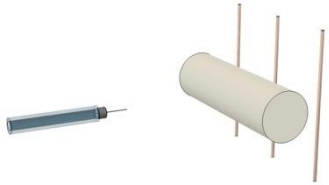	8 w/v% PCL	Dichloromethane/methanol	2.5	23	15	Take-up speed: 0.5–4 m/s	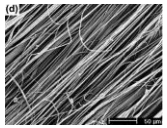	[202]
	12 wt% PVDF	DMF/acetone	0.18	10	5–20	2–50 cm cylinder diameter with 2–10 cm gap width.	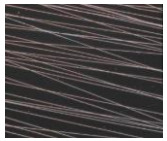	[482]
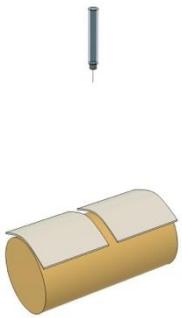	30 wt% PVDF	DMF	N/A	.10	10	10 cm diameter mandrel. Take-up speed: 1500–3500 rpm	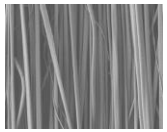	[200]
	10, 13wt% PVA	Distilled water	0.03	3.3, 4.5	14	Take-up speed: 3–14.9 m/s		[7]
	1,8,10,12 wt% PVP	Ethanol	0.96, 0.84	3.8, 4				

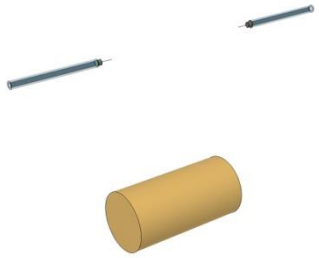	13-15 wt% PAN	DMF	0.293	10.5, 11	20	Needle distance: 13 cm. Take-up speed: 0.375–1.123 m/s		[283]
	13.5 wt% PAN	DMF	N/A	8	5	Needle distance: 13 cm. Take-up speed: 0.002 m/s	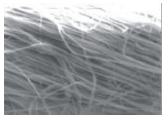	[483]
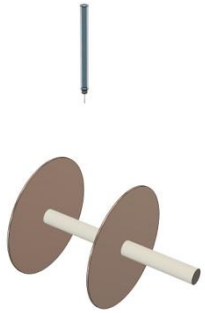	0.1 g/ml PVP	Ethanol	0.5	–10	10	Gap width: 1.5 cm. Rotating speed: 0.075 m/s.	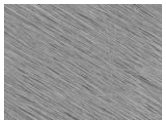	[484]
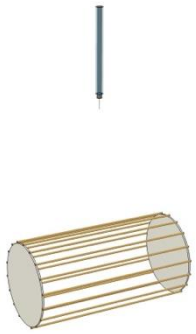	20 wt% Nylon-6	Formic acid	0.002	20	N/A	12.7 cm diameter mandrel. Take-up speed: 1 rpm.	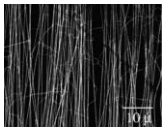	[178]

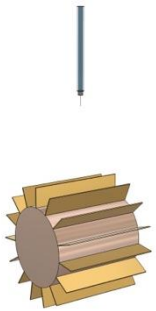	8 wt% PLLA	DCM	0.06	10	20	14 cm diameter mandrel. 3 cm fin gap. Take-up speed: 7.3 m/s.		[22]
	20 wt% PS	THF	3	20	8	18×16 cm frame collector. Take-up speed: 600 rpm	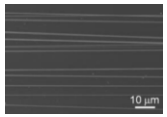	[485]
	20 wt% PVDF	DMF/acetone						
Other Electro-spinning Methods								
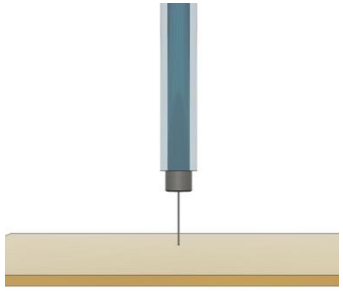	5 wt% PEO	Distilled water	N/A	1	0.1	Collector moving speed: 5–15 cm/s	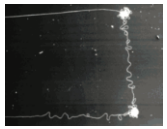	[216]
	7 wt% PEO	Distilled water	1E–4	1.5	500 µm	Collector moving speed: 120 mm/s		[218]
	4 wt% PEO/	Distilled water	N/A	1	0.1 mm	Collector moving speed: 0.47–5 cm/s	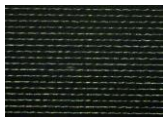	[217]
	15–20 wt% PA-6	formic acid		2	0.5 mm			

	10–14 wt% PAN	DMF						
	1–3 wt% PEO/DI water		0.001	0.2–0.6	1 mm	Collector moving speed: 120–1500 mm/s	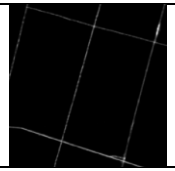	[214]
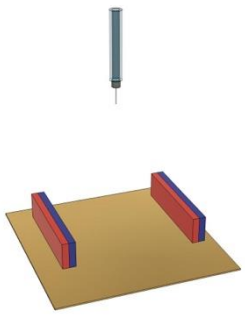	8 wt% PVA+0.22 wt% Fe3O4	Distilled water	N/A	10–18	10	Magnets dimension: 6.5 cm heigh		[20]
	22–28 (w/v)% PLGA	HFIP	0.5–3	15	14	Magents dimension: 2.5×2.5×15 cm. Gap width: 0.5–4 cm	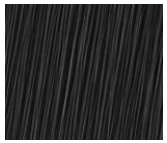	[23]
	11 (w/v)% PVP	Ethyl alcohol/distilled water						
	10 wt% PVP+Fe3O4	Ethanol	2	15	20	Magnets gap width: 2 cm	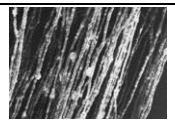	[207]

APPENDIX B

Table B A compiled list of the literature on tensile test of nano-fibres.

Materials/Solvent	Spinning Condition	Techniques	Testing Condition	Sample Preparation	Data Analysis	Sample Type	Tensile Strength	Tensile Modulus	Failure Strain %	Refs
12 wt% PAN/(DMF)-CNF	0.8 ml/h; WD 20 cm; 16 kV; 23°C; 0.5–5.6 m/s take-up speed.	Custom MEMS device		Use a W prob to separate single fibre; Pt end-tabs deposited by FIB; 8 repeats.	Diameter measured using TEM;	Single	5.4 GPa	287 GPa	2.4	[37]
10 wt% PAN-CNF/0.12 wt% DWNT/(DMF)	20-G needle; 12 kV; 0.6 ml/h; WD 20 cm	In suit TEM MEMS device		Gauge length 2.5 um; End-tab electron beam pt deposition;	Diameter measured using TEM;	Single	7.3 GPa	262 GPa		[28]
4–10 wt% PAN/(DMF)	22-G needle; 0.5 ml/h; WD 14 cm; 16 kV; 5 h dried in air; 300 fibre per yarn	Universal tensile tester	Cross-head 35 mm/minute; 10 N load-cell	Gauge length 100 mm; Epoxy glue end-tab;	Fibre diameter measured using SEM; Force and strain graph plotted	Bundle				[224]
10 wt% PAN/0.05 wt% BTEAC(organic salt)/(DMF)	9 kV; WD 15 cm; 10 ul/minute;	Universal tensile tester	Cross-head 15 mm/minute; room temp;	Draw in 95 °C water with 100 mm/minute; annealed at 130 °C in oven for 1 h; 30 mm gauge length	Fibre diameter measured using SEM; stress and modulus were calculated using equation provided;	Bundle	45 MPa	0.8 GPa		[35]
						Random mat	14 MPa	0.03 GPa	13	
10–15 wt% PAN/ (DMF)	0.7 mm diameter needle; WD	Universal tensile tester	Cross-head 30	70 °C dried for 2 h; post-treat 94 °C 10 minutes	fibre diameter measured using SEM;	Bundle	99 MPa	2.79 GPa	18.37	[36]

	15–20 cm; 9–11 kV;		mm/minute;	then dried at 110 °C; bundle linear density 60 den; 30 mm gauge length						
PAN/DMF	12.5 kV; WD 20 cm; 0.25 ml/h	AFM-Microcantilever	Fibre placed between 2 AFM-cantilever beam by adhesion and wrapping.		Use the change of vibration frequency to calculate the stiffness and youngs modulus. Equation provided	Single		26.8 GPa		[241]
11 wt% PAN/(DMF)	0.5 mm needle; WD 17 cm; 10 kV;	Universal tensile tester Instron 1185		Hot stretched in oven at 135 °C for 5 minutes under 75 g load; 5 mm x 20 mm specimen;	Diameter measured from cross section of fibre using SEM; cross sectional area was calculated from weights and density of PAN;	Aligned mat	45 MPa	425 MPa	20	[229]
						Stretched Aligned mat	170 MPa	2243 MPa	9.5	
10 wt% PAN/(DMF)	0.394 mm diameter; 15 kV; 1 ml/h; WD 20 cm; working temp 30 °C;	Universal tensile tester Instron 3369 with 100 N load-cell	Cross-head 1,5,10 mm/minute; 1 cm^2 gripping area	Gauge length 20,30,40 mm; adhesive cushion tape as end-tabs;	Thickness measure using image analysis; porosity measured use equation provided; fibre diameter measured using SEM;	Random mat		0.02 MPa		[38]
18 wt% PAN/(DMF)	21-G needle; 1.5 ml/h; 10–40 % humidity;	Shimazdu EZ-SX tensile tester with a 2 N load-cell	Cross-head speed 3 mm/minute;	1x1 cm aligned fibre sheet;	Fibre diameter measured using SEM; cross sectional area are calculated from	Aligned mat	354 MPa	16.5 GPa	18	[84]

	45°C; 15 kV; WD 15 cm				individual fibre times the average number of fibres; Youngs modulus of 0.01 strain; toughness calculated as the area of the s-s curve;					
10 wt% PAN/(DMF)	9–14 kV; 0.004 ml/minute; WD 14 cm; 18-G needle; flat and rotating drum with 9.8 m/s take-up speed;	Universal tensile tester Instron 5564	Cross-head 2 mm/minute; room temp;	gauge length 20 mm; Manila paper tabs;	SEM measured fibre diameter; cross-sectional area determined from measured density 1.1 g/ml;	Aligned mat	78 MPa	4.3 GPa	25.4	[39]
10 % PAN/0.1 %MWCNT/(DMF)							109 MPa	1.8 GPa	44.5	
10 wt% PAN/MWCNT/(DMF)	0.4 ml/h; room temp; 28 kV; WD 20cm; 70 °C dried for 24 h;	Tensimeter tensile tester	ASTM D3039; 5 mm/minute cross-head speed;	Specimen dimention 20 mm*60 mm; 5 repeats;	SEM measured fibre diameter; The Young's modulus of the samples is derived from the slope of the initial linear part of the stress–strain curves.	Random mat	122 MPa	400 MPa		[220]
10 wt% PAN/(0.05–0.3 wt%)MWCNT/(DMF)	0.5 ml/h; 25 kV; dried	Agilent T150 universal testing machine	ASTM 3039; Cross-head 5 mm/minute;	Sample dimension 6 cm x 2 cm; gauge length 3 cm; 3 times repeat	SEM measured fibre diameter	Random mat	130 MPa	1.2–4.7 GPa		[357]

8% PAN-CNF/(DMF)	Electric field strength 0.9 kV/cm; 5 cm/s take-up speed;	AFM cantilever		Single fibre bonded to W tip using Hysol glue.	SEM measured fibre diameter	Single	0.64 GPa			[242]
Various PAN/Lignin combination-CNF/(DMF)	0.36 mm needle; 0.2 ml/minute feed rate; 15 kV; WD 100 mm	Universal tensile tester Instron 5569	ASTM D638; 5 mm/minute cross-head speed;			Random mat	810 MPa			[486]
12 wt% PAN/1%PVP/(DMF)	22-G needle; 0.25 ml/h; 16 kV; 100 rpm; WD 18 cm; 22 °C; 30–35% RH;	Universal tensile tester Instron 5566 with	Cross-head rate 10 mm/minute; 10N load-cell	Specimen dimension 1 cm * 3 cm;	SEM measured fibre diameter; The strength calculated from the equation provided; The modulus and elongation at break were obtained from the stress-strain curves.	Random mat	3.93 MPa	61.39 GPa	43.7	[226]
12 wt% PAN/1%PVP/0.5–2 wt% SWCNT/(DMF)							10.74 MPa	605.39 GPa	16.78	
9 wt% PAN-CNF/ (DMF)	15–25 kV; WD 15–25 cm;	MEMS				Single	3.52 GPa	172 GPa		[248]
8–11 wt% PAN/(DMF)	20-G needle; 10–12 kV; WD 20 cm; Annealing 130 °C 1 h;	NANO UTM testing system	Strain rate 0.001 /s	Gauge length 5-10 mm; Epoxy adhesive end-tab;	SEM measured fibre diameter; True stress and strain plotted diagram. Modulus, toughness was computed using engineering stress-strain.	Single	1750 MPa	48 GPa		[239]
10 wt% PAN/(DMF)	WD 18 cm; 28 kV; 1 ml/h; 70 rpm; 0–60% RH; 21–22 °C;	Micro force testing system		Specimen dimension 40 mm*6.5 mm;	SEM measured fibre diameter	Random mat	6.25 MPa	95 MPa		[147]

9% PAN/(DMF)	22-G needle; 1700–3100 rpm; 21 kV; WD 20 cm; 1 ml/h feed rate	Universal tensile tester	ASTM D882-12;	Gauge length 25 mm; mass used instead of thickness; specific strength, tensile strength and porosity were calculated with equation given.	SEM measured fibre diameter	Random mat	24.8 × 10^3 N kg−1 m			[457]
PAN/(DMF)	CO-axial with 0.61 mm ID core and 1.36 mm ID shell; core 0.07 mL/h, shell 0.9 mm/h; 12–13 kV; WD 10 cm; 200 rpm	Universal tensile tester	1 mm/minute cross-head speed;	20 mm gauge length;	SEM measured fibre diameter;	Random mat	2.5 MPa	46.45 MPa	32.5	[458]
2 wt% Collagen/PEO /(HCl)	22-G needle;	Minimat 2000	2 mm/minute cross-head speed; 20N load-cell;	8 mm gauge length; 5 mm wide	Sample thickness determined by profilometer;	Random mat	370 kPa	12 MPa		[147]
16.6 wt% PVP/(DMF)	20-G needle; 1 mL/h; WD 20 cm; 18 kV;	TA AR2000 rheometer with solid fixture	10 µm/s cross-head speed;	10 mm gauge length; Specimen dimension 15*5*0.2 mm;		Random mat	2.3 MPa		9.1	[385]
6 wt% PEO/(DI water)	0.04 ml/h; 12 kV; 160 mm parallel electrodes;	Custom AFM cantilever	The incremental force applied as the fibre is	The gauge length of the fibre is calculated from the initial and	SEM measured fibre diameter; cross-sectional area calculated from diameter;	Single		45 MPa		[31]

			stretched is calculated by the incremental change in resistance divided by the coefficient of resistance change per unit force applied	final stage positions; fibre attached to cantilever using super glue;						
25 wt% Nylon 6/(formic acid)	Room temp; 45% RH; 14 kV; WD 5–20 cm; parallel rods collector with 0.5–7 cm separation;	Custom build air-stream-assisted set-up	The air velocity ranged from 0.16 to 7.20 m/s;	Use double sided tapes to fix the fibre on the rods;	Camcorder recorded imaged of fibre movement at 30 fps; SEM measured fibre diameter; equation provided to convert the result into stress strain and modulus;	Single	230 MPa	4–5 GPa	10–23	[487]
6 wt% PEO/(DI water)						Single	22 MPa	60–70 MPa	100–150	
18 wt% PVP/(ethanol)						Single	7 MPa	500 MPa	14–15	
12 wt% Nylon-6/(Formic acid)	24-G needle; 0.1 ml/h; WD 14 cm; 29 kV;	Instron 5566	100 N load-cell; 65% RH; 23 °C; 5 mm/minute cross-head speed;	50 mm * 10 mm *0.03 mm; 3 to 6 repeats;	SEM measured fibre diameter;	Random mat	6.8 MPa	43.8 MPa	25.7	[227]
		AFM-based 3-point bending test				Single		30GPa		
		Custom build tensile tester	a typical micro	20 mm gauge length; 12	SEM measured fibre diameter;	Random mat	10.45 MPa	19.4 MPa		[351]

20 wt% Nylon 6/(formic acid)	0.2 mL/h; 15 kV; WD 8 cm; 2 min;		spring with stiffness constant of 3.75 mg (wt)/mm ‘‘0.03823 N/m’’ and wire diameter of 100 um to measure the force applied; 7.2 mm/minute cross-head speed;	repeats; double-sided tapes as end-tab; single fibre picked up using cardboard frame;		Single	304 MPa	901.65 MPa	40	
10–14 wt% PCL/(dichloromethane/DMF)	23 °C; 74 %RH; 0.6 ml/h; 10 kV;	Nano tensile testing system	1%/strain rate; room temp	10 mm gauge length	SEM measured fibre diameter	Single	40 MPa	120 MPa		[31]
PCL/(aceton/DMF/chloroform)		Nano tensile tester	50nN load resolution; extension resolution 35 nm; 10 %/s loading rate;	Double sided tape end-tab; Trimmed paper frame;	SEM micrograph to calculate the fibre area density is quantified by counting the number of fibres.	Single	55 MPa	280 MPa		[234]
		Instron 5582	10 mm/minute cross-head speed	3.10x55.12x0.008 mm		Compression moulded random mat	58 MPa	307 MPa		

12 wt% PHBV/(Chloroform and 1,2-dichloroethane 2:3)	22-ga needle; WD 15 cm; 0.5 ml/h; 470–940 m/minute	Nano tensile tester	50 nN load resolution; within 500 mN load range; 1% /minute strain rate;	10 mm gauge length; 5 repeats;	SEM measured fibre diameter	Single	268.01 MPa	2.67 GPa		[233]
7.5 & 12.5 wt% PLLA/(DCM)	0.2 ID needle; 0.5 ml/h; 10-15 kV; 63 & 630 m/minute; annealed at 80 °C for 10 h;	Nano tensile tester	500 mN load range; 50 nN load resolution; 25 %/minute strain rate;	20 mm gauge length; 5 repeats	SEM measured fibre diameter	Single	183 MPa	2.9 GPa	0.45	[231]
1 wt% PLLA/(DCM/DMF7:3)	1 ml/h; 12 kV; 50–70 %RH;	Nano tensile tester	50 nN load resolution; extension resolution of 35nm; 0.1 %/s strain rate;	10 mm gauge length;	SEM measured fibre diameter	Single	204 MPa	4.8 GPa	4.5	[232]
7.5 wt% PCL/(chloroform/methanol 3:1)	0.5 ml/h; 9–10 kV;	Nano tensile tester	0.1 %/s strain rate;	10 mm gauge length;	Optical microscope image analysed diameter; Double sided tape as end-tab;	Single	40 MPa	120 MPa	200	[235]
20 wt% Nylon 6,6/(Formic acid)	0.1 mm ID needle; 5 mL/h; 1.7 kV/cm; 30 kV; 20 °C; 40 %RH; Vacuumed under 10^{-2} Toor for 24 h;	AFM cantilever	4 um/s pull rate;		Fibre ends fixed using Loctite epoxy glue; deflection observed by microscope;	Single	150 MPa	950 MPa	61	[244]

8 wt% (1:1) PLLA/PDLA/(8:2 DCM/DMF)	18 °C; 30–60%; 15 kV; $3x10^{-4}$ ml/s; parallel electrodes with 30 mm distance with 3 V potential difference;	Nano tensile tester	Cross-head 0.6 mm/minute; 500 mN load-cell, 12.5 nN resolution	Double sided tape and adhesive as end-tabs;	Diameter measured using SEM	Single	204 MPa			[29]
22 wt% PCL/(Chloroform)	0.8 ID needle; 16–20 kV; WD 17.5 cm; 24 °C; 40% RH; 26 uL/minute	FemtoTool mechanical testing machine	100 uN load-cell; 60 um/s displacement rate;	The fibres fixed in the holder were placed into the FemtoTool and optical microscope assembly;	Liner extension, stress and strain were calculated from geometry using the equations provided;	Single		300–250 MPa		[221]
PCL		nano tensile tester				Single		100–300 MPa		[236]
10 w:v% PCL/(HFP)	20 ga needle; 20 kV; WD 15 cm; 0.8 ml/h	AFM	stretch the fibres at a rate of 300 nm/s;		Lateral force, stress and strain measured and calculated using the equation provided; Diameter measured using SEM;	Single		10–310 MPa	98	[32]
10–30 wt% Nylon 6/formic acid	22-G needle; 10–30 kV; WD 5–10 cm	Dynamic mechanical analyser (DMA)	1 mm gauge length	Adhesive tapes ad end-tabs;	SEM micrograph measured diameter and number of fibres counted over time.	Aligned mat	345 MPa	5.47 GPa	73	[256]
16 wt% PA-6/ formic acid	0.2 m/s take-up speed; WD 120 mm; 0.3 ml/h; 35 °C; 40–50% RH;	universal tensile tester with 20 N load-cell with	2 mm/minute cross-head speed;	Specimen dimension 6 mm * 20 mm; paper frame with 10 mm gap; tape	The cross section of each sample was estimated by measuring the area and weight of the	Aligned mat	34.9 MPa			[225]
						Single fibre	85.5 MPa			

		0.001 N resolution;		adhesive end-tab; gauge length 10 mm; 80 repeats;	sample and by the known density of the bulk material.					
15 wt% Cellulose acetate/(DMAc)	23-G needle; 1 mL/h; 14.25 kV; 27 °C; 34% RH; WD 25 cm;	Universal tensile tester Instron 5566	5 mm/minute cross-head speed; 21 °C; 65% RH;	10 mm gauge length; Specimen dimension 5*20 mm; 10 repeats;	The thickness were measured by thickness tester; weight measured by balance with 0.01 mg accuracy;	Random mat	21.9 MPa	553 MPa	8.04	[488]
15 wt% Cellulose acetate/0.11–0.55 wt% MWCNT/(DMAc)							40.7 MPa	1144MPa	10.46	
4 wt% PEO/(DI water)	5–55 uL/minute; 10–20kV; 1kV/cm electric field; 20-G needle;	Universal tensile tester Instron 5544	ASTM standard D4762-04; 25.4 cm/minute cross-head speed;	2 cm wide; 2.54 cm gauge length; 7 repeats;	The volume of voids in the random fibrous mats was calculated using Image-J analyser of SEM micrograph;	Random mat	9.96 MPa	12.28MPa		[489]
4 wt% PEO/0-3 wt% MWCNTs/(DI water)							5.04 MPa	23.56MPa		
6 wt% PEO/3 wt% MWNT/(GA) Annealed	20-G needle; 12–14 kV; WD 19.5 cm; 7 ml/minute; 5 h spinning time; anneal in oven at 60 °C;	Universal tensile tester Instron 5544	Cross-head speed 10 mm/minute	1.5 cm gauge length; Specimen dimension 1 * 1.5 cm * 0.3 mm measured by calliper and thickness gauge; cross sectional area calculated using the equation provided with porosity considered.	Diameter measured using SEM;	Random mat	17 MPa	250 MPa		[284]

9 wt% PVA/(DI water)	0.1–5 ml/h; 0.2 mm ID needle; WD 10–15 cm; 10–20 kV;	Universal tensile tester.	250 N load-cell; room temp; cross-head speed 50 mm/minute;	30 mm gauge length; specimen dimension 2 cm * 5 cm * 100–150 um;		Random mat	5.8 MPa	175 MPa	100	[228]
9 wt% PVA/1-7.5% MWCNT/(DI water)							9.4 MPa	180 MPa	145	
7% PVA/0–15% CNs/(DI water)	22-G needles; WD 15 cm;	DMA tensile mode	DMA measurements used a constant frequency of 1 Hz, strain amplitude of 0.03%, and a temperature range of –100 to 250 °C (heating rate of 3 °C/minute).	6 mm wide strip; 10 mm gauge length;		Random mat	1.0 MPa	2.0 MPa	0.33	[255]
3 wt% PLCL/(HFIP)	5 or 10 ml/h; 15 or 30 kV; WD 20 cm;	Universal tensile tester	Cross-head speed 0.5 mm/s	Sample dimension 5*20*0.14mm	Porosity measured by mercury porosimeter	Random mat		2.2 MPa		[490]
8 wt% Co-PI/DMAc	38 uScm conductivity; 100 kV/m electric field strength; 15 kV; WD 15 cm; 24 m/s	Dynamic mechanical analysis (DMA)	3 °C/minute; 1 Hz and 20 um;		The densities of the co-PI nanofibres were determined by the weight and volume; Thickness calculated from	Aligned belt	983 MPa	6.3 GPa	22.2	[230]

	take-up speed;				weight and density;					
5 w:v% PLGA/(THF/DMF)	18-G needle; 18 kV; WD 20 cm;	Kawabata Evaluation System	1*1 cm grip; 4 cm gauge length; 0.05 cm/s deforming speed;	Sample dimension 1*10*60 mm;	Porosity measured by mercury porosimeter;	Random mat	323 MPa	23 MPa	96	[491]
10–20% PCL/(chloroform/methanol)	21-G needle; 2–5 ml/h;15–25 kV; WD 12–16 cm; 500 rpm	universal tensile testing machine	10 mm/minute cross-head speed; 20 °C; 500 N load-cell	Sample dimension 3*1 cm;	Thickness measured by digital micrometre; pour size measure by SEM	Random mat	2.2 MPa			[492]
4.5 wt% BPDA/ODA/PDA/(DMF)	0.5 ml/h; 25 kV; 2200 rpm; dried at 70 °C for 3 h;	Instron 5566 universal testing machine	100 N load-cell;	Sample dimension 4*50 mm;	Thickness determined using equations; Density measured using gas pycnometer;	Aligned mat	1040 MPa	10 GPa	13.5	[493]
9–18 wt% Nylon 66/(TFA/formic acid/chloroform 1:6:3 v%)	0.84 mm ID needle; take-up speed 0.39 m/s;	universal testing machine	10 N load-cell; 10 mm/minute cross-head speed;	10 mm width; Gauge length 30&45 mm;	Thickness measured by 6 different instruments: SEM, an analog centesimal indicator, a digital millesimal indicator, an analog millesimal indicator with two different pressure configurations, a	Random mat	36	1071MPa	13	[494]

					micrometer, a digital caliper.					
10–15 wt% PVC/(THF/DMF)	8–15 kV; WD 6–15 cm	universal testing machine	10 mm/minute cross-head speed; room temp; ASTM D638	Doumbell shape;		Random mat	1.75 MPa		220	[495]
PA6(3)T/(DMF)	WD 25 cm; 22 kV; 1 mm ID needle; 0.01 ml/minute;	universal testing machine	2.5 kN load-cell; 0.5 mm/s cross-head speed;	50 mm gauge length; 5 repeats	Thickness measured by digital micrometer; porosity calculated from volume and mass of specimen using the bulk density of material;	Random mat	9.5 MPa	480 MPa	<10	[496]
BPDA/PPA/(DMAc)	50 kV; WD 25 cm; 2.5 ml/h;	micro tensile testing machine	19.6 mN load-cell; 1 mm/minute cross-head speed;	adhesives used as end-tabs; single fibre mounted on paper frame;	Diameter measured using SEM;	Single	1708 MPa	76 GPa	2.8	[230]
8–12 wt% PCL/(DCM/MtOH)	0.8–1.2 ml/h; 6–9 kV; 31–43% RH 20–25 °C;	ASTM D3822-01;	0.001 /s strain rate;	20 mm gauge length;	Diameter measured using SEM;	Single	190 MPa	3200MPa	0.7	[165]
6 wt% PCLEEP/(DCM/MtOH)	0.3 ml/h; 6 kV; 31–72% RH 20–25 °C;						50 MPa	140 MPa	0.6	
15 wt% PCL(THF/DMF 1:1)	21-G needle; 1 ml/h; 12 kV; WD 18 cm;	Universal tensile tester	5 mm/minute cross-head	10 mm gauge length; specimen	Thickness was measured with a Kafer Mechanical Thickness Gauge;	Random mat	4000 kPa	3.8 MPa	170	[30]

			speed; 21 °C;	dimension 3*0.5 cm	porosity determined by mercury porsimetry.					
10–30 wt% PET/(TFA/CDM)	1.07 mm ID needle; 26 kV; 0.2 mL/minute; WD 12 cm; 20 °C; 900 rpm; 24–50% RH; dried at 30 °C for 16 h	Micro tensile tester	0.5 mm/s cross-head speed; 23 °C; 50% RH;	Specimen dimension 90*10 mm; 50 mm gauge length;	Porosity calculated with known weight, bulk density, and volume;	Random mat	3.5 MPa	60 MPa	40	[497]
3.5 wt% SNF-PI/DMF	100 kV/m; 0.3 ml/h	Micro tensile tester	0.094 mm/minute cross-head speed;	4 mm gauge length;	Diameter measured using SEM;	Random mat	2494 MPa	174 GPa	1.43	[498]
PCL/(MC/DMF)	20-G needle; 15 kV; 3 ml/h; WD 40 cm;	Universal tensile tester	50 mm/minute cross-head speed;	30 mm gauge length; 12 mm wide; 5 repeats;	The pore size was determined using capillary flow analysis; porosity calculated using density value with equation given;	Random mat	3.2 MPa	21 MPa		[499]

APPENDIX C

Table C A compiled list of the literature on the carbonisation condition for CNFs and their characterisation methods.

Material/Solution	Stabilisation	Carbonisation	XRD (2θ)	Raman	Reference
9 wt% PAN/(DMF)	300 °C in (air); 5 °C/minute; Hold 1 h	800, 1100, 1400 and 1700 °C in (N_2); 5 °C/minute; Hold 1 h.			[248]
8 wt% PAN/(DMF)	250 °C; 5°C/minute; 30 min; air	1h 750 °C ,1h 1100oC 5 °C/minute (N2)		1100 °C (R=0.93)	[242]
PAN/(DMF)	270 °C 5 °C/minute hold 90min (air)	1h 1000°C 3°C/minute	As-spun: 17°; 28° 1000°C: 24°; 43°	1000 °C (R=3.5)	[305]
6 w:v% PAN/(DMF)		564, 800, 1000 and 1200 °C 0.5h (vacuum 10^{-6} Torr)		564°C (R=2.92) 800°C (R=2.45) 1000°C (R=1.78) 1200°C (R=1.67)	[324]
10 wt% PAN/(DMF)	280 °C for 2 h 2°C/minute	600 °C for 2 h (N2)	25.0° 43.6°	600 °C (R= 1.39)	[448]
10–20 wt% PAN/(DMF)	280 °C for 1 h （Air）	700, 800, 900 and 1000°C for 1h (Ar)	24° 44°	700°C (R=2.73) 800°C (R=2.26) 900°C (R=1.95) 1000°C (R=1.39)	[325]
10 wt% PAN/ (DMF/Acetone/dod	280 °C for 3 h 2°C/minute（Air）	1000°C for 1h 2°C/minute (N2)	As-spun: 16.8°	Graph shown with no R-value reported	[312]

ecylethyldimethylammonium bromide)		1400°C 1800°C 2200°C 2°C/minute (6Pa vacuum)	28.6 ° Carbonised: 25.3 °		
10 wt% PAN/(DMF/Acetone 9:1)	290 °C for 3 h 1°C/minute（Air）	1000°C for 30h 5°C/minute (N2)	25°–26° 44 °		[439]
10wt%PAN/(DMF)	280 °C for 2 h 1 °C/minute（Air）	750–900°C for 0.5 5°C/minute (CO2/Ar)	20°–30° 43°	750°C (R=1.03) 800°C (R=0.97) 900°C (R=0.92)	[449]
2.1–17.4 wt% PAN/(DMF)	230 °C for 2 h 1°C/minute（Air）	1000 °C for 2 h 1°C/minute（N2）	As-spun: 17° Carbonised: 24°		[323]
PAN/(DMF)	210 °C for 1 h （Air）	1000 °C–2800 °C (N2/Ar)	25° sharpens as the heat-treatment time increase	700°C (R=3.81) 1000°C (R=3.41) 1500°C (R=1.51) 2000°C (R=1.31) 2500°C (R=0.93) 2800°C (R=0.29)	[446]